Synthesis, Characterization and Reactivity of Ylidyne and μ-Ylido Complexes Supported by Scorpionato Ligands

Dissertation

Submitted in fulfillment of the degree
doctor rerum naturalium
(Dr. rer. nat)

of
The Faculty of Mathematics and Natural Sciences
of
The Rheinische Friedrich-Wilhelms-University of Bonn

By
MSc. Priyabrata Ghana

Bonn, 2017

Prepared with the consent of the Faculty of Mathematics and Natural Sciences of the Rheinische Friedrich-Wilhelms-Universität Bonn.

Members of the promotion committee:

Prof. Dr. A. C. Filippou (1st reviewer)

Prof. Dr. R. Streubel (2nd reviewer)

Prof. Dr. O. Schiemann (Examiner)

Prof. Dr. U. Deppenmeier (Examiner)

Prof. Dr. Werner Uhl (External examiner)

Date of dissertation defense: 06.07.2017

Year of Publication: 2018

The greatest challenge to any thinker is stating the problem in a way that will allow a solution.

– Bertrand Russell

Acknowlegement

It is a great pleasure to have the chance to thank everyone who have helped and supported me during this exciting journey of my PhD. It has been an amazing adventure of my life.

First of all, I would like to express my gratitude to Prof. Alexander C. Filippou for giving me the opportunity to pursue my PhD in his research group. I thank him for his excellent guidance and helpful advices throughout the last five years, and also for the final corrections and amendments of my thesis.

I am also very thankful to many of my colleagues who helped me immensely throughout this journey and enabled this work to come to completion:

Prof. Dr. Olav Schiemann, Dr. Yaser Nejaty Jahromy, Andreas Meyer for EPR measurements.
Cornelia Piloth, Brigitta Poth and Dorothe Sommershof (†) for their academic/non-academic help.
Dr. Gregor Schnakenburg for the X-ray diffraction measurements, quantum chemical calculations and also for many valuable discussions.
Martin Straßmann not only for some quantum chemical calculations but also for everyday help with computers.
Dr. Jürgen Tirrée for his great help in lab organization.
Dr. Uttam Chakraborty for his excellent guidance and advices at the beginning of my PhD.
Dietmar Kühlmorgen, Katrin Puffler, Kerstin Kühnel-Lysek, Bernhard Beile, Gabriele Hofer for the synthesis of starting materials and everyday help.
Dr. Burhanshah Lewall for the cyclic voltammetry studies.
Charlotte Rödde for the crystal structure determinations.
Karin Prochnicki, Hannelore Spitz, Claus Schmidt and Dr. Senada Nozinovic for the NMR spectroscopy.
Dr. Sabine Rings and her colleagues for the elemental analyses.
Ioannis Papazoglou and Dr. Uttam Chakraborty for correcting my thesis.
All the group members for the friendly support and help.

Finally, I would like to thank my family and friends for their immense support, patience and encouragement throughout my life and also allowing me to pursue my dreams.

Index

1 Introduction

1.1 Heavy group 14 elements

The introduction of the periodic table by Mendeleev and Meyer was a renaissance in chemistry which provided a useful tool to chemists to assimilate such a vast array of elements of different physical and chemical properties. But, albeit the elements which are placed in the same column were proposed to exhibit similar properties, continuous research in last century made it increasingly clear that heavier congeners of the column display remarkably different behavior compared to their lightest member, which is even more pronounced for the p-block elements. A representative example of this difference is the divergent tendency of carbon and its heavier congeners (e.g., Si, Ge, Sn, and Pb) of the group 14 elements, which are well known as tetrel elements, towards participation in multiple bondings. Carbon is well known for its tendency to form double or triple bonds, which enriched the organic chemistry in last two centuries, but in sharp contrast, compounds containing multiple bonds with the heavier congeners of carbon are far less developed and only started to flourish from the 1980's.[1-4] This striking difference was rationalized by the increasing size difference of the valence s- and p-orbitals down the group, resulting from the increasing Pauli repulsions (Figure I, left). This large size difference makes the orbital mixing, which is necessary to form the multiple bonds, harder for the heavier congeners.[5] Another reason for such different behavior is the significantly reduced electronegativity of the heavier congeners compared to their sister congener carbon (Figure I, right), which makes the compound comprising of multiply bonded heavier elements more reactive and unstable compared to the analogous carbon compounds.[6]

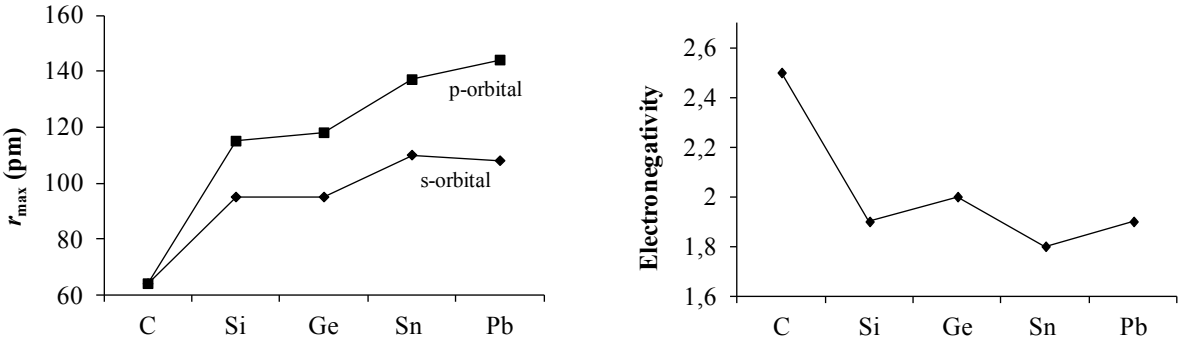

Figure I. A plot of the most probable radii of maximal electron density (r_{max}) of the ns and np valence orbitals (left) and the Pauling electronegativity (right) of tetrel elements.

1.2 Heavy group 14 element analogues of alkynes

Although the alkynes are ubiquitous and known since centuries, the heavier alkynes were completely unknown until 2000, when Power and co-workers serendipitously discover the formation of the diplumbylene 2,6-$Trip_2H_3C_6PbPbC_6H_3$-2,6-$Trip_2$ (Trip = C_6H_2-2,4,6-iPr$_3$), in an attempt to prepare $PbH(C_6H_3$-2,6-$Trip_2)$ upon reaction of $PbBr(C_6H_3$-2,6-$Trip_2)$ with $LiAlH_4$ (Figure II).[7] This was soon followed by the report of the digermyne 2,6-$Dipp_2H_3C_6GeGeC_6H_3$-2,6-$Dipp_2$ (Dipp = C_6H_3-2,6-iPr$_2$) in 2002, and the distannyne 2,6-$Dipp_2H_3C_6SnSnC_6H_3$-2,6-$Dipp_2$ in the same year by Power and co-workers (Figure II).[8, 9] Finally, the series of heavy alkynes was completed in 2004, when Sekiguchi and co-workers prepared the first disilyne R_2(iPr)SiSi(iPr)R_2 (R = $CH(SiMe_3)_2$) upon reduction of the corresponding tetrabromodisilane with KC_8 (Figure II).[10] Conspicuously, in contrast to the linear alkyne, molecular structures of these heavier alkynes revealed significant *trans*-bent geometry and the *trans*-bending gradually increases upon descending from disilyne (∠Si-Si-Si = 137.44(4)°) to diplumbylene (∠Pb-Pb-C1 = 94.26(4)°).[11] Furthermore, subsequent experimental and quantum chemical studies revealed that the E–E bond order decreases down the group from 2.5 (E = Si) to 1 (E = Pb).[11] Even though, these complexes were soon succeeded with few more analogous disilynes,[12-14] digermynes,[15-19] and distannynes,[16, 19, 20] still their syntheses remain a highly challenging issue in modern main group chemistry.

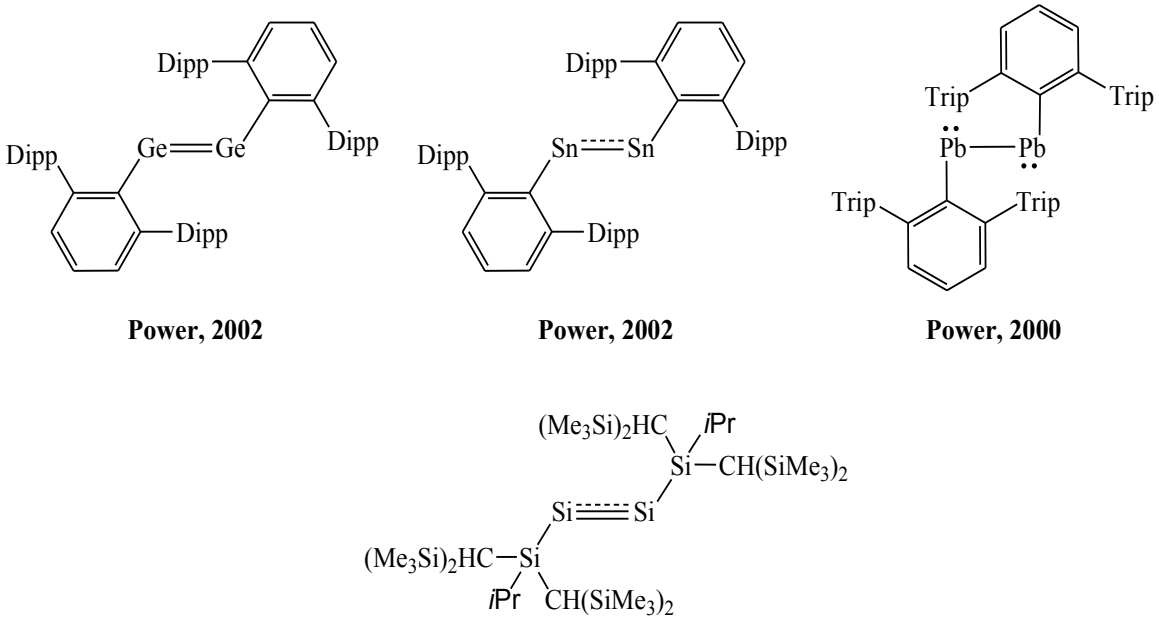

Figure II. First examples of the structurally characterized heavier alkynes.

This striking structural difference between alkynes and their heavier group 14 element analogues can be easily understood with the help of the CGMT model, according to which a linear structure with a triple bond will be observed by a combination of two E–R (E = C – Pb) fragments in a quartet state, whereas a *trans*-bent geometry will be observed, when two E–R fragments combine in a doublet state.[21] The E–R fragments exist in a doublet ground state and the difference between the energy required exciting two doublet E–R fragments into the quartet state ($2\Delta E_{D\rightarrow Q}$) and the energy gained from the two emerging π-bonds ($E_{2\pi}$) determine the geometry of the R–EE–R species. In general, the energy $E_{2\pi}$ exceeds from $2\Delta E_{D\rightarrow Q}$ for the C–R fragments and results in a linear structure, whereas for the E–R fragment (E = Si – Pb), the energy $E_{2\pi}$ is less than $2\Delta E_{D\rightarrow Q}$ leading to a *trans*-bent geometry (Figure III).[21]

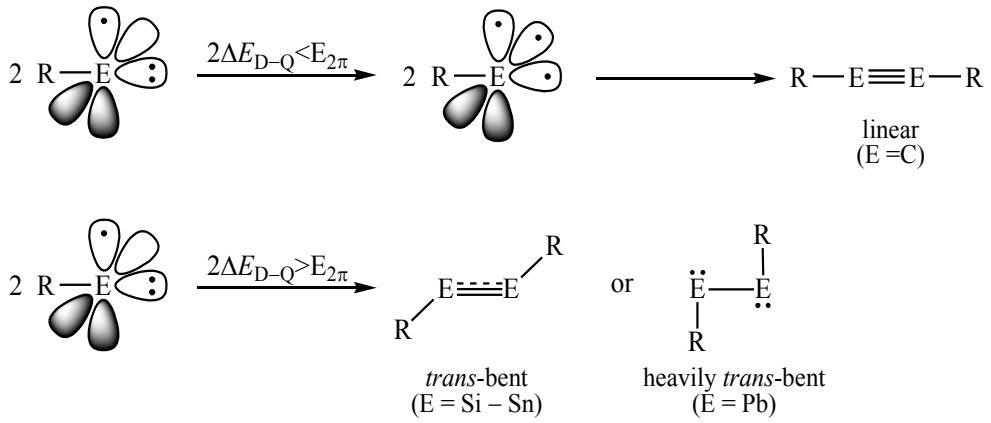

Figure III. Schematic portrayal of the difference between the linear and *trans*-bent geometry of alkynes and their heavier group 14 element homologues according to the CGMT model.

1.3 Heavy group 14 element analogues of alkylidyne complexes

Since the first report of transition metal alkylidyne complexes of the general formula *trans*-$[X(CO)_4M{\equiv}C–R]$ (X = Cl, Br, I; M = Cr, Mo, W; R = Me, Ph) by Fischer and co-workers in 1973, interest in alkylidyne complexes has grown substantially.[22] Soon after this report, Schrock and co-workers reported the first examples of alkylidyne complexes of the general formula $[(\eta^5\text{-}C_5R_5)(Cl)(PMe_3)_2Ta{\equiv}C–R']$ (R = H, Me; R' = *t*Bu, Ph) of a transition metal in high oxidation state in 1978.[23] Studies on high oxidation state alkylidyne complexes have shown that some of them can efficiently catalyze alkyne metathesis, which further stimulated the advancement of this new class of compounds and consequently makes it ubiquitous.

The Fischer-type alkylidyne complexes differ markedly from the Schrock-type. The most striking differences are the low oxidation state of the transition metal and the electrophilic carbyne carbon in Fischer alkylidyne complexes compared to the high oxidation state of the transition metals and the nucleophilic carbyne carbon in Schrock-type alkylidyne complexes. The bonding difference of Fischer-type and Schrock-type alkylidyne complexes can be rationalized by the Dewar-Chatt-Duncanson model (DCD model).[24, 25] In Fischer-type alkylidyne complexes, the triple bond is built by σ-donation from the positively charged $[ER]^+$ fragment to an empty orbital of the negatively charged $[ML_n]^-$ fragment and two π-back donations from the filled orbitals of the $[ML_n]^-$ fragment to two orthogonal empty p-orbitals of the $[ER]^+$ fragment, whereas, in Schrock-type alkylidyne complexes the triple bond is composed by electron sharing of neutral $[ML_n]$ and [CR] fragments (Figure IV).[26]

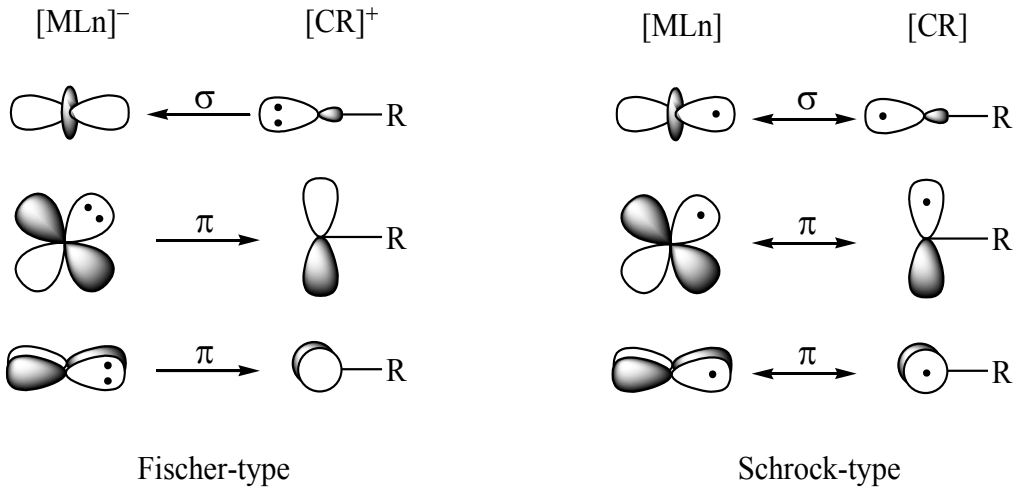

Figure IV. Schematic representation of the orbital interactions in Fischer-type (left) and Schrock-type alkylidyne complexes, according to the Dewar-Chatt-Duncanson model.

Akin to the heavier alkynes, heavier alkylidyne complexes are far less advanced compared to the alkylidyne complexes. The heavier analogues are inherently more reactive, which prevented the isolation of this class of compounds until 1996, when Power and co-workers reported the first germylidyne complex $[Cp(CO)_2Mo{\equiv}Ge(C_6H_3\text{-}2,6\text{-}Mes_2)]$ featuring a triple bond between the Mo and Ge atoms.[27] In fact, this was the first report of a compound featuring a triple bond to a heavier group 14 element. The germylidyne complex was prepared by salt elimination method from $Na[CpMo(CO)_3]$ and $GeCl(C_6H_3\text{-}2,6\text{-}Mes_2)$ (Scheme I).[27] Following the same method, analogous germylidyne complexes of Cr and W were also prepared. The reactions proceed through the intermediate formation of metallogermylenes of the general formula $[Cp(CO)_3M–$

$Ge(C_6H_3\text{-}2,6\text{-}R_2)]$ (M = Cr – W; R = Mes, Trip), which upon heating or photolysis loose one carbonyl ligand to yield the corresponding germylidyne complexes $[Cp(CO)_2M{\equiv}Ge(C_6H_3\text{-}2,6\text{-}R_2)]$ (Scheme I).[28] In 2010 the first genuine silylidyne complex $[Cp(CO)_2Mo{\equiv}Si(C_6H_3\text{-}2,6\text{-}Trip_2)]$ have been reported by Filippou and co-workers following a similar method.[1][29, 30] However, attempts to prepare analogous stannylidyne or plumbylidyne complexes of group 6 metals by this approach were unsuccessful and only afforded corresponding metallostannylenes or metalloplumbylenes.[31, 32] This difference was explained by a combination of electronic and steric reasons.[32] Even an attempt to prepare a stannylidyne complex by this approach using a bulkier cyclopentadienyl ligand η^5-1,3-tBu$_2$-C_5H_3 on the metal center also failed. Although several silylidyne and germylidyne complexes were successfully prepared so far, group 6 metal stannylidyne and plumbylidyne complexes remain unattainable by salt metathesis.[33-38]

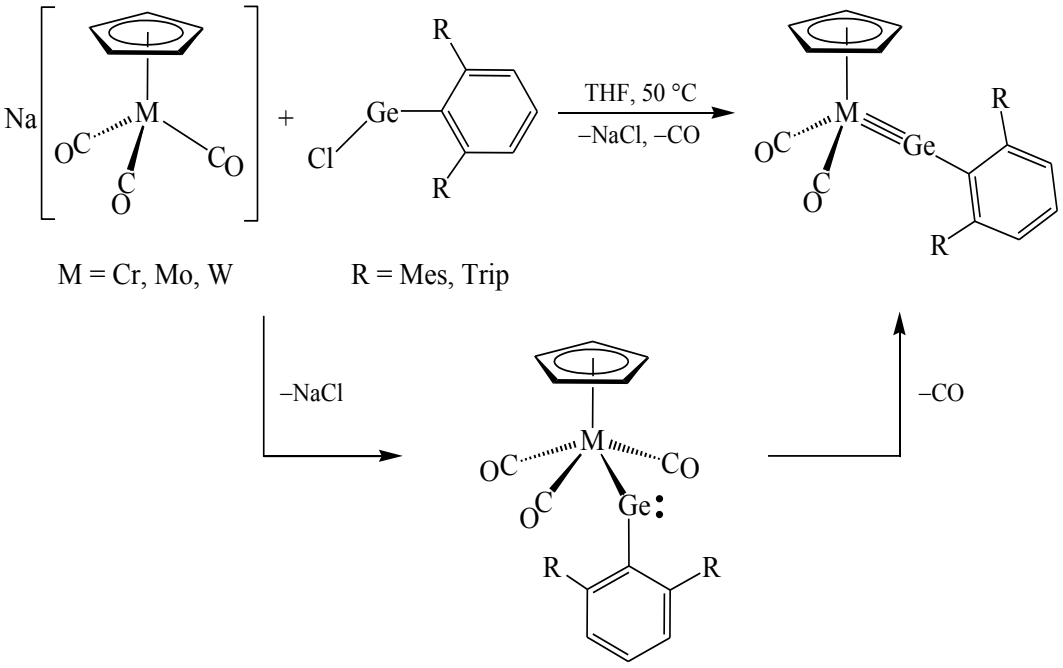

Scheme I. Synthesis of germylidyne complexes by salt metathesis as reported by Power.

The second step, and perhaps the most important step towards the synthesis of the heavier alkylidyne complexes was taken in 2000, when Filippou and co-workers reported the synthesis of germylidyne complexes *trans*-$[X(dppe)_2W{\equiv}Ge{-}(\eta^1\text{-}Cp^*)]$ (X = Cl, Br; dppe =

1 In 2003, Tilley and co-workers reported the complex $[\{Cp^*(dmpe)(H)MoSi{-}Mes)\}\{B(C_6F_5)_4\}]$ ($Cp^* = \eta^5\text{-}C_5Me_5$) with considerable silylidyne character but due to the weak interaction of the H atom with the silicon center, the bonding situation is quite different from that of a genuine silylidyne complex.

$Ph_2PCH_2CH_2PPh_2$; Cp* = C_5Me_5) via a new procedure, called N_2-elimination method.[39] Unlike to the salt metathesis, in the N_2-elimination method the neutral electron rich metal precursor *trans*-[$W(dppe)_2(N_2)_2$] was reacted with a halogermylene [Cp*GeX] in refluxing toluene, which resulted in a clean formation of the germylidyne complexes with concomitant elimination of the N_2 ligands and halide migration from the Ge atom to the metal center (Scheme II).

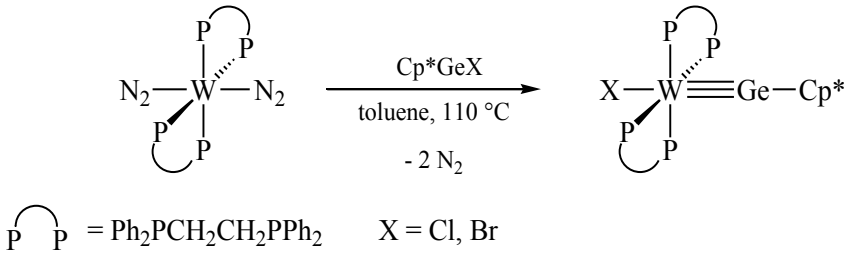

Scheme II. Synthesis of germylidyne complexes using the N_2-elimination method introduced by Filippou.

Conspicuously, this N_2-elimination strategy not only led to the isolation of several neutral and cationic germylidyne complexes of group 6 transition metals,[40, 41] but also enabled the isolation of the first stannylidyne complex, *trans*-[$Cl(PMe_3)_4W{\equiv}Sn(C_6H_3\text{-}2,6\text{-}Mes_2)$] by reaction of *trans*-[$W(PMe_3)_4(N_2)_2$] with the chlorostannylene [$SnCl(C_6H_3\text{-}2,6\text{-}Mes_2)$],[42] and the first plumbylidyne complex *trans*-[$Br(PMe_3)_4Mo{\equiv}Pb(C_6H_3\text{-}2,6\text{-}Trip_2)$] upon reaction of *cis*-[$Mo(PMe_3)_4(N_2)_2$] with the bromoplumbylene [$PbBr(C_6H_3\text{-}2,6\text{-}Trip_2)$] (Scheme III).[43] Furthermore, these unprecedented complexes were soon succeeded by the cationic tungsten stannylidyne complex [$(dppe)W{\equiv}Sn(C_6H_3\text{-}2,6\text{-}Mes_2)][PF_6]$,[44] and the tungsten plumbylidyne complexes *trans*-[$X(PMe_3)_4W{\equiv}Pb(C_6H_3\text{-}2,6\text{-}Trip_2)$] (X = Br, I)[45] following the same strategy and thus displaying the importance and superiority of the N_2-elimination method over the salt metathesis.

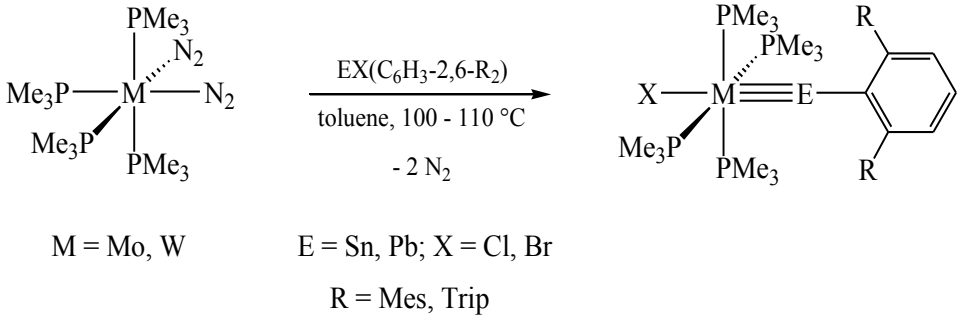

Scheme III. First stannylidyne and plumbylidyne complexes obtained by the N_2-elimination method.

Akin to the N_2-elimination method, the trimethylphosphine (PMe_3) elimination method was also employed starting from the electron rich PMe_3 complexes $[Mo(PMe_3)_6]$ and $[W(\eta^2\text{-}CH_2PMe_2)H(PMe_3)_4]$, which also enabled the isolation of many unprecedented heavier tetrylidyne complexes. Some representative examples are the germylidyne complexes *trans*-$[Cl(PMe_3)_4M{\equiv}Ge(C_6H_3\text{-}2,6\text{-}Trip_2)]$ (M = Mo, W), and the plumbylidyne complexes *trans*-$[X(PMe_3)_4W{\equiv}Pb(C_6H_3\text{-}2,6\text{-}Trip_2)]$ (X = H, Br).[46, 47] Apart from the salt metathesis and the N_2/PMe_3-elimination methods, recently few more strategies were also employed for the synthesis of the heavier tetrylidyne complexes of group 6 transition metals. For example, the germylidyne complex $[Cp^*(CO)_2W{\equiv}Ge{-}C(SiMe_3)_3]$ was prepared by the dehydrogenation of the hydrido germylidene complex $[Cp^*(CO)_2(H)W{=}Ge(H)\{C(SiMe_3)_3\}]$ with MesNCO.[48] Accordingly, the silylidyne complex $[Cp^*(CO)_2W{\equiv}Si{-}C(SiMe_3)_3]$ was obtained by a stepwise proton and hydride abstraction from the hydrido hydrosilylene complex $[Cp^*(CO)_2(H)W{=}Si(H)\{C(SiMe_3)_3\}]$ using IMe_2iPr_2 and $B(C_6F_5)_3$, respectively.[49]

Although all tetrylidyne complexes mentioned above contain group 6 transition metals, recent studies by Filippou and co-workers, and Tilley and co-workers have shown that this chemistry can also be extended to early transition metals of group 4[50, 51] and 5,[52, 53] as well as to late transition metals of group 7 – 10.[38, 54-58] Some representative examples are depicted in Figure V. The N_2/PMe_3-elimination strategy was also found to be a very efficient method for other transition metals outside group 6 which enabled the isolation of a series of tetrylidyne complexes of group 7, 8 and 10 transition metals.[54, 56, 57] The titanium tetrylidyne complexes were prepared by salt metathesis of the carbonyl metalate $NEt_4[Cp^*Ti(CO)_4]$ with the suitable tetrylene precursors and represent the first examples of compounds featuring a triple bond between Ti and a heavier group 14 element. The cobalt germylidyne complex $[Cp(Idipp)CoGe{-}N(Mes^*)TMS][B\{C_6H_3\text{-}3,5\text{-}(CF_3)_2\}_4]$ was prepared in two steps starting from $[CpCo(C_2H_4)(Idipp)]$. In the first step ethylene exchange by [Ge(Cl)N(Mes*)TMS)] afforded the chlorogermylidene complex $[Cp(Idipp)Co{=}Ge(Cl)N(Mes^*)TMS]$, which was then treated with $Na[B\{C_6H_3\text{-}3,5\text{-}(CF_3)_2\}_4]$ in fluorobenzene at ambient temperature.[38]

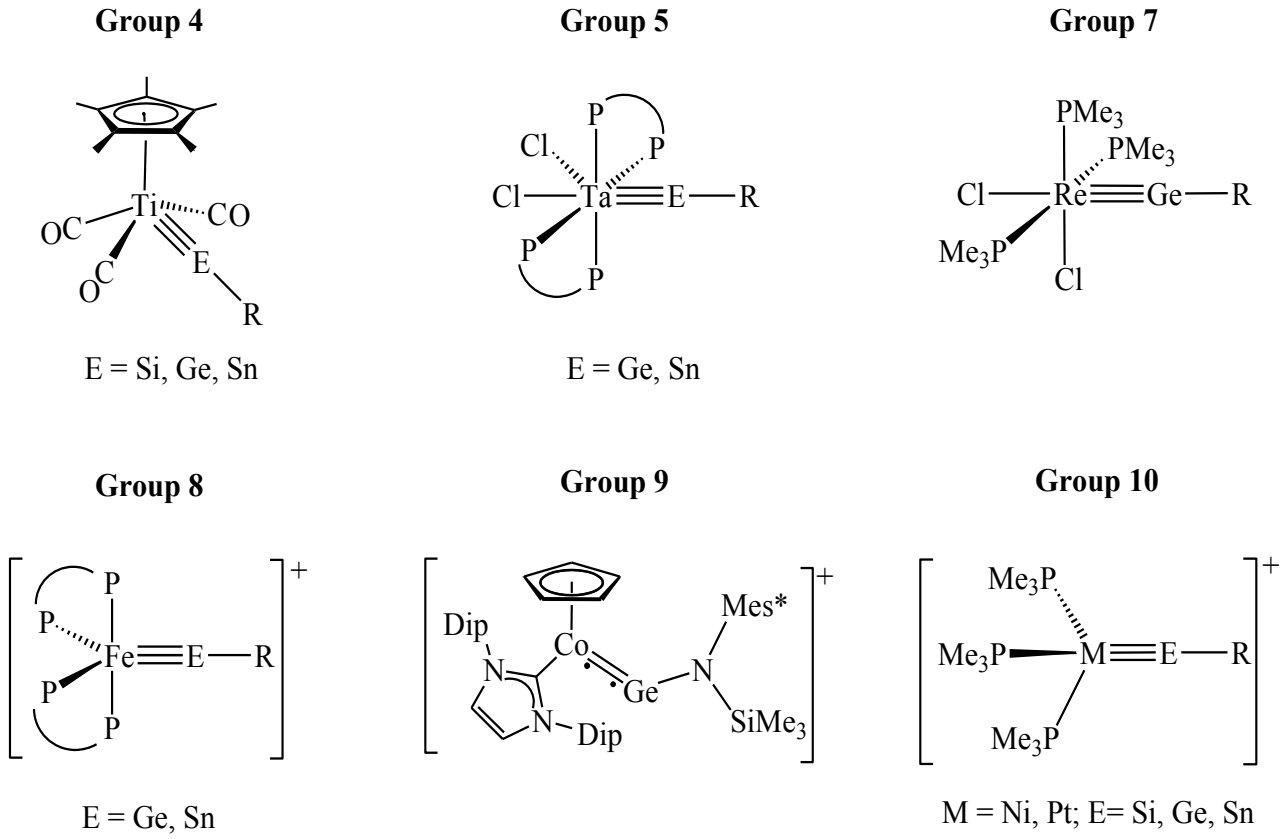

Figure V. Tetrylidyne complexes of transition metals other than group 6. Counter anions are omitted for simplicity.

All the heavier tetrylidyne complexes mentioned above are closed-shell 18 VE complexes, with the only exception of the cobalt germylidyne complex [Cp(Idipp)CoGe–N(Mes*)TMS][B{C_6H_3-3,5-$(CF_3)_2$}$_4$], which exists in a triplet ground state. Despite these enthralling advancement of the chemistry of tetrylidyne complexes, open-shell congeners of this interesting class of compounds were elusive up until 2012, when Filippou and co-workers reported the first open-shell germylidyne complexes *trans*-[Cl$(PMe_3)_4$M≡Ge(C_6H_3-2,6-Mes_2)][B$(C_6F_5)_4$] (M = Mo, W). These compounds were obtained upon one-electron oxidation of the corresponding closed-shell precursors *trans*-[Cl$(PMe_3)_4$M≡Ge(C_6H_3-2,6-Mes_2)] with one equivalent of (Ph_3C)[B$(C_6F_5)_4$] (Scheme IV).[59] Quantum chemical calculations of the neutral closed-shell germylidyne complexes *trans*-[Cl$(PMe_3)_4$M≡Ge(C_6H_3-2,6-Mes_2)] revealed that the HOMOs of these molecules is a metal centered d-orbital, which is nonbonding with respect to the germylidyne ligand.[59] Consequently, one-electron oxidation of these complexes did not affect

the Mo≡Ge triple bond. This was further verified by EPR and single-crystal X-ray diffraction studies.[59]

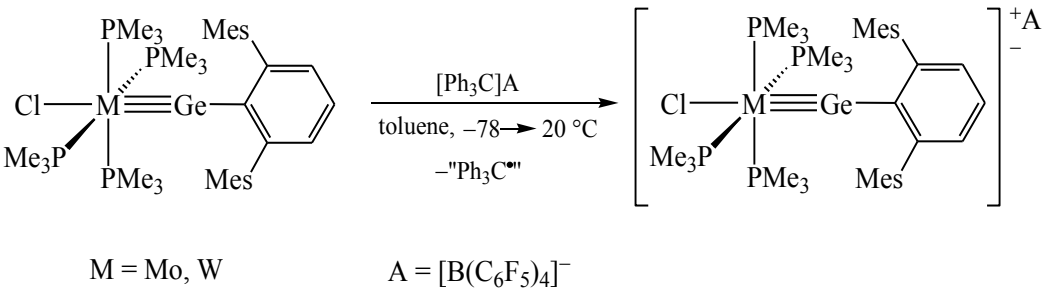

Scheme IV. First examples of open-shell germylidyne complexes prepared by one-electron oxidation of corresponding closed-shell germylidyne complexes.

These results were soon followed by another class of open-shell complexes of the general formula $[Cp(PMe_3)_2Mo{\equiv}E(C_6H_3\text{-}2,6\text{-}Mes_2)][BAr^f{}_4]$ (E = Ge, Sn; $Ar^f = C_6F_5$, C_6H_3-3,5-$(CF_3)_2$) by Filippou and co-workers.[60] Entry into these three-legged piano-stool structured open-shell complexes was provided by the neutral tetrylidyne complexes $[Cp(PMe_3)_2Mo{\equiv}E(C_6H_3\text{-}2,6\text{-}Mes_2)]$, which were prepared by the reaction of *trans*-$[Cl(PMe_3)_4Mo{\equiv}E(C_6H_3\text{-}2,6\text{-}Mes_2)]$ with NaCp in boiling toluene or xylene.[60] Finally, the open-shell complexes were prepared by oxidation of the neutral 18VE complexes using either $(Ph_3C)[B(C_6F_5)_4]$ or $[Fe(C_5Me_5)_2][B\{C_6H_3\text{-}3,5\text{-}(CF_3)_2\}_4]$ in fluorobenzene at ambient temperature (Scheme V).[60] Single crystal X-ray diffraction and ESR studies of these complexes revealed that they also feature a metal-centered unpaired electron.

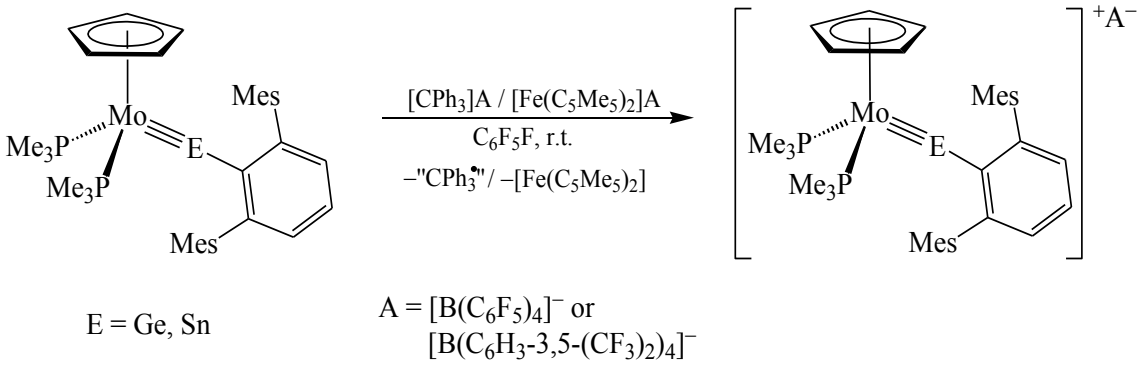

Scheme V. Synthesis of three-legged piano-stool structured, open-shell germylidyne and stannylidyne complexes.

1.4 Heavy group 14 element analogues of μ-carbido complexes

1.4.1 μ-carbido complexes

Transition metal carbido complexes are an intriguing class of compounds in organometallic chemistry which drawn considerable attention due to their involvement as models for surface carbide intermediates in heterogeneous catalysis and also as a building block for the synthesis of cluster compounds.[61-63] Based on the coordination number of the coordinated carbon, carbido complexes can exhibit a variety of structures ranging from highly exposed triply bonded terminal carbido complexes $L_nM{\equiv}C$: to high-nuclearity clusters containing interstitial carbon atoms.[63-71] In μ_2-carbido complexes, where a ''naked'' carbon atom is only bonded to two metal fragments, the bonding can be delineate by two major canonical forms – metallacarbyne ($L_nM{\equiv}C{-}M'L_n$) with a localized triple and a single metal-carbon bonds, and dimetallacumulene ($L_nM{=}C{=}ML_n$) with two symmetrical metal-carbon double bonds. In 1980, in an attempt to prepare [Fe(TPP)(CI_2)] (TPP = tetraphenylporphyrin) to an analogous way to that used for the preparation of [Fe(TPP)(CCl_2)] by reacting Fe(TPP) with CI_4 in the presence of an excess of the reducing agent sodium dithionite, Mansuy serendipitously discovered the first μ_2-carbido complex of the general formula [(TPP)Fe=C=Fe(TPP)], which was proposed to have a dimetallacumulene structure (Scheme VI).[72]

$$2\,[Fe(TPP)] \;+\; CI_4 \;+\; Na_2S_2O_4\,(\text{excess}) \xrightarrow[-4\ NaI]{C_6H_6} [(TPP)Fe{=}C{=}Fe(TPP)]$$

TPP = Tetraphenylporphyrin

Scheme VI. Synthesis of the first μ-carbido complex of dimetallacumulene class.

Although the molecular structure of this compound was not determined by a single-crystal X-ray diffraction study at that time, its spectroscopic properties and elemental analysis as well as a molecular weight determination were in good agreement with the proposed structure.[73] This was supported by a theoretical study, which predicted that this compound should be diamagnetic and display a linear Fe-C-Fe spine.[74] Finally, the structure of the first μ_2-carbido complex [(TPP)Fe=C=Fe(TPP)] was reported by Goedken and Bottomley in 1982, and it indeed exhibits a linear Fe-C-Fe unit with a short Fe–C bond length of 1.675 Å.[75] In 1987 Latesky and Selegue reported the first example of the metallacarbyne complex [$(Me_3CO)_3W{\equiv}C{-}Ru(CO)_2Cp$], which

was prepared by alkyne metathesis from [$(Me_3CO)_3W{\equiv}C–Et$] and [$Cp(CO)_2Ru–C{\equiv}C–Me$] at ambient temperature (Scheme VII).[76]

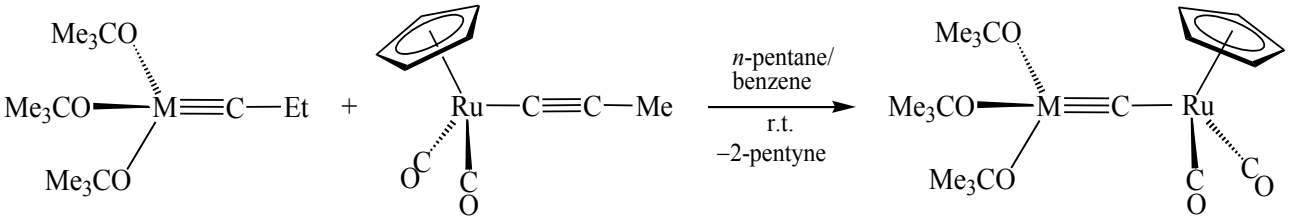

Scheme VII. Synthesis of the first metallacarbyne complex.

Following these results a large array of metallacarbynes, as well as dimetallacumulenes with different transition metals were reported in the literature, which display interesting reactivity.[77-85]

1.4.2 Heavy group 14 analogues of metallacumulene complexes

In 1981, soon after the first report of a dimetallacumulene by Mansuy, Weiss and Gäde reported the first compound, [(μ-Ge){(η^5-C_5H_4Me)$Mn(CO)_2$}$_2$], featuring a multiply-bonded Ge atom bridging between two Mn centers.[86] In an attempt to prepare the acyl complex K[(η^5-C_5H_4Me)$(CO)_2Mn–C(O)GeH_3$] by reacting $KGeH_3$ with the carbonyl manganese complex [(η^5-C_5H_4Me)$Mn(CO)_3$], Weiss et al. serendipitously discovered the formation of K[(η^5-C_5H_4Me)$(CO)_2Mn–GeH_3$], which upon treatment with a non-oxidizing mineral acid produced the compound [(μ-Ge){(η^5-C_5H_4Me)$Mn(CO)_2$}$_2$] (Scheme VIII).[86] The molecular structure of this compound revealed a centrosymmetric molecule with a linear Mn-Ge-Mn spine. In 1983, Herrmann and co-workers reported an another method for the preparation of an analogous compound [(μ-Ge){Cp*$Mn(CO)_2$}$_2$] by directly reacting GeH_4 with [Cp*$Mn(CO)_2$(THF)] with traces of sulphuric acid.[87] The mechanism of formation of these complexes remains unclear, but it has been predicted to occur by reductive cleavage of the labile Ge–H bonds.[71] Interestingly, although Weiss and Gäde described that the compound [(μ-Ge){(η^5-C_5H_4Me)$Mn(CO)_2$}$_2$] was the first one to contain Mn–Ge double bonds with a heteroallene structure, Kostić and Fenske suggested on the basis of quantum chemical calculations that the Mn–Ge bonds can be viewed as partial triple bonds.[88]

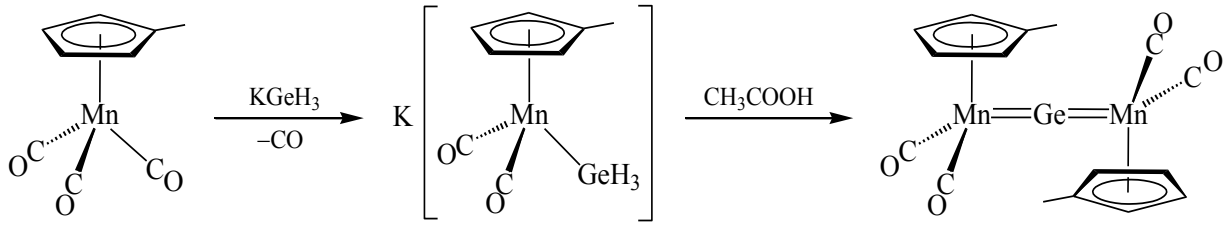

Scheme VIII. Synthetic route to the first germanium analogue of a μ_2-carbido complex with a cumulene structure.

Later, in 1985 Herrmann and co-workers reported the first lead analogue [(μ-Pb){(CpMn(CO)$_2$}$_2$] of dimetallacumulenes.[89] This complex was prepared by the reaction of $PbCl_2$ with the labile solvent complex [CpMn(CO)$_2$(THF)] in THF at ambient temperature (Scheme IX). A possible mechanism for the formation of this compound was proposed involving a dichloroplumbanediyl complex [CpMn(CO)$_2$($PbCl_2$)],[2] which undergoes consecutive reduction by the metal precursor.[89] Notably, complex [(μ-Pb){(CpMn(CO)$_2$}$_2$] was the first example of a compound containing transition metal-lead multiple bonds. Soon after, isolation of a tin analogue [(μ-Sn){CpMn(CO)$_2$}$_2$] was achieved by Herrmann and co-workers using a similar method, i.e. upon reacting $SnCl_2$ with [CpMn(CO)$_2$(THF)].[90, 91] A similar dimetallastannacumulene [(μ-Sn){(η^5-C_5H_4Me)Mn(CO)$_2$}$_2$] was also reported by Huttner and co-workers in 1990 following a different route, in which $SnCl_2$ was reacted with Na[{(η^5-C_5H_4Me)(CO)$_2$Mn}$_2$H] in THF at –30 °C.[92]

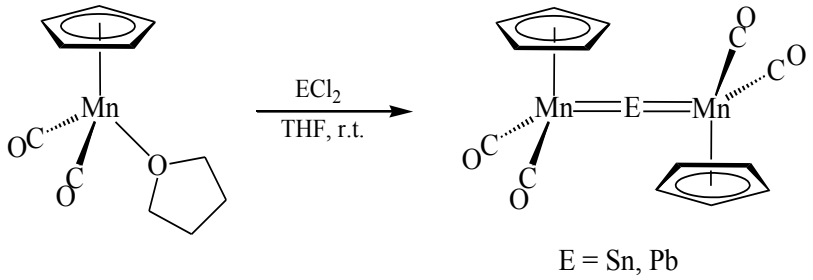

Scheme IX. Synthesis of the first Sn and Pb analogue of the μ_2-carbido complex with a cumulene structure.

2 An analogoues Ge compound [(η^5-C_5H_4Me)Mn(CO)$_2$($GeCl_2$)] is a stable and isolable species as a THF or benzothiazole adduct; see: P. Jutzi, W. Steiner, *Chem. Ber.* **1976**, *109*, 3473.

In contrast, a genuine silicon analogue of the μ_2-carbido complex is still elusive. Thus, attempts to prepare the silicon analogue [(μ-Si){Cp*Mn(CO)$_2$}$_2$] by reacting SiH_4 and the labile solvent complex [Cp*Mn(CO)$_2$(THF)] only afforded the silane [(μ-SiH$_2$){Cp*Mn(CO)$_2$H}$_2$], which feature a four coordinated silicon with an expected bent Mn-Si-Mn skeleton (Figure VI).[93] Attempts to remove H_2 from the dimanganosilane by thermal treatment were unsuccessful, probably due to the high stability of the Si-H bond.[71] It was only in 1988, when Zybill and co-workers reported the first example of the base stabilized μ_2-silicido complex [(μ-Si)(HMPT)$_2${Fe(CO)$_4$}$_2$] (HMPT = (Me$_2$N)$_3$PO), generated by metathetical exchange from Na$_2$[Fe(CO)$_4$] and $SiCl_4$ in the presence of excess HMPT in THF at –40 °C.[94] In contrast to the related Ge or Pb compounds, the molecular structure of [(μ-Si)(HMPT)$_2${Fe(CO)$_4$}$_2$] revealed an approximate tetrahedral coordination of Si with a Fe-Si-Fe bond angle of 122.6(1)°. Therefore this complex should better described by the zwitterionic structure shown in Figure VI.[94] Remarkably, metalloylidyne complexes of the general formula [L$_n$M≡E–M'L'$_n$] are still elusive.

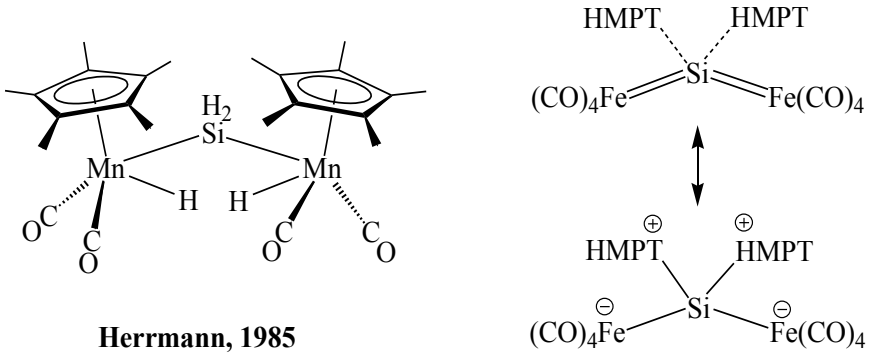

Herrmann, 1985

HMPT = (Me$_2$N)$_3$PO

Zybill, 1988

Figure VI. The dimanganosilane (left) and the bis(base) stabilized μ-silicido complex (right).

1.5 Goals and Objectives

As discussed in the introduction, closed-shell complexes comprising triple bonds between transition metals and the tetrel atoms (Si – Pb) are already known, and they are not only limited to group 6 transition metals, but also were extended to early transition metals of the groups 4 and 5 and late transition metals of the groups 7 – 10. In contrast, open-shell tetrylidyne complexes are far less common. Only very recently, a handful of open-shell tetrylidyne complexes featuring mainly a metal-centered unpaired electron have been reported. But, so far no examples of open-shell tetrylidyne complexes with of a tetrel-centered unpaired electron exist. Furthermore, heavier analogues of the μ-carbido complexes are not well developed. Only few examples with the tetrel elements Ge–Pb are known with dimetallacumulene structure. Silicon congeners of these dimetallacumulenes are missing. In addition, no metalloylidyne of the elements Si – Pb have been reported. This situation constituted the following goals of this thesis:

- To prepare suitable closed-shell tetrylidyne complexes that can be used as precursors for open-shell tetrylidyne complexes.
- To isolate and characterize unprecedented open-shell tetrylidyne complexes featuring a tetrel-centered unpaired electron.
- To isolate and characterize the metallatetrylidyne complexes $[L_nM{\equiv}E{-}M'L'_n]$.
- To complete the series of metallacumulenes with the isolation of most challenging missing member containing a [M]=Si=[M] functionality.
- To explore the reactivity of these new classes of compounds.

2 Results & Discussion

2.1. Closed shell heavier tetrylidyne complexes of group 6 metals

One of the ultimate goals of this work was to prepare open-shell tetrylidyne complexes featuring a tetrel-centered unpaired electron. This could be accomplished by one-electron reduction of suitable closed-shell tetrylidyne complexes, since it is well-known for a Fischer-type tetrylidyne complex that the HOMO is a metal-centered orbital and the LUMO is a tetrel-centered orbital.[95] So, addition of one electron to a closed-shell tetrylidyne complex is expected to give an open-shell tetrylidyne complex featuring an unpaired electron at the tetrel atom. To achieve this target, we envisaged a synthetic strategy by introducing electron withdrawing ligands on the metal fragment, such as CO, which will lower the energy of the LUMO and therefore stabilize the additional unpaired electron in the new open-shell complex.

As pointed out in the introduction, tetrylidyne complexes of the general formula $[Cp(CO)_2M{\equiv}E(C_6H_3\text{-}2,6\text{-}R_2)]$ (M = Cr, Mo, W; E = Si, Ge; R = Mes, Trip), consisting of two carbonyl ligands on the metal center, can be obtained by salt metathesis, as described by Power and co-workers, and Filippou and co-workers.[27, 28, 30] But, so far only silylidyne and germylidyne complexes have been obtained following this method. In contrast, attempts to synthesize analogous stannylidyne or plumbylidyne complexes using this approach only led to the corresponding metallotetrylenes $[Cp(CO)_3M{-}E(C_6H_3\text{-}2,6\text{-}R_2)]$ (M = Cr, Mo, W; E = Sn, Pb; R = Mes, Trip).[31, 32, 96] This aberration was explained by a combined effect of electronic and steric reasons.[32] The bulkier cyclopentadienyl ligand η^5-1,3-*t*Bu_2-C_5H_3 was also employed to generate sufficient steric crowding to induce CO elimination and produce the corresponding triple bonded compounds, but this approach failed.[31] Furthermore, metallostannylenes and metalloplumbylenes containing a potentially labile trimethylphosphane (PMe_3) ligand instead of ar CO ligand, of the general formula $[Cp^*(CO)_2(PMe_3)Mo{-}E(C_6H_3\text{-}2,6\text{-}Mes_2)$ (E = Sn, Pb) were also prepared, by reacting $[Cp^*Mo(CO)_2(PMe_3)(SiMe_3)]$ with the corresponding chlorotetrylenes $E(Cl)(C_6H_3\text{-}2,6\text{-}Mes_2)$ (E = Sn, Pb), to check the possibility of a smooth elimination of PMe_3 ligand to form the corresponding tetrylidyne complexes.[97] However, the metalloylenes proved to be inert to a PMe_3 elimination.

2.1.1 Synthesis of scorpionate metalate salts

Hydridotris(pyrazolyl)borate (Tp) and hydridotris(3,5-dimethylpyrazolyl)borate (Tp') ligands, which are well known as scorpionate ligands, were first introduced by Trofimenko in 1966.[98] Following this discovery, these ligands were successfully utilized in the synthesis of a wide range of organometallic complexes.[99] These Tp/Tp' ligands are frequently compared with the Cp/Cp* ligands since both classes of ligands are six-electron donor anionic ligands and bind the metal center in a facial geometry. Despite these similarities, they also differ in many aspects, as pointed out below.

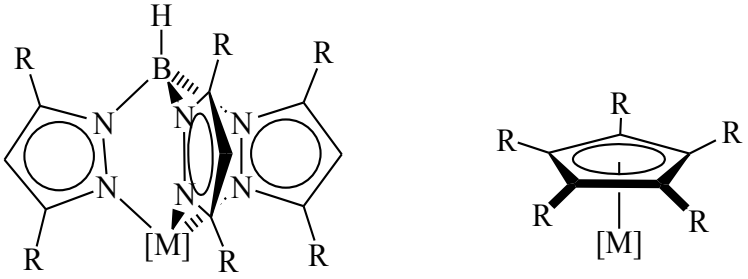

R = H, Me

Figure 1. Comparison of the hydridotris(pyrazolyl)borate ligand and the cyclopentadienyl ligand.

1. Tp/Tp' ligands provide much better steric protection (cone angle: Tp 180°, Tp' 224°) than the Cp/Cp* ligands (cone angle: Cp 100°, Cp* 146°).[100, 101]

2. Although, the electron donating properties of the Tp/Tp' ligands are highly dependent on the metal center as well as the other ligands on the metal, in the case of group 6 metals Tp/Tp' ligands are more donating than the Cp ligand.

3. Tp/Tp' ligands are weak-field ligands carrying relatively hard nitrogen σ-donors, while the Cp/Cp* groups are comparatively soft and capable of π-donation.[102]

4. Most importantly, in contrast to Cp/Cp* ligands, Tp/Tp' ligands strictly enforce an octahedral geometry around the metal center.[102]

As pointed above, hydridotris(pyrazolyl)borate ligands are more sterically protecting than Cp/Cp* ligands, which is necessary for the stabilization of highly reactive tetrylidyne complexes, and force an octahedral geometry around the metal center, which is important to trigger the elimination of a third ligand from the metal center in metallotetrylenes which are formed as intermediates during the formation of tetrylidyne complexes. Thus, we decided to use the

hydridotris(3,5-dimethylpyrazolyl)borate (Tp') ligand instead of Cp/Cp* ligands on the metal center to pursue the whole series of tetrylidyne complexes of the general formula [Tp'(CO)$_2$M≡E(C$_6$H$_3$-2,6-Ar$_2$)] (M = Mo, W; E = Si – Pb; Ar = Mes, Trip) by salt metathesis.

To accomplish this target, we developed two new scorpionate metalate salts Na[Tp'M(CO)$_2$(PMe$_3$)] (**3-Mo**, M = Mo; **3-W**, M = W) with a potentially labile phosphane ligand. These metalates were prepared by two electron reduction of the M(II) complexes [Tp'M(CO)$_2$(PMe$_3$)Cl] (**1-Mo**, M = Mo; **1-W**, M = W) in THF at ambient temperature. Compounds **3-Mo** and **3-W** were isolated after workup as extremely air-sensitive, thermally robust (**3-Mo**: m.p. 288 °C (dec)), yellow solids in 90 – 95% yields (Scheme 1). Both metalates are well soluble in THF and DME, sparingly soluble in fluorobenzene and insoluble in benzene or common aliphatic solvents. The precursor **1-Mo** was prepared following a modified procedure described for **1-W**,[103] and was isolated as a bright yellow solid. Similar to **1-W**, complex **1-Mo** is also well soluble in CH_2Cl_2, THF, and fluorobenzene, moderately soluble in toluene or Et_2O and insoluble in common aliphatic solvents.

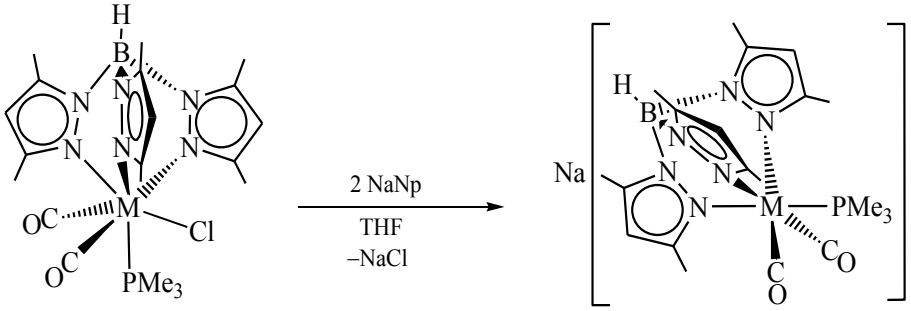

NaNp = Sodium naphthalenide

3-Mo (M = Mo), yellow solid, 95%

3-W (M = W), yellow solid, 95%

Scheme 1. Synthesis of the metalate salts **3-Mo**/**3-W** by two-electron reduction of **1-Mo**/**1-W**.

Compound **1-Mo** was fully characterized by IR and multinuclear NMR spectroscopy, single-crystal X-ray diffraction analysis, and the composition was determined by elemental analysis. The IR spectrum of **1-Mo** in THF displays two ν_{CO} absorption bands at 1936 (s) and 1840 (vs) cm^{-1}, which appear at slightly higher wavenumbers compared to those of the analogous tungsten compound **1-W** (ν_{CO} in THF: 1921 (s) and 1819 (vs) cm^{-1}).[103] Furthermore, the ν_{CO} absorption bands of **1-Mo** appear almost 70 cm^{-1} at lower wave numbers compared to those of the 16VE precursor [Tp'Mo(CO)$_2$Cl] (ν_{CO} in THF: 2007 (s), 1923 (s) cm^{-1}), which is in accordance with

the increased electron density at the Mo center due to the added electron donating phosphane ligand.[104] The $^{31}P\{^{1}H\}$ NMR spectrum of **1-Mo** in CD_2Cl_2 reveals a singlet resonance signal at δ = 33.6 ppm, which is remarkably downfield shifted compared to that of **1-W** (–1.93 ppm, ^{1}J(W, P) = 63 Hz). The most characteristic signal in the $^{13}C\{^{1}H\}$ NMR spectrum of **1-Mo** is that of the low-field shifted carbonyl carbon atom at δ = 252.9 ppm (d, ^{2}J(C, P) = 51.1 Hz).

To establish the molecular structure, yellow plates of **1-Mo**, suitable for X-ray diffraction analysis, were grown from a concentrated THF solution at –60 °C. The molecular structure revealed a distorted face-capped octahedral geometry with the PMe_3 ligand capping the one face of the octahedron, which is built from the chloride and two CO ligands. As expected, three pyrazolyl groups of the scorpionate ligand are bonded to the Mo center in a facial mode and constitute the other face of the octahedron (Figure 2). Notably, due to the presence of disorder in the chloride and the carbonyl (C(20)≡O(2)) positions the Mo–Cl and Mo–C20 bond lengths has significant inaccuracy, which explains the difference between Mo–C19 (2.026 (4) Å) and Mo–C20 (1.880 (9) Å) bond lengths.

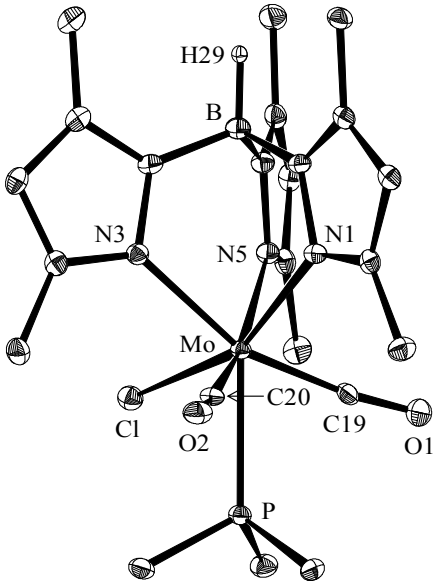

Figure 2. DIAMOND plot of the molecular structure of **1-Mo** in the crystal lattice of **1-Mo**·2(C_4H_8O) at 100(2) K. Thermal ellipsoids are set at 30 % electronic probability. Hydrogen atoms (except the B-bonded H atom) were omitted for clarity reasons. Selected bond lengths [Å] and bond angles [°]: Mo-P 2.4806 (9), Mo-Cl 2.540 (3), Mo-N1 2.259 (3), Mo-N3 2.260 (3), Mo-N5 2.239 (3), Mo-C19 2.026 (4), Mo-C20 1.880 (9), N1-Mo-Cl 157.40 (9), N3-Mo-Cl 80.12 (9), N5-Mo-Cl 80.53 (8), P-Mo-Cl 72.77 (5), P-Mo-C20 70.5 (3).

Both scorpionate metalate salts **3-Mo** and **3-W** were also characterized by IR and multinuclear NMR spectroscopy and the solid state structure of **3-Mo** was established by single-crystal X-ray diffraction analysis. The solution IR spectra of the metalate salts are highly solvent-dependent. For example, metalates **3-Mo** and **3-W** exhibit five resolvable ν_{CO} absorption bands (**3-Mo**: 1766 (m), 1726 (vs), 1644 (m), 1620 (s) and 1596 (s) cm^{-1}; (Figure 3) **3-W**: 1756 (m), 1715 (vs), 1639 (m), 1614 (s) and 1594 (s) cm^{-1}) in THF, which indicates the existence of at least three different species in solution, among which two species are arising from the contact ion pairs (CIP) of the sodium gegencation with the metal centers and the carbonyl oxygen atom, whereas the third species is the solvent-separated ion pair (SSIP).[105, 106] These two CIPs and the SSIP are in equilibrium and the equilibrium was found to be solvent dependent as indicated by the presence of four ν_{CO} absorption bands in DME (**3-Mo**: 1762 (vs), 1727 (vs), 1645 (s) and 1623 (s) cm^{-1}; **3-W**: 1753 (vs), 1716 (vs), 1639 (s) and 1619 (s) cm^{-1}), and only two in acetonitrile (**3-Mo**: 1755 (vs) and 1663 (vs) cm^{-1}; **3-W**: 1743 (vs) and 1654 (vs) cm^{-1}) (Figure 3).

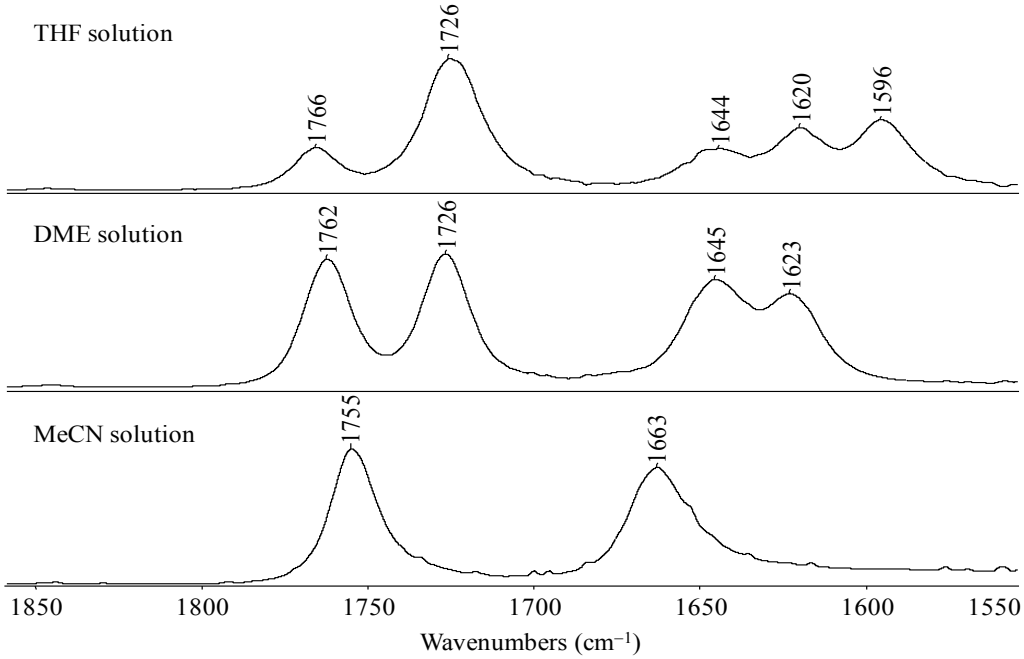

Figure 3: FT-IR spectra (1850 – 1550 cm^{-1}) of **3-Mo** showing the characteristic ν_{CO} absorption bands in different solvents.

The IR spectrum of **3-Mo** in the solid-state displays only two ν_{CO} absorption bands at 1676 (vs) and 1576 (s) cm^{-1}, but surprisingly that of **3-W** displays four ν_{CO} absorption bands at 1709 (w, sh), 1671 (s), 1586 (w) and 1528 (vs) cm^{-1}. The $^{31}P\{^{1}H\}$ NMR spectrum of **3-Mo** and **3-W**

displays a characteristic singlet signal (δ = 15.8 ppm (**3-Mo**); δ = –11.0 ppm (^1J(W,P) = 397.5 Hz) (**3-W**)), which appears at higher field compared to that of the corresponding starting material **1-Mo** (δ = 33.6 ppm) and **1-W** (δ = –1.9 ppm (^1J(W, P) = 63 Hz)). Interestingly, the ^1J(W, P) coupling constant of **3-W** appears significantly higher than that found in **1-W**, indicating the higher s-character of the hybride orbital used by the phosphorus atom for the W–P bond of the metalate **3-W**.

Yellow plates of **3-Mo**·2.5($C_4H_{10}O_2$), suitable for single crystal X-ray diffraction, were grown upon cooling a saturated solution of **3-Mo** in DME at –35 °C. The molecular structure displays a distorted octahedral arrangement of ligands around the Mo center, with three pyrazolyl groups of the Tp' ligand bonded in a facial arrangement (Figure 4). In solid state the sodium cations, which are coordinated with two molecules of DME, are also in close contact with the metalates via complexation with the carbonyl carbon atoms, as demonstrated by the very short Na–O_{CO} distances (Na–O1 2.497 (4) Å, Na–O2 2.478 (3) Å). The most interesting bonding feature of **3-Mo** is the very short Mo–P bond (2.428 (1) Å) compared to that of the Mo(II) complex **1-Mo** (d(Mo–P): 2.4806 (9) Å). This shortening can be rationalized by the higher Mo–P bond order resulting from the increased back donation from the electron rich Mo(0) d-orbital into the π-accepting orbitals of the PMe_3 ligand, which are mainly σ*(P–C) in character.[59]

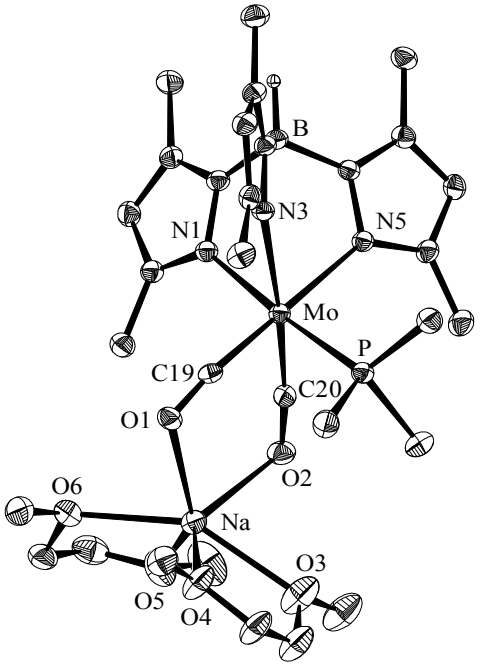

Figure 4. DIAMOND plot of the molecular structure of **3-Mo**·2($C_4H_{10}O_2$) in the crystal lattice of **3-Mo**·2.5($C_4H_{10}O_2$) at 123(2) K. Thermal ellipsoids are set at 30 % electronic probability. Hydrogen atoms

(except the B-bonded H atom) were omitted for clarity. Selected bond lengths [Å] and angles [°]: Mo-P 2.428 (1), Mo-N1 2.251 (3), Mo-N3 2.356 (3), Mo-N5 2.344 (3), Mo-C19 1.892 (4), Mo-C20 1.892 (4), Na-O1 2.497 (4), Na-O2 2.478 (3); P-Mo-N1 175.88 (9), P-Mo-N3 97.01 (8), P-Mo-N5 97.54 (8), P-Mo-C19 85.4 (1), P-Mo-C20 86.5 (1).

Slow addition of the sodium naphthalenide solution to the THF solution of **1-Mo** revealed that the two-electron reduction of **1-Mo** to give **3-Mo** proceeds via the 17VE radical [Tp'Mo(CO)$_2$(PMe$_3$)] (**2-Mo**), which could be detected by IR spectroscopy. Therefore, we assumed that reduction of **1-Mo** with one equivalent of a suitable reducing agent could selectively lead to the radical **2-Mo**. Indeed, one-electron reduction of **1-Mo** by one equivalent of Na-sand in the presence of a catalytic amount of naphthalene in THF leads slowly but selectively to the radical **2-Mo**, which could be isolated after workup and crystallization as an analytically pure, light yellow solid in 56% yield (Scheme 2). The light yellow solid is highly air-sensitive, turning immediately brown upon exposure to air, and is well soluble in organic solvents such as THF, toluene and *n*-pentane.

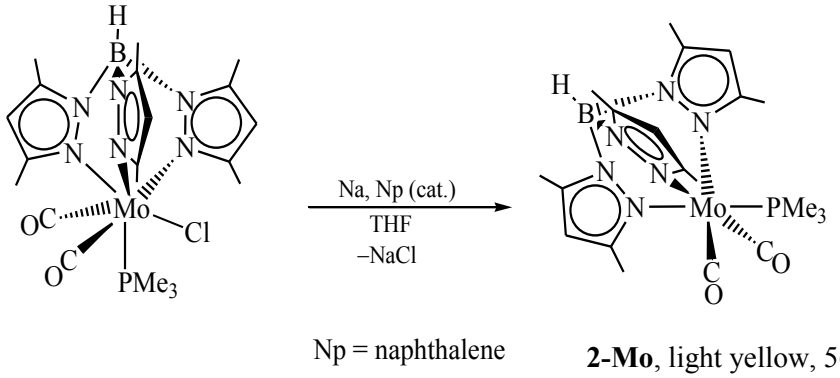

Scheme 2. Synthesis of the 17VE radical **2-Mo** upon one-electron reduction of **1-Mo**.

The molecular structure of the radical **2-Mo** was determined by single crystal X-ray diffraction, and the composition was confirmed by elemental analysis. It was further characterized by solid state and solution IR spectroscopy. The solid state IR spectrum of the Mo(I) radical **2-Mo** displays two ν_{CO} absorption bands (ν_{CO}: 1883 (vs) and 1737 (s) cm^{-1}), which appear in-between those of the Mo(II) complex **1-Mo** (ν_{CO}: 1930 (s) and 1825 (vs) cm^{-1}), and the Mo(0) metalate salt **3-Mo** (ν_{CO}: 1676 (vs) and 1576 (s) cm^{-1}). This observation is in accordance with the increased electron density at the Mo center on going from the Mo(II) complex **1-Mo** to

the Mo(0) complex **3-Mo**, leading to increased Mo(d)→π*(CO) back donation. As expected, the IR spectrum of **2-Mo** in THF also displays two ν_{CO} bands at 1893 (vs) and 1756 (s) cm^{-1}.

Single crystal X-ray diffraction analysis of orange crystals of **2-Mo**·(C_7H_8), obtained upon cooling a toluene/*n*-pentane mixture of **2-Mo** at +5 °C, revealed a distorted octahedral arrangement of ligands around the molybdenum center (Figure 5). The most striking structural differences between the octahedral **2-Mo** and the anion in **3-Mo**, where in both cases the Mo center features a distorted octahedral geometry, are those of the Mo–P and the Mo–C_{CO} bond lengths. In **2-Mo**, the Mo–P bond (2.506 (1) [2.498 (1)] Å) and the Mo–C_{CO} bonds (Mo1-C19: 1.944 (4) [1.961 (4)] Å; Mo1-C20: 1.949 (4) [1.958 (4)] Å) are longer compared to that in **3-Mo** (Mo–P: 2.428 (1) Å; Mo–C19 1.892 (4) Å, Mo–C20 1.892 (4) Å). This suggest a weaker Mo(d)→π*(CO) back donation in **2-Mo** than in **3-Mo**.

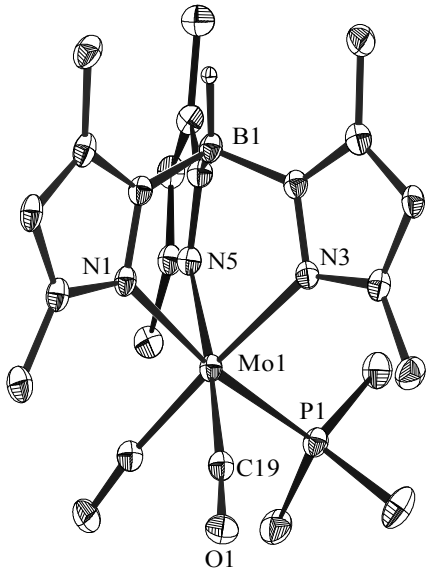

Figure 5. DIAMOND plot of the molecular structure of **2-Mo** in the crystal lattice of **2-Mo**·(C_7H_8) at 123(2) K. Thermal ellipsoids are set at 30% probability. Hydrogen atoms (except the B-bonded H atom) were omitted for clarity. Selected bond lengths [Å] and bond angles [°] (bond lengths and bond angles in square brackets are of the second independent molecule of **2-Mo**·(C_7H_8)): Mo1-P1 2.506 (1) [2.498 (1)], Mo1-N1 2.195 (3) [2.183 (3)], Mo1-N3 2.277 (3) [2.279 (4)], Mo1-N5 2.257 (3) [2.284 (3)], Mo1-C19 1.944 (4) [1.961 (4)], Mo1-C20 1.949 (4) [1.958 (4)], N1-Mo1-P1 169.7 (1) [173.44 (9)], N3-Mo1-P1 93.52 (9) [93.59 (9)], N5-Mo1-P1 90.83 (9) [94.61 (9)], P1-Mo1-C19 89.7 (1) [90.5 (1)], P1-Mo1-C20 87.6 (1) [86.6 (1)].

2.1.2 Access to the zwitterionic silylidene complexes of Mo and W

In the previous chapter the synthesis and characterization of the scorpionate group 6 metalates were reported. In this section, the reaction of these highly nucleophilic metalates with suitable Si(II) species will be presented, which provides an access to zwitterionic silylidene complexes.

In order to obtain the target silylidene complexes, NHC-stabilized arylchlorosilylenes $SiCl(C_6H_3\text{-}2,6\text{-}R_2)(IMe_4)$ (R = Mes, Trip; IMe_4 = C[N(Me)C(Me)]$_2$))[33, 107] were first selected as Si(II) precursors. But, despite several attempts under several reaction conditions,[3] the reactions between the scorpionate metalates **3-Mo**/**3-W** and the NHC-stabilized arylchlorosilylenes were unselective. Therefore, we decided to switch to other suitable Si(II) compounds, which can be employed for the envisaged synthesis. Recent studies have shown that 1,2-dibromodisilenes (*E*)-R(Br)Si=Si(Br)R (R = bulky organic groups) can act as a source of bromosilylenes Si(Br)R.[108-110] Thus, we decided to test the feasibility of using (*E*)-Tbb(Br)Si=Si(Br)Tbb (Tbb = C_6H_2-2,6-[$CH(SiMe_3)_2$]$_2$-4-*t*Bu) as a precursor for the anticipated synthesis.[110] Indeed, heating of a mixture of one equiv. of **3-Mo**/**3-W** and half equiv. of (*E*)-Tbb(Br)Si=Si(Br)Tbb in the presence of one equivalent of 4-dimethylaminopyridine (4-dmap) in toluene at 80 – 100 °C was accompanied by a fast color change from orange to brown. Monitoring of both reactions by IR spectroscopy revealed the selective formation of dicarbonyl complexes, which were isolated as brown solids in 72 – 74% yields and characterized as the zwitterionic silylidene complexes [Tp'$(CO)_2$M=Si(4-dmap)Tbb] (**6-Mo**, M = Mo; **6-W**, M = W) (Scheme 3). Notably, these complexes can also be considered as 4-dmap-stabilized silylidyne complexes. The silylidene compounds **6-Mo** and **6-W** are highly air-sensitive and decolorize instantaneously upon exposure to air. Compounds are well soluble in THF, fluorobenzene, Et_2O, moderately soluble in toluene, and insoluble in common aliphatic solvents. The silylidene compounds are thermally quite stable, but loose 4-dmap upon heating under vacuum in a sealed tube at 170 °C (**6-Mo**) and 161 – 163 °C (**6-W**) to give the corresponding silylidyne complexes [Tp'$(CO)_2$M≡Si–Tbb] (**7-Mo**, M = Mo; **7-W**, M = W).

---

3 Reactions were carried out in different solvents such as THF, fluorobenzene, chlorobenzene, DME, xylene starting from room temperature to boiling temperature of the corresponding solvents. Furthermore, some reactions were also carried out in the presence of LiBr or LiI. All the reactions were followed by IR and ^{1}H NMR spectroscopy, which revealed the formation of a mixture of the 17VE radical **2-Mo** and **2-W** and some unknown compounds. Several attempts to isolate these unknown complexes in pure form were unsuccessful.

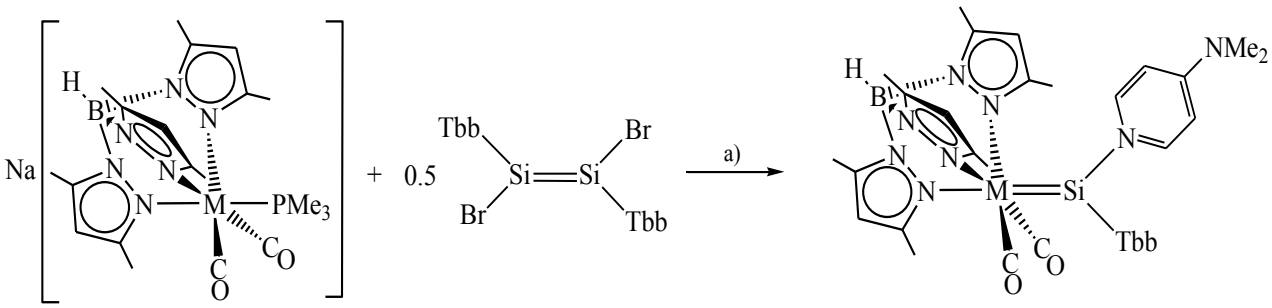

6-Mo, brown solid, 72%

6-W, brown solid, 74%

Scheme 3. Synthesis of zwitterionic silylidene complexes; a) 4-dimethylaminopyridine (4-dmap), toluene, –NaBr, –PMe_3. Formal charges are omitted for clarity.

The silylidene compounds **6-Mo** and **6-W** were fully characterized by single crystal X-ray diffraction, elemental analysis, IR and multinuclear NMR spectroscopy. Both compounds display similar structural and spectroscopic properties. The molecular structures of **6-Mo** and the solvate **6-W**·5(C_4H_8O) were determined by single crystal X-ray diffraction analysis and reveal a distorted octahedral environment around the metal centers with the silylidene ligand in *trans*-orientation to one of the pyrazolyl groups of the Tp' ligand (N3-Mo-Si1 170.7(2)°; N7-W-S1 172.8(1)°) (Figure 6).[4] The very short M–Si bond lengths found in **6-Mo** and **6-W** (Mo–Si1 2.337(3) [2.328(3)] Å, W–Si1 2.338(2) Å) are comparable with rare examples of molybdenum and tungsten silylidene complexes with a three-coordinated silicon center (*d*(Mo=Si): 2.2853(8)-2.3872(7) Å;[29, 30, 33, 111-113] *d*(W=Si) = 2.354(3)-2.420(1) Å)[114-118]. Notably, the trigonal planar coordinated silicon centers (sum of angles at Si1 = 359.5° [359.7°] (**6-Mo**), 359.2° (**6-W**)) of the silylidene complexes exhibit a widened M-Si1-C_{Tbb} angle (155.1(3)° [153.7(3)°] (**6-Mo**), 150.7(2)° (**6-W**)) and a narrow C1-Si1-N1 angle (**6-Mo**: 92.5(4)° [93.7(5)°], **6-W**: 95.2(2)°). This situation can be rationalized by an increased s-character of the hybrid orbital used by the Si atom for the M–Si double bond and an increased p-character for the Si1–N1 and Si1–C1 bonds resulting from the decreased sp^2 hybridization of the Si1 center. This is also evidenced by a natural bond orbital (NBO) analysis of **6-W**, which revealed the use of an $sp^{0.74}$ hybrid orbital instead of sp^2 hybrid orbital from the silicon atom for the W–Si1 σ-bond.[5] The quite elongated Si1–N1 bond (**6-Mo**: 1.929(8) Å [1.931(8) Å] **6-W**: 1.928(5) Å) of **6-Mo** and **6-W**, which also

4 The DIAMOND plot of the compound **6-Mo** is not depicted as it shows similar structural motif as **6-W**, but selected bond lengths [Å] and angles [°] are presented in the brackets.

5 The NBO analysis was carried out at the RIJCOSX-B97-D3/TZVP level of theory by Dr. G. Schnakenburg.

compares well with the Si–N bond length (1.913(7) Å) of the tungsten silylidene complex [Cp*(CO)$_2$(H)W=Si(H)(4-dmap){C(SiMe$_3$)$_3$}] containing a tetra-coordinate silicon atom,[119] suggests a rather weak coordination of the 4-dmap substituent at the silicon center.

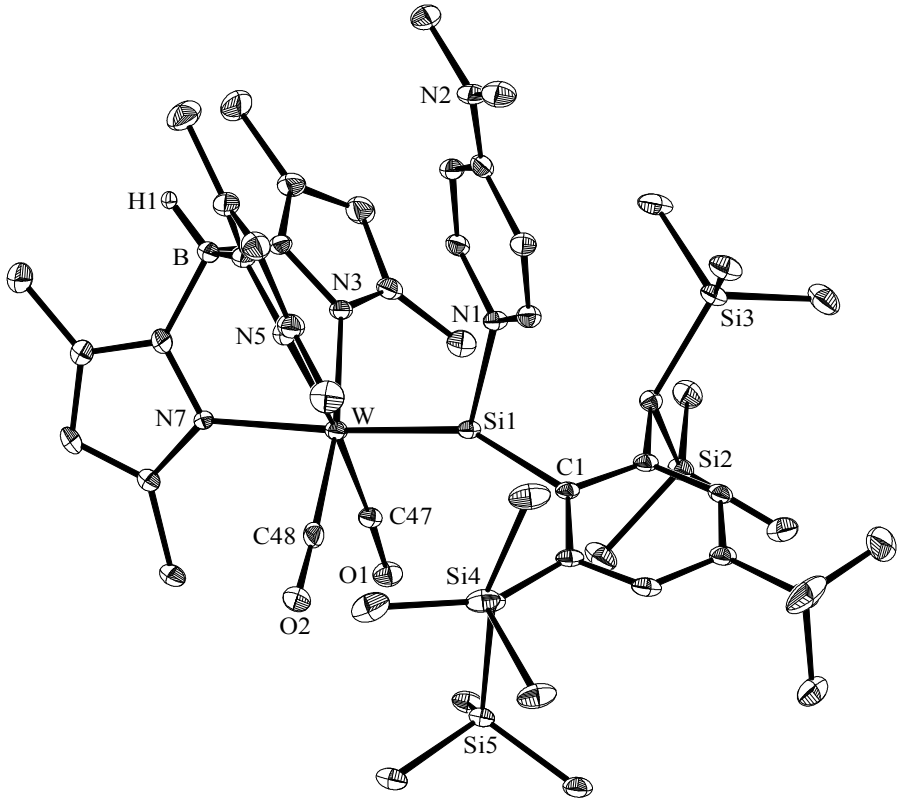

Figure 6. DIAMOND plot of the molecular structure of complex **6-W** in the crystal lattice of the THF solvate **6-W**·5(C_4H_8O). The thermal ellipsoids represent 30% of the electronic probability at 100(2) K. Hydrogen atoms (except B-H) and the solvent molecules are omitted for clarity. Selected bond lengths [Å] and angles [°] {values in braces are given for complex **6-Mo** (values in square brackets correspond to the second independent molecule in the unit cell)}: W-Si1 2.338(2) {2.337(3) [2.328(3)]}, W-C47 1.942(6) {1.942(8) [1.93(1)]}, W-C48 1.936(6) {1.93(1) [1.93(1)]}, Si1-N1 1.928(5) {1.929(8) [1.931(8)]}, Si1-C1 1.904(6) {1.902(9) [1.90(1)]}, W-N3 2.284(5) {2.282(8) [2.301(8)]}, W-N5 2.282(5) {2.320(6) [2.300(9)]}, W-N7 2.238(5) {2.282(9) [2.252(9)]}; C1-Si1-W 150.7(2) {155.1(3) [153.7(3)]}, N1-Si1-W 113.3(2) {111.9(3) [112.3(3)]}, C1-Si1-N1 95.2(2) {92.5(4) [93.7(5)]}, N3-W-Si1 102.0(1) {99.6(2) [91.6(2)]}, N5-W-Si1 93.2(1) {90.6(2) [100.3(3)]}, N7-W-Si1 172.8(1) {170.7(2) [171.0(2)]}.

The solid-state structures of the silylidene complexes were further supported by solution NMR spectroscopy. The ^{1}H and ^{13}C{^{1}H} NMR spectra of the silylidene complexes suggest overall C_s-symmetric structures in solution and show broad signals at ambient temperature. Furthermore, a

variable temperature ^{1}H NMR spectroscopic study (298 – 193 K, THF-d_8) for **6-W** revealed an interesting equilibrium process arising from the partial dissociation of the 4-dmap substituent from the Si1 center to form the corresponding silylidyne complex [Tp'(CO)$_2$W≡Si–Tbb] (**7-W**). This is evidenced by the appearance of a single set of averaged signals at ambient temperature (Figure 7), due to a fast equilibrium with respect to the NMR timescale. Upon lowering the temperature from 298 K to 193 K, the equilibrium shifts towards the silylidene complex (**6-W**) and the spectrum shows a single set of sharp signals for the silylidene complex (**6-W**) (Figure 7). All the three components, the silylidene (**6-W**), silylidyne (**7-W**) and free 4-dmap were never observed by ^{1}H NMR spectroscopy. This prevents the determination of the equilibrium constant (K_{eq}) and the Gibbs free energy (ΔG^0) of the dissociation equilibrium by NMR spectroscopy. The dissociation equilibrium was further proved by the addition of free 4-dmap into a solution of the silylidyne complex (**7-W**) and subsequent investigation of those mixtures by ^{1}H NMR spectroscopy, which also revealed a single set of averaged signals. The ^{29}Si{^{1}H} NMR spectrum of the silylidene complexes in THF-d_8 shows a distinctive low-field shifted signal for the silylidene ligands at δ = 212.1 ppm (**6-Mo**) and 201.5 ppm (**6-W**), which is broad at ambient temperature. But, the ^{29}Si{^{1}H} NMR spectrum of **6-W** at 208 K in THF-d_8 revealed a sharp singlet signal for the silylidene ligand at δ = 202.6 ppm, which is accompanied by a pair of tungsten satellite with a $^{1}J_{W,Si}$ coupling constant of 298 Hz.

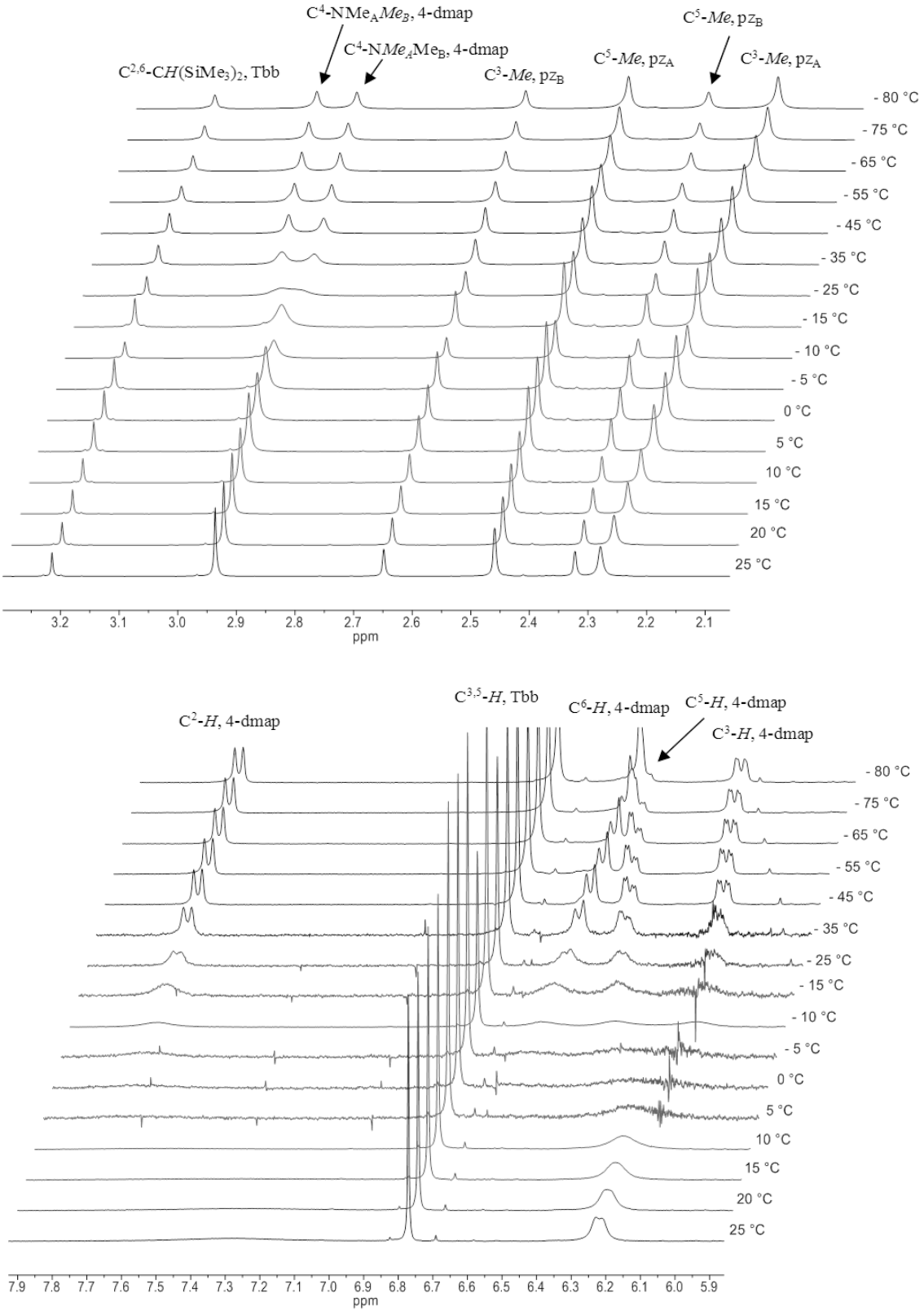

Figure 7. Expanded sections (δ = 2.05 – 3.30 ppm, top; δ = 5.85 – 7.95 ppm, bottom) of the ^{1}H NMR spectrum (300.1 MHz) of **6-W** in THF-d_8 between 298 K and −193 K.

The solution IR spectrum of the silylidene complexes indeed shows the presence of the corresponding silylidyne complexes, resulting from the dissociation of the 4-dmap substituent from the silicon center. For example, the IR spectrum of the silylidene complexes in THF displays two additional carbonyl absorption bands at higher frequency (**7-Mo**: 1912 (s) and 1836 (vs) cm^{-1}; **7-W**: 1901 (s) and 1822 (vs) cm^{-1}), corresponding to the silylidyne complexes, along with two additional bands of higher intensity for the silylidene complexes (**6-Mo**: 1862 (vs) and 1779 (vs) cm^{-1}; **6-W**: 1852 (vs) and 1768 (vs) cm^{-1}). In contrast to NMR spectroscopy, the appearance of the silylidyne complexes along with the silylidene complexes in the IR spectra allows us to carry out a quantitative analysis of the dissociation equilibrium following the Beer-Lambert Law.[120] The equation for the dissociative equilibrium is depicted in Scheme 4.

$$\underset{\textbf{ML}}{Tp'(CO)_2M{=}Si(4\text{-}dmap)Tbb} \underset{k_{-1}}{\overset{k_1}{\rightleftharpoons}} \underset{\textbf{M}}{Tp'(CO)_2M{\equiv}Si(Tbb)} + \underset{\textbf{L}}{4\text{-}dmap}$$

Scheme 4. Dissociation equilibrium among the silylidene complex (ML), the silylidyne complex (M) and free 4-dmap (L).

The equilibrium constant K_{eq} for the dissociative process is defined as:

$$K_{eq} = \frac{[M][L]}{[ML]} \qquad (1)$$

Since dissociation of the silylidene complex leads to the formation of an equimolar amount of the silylidyne complex (M) and 4-dmap (L), the concentrations of the silylidyne complex and free 4-dmap will be equal in solution. Furthermore, the initial concentration of the silylidene complex ($[ML_0]$) will be diminished by the amount of the formed silylidyne complex (M). Therefore K_{eq} is given by equation (2):

$$K_{eq} = \frac{[M]^2}{[ML]} = \frac{[M]^2}{[ML_0]-[M]} \qquad (2)$$

According to the Beer-Lambert law the concentration of the silylidyne complex ([M]) can be expressed using the absorbance (A_M), the molar attenuation coefficient (ε_M) and the path length of the IR cell (d), and replacing these terms in equation (2) leads to equation (3):

$$K_{eq} = \frac{\left(\frac{A_M}{\varepsilon_M \cdot d}\right)^2}{[ML_0]-\left(\frac{A_M}{\varepsilon_M \cdot d}\right)} \qquad (3)$$

The molar attenuation coefficient (ε_M) could be easily obtained from Beer-Lambert law by measuring a solution IR spectrum of known concentration of the pure silylidyne complex. For example, the IR spectrum of the silylidyne **7-W** in THF with a concentration of 0.0187 molL^{-1} , measured in an IR cell of 0.02 cm path length shows an absorbance of 1.132 (from the peak at 1901 cm^{-1}). Using this value and the cell path length, the molar attenuation coefficient ($\varepsilon_M = A_{M(pure)} / ([M_{(pure)}].d)$) of **7-W** was calculated to be 2873 L.mol^{-1}.cm^{-1}.

In order to determine the equilibrium constant (K_{eq}) at room temperature, a solution IR spectrum of **6-W** at the initial concentration ([ML_0]) of 0.00414 mol.L^{-1} was measured in THF (Figure 8). From this spectrum, the relative concentration of the resulting silylidyne complex was obtained by its absorbance at ν_{CO} = 1901 cm^{-1} and found to be 0.037. Using this values, the equilibrium constant (K_{eq}) for the dissociative equilibrium was calculated to be 1.186 × 10^{-4} mol.L^{-1}.

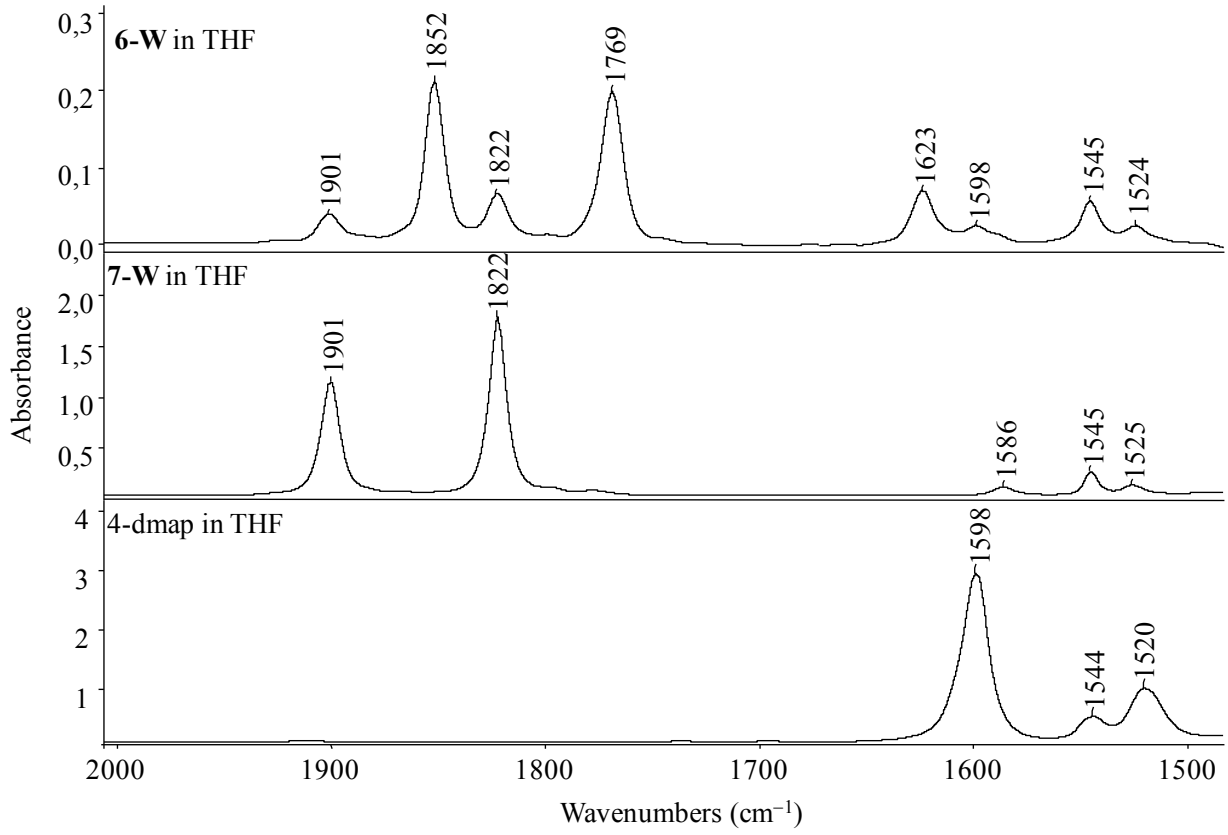

Figure 8. FT-IR spectra of the silylidene complex **6-W** in THF showing the formation of the silylidyne complex **7-W** by dissociation of 4-dmap ([ML_0] = 0.00414 mol.L^{-1}) (top), the silylidyne complex **7-W** in THF (middle) and pure 4-dmap in THF (bottom).

At equilibrium, the Gibbs dissociation energy (ΔG^0) at room temperature (298 K) could be obtained using equation (4).

$$(\Delta G^0) = - RT\ln K_{eq} \quad (4)$$

Using the values K_{eq} = 1.186 × 10^{-4} mol.L^{-1} and RT = 2.478 kJ mol^{-1} (at T = 298 K), the Gibbs dissociation energy (ΔG^0) was found to be 22.4 kJ mol^{-1}. Experimentally obtained values were further supported by quantum chemical calculations, which also show a rather low dissociation energy (D(0)°) of the 4-dmap ligand of 83 $kJmol^{-1}$, which further reduces to a Gibbs dissociation energy of $\Delta G°$ = 22 $kJmol^{-1}$ due to the entropy gain. Therefore, this gives an explanation for the elongated Si1–N1 bond in the silylidene complexes.

2.1.3 Access to the silylidyne complexes of Mo and W

Following the successful isolation of the zwitterionic silylidene complexes **6-Mo** and **6-W**, my next target was to synthesize the corresponding silylidyne complexes of the general formula [Tp'$(CO)_2$M≡Si–Tbb] (M = Mo, W) by abstraction of the 4-dmap base from the zwitterionic silylidene complexes. As shown in the previous chapter, the 4-dmap base is weakly bonded to the silicon atom, and dissociates readily in solution thus leading to an equilibrium between the zwitterionic silylidene and the corresponding silylidyne complex. This suggested that a suitable Lewis acid could trap 4-dmap as a acid-base adduct and shift the equilibrium towards the silylidyne complex. Indeed, treatment of diethyl ether solutions of the silylidene complex **6-Mo** and **6-W** with one equivalent of the borane $B(C_6F_5)_3$ at ambient temperature selectively afforded the silylidyne complexes [Tp'$(CO)_2$M≡Si–Tbb] (**7-Mo**, M = Mo; **7-W**, M = W). Compounds **7-Mo** and **7-W** were isolated after workup as analytically pure, extremely air-sensitive, thermally robust (m.p. 253 °C (dec.) for **7-Mo**, and 252 °C (dec.) for **7-W**), reddish-orange to red solids in quite good yields (Scheme 5). After the successful isolation of the silylidyne complexes via the zwitterionic silylidene complexes, a direct access to **7-Mo** and **7-W** was attempted. It was recently observed that in the presence of a Lewis base, the disilene (*E*)-Tbb(Br)Si=Si(Br)Tbb serves as a source of Si(Br)Tbb.[121] Therefore, I decided to react the strongly nucleophilic metalates **3-Mo** and **3-W** with the disilene (*E*)-Tbb(Br)Si=Si(Br)Tbb in the absence of 4-dmap. Indeed, heating of a mixture of (*E*)-Tbb(Br)Si=Si(Br)Tbb and the metalate salts **3-Mo** or **3-W** in boiling toluene resulted in the selective formation of the corresponding silylidyne complexes [Tp'$(CO)_2$M≡Si–Tbb] (**7-Mo** (M = Mo), **7-W** (M = W)). Both compounds were isolated after workup as analytically pure solids in very good yields (**7-Mo**: 67%, **7-W**: 66%). The silylidyne

complexes **7-Mo** and **7-W** are very well soluble in THF, toluene or Et_2O and moderately soluble in common aliphatic solvents.

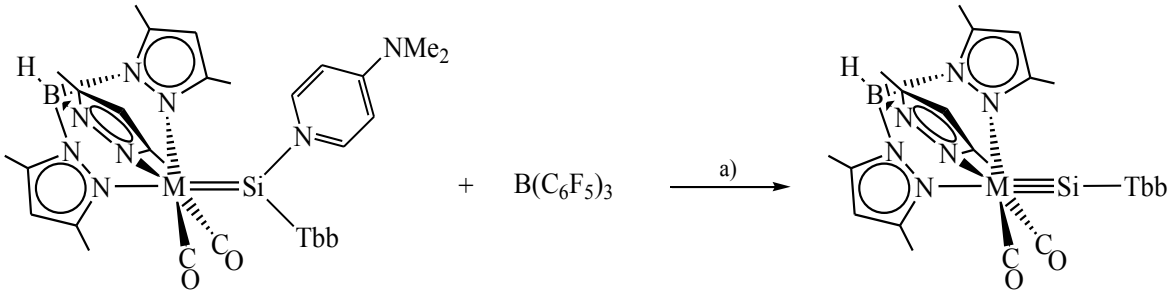

7-Mo, reddish-orange solid, 59%

7-W, red solid, 67%

Scheme 5. Synthesis of the silylidyne complexes **7-Mo** and **7-W**. a) Et_2O, r.t., –(4-dmap·$B(C_6F_5)_3$). Formal charges are omitted for clarity.

The silylidyne complexes were comprehensively characterized by single crystal X-ray diffraction, elemental analysis, IR and multinuclear NMR spectroscopy. Compounds **7-Mo** and **7-W** are isostructural with similar bonding features. Therefore, only the structure of **7-W** will be discussed. Although, while the work was in progress a tungsten silylidyne of the formula [Cp*$(CO)_2$W≡Si(C$(SiMe_3)_3$)] was reported by Tobita and coworkers, the silylidyne complex **7-W** is the first example of a structurally characterized neutral tungsten silylidyne prepared in this group.[49] The molecular structure of **7-W** reveal a distorted octahedral coordination sphere around the tungsten center with a terminal silylidyne ligand (Si–Tbb) situated in a *trans*-orientation to one of the pyrazolyl groups of the Tp' ligand, as indicated by the Si1-W-N1 bond angle of 168.27(7)° (Figure 9). Conspicuously, in contrast to the previously reported three-legged piano-stool silylidyne complexes, **7-Mo** and **7-W** are the first examples of silylidyne complexes featuring an octahedrally coordinated metal center. Compound **7-W** features a short W−Si1 bond with a length of 2.2706(8) Å, which is almost 7 pm shorter than the W–Si double bond of **6-W** (W–Si 2.338(2) Å) and is also much shorter (3.6% − 6.6%) than the W–Si double bonds of presently known silylidene complexes.[114-118, 122-127] Notably, the W≡Si bond of **7-W** is *ca.* 4 pm longer than that in the recently published piano-stool silylidyne complex [Cp*$(CO)_2$W≡Si(C$(SiMe_3)_3$)] (W–Si 2.2297(9) Å) and also *ca.* 5 pm longer than that in the cationic tungsten silylidyne complex [(Cp*)$(CO)_2$W≡Si(SIdipp)][B{C_6H_3-3,5-$(CF_3)_2$}$_4$] (*d*(W-Si) = (2.224(3) Å) prepared by Filippou and coworkers.[49, 128]

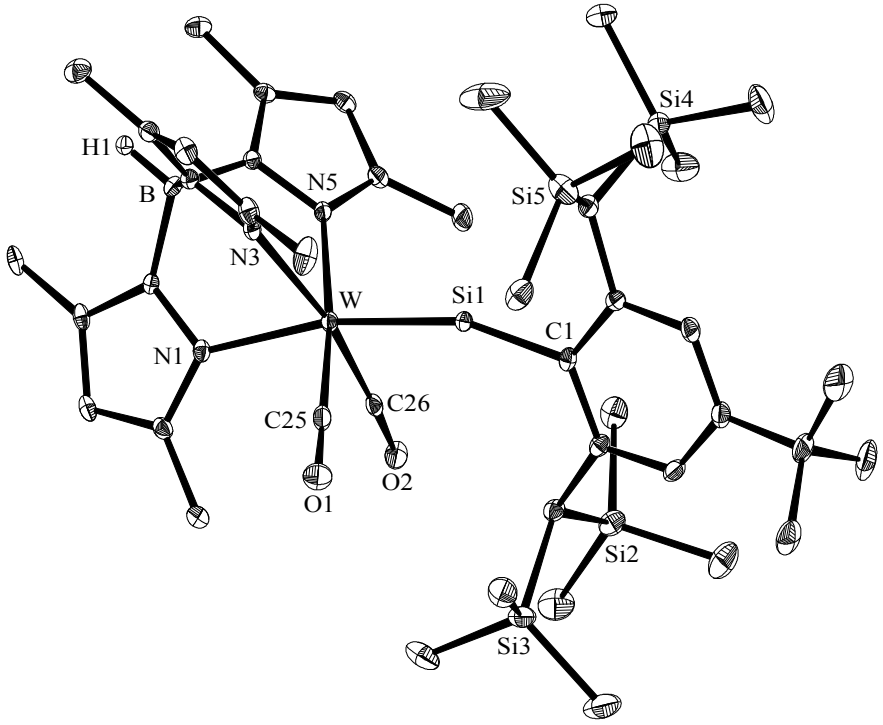

Figure 9. DIAMOND plot of the molecular structure of complex **7-W** in the crystal lattice of the benzene solvate **7-W**·1.5(C_6H_6). The thermal ellipsoids represent 30% of the electronic probability at 100(2) K. The solvent molecules and the hydrogen atoms (except B-H) are omitted for clarity. Selected bond lengths [Å] and angles [°] (bond lengths and bond angles of **7-Mo** are given in the squre brackets): W-Si1 2.2706(8) [2.2614(9)], Si1-C1 1.864(3) [1.861(3)], W-C25 1.968(4) [1.956(4)], W-C26 1.958(3) [1.950(4)], W-N1 2.226(2) [2.233(2)], W-N3 2.242(2) [2.249(3)], W-N5 2.237(2) [2.255(3)]; W-Si1-C1 161.7(1) [160.8(1)], C25-W-Si1 81.19(9) [80.3(1)], C26-W-Si1 82.31(9) [82.24(9)], N1-W-Si1 168.27(7) [167.19(7)], N3-W-Si1 110.24(6) [111.01(7)], N5-W-Si1 104.77(7) [105.13(7)].

Apparently, a general tendency of elongated M≡Ge bonds (M = Mo, W) was also observed in octahedral germylidyne complexes compared to those of three-legged piano-stool germylidyne complexes.[27, 28, 34, 37, 39, 40, 48] This M≡E bond (M = Mo, W; E = Si, Ge) elongation is attributed to the increased steric congestion at the metal center, and the influence of the pyrazolyl group *trans* to the tetrylidyne ligand. In addition to the short W–Si1 bond, the very wide W-Si1-C1 angle (161.7(1)°) in **7-W** confirms the presence of a triple bond between the W and Si1 atoms. The W-Si1-C1 array in **7-W** appears to deviate even more from linearity compared to those in the previously reported silylidyne complexes ([$Cp(CO)_2Mo{\equiv}Si(C_6H_3$-2,6-$Trip_2)$] 173.49(8)°; [$Cp^*(CO)_2W{\equiv}Si(C(SiMe_3)_3)$] 173.71(11)° and [$(Cp^*)(CO)_2W{\equiv}Si(SIdipp)$][$B\{C_6H_3$-3,5-$(CF_3)_2\}_4$] 172.1(3)°).[30, 33, 49, 128] An explanation for this higher bending is provided by the DFT

analysis of the model compound [Tp(CO)$_2$W≡SiH] (**7-W-H**). Surprisingly, quantum chemical calculations on **7-W-H** at the RIJCOSX-B97-D3/TZVP level of theory leads to a global minimum structure **7-W-H$_{min}$** on the potential energy hypersurface with a W-Si-H bending angle of 148.8° (Figure 10, Table 1). Furthermore, the constrained geometry transition state **7-W-H$_{lin}$** with a linearly coordinated silicon atom (∠W-Si-H = 180.0°) appears to be higher in energy (11 kJmol^{-1}) compared to **7-W-H$_{min}$**. Notably, the W–Si bond length in **7-W-H$_{min}$** (2.261 Å) was found slightly longer than that in **7-W-H$_{lin}$** (2.242 Å) and compares well with the experimental value of **7-W** (2.2706(8) Å) (Table 1).

$\Delta E = 0$ kJmol^{-1} $\Delta E = 11$ kJmol^{-1}

Figure 10. Calculated (RIJCOSX-B97-D3/TZVP) global minimum structure (left, **7-W-H$_{min}$**) and the transition state with constrained linear coordination around the Si atom (right, **7-W-H$_{lin}$**) of [Tp(CO)$_2$W≡SiH] (**7-W-H**).

Table 1. Comparison of the selected experimental and calculated[a)] bonding parameters of **7-W**, **7-W-H$_{min}$**, and **7-W-H$_{lin}$**

Compound	W−Si [pm]	Si−R [pm]	W−CO [pm]	W-N$_{trans}$ [pm]	W-N$_{cis}$ [pm]	W-Si-R [°]	CO-W-Si [°]
7-W	227.06(8)	186.4(3)	196.8(4) / 195.8(3)	222.6(2)	224.2(2) / 223.7(2)	161.7(1)	81.19(9) / 82.31(9)
7-W-H$_{min}$	226.1	150.7	196.8 / 196.8	220.6	223.0 / 222.9	148.8	81.6 / 81.7
7-W-H$_{lin}$	224.2	150.8	197.6 / 197.6	223.3	224.1 / 224.1	180.0	88.1 / 88.1

a) RIJCOSX-B97-D3/TZVP

A look at the Kohn-Sham frontier orbitals of **7-W-H$_{lin}$** shows that HOMO–9 is the σ-bonding orbital, HOMO–1 and HOMO–2 are the two orthogonal π-orbitals and the corresponding π^*-orbitals are the LUMO and LUMO+1, respectively (Figure 11).

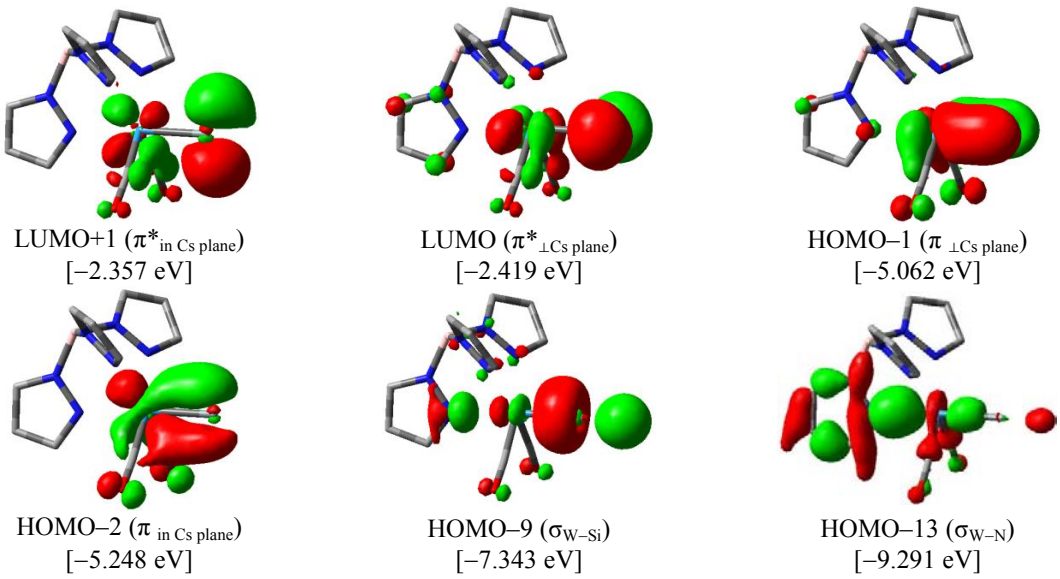

Figure 11. Selected Kohn-Sham frontier orbitals of **7-W-H$_{lin}$** calculated at RIJCOSX-B97-D3/TZVP level of theory; isosurface value correspond to 0.04 e bohr^{-3}.

The reason for the bending at the silicon atom in **7-W** and **7-W-H$_{min}$** can be attributed to the electronic effect as predicted from the Extended Transition State Coupled with Natural Orbital for Chemical Valence (ETS-NOCV) analysis carried out at the BP86/TZ2P level of theory. Upon decrease of the W-Si-R bond angle (R = H in **7-W-H**) from 180.0° (in **7-W-H$_{lin}$**) to 148.8° (in **7-W-H$_{min}$**) the energy of the HOMO–9, which is the W–Si σ bonding MO, rises due to the weaker overlap between W and Si atoms. Along with this, the HOMO–13, which is the N_{trans}–W σ bonding MO, is lowered in energy due to the weaker *trans*-effect of the silylidyne ligand. Both effects are almost equal in energy. The most pronounced energetic stabilization upon bending of the W-Si-R bond occurs at the HOMO–2, which is the in-plane π-bonding orbital with some contribution of W–C_{CO} π-backbonding. This orbital rehybridises to get higher lone-pair character at the silicon atom (Figure 12). This process lowers the positive partial charge at the Si atom and slightly shortens the W–C_{CO} bonds. The overall energy change, as well as the individual change of the orbitals energy is shown in a Walsh diagram. The relative energy is minimised at a W-Si-H bond angle of 148.8° (Table 3, Figure 13). In **7-W**, this effect is weakened due to the high steric demand of the Tbb substituent, which hinders a pronounced bending at the Si center.

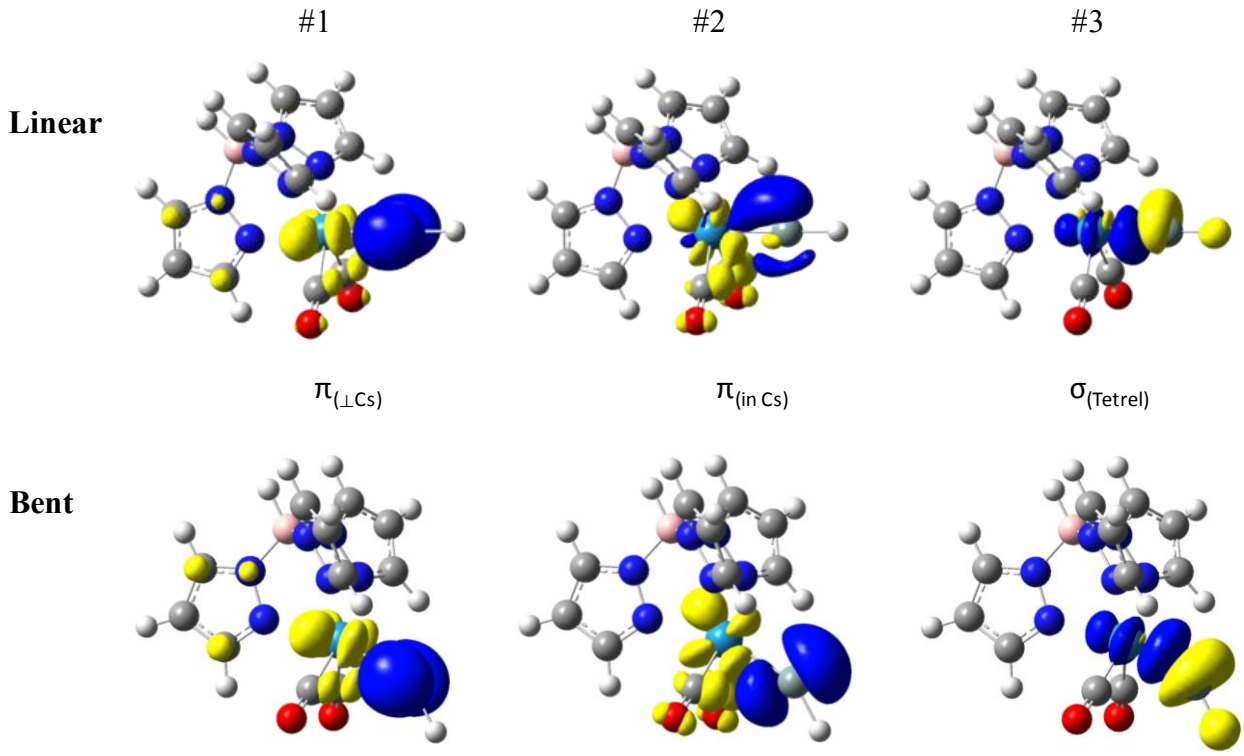

Figure 12. Deformation density contributions of the linear (**7-W-H$_{lin}$**) and bent (**7-W-H$_{min}$**) structures obtained by ETS-NOCV analysis at BP86/TZ2P level of theory. The blue and yellow colors correspond to the accumulation and depletion of electron density.

Table 2. ETS-NOCV bond-energy decomposition results of the W≡Si bond of **7-W-H**.

Angle W-Si-H [°]	ΔE_{Pauli} [kJmol^{-1}]	ΔE_{orb} [kJmol^{-1}]	ΔE_{elstat} [kJmol^{-1}]	ΔE_{int} [kJmol^{-1}]	NOCV-ν [e$^-$] #1	NOCV-ν [e$^-$] #2	NOCV-ν [e$^-$] #3	Orb-Int-energie #1	Orb-Int-energie #2	Orb-Int-energie #3
180,0	604,5	-865,7	-749,7	-1010,9	1,01	0,96	0,57	-356,3	-335,1	-121,6
148,8	683,9	-869,0	-833,4	-1018,5	0,97	0,91	0,59	-334,0	-354,6	-115,0
Delta's:	79,4	-3,3	-83,7	-7,6	-0,04	-0,05	0,02	22,2	-19,5	6,5

Table 3. Energies of selected Kohn-Sham orbitals and NPA partial charges of **7-W-H** in the relaxed potential energy scan of the W-Si-H angle from 180 to 120°.

angle W-Si-H [°]	Rel. energy [kJmol^{-1}]	HOMO–31 [eV]	HOMO–13 [eV]	HOMO–9 [eV]	HOMO–2 [eV]	HOMO–1 [eV]	HOMO [eV]	LUMO [eV]	LUMO+1 [eV]	rel. energies of the orbitals HOMO–13, –9, –2, –1, 0 [kJmol^{-1}]	NPA partial charges		
		$\sigma_{(Si-H)}$	$\sigma_{(trans\ N)}$	$\sigma_{(W-Si)}$	$\pi_{(W-Si\ in\ Cs)}$	$\pi_{(W-Si\ \perp Cs)}$	LP	$\pi^*_{(W-Si\ \perp Cs)}$	$\pi^*_{(W-Si\ in\ Cs)}$		W	Si	H
180.0	11.2	-11.730	-9.291	-7.343	-5.248	-5.062	-4.456	-2.419	-2.357	11.35	-0.3926	0.7392	-0.1836
176.4	8.8	-11.734	-9.295	-7.342	-5.260	-5.063	-4.452	-2.408	-2.314	9.79	-0.3860	0.7346	-0.1825
173.0	6.7	-11.737	-9.299	-7.339	-5.272	-5.064	-4.449	-2.396	-2.286	8.38	-0.3784	0.7288	-0.1813
169.5	4.8	-11.741	-9.303	-7.335	-5.284	-5.064	-4.447	-2.384	-2.273	7.13	-0.3698	0.7224	-0.1801
166.1	3.3	-11.745	-9.308	-7.331	-5.295	-5.063	-4.444	-2.372	-2.275	5.93	-0.3604	0.7154	-0.1791
162.6	2.0	-11.750	-9.314	-7.325	-5.305	-5.061	-4.443	-2.360	-2.292	4.76	-0.3502	0.7077	-0.1784
159.2	1.0	-11.756	-9.321	-7.319	-5.315	-5.058	-4.442	-2.349	-2.322	3.56	-0.3392	0.6993	-0.1778
155.7	0.4	-11.762	-9.328	-7.312	-5.325	-5.054	-4.442	-2.361	-2.339	2.34	-0.3273	0.6899	-0.1774
152.3	0.0	-11.769	-9.336	-7.305	-5.334	-5.050	-4.443	-2.405	-2.330	1.11	-0.3144	0.6795	-0.1770
148.8	0.0	-11.776	-9.345	-7.295	-5.341	-5.042	-4.443	-2.458	-2.323	0.57	-0.3012	0.6690	-0.1769
145.6	0.3	-11.781	-9.351	-7.285	-5.349	-5.036	-4.444	-2.504	-2.314	0.00	-0.2881	0.6586	-0.1765
142.4	0.9	-11.787	-9.358	-7.273	-5.354	-5.028	-4.446	-2.553	-2.306	0.07	-0.2743	0.6471	-0.1762
139.2	1.9	-11.792	-9.363	-7.259	-5.359	-5.019	-4.448	-2.603	-2.300	0.68	-0.2607	0.6356	-0.1758
136.0	3.2	-11.795	-9.368	-7.241	-5.362	-5.010	-4.451	-2.654	-2.295	1.97	-0.2467	0.6234	-0.1753
132.8	5.0	-11.795	-9.371	-7.221	-5.365	-5.000	-4.454	-2.704	-2.290	4.01	-0.2324	0.6103	-0.1745
129.6	7.2	-11.792	-9.373	-7.199	-5.367	-4.990	-4.456	-2.750	-2.286	6.85	-0.2171	0.5964	-0.1739
126.4	9.8	-11.784	-9.374	-7.175	-5.368	-4.979	-4.459	-2.793	-2.281	10.48	-0.2012	0.5820	-0.1734
123.2	12.9	-11.774	-9.374	-7.149	-5.366	-4.966	-4.462	-2.838	-2.278	15.09	-0.1859	0.5684	-0.1733
120.0	16.6	-11.760	-9.371	-7.123	-5.364	-4.953	-4.464	-2.879	-2.275	20.44	-0.1706	0.5551	-0.1733

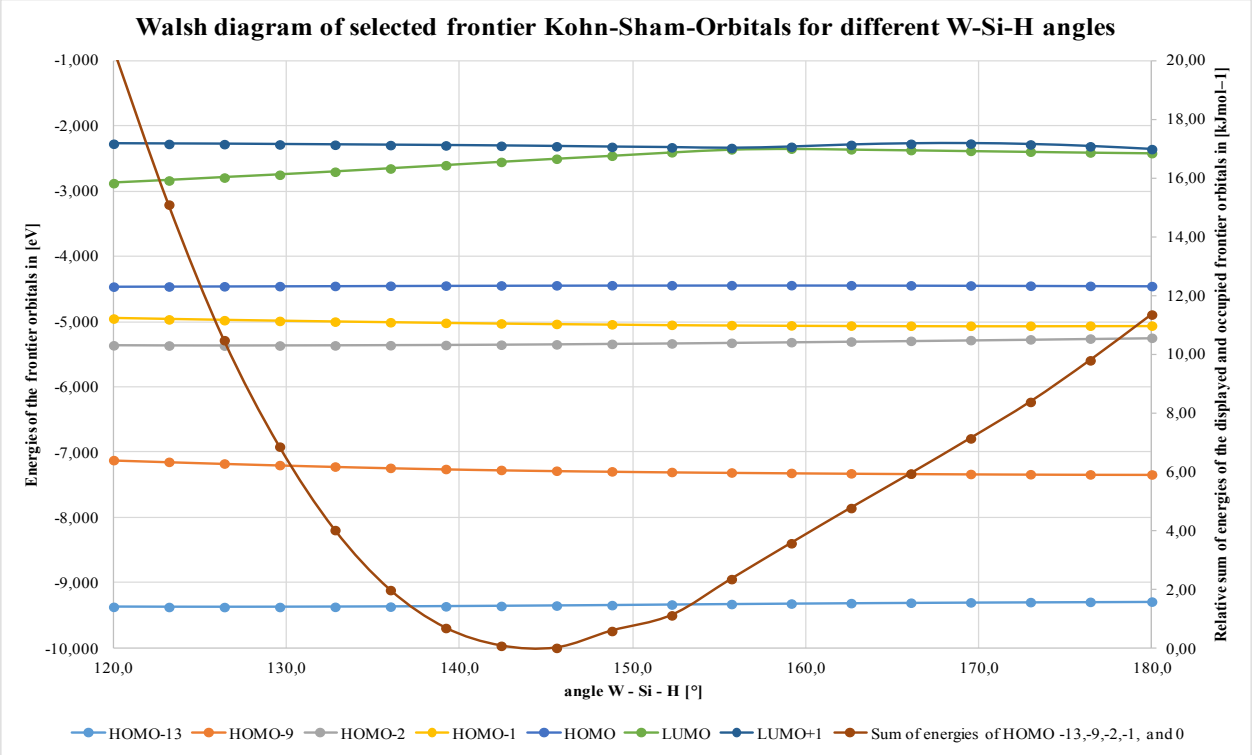

Figure 13. Walsh diagram of selected frontier Kohn-Sham orbitals for different W-Si-H angles of **7-W-H**.[6]

Further insight into the structures of the silylidyne complexes was provided by multinuclear NMR and IR spectroscopy. The ^{1}H and ^{13}C{^{1}H} NMR data of both silylidyne complexes suggest a time averaged C_s-symmetric structure in solution. The ^{29}Si{^{1}H} NMR spectrum displays a characteristic low-field shifted signal for the silylidyne silicon atom at δ = 258.5 ppm (**7-Mo**), and 259.8 ppm (^{1}J(W, Si) = 272 Hz) (**7-W**), which appears at slightly higher field compared to those of the previously reported silylidyne complexes [Cp(CO)$_2$Mo≡Si(C$_6$H$_3$-2,6-Trip$_2$)] (δ = 320 ppm), [Cp*(CO)$_2$W≡Si(C(SiMe$_3$)$_3$)] (δ = 339.1 ppm, ^{1}J(W, Si) = 316.2 Hz).[30, 49] The very large $^{1}J_{W,Si}$ coupling constant of 272 Hz, which is characteristic for a silylidyne complex, is indicative of a very high s-character of the orbital used by Si for the W–Si triple bond. The solution IR spectra of both silylidyne complexes in THF display two carbonyl absorption bands (**7-Mo**: 1912 (s) and 1835 (vs) cm^{-1}; **7-W**: 1901 (s) and 1822 (vs) cm^{-1}) of equal intensity, which are shifted to higher wavenumbers by roughly 50 cm^{-1} compared to those of the silylidene complexes (**6-Mo**: 1862 (vs) and 1779 (vs) cm^{-1}; **6-W**: 1852 (vs) and 1768 (vs) cm^{-1}) testifying the higher π-accepting properties of the silylidyne ligand.

6 Notable, the change of the W-Si-H angle not only change the energy of the LUMO and LUMO+1, but also alter the symmetry of the orbitals at the angle of ~158 °.

Another new strategy was employed to prepare an unprecedented silylidyne complex starting from the pentamethylsilicocenium borate salt $[(Cp^*)Si][B(C_6F_5)_4]$.[7][129] The salt $[(Cp^*)Si][B(C_6F_5)_4]$ can be viewed as a source of the silicon analogue of Cp*GeCl, where the later one was shown to be a very useful precursor for the successful syntheses of a series of germylidyne complexes of the general formula *trans*-$[X(dppe)_2M{\equiv}Ge\{\eta^1\text{-}Cp^*]$ (X = Cl, Br, I; M = Mo, W; dppe = $Ph_2PCH_2CH_2PPh_2$).[39-41] Indeed, treatment of **3-Mo** with one equivalent of $[(Cp^*)Si][B(C_6F_5)_4]$ in THF at ambient temperature resulted in a rapid color change from yellow to orange. Inspection of the orange solution by IR spectroscopy revealed the formation of the new silylidyne complex $[Tp'(CO)_2Mo{\equiv}Si(Cp^*)]$ (**5-Mo**) together with a small amount of the radical **2-Mo**. Formation of the radical **2-Mo** suggests a concomitant redox side reaction, in which the $[(Cp^*)Si]^+$ ion acts as a one-electron oxidant. Compound **5-Mo** was isolated after workup as an analytically pure, highly air-sensitive, orange solid in 49% yield (Scheme 6). The orange solid is well soluble in THF or fluorobenzene, sparingly soluble in Et_2O and toluene, and insoluble in aliphatic solvents. Compound **5-Mo** is a highly thermally stable solid, which decomposes upon melting to a black liquid at 319 – 322 °C.

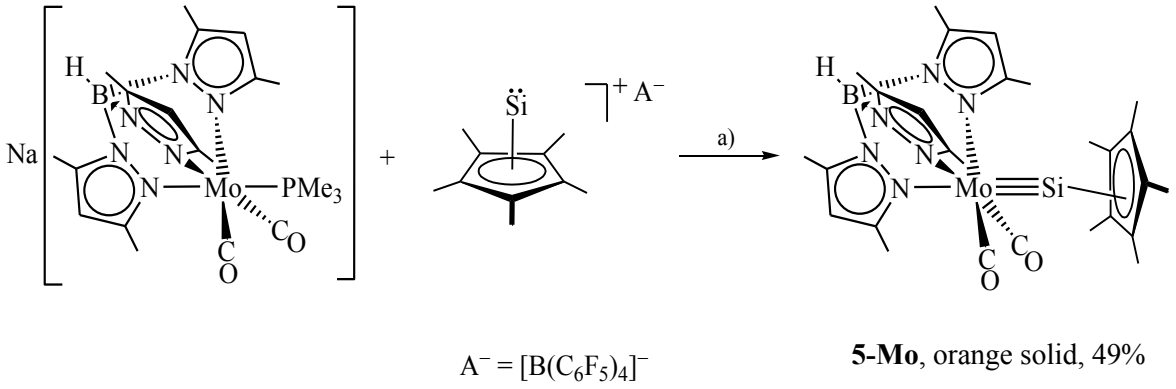

Scheme 6. Synthesis of the silylidyne complex **5-Mo**; a) THF, r.t., $-Na[B(C_6F_5)_4]$, $-PMe_3$.

In order to establish the molecular structure, suitable orange blocks of **5-Mo** were grown by slow evaporation of a benzene solution of **5-Mo** at ambient temperature and analysed by single-crystal X-ray diffraction. Surprisingly, the structural analysis shows an interesting bonding feature in **5-Mo**, displaying an asymmetric η^3-coordination of the Cp* substituent to the silicon center. Thus, in contrast to the germylidyne complexes *trans*-$[X(dppe)_2M{\equiv}Ge\{\eta^1\text{-}Cp^*]$, where

7 The salt $[(C_5Me_5)Si][B(C_6F_5)_4]$ was prepared following a modified procedure, than that described by Jutzi et al., starting from $SiX_2(NHC)$ (X = Br, I; NHC = Idipp, SIdipp) as Si(II) source. M. I. Arz, *personal communication*.

the Cp* substituent is σ-bound to the Ge-center, the Cp* group in **5-Mo** is π-bound to the silicon center as evidenced by the characteristic orientation of all methyl groups of the Cp* substituent almost in the plane of the Cp* ring.[130][8] A similar geometry was also observed in the silylene (C_6H_3-2,6-$Trip_2$)(η^3-Cp*)Si, where the Cp* group is attached to the silicon atom in a η^3-fashion as a π-bound substituent.[131] Notably, σ-bonding of the Cp* group to the silicon center would lead to a change of the hybridization of the silicon-bound carbon atom, from sp^2 to sp^3, and that would accordingly lead to a deformation of the geometry around the respective carbon atom. This change of hybridization would result in a deviation of the methyl group attached to the silicon-bonded carbon atom from the plane of the Cp* ring, and indeed this has been observed in the above mentioned germylidyne complexes.[39-41] The η^3-bonding of the Cp* substituent is documented by the Si–C distances of 2.078(2) Å (Si-C3), 2.171(2) Å (Si-C2) and 2.158(2) Å (Si-C4), which are significantly shorter than the remaining two Si–C distances (2.318(2) Å (Si···C1), 2.302(2) Å (Si···C5)). Similar bonding features were observed in [Cp*$(CO)_2$Fe–Si(η^3-Cp*)] and (C_6H_3-2,6-$Trip_2$)(η^3-Cp*)Si, which were prepared from [(Cp*)Si][$B(C_6F_5)_4$] upon treatment with Na[Cp*$Fe(CO)_2$] and Li(C_6H_3-2,6-$Trip_2$), respectively.[131, 132] Interestingly, in contrast to the compounds [Cp*$(CO)_2$Fe–Si(η^3-Cp*)] and (C_6H_3-2,6-$Trip_2$)(η^3-Cp*)Si, the C–C bond lengths of the Cp* ring in the silylidyne complex **5-Mo** are very similar and appear in the range of 1.413(2) – 1.443(3) Å, suggesting an extensive π-electron delocalisation in the Cp* ring. The Mo–Si bond length of 2.3092(4) Å in **5-Mo** is slightly longer than that found in the silylidyne complex **7-Mo** (*d*(Mo–Si): 2.2614(9) Å) or [Cp$(CO)_2$Mo≡Si(C_6H_3-2,6-$Trip_2$)] (*d*(Mo–Si): 2.2241(7) Å) and appears at the short end of the range of Mo=Si double bonds (2.2853(8)-2.3872(7) Å).[29, 30, 33, 111-113] Elongation of the Mo–Si bond in the silylidyne complex **5-Mo** can be rationalized by the competitive strong π-donation from the Cp* ring to the p-orbitals of the silicon atom, which significantly decreases the Mo(d)→Si(p) back-donation as confirmed by the quantum chemical calculations (vide infra). As expected for a silylidyne structure, the Mo-Si-C3 angle of 130.61(5)° of compound **5-Mo** is remarkably wider than that observed in the ferriosilylene Cp*$(CO)_2$Fe–Si(η^3-Cp*)] (112.8(1)°) and the arylsilicon(II) compound (C_6H_3-2,6-$Trip_2$)(η^3-Cp*)Si (101.98(7)°).

[8] The deviation of methyl groups from the plane of the C_5 ring plane of Cp* substituent ranges from 0.4(2)° to 2.8(1)°.

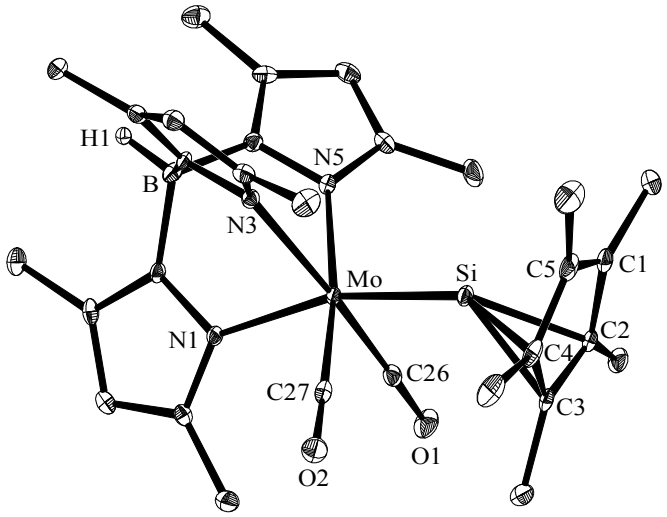

Figure 14. DIAMOND plot of the molecular structure of compound **5-Mo**. The thermal ellipsoids represent 30% of the electronic probability at 123(2) K. Hydrogen atoms (except B-H) are omitted for clarity. Selected bond lengths [Å] and angles [°]: Mo-Si 2.3092(4), Mo-N1 2.217(1), Mo-N3 2.281(2), Mo-N5 2.252(2), Mo-C26 1.929(2), Mo-C27 1.938(2), Si···C1 2.318(2), Si-C2 2.171(2), Si-C3 2.078(2), Si-C4 2.158(2), Si···C5 2.302(2), C1-C2 1.421(3), C1-C5 1.413(2), C2-C3 1.428(3), C3-C4 1.443(3), C4-C5 1.422(3); Mo-Si-C3 130.61(5), Mo-Si-C2 138.94(6), Mo-Si-C4 140.34(6), N1-Mo-Si 164.30(3), N3-Mo-Si 109.46(4), N5-Mo-Si 107.90(4), C26-Mo-Si 78.55(6), C27-Mo-Si 79.12(6).

The solution IR and NMR spectra of compound **5-Mo** corroborate well with the solid-state structure. The solution IR spectrum of **5-Mo** in THF displays two ν_{CO} absorption bands at 1849 (s) and 1772 (vs) cm^{-1}, which are at remarkably lower frequency compared to those observed for the Tbb-substituted silylidyne complex **7-Mo** (ν_{CO} in THF: 1912 (s) 1835 (vs) cm^{-1}), but compare well with those of the base-stabilized silylidyne complex **6-Mo** (ν_{CO} in THF: 1862 (s) 1779 (vs) cm^{-1}), suggesting a larger σ-donor/π-acceptor ratio of the [SiCp*] ligand compared to the [SiTbb] ligand. The low-frequency ν_{CO} absorption bands of **5-Mo** can be easily explained by the significant contribution of the resonance form **B/B'** to the overall bonding, as shown in Figure 15, which illustrate the strong π-donation from the Cp* group to the silicon atom. Akin to the solution IR spectrum, the solid-state IR spectrum also exhibit two ν_{CO} absorption bands at 1846 (s) and 1761 (vs) cm^{-1}. The ^{1}H and $^{13}C\{^{1}H\}$ NMR spectra support the presence of a fluxional structure in solution as evidenced by an averaged resonance signal for the methyl groups and the carbon atoms of the Cp* ring. Thus, only one singlet signal is observed at 1.90 ppm in C_6D_6 solution for the methyl protons of the Cp* group and also one singlet is found at 122.5 ppm in THF-d_8 solution for the ring carbon atoms of the Cp* group with a $^{1}J_{SiC}$ coupling constant of 13.4

Hz. Notably, fluxionality in solution for η^1- or $\eta^{2,3}$-bound Cp* groups is a typical phenomenon observed for main-group element compounds.[133] The $^{29}Si\{^1H\}$ NMR spectrum of **5-Mo** in THF-d_8 displays a singlet resonance at –272.4 ppm, which is *ca*. 128 ppm downfield-shifted compared to that of the precursor $[(Cp^*)Si][B(C_6F_5)_4]$ (δ = –400.2 ppm, in CD_2Cl_2). Notably, high field shifted ^{29}Si resonance signals are characteristic for π-complexes of silicon(II).[129, 134, 135] In comparison, the $^{29}Si\{^1H\}$ NMR signal of the silylidyne complexes **7-Mo** (258.5 ppm in C_6D_6) and $[Cp(CO)_2Mo{\equiv}Si(C_6H_3\text{-}2,6\text{-}Trip_2)]$ (δ = 320 ppm in C_6D_6) appears at considerably lower field than that of **5-Mo**.

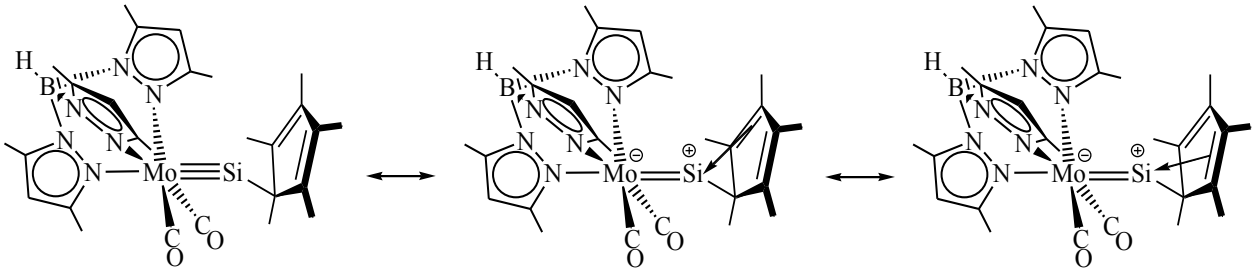

Figure 15. Three extreme possible canonical forms of the silylidyne complex **5-Mo**.

Quantum chemical calculations fully support the description of **5-Mo** as a silylidyne complex. The structural parameters of the optimized minimum structure **(5-Mo)$_{calc}$** at the RIJCOSX/B97-D3/def2-TZVP level of theory are in a very good agreement with the experimental values obtained by the single crystal X-ray diffraction analysis. A look at the Kohn-Sham frontier orbitals reveals that the HOMO−1 and HOMO−2 are the two π-bonds ($\perp$ to C_s plane and in C_s plane, respectively), which together with HOMO−11, which is the Mo–Si σ-bond, form the triple bond core between the molybdenum and the silicon atoms (Figure 16). Notably, the HOMO–2, which is mainly the in-plane π-bonding orbital with a small Mo-C_{CO} π-backbonding contribution, also shows some extent of lone pair-character at the silicon atom which is accumulated by the rehybridisation of the silicon orbitals to minimize the high positive partial charge at the electrophilic silicon center. Conspicuously, a similar situation was also observed in the calculated minimum structure of the silylidyne complex **7-W-H$_{min}$** (Figure 12, *vide supra*). The HOMO–9 and HOMO–10 correspond to two π-bonds (in C_s plane and $\perp$ to the C_s plane, respectively), which arise upon π-donation from the Cp* group to the silicon p-orbitals (Figure 16). These competitive π-donations into the same Si p-orbitals significantly lower the extent of electron donation from the molybdenum to the silicon center, and this results in a weakening, as well as

elongation of the Mo≡Si bond in the silylidyne complex **5-Mo**. As expected, the HOMO corresponds to the molybdenum-centered nonbonding orbital, and the LUMO and LUMO+1 correspond to the two Mo–Si π*-orbitals (Figure 16).

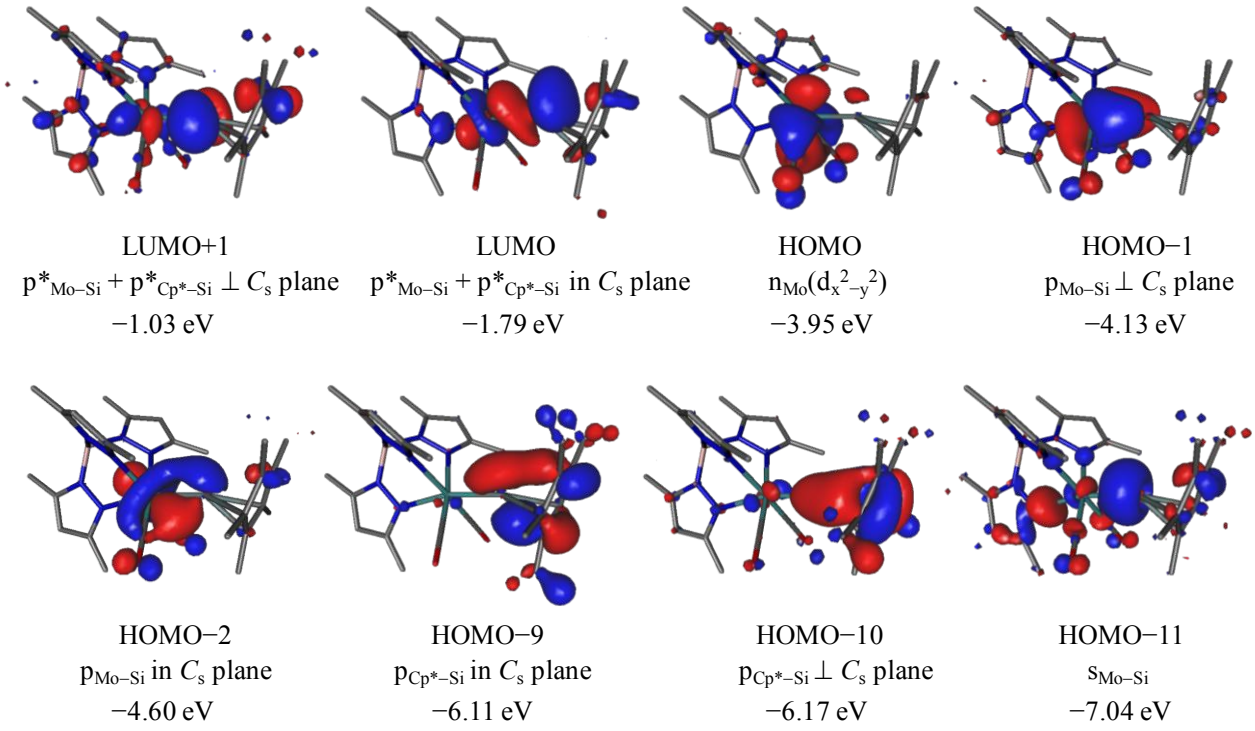

Figure 16. Selected Kohn-Sham frontier orbitals of **5-Mo** calculated at RIJCOSX-B97-D3/TZVP level of theory, isosurface value correspond to 0.04 e bohr^{-3}.

The presence of a triple bond between the Mo and Si atoms was further supported by a natural bond orbital (NBO) analysis of **(5-Mo)$_{calc}$**. Thus, one σ and two π NBOs were found between the Mo and Si centers (Table 4), which is characteristic for a silylidyne complex.[35, 58] The σ NBO is highly localized compared to the two π NBOs as evidenced by their occupancies of 1.96e, and 1.51e, 1.62e, respectively (Table 4). As expected, the σ and the two π NBOs are significantly more polarized towards the silicon (74.2%) and the molybdenum atoms (75.9 and 82.1%), respectively (Table 4), compared to the known cationic chromium silylidyne complex [Cp*(CO)$_2$Cr≡Si(SIdipp)][B{C$_6$H$_3$-3,5-(CF$_3$)$_2$}$_4$] (σ NBO: 65.2% (Si); π NBOs: 78.8 and 67.6% (Cr)).[35] The decreased occupancies of the π(Mo–Si) NBOs can be explained by the competitive π-donation of the η^3-coordinated Cp* ring to the Si atom, which is also reflected in the presence of two 3c2e interactions between the Si and the Cp* ring carbon atoms with decreased occupancies (1.67 and 1.71 electrons) (Table 4) displaying strong donor-acceptor interactions

with the antibonding π*(Mo–Si) orbitals according to second-order pertubation theory analysis (Table 5). This high delocalization of the electron density also rationalize the weakening of the Mo–Si bond in compound **5-Mo**. Finally, the natural population analysis (NPA) also revealed a highly polarized Mo≡Si bond as evidenced by high opposite partial charges of Mo (−0.57) and Si atoms (+1.13), which is indeed characteristic for heavier alkylidyne complexes.[35, 39, 43, 58, 136]

Table 4. Selected results of the natural bond orbital (NBO) analysis of **(5-Mo)$_{calc}$** at the RI-JCOSX/B97-D3/def2-TZVP level of theory. Atom numbering of the experimental structure was taken over in the calculated structure **(5-Mo)$_{calc}$**.[a]

NBO analysis					NPA partial charges[b]	
	occ.	pol. [%]	hyb.	WBI		
σ(Mo–Si)	1.94	23.4 (Mo) 76.6 (Si)	$sd^{1.55}$ (Mo) $sp^{0.11}$ (Si)	1.03	Mo	−0.57
π_1(Mo–Si)	1.65	83.5 (Mo) 16.5 (Si)	d (Mo) p (Si)		Si	1.13
π_2(Mo–Si)	1.41	98.8 (Mo) 1.2 (Si)	d (Mo) $sp^{14.92}d^{2.01}$ (Si)		Cp*	−0.33
LP(Mo)	1.46		d			
LP(C1)	1.06		p			
3c(Si-C2-C3)	1.67	3.5 (Si) 45.9 (C2) 50.6 (C3)	$sp^{14.71}d^{23.94}$ (Si) p (C2) p (C3)			
3c(Si-C4-C5)	1.71	5.7 (Si) 46.8 (C4) 47.6 (C5)	$sp^{30.77}d^{9.02}$ (Si) p (C4) p (C5)			
σ*(Mo–Si)	0.34	76.6 (Mo) 23.4 (Si)	$sd^{1.55}$ (Mo) $sp^{0.11}$ (Si)			
π^*_1(Mo–Si)	0.25	16.5 (Mo) 83.5 (Si)	d (Mo) p (Si)			
π^*_2(Mo–Si)	0.38	1.2 (Mo) 98.8 (Si)	d (Mo) $sp^{14.92}d^{2.01}$ (Si)			
3c*(Si-C2-C3)	0.59	6.0 (Si) 52.1 (C2) 47.5 (C3)	$sp^{14.71}d^{23.94}$ (Si) p (C2) p (C3)			
3c*(Si-C2-C3)	0.03	96.5 (Si) 1.6 (C2) 1.9 (C3)	$sp^{14.71}d^{23.94}$ (Si) p (C2) p (C3)			
3c*(Si-C4-C5)	0.52	2.3 (Si) 53.0 (C4) 44.8 (C5)	$sp^{30.77}d^{9.02}$ (Si) p (C4) p (C5)			
3c*(Si-C4-C5)	0.15	92.1 (Si) 0.3 (C4) 7.6 (C5)	$sp^{30.77}d^{9.02}$ (Si) p (C4) p (C5)			

[a]: occ. = occupancy, pol. = polarization, hyb. = hybridization, WBI = Wiberg bond index, LP = lone pair, 3c = three-center bond. [b]: Partial charges obtained by natural population analysis (NPA).

Table 5. Selected results of the second order perturbation theory analysis of the Fock matrix in the NBO basis of **(5-Mo)$_{calc}$**; atom numbering of the experimental structure was taken over in the calculated structure.

Donor orbital	Acceptor orbital	Interaction energy [kcal mol^{-1}]
LP(Mo)	π^*_2(Mo–Si)	18.00
LP(C1)	3c*(Si-C2-C3)	108.75
LP(C1)	3c*(Si-C4-C5)	93.03
3c(Si-C2-C3)	σ*(Mo–Si)	2.12
3c(Si-C2-C3)	π^*_1(Mo–Si)	8.53
3c(Si-C2-C3)	π^*_2(Mo–Si)	76.37
3c(Si-C4-C5)	σ*(Mo–Si)	5.20
3c(Si-C4-C5)	π^*_1(Mo–Si)	20.24
LP(N3)	σ*(Mo–Si)	64.67

Thus, both the experimental and quantum chemical calculation results clearly demonstrate that compound **5-Mo** is a silylidyne complex featuring an η^3-coordinated Cp* at the silicon atom.

2.1.4 The tetrylidyne complexes [Tp'(CO)$_2$M≡E–R] (E = Ge, Sn, Pb; M = Mo, W)

As it was discussed earlier, the synthesis of carbonyl-containing stannylidyne and plumbylidyne complexes of group 6 transition metals was hampered due to hindrance of elimination of the third ligand (e.g. CO, PMe_3) from the corresponding metallotetrylenes (*vide supra*). In an attempt to overcome this problem, the metalates Na[Tp'M(CO)$_2$(PMe_3)] (**3-Mo**, M = Mo; **3-W**, M = W) comprising of a bulky scorpionate ligand were prepared. In this chapter, the reactivity of these metalates **3-Mo** and **3-W** with halotetrylenes of the type [EXR][9] (E = Ge, Sn, Pb; X = Cl – I; R = bulky organic groups) will be presented, which indeed provided access to a series of unprecedented tetrylidyne complexes of the general formula [Tp'(CO)$_2$M≡E–R].

2.1.4.1. Syntheses of the heavier tetrylidyne complexes

To access the aforementioned tetrylidyne complexes, the reaction of the tricarbonyl metalates K[Tp'M(CO)$_3$] (M = Mo, W) were initially tested toward different halotetrylenes, [EXR]. Surprisingly, only the reactions with the chlorogermylenes, Ge(Cl)R (R = C_6H_3-2,6-Mes_2, C_6H_3-2,6-$Trip_2$) led to the desired products at elevated temperature. For example, heating of a mixture of K[Tp'M(CO)$_3$] (M = Mo, W) with an equimolar amount of GeCl(C_6H_3-2,6-Mes_2) in toluene at 110 °C for 1 hour resulted in a color change from orange to yellowish-brown and lead to a selective and complete conversion of the metalates to the corresponding germylidyne complexes [Tp'(CO)$_2$M≡Ge(C_6H_3-2,6-Mes_2)] (**8-Mo**, M = Mo; **8-W**, M = W) (Scheme 7), as evidenced by *in situ* IR monitoring. Furthermore, the metalate K[Tp'Mo(CO)$_3$] also reacts with GeCl(C_6H_3-2,6-$Trip_2$) in toluene at 110 °C to afford the germylidyne complex [Tp'(CO)$_2$Mo≡Ge(C_6H_3-2,6-$Trip_2$)] (**13-Mo**) (Scheme 7), but this reaction takes a longer reaction time (>2 hours)[10] for completion. This suggests that the reaction rate decreases upon increasing the steric bulk at the germanium center. All the germylidyne complexes were isolated after workup as analytically pure, extremely air-sensitive, yellowish-brown solids in excellent yields (Table 6).

---

9 For simplicity, the halotetrylenes will be presented as monomeric species in the entire dissertation, despite the fact that they forms dimer in the solid state.

10 Monitoring of the reaction by IR spectroscopy showed ~98% completion after 2 hours without any further conversion occurring after prolonged heating.

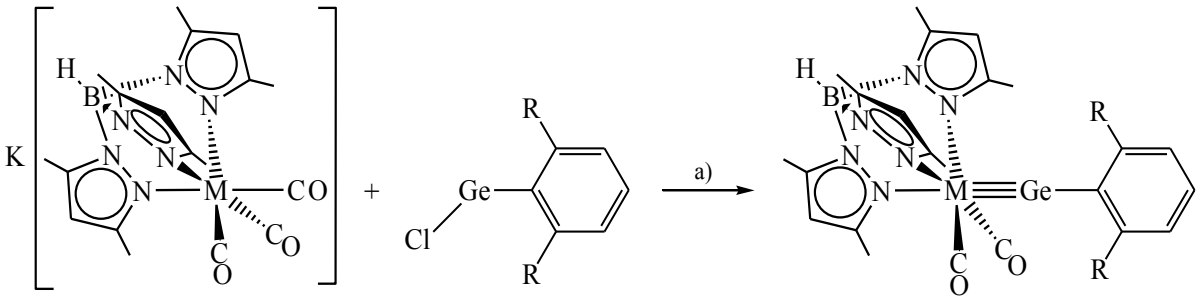

Scheme 7. Synthesis of germylidyne complexes by salt metathesis from triscarbonyl metalate salts; a) toluene, 110 °C, –KCl, –CO.

Similarly, heating of a mixture of $K[TpMo(CO)_3]\cdot 0.8THF$ with one equivalent of $GeCl(C_6H_3\text{-}2,6\text{-}Mes_2)$ in toluene at 110 °C for 4 hours leads to the selective formation of the germylidyne complex $[Tp(CO)_2Mo{\equiv}Ge(C_6H_3\text{-}2,6\text{-}Mes_2)]$ (**12-Mo**), which was isolated after workup as an analytically pure, air-sensitive, brown solid in 73% yield (Table 6). Compound **12-Mo** was prepared to compare the decreased steric demand of the Tp ligand on the structural and spectroscopic properties of the germylidyne complexes. In comparison, the reaction of $K[Tp'Mo(CO)_3]$ with the halostannylene $SnCl(C_6H_3\text{-}2,6\text{-}Mes_2)$ and the haloplumbylene $PbBr(C_6H_3\text{-}2,6\text{-}Mes_2)$ in toluene at elevated temperature led only to the redox products $[Tp'Mo(CO)_3]$, $C_6H_4\text{-}2,6\text{-}Mes_2$ and elemental tin and lead, respectively. Formation of these products was confirmed by IR and ^{1}H NMR spectroscopy.

Whereas the desired stannylidyne and plumbylidyne complexes could not be obtained upon treatment of the tricarbonyl metalate $K[Tp'Mo(CO)_3]$ with a halostannylene or haloplumbylene, they can be however easily prepared from the more labile trimethylphosphine substituted metalates $Na[Tp'M(CO)_2(PMe_3)]$ (**3-Mo**, M = Mo; **3-W**, M = W). Interestingly, unlike to the tricarbonyl metalates, compounds **3-Mo** and **3-W** immediately reacted with the halotetrylenes $E(X)(C_6H_3\text{-}2,6\text{-}Mes_2)$ (E = Ge, Sn; Pb; X = Cl – I) at ambient temperature to produce the corresponding tetrylidyne complexes $[Tp'(CO)_2M{\equiv}E(C_6H_3\text{-}2,6\text{-}Mes_2)]$ (M = Mo: **8-Mo** (E = Ge), **9-Mo** (E = Sn), **10-Mo** (E = Pb); M = W; **9-W** (E = Sn), **10-W** (E = Pb)) (Scheme 8). For example, treatment of a THF solution of **3-Mo** with one equivalent of $SnCl(C_6H_3\text{-}2,6\text{-}Mes_2)$ at ambient temperature led to an immediate color change from yellow to dark greenish-brown. Monitoring of the reaction by IR spectroscopy revealed the complete consumption of the starting

material within 5 minutes and the formation of the unprecedented stannylidyne complex **9-Mo** along with a small amount of the 17VE radical [Tp'Mo(CO)$_2$(PMe$_3$)] (**2-Mo**). Compounds **9-Mo**/**9-W** and **10-Mo**/**10-W** are first examples of group 6 transition metals stannylidyne and plumbylidyne complexes obtained by salt metathesis and thus, their synthesis using scorpionate-based metalates represent a significant development in this field. The radical **2-Mo**, which was independently synthesized as previously reported by one-electron reduction of **1-Mo** arises from a competing one-electron redox side reaction of **3-Mo** with the chlorostannylene (*vide supra*). This redox side reaction was observed in many of the reactions of the metalates **3-Mo** and **3-W** with halotetrylenes. All tetrylidyne complexes were isolated after workup as extremely air-sensitive, analytically pure solids in moderate to excellent yields (Table 6).

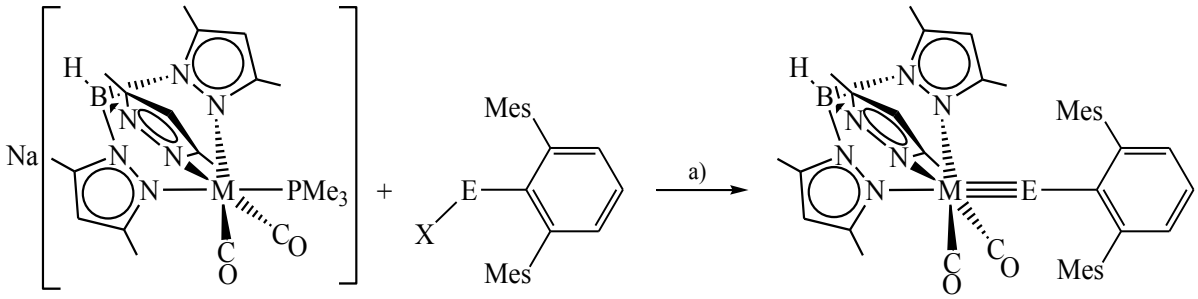

Scheme 8. Synthesis of the tetrylidyne complexes by salt metathesis from the biscarbonyl metalate salts; a) THF, r.t., –NaX, –PMe$_3$.

With the goal of expanding the range of tetrylidyne complexes carrying different substituents at the tetrel atoms the metalate salts **3-Mo** and **3-W** were reacted with a variety of other halotetrylenes E(X)R (E = Ge –Pb, X = Cl, Br, R = N(TMS)Mes*, Mes*, Eind, C$_6$H$_3$-2,6-Trip$_2$) leading to a series of unprecedented tetrylidyne complexes of the general formula [Tp'(CO)$_2$M≡E–R]. For instance, when a THF solution of **3-Mo** or **3-W** was treated with a THF solution of GeCl{N(TMS)Mes*} at ambient temperature, a rapid color change from yellow to red orange was observed. Monitoring of the reactions by IR spectroscopy revealed the immediate formation of the aminogermylidyne complexes [Tp'(CO)$_2$M≡Ge{N(TMS)Mes*}] (**11-Mo**, M = Mo; **11-W**, M = W) together with small amount of **2-Mo** and **2-W**, respectively. Compounds **11-Mo** and **11-W** were isolated as analytically pure, air-sensitive, orange solids in moderate yields (Table 6). The analogous aminostannylidyne complex **16-Mo** was also prepared in a same way,

as a brown solid in 16 % yield. The extremely high light sensitivity of the novel stannylidyne complex **16-Mo** hindered its isolation in a high yield and its complete characterization. The germylidyne complex [Tp'$(CO)_2$M≡GeMes*] (**14-Mo**) was obtained upon reaction of **3-Mo** with Ge(Cl)Mes*, which was *in situ* prepared by the reaction of Mes*Li·2(THF) and $GeCl_2$·(1,4-dioxane) in THF at −78 °C, and was isolated as an analytically pure, air-sensitive, brown solid in 34 % yield. Furthermore, the addition of a yellow solution of (*E*)-Eind(Cl)Ge=Ge(Cl)Eind to a yellow suspension of **3-Mo** led to an immediate color change from yellow to red-brown. Similar to other reactions, inspection of the reaction mixture after 10 minutes revealed the formation of the germylidyne complex [Tp'$(CO)_2$Mo≡Ge–Eind] (**15-Mo**) along with small amount of **2-Mo**. Compound **15-Mo** was isolated after workup as an analytically pure, air-sensitive, red-brown solid in 53 % yield (Table 6). The plumbylidyne complex [Tp'$(CO)_2$Mo≡Pb(C_6H_3-2,6-$Trip_2$)] (**17-Mo**) was prepared by the reaction of **3-Mo**·DME with an equimolar amount of PbBr(C_6H_3-2,6-$Trip_2$) in THF at ambient temperature under complete exclusion of light. Interestingly, monitoring of the reaction by IR spectroscopy revealed the formation of the metalloplumbylene [Tp'$(CO)_2(PMe_3)$Mo–Pb(C_6H_3-2,6-$Trip_2$)] (ν_{CO}: 1910 and 1808 cm^{-1}) as an intermediate which slowly converted to the plumbylidyne complex **17-Mo** (ν_{CO}: 1896 and 1827 cm^{-1}) upon stirring for 3.5 hours at ambient temperature. Compound **17-Mo** was isolated after workup as a green solid in 24 % yield (Table 6). Akin to the aminostannylidyne complex **16-Mo**, the plumbylidyne complex **17-Mo** is also extremely light sensitive in solution. This property prevented its isolation in analytically pure form.

The most important general physical properties of all tetrylidyne complexes are as follows:

- As expected, all tetrylidyne complexes are highly colored. The color changes from orange to dark green on moving from the silylidyne to plumbylidyne complexes, suggesting a lower HOMO–LUMO gap as one move down the group 14 of the periodic table. The lower HOMO–LUMO gap for heavier elements is results from the decreased metal-tetrel π-bond strengths, and was verified by UV-Vis spectroscopy (*vide infra*). Furthermore, the color of the complexes also changes upon replacing the substituent at the tetrel atom, indicating a significant effect on the HOMO–LUMO energy gap. For example, the germylidyne complex **8-Mo** with a C_6H_3-2,6-Mes_2 substituent is yellowish-brown colored, whereas the germylidyne **14-Mo** with a Mes* substituent is brown colored.

- All tetrylidyne complexes are thermally very stable solids, which typically decompose upon heating in vacuum-sealed glass capillaries above 220 °C.
- All tetrylidyne complexes, except the aminotetrylidyne complexes, are extremely soluble in THF, fluorobenezene, toluene and Et_2O, and moderate to well soluble in common aliphatic solvents, such as *n*-pentane, *n*-hexane (Table 6). The aminotetrylidyne complexes are well soluble in THF and toluene, moderately soluble in Et_2O and sparingly soluble in aliphatic solvents.
- In general, all tetrylidyne complexes are extremely oxygen and moisture sensitive and immediately decompose upon exposure to air. Additionally, the plumbylidyne complexes and the aminostannylidyne complex are light sensitive, and decompose upon exposure to light both in the solid state and in solution.

Table 6. Summary of properties and yields of the tetrylidyne complexes **7-Mo** – **17-Mo**.

Complex	Color	Yield [%]	M.P. [°C]	Solubility in *n*-hexane
[Tp'$(CO)_2$Mo≡Si–Tbb] (**7-Mo**)	reddish-orange	67/59[a]	283 – 285	moderate
[Tp'$(CO)_2$W≡Si–Tbb] (**7-W**)	red	66/67[a]	252 – 253	moderate
[Tp'$(CO)_2$Mo≡Ge(C_6H_3-2,6-Mes_2)] (**8-Mo**)	yellowish-brown	91/86[a]	> 240	good
[Tp'$(CO)_2$W≡Ge(C_6H_3-2,6-Mes_2)] (**8-W**)	light purple	84	221 – 224	good
[Tp'$(CO)_2$Mo≡Sn(C_6H_3-2,6-Mes_2)] (**9-Mo**)	greenish-brown	68	231 – 233	moderate
[Tp'$(CO)_2$W≡Sn(C_6H_3-2,6-Mes_2)] (**9-W**)	brown	72	228 – 231	moderate
[Tp'$(CO)_2$Mo≡Pb(C_6H_3-2,6-Mes_2)] (**10-Mo**)	dark green	72	240 – 241	moderate
[Tp'$(CO)_2$W≡Pb(C_6H_3-2,6-Mes_2)] (**10-W**)	green	61	215 – 218	moderate
[Tp'$(CO)_2$Mo≡Ge{N(TMS)Mes*}] (**11-Mo**)	orange	58	> 240	very low
[Tp'$(CO)_2$W≡Ge{N(TMS)Mes*}] (**11-W**)	orange	49	280 – 282	very low
[Tp$(CO)_2$Mo≡Ge(C_6H_3-2,6-Mes_2)] (**12-Mo**)	brown	73	233 – 235	moderate
[Tp'$(CO)_2$Mo≡Ge(C_6H_3-2,6-$Trip_2$)] (**13-Mo**)	yellowish-brown	71	281 – 283	very good
[Tp'$(CO)_2$Mo≡Ge–Mes*] (**14-Mo**)	brown	34	253 – 256	moderate
[Tp'$(CO)_2$Mo≡Ge–Eind] (**15-Mo**)	red-brown	53	239 – 234	very good
[Tp'$(CO)_2$Mo≡Sn{N(TMS)Mes*}] (**16-Mo**)	brown	16	–	very low
[Tp'$(CO)_2$Mo≡Pb(C_6H_3-2,6-$Trip_2$)] (**17-Mo**)	green	24	–	moderate

[a]: The two different values correspond to the yields obtained using the two different methods of synthesis described in the text.

2.1.4.2. Molecular structures of the heavier tetrylidyne complexes

The solid-state structures of all the tetrylidyne complexes, except **16-Mo**, were determined by single-crystal X-ray diffraction studies. Selected bonding parameters of all compounds are summarized in Table 7. The tetrylidyne complexes containing C_6H_3-2,6-Mes_2 substituent on the tetrel atoms are isostructural. The molecular structure of **9-Mo** is depicted in Figure 17 as an example. In all complexes, the central aryl ring of the C_6H_3-2,6-Mes_2 substituent is oriented orthogonal to the molecular plane of the C_s-symmetric molecule. This orientation differs from that of the C_6H_3-2,6-$Trip_2$ substituted tetrylidyne complexes **13-Mo** and **17-Mo**, in which the central aryl ring is located in the molecular plane (Figure 18).

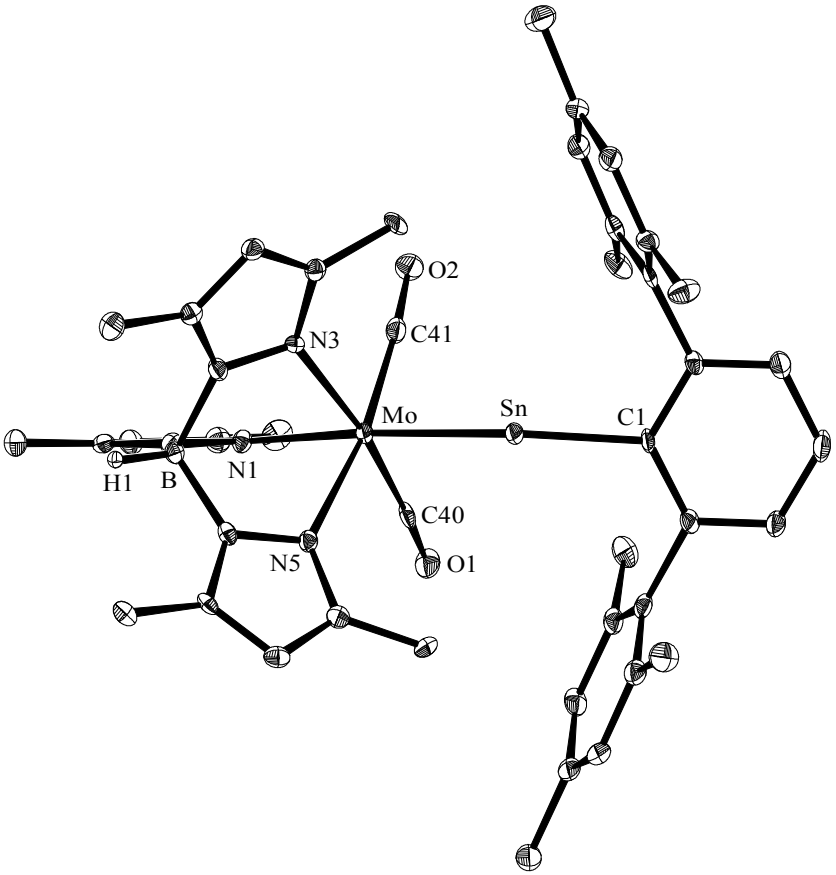

Figure 17. DIAMOND plot of the molecular structure of complex **9-Mo** in the crystal lattice of the Et_2O solvate **9-Mo**·($C_4H_{10}O$). The thermal ellipsoids represent 30% of the electronic probability at 123(2) K. The solvent molecule and the hydrogen atoms (except B-H) are omitted for clarity.

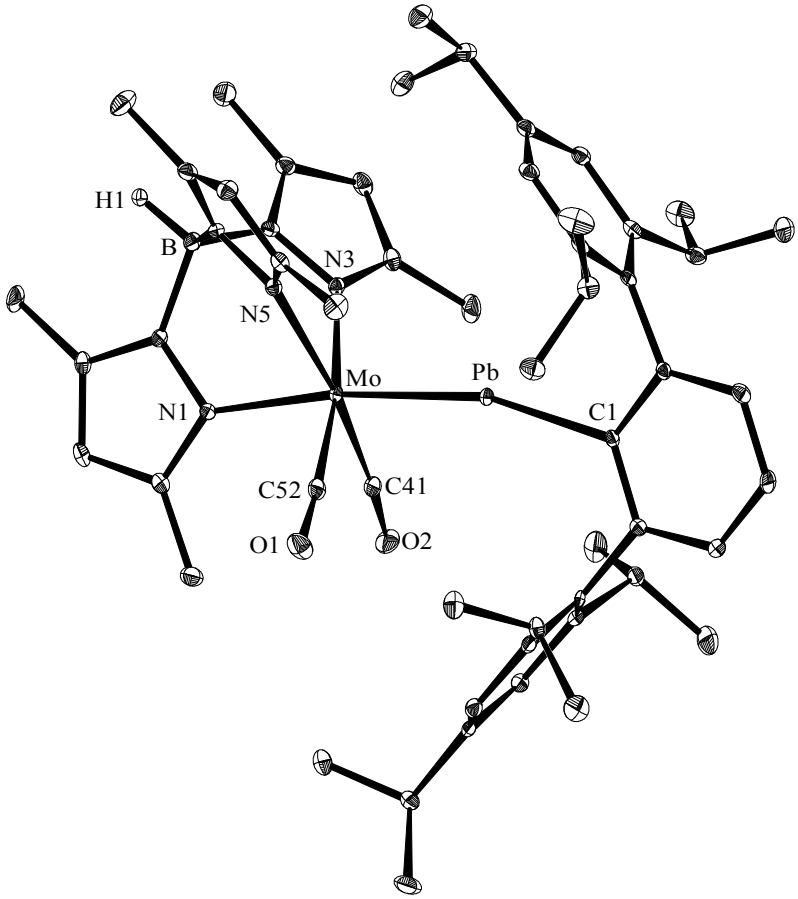

Figure 18. DIAMOND plot of the molecular structure of complex **9-Mo** in the crystal lattice of the Et_2O solvate **9-Mo**·($C_4H_{10}O$). The thermal ellipsoids represent 30% of the electronic probability at 123(2) K. The solvent molecule and the hydrogen atoms (except B-H) are omitted for clarity.

Akin to the germylidyne complex **13-Mo**, the aryl ring of the germylidyne **14-Mo** and **15-Mo** is also oriented in the C_s-plane of the molecules. Apart from this spatial orientation, all the tetrylidyne complexes display the following trends –

- The metal centers in the tetrylidyne complexes have distorted octahedral geometry, and the tetrylidyne fragments are situated in a *trans*-orientation to one of the pyrazolyl groups of the scorpionate ligand, as evidenced by the wide N_{trans}-M-E angles (>165°, Table 7).
- The Mo–E triple bond lengths are identical to the corresponding W–E triple bond lengths, which is in aggrement with the almost identical atomic radii of Mo (1.90 Å) and W (1.93 Å) due to the lanthanide contraction.[137] Furthermore, upon increasing the principle number of the tetrel, the M–E bond length increases to *ca.* 0.19 Å (E = Sn) and 0.24 Å (E =

Pb), respectively. This increase is in harmony with the increasing atomic radii of the tetrel atoms (Ge: 1.25 Å, Sn: 1.45 Å, 1.54 Å).

- The Mo–Ge triple bond lengths of all Tp'-substituted germylidyne complexes are slightly longer than those of the Cp-substituted germylidyne complexes but comparable with the phosphane-substituted octahedral germylidyne complexes (Table 7, Table 8). For instance, the Mo–Ge bond (2.3117(9) [2.3121(9)] Å) in **8-Mo** is ca. 4 pm longer than that found in the germylidyne complex [Cp(CO)$_2$Mo≡Ge(C$_6$H$_3$-2,6-Mes$_2$)] (M–Ge 2.271(1) Å) (Table 8). This trend of longer bond length in the octahedral complexes can be attributed to the higher coordination number at the metal center as well as the *trans*-influence of the ligand in *trans* position to the tetrylidyne ligand.
- The M-E-C bond angles of all C$_6$H$_3$-2,6-Mes$_2$ substituted tetrylidyne complexes, for which the central aryl ring of the C$_6$H$_3$-2,6-Mes$_2$ substituent is oriented orthogonal to the molecular plane, deviate from 180° and are in general lower than corresponding angles of known tetrylidyne complexes (Table 7, Table 8). Furthermore, in all cases, the bending of the aryl groups occurs towards the carbonyl ligands. In contrast, the M-E-C bond angles of those tetrylidyne complexes, for which the central aryl rings of the m-terphenyl substituents are oriented in the molecular C_s-symmetry plane, are much wider (Table 7). As shown by the DFT calculations for the silylidyne complex **7-W** (*vide supra*, chapter 2.1.3), such bending results in an electronic stabilization of the molecule. Notably, a similar bending was also observed in Tp'-substituted alkylidyne complexes [Tp'(CO)$_2$M≡C–*p*-Tol] (M = Mo, 163.1(3)°; M = W, 163.2(3)°) (Table 7).[138]
- The *trans* influence of the heavier tetrylidyne ligands is weaker than that of the alkylidyne ligand, and decreases in the series silylidyne → plumbylidyne, as evidenced by the decreased M–N$_{trans}$ bond lengths (Table 7). For example, the Mo–N$_{trans}$ bond length of the alkylidyne complex [Tp'(CO)$_2$Mo≡C–*p*-Tol] is 2.306(3) Å, which is ca. 0.07 Å longer than that of the silylidyne complex **7-Mo** (Mo–N$_{trans}$: 2.233(3) Å) and ca. 0.11 Å longer than that of the plumbylidyne complex **10-Mo** (Mo–N$_{trans}$: 2.193(3) Å).[138]
- In the aminogermylidyne complexes **11-Mo** and **11-W**, the nitrogen atoms are in a planar environment (sum of angles at N = 359.96° (**11-Mo**) and 360.0° (**11-W**)) (Figure 19). This phenomenon was also observed in the corresponding amino germylene Ge(Cl)N(Mes*)TMS (sum of angles at N = 359.9°)[38] and the three-legged piano-stool germylidyne complexes [Cp*(CO)$_2$M≡GeN(Mes*)TMS] (sum of angles at N = 359.79°

[359.92°, 359.83°] (M = Mo), 360.0° [359.9°] (M = W))[38] and [Cp(CO)$_2$M≡GeN(C$_6$H$_2$-2,6-{C(H)Ph$_2$}$_2$-4-Me)TMS] (sum of angles at N = 359.9°).[37] This suggests a certain degree of N→Ge π-donation as also found in the germylidyne complex [Cp(CO)$_2$Mo≡GeN(C$_6$H$_2$-2,6-{C(H)Ph$_2$}$_2$-4-Me)TMS],[37] and is reflected in the Ge–N distance of 1.822(1) Å (**11-Mo**) and 182.3(3) Å (**11-W**) (Figure 19), which is significantly shorter than the sum of single bond covalent radii of the Ge and N atoms (1.91 Å).[139]

Table 7. Selected bond lengths and angles of alkylidyne and the heavier analogues of the alkylidyne complexes of Mo and W comprising of scorpionate ligands.

Complex	M–E [Å]	M–N$_{trans}$ [Å]	M–N$_{cis(av)}$ [Å]	M-E-C1/N [°]	N$_{trans}$-M-E [°]
[Tp'(CO)$_2$Mo≡C–*p*-Tol][138]	1.804(4)	2.306(3)	2.25	163.1(3)	166.372
[Tp'(CO)$_2$W≡C–*p*-Tol][138]	1.829(3)	2.288(3)	2.2065	163.2(3)	166.748
[Tp'(CO)$_2$Mo≡Si–Tbb] (**7-Mo**)	2.2614(9)	2.233(3)	2.252	160.8(1)	167.19(7)
[Tp'(CO)$_2$W≡Si–Tbb] (**7-W**)	2.2706(8)	2.226(3)	2.2395	161.73	168.27(7)
[Tp'(CO)$_2$Mo≡Ge(C$_6$H$_3$-2,6-Mes$_2$)] (**8-Mo**)[a]	2.3117(9)	2.221(3)	2.254	159.4(2)	167.1(2)
	2.3121(9)	2.233(3)	2.244	160.6(2)	164.8(1)
[Tp'(CO)$_2$W≡Ge(C$_6$H$_3$-2,6-Mes$_2$)] (**8-W**)[a]	2.3133(3)	2.224(2)	2.238	165.73(9)	169.17(6)
	2.3084(3)	2.206(2)	2.231	159.66(9)	165.96(6)
[Tp'(CO)$_2$Mo≡Sn(C$_6$H$_3$-2,6-Mes$_2$)] (**9-Mo**)	2.5068(6)	2.214(4)	2.246	159.5(2)	168.4(1)
[Tp'(CO)$_2$W≡Sn(C$_6$H$_3$-2,6-Mes$_2$)] (**9-W**)	2.5099(3)	2.199(3)	2.239	160.31(8)	169.41(7)
[Tp'(CO)$_2$Mo≡Pb(C$_6$H$_3$-2,6-Mes$_2$)] (**10-Mo**)	2.5545(2)	2.193(3)	2.2465	158.89(5)	169.92(4)
[Tp'(CO)$_2$W≡Pb(C$_6$H$_3$-2,6-Mes$_2$)] (**10-W**)	2.561(2)	2.190(9)	2.2325	160.6(3)	170.6(2)
[Tp'(CO)$_2$Mo≡Ge{N(TMS)Mes*}] (**11-Mo**)	2.3147(2)	2.232(1)	2.246	166.37(4)	173.56(3)
[Tp'(CO)$_2$W≡Ge{N(TMS)Mes*}] (**11-W**)	2.3218(6)	2.220(6)	2.2325	166.9(1)	173.92(9)
[Tp(CO)$_2$Mo≡Ge(C$_6$H$_3$-2,6-Mes$_2$)] (**12-Mo**)	2.2966(5)	2.221(3)	2.2195	163.1(1)	175.16(8)
[Tp'(CO)$_2$Mo≡Ge(C$_6$H$_3$-2,6-Trip$_2$)] (**13-Mo**)	2.306(2)	2.25(2)	2.2765	169.4(5)	173.1(4)
[Tp'(CO)$_2$Mo≡Ge–Mes*] (**14-Mo**)	2.3112(7)	2.248(4)	2.2525	173.2(1)	176.0(1)
[Tp'(CO)$_2$Mo≡Ge–Eind] (**15-Mo**)[a]	2.3023(6)	2.224(4)	2.255	175.3(1)	178.0(1)
	2.2956(6)	2.201(4)	2.2545	174.9(1)	177.10(9)
[Tp'(CO)$_2$Mo≡Pb(C$_6$H$_3$-2,6-Trip$_2$)] (**17-Mo**)	2.5723 (2)	2.209(1)	2.259	164.64(4)	172.24(4)

[a]: Two independent molecules in the unit cell.

Table 8. M–E bond lengths and M-E-C1 angles of selected literature known molybdenum and tungsten tetrylidyne complexes.

Complex	M–E [Å]	M-E-C1/N [°]	Refereces
$[Cp(CO)_2Mo{\equiv}Si(C_6H_3\text{-}2,6\text{-}Trip_2)]$	2.2241(7)	173.49(8)	[30]
$[Cp(CO)_2Mo{\equiv}Ge(C_6H_3\text{-}2,6\text{-}Mes_2)]$	2.271(1)	172.2(2)	[27]
$[Cp(CO)_2W{\equiv}Ge(C_6H_3\text{-}2,6\text{-}Mes_2)]$	2.277(1)	170.9(3)	[28]
trans-$[Cl(PMe_3)_4Mo{\equiv}Ge(C_6H_3\text{-}2,6\text{-}Mes_2)]$	2.3041(3)	176.27(8)	[59]
trans-$[Cl(PMe_3)_4W{\equiv}Ge(C_6H_3\text{-}2,6\text{-}Mes_2)]$	2.3106(4)	176.3(1)	[59]
trans-$[Cl(PMe_3)_4Mo{\equiv}Sn(C_6H_3\text{-}2,6\text{-}Mes_2)]$	2.4808(4)	178.02(9)	[140]
trans-$[Cl(PMe_3)_4W{\equiv}Sn(C_6H_3\text{-}2,6\text{-}Mes_2)]$	2.4901(7)	178.2(1)	[42]
trans-$[Br(PMe_3)_4Mo{\equiv}Pb(C_6H_3\text{-}2,6\text{-}Trip_2)]$	2.5495(8)	177.8(2)	[43]
trans-$[Br(PMe_3)_4W{\equiv}Pb(C_6H_3\text{-}2,6\text{-}Trip_2)]$	2.5464(5)	177.5(2)	[45]

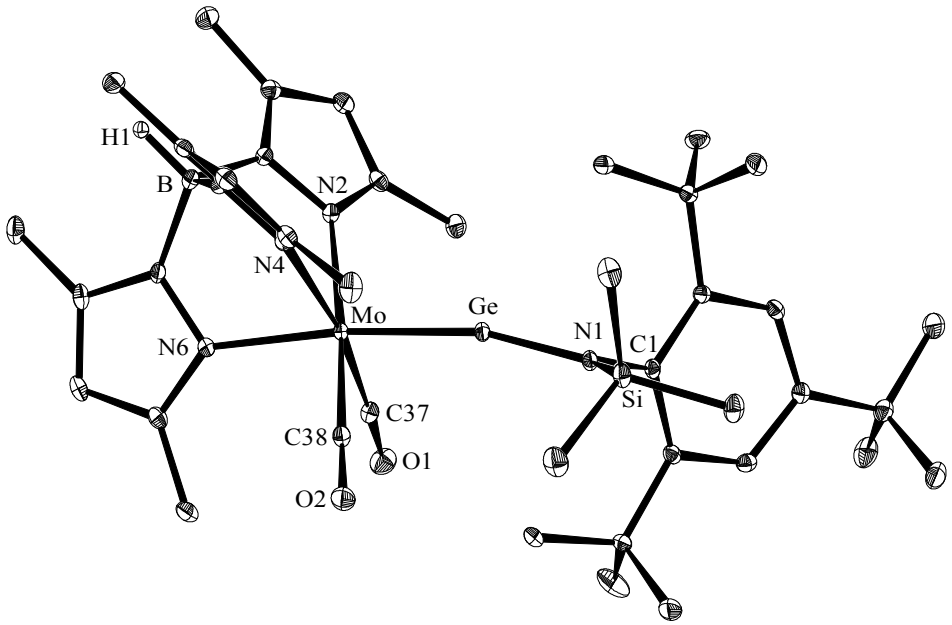

Figure 19. DIAMOND plot of the molecular structure of complex **11-Mo**. The thermal ellipsoids represent 30% of the electronic probability at 100(2) K. The hydrogen atoms (except B-H) are omitted for clarity. Selected bond lengths [Å] and angles [°] (bond lengths and bond angles of **11-W** are given in squre brackets): Mo-Ge 2.3147(2) (2.3218(6)), Ge-N1 1.822(1) [1.823(3)], Mo-N6 2.232(1) [2.220(3)]; Mo-Ge-N1 166.37(4) [166.9(1)], Si-N1-Ge 121.14(7) [120.5(2)], Si-N1-C1 118.06(9) [118.2(3)], Ge-N1-C1 120.76(9) [121.3(3)], N6-Mo-Ge 173.56(3) [173.92(9].

2.1.4.3. Infrared spectroscopic studies of the heavier tetrylidyne complexes

All tetrylidyne complexes have been characterized by solid-state and solution IR spectroscopy. The IR spectra display in all cases two ν_{CO} absorption bands of slightly different intensity, as expected for a cis-dicarbonyl complex. The two bands originate from the symmetric (A') and antisymmetric (A'') CO stretching modes. Selected results of the solution IR-spectra are summarized in Table 9. The IR-spectra were recorded in solvents of different polarity to investigate the solvent's effect on the carbonyl absorption bands. Furthermore, the results were compared with the ν_{CO} absorption bands of literature known alkylidyne complexes and Cp-substituted heavier tetrylidyne complexes. From this comparison the following trends were derived:

- The ν_{CO} bands of all tetrylidyne complexes are solvent dependent and display a shift towards lower wavenumbers, when the polarity of the solvent is increased (Table 9). For example, the ν_{CO} absorption bands of the germylidyne complex **8-Mo** in *n*-hexane appear at 1929 (s) and 1858 (vs) cm^{-1}, whereas in THF these bands appear at 1924 (s) and 1850 (vs) cm^{-1}. Notably, the solvent dependence of ν_{CO} absorption bands of carbonyl complexes is a common phenomenon that arises from the dipolar and dispersive interactions of complex with the solvent molecules.[34, 141]
- The ν_{CO} absorption frequencies of the tetrylidyne complexes decrease in the series alkylidyne → plumbylidyne (Table 9). Replacement of the alkylidyne ligand [C(*p*-Tol)] in the complex [Tp'$(CO)_2$Mo≡C–*p*-Tol] with the heavier tetrylidyne ligands [ER] (E = Ge – Pb, R = C_6H_3-2,6-Mes_2) leads to the shift of the two ν_{CO} absorption bands in THF solution from 1982 (m), 1899 (s) cm^{-1} to 1924 (s), 1850 (vs) cm^{-1} (E = Ge, **8-Mo**), 1897 (s), 1828 (vs) cm^{-1} (E = Sn, **9-Mo**) and 1890 (s), 1818 (vs) cm^{-1} (E = Pb, **10-Mo**). The same trend was also observed in *n*-hexane solution as shown in Figure 20. This trend can be rationalized by the increased Mo(d)→π*(CO) back donation in the direction C→Pb, and indicates that the σ-donor/π-acceptor ratio of the tetrylidyne ligand increases in the series – [C(*p*-Tol)]< [GeR]< [SnR]< [PbR].

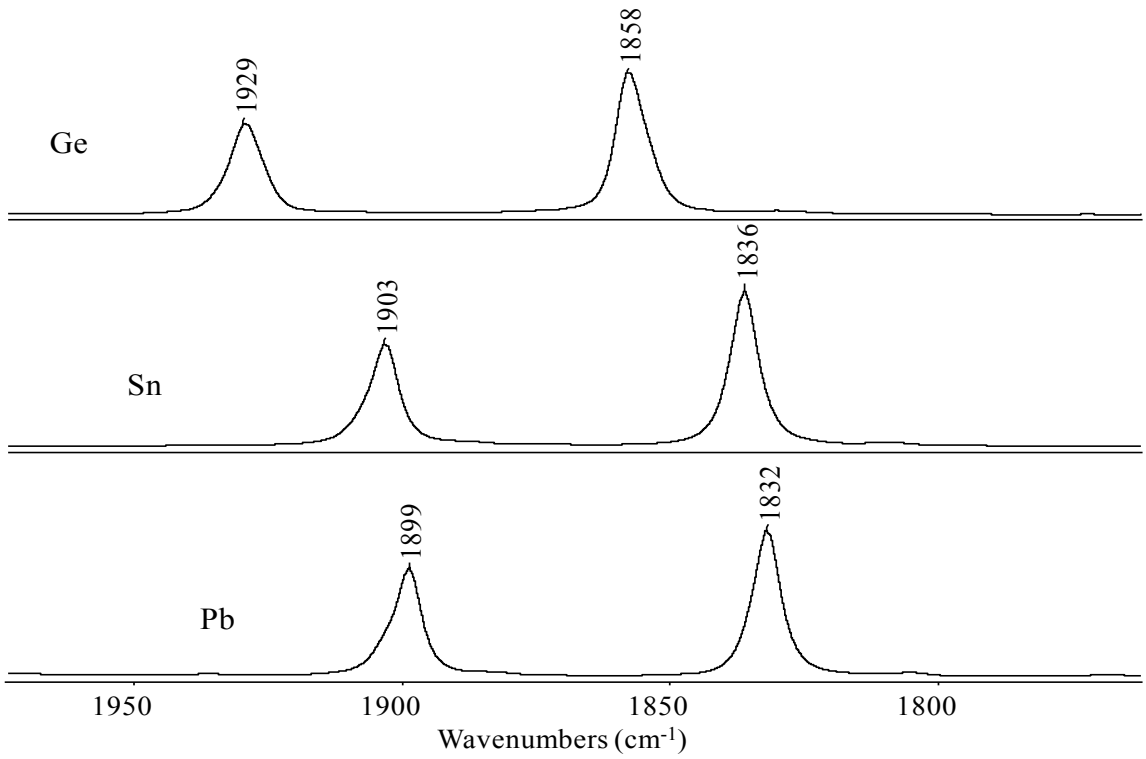

Figure 20. FT-IR spectra of the tetrylidyne complexes [Tp'(CO)$_2$Mo≡E(C$_6$H$_3$-2,6-Mes$_2$)] (E = Ge (**8-Mo**), Sn (**9-Mo**), Pb (**10-Mo**)) in *n*-hexane showing the shift of the ν_{CO} absorption bands to lower frequency in the direction Ge→Pb.

- Akin to the tetrel atoms, the ν_{CO} absorption bands of the tetrylidyne complexes also shift to lower frequency upon descending from molybdenum to tungsten (Table 9), suggesting a better W→CO back donation compared to the Mo→CO back donation. For instance, the IR spectrum of the germylidyne complex **8-Mo** displays two ν_{CO} absorption bands in THF at 1924 (s), 1850 (vs) cm^{-1}, whereas that of **8-W** shows two bands at 1913 (s) and 1836 (vs) cm^{-1}.
- The position of the ν_{CO} bands not only depends on the metal and tetrel atoms but also varies with the ligands sphere and the tetrel substituents. For example, replacement of the Tp' ligand by the Tp ligand results in a hypsochromic shift of the ν_{CO} absorption bands (cf. ν_{CO} of **8-Mo** in THF at 1924 (s), 1850 (vs) cm^{-1} and of **12-Mo** at 1930 (s), 1857 (vs) cm^{-1}) suggesting that the Tp' group is a better donor ligand than Tp. Furthermore, replacement of the Tp' ligand with the Cp/Cp* ligand also causes a shift of the ν_{CO} absorption bands to higher wavenumbers (Table 9) (cf. ν_{CO} of **8-Mo** in *n*-hexane (1929 (s), 1858 (vs) cm^{-1}),

[$Cp(CO)_2Mo{\equiv}Ge(C_6H_3$-2,6-$Mes_2)$] in *n*-pentane (1945 (vs), 1885 (s) cm^{-1}) and [$Cp^*(CO)_2Mo{\equiv}Ge(C_6H_3$-2,6-$Mes_2)$] in *n*-pentane (1932 (vs), 1873 (s) cm^{-1})),[34, 36] suggesting the following trend of their donor properties[11]–

Tp'>Tp>Cp*>Cp

- A comparison of the ν_{CO} absorption bands of the germylidyne complexes **8-Mo** and **13-Mo** shows that replacement of the C_6H_3-2,6-Mes_2 substituent by the C_6H_3-2,6-$Trip_2$ substituent results in a tiny shift of the ν_{CO} absorption bands towards higher wavenumbers (cf. ν_{CO} of **8-Mo** in THF (1924 (s), 1850 (vs) cm^{-1}) and of **13-Mo** (1926 (s), 1852 (vs) cm^{-1}), whereas replacement by the Eind, Mes* or the Ge{N(TMS)Mes*} substituent leads to a shift of the ν_{CO} absorption bands towards lower frequency (Table 9, Figure 21). This suggest the following trend of the σ-donor/π-acceptor ratio of different germylidyne ligands –

$Ge(C_6H_3$-2,6-$Trip_2) \approx Ge(C_6H_3$-2,6-$Mes_2) <$ GeEind $\approx$ GeMes* $\approx$ Ge{N(TMS)Mes*}

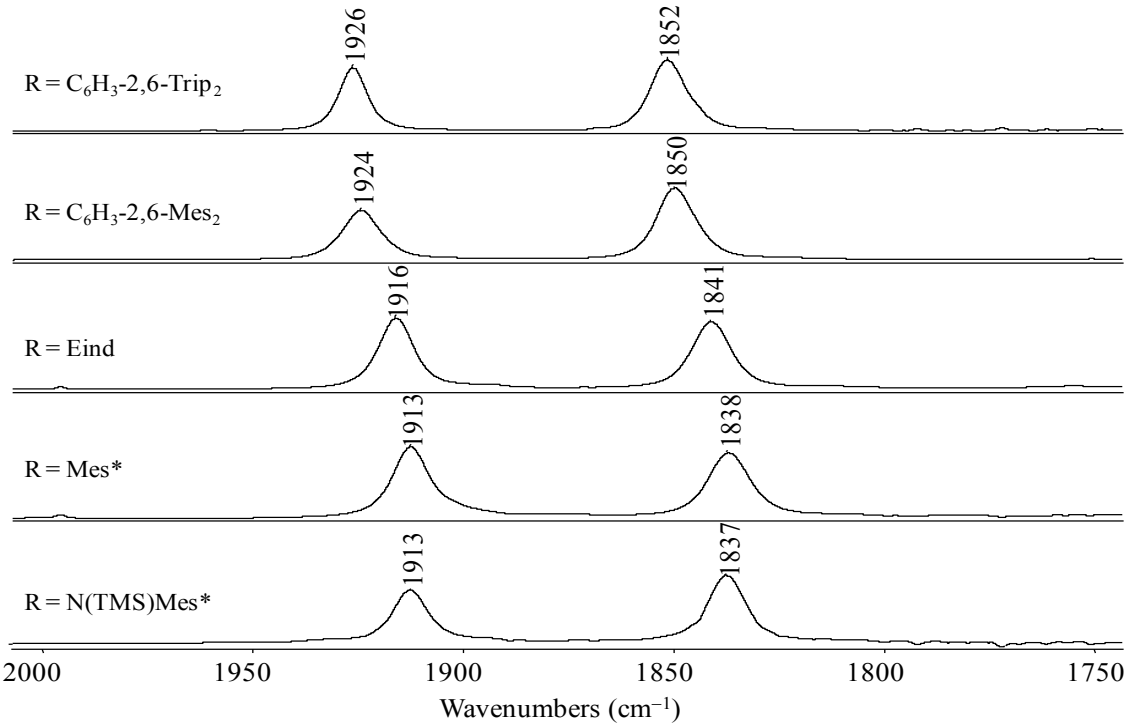

Figure 21. FT-IR spectra of the germylidyne complexes [Tp'$(CO)_2Mo{\equiv}$GeR] (R = C_6H_3-2,6-$Trip_2$, C_6H_3-2,6-Mes_2, Eind, Mes* and N(TMS)Mes*) in THF showing the change of the ν_{CO} absorption bands on changing the substituent in the germylidyne ligands.

11 This trend may also reflect the more pronounced bendeing at the tetrel centers in the Tp/Tp'-germylidyne complexes compared to the Cp/Cp*-germylidyne complexes.

A similar trend is also observed for the plumbylidyne complexes **10-Mo** and **17-Mo**, where replacement of the C_6H_3-2,6-Mes_2 substituent by the C_6H_3-2,6-$Trip_2$ substituent causes a shift of the ν_{CO} absorption bands in THF from 1890 (s), 1818 (vs) cm^{-1} to 1896 (s), 1827 (vs) cm^{-1} (Table 9).

Table 9. Infrared absorption bands (ν_{CO}) of the tetrylidyne complexes and related alkylidyne complexes.

Complex	IR [cm^{-1}]	Solvent	Reference
[Tp'$(CO)_2$Mo≡C–*p*-Tol]	1982 (m), 1899 (s)	THF	[138]
[Tp'$(CO)_2$W≡C–*p*-Tol]	1974 (m), 1888 (s)	*n*-hexane	[142]
[Tp'$(CO)_2$Mo≡Si–Tbb] (**7-Mo**)	1912 (s), 1835 (vs) 1918 (s), 1844 (vs)	THF *n*-pentane	this work
[Tp'$(CO)_2$W≡Si–Tbb] (**7-W**)	1901 (s), 1822 (vs)	THF	this work
[Cp$(CO)_2$Mo≡Si(C_6H_3-2,6-$Trip_2$)]	1945 (vs), 1886 (vs)	*n*-pentane	[33]
[Tp'$(CO)_2$Mo≡Ge(C_6H_3-2,6-Mes_2)] (**8-Mo**)	1924 (s), 1850 (vs) 1929 (s), 1858 (vs)	THF *n*-hexane	this work
[Tp'$(CO)_2$W≡Ge(C_6H_3-2,6-Mes_2)] (**8-W**)	1913 (s), 1836 (vs)	THF	this work
[Tp'$(CO)_2$Mo≡Sn(C_6H_3-2,6-Mes_2)] (**9-Mo**)	1897 (s), 1828 (vs) 1903 (s), 1836 (vs)	THF *n*-hexane	this work
[Tp'$(CO)_2$W≡Sn(C_6H_3-2,6-Mes_2)] (**9-W**)	1886 (s), 1814 (vs)	THF	this work
[Tp'$(CO)_2$Mo≡Pb(C_6H_3-2,6-Mes_2)] (**10-Mo**)	1890 (s), 1818 (vs) 1899 (s), 1832 (vs)	THF *n*-hexane	this work
[Tp'$(CO)_2$W≡Pb(C_6H_3-2,6-Mes_2)] (**10-W**)	1880 (s), 1809 (vs)	THF	this work
[Tp'$(CO)_2$Mo≡Ge{N(TMS)Mes*}] (**11-Mo**)	1913 (s), 1838 (vs)	THF	this work
[Tp'$(CO)_2$W≡Ge{N(TMS)Mes*}] (**11-W**)	1902 (s), 1824 (vs)	THF	this work
[Tp$(CO)_2$Mo≡Ge(C_6H_3-2,6-Mes_2)] (**12-Mo**)	1930 (s), 1857 (vs) 1937 (s), 1867 (vs)	THF *n*-hexane	this work
[Tp'$(CO)_2$Mo≡Ge(C_6H_3-2,6-$Trip_2$)] (**13-Mo**)	1926 (s), 1852 (vs)	THF	this work
[Tp'$(CO)_2$Mo≡Ge–Mes*] (**14-Mo**)	1913 (s), 1837 (vs)	THF	this work
[Tp'$(CO)_2$Mo≡Ge–Eind] (**15-Mo**)	1916 (s), 1841 (vs)	THF	this work
[Cp$(CO)_2$Mo≡Ge(C_6H_3-2,6-Mes_2)]	1945 (vs), 1885 (s)	*n*-pentane	[34]
[Cp*$(CO)_2$Mo≡Ge(C_6H_3-2,6-Mes_2)]	1932 (vs), 1873 (s)	*n*-pentane	[36]
[Tp'$(CO)_2$Mo≡Sn{N(TMS)Mes*}] (**16-Mo**)	1893 (s), 1828 (vs)	THF	this work
[Tp'$(CO)_2$Mo≡Pb(C_6H_3-2,6-$Trip_2$)] (**17-Mo**)	1896 (s), 1827 (vs)	THF	this work

2.1.4.4. NMR spectroscopic studies of the heavier tetrylidyne complexes

All tetrylidyne complexes were characterized by multinuclear NMR spectroscopy, which corroborate well with their solid-state structures. The ^{1}H and $^{13}C\{^{1}H\}$ NMR spectra of all complexes reveal a C_s-symmetric structure in solution. In the ^{1}H and $^{13}C\{^{1}H\}$ NMR spectra, all compounds comprising of the Tp' ligand show two sets of singlet signals in a 2:1 ratio for the C^3-*Me* and C^5-*Me*, as well as for the C^3 and C^5 ring carbons of the 3,5-dimethylpyrazolyl groups of the Tp' ligand (Figure 22). As expected, all tetrylidyne complexes featuring the C_6H_3-2,6-Mes_2 substituent show a similar pattern of the ^{1}H and $^{13}C\{^{1}H\}$ NMR signals, and display only two singlet signals for the $C^{2,6}$- and C^4-Me of the Mes groups (Figure 22), suggesting a fast rotation of the *m*-terphenyl substituent about the E–C_{aryl} bonds on the NMR timescale at ambient temperature.

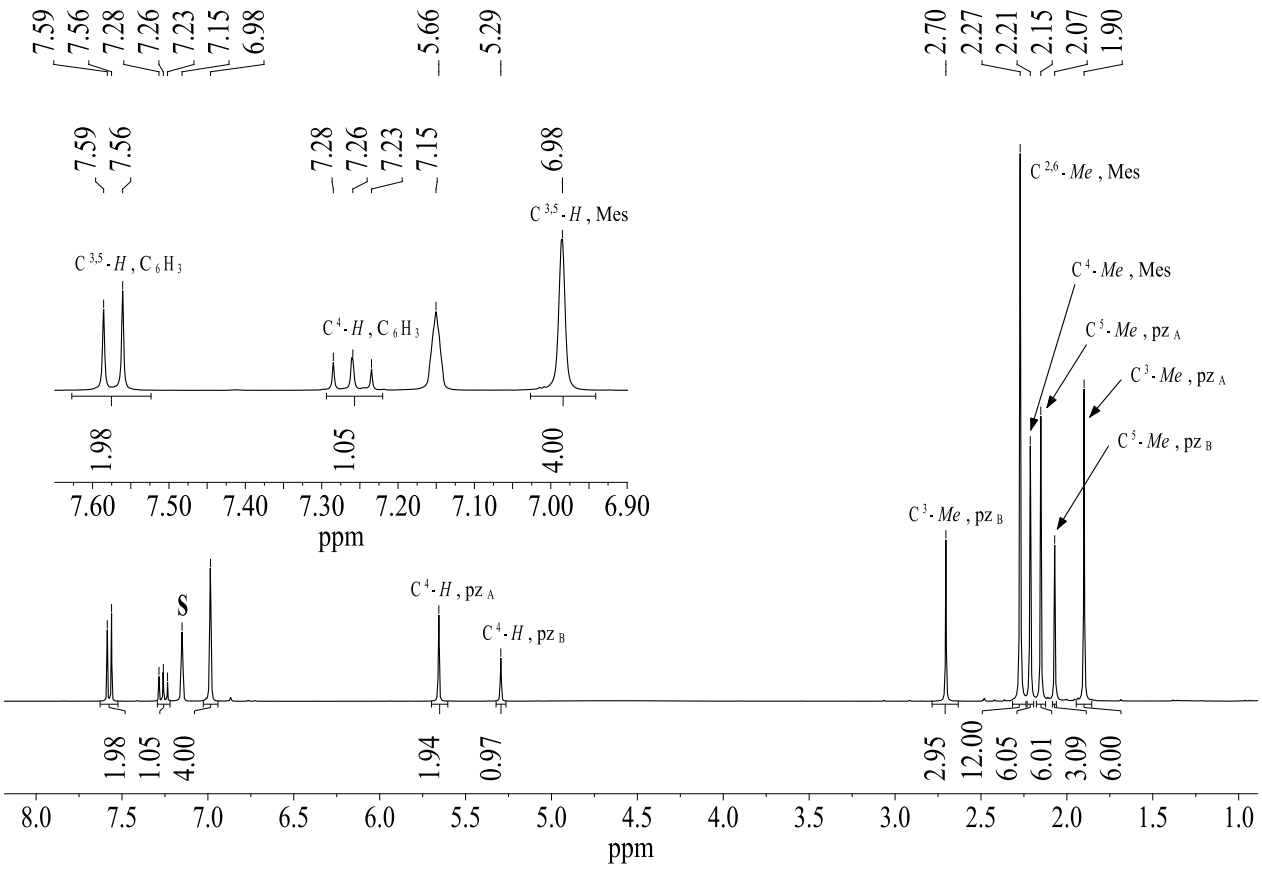

Figure 22. ^{1}H NMR spectrum (300.1 MHz) of **10-Mo** in C_6D_6. The character S denotes the residual proton signal of the deuterated solvent.

In the ^{1}H NMR spectra, the $C^{3,5}$- and C^4-*H* proton signals of the central aryl ring of the *m*-terphenyl substituted tetrylidyne complexes shift progressively to higher frequency (lower field)

from Ge→Pb (Table 10). Similarly, a comparison of the signals of the tetrel atom bonded carbon atoms (C_{ipso}) in the $^{13}C\{^1H\}$ NMR spectra also shows a significant shift towards lower-field upon going from Si→Pb (Table 10). For example, the C_{ipso} signal of the germylidyne complex **8-Mo** appears at δ = 164.3 ppm, whereas that of the plumbylidyne complex **10-Mo** appears at δ = 266.8 ppm. This trend can be rationalized with the increased relativistic effect of the heavier tetrel atoms on the light atom (e.g. H, C), abbreviated as HALA effect. This HALA effect induces a spin-orbit contribution to the chemical shift of the light atoms via mixing of the triplet state with the ground-state wave function due to spin-orbit coupling at the heavy atom.[143] Interestingly, in contrast to the C_{ipso} atoms, the carbonyl carbon signals in the $^{13}C\{^1H\}$ NMR spectra exhibit a slight upfield-shift from Si→Pb (Table 10). This can be explained by the increasing σ-donor/π-acceptor ratio of the [ER] ligand from Si→Pb, as evident by the IR spectra (*vide supra*), which indicate an increased M→CO back donation leading to a high field shift of the carbonyl carbon signal.

Table 10. Selected ^1H and $^{13}C\{^1H\}$ NMR signals of the tetrylidyne complexes measured in C_6D_6.

Complex	^1H		^{13}C	
	$C^{3,5}$-*H*	C^4-*H*	*C*^{1}	*C*O
[Tp'(CO)$_2$Mo≡Si–Tbb] (**7-Mo**)	6.87	-	148.6	229.0
[Tp'(CO)$_2$W≡Si–Tbb] (**7-W**)	6.93	-	150.7	223.8
[Tp'(CO)$_2$Mo≡Ge(C$_6$H$_3$-2,6-Mes$_2$)] (**8-Mo**)	6.87	7.14	164.3	228.1
[Tp'(CO)$_2$W≡Ge(C$_6$H$_3$-2,6-Mes$_2$)] (**8-W**)	6.934	7.18	166.9	222.7
[Tp(CO)$_2$Mo≡Ge(C$_6$H$_3$-2,6-Mes$_2$)] (**12-Mo**)	6.89	7.11	164.3	226.7
[Tp'(CO)$_2$Mo≡Ge(C$_6$H$_3$-2,6-Trip$_2$)] (**13-Mo**)	-	-	166.9	228.9
[Tp'(CO)$_2$Mo≡Ge–Mes*] (**14-Mo**)	7.47	-	161.0	230.7
[Tp'(CO)$_2$Mo≡Ge–Eind] (**15-Mo**)	-	-	160.2	230.5
[Tp'(CO)$_2$Mo≡Sn(C$_6$H$_3$-2,6-Mes$_2$)] (**9-Mo**)	6.965	7.16	182.9	227.9
[Tp'(CO)$_2$W≡Sn(C$_6$H$_3$-2,6-Mes$_2$)] (**9-W**)	7.02	7.19	183.3	222.3
[Tp'(CO)$_2$Mo≡Pb(C$_6$H$_3$-2,6-Mes$_2$)] (**10-Mo**)	7.57	7.26	266.8	222.7
[Tp'(CO)$_2$W≡Pb(C$_6$H$_3$-2,6-Mes$_2$)] (**10-W**)	7.57	7.29	255.9	218.3
[Tp'(CO)$_2$Mo≡Pb(C$_6$H$_3$-2,6-Trip$_2$)] (**17-Mo**)	7.84	7.25	272.5	224.7

For the stannylidyne complexes, a sharp singlet is observed in the $^{119}Sn\{^1H\}$ NMR spectrum at δ = 642.4 ppm (**9-Mo**) and 616.9 ppm (**9-W**) in C_6D_6 at room temperature, with the latter one being accompanied by a characteristic set of ^{183}W satellite signals with a very large $^1J_{W,Sn}$ coupling constant of 1740 Hz (Figure 23). The $^{119}Sn\{^1H\}$ signals of both compounds appear at lower field than that of the chlorostannylene $SnCl(C_6H_3\text{-}2,6\text{-}Mes_2)$ (δ = 562 ppm, in C_6D_6).[144] Furthermore, the signals are significantly low-field shifted compared to those in the phosphane-substituted stannylidyne complexes *trans*-$[Cl(PMe_3)_4Mo{\equiv}Sn(C_6H_3\text{–}2,6\text{–}Mes_2)]$ (δ = 318 ppm (quint)), *trans*-$[I(PMe_3)_4Mo{\equiv}Sn(C_6H_3\text{–}2,6\text{–}Mes_2)]$ (δ = 343 ppm (quint)) and *trans*-$[Cl(PMe_3)_4W{\equiv}Sn(C_6H_3\text{–}2,6\text{–}Mes_2)]$ (δ = 340.1 ppm (quint)).[42, 140] Notably, the $^1J_{W,Sn}$ coupling constant of 1740 Hz for the stannylidyne complex **9-W** is significantly larger than that observed for the stannylidene complex $[(CO)_5W{=}SnRR']$ (R = Mes*, R' = $CH_2C(CH_3)_2(C_6H_3\text{-}3,5\text{-}t\text{Bu}_2)$) ($\delta$ = 799 ppm, $^1J_{W,Sn}$ = 940 Hz), indicating the high s-character in the orbital used by the Sn atom to form the W≡Sn bond in compound **9-W**.[145] Unfortunately, no signal could be detected in the $^{119}Sn\{^1H\}$ NMR spectrum of the aminostannylidyne complex **16-Mo**, presumably due to the low concentration of the measured NMR solution.

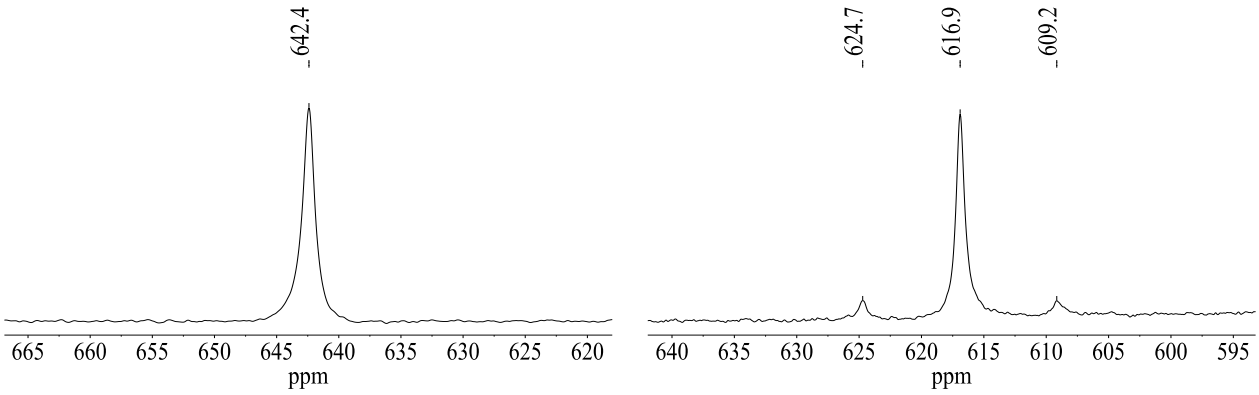

Figure 23. $^{119}Sn\{^1H\}$ NMR spectra of **9-Mo** (left) and **9-W** (right) in C_6D_6 at room temperature. In the spectrum of **9-W** the ^{183}W satellite signals flanking the main signal are clearly visible.

The ^1H NMR spectra of the aminotetrylidyne complexes **11-Mo**, **11-W** and **16-Mo** display four singlet signals for the –Si*Me*$_3$, –C^4-C(C*H*$_3$)$_3$, –C^{2,6}-C(C*H*$_3$)$_3$ and C^{3,5}-*H* groups in a 9:9:18:2 ratio, apart from the six singlet signals for the C_s-symmetric Tp' ligand (Figure 24). The $^{29}Si\{^1H\}$ NMR spectra of the aminotetrylidyne complexes exhibit a singlet signal for the *Si*Me$_3$ group at δ = 9.64 (**11-Mo**), 8.54 (**11-W**) and 6.95 ppm (**16-Mo**). These signals are marginally low-field

shifted compared to those of the aminogermylene GeCl{N(Mes*)TMS}(δ = 7.2 ppm) and the dimeric aminostannylene [Sn(μ-Cl){N(Mes*)TMS}]$_2$ (δ = 0.9 ppm).[38]

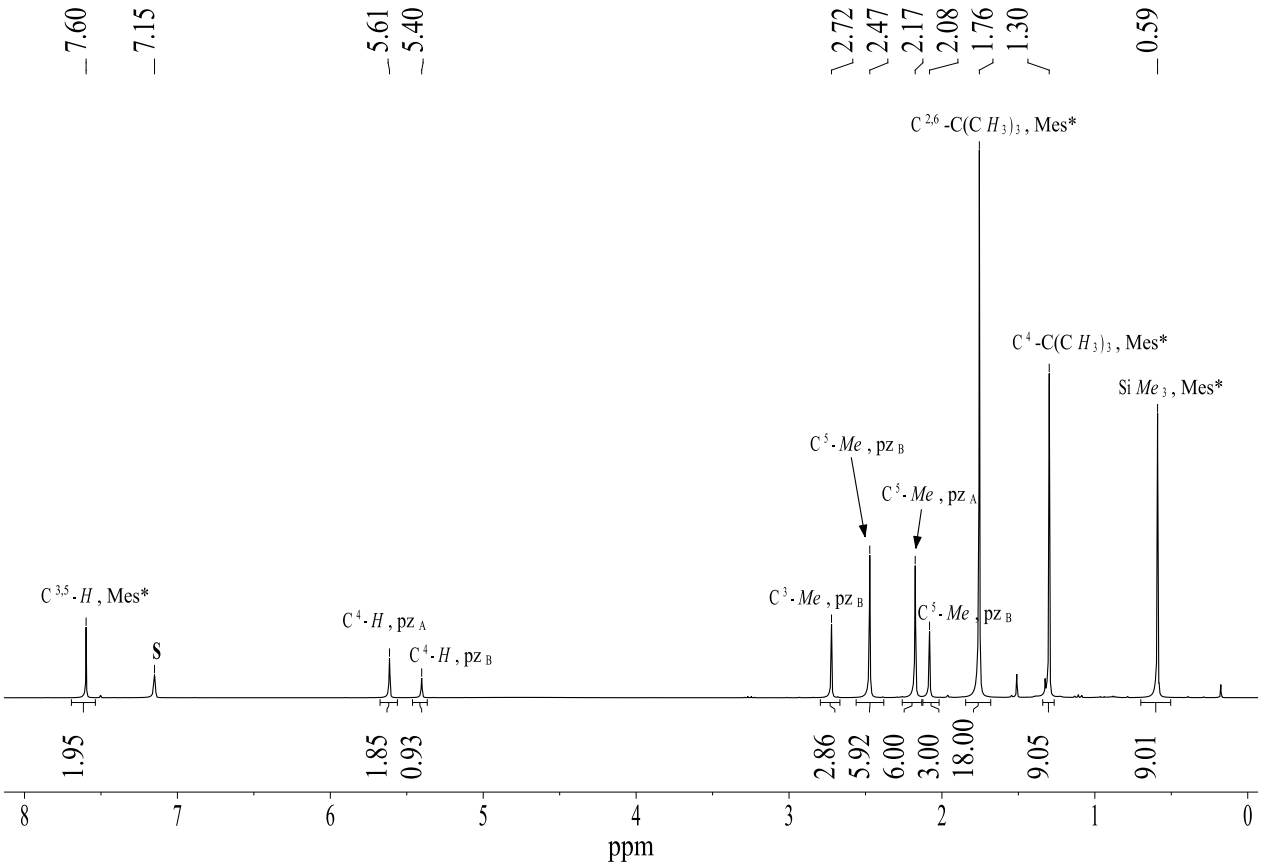

Figure 24. ^{1}H NMR spectrum (300.1 MHz, 298 K) of the aminostannylidyne complex **16-Mo** in C_6D_6. The character S denotes the residual proton signal of the deuterated solvent.

2.1.4.5. UV-Vis spectroscopic studies of the heavier tetrylidyne complexes

The color of the tetrylidyne complexes changes from reddish-orange or red to green from Si→Pb for both the molybdenum and tungsten analogues. This prompted us to investigate the UV-Vis spectra of the closed-shell tetrylidyne complexes. The UV-Vis spectra of the silylidyne complexes **7-Mo** and **7-W** were recorded in *n*-hexane and the tetrylidyne complexes **8-Mo** to **10-Mo** along with their tungsten analogues were measured in THF at ambient temperature. Furthermore, measurements were performed using three different cuvettes with three different layer thickness (*d* = 1 mm, 5 mm and 10 mm) in Young-taped quartz cells at different concentrations. The results are summarized in Table 11, and representative spectra of **7-Mo** in *n*-hexane and **8-Mo** in THF are depicted in Figure 25 and Figure 26, respectively. All complexes

display mainly three absorption maxima in the wavelength (λ) range of 300 – 650 nm (Table 11). The long-waved absorption maximum is of low intensity and appears in the wavelength range of 520 – 650 nm. This band is followed by two lower wavelength absorption bands in the spectral region of 416 – 452 nm and 318 – 378 nm, respectively, the first ones being intensive absorption bands and the latter ones very intensive bands. A comparison of the absorption bands of the tetrylidyne complexes revealed the following trends –

- From Si→Pb a bathochromic- or red-shift of the very weak and the very strong absorption bands is observed (Table 11, Figure 27).
- Replacement of the metal center from Mo to W leads to a red-shift of the long-waved absorption band, whereas a hypsochromic- or blue-shift for other two strong bands is observed (Table 11).

Table 11. Summary of the experimental UV-Vis spectra of the tetrylidyne complex **7-Mo** to **10-Mo** and its tungsten analogues showing three major absorption bands.

Complex	Absorption bands		
	Very weak λ[nm]	Strong λ[nm]	Very strong λ[nm]
[Tp'(CO)$_2$Mo≡Si–Tbb] (**7-Mo**)[a]	520	421	323
	(1032)	(11364)	(64161)
[Tp'(CO)$_2$W≡Si–Tbb] (**7-W**)[a]	548	417	318
	(346)	(6108)	(32236)
[Tp'(CO)$_2$Mo≡Ge(C$_6$H$_3$-2,6-Mes$_2$)] (**8-Mo**)	565	421	331
	-	(1230)	(10031)
[Tp'(CO)$_2$W≡Ge(C$_6$H$_3$-2,6-Mes$_2$)] (**8-W**)	576	416	320
	(72)	(1106)	(10512)
[Tp'(CO)$_2$Mo≡Sn(C$_6$H$_3$-2,6-Mes$_2$)] (**9-Mo**)	640	452	370
	-	(1771)	(30951)
[Tp'(CO)$_2$W≡Sn(C$_6$H$_3$-2,6-Mes$_2$)] (**9-W**)	650	428	363
	(360)	(2661)	(44509)
[Tp'(CO)$_2$Mo≡Pb(C$_6$H$_3$-2,6-Mes$_2$)] (**10-Mo**)	628	431	378
	(598)	-	(26230)
[Tp'(CO)$_2$W≡Pb(C$_6$H$_3$-2,6-Mes$_2$)] (**10-W**)	611	420	369
	(360)	-	(24954)

[a]: These were measured in *n*-hexane, rest werere measured in THF. Values in the brackets represent the extinction coefficient in Lmol^{-1}cm^{-1} unit.

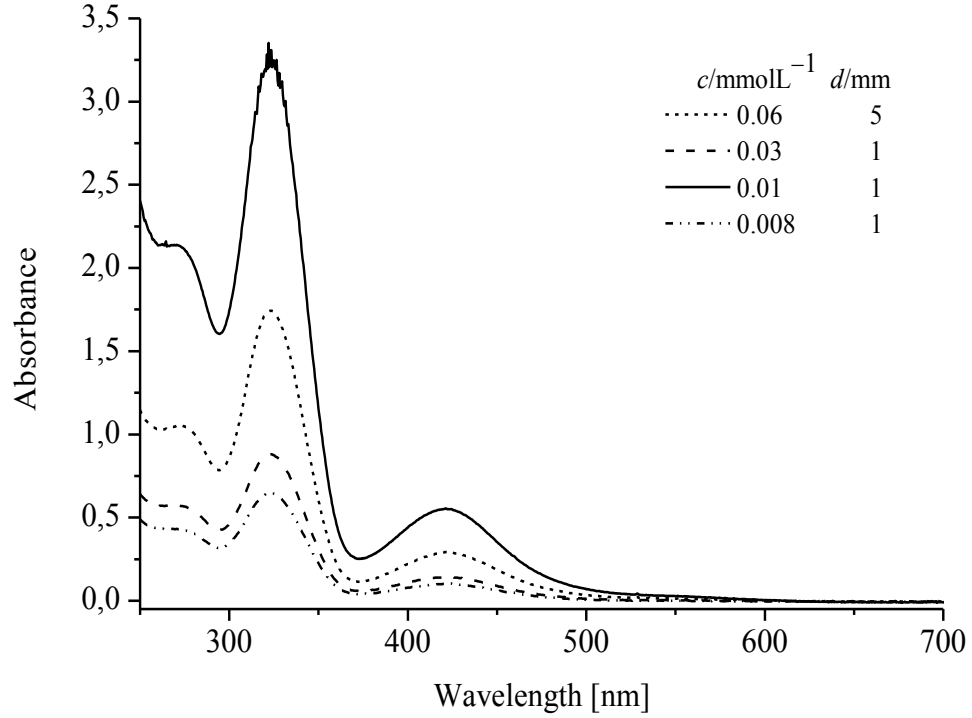

Figure 25. UV-Vis spectra of **7-Mo** at different concentrations in *n*-hexane.

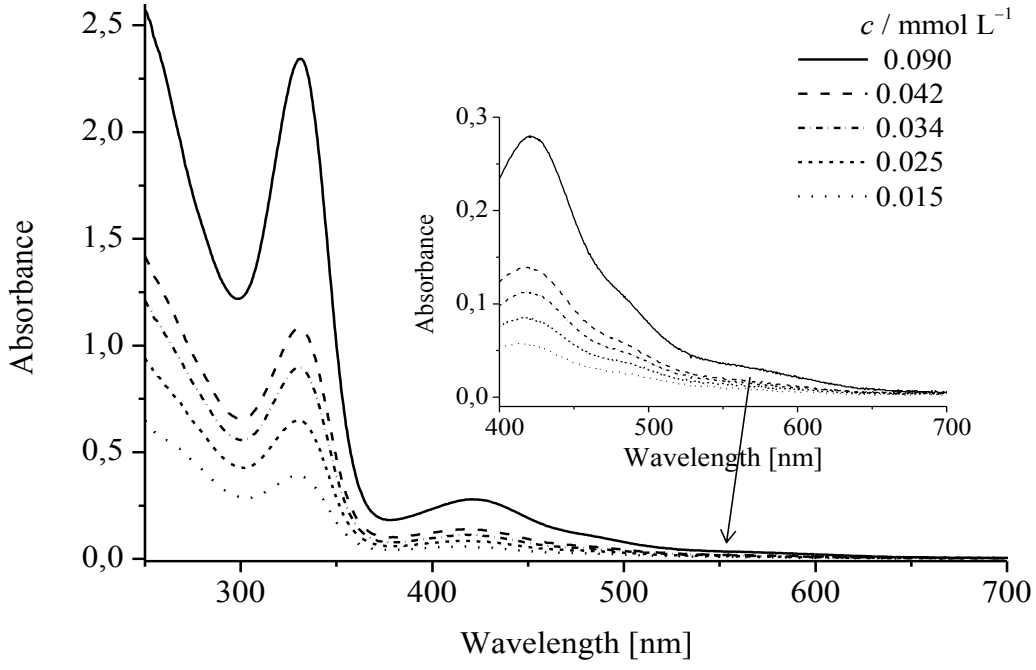

Figure 26. UV-Vis spectra of **8-Mo** at different concentrations in THF.

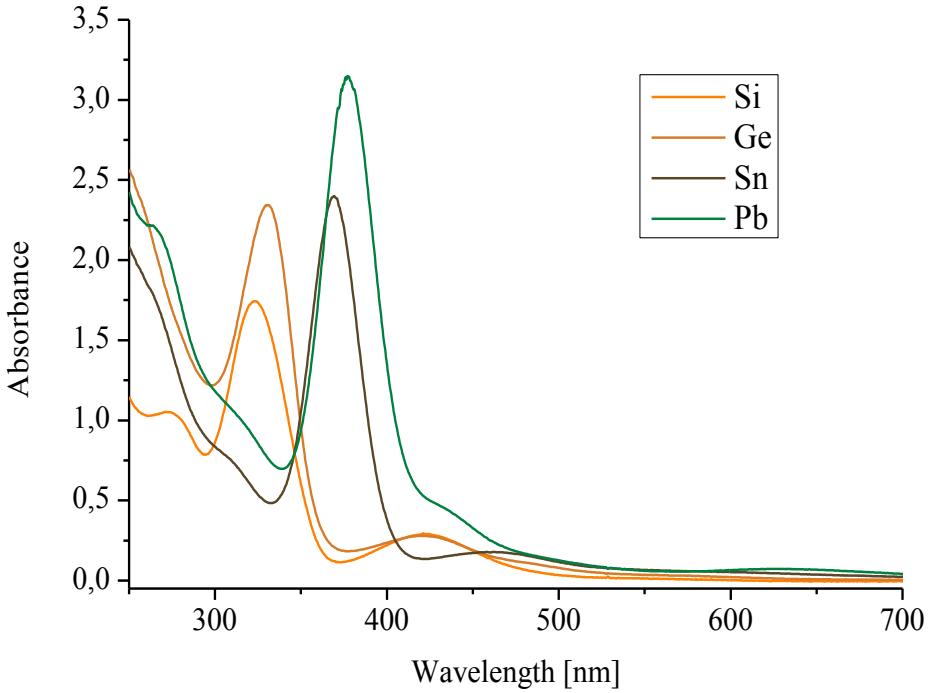

Figure 27. UV-Vis spectra of the tetrylidyne complexes [Tp'(CO)$_2$Mo≡E–R] (E = Si – Pb; R = Tbb (E = Si), C$_6$H$_3$-2,6-Mes$_2$ (E = Ge –Pb)) showing the bathochromic shift of the absorption bands from Si→Pb.

In an attempt to interpret the experimental UV-Vis spectra, a deconvolution of the spectrum of the germylidyne complex **8-Mo** was carried out to determine the actual absorption bands, which are depicted in Figure 28. The parameters used for the deconvolution are summarized in Table 12. The absorption bands were further analyzed by TD-DFT (time dependent-density functional theory) calculations of the geometry optimized minimum structures. The first 40 dipole-allowed electronic excitations were calculated at the B97-D3/RI-JCOSX/def2-TZVP level of theory. A summary of the calculated wavelengths and their corresponding MO-contribution with oscillator strength is given in Table 13. Selected Kohn-Sham frontier orbitals of the calculated minimum structure of **8-Mo** are depicted in Figure 29. A close look at the Kohn-Sham orbitals reveals that the HOMO corresponds to a metal centered nonbonding orbital. The HOMO–1 and HOMO–2 represent the two M–E π-bonding orbitals out of plane and in plane of the molecular C_s-symmetry plane, respectively. The LUMO+1 and LUMO represent their corresponding π^*-orbitals. The rest of the Kohn-Sham orbitals depicted in Figure 29 are mainly other ligand-centered orbitals.

Deconvolution of the experimental spectrum afforded five absorption bands at 565, 475, 420, 375 and 330 nm. The very weak band at λ = 565 nm arises from the symmetry forbidden HOMO(n(Mo))→LUMO(π*(Mo–Ge)) transition, which was theoretically calculated at 581 nm (Figure 29, Table 13). Thus, gradual increase of λ_{max} from Si→Pb suggest that the energy gap between the HOMO and LUMO decreases from Si→Pb. Since the HOMO is a Mo-centered nonbonding orbital and the LUMO is mainly a Ge-centered orbital, this transition can be regarded as a metal to ligand charge transfer (MLCT) transition. The position of the absorption band at 475 nm compares well with the calculated one at 484 nm, which is also a MLCT transition and originates from the electronic excitation from the HOMO(n(Mo))→LUMO+1(π*(Mo–Ge)). The band at 420 nm compares well with the calculated one at 431 nm, which includes the HOMO–1(π(Mo–Ge))→LUMO+1(π*(Mo–Ge) and HOMO–2(π(Mo–Ge))→LUMO(π*(Mo–Ge) transitions. Thus, the blue shift of this particular band in the tungsten complexes suggests that the π–π* energy difference increases in the tungsten complexes. According to the claculations, the deconvoluted band at 375 is also originating from the HOMO–2(π(Mo–Ge))→LUMO+1(π*(Mo–Ge) transition. Finally, the very strong band at 330 nm involves several transitions mainly from HOMO–3, HOMO–4, HOMO–5, HOMO–6 and HOMO–7 to LUMO.

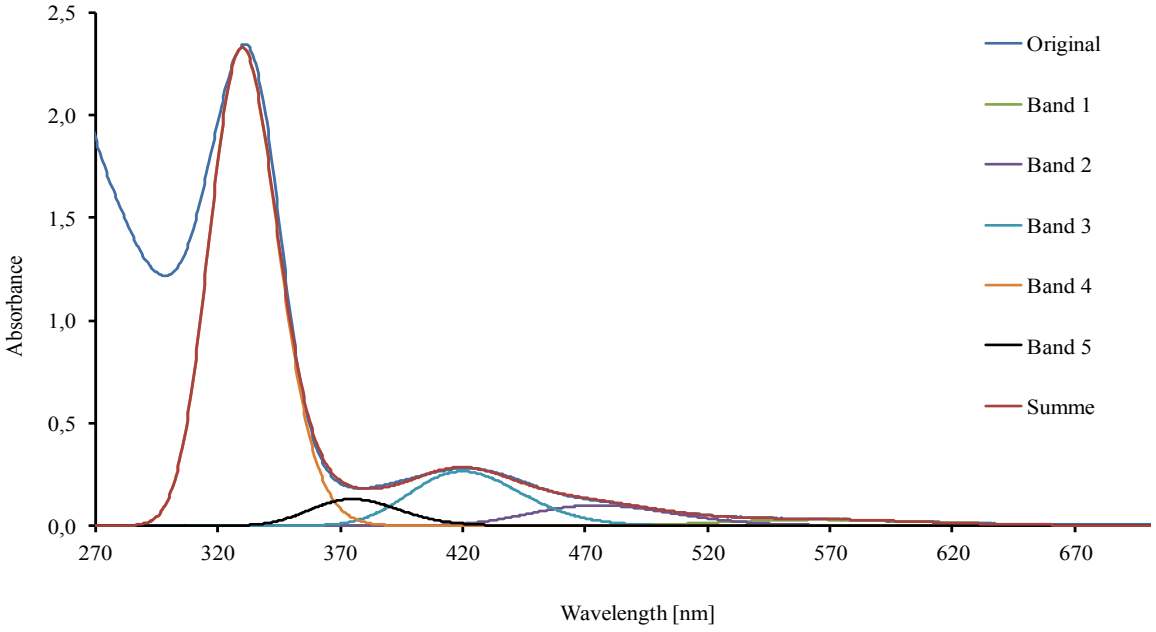

Figure 28. Deconvoluted and experimental UV-Vis spectrum of **8-Mo** in THF.

Table 12. Parameters used for the band deconvolution of the UV-Vis spectrum depicted in Figure 28.

		Band 1	Band 2	Band 3	Band 4	Band 5
Wavelength [nm]	λ_{max}	565	475	420	330	375
Absorbance	A_{max}	0,030	0,100	0,265	2,330	0,130
Bandwidth [cm^{-1}]	σ_{max}	1800	1800	1800	1800	1800

Table 13. Calculated energies and assignment of electronic transitions of **8-Mo**.[a]

Excited State	λ / nm	MO contributions[b]	Contribution [%]	*f*
1	581	HOMO→LUMO	91	0.00884
2	515	HOMO−1→LUMO	95	0.00001
3	484	HOMO→LUMO+1	98	0.00070
4	431	HOMO−2→LUMO HOMO−1→LUMO+1	57 39	0.00553
5	393	HOMO−2→LUMO+1	96	0.00266
6	343	HOMO→LUMO+2	83	0.00196
7	336	HOMO−3→LUMO HOMO−4→LUMO	82 14	0.00186
8	333	HOMO→LUMO+3 HOMO→LUMO+11	63 11	0.01807
9	330	HOMO−5→LUMO HOMO−4→LUMO	61 30	0.02242
10	329	HOMO−6→LUMO HOMO−7→LUMO	61 37	0.00573
11	327	HOMO−4→LUMO HOMO−5→LUMO HOMO−3→LUMO	52 26 12	0.02170
12	324	HOMO−6→LUMO	92	0.00021
13	323	HOMO−7→LUMO HOMO−6→LUMO	59 33	0.00065
14	319	HOMO→LUMO+5 HOMO−1→LUMO+3	44 20	0.00034
15	317	HOMO−1→LUMO+1 HOMO−1→LUMO+5 HOMO−2→LUMO	27 22 16	0.42903
16	308	HOMO→LUMO+4 HOMO→LUMO+3	58 13	0.05589
17	304	HOMO−1→LUMO+3 HOMO→LUMO+5	44 23	0.04732

[a]: λ is the wavelength of the excitation, *f* is the oscillator strength of the electronic transition. [b]: only MO contribution >10 % are given.

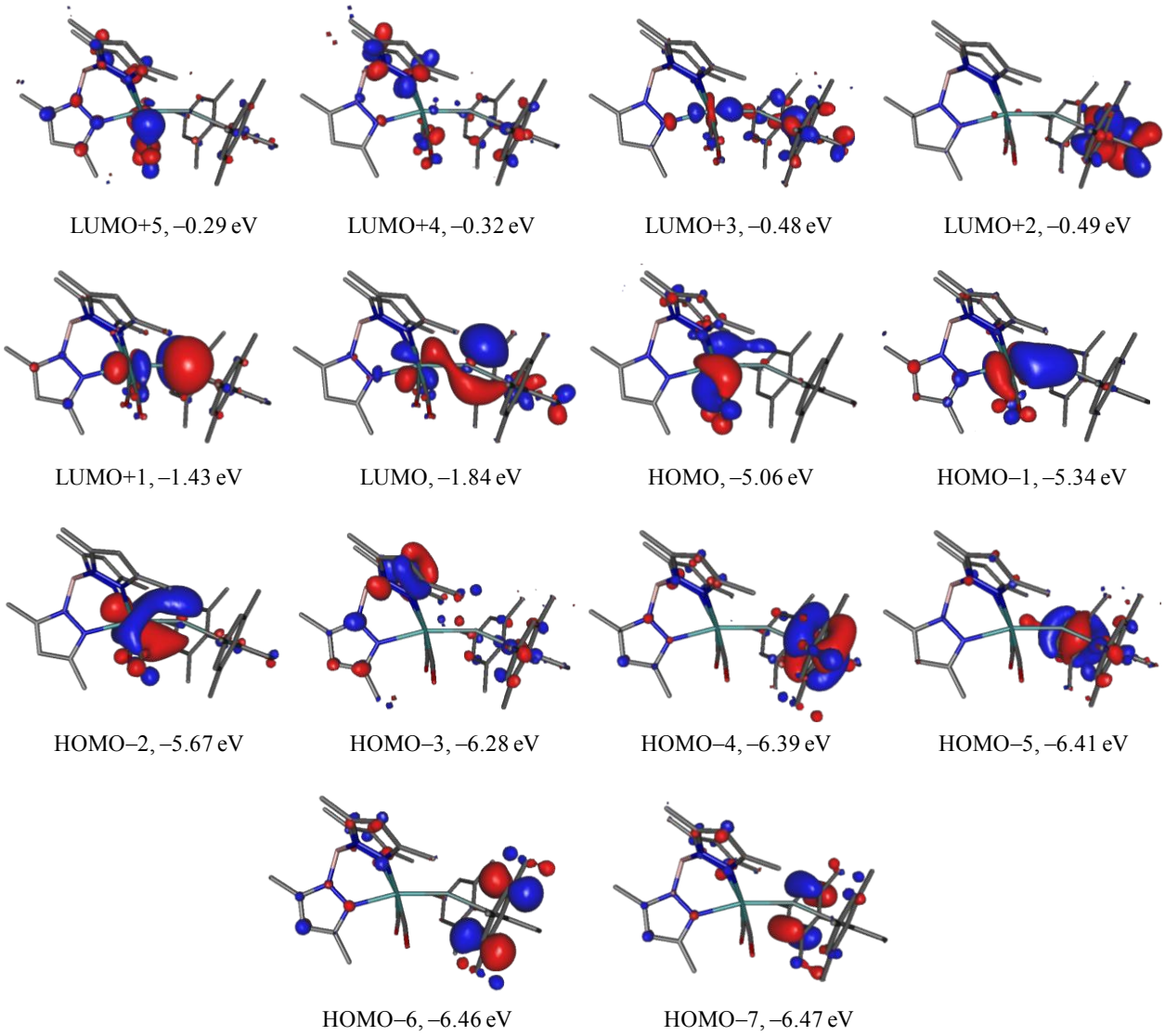

Figure 29. Selected Kohn-Sham frontier orbitals of **8-Mo** and their energy eigenvalues; the isosurface value corresponds to 0.04 e bohr^{-3}.

2.1.4.6. Cyclic voltammetric studies of the heavier tetrylidyne complexes

Following the successful isolation of the tetrylidyne complexes **7-Mo** – **10-Mo** and **7-W** – **10-W**, a detailed electrochemical study of these closed-shell complexes was performed in order to elucidate whether a one-electron reduction is reversible. The ultimate goal was to obtain open-shell complexes containing a tetrel-centered unpaired electron. The cyclic voltammograms (CV) of the complexes were measured in THF either at room temperature or −11 °C using a 4 mM $Fe(C_5Me_5)_2/Fe(C_5Me_5)_2^+$/0.1 M $(NBu_4)PF_6$/THF reference electrode and a 0.1 M $(NBu_4)PF_6$ solution in THF as the electrolyte. The results of these CV studies are summarized in Tables 14 and 15, and selected cyclic voltammograms are depicted in Figure 30 and Figure 31. Auspiciously, studies exhibit a reversible one-electron reduction in the potential range (−2.038) – (−1.729) V for the Ge, Sn and Pb analogues. In comparison, the molybdenum silylidyne **7-Mo** shows a quasi-reversible one-electron reduction at $E_{1/2}$ = −1.940 V, and the corresponding tungsten silylidyne **7-W** exhibit an irreversible reduction at a cathodic peak potential (E_{pc}) of −1.745 V. Furthermore, the cyclic voltammogram of the silylidyne complex **7-Mo** also displays a reversible one-electron oxidation at $E_{1/2}$ = +0.147 V and all other complexes display an either irreversible or a quasi-reversible one-electron oxidation around a similar potential.

Table 14. Comparison of half-wave reduction potentials ($E_{1/2}$) of the heavier alkylidyne complexes measured by cyclic voltammetry in THF.[a]

Complex	T [°C]	v [mV s^{-1}]	ΔE_p [mV]	i_{pa}/i_{pc}	$E_{1/2} = (E_{pa} + E_{pc})/2$ [mV]
[Tp'(CO)$_2$Mo≡Si–Tbb] (**7-Mo**)	25	100	118	1.02	−1940
[Tp'(CO)$_2$Mo≡Ge(C$_6$H$_3$-2,6-Mes$_2$)] (**8-Mo**)	−11	100	58	0.86	−1920
[Tp'(CO)$_2$Mo≡Sn(C$_6$H$_3$-2,6-Mes$_2$)] (**9-Mo**)	25	100	80	1.00	−1800
[Tp'(CO)$_2$Mo≡Pb(C$_6$H$_3$-2,6-Mes$_2$)] (**10-Mo**)	−11	100	68	1.01	−1729
[Tp'(CO)$_2$W≡Si–Tbb] (**7-W**)	25	100	74	0.46	*
[Tp'(CO)$_2$W≡Ge(C$_6$H$_3$-2,6-Mes$_2$)] (**8-W**)	−11	100	60	0.92	−2038
[Tp'(CO)$_2$W≡Sn(C$_6$H$_3$-2,6-Mes$_2$)] (**9-W**)	−11	100	62	1.02	−1879
[Tp'(CO)$_2$W≡Pb(C$_6$H$_3$-2,6-Mes$_2$)] (**10-W**)	−11	100	66	1.01	−1823

[a] v: scan rate; ΔE_p: peak potential separation; $\Delta E_p = E_{pa} - E_{pc}$, E_{pa} is the anodic peak potential and E_{pc} the cathodic peak potential; i_{pa}/i_{pc}: ratio of anodic and cathodic peak current; $E_{1/2}$: half wave potential. Potentials are given vs. the $[Fe(C_5Me_5)_2]^{+1/0}$ reference electrode; [*] no reversible one-electron reduction process was observed for **7-W**.

Table 15. Comparison of half-wave oxidation potentials ($E_{1/2}$) of the silylidyne complexes measured by cyclic voltammetry in THF.[a]

Complex	T [°C]	v [mV s^{-1}]	ΔE_p [mV]	i_{pa}/i_{pc}	$E_{1/2} = (E_{pa} + E_{pc})/2$ [mV]
[Tp'$(CO)_2$Mo≡Si–Tbb] (**7-Mo**)	25	100	62	1.01	+147
[Tp'$(CO)_2$W≡Si–Tbb] (**7-W**)	25	100	70	1.05	–203

[a] v: scan rate; ΔE_p: peak potential separation; $\Delta E_p = E_{pa} - E_{pc}$, E_{pa} is the anodic peak potential and E_{pc} the cathodic peak potential; i_{pa}/i_{pc}: ratio of anodic and cathodic peak current; $E_{1/2}$: half wave potential. Potentials are given vs. the $[Fe(C_5Me_5)_2]^{+1/0}$ reference electrode.

The reversibility of the one-electron reduction (for Ge, Sn and Pb analogues) and the one-electron oxidation (for **7-Mo**) were confirmed by the following criteria –

- In general, the half-wave potentials ($E_{1/2}$) were found to be constant in the scan rate (ν) range of 50 – 1000 mV s^{-1} as shown for the one-electron reduction of germylidyne complex **8-Mo** (Table 16) and the one-electron oxidation of the silylidyne complex **7-Mo** (Table 17).
- The cathodic to anodic peak potential differences (ΔE_p) are in the range expected for an ideal Nernstian process (58 mV) as shown in Tables 16 and 17 and the observed slow increase of the ΔE_p values with increasing scan rates can be rationalized by the incomplete *iR*-drop compensation.
- Almost in all cases, the anodic and cathodic peak currents were almost identical ($i_{pa} / i_{pc} \approx 1$) and independent of the scan rates (Table 16 and Table 17).
- Finally, a plot of the cathodic peak currents (i_{pc}) *versus* the square root of scan rates ($\nu^{1/2}$) revealed an almost linear relationship (Figure 32).

All these criteria clearly support a reversible one-electron reduction of the Ge, Sn and Pb complexes and a reversible one-electron oxidation of the silylidyne complex **7-Mo**.

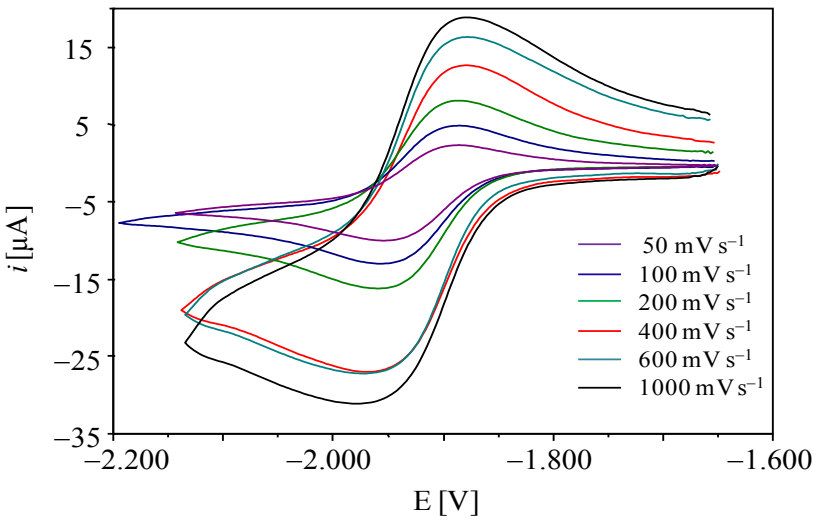

Figure 30. Single-scan cyclic voltammograms of **8-Mo** in THF at −11 °C from (−1.600) – (−2.200) V at different scan rates (50 – 1000 mV s^{-1}); reference electrode: 4 mM $Fe(C_5Me_5)_2/Fe(C_5Me_5)_2^+$ /0.1 M $(NBu_4)PF_6$/THF; electrolyte: 0.1M $(NBu_4)PF_6$.

Table 16. Cyclic voltammetric results of the compound **8-Mo**, presenting half-wave reduction potential at different scan rates.[a]

v [mV s^{-1}]	ΔE_p [mV]	i_{pa}/i_{pc}	$E_{1/2} = (E_{pa} + E_{pc})/2$ [mV]
50	62	0.70	−1919
100	58	0.86	−1920
200	60	0.98	−1918
400	62	1.02	−1919
800	64	1.04	−1919
1000	66	1.01	−1919

[a] v: scan rate; ΔE_p: peak potential separation; $\Delta E_p = E_{pa} - E_{pc}$, E_{pa} is the anodic peak potential and E_{pc} the cathodic peak potential; i_{pa}/i_{pc}: ratio of anodic and cathodic peak current; $E_{1/2}$: half wave potential. Potentials are given vs. the $[Fe(C_5Me_5)_2]^{+1/0}$ reference electrode.

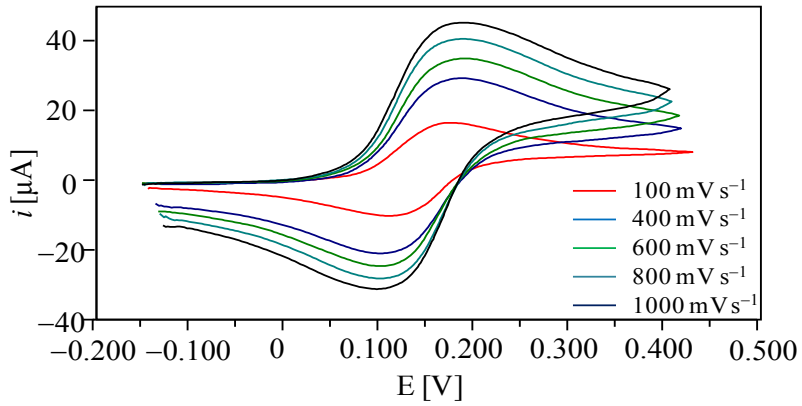

Figure 31. Single-scan cyclic voltammograms of **7-Mo** in THF at room temperature from (−0.200) – (0.500) V at different scan rates (100 – 1000 mV s^{-1}); reference electrode: 4 mM $Fe(C_5Me_5)_2/Fe(C_5Me_5)_2^+$ /0.1 M $(NBu_4)PF_6$/THF; electrolyte: 0.1M $(NBu_4)PF_6$.

Table 17. Cyclic voltammetric results of compound **7-Mo**, presenting half-wave oxidation potential at different scan rates.[a]

v [mV s^{-1}]	ΔE_p [mV]	i_{pa}/i_{pc}	$E_{1/2} = (E_{pa} + E_{pc})/2$ [mV]
100	62	1.01	+147
400	70	1.01	+147
600	70	1.02	+147
800	70	1.01	+147
1000	76	1.01	+148

[a] v: scan rate; ΔE_p: peak potential separation; $\Delta E_p = E_{pa} - E_{pc}$, E_{pa} is the anodic peak potential and E_{pc} the cathodic peak potential; i_{pa}/i_{pc}: ratio of anodic and cathodic peak current; $E_{1/2}$: half wave potential. Potentials are given vs. the $[Fe(C_5Me_5)_2]^{+1/0}$ reference electrode.

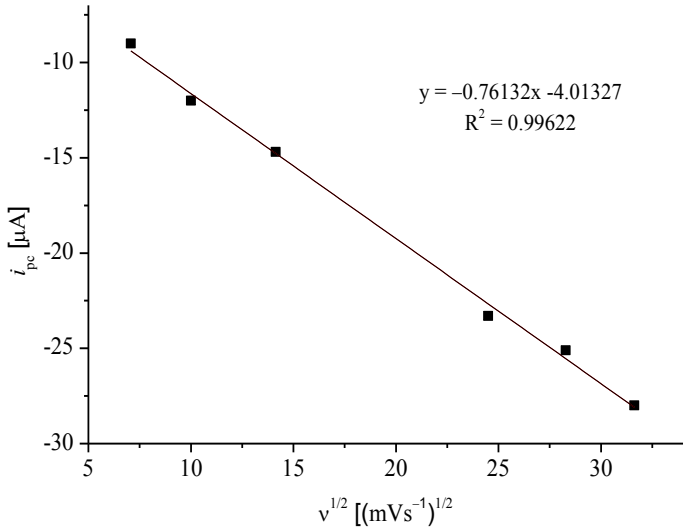

Figure 32. Plot of the cathodic peak current (i_{pc}) *versus* the square root of the scan rate ($v^{1/2}$) for the reversible reduction of **8-Mo** at $E_{1/2} = -1.919$ V.

The half-wave potential ($E_{1/2}$(red)) of the one-electron reduction of the tetrylidyne complexes was found to be strongly dependent on the metal and tetrel atoms. Thus, the reduction potential decreases on going from Mo to W (Table 14), indicating that the ease of reduction decreases upon going from the molybdenum to the tungsten analogues. For instance, the $E_{1/2}$(red) for the molybdenum germylidyne **8-Mo** was found to be −1.920 V, whereas that for the tungsten germylidyne **8-W** was found to be −2.038 V, thus showing a 118 mV decrease of the reduction potential from Mo to W. In contrast, an increase of the reduction potential ($E_{1/2}$(red)) is observed from Si → Pb, with the only exception of the tungsten silylidyne **7-W** (Table 14). Comparative cyclic voltammograms are depicted in Figure 33 showing the shift of the half-wave potentials towards higher values. As an example, the $E_{1/2}$(red) of the silylidyne complex **7-Mo** was observed at −1.940 V, whereas that for the plumbylidyne complex **10-Mo** was found at −1.729 V,

i.e. a difference of 211 mV. This increase of the reduction potential upon going from the silylidyne to the plumbylidyne complexes clearly indicates that the energy of the LUMO decreases in the same direction, and illustrates that the plumbylidyne complexes should be more easily reduced by one-electron than the corresponding silylidyne complexes.

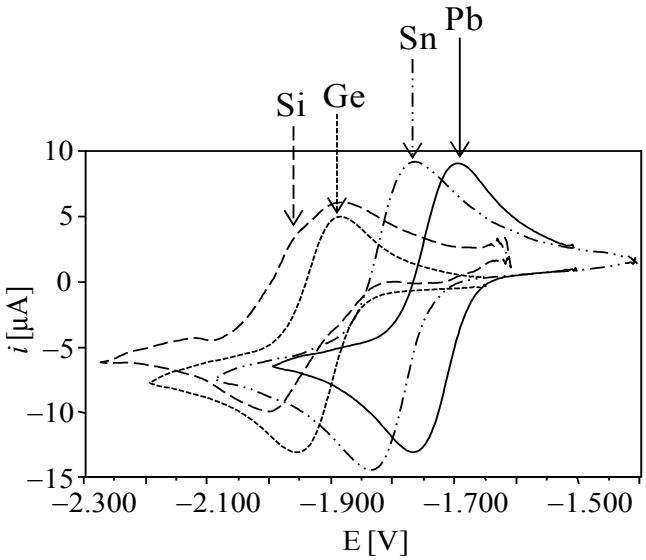

Figure 33. Single-scan cyclic voltammograms of the tetrylidyne complexes [Tp'$(CO)_2$Mo≡E–R] (R = Tbb (E = Si), R = C_6H_3-2,6-Mes_2 (E = Ge - Pb) at a scan rate of 100 mVs^{-1} showing the change of the half-wave potential on changing the tetrel atoms.

The reversible one-electron oxidation at $E_{1/2}$ = +147 mV for the silylidyne complex **7-Mo** suggests that the silylidyne radical cation [Tp'$(CO)_2$Mo≡Si(Tbb)]$^+$ might be accessible by oxidation with a suitable oxidizing agent. Irreversible one-electron oxidation for the other tetrylidyne complexes indicates the instability of the resulting radical cations, which leads to rapid follow-up reactions.

2.2. Open-shell heavier tetrylidyne complexes of group 6 transition metals

Following the successful isolation of a series of closed-shell tetrylidyne complexes of the general formula [Tp'(CO)$_2$M≡E–R] (M = Mo, W; E = Si – Pb; R = Tbb, C$_6$H$_3$-2,6-Mes$_2$), my next target was to obtain open-shell tetrylidyne complexes containing a tetrel-centered unpaired electron. As discussed earlier (*vide supra*), the quantum chemical calculations of the molybdenum germylidyne **8-Mo** revealed that the HOMO is a molybdenum centered nonbonding orbital with respect to the Mo≡Ge bond and that the HOMO–1, and HOMO–2 correspond to the two orthogonal Mo-Ge π-bonds. Furthermore, the LUMO and LUMO+1 are the corresponding orthogonal Mo–Ge π*-orbitals. Therefore, addition of one electron was expected to yield an open-shell radical anion with a tetrel centered unpaired electron. Auspiciously, the electrochemical study of these closed-shell tetrylidyne complexes also revealed that these complexes can be reversibly reduced by one electron (*vide supra*). In order to test, whether this reduction is also chemically reversible, the germylidyne complex **8-Mo** was chosen as a substrate in a first attempt. Thus, vacuum transfer of THF into a 1:1 mixture of **8-Mo** and KC$_8$ at –196 °C, followed by warming to –50 °C resulted in a distinct color change from yellowish-brown to dark green. Stirring the dark green suspension for 1 hour at –50 °C, followed by workup of the reaction mixture, afforded the thermolabile radical anion K(THF)$_3$[Tp'(CO)$_2$MoGe(C$_6$H$_3$-2,6-Mes$_2$)] (**18-Mo**) as an extremely air-sensitive, green solid in 33 % yield (Scheme 9). Compound **18-Mo** is well soluble in THF or fluorobenzene but insoluble in common aliphatic solvents.

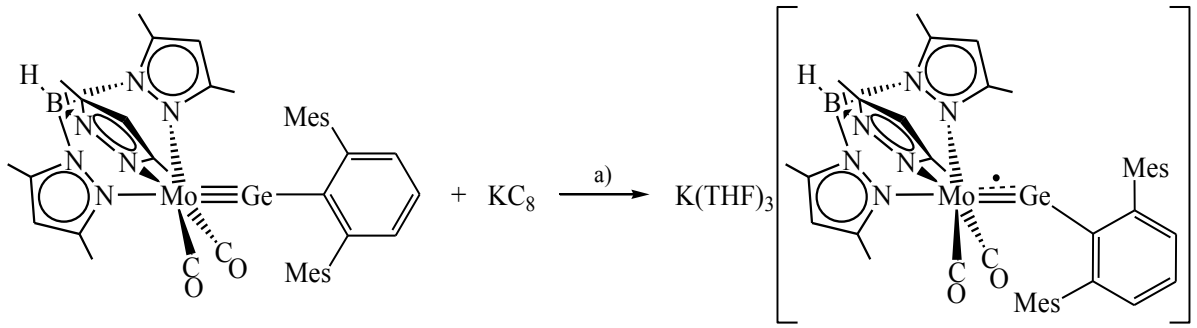

18-Mo, green solid, 33%

Scheme 9. Synthesis of the complex salt K(THF)$_3$[Tp'(CO)$_2$MoGe(C$_6$H$_3$-2,6-Mes$_2$)] (**18-Mo**) upon one-electron reduction of **8-Mo**; a) –8C, THF, –196 → –50 °C; formal charges are omitted for clarity.

The green solid slowly decompose at ambient temperature to a brown solid, but in solution it decomposes much faster even above –40 °C to give a yellow-brown solution. An inspection of

this yellow-brown solution by IR spectroscopy revealed the formation of the parent germylidyne complex **8-Mo** and some other unknown compounds displaying multiple carbonyl absorption bands at a lower frequency (<1750 cm^{-1}). These results suggest that **18-Mo** disproportionates in solution to give **8-Mo** and more reduced species.

The molecular structure of **18-Mo** was determined by single crystal X-ray diffraction analysis. The green plates of **18-Mo**·3(C_4H_8O) were grown upon cooling a solution of **18-Mo** in THF/*n*-pentane mixture at −60 °C. The molecular structure revealed a C_s-symmetric structure with the molecular plane passing through the N5, Mo, Ge and C1 atoms (Figure 34). The potassium cations are well separated from the germylidyne radical anions as evidenced by the shortest Ge···K distance of 6.479(3) Å (cf. $\Sigma r(Ge\cdots K)_{vdW}$ = 4.9 Å). Akin to the closed-shell germylidyne complex **8-Mo**, the Mo center in **18-Mo** also adopts a distorted octahedral geometry with the Ge atom being in *trans*-orientation to one of the pyrazolyl groups of the Tp' ligand, as evidenced by the N5-Mo-Ge angle of 175.3(2)°. One-electron reduction of **8-Mo** gives rise to a remarkable change of the Mo–Ge bond length, as well as the Mo-Ge-C1 angle. Thus, the Mo–Ge bond in **18-Mo** (*d*(Mo–Ge) = 2.423(2) Å) is ca. 10 pm longer than that in **8-Mo** (*d*(Mo–Ge) = 2.3117(9) [2.3121(9)] Å] and the Mo-Ge-C1 angle (147.0(4)°) becomes ca. 13° smaller than that in **8-Mo** (159.4(2) [160.6(2)]°). Notably, the Mo–Ge bond of **18-Mo** is even longer than those observed in the molybdenum germylidene complexes [$Cp(CO)_2(H)Mo{=}GeX(C_6H_3$-2,6-$Mes_2)$] (2.3921(5) Å (X = Cl), 2.4031(7) Å (X = OH), 2.4119(5) Å (X = OMe)), whereas the Mo-Ge-C1 bond angle of **18-Mo** is slightly wider than those found in these complexes (140.2(1)° (X = Cl), 139.1(2)° (X = OH), 139.1(1)° (X = OMe)).[34, 36] Furthermore, the reduction leads to an increase of the electron density on the molybdenum center as evidenced by the significant decrease of the Mo–C_{CO} bond lengths (Mo-C40 1.88(2) Å, Mo-C41 1.92(1) Å), compared to that of the closed-shell germylidyne complex **8-Mo** (Mo-$C_{CO(av)}$ 1.972 Å),[12] resulted from the increased Mo→CO back donation. These structural changes can be rationalized by the occupation of one of the two Mo≡Ge π^*-orbitals of $K(THF)_3$[Tp'$(CO)_2$MoGe(C_6H_3-2,6-Mes_2)] by one electron, which reduces the Mo–Ge bond order from 3 to 2.5. This leads to a rehybridization of the Ge orbitals and an increased σ-donor/π-acceptor ratio of the [Ge(C_6H_3-2,6-Mes_2)] ligand.

12 The Mo-C_{CO} bond lengths (Mo-C40 and Mo-C41) in compound **8-Mo** are 1.973(7) [1.966(7)] Å and 1.979(7) [1.971(7)] Å, respectively, leading to an average Mo–CO bond length of 1.972 Å.

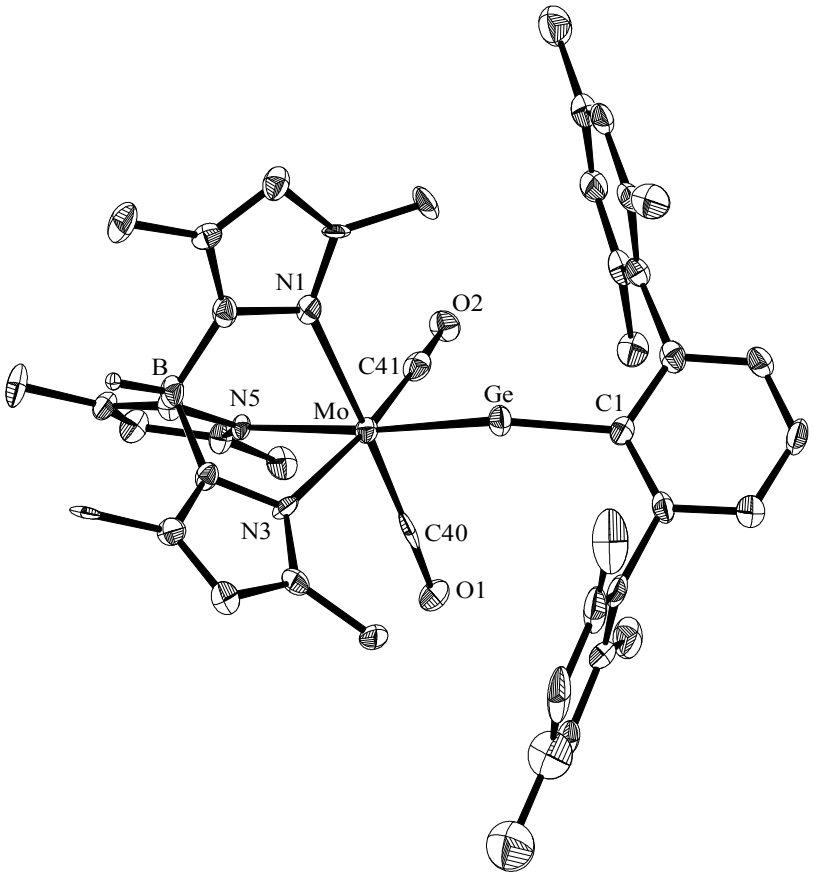

Figure 34. DIAMOND plot of the molecular structure of the anion $[Tp'(CO)_2MoGe(C_6H_3\text{-}2,6\text{-}Mes_2)]^-$ in the crystal lattice of **18-Mo**·3(C_4H_8O) at 100(2) K. Thermal ellipsoids are set at 30% probability. Hydrogen atoms (except the B-bonded H atoms), solvent molecules and the potassium cation are omitted for clarity. Selected bond lengths [Å] and bond angles [°]: Mo-Ge 2.413(2), Ge-C1 1.97(1), Mo-N1 2.30(1), Mo-N3 2.29(1), Mo-N5 2.274(9), Mo-C40 1.88(2), Mo-C41 1.92(1); Mo-Ge-C1 147.0(4), N1-Mo-Ge 95.6(3), N3-Mo-Ge 104.0(3), N5-Mo-Ge 175.3(2).

The solid-state FT-IR spectrum of the radical anion displays two equally intense ν_{CO} stretching absorption bands at 1794 and 1723 cm^{-1}, which are shifted towards lower wavenumbers than those of the parent germylidyne complex **8-Mo**. The shift of the ν_{CO} frequency towards lower wavenumbers suggests an increased $Mo \rightarrow C_{CO}$ backdonation accompanying the one-electron reduction of the neutral germylidyne complex.

Further insight of the electronic structure of the radical anion **18-Mo** was provided by continuous-wave (*cw*) EPR spectroscopy using S- and X-band resonators and was backed up by DFT calculations carried out at the B97-D3/RI-JCOSX/def2-TZVP level of theory. The samples were prepared in THF and measured at 5 K for the S-band and 10 K for the X-band. Simulation

of the experimental spectra suggest a weakly rhombic *g*-tensor (g_{xx} = 1.850, g_{yy} = 1.963, g_{zz} = 1.997) and a g_{iso} value of 1.937. The experimental values are in excellent agreement with the calculated values of the g-tensor (g_{xx} = 1.853, g_{yy} = 1.996, g_{zz} = 2.018, and g_{iso} = 1.955) (Figure 35, Table 18). The g_{iso} value of 1.937 is slightly lower than those usually found for Ge-centered radicals (1.9991 – 2.0107).[146] This indicates a partial delocalization of the unpaired electron towards the Mo-center. Surprisingly, hyperfine coupling with the ^{73}Ge nucleus (*I* = 9/2, 7.8 % abundance) or the $^{95/97}$Mo nuclei (*I* = 5/2, 15.92 and 9.55 abundance) was not resolved experimentally, possibly due to low resolution of the spectra, but the DFT-derived values suggest that **18-Mo** is a π-type radical. Thus, the value of the hyperfine coupling tensor of –42.7 MHz, which is significantly higher than the other two values (11.9 and 13.0 MHz), compares well with previously known Ge-centered π-type radicals, [(^{But}Nacnac)Ge:]$^{\bullet}$ (^{But}Nacnac = [{N(Dip)C(*t*Bu)}$_2$CH]$^-$) (A(^{73}Ge) = ±37.5 – 82.5),[147] [{CH(SiMe$_3$)$_2$}$_2$Ge:]$^{\bullet-}$ (A(^{73}Ge) = 35 MHz)[148] and [Ge(SiMe*t*Bu$_2$)$_3$]$^{\bullet}$ (A(^{73}Ge) = 56 MHz)[149] but is significantly lower than that observed for the σ-type radical [Ge{N(SiMe$_3$)$_2$}$_3$]$^{\bullet}$ (A(^{73}Ge) = 479 MHz).[150] Additionally, the very small hyperfine coupling constants of (–20.6) – (–61.6) MHz with the $^{95/97}$Mo nuclei are also indicative of a Ge-centered radical.[59, 60]

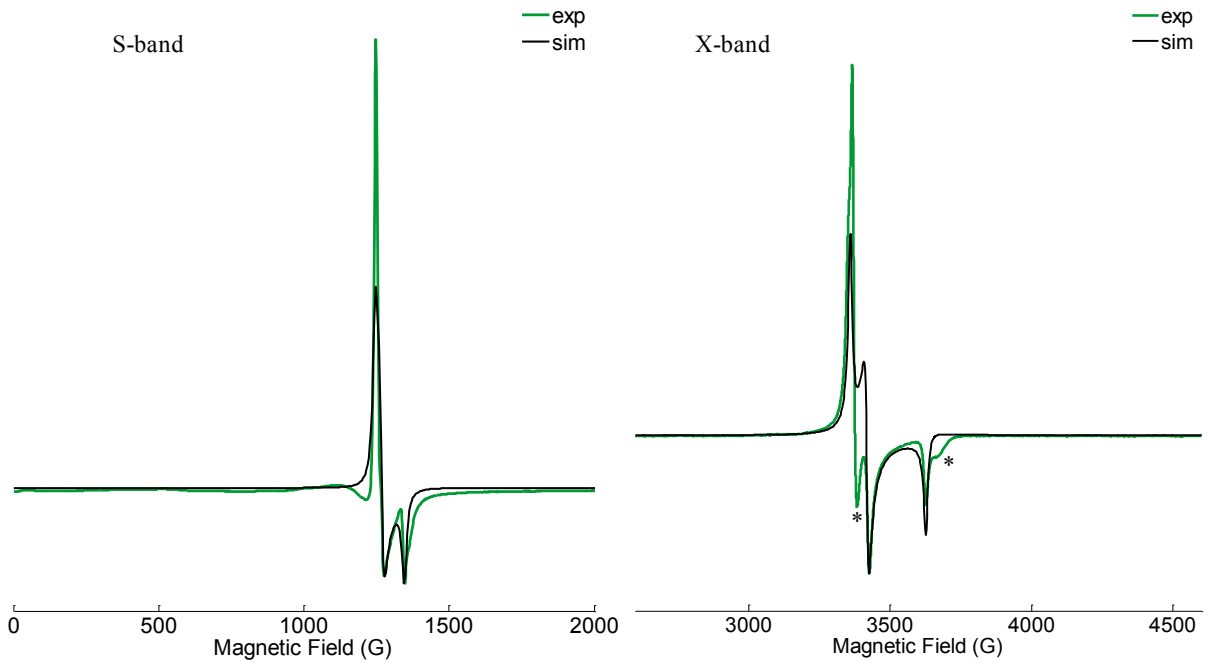

Figure 35. S-band (left, 5 K) and X-band (right, 10 K) *cw*-EPR spectrum of the germylidyne radical anion salt **18-Mo** in THF; green line represent an experimental spectrum, and the black line represents the simulated spectrum. The asterisk (*) on the X-band spectrum represents one unknown impurity.

Table 18. Experimental and calculated *g*-tensors and calculated A(^{97}Ge)- and A(^{98}Mo)-tensors of the germylidyne radical anion in **18-Mo**.

Method	*g*			A(^{73}Ge) [MHz]			A($^{95/97}$Mo) [MHz]		
	g_{xx}	g_{yy}	g_{zz}	A_x	A_y	A_z	A_x	A_y	A_z
Experimental	1.850	1.963	1.997	*	*		*	*	*
		g_{iso} = 1.937							
DFT	1.853	1.996	2.018	11.9	–42.7	13.0	–44.2	–61.6	–20.6
(B97-D3)		g_{iso} = 1.955							

*: No hfcc's could be resolved experimentally.

Although more detailed quantum chemical calculations will be necessary to describe the actual electronic structure of the open-shell germylidyne complex **18-Mo**, the solid-state structure and the ESR spectra so far suggest that the compound **18-Mo** is an open-shell germylidyne complex, which features an unpaired electron at the germanium center. Thus, despite its thermal instability, isolation and characterization of this novel compound represent a significant success in this field.

2.3. Germylidyne mediated C–C coupling reaction of isonitriles – formation of an N-heterocyclic germylene

Reactions of alkynes or phosphaalkynes with heavier alkylidyne complexes are very well known, and generally resulted in very fascinating [2+2] cycloaddition products.[33, 38, 58] This inspired us to study the reactivity of the Tp'-substituted tetrylidyne complexes towards analogous isonitriles. Surprisingly, the reaction of *i*PrNC with the molybdenum germylidyne **8-Mo** produces a different type of product, rather than just the [2+2] cycloaddition product. Heating of a mixture of **8-Mo** with an excess *i*PrNC in *n*-heptane at 100 °C resulted in a complete splitting of the Mo≡Ge bond and coupling of two isonitrile groups, thus resulting in the formation of an N-heterocyclic germylene (**19-Mo**), which forms the backbone of a diaminoalkyne liagnd (Scheme 10). Compound **19-Mo** was isolated after workup as an analytically pure, air-sensitive, yellowish-brown solid in 60 % yield. The yellowish brown solid decompose upon melting to a reddish brown liquid at 155 – 158 °C. Compound **19-Mo** is very well soluble in THF, toluene, and Et_2O and moderately soluble in aliphatic solvents.

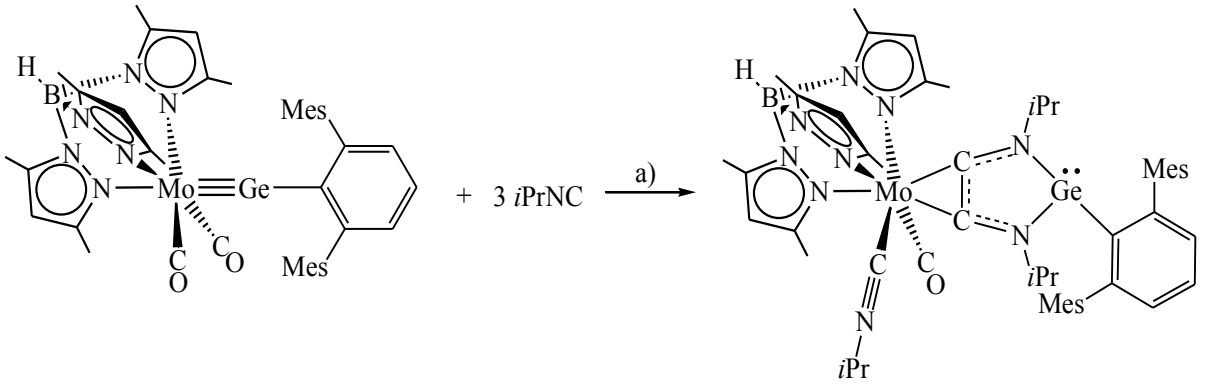

19-Mo, yellowish-brown solid, 60%,

Scheme 10. Reaction of the germylidyne complex **8-Mo** with isonitrile. a) –CO, *n*-heptane, 6 hours, 100 °C; formal charges are omitted for clarity.

The molecular structure of **19-Mo** was determined by single-crystal X-ray diffraction analysis. Red plates of **19-Mo**·0.25(C_5H_{12}) were grown by storing a saturated solution of **19-Mo** in *n*-pentane/*n*-heptane mixture at room temperature. It revealed a C_1-symmetric structure with no Mo···Ge interaction ($d(\text{Mo}\cdots\text{Ge})_{\text{shortest}}$ = 4.5599(5) Å) and a puckered C_2N_2Ge five-membere ring (Figure 36). The bonding parameters of the N-heterocyclic germylene moiety compare very well with that of literature known N-heterocyclic germylenes, such as [(*t*Bu)$_2$ATI]GeCl (ATI = aminotroponimine).[151] Thus, the Ge–N bond lengths (Ge-N1 2.035(2) [2.013(2)] Å, Ge-N2 2.009(2) [2.037(2)] are slightly longer than the sum of the single-bond covalent radii of the Ge and N atom (1.92 Å), but fits quite well with the Ge–N bond lengths of [(*t*Bu)$_2$ATI]GeCl ($(\text{Ge-N})_{\text{av}}$ 1.978 Å).[151, 152] The N1–C25 and N2–C26 bond lengths of 1.309(3) [1.321(3)] Å and 1.315(3) [1.316(3)] Å are also slightly longer than the sum of double bond covalent radii of 1.27 Å, but again fits well with the N–C bond lengths of [(*t*Bu)$_2$ATI]GeCl ($(\text{N–C})_{\text{av}}$ 1.331 Å).[151, 152] Furthermore, the C25-C26 bond length of 1.408(3) Å is in between the calculated value for a C-C single (1.50 Å) and a C-C double bond (1.34 Å).[152] Finally, the Mo–C25 and Mo–C26 bond lengths of 2.062(2) [2.067(3)] and 2.070(2) [2.075(3)], respectively, compare well with the sum of the Mo and C(sp^2) single bond radii of 2.05 Å indicating a Mo-C single bond. The Ge atom adopts a distorted trigonal pyramidal geometry, as evidenced by the sum of angles around Ge of 292.51°, suggesting the presence of a stereochemically active lone pair on the germanium atom. This kind of pyramidalization is a common feature of three coordinated germylenes.[151, 153-155]

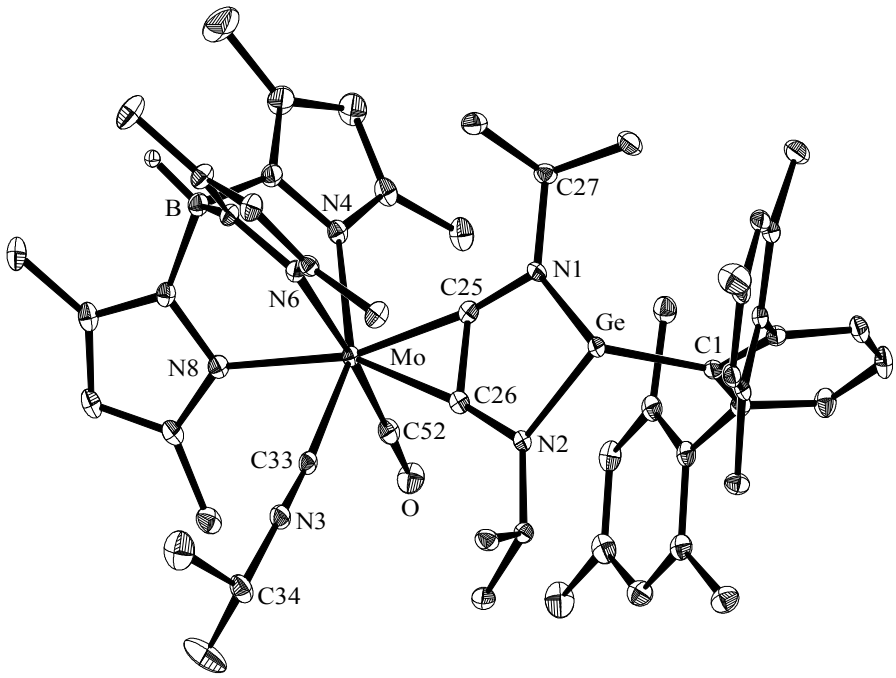

Figure 36. DIAMOND plot of the molecular structure of compound **19-Mo** in the crystal lattice of **19-Mo**·0.25(*n*-C_5H_{12}) at 100(2) K. Thermal ellipsoids are set at 30% probability. Hydrogen atoms (except the B-bonded H atoms) were omitted for clarity. Selected bond lengths [Å] and bond angles [°] (values in the square brackets are for the second independent molecule present in the unit cell): Mo-C25 2.062(2) [2.067(3)], Mo-C26 2.070(2) [2.075(3)], Mo-C33 2.074(3) [2.070(3)], Mo-C52 1.965 [1.963(3)], C25-C26 1.408(3) [1.391(3)], N1-C25 1.309(3) [1.321(3)], N2-C26 1.315(3) [1.316(3)], Ge-N1 2.035(2) [2.013(2)], Ge-N2 2.009(2) [2.037(2)], Ge-C1 2.052(3) [2.077(3)], C33-N3 1.157(3) [1.162(3)]; N1-Ge-C1 105.48(9) [103.22(9)], N1-G-N2 80.73(8) [80.68(8)], N2-Ge-C1 106.30(9) [111.75(9)], Ge-N1-C27 126.4(2) [123.5(2)], Ge-N1-C25 109.6(2) [111.6(2)], C25-N1-C27 119.9(2) [122.1(2)], Mo-C25-N1 170.5(2) [169.4(2)], Mo-C26-N2 172.4(2) [170.9(2)].

The solution NMR and IR spectra of **19-Mo** corroborate well with the solid-state structure. Thus, the ^{1}H NMR spectrum confirms the C_1-symmetric structure of the complex resulting in six singlet signals for the methyl groups of the Tp' ligand and three singlet signals for the $C^{2,6}$- and C^4-bonded methyl groups of the Mes substituents (Figure 37). Furthermore, the $C^{3,5}$-*H* of the Mes substituents also split into two singlet signals. The $^{13}C\{^1H\}$ NMR spectrum also verifies the C_1-symmetric structure of the complex. The most distinctive signals in the $^{13}C\{^1H\}$ NMR spectrum are those of the Mo bonded isonitrile carbon atom (*i*PrN*C*) and the carbonyl carbon (*C*O) appearing at 176.5 and 232.7 ppm, respectively. Furthermore, the $^{13}C\{^1H\}$ NMR spectrum displays two signals for the Mo-bonded C-atoms of the C_2N_2Ge heterocycle at 209.4 and 222.0

ppm. The solution IR spectrum of **19-Mo** in THF displays a medium intensity band at 2131 cm^{-1} for the ν_{NC} stretching vibration of the isonitrile group and a very strong band at 1870 cm^{-1} for the ν_{CO} stretching vibration. In addition, the IR spectrum displays two more absorption bands at 1903 (w) and 1782 (m) cm^{-1}, which so far could not be assigned to any particular stretching mode.

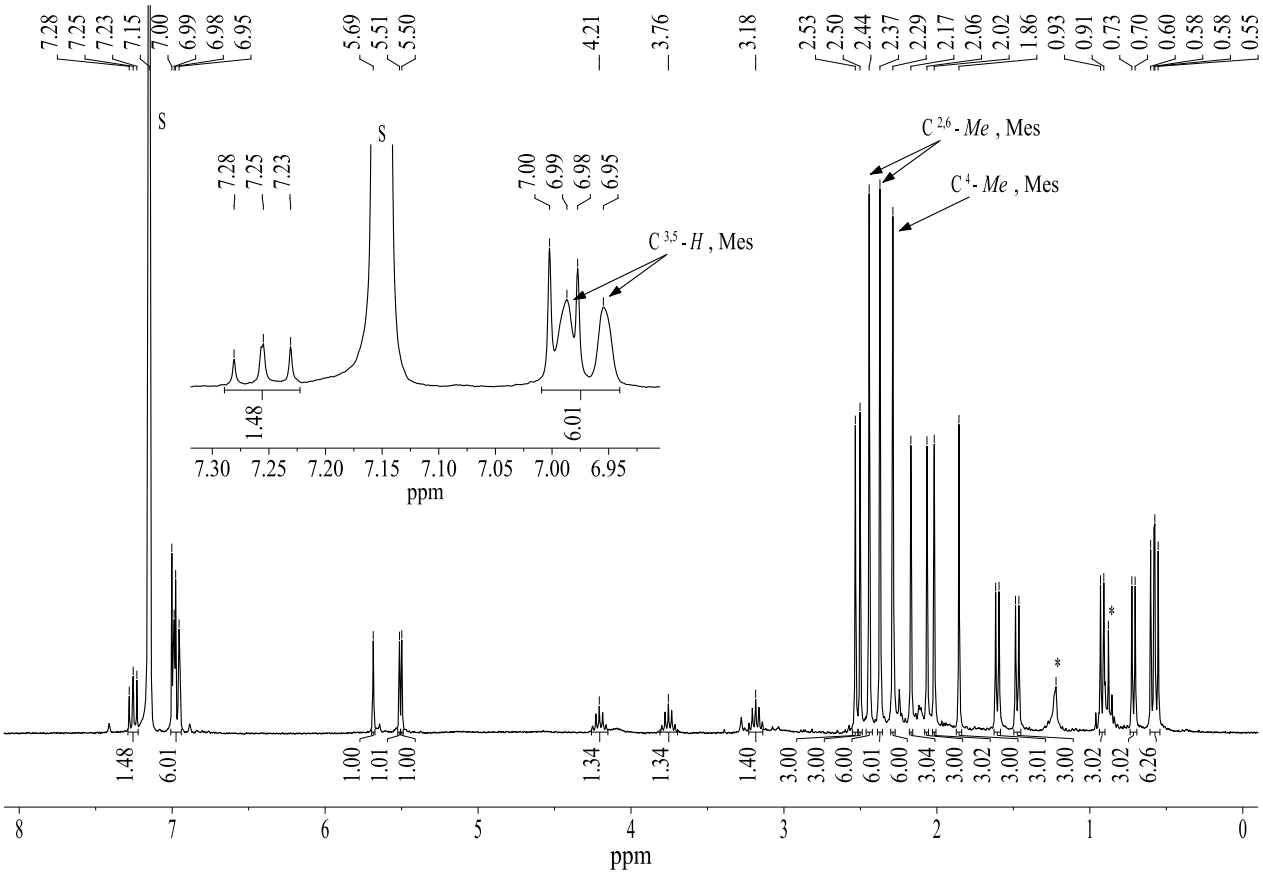

Figure 37. ^{1}H NMR spectrum of **19-Mo** in C_6D_6 at room temperature verifying the C_1-symmetric structure. The character S denotes the residual solvent peak and the symbol * denotes the signals of residual *n*-hexane.

In summary, isolation of the unprecedented N-heterocyclic germylene by the reaction of the germylidyne complex **8-Mo** with an excess of isonitrile shows the potential of Tp'-substituted tetrylidyne complexes for the construction of new molecules featuring low-valent tetrel centers.

2.4. A new method for the synthesis of manganese tetrylidyne complexes

Thus far, only tetrylidyne complexes of group 6 transition metals were discussed and the chemistry was explored to a certain extend in the last two decades. In comparison, tetrylidyne complexes of transition metals of other groups are rare.[38, 54-56, 58, 156] More importantly, examples for open-shell tetrylidyne complexes of metals other than group 6 have not been reported so far. This set up my next target to develop open-shell tetrylidyne complexes of group 7 transition metals. In order to achieve this goal, suitable manganese tetrylidyne complexes were targeted which should be then reduced to obtain the desired open-shell tetrylidyne complexes containing a tetrel-centered unpaired electron. In general, compounds featuring multiple bonds between manganese and the heavier tetrel elements are very rare. In fact, up to 2013, when a series of manganese tetrylidyne complexes were reported by Filippou and co-workers, there were no complexes known featuring a manganese–tetrel (Si – Pb) triple bond.[54]

So far two synthetic routes have been mainly used for the synthesis of tetrylidyne complexes. The first route involves a salt metathesis as developed by Power *et al.* and the second route, a N_2/PMe_3-elimination developed by Filippou *et al.*.[27, 39] In order to access manganese tetrylidyne complexes a new synthetic route was envisaged employing transition metals with labile ligands other than the one used so far for the synthesis of group 6 tetrylidyne complexes. In recent years, transition metal polyhydride[157] and dihydrogen complexes[158] have attracted considerable attention for their potential applications in hydrogen storage.[159-161] Given the propensity of these complexes to eliminate dihydrogen under certain conditions, these compounds appeared to be promising starting materials for the preparation of group 7 transition metal tetrylidyne complexes.

In this respect, the easily accessible manganese dihydrogen hydride complex [$MnH(\eta^2$-$H_2)(dmpe)_2$][162] (**1-Mn**) was employed as a precursor. Complex **1-Mn** can be easily prepared from $MnBr_2$ in three steps following literature known procedures.[162, 163] The first step comprises the complexation of $MnBr_2$ with two equiv. dmpe liagnds (dmpe = 1,2-bis(dimethylphosphino)ethane) to afford the paramagnetic Mn(II) complex $MnBr_2(dmpe)_2$ as a colorless solid in almost quantitative yield (Scheme 11). In the 2nd step the Mn(II) complex was reduced to the dimeric Mn(I) complex $[Mn(AlH_4)(dmpe)_2]_2$ by $LiAlH_4$. Finally hydrolysis of the resulting dimer $[Mn(AlH_4)(dmpe)_2]_2$ afforded the hydrido-dihydrogen complex **1-Mn** as a highly air-sensitive yellow solid in good yield (Scheme 11).

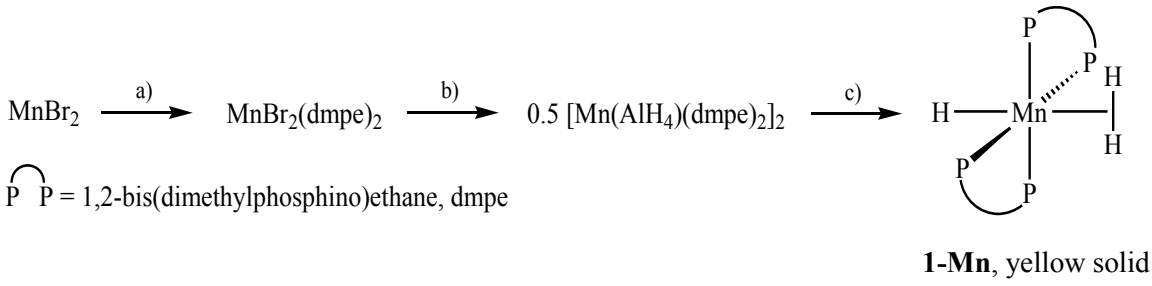

Scheme 11. Synthesis of **1-Mn** from $MnBr_2$. a) +2 dmpe, THF; b) + excess $LiAlH_4$, toluene; c) + H_2O, toluene.

The 18VE complex **1-Mn** is known to lose dihydrogen to form the 16VE intermediate $[MnH(dmpe)_2]$, which can be trapped selectively by a variety of ligands.[162] For example, the reaction of **1-Mn** with N_2, CO or C_2H_4 at moderately elevated temperature afforded the complexes $[MnH(L)(dmpe)_2]$ (L = N_2, CO or C_2H_4) after elimination of dihydrogen. Thus, my envisaged synthetic strategy involved the reaction of one equivalent of a tetrylene (EXR) (E = Ge – Pb; X = Cl, Br; R = terphenyl) with **1-Mn**, which was expected to give a halo-ylidene complex after elimination of dihydrogen. The next step should then involve the abstraction of the halide from the tetrel center with a suitable halide abstracting agent to form the desired complexes featuring triple bonds between manganese and the heavier tetrel atoms (Scheme 12).

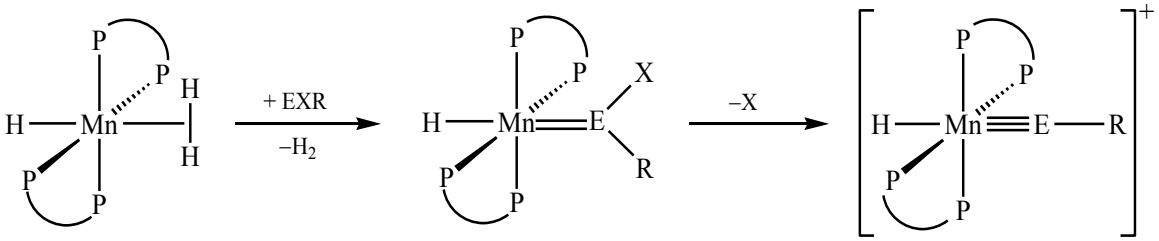

Scheme 12. Synthetic strategy to access manganese tetrylidyne complexes.

2.4.1 Access to the manganese chlorostannylidene complex

The implementation of this synthetic strategy indeed resulted in the successful isolation of a manganese chlorostannylidene complex. Treatment of **1-Mn** with one equivalent of $SnCl(C_6H_3$-2,6-$Mes_2)$ in toluene at ambient temperature was accompanied by a rapid color change from yellow to dark red-brown with concomitant evolution of dihydrogen gas and resulted in the selective formation of the stannylidene complex *trans*-$[H(dmpe)_2Mn{=}Sn(Cl)(C_6H_3$-2,6-$Mes_2)]$ (**40**), which was isolated as an air-sensitive, red-brown solid in 93 % yield (Scheme 13). The red-

brown solid is insoluble in aliphatic solvents, moderately soluble in toluene and diethylether and very good soluble in THF and fluorobenzene. Compound **40** shows very high thermal stability and does not melt or decompose upon heating up to 240 °C.

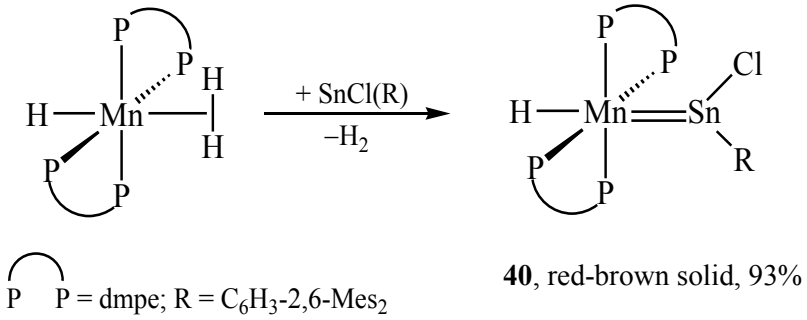

Scheme 13. Synthesis of the manganese chlorostannylidene complex **40**.

Red-brown single-crystals of compound **40**, suitable for X-ray diffraction analysis, were grown upon cooling a saturated toluene solution at +5 °C. Compound **40** represents the second example of a structurally characterized manganese halostannylidene complex after the recently synthesized complex [$Cp(CO)_2Mn{=}Sn(Cl)(C_6H_3$-2,6-$Trip_2)$] in our group.[54] The molecular structure reveals a distorted octahedral geometry around the manganese center with a *trans* arrangement of the stannylidene ligand to the hydrido ligand (Sn-Mn-H37 176.6(9)°). The hydrido ligand could be located in the difference Fourier map and refined isotropically to a Mn–H distance of 1.51(2) Å (Figure 38). Notably, the P atoms are inclined toward the hydrido ligand, as evidenced by the Sn-Mn-P bond angles of 96 – 102 °, to minimize the steric repulsion exerted by the bulky chlorostannylidene ligand. The Mn–Sn bond (2.3997(3) Å) of **40** is considerably shorter than a Mn–Sn single bond (median value 2.620 Å)[13] and also shorter than all previously reported Mn–Sn double bonds (2.427 – 2.52 Å),[54, 164-168] which suggests a very strong Mn–Sn bonding interaction. The C_{aryl}-Sn-Cl bond angle of 87.69(5) ° together with the Mn-Sn-C_{aryl} angle of 158.53(4) ° and the Mn-Sn-Cl angle of 113.66(1) ° suggest a planar coordination geometry around the Sn center, as evidenced by the arithmetic sum of these angles ($\Sigma\angle$Sn = 359.88°). The deviation from the ideal bonding angles of 120 ° in a trigonal planar arrangement can be

13. A Cambridge Structural Database survey (29/02/2016) gave 50 hits of Mn complexes containing single bonds to four-coordinate Sn atoms. The Mn−Sn single bond lengths ranged from 2.455 to 2.758 Å with mean and median values of 2.619 and 2.620 Å, respectively. For the shortest and longest reported Mn−Sn single bonds, respectively, see (a) Schiemenz, B.; Ettel, F.; Huttner, G.; Zsolnai, L. *J. Organomet. Chem*. **1993**, *458*, 159; (b) Haupt, H.-J.; Preut, H.; Wolfes, W. Z. *Anorg. Allg. Chem*. **1978**, *446*, 105.

explained by the decreased sp^2 hybridization of the Sn atom, which results in a high s-character of the Sn hybride orbital in the Mn–Sn double bond and a high p character of the Sn hybrid orbitals employed in the Sn–Cl and Sn–C_{aryl} bonds.

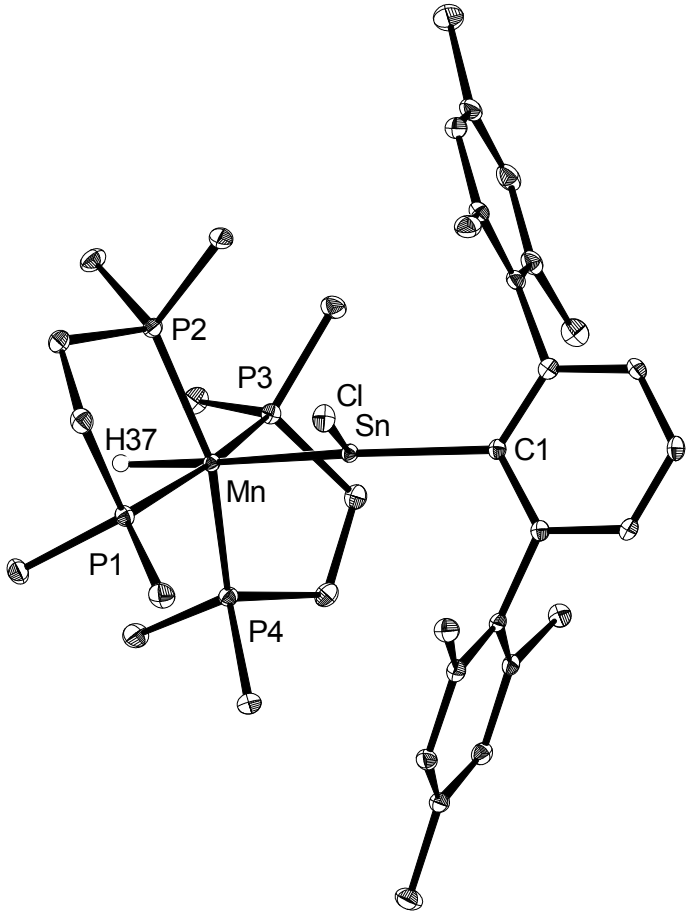

Figure 38. DIAMOND plot of the molecular structure of complex **40**. Thermal ellipsoids are set at 30% probability. Hydrogen atoms are omitted for clarity except the H37 atom bonded to manganese. Selected bond lengths [Å] and bond angles [°]: Mn-Sn 2.3997(3), Mn-H(37) 1.51(2), Sn-Cl 2.5566(5), Sn-C1 2.209(2), Mn-Sn-C(1) 158.53(4), Mn-Sn-Cl 113.66(1), C1-Sn-Cl 87.69(5), Sn-Mn-H(37) 176.6(9), Sn-Mn-P1 96.24(2), Sn-Mn-P2 98.50(2), Sn-Mn-P3 96.02(2), Sn-Mn-P4 101.50(2).

Another salient structural feature of compound **40** is the Sn–Cl bond (2.5566(5) Å), which is considerably elongated compared to the Sn–Cl bond of two or three coordinated Sn^{II} centers in organotin chlorides [$SnCl(C_6H_3\text{-}2,6\text{-}Trip_2)$, 2.4088(8) Å; $SnCl(C_6H_3\text{-}2,6\text{-}Trip_2)(py)$ 2.448(2) Å).[169] Similar structural features (short M=E bonds, large M-E-C_{aryl} angles and long E–Cl bonds) were also observed in other chlorotetrylidene complexes of electron-rich metal centers recently isolated in our group[55, 56] and can be rationalized in valence-bond terms by a contribution of the tetrylidyne resonance form **d** to the overall bonding of **40** (Figure 39).

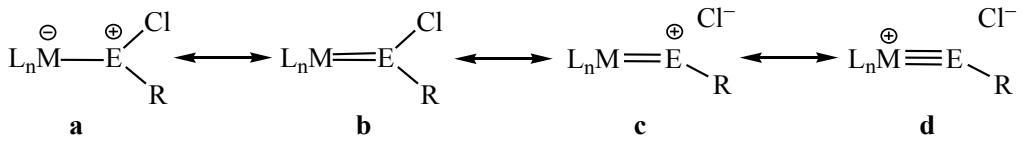

E = Si - Pb; M= transition metal; R = *m*-terphenyl

Figure 39. Resonance forms for the metal-tetrel bond in electron-rich metal chlorotetrylidene complexes.

A natural resonance theory (NRT) analysis of compound **40** calculated at the B3LYP/6-31G* level of theory supported the partial contribution of the tetrylidyne resonance form to electronic structure of **40**. The NRT analysis revealed a major triply-bonded resonance structure similar to **d** with a weight of 23 %, followed by several doubly-bonded (overall weight 50%) and singly-bonded (overall weight 21%) resonance structures, leading to an NRT bond order of 2.08 (Table 19). Furthermore, NBO analysis of compound **40** showed that the Mn-Sn σ and π bonds are strongly polarized towards the Sn and Mn atoms, respectively, as generally observed for Fischer-type carbene complexes. The NBO analysis also revealed that the Mn–Sn double bond has a low covalent character, as evidenced by the low covalent (0.69) and high ionic (1.39) contributions to the natural bond order (Table 19). The high polarity of the Mn–Sn double bond is also reflected in the high opposite charges of the Mn (q(Mn) = –0.87) and Sn atoms (q(Sn) = +1.46), obtained by a natural population analysis (NPA).

The NMR and IR spectra corroborate the solid state structure of compound **40**. The ^{1}H and ^{13}C{^{1}H} NMR spectra suggest an overall C_s-symmetric structure in solution in which the *m*-terphenyl substituent is rotationally locked as evidenced by the three methyl signals of the mesityl rings and two sets of signals observed for C^{3,5}-*H* protons (Figure 40). The ^{1}H NMR spectrum also displays a characteristic high field shifted signal (–13.73 ppm) for the hydrido ligand, which appears as a quintet due to coupling with the four equivalent ^{31}P nuclei [^{2}J(P,H) = 59 Hz] (Figure 40). The presence of the hydrido ligand was further verified by the solid state IR spectroscopy, which displays a characteristic absorption band at 1760 cm^{-1} originating from the Mn-H stretching vibration. The ^{31}P{^{1}H} NMR spectrum displays a singlet signal at 79.1 ppm, accompanied by a pair of tin satellites [^{2}J(Sn, P) = 210 Hz], indicating the *trans*-configuration of compound **40**. In the ^{13}C{^{1}H} NMR spectrum, the most notable signal is that of the low field shifted tin bonded carbon atom at δ = 184.7 ppm. Interestingly, the ^{119}Sn{^{1}H} NMR spectrum of **40** displays a very broad signal at 540 ppm due to the high quadrupole moment of the manganese atom.[170]

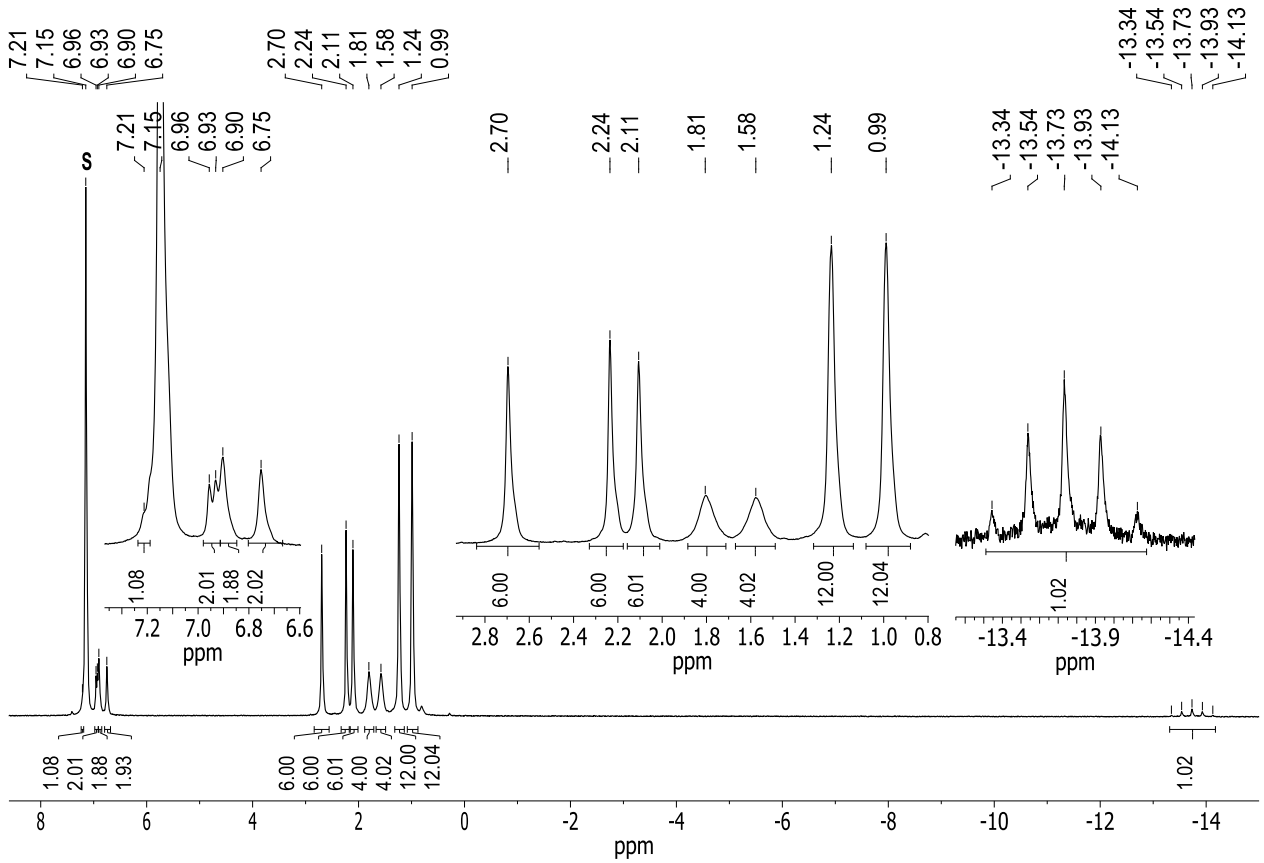

Figure 40. The ^{1}H NMR spectrum (300.1 MHz, 298 K) of **40** in C_6D_6. The character S denotes the residual signal of the deuterated solvent.

Attempts to extend this dihydrogen elimination strategy to other halotetrylenes [EXR] (E = Ge, Pb; X = Cl – I; R = C_6H_3-2,6-Mes_2, C_6H_3-2,6-$Trip_2$) for the synthesis of the corresponding halotetrylidene complexes was not successful. In all cases a mixture of products was obtained. For example, the reaction of **1-Mn** with one equivalent of GeCl(C_6H_3-2,6-Mes_2) in toluene at ambient temperature led to a mixture of products and the ^{1}H NMR spectrum of the crude reaction mixture revealed the formation of the germane GeH_3(C_6H_3-2,6-Mes_2)[171] as one of the primary products of the reaction. Furthermore, the reaction of **1-Mn** with one equivalent of PbBr(C_6H_3-2,6-Mes_2) led to the formation of elemental lead and C_6H_4-1,3-Mes_2 as the major products.

Attempts to prepare the corresponding silylidene complex using the NHC-stabilized chlorosilylene SiCl(C_6H_3-2,6-Mes_2)(IMe_4) were also not successful. A 1:1 reaction mixture does not react at ambient temperature in toluene but heating of this mixture at 110 °C resulted in the formation of the Mn(I) dimer [MnH(dmpe)$_2$]$_2$(μ-dmpe) (**2-Mn**) as one of the major products. Compound **2-Mn** was characterised by ^{1}H and ^{31}P{^{1}H} NMR spectroscopy, and single crystal X-ray diffraction. The ^{31}P{^{1}H} NMR spectrum in C_6D_6 displays two broad singlets in a 1:4 ratio for

the two different sets of phosphorus nuclei at δ = 27.0 ($\Delta\nu_{1/2}$ = 148 Hz) and 79.5 ($\Delta\nu_{1/2}$ = 84 Hz) ppm, respectively.

The molecular structure of **2-Mn** shows a distorted octahedral arrangement of the ligands around the Mn center (Figure 41). The most salient structural feature of **2-Mn** is the zigzag configuration of the bridging phosphane ligand along with the *trans*-arrangement of two Mn fragments about the P···P linkage. Similar to compound **40**, the chelating phosphane ligands are inclined towards the hydrido ligand as evidenced by the P-Mn-P angles of 96 – 100°.

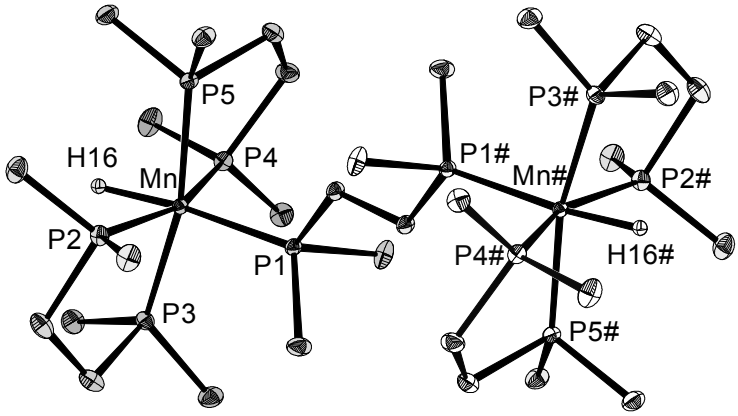

Figure 41. DIAMOND plot of the molecular structure of complex **2-Mn**. Thermal ellipsoids are set at 30% probability. Hydrogen atoms are omitted for clarity except the H16/H16# atoms bonded to manganese. Selected bond lengths [Å] and bond angles [°]: Mn-H16 1.50(2), Mn-P1 2.2291(4), Mn-P2 2.2010(4), Mn-P3 2.2089(4), Mn-P4 2.1998(4), Mn-P5 2.2071(4); H16-Mn-P1 173.1(6), P1-Mn-P2 99.32(2), P1-Mn-P3 96.68(2), P1-Mn-P4 100.06(2), P1-Mn-P5 98.18(2).

2.4.2 Manganese stannylidyne complexes

After the successful isolation of the manganese chlorostannylidene complex **40**, the next target was to prepare the corresponding cationic manganese stannylidyne complex. The strong polarization of the Sn–Cl bond indicated that the chloride group might be easily removed using a suitable halide abstracting agent. Indeed, treatment of **40** with one equivalent of a nonoxidizing halide abstracting agent such as $Na[B(C_6H_3\text{-}3,5\text{-}(CF_3)_2)_4]$ or $Li[Al(OC(CF_3)_3)_4]$ in fluorobenzene at ambient temperature was accompanied by a rapid color change from red-brown to dark purple and concomitant precipitation of MCl (M = Li, Na) (Scheme 14). Monitoring of the reaction *in situ* by ^{31}P NMR spectroscopy revealed the selective formation of the stannylidyne complexes *trans*-$[H(dmpe)_2Mn{\equiv}Sn(C_6H_3\text{-}2,6\text{-}Mes_2)][B(C_6H_3\text{-}3,5\text{-}(CF_3)_2)_4]$ (**41**) and *trans*-$[H(dmpe)_2Mn{\equiv}Sn(C_6H_3\text{-}2,6\text{-}Mes_2)][Al(OC(CF_3)_3)_4]$ (**42**), which were isolated after workup and crystallization as extremely air-sensitive, microcrystalline dark purple solids in high yields (90%). The complex salts are soluble in fluorobenzene or THF but insoluble in benzene or aliphatic solvents. Both complexes exhibit an exceptionally high thermal stability – complex **41** melts at 195 °C to a dark purple liquid, whereas complex **42** does not melt or decompose upon heating up to 240 °C.

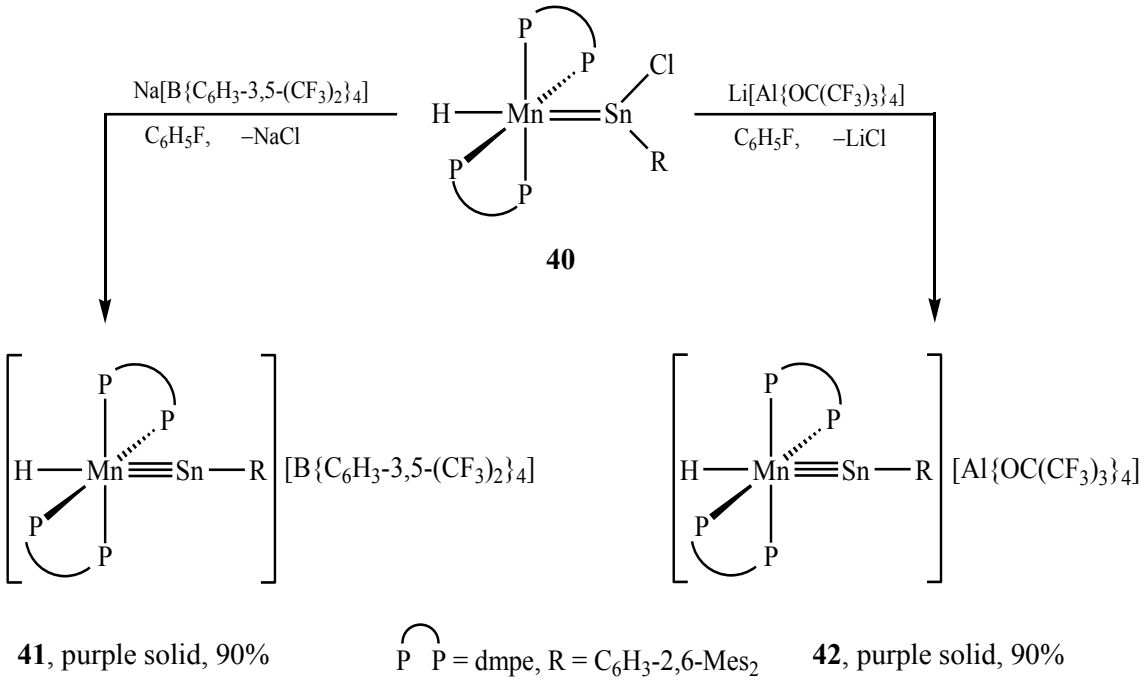

Scheme 14. Synthesis of manganese stannylidyne complexes **41** and **42**.

Purple single crystals of **41**·(C_6H_5F), suitable for X-ray diffraction analysis, were grown upon cooling a saturated solution of **41** in fluorobenzene/petrol ether mixture at –30 °C.[14] Compound **41** represents the first example of a structurally characterized complex featuring a triple bond between the manganese and tin atoms. The solid state structure revealed well-separated cations and anions, excluding any bonding interaction between the highly electrophilic tin center and the counteranion.[15] Compound **41** features a distorted octahedral geometry about the manganese atom with a *trans*-configured stannylidyne ligand relative to the hydrido ligand as evidenced by the H75-Mn-Sn bond angle of 177.1(14)°. The structure displays a near linearly coordinated tin atom as exemplified by the Mn-Sn-C1 bond angle of 176.85(9)°, which together with the very short Mn–Sn bond length of 2.3434(5) Å are indicative of a triple bond between the Mn and Sn atoms. In fact, the Mn–Sn bond length in **41** is the shortest one reported to date. Notably, the Mn–Sn bond is almost 6 pm shorter than that observed in chlorostannylidene complex **40**, and 29 pm shorter than that found in the manganostannylene *mer,trans*-[$Mn(CO)_3(CNR)_2SnCl$] (Mn–Sn 2.6359(8) Å; R = C_6H_3-2,6-$Dipp_2$; Dipp = C_6H_3-2,6-*i*Pr_2), which contains a singly bonded, V-shaped SnCl ligand,[172] and compares very well with the predicted Mn–Sn triple bond length (*d*(Mn≡Sn) = 2.35 Å) derived from the theoretically calculated sum of triple bond radii for Mn (1.03 Å) and tin (1.32 Å).[173] Akin to the chlorostannylidene complex **40**, the P atoms of **41** are also inclined towards the hydrido ligand, as evidenced by the Sn-Mn-P bond angles of 97.40 (3)–100.94(3)°, to minimize the steric pressure exerted by the bulky stannylidyne ligand.

14 The solid state structure of **42** was also determined by single crystal X-ray diffraction analysis and showed the same structural motif and bonding parameters for the complex cation as in **41**. However, due to the low quality of the two data sets for two different samples, the structure of **42** was not further considered.

15 The closest interionic contact (2.399 Å) exists between a F atom of the counteranion and a *m*-CH group of the central phenyl ring of the *m*-terphenyl substituent. No contacts to the Sn atom were found that are shorter than van der Waals contacts.

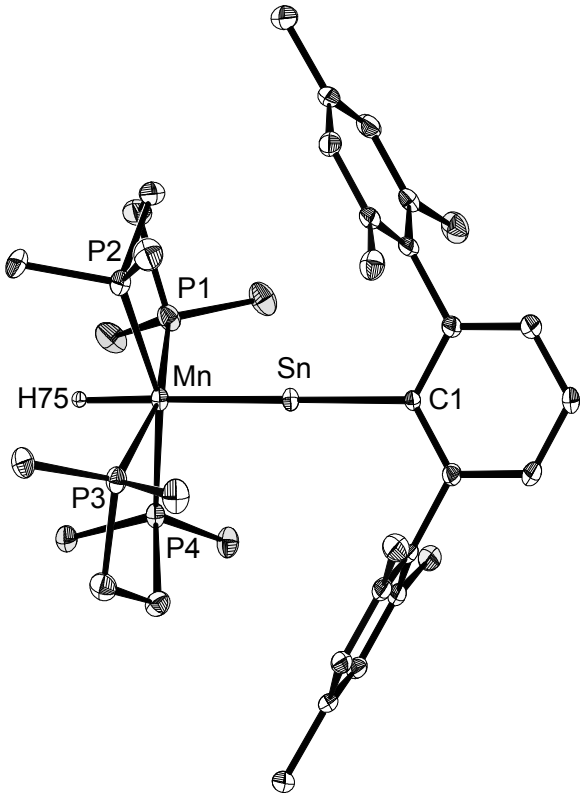

Figure 42. DIAMOND plot of the molecular structure of the complex cation in **41**·(C_6H_5F). Thermal ellipsoids are set at 30% probability. Solvent molecule, counter anion and the hydrogen atoms are omitted except the H75 atom bonded to manganese. Selected bond lengths [Å] and bond angles [°]: Mn-Sn 2.3434(5), Sn-C1 2.159(3), Mn-H75 1.44(3), Mn-P1 2.262(1), Mn-P2 2.258(1), Mn-P3 2.266(1), Mn-P4 2.253(1); Mn-Sn-C1 176.85(9), Sn-Mn-H75 177.1(14), Sn-Mn-P1 97.40(3), Sn-Mn-P2 100.94(3), Sn-Mn-P3 98.16(3), Sn-Mn-P4 99.17(3).

Similar to compound **40**, the $^{31}P\{^1H\}$ NMR spectra of complex **41** and **42** in CD_2Cl_2 show a singlet signal flanked by tin satellites [^2J(Sn,P) = 200 – 215 Hz] at slightly higher field (71.0 ppm) than that of **40** (δ (in THF-d_8) = 79.5 (s, $^2J(^{119}Sn,^{31}P)$ = 210 Hz)). Accordingly, the ^1H NMR spectrum displays a characteristic quintet signal [^2J(P,H) = 66 Hz] for the hydrido ligand [Mn–*H*] at δ = –14.59 (**41**) and –14.58 ppm (**42**), which appear at slightly higher field than that of **40** (δ = –13.73 ppm). The ^1H and $^{13}C\{^1H\}$ NMR spectra of both complexes revealed a time-averaged C_{2v}-symmetric structure in solution, which renders the mesityl substituents of the *m*-terphenyl group homotopic. Therefore, only a single set of signals is observed for the ortho and meta ^1H and ^{13}C nuclei of the mesityl groups, respectively. In the $^{13}C\{^1H\}$ NMR spectra of complexes **41** and **42**, the most distinctive signal is that of the low field shifted tin bonded C_{aryl} atom at 188.2 ppm, which is characteristic for stannylidyne complexes.[42, 44] In the solid state IR

spectrum the ν_{Mn-H} absorption band of the stannylidyne complex cation appeares at slightly higher wave numbers (**41**: 1792 cm^{-1}; **42**: 1778 cm^{-1}) than that observed for the stannylidene complex **40** (ν_{Mn-H} = 1760 cm^{-1}), and interestingly this absorption band is counteranion dependent. The $^{119}Sn\{^1H\}$ NMR spectrum of complex **41** shows a very broad signal for the stannylidyne ligand at a considerably lower field ($\delta(^{119}Sn\{^1H\})$ = 761 ppm) than that observed for compound **40** ($\delta(^{119}Sn\{^1H\})$ = 540 ppm).

Geometric optimization of the complex cation of **41** and **42** at the B3LYP level of theory afforded a minimum structure with a good agreement between experimental and calculated bonding parameters (Table 19). Furthermore, NRT analysis of the DFT derived minimum structure (**41$_{calc}$**) of the complex cation suggest a highly polar Mn≡Sn bond, as supported by the low covalent (0.85) and high ionic (1.45) contributions to the total Mn–Sn bond order of 2.25, which is slightly higher than that found for the Mn=Sn bond in **40** (Table 19). The increased NRT bond order of the complex cation of **41**/**42** rationalizes the observed shortening of the Mn–Sn bond length compared to that of the stannylidene complex **40**. A natural population analysis (NPA) of the minimum structure of the complex cation also indicates the high polarity of the Mn≡Sn bond as evidenced by the high opposite NPA charges of Mn (–0.87) and Sn (+1.35) (Table 19).

Table 19. Selected calculated (B3LYP)[a] and experimental bonding parameters, and selected results of the NBO and NRT analysis of **40** and **41**/**42**.

	Mn-Sn	**Mn-H**	**Mn-Sn-C1**	**H-Mn-Sn**	**NPA charges**			**NBO analysis[b]**			**NRT-BO[c]**
	[pm]	[pm]	[°]	[°]	Mn	Sn	H	NBO	occ.	pol.	bond: sum (cov/ionic)
40$_{calc.}$	2.486	1.566	158.2	173.8				Mn–Sn (σ)	1.92	72.6%(Sn)	Mn-Sn: 2.08 (0.69/1.39)
40$_{exp.}$	2.3997(3)	1.51(2)	158.53(4)	176.6(9)	–0.87	+1.46	–0.18	Mn–Sn (π)	1.82	83.3%(Mn)	Mn-H37: 0.35 (0.04/0.31)
41$_{calc.}$	2.373	1.552	180.0	180.0				Mn–Sn (σ)	1.93	73.0% (Sn)	Mn-Sn: 2.25 (0.80/1.45)
41$_{exp.}$	2.3434(5)	1.44(3)	176.85(9)	177.1(14)	–0.87	+1.35	–0.14	Mn–Sn (π)	1.44	76.6% (Mn)	Mn-H75: 0.50 (0.39/0.11)

[a] basis sets: TZVPP for Mn, Sn, P, Cl, $H_{hydride}$, 6-31G* for all other atoms. [b] NBO occupancy (occ.) and bond polarisation (pol.) in %; [c] NRT bond order, sum of covalent and ionic bond order and respective individual values.

A look at the Kohn-Sham frontier orbitals of the complex cation **41**/**42** reveals that the LUMO+1 and LUMO correspond to the π_{in}* and π_{out}* Mn–Sn bonds. The HOMO and HOMO–2 correspond to the π_{out} and π_{in} orbitals respectively, which together with the Mn–Sn σ-bonding orbital (HOMO–8) contribute to the formation of Mn–Sn triple bond (Figure 43). Furthermore,

the HOMO–1 is a manganese centered non-bonding orbital, that is non bonding with respect to the Mn-Sn triple bond (Figure 43).

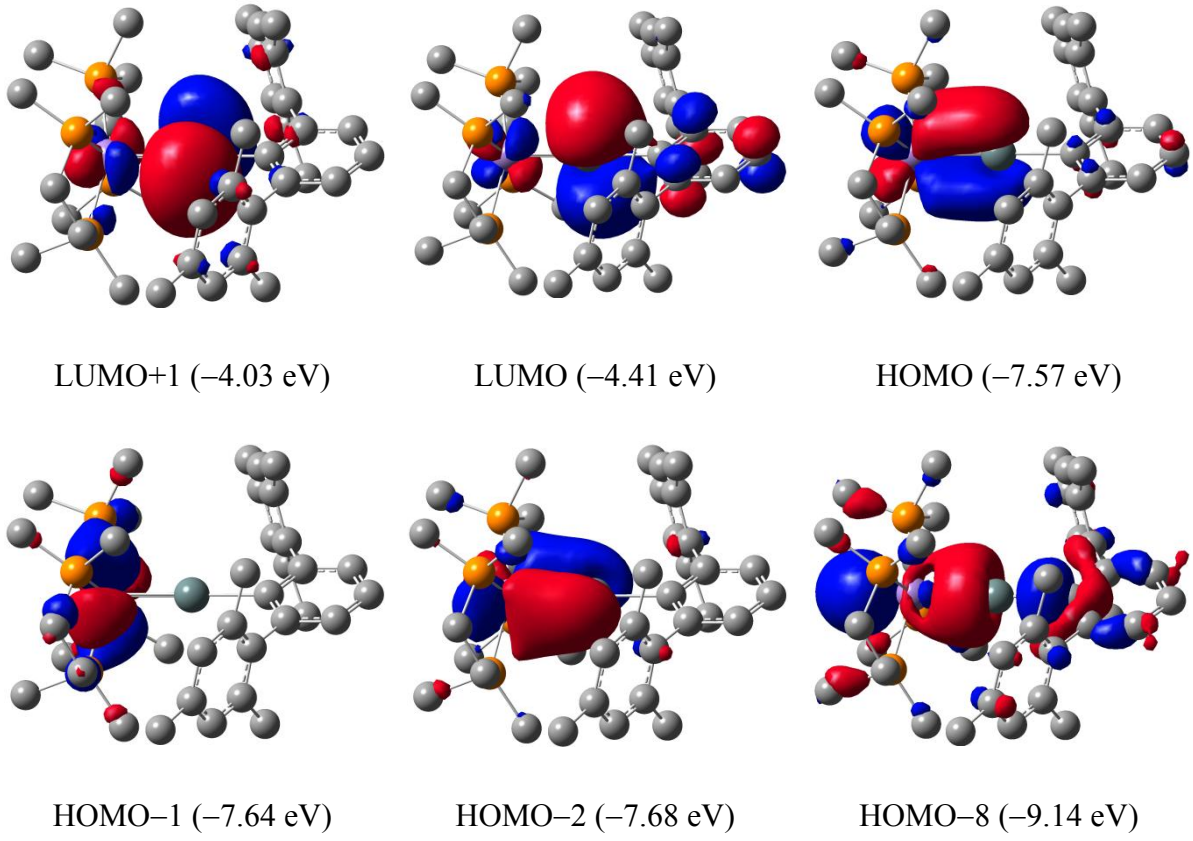

Figure 43. Frontier Kohn-Sham orbitals of the complex cation of **41**/**42** (isosurface value: 0.04 e $Å^{-3}$).

2.4.3 Access to a hydridostannylidene complex of manganese

The presence of a very electrophilic tin center in the stannylidyne complex **41** prompted us to study the reactivity of this compound towards nucleophiles, such as potassium hydride, which resulted in the formation of the first manganese hydridostannylidene complex *trans*-[H(dmpe)$_2$Mn=SnH(C$_6$H$_3$-2,6-Mes$_2$)] (**44**). Thus, stirring of a mixture of **41** and KH (1.4 equiv.) in THF at ambient temperature for 18 hours led to a distinct color change from purple to dark red and the formation of the hydridostannylidene complex **44**, which was isolated after workup and crystallization as an analytically pure, air-sensitive, dark red solid in 43 % yield (Scheme 15). The red solid decomposes upon melting at 185 – 188 °C to a dark red liquid, as suggested by the $^{31}P\{^1H\}$ NMR spectrum of the molten sample. Compound **44** is well soluble in THF, fluorobenezene, benzene, Et_2O and moderately soluble in common aliphatic solvents.

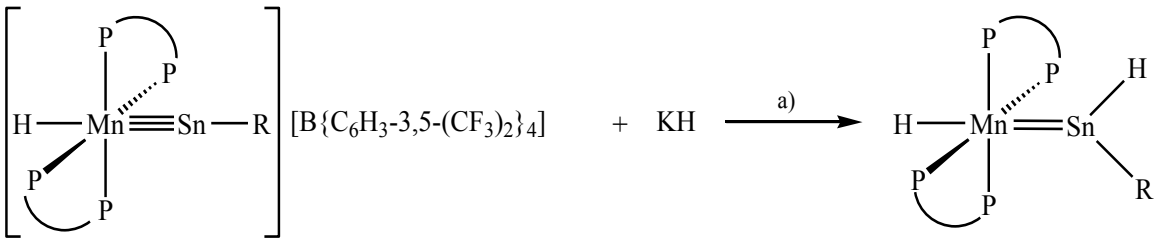

P P = dmpe, R = C_6H_3-2,6-Mes_2

44, dark red solid, 43 %

Scheme 15. Synthesis of the hydridostannylidene complex **44** upon reaction of the stannylidyne complex **41** with KH; a) –K[B{C_6H_3-3,5-$(CF_3)_2$}$_4$], THF, r.t.; formal charges are omitted for clarity.

Dark red, block-like crystals of **44** were grown upon cooling a concentrated *n*-pentane solution of **44** at –30 °C and analysed by single-crystal X-ray diffraction. Compound **44** is the first example of a hydridostannylidene complex of manganese and also one of the rare example of structurally characterized hydridostannylidene complexes.[56, 174] Akin to the chlorostannylidene complex **40**, the molecular structure of **44** reveals a distorted octahedral complex with a *trans* arrangement of the stannylidene and the hydrido (Mn-H) ligand, as evidenced by the H76-Mn-Sn angle of 174.2(13)° (Figure 44). Furthermore, the P atoms are inclined towards the hydrido ligand with Sn-Mn-P bond angles ranging from 92.17(3) – 103.29(3) ° to reduce the steric repulsion imposed by the bulky hydridostannylidene ligand. The Mn–Sn bond length of 2.4531(5) Å in **44** is significantly larger (4.7 %) than that observed in the stannylidyne complex **41** (2.3434(5) Å) and also larger (2.2 %) than that in the chlorostannylidene complex **40** (2.3997(3) Å) (*vide supra*), thus suggesting a smaller multiple bond character in the Mn–Sn bond. The Sn center features a trigonal-planar geometry as evidenced by the sum of angles around the Sn atom (Σ∠Sn = 359.44°). The Mn-Sn-C1 bond angle of 142.84(7)° is markedly lower than that found in **40** (158.53(4)°), indicating the presence of a double bond between the Mn and Sn atoms, whereas the C1-Sn-H angle of 93.6(12)° is slightly widened compared to that in **40** (87.69(5)°). The significant difference between the Mn-Sn-C1 and C1-Sn-H bond angles clearly indicates that the tin center mainly uses p-orbitals for the σ-bonding to its substituents.

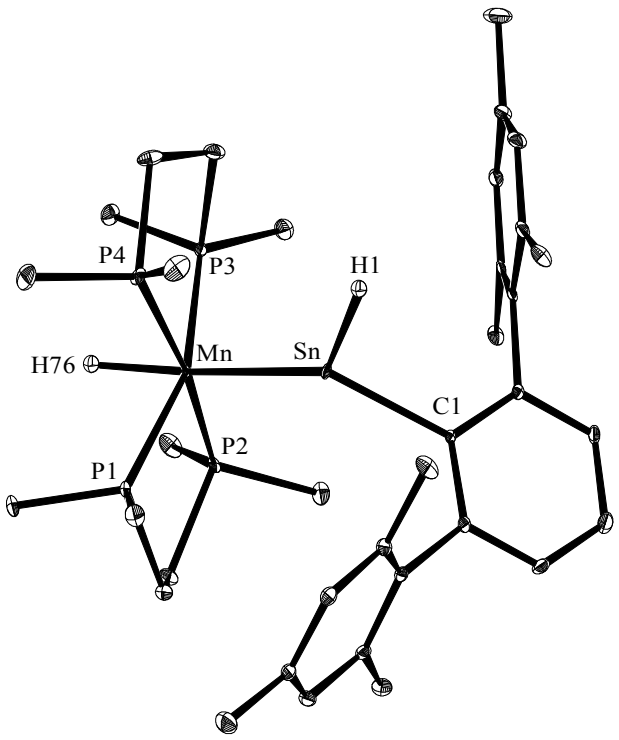

Figure 44. DIAMOND plot of the molecular structure of the hydridostannylidene complex **44** at 100(2) K. Thermal ellipsoids are set at 30% probability. Hydrogen atoms, except the H1 and H75 atom bonded to tin and manganese, respectively, are omitted for clarity. Selected bond lengths [Å] and bond angles [°]: Mn-Sn 2.4531(5), Sn-C1 2.227(3), Mn-H75 1.61(4), Sn-H 1.73(4), Mn-P1 2.2335(9), Mn-P2 2.2148(9), Mn-P3 2.2244(9), Mn-P4 2.2256(9); Mn-Sn-C1 142.84(7), Mn-Sn-H 123.0(12), C1-Sn-H 93.6(12), Sn-Mn-H75 174.2(13), Sn-Mn-P1 103.29(3), Sn-Mn-P2 97.16(3), Sn-Mn-P3 97.59(3), Sn-Mn-P4 92.17(3).

Complex **44** was further studied IR spectroscopy. The ATR-IR spectrum of **44** displays a characteristic absorption band for the Mn-H stretching vibration at 1743 cm^{-1}, which is significantly lower than that observed for the stannylidyne complex **41** (1792 cm^{-1}) or the chlorostannylidene complex **40** (1760 cm^{-1}) (Table 20), suggesting the following *trans*-effect of these ligands – $[SnH(C_6H_3\text{-}2,6\text{-}Mes_2)]$> $[SnCl(C_6H_3\text{-}2,6\text{-}Mes_2)]$>> $[Sn(C_6H_3\text{-}2,6\text{-}Mes_2)]^+$. Furthermore, the solid-state IR spectrum shows another characteristic signal for the Sn-H stretching vibration at 1627 cm^{-1}, which is remarkably lower than that found for the DMAP stabilized hydridostannylene [Sn(H)N(Ar*)(Si*i*Pr$_3$)] (Ar* = 2,6-[C(H)Ph$_2$]$_2$-4-*i*PrC$_6$H$_2$) ($\nu_{Sn\text{-}H}$ = 1759 cm^{-1}),[18] suggesting a relatively high p-character of the hybride orbital of Sn used in the Sn-H bond of **44**.

The solution NMR spectra also corroborate well with the solid-state structure. In contrast to the chlorostannylidene complex **40**, the ^{1}H NMR spectrum of **44** in C_6D_6 at room temperature displays a 1:2 ratio of the resonance signals for the *para* and *ortho* methyl groups of the mesityl rings, suggesting a free rotation of the *m*-terphenyl substituent about the Sn–C_{ipso} bond in solution. This observation can be rationalized with the reduced steric bulk at the tin atom in **44**. This is further confirmed by the presence of only two signals for the *ortho* and *para* methyl groups of the mesityl rings in the ^{13}C{^{1}H} NMR spectrum. The most characteristic signals in the ^{1}H NMR spectrum of **44** are that of the Sn–*H* functionality at δ = 18.46 ppm, which is flanked by a set of tin satellites (quintet, $^{3}J(^{31}P,^{1}H)$ = 4.6 Hz, $^{1}J(^{117/119}Sn,^{1}H)$ = 425 Hz) (Figure 45), and of the Mn-*H* functionality at δ = –11.93 ppm (quintet, $^{2}J(^{31}P,^{1}H)$ = 57 Hz). The quintet multiplicity of both signals arises from the coupling with the four equivalent ^{31}P nuclei. The Sn-*H* resonance signal at δ = 18.46 ppm compares well with that of the osmium hydridostannylidene complex [η^5-C_5Me_5)(*i*Pr_3P)(H)Os=SnH(Trip)] (δ = 19.4 ppm, $^{1}J(^{117/119}Sn,^{1}H)$ = 775 Hz) and appears at a slightly lower field than that of the iron hydridostannylidene [(depe)$_2$Fe=SnH(C_6H_3-2,6-Mes_2)] (δ = 14.5 ppm, $^{1}J(^{117/119}Sn,^{1}H)$ = 509 Hz).[56, 174] The $^{1}J_{Sn,H}$ coupling constant of 425 Hz in **44** is smaller than that found in other two hydridostannylidene complexes, suggesting the presence of a relatively low s-character of the orbital used for the Sn-H bond of **44**. In the ^{13}C{^{1}H} NMR spectrum, the most characteristic signal is that of the tin bonded carbon atom at δ = 173.4 ppm. Interestingly, the chloride/hydride substitution at the tin atom has almost no effect on the ^{31}P{^{1}H} chemical shift, but has a significant effect on the $^{2}J_{Sn,P}$ coupling constant. Thus, the ^{31}P{^{1}H} NMR spectrum of **44** displays a singlet signal at 78.9 ppm, which appears at almost the same position as that observed for **40** (δ = 79.5 ppm, $^{2}J(^{117/119}Sn,^{31}P)$ = 210 Hz)), but the $^{2}J_{Sn,P}$ coupling constant of 248 Hz in **44** is larger than that found in the chlorostannylidene complex **40** (Table 20). A similar trend was also observed in related iron complexes, where the $^{2}J_{Sn,P}$ coupling constant values only 100 Hz in the chlorostannylidene complex [(depe)$_2$Fe=SnCl(C_6H_3-2,6-Mes_2)], but 206 Hz in the hydridostannylidene complex [(depe)$_2$Fe=SnH(C_6H_3-2,6-Mes_2)].[56] Finally, the ^{119}Sn{^{1}H} NMR spectrum of **44** displays a broad signal at 531.7 ppm, which is only slightly upfield-shifted compared to that of the corresponding chlorostannylidene complex **40** (δ = ~540 ppm) (Table 20).

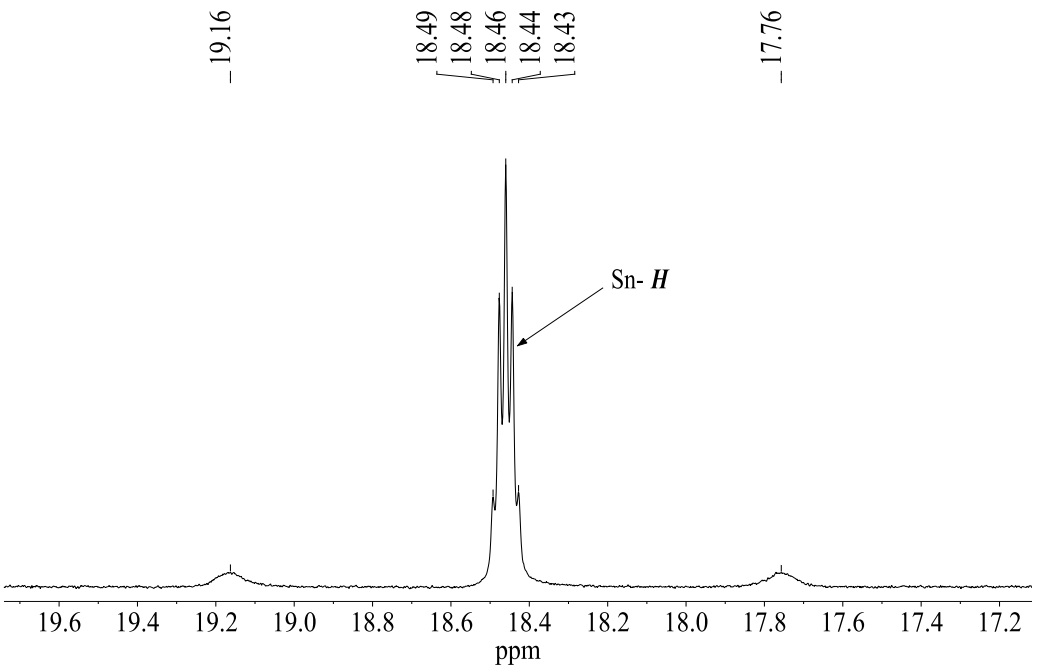

Figure 45. Expanded region (19.7 – 17.1 ppm) of the ^{1}H NMR spectrum of **44** in C_6D_6 showing the characteristic Sn-*H* quintet resonance signal flanked by a pair of tin-satellites.

Table 20. Summary of the $\nu_{Mn\text{-}H}$, and $^{31}P\{^{1}H\}$ and $^{119}Sn\{^{1}H\}$ NMR chemical shift of the stannylidene and stannylidyne complexes **40**, **41**, **42** and **44**.

Complex	$\nu_{Mn\text{-}H}$ [cm^{-1}]	$^{31}P\{^{1}H\}$ NMR [ppm]	$^{119}Sn\{^{1}H\}$ NMR [ppm]
40	1760	79.5 (s, $^{2}J(^{119/117}Sn,^{31}P)$ = 210 Hz)[a]	~540 (br, $\Delta\nu_{1/2}$ = 7100 Hz)[a]
41	1792	71.0 (s, $^{2}J(^{119/117}Sn,^{31}P)$ = 200 Hz)[a]	761 (br, $\Delta\nu_{1/2}$ = 1600 Hz)[b]
42	1778	71.0 (s, $^{2}J(^{119/117}Sn,^{31}P)$ = 215 Hz)[b]	-
44	1743	78.9 (s, $^{2}J(^{119/117}Sn,^{31}P)$ = 248 Hz)[c]	531.7 (br, $\Delta\nu_{1/2}$ = 1322 Hz)[c]

[a] : in THF-d_8 ; [b] : in CD_2Cl_2; [c]: in C_6D_6.

2.5. An open-shell manganese stannylidyne comprising of a tin-centered unpaired electron

The manganese stannylidyne complex **41** appeared to be a suitable precursor to prepare an open-shell stannylidyne complex featuring a tin-centered unpaired electron. As expected for a Fischer-type tetrylidyne complex, quantum chemical calculations of **41** revealed that the LUMO+1 and LUMO corresponding to the π_{in}* and π_{out}* Mn–Sn bonds are mainly tin centered (*vide supra*). Auspiciously, the energy of the LUMO of **41** (–4.41 eV) is much lower than that observed for the isolobal group 6 metal tetrylidyne complexes.[95] For example, the energy of the LUMO of the neutral molybdenum stannylidyne [$Cp(PMe_3)_2Mo{\equiv}Sn(C_6H_3\text{-}2,6\text{-}Mes_2)$] was calculated to be –1.7886 eV, i.e. 2.62 eV higher compared to that of **41**.[60]16 This let one assume that the cationic stannylidyne complex should be more easily reduced. Indeed, cyclic voltammetric (CV) studies of **41** in THF at –11 °C revealed a reversible one-electron reduction at a very low half-wave potential ($E_{1/2}$) of –1.568 V *versus* the $[Fe(\eta^5\text{-}C_5Me_5)_2]^{+1/0}$ reference electrode (Figure 46, Table 21).

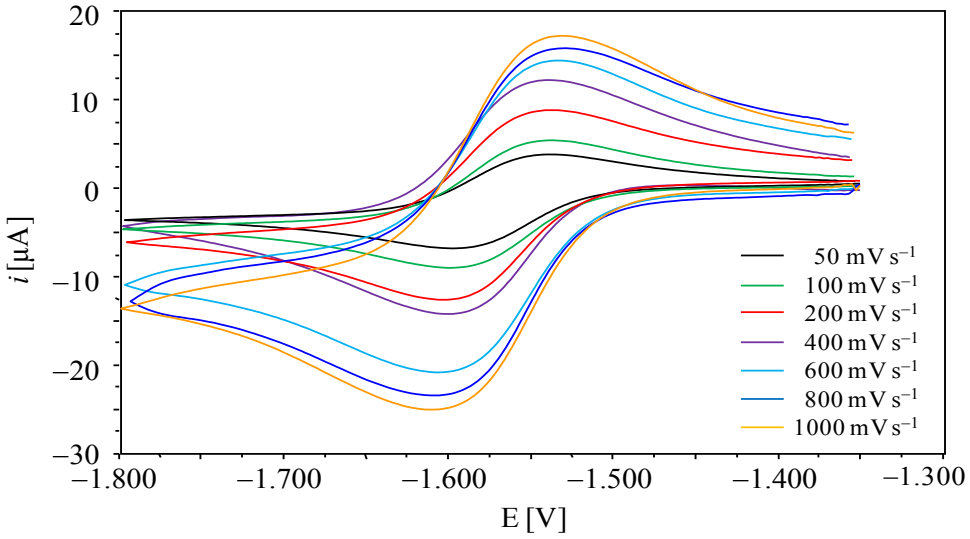

Figure 46. Single-scan cyclic voltammograms of **41** in THF at –11 °C from (–1.300) – (–1.800) V at different scan rates (50 – 1000 mV s^{-1}); reference electrode: 4 mM $Fe(C_5Me_5)_2/Fe(C_5Me_5)_2^+$ / 0.1 M $(NBu_4)PF_6$/THF; electrolyte: 0.1 M $(NBu_4)PF_6$.

16 Personal communication, M. Straßmann.

Table 21. Cyclic voltammetric results of complex **41**.[a]

v [mV s^{-1}]	ΔE_p [mV]	i_{pa}/i_{pc}	$E_{1/2} = (E_{pa} + E_{pc})/2$ [mV]
50	56	1.00	−1568
100	60	1.01	−1568
200	60	1.02	−1569
400	60	1.02	−1568
600	60	1.01	−1568
800	64	1.01	−1568
1000	64	1.01	−1570

[a] v: scan rate; ΔE_p: peak potential separation; $\Delta E_p = E_{pa} - E_{pc}$, E_{pa} is the anodic peak potential and E_{pc} the cathodic peak potential; i_{pa}/i_{pc}: ratio of anodic and cathodic peak current; $E_{1/2}$: half wave potential. Potentials are given vs. the $[Fe(C_5Me_5)_2]^{+1/0}$ reference electrode.

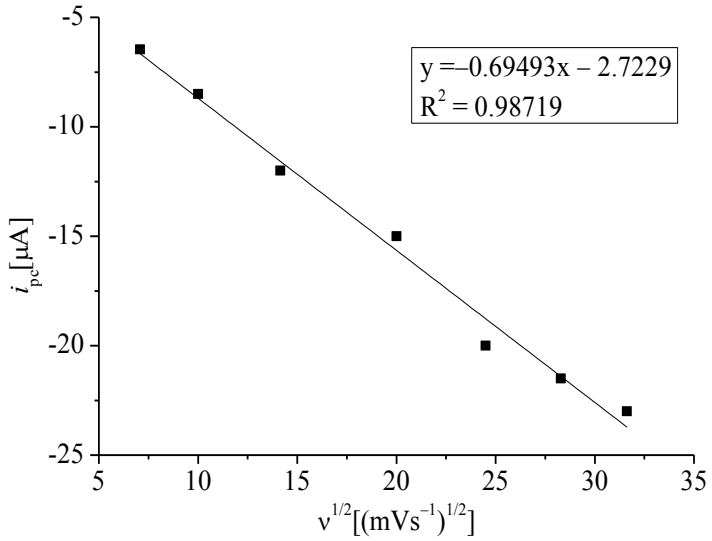

Figure 47. Plot of the cathodic peak current (i_{pc}) *versus* the square root of scan rates ($\nu^{1/2}$) for the reversible reduction of **41** at $E_{1/2}$ = –1.568 V.

The reversibility of the one-electron reduction at $E_{1/2}$ = −1.568 V was confirmed by the following criteria:

- The half-wave potential ($E_{1/2}$) was found to be constant at all scan rates (ν) ranging from 50 – 1000 mV s^{-1} (Table 21).
- The cathodic and anodic peak potential difference (ΔE_p) varied between 56 – 64 mV at all scan rates between 50 – 1000 mV s^{-1} (Table 21) as expected for an ideal Nernstian process (58 mV). The slow increase of the ΔEp value with increasing scan rate can be attributed to incomplete *iR*-drop compensation.

- The anodic and cathodic peak currents were almost identical (i_{pa} / i_{pc} ≈ 1) and independent of the scan rates (Table 21).
- Finally, a plot of cathodic peak current (i_{pc}) *versus* the square root of the scan rate ($\nu^{1/2}$) revealed an almost linear relationship (Figure 47).

The CV results prompted me to study the chemical reduction of the stannylidyne complex **41**. Indeed, vacuum transfer of THF into an equimolar mixture of **41** and KC_8 at −196 °C, followed by warming to −78 °C and stirring for 2 hours at this temperature resulted in a noticeable color change from purple to dark brown. Warming of the brown suspension to 0 °C, and workup at this temperature followed by crystallization at −60 °C from an *n*-pentane solution afforded the open-shell stannylidyne complex *trans*-[H(dmpe)$_2$MnSn(C_6H_3-2,6-Mes_2)] (**43**) as a microcrystalline brown solid in 49 % yield (Scheme 16). Notably, the radical **43** constitutes the first example of an open-shell stannylidyne complex featuring a tin-centered unpaired electron. Compound **43** is extremely air-sensitive and instantaneously decolorizes upon exposure to air. The brown stannylidyne radical is a quite thermally stable solid, which decomposes in a vacuum-sealed glass capillary to a dark-brown to black solid at 152 °C. It is very good soluble in THF, fluorobenzene, Et_2O and toluene, and moderately soluble in common aliphatic solvents.

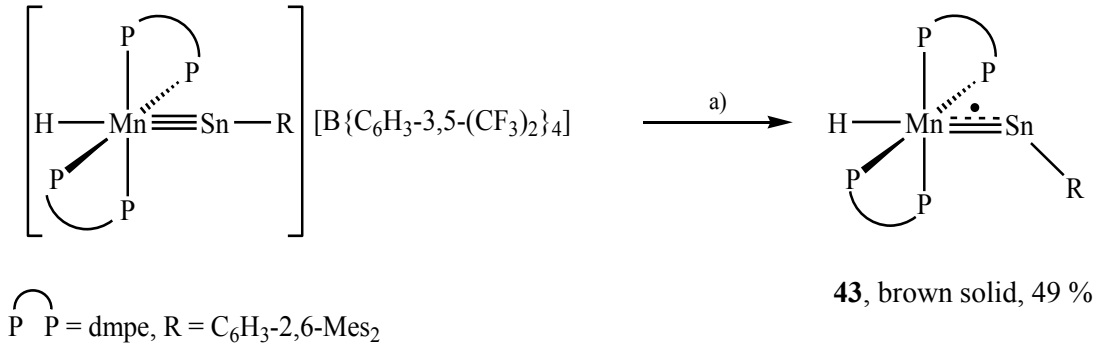

Scheme 16. Synthesis of the stannylidyne radical **43** upon one-electron reduction of **41**; a) +KC_8, −K[B{C_6H_3-3,5-$(CF_3)_2$}$_4$], −8C; THF; −196 °C → 0 °C. The dot indicates the unpaired electron; formal charges are omitted for clarity.

Compound **43** was fully characterized by single-crystal X-ray diffraction, IR, UV-Vis and EPR spectroscopy. Furthermore, the composition and the purity were confirmed by elemental analysis. Brown block-like single-crystals of **43**, suitable for X-ray diffraction analysis, were grown upon cooling a saturated *n*-pentane solution of **43** at −60 °C. The molecular structure revealed a distorted octahedral geometry around the manganese center with a *trans* arrangement

of the stannylidyne ligand to the hydrido ligand, as evidenced by the Sn-Mn-H75 angle of 178.2833(3)° (Figure 48). The hydrido ligand could be located in the difference Fourier map and was refined isotropically to a Mn–H distance of 1.5617(3) Å.

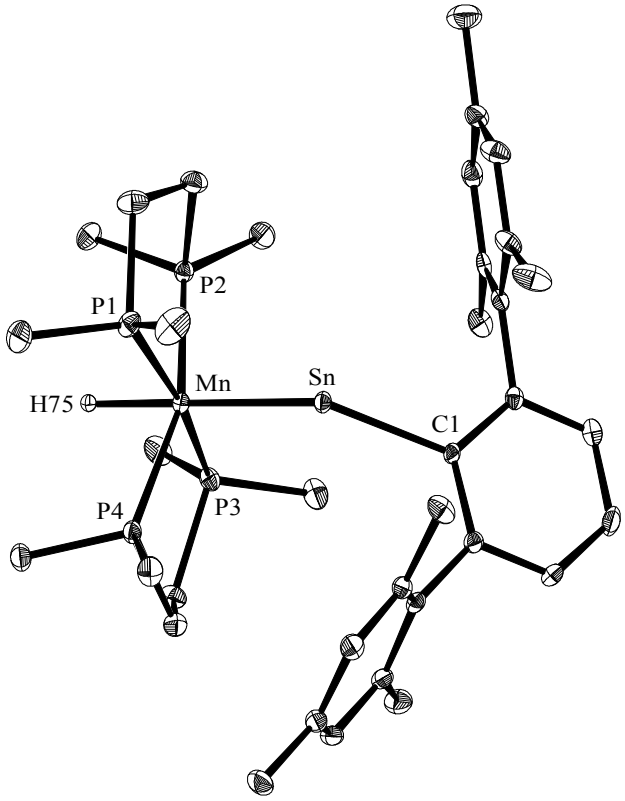

Figure 48. DIAMOND plot of the molecular structure of the stannylidyne radical **43** at 100(2) K. Thermal ellipsoids are set at 30% probability. Hydrogen atoms, except the H75 atom bonded to manganese, are omitted for clarity. Selected bond lengths [Å] and bond angles [°]: Mn-Sn 2.4486(6), Sn-C1 2.229(4), Mn-H75 1.5617(3), Mn-P1 2.238(1), Mn-P2 2.224(1), Mn-P3 2.215(1), Mn-P4 2.231(1); Mn-Sn-C1 144.29(8), Sn-Mn-H75 178.2833(3), Sn-Mn-P1 93.39(3), Sn-Mn-P2 98.17(3), Sn-Mn-P3 96.66(3), Sn-Mn-P4 101.59(3).

Reduction of the closed-shell stannylidyne complex **41** causes a significant change in the Mn–Sn bond length and the Mn-Sn-C1 angle (Table 22). Thus, the Mn–Sn bond in **43** (2.4486(6) Å) is *ca*. 11 pm (4.3 %) longer than that in **41** (2.3434(5) Å), and the Mn-Sn-C1 atom array deviates considerably from linearity in **43** (∠Mn-Sn-C1 144.29(8)°) in contrast to the almost linear coordination of the tin atom in **41** (∠Mn-Sn-C1 = 176.85(6)°). Furthermore, the reduction leads to a decrease of the Mn–P bond lengths ($Mn–P_{(av)}$ = 2.227 Å (**43**), 2.26 Å (**41**)) and an increase of the Sn–C1 bond length (2.229(4) Å (**43**), 2.159(3) Å (**41**)) (Table 22). All these structural

changes can be rationalized with the population of one of two Mn≡Sn π*-orbitals with one unpaired electron, which reduces the formal Mn–Sn bond order from 3 to 2.5. Since the π*-orbitals are mainly tin centered p-orbitals (*vide supra*), the unpaired electron resides primarily on one of the p-orbitals of the tin atom leading to a bending of the terphenyl substituent at the tin atom. Furthermore, addition of one electron to a mainly Sn-centered π*-orbital reduces the π-backdonation from Mn→Sn, which leads to an increase of the electron density on the Mn center. This induces an increased Mn→P back-doantion and a Mn–P bond shortening. Finally, elongation of the Sn–C1 bond can be explained with an increased hyperconjugartion leading to a population of the σ*(Sn–C1) orbital, which reduces the Sn–C1 bond order. The latter observation was further supported by quantum chemical calculations (*vide infra*).

Table 22. Comparison of selected bonding parameters of the open-shell and closed-shell stannylidyne complex **43** and **41**, respectively.

Complex	Mn-Sn [Å]	Mn-H75 [Å]	Sn-C1 [Å]	Mn-P1 [Å]	Mn-P2 [Å]	Mn-P3 [Å]	Mn-P4 [Å]	Mn-Sn-C1 [°]
43	2.4486(6)	1.5617(3)	2.229(4)	2.238(1)	2.224(1)	2.215(1)	2.231(1)	144.29(8)
41	2.3434(5)	1.44(3)	2.159(3)	2.262(1)	2.258(1)	2.266(1)	2.253(1)	176.85(9)

The stannylidyne radical **43** was further characterized by solid-state IR spectroscopy. The solid-state IR spectrum of **43** reveals a considerable shift of the Mn-H absorption band to lower wavenumbers than **41** (ν(Mn-H) = 1747 (**43**), 1792 cm^{-1} (**41**)) (Figure 49). This can be rationalized with the occupation of one of the π*-orbitals of the Mn≡Sn bond leading to a rehybridisation of the Sn orbitals, which results in an increase of the *trans*-influence of the stannylidyne ligand in the open-shell complex **43** and consequently a weakening of the Mn-H bond.

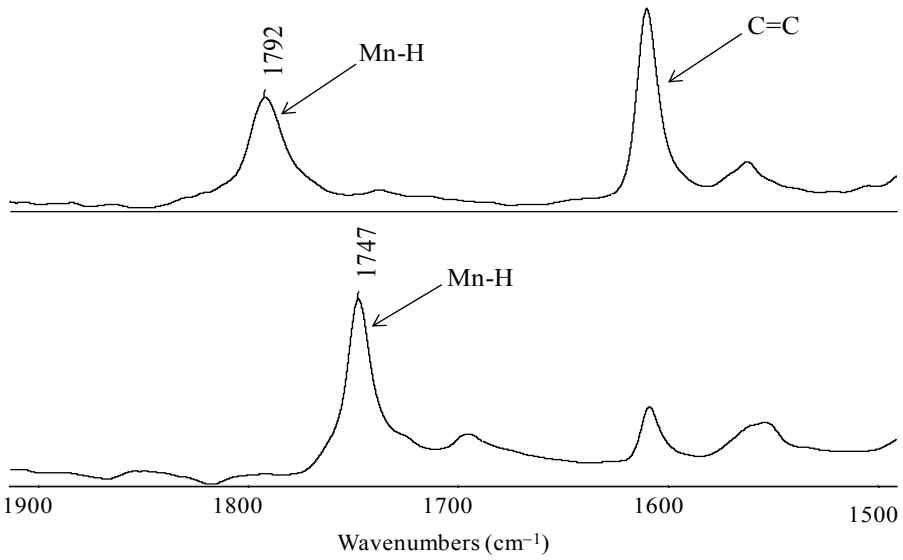

Figure 49. Comparison of the ATR FT-IR spectra (1900 – 1500 cm^{-1}) of the solid sample of the closed-shell (top) and the open-shell (bottom) stannylidyne complexes **41** and **43**, respectively.

The UV-Vis spectrum of the stannylidyne radical **43** was measured in THF at room temperature (Figure 50). In addition, the spectrum was compared with the UV-Vis spectra of the corresponding closed-shell stannylidyne complex **41** (Figure 51) and the hydridostannylidene complex **44** (Figure 52), which were also measured under the same conditions. The main absorption bands and the associated molar extinction coefficients are summarized in Table 23.[17] Compound **43** displays two closely spaced absorption maxima at 489 (3275) and 428 (3768) nm, accompanied by a red-shifted low-intensity shoulder at 640 (216) nm (the values in brackets are the molar absorption coefficients in L mol^{-1} cm^{-1}) in the visible range of the spectrum. These three absorption bands are responsible for the intense brown color of the radical. In contrast, only two well-separated absorption maxima were observed for the closed-shell stannylidyne complex **41** at 533 (1088) and 394 (12870) nm, which arise presumably from the two different $\pi \rightarrow \pi^*$ transitions, and are responsible for the purple color of the compound. The red shift ($\Delta\lambda_{max}$) of 107 nm for the neutral metal stannylidyne radical **43** compared to that for the stannylidyne cation **41** indicates the presence of an unpaired electron in the former molecule. In contrast to the stannylidyne complexes, the stannylidene complex **44** displays only one strong absorption band at 490 (6977) nm in the visible range of the spectrum. This intense band at 490 nm covers the

[17] The plot of the extinction vs concentration always showed a linear dependence with $R^2 \geq 0.968$ indicating that the Lambert-Beer law is obeyed in the range of concentrations employed.

blue-green region of the visible spectrum and gives rise to the observed red color of the stannylidene complex. Apart from these absorption bands, all complexes display a very strong shoulder in the range 300 – 340 nm. In summary, the solution UV-Vis spectra of these complexes provide a rationale for the observed color in solution. An assignment of these bands could not be undertaken.

Table 23. Comparison of the major UV-Vis absorption bands and their corresponding molar extinction coefficients of the closed-shell and open-shell stannylidyne complexes (**41** and **43**, respectively), and the hydridostannylidene complex **44** in THF.

Complex	**Band 1**		**Band 2**		**Band 3**		**Band 4**	
	λ [nm]	ε [L·mol^{-1}·cm^{-1}]	λ [nm]	ε [L·mol^{-1}·cm^{-1}]	λ [nm]	ε [L·mol^{-1}·cm^{-1}]	λ [nm]	ε [L·mol^{-1}·cm^{-1}]
41			533	1088	394	12870	335	2469
43	640	216	489	3275	428	3768	300	-
44	-	-	490	6977	-	-	341	-

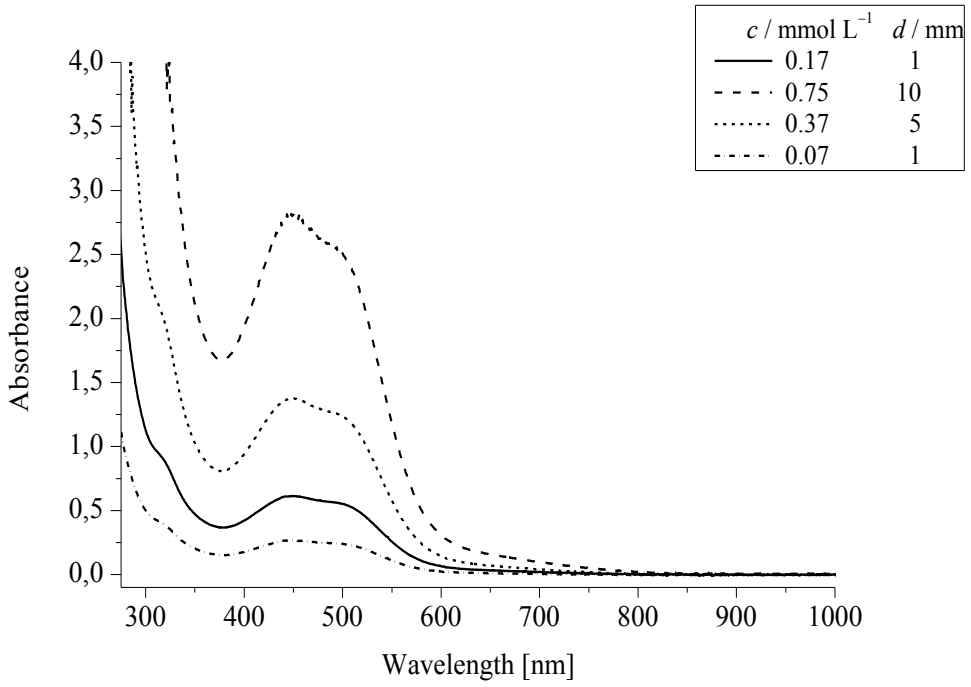

Figure 50. UV-Vis spectrum of the open-shell stannylidyne complex **43** in THF at different concentrations (*c*) and thickness (*d*) of the cuvette at room temperature.

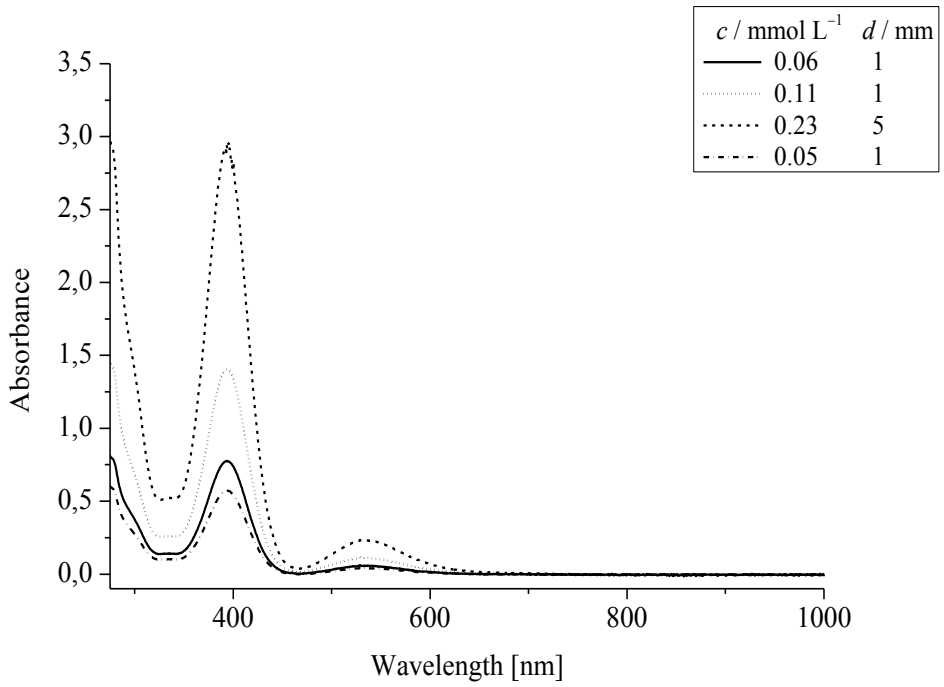

Figure 51. UV-Vis spectrum of the closed-shell stannylidyne complex **41** in THF at different concentrations (*c*) and thickness (*d*) of the cuvette at room temperature.

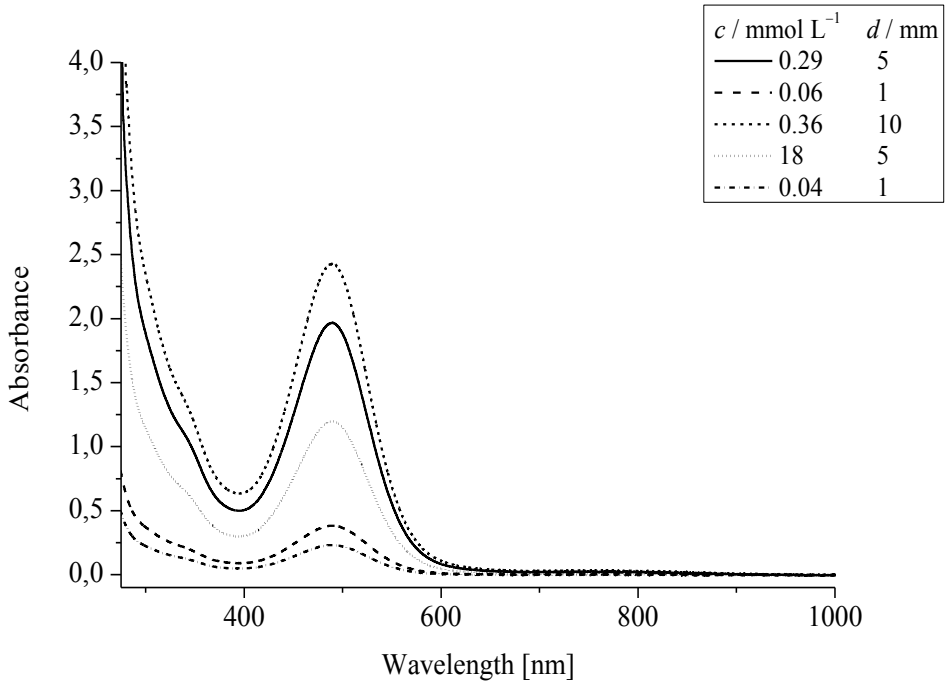

Figure 52. UV-Vis spectrum of the hydridostannylidene complex **44** in THF at different concentrations (*c*) and thickness (*d*) of the cuvette at room temperature.

Further evidence for presence of a tin-centered unpaired electron in compound **43** was provided by the continuous-wave (*cw*) EPR spectroscopy using X- and Q-band resonators. Samples for the measurement were prepared in *n*-pentane in the concentration range of 1 mM – 10 mM and were measured at 10 K for the X-band and 25 K for the Q-band. The X-band *cw*-EPR spectrum revealed an orthorhombic splitting with a large *g*-anisotropy (g_{xx} = 1.606, g_{yy} = 1.947 and g_{zz} = 1.970; g_{iso} = 1.841) and with hyperfine coupling to ^{119,117}Sn (A(^{119,117}Sn) = 54.4 mT) and ^{55}Mn (A(^{55}Mn) = 2.9 – 3.3 mT) (Figure 53, left). The results of the X-band spectrum were further verified by measuring the Q-band *cw*-EPR spectrum, which revealed the same splitting pattern with better resolution as evidenced by the well fitting with the simulated spectrum using the same g-tensor and A(^{119}Sn) and A(^{55}Mn) tensors (Figure 53, right).[18] Furthermore, the experimental spectrum was also compared with the DFT derived g-tensor and the ^{119}Sn and ^{55}Mn hyperfine coupling constants, which fit quite well. The large shift of the g_{xx}-value from the ideal g_e value of 2.0023 is indicative of a strong spin-orbit interaction of the unpaired electron with Mn d-orbitals.

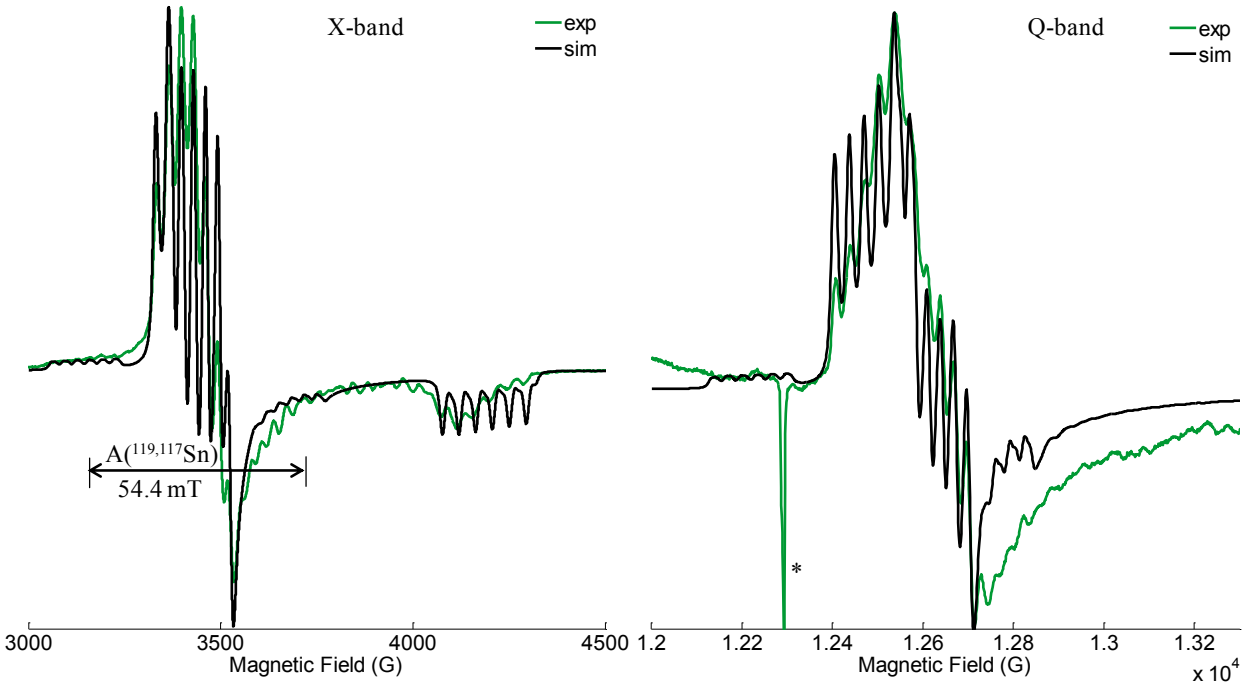

Figure 53. X-band (left, 10 K) and Q-band (right, 25 K) *cw*-EPR spectrum of the stannylidyne radical **43** in *n*-pentane; green line represents the experimental spectrum, and the black line represents the simulated spectrum. The * marks corresponds to a spike arising from the instrument.

18 In the Q-band spectrum, the third component of the *g*-tensor was not observed as it appeared outside of the measured spectral window.

Table 24. Experimental and calculated g-tensors and associated A(^{119}Sn)- and A(^{55}Mn)-tensors of the stannylidyne radical **43**.

Method	g			A(^{119}Sn) [mT]			A(^{55}Mn) [mT]		
	g_{xx}	g_{yy}	g_{zz}	A_x	A_y	A_z	A_x	A_y	A_z
Experimental	1.606	1.947	1.970	*	*	54.4	–4.4	2.9	3.3
		g_{iso} = 1.841							
DFT	1.591	1.998	2.015	–14.8	–11.5	–52.9	–3.9	2.5	0.4
		g_{iso} = 1.868							

*: These hyperfine coupling constant could not be resolved due to the weak and overlapping with the other intense lines of the spectrum.

Unfortunately, two separate pair of satellites were not observed for the two ^{117}Sn and ^{119}Sn nuclei, presumably due to the very small difference between the hyperfine coupling constants (hfcc). The ^{119,117}Sn hfcc of 54.4 mT is significantly larger than that observed for the previously reported tin-centered radicals $(tBu_2MeSi)_3Sn$ (A(^{119,117}Sn) = 32.9 mT)[175] and $Na[\{(Me_3Si)_2CH\}_2Sn]$ (A(^{119,117}Sn) = 11.6 mT),[148] thus supporting the tin-centered radical character of compound **43**. Furthermore, the ^{119,117}Sn hfcc of 54.4 mT is much smaller than that expected for a σ-type tin-centered radical (≥132.5 mT),[146] thus suggesting a π-type tin-centered radical. The very weak ^{55}Mn superhyperfine coupling constant of 2.9 – 3.3 mT and the absence of a resolvable hyperfine coupling with the ^{31}P nuclei is also consistent with the presence of a tin-centered unpaired electron.

Additional information about **43** was provided by quantum chemical calculations, which were carried out at the RI-JCOSX/B97-D3/def2-TZVP level of theory. The preliminary calculations indeed support the description of **43** as a stannylidyne radical that features the major spin density at the tin center. Geometric optimization of **43** afforded a minimum structure (**43$_{calc}$**) with an excellent agreement between the calculated and experimental bonding parameters (Table 25).

Table 25. Comparison of selected experimental and calculated bonding parameters of **43** and **43$_{calc}$**. Atom numbering of the experimental structure was taken over in the calculated structure.

Complex	Mn-Sn [Å]	Mn-H75 [Å]	Sn-C1 [Å]	Mn-P1 [Å]	Mn-P2 [Å]	Mn-P3 [Å]	Mn-P4 [Å]	Mn-Sn-C1 [°]
43	2.4486(6)	1.5617(3)	2.229(4)	2.238(1)	2.224(1)	2.215(1)	2.231(1)	144.29(8)
43$_{calc}$	2.458	1.557	2.231	2.228	2.210	2.209	2.210	147.94

A look at the Kohn-Sham orbitals revealed the SOMO as the Mn≡Sn π^* orbital, which is mainly a tin-centered p-orbital and affirms that the reduction of the closed-shell stannylidyne complex **41** results in the population of one of the Mn≡Sn π^* orbitals of **41** with one electron (Figure 54). The DOMO is one of the Mn≡Sn π-bonds and located in the same plane as that of the SOMO, and becomes almost a Mn-centered lone pair orbital due to the decreased back donation to the occupied Sn p-orbital. The DOMO–1 is a metal centered d orbital that is nonbonding with respect to the Mn-Sn multiple bond and the DOMO–2 represent the Mn-Sn π-orbital (Figure 54). Finally, the DOMO–3 represents the σ-bond between Mn and Sn (Figure 54).

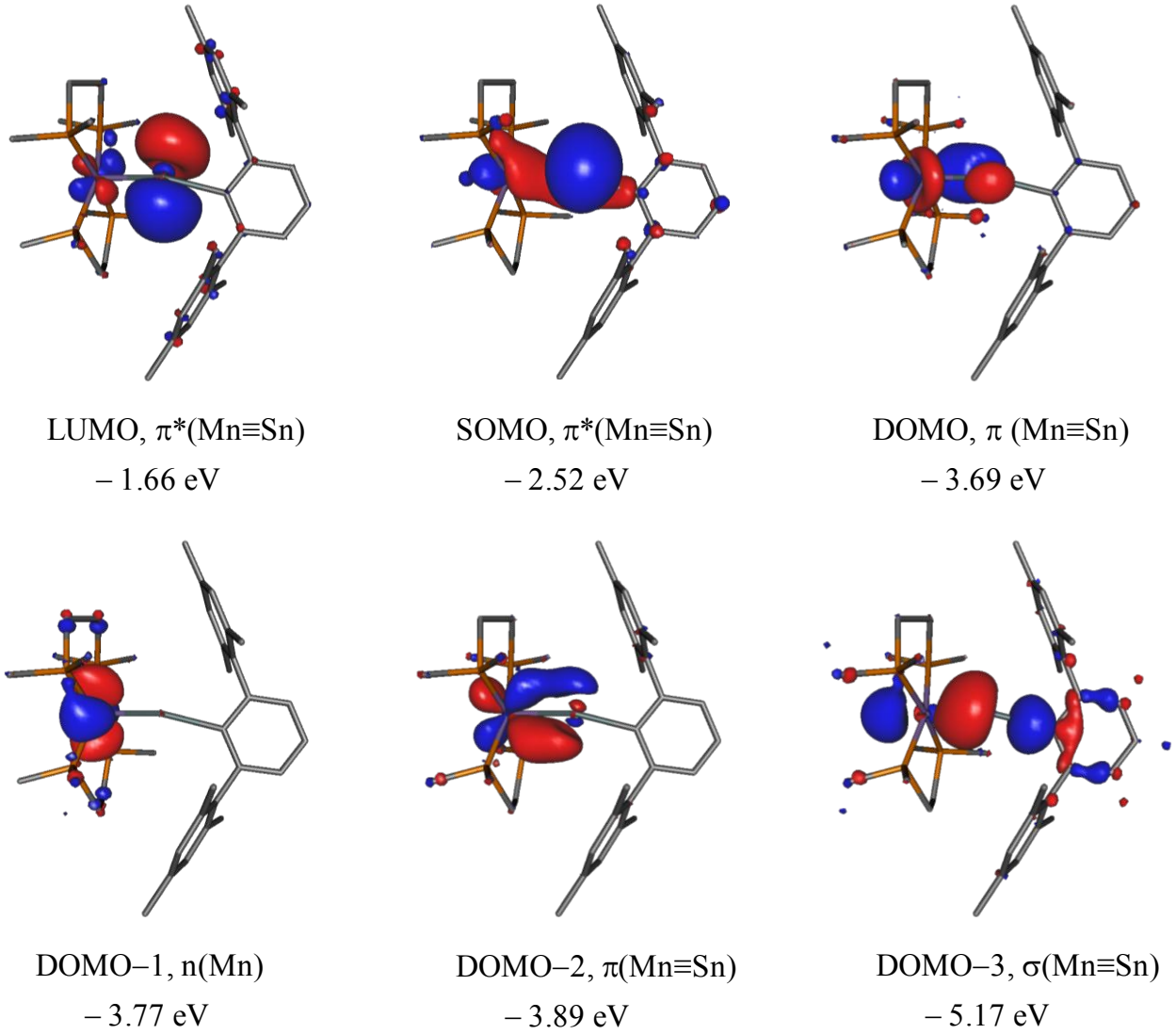

Figure 54. Selected Kohn-Sham frontier orbitals of the stannylidyne radical **43**; isosurface value corresponds to 0.04 e bohr^{-3}.

Further insight into the electronic structure of the stannylidyne radical **43** was provided by the natural bond orbital (NBO) analysis at the RI-JCOSX/B97-D3/def2-TZVP level of theory (Table 26). The NBO analysis revealed that the Mn–Sn bond is composed of one σ and one π-bond with occupancies of 1.57 and 1.80 electrons, respectively (Table 26). Furthermore, the Mn atom contains one more lone electron pair compared to the closed-shell stannylidyne complex. In addition, the Sn atom features a p orbital populated with 0.65 electrons, which indicates indirectly a population of the Mn≡Sn π^*-orbital with one unpaired electron, resulting in a decrease of the formal Mn–Sn bond order from 3 in **41** to 2.5 in **43**. The lowering of the Mn–Sn bond order is also reflected in a very low Wiberg bond index (WBI) of 0.72 (Table 26). Finally, a natural population analysis (NPA) of **43** revealed that the reduction leads to a significant decrease of the positive partial charge of the Sn atom from +1.35 in **41** (*vide supra*) to +0.84 in **43** (Table 26). Furthermore, the high polarity of the Mn-Sn bond in the open-shell stannylidyne complex **43** is also reflected by the high opposite NPA charges of Mn (−1.62) and Sn (+1.35) (Table 26).

Table 26. Selected results of the natural bond orbital (NBO) analysis of **43** (RI-JCOSX/B97-D3/def2-TZVP).[a]

	α-spin			β-spin				NPA parital charges	
	occ.	pol. [%]	hyb.	occ.	pol. [%]	hyb.	WBI		
σ(Mn–Sn)	0.84	39.7 (Mn) 60.3 (Sn)	$sd^{1.05}$ (Mn) $sp^{0.75}$ (Sn)	0.73	54.8 (Mn) 45.2 (Sn)	$sd^{1.40}$ (Mn) $sp^{0.95}$ (Sn)	0.72	Mn	−1.62
π(Mn–Sn)	0.92	89.6 (Mn) 10.4 (Sn)	d (Mn) p (Sn)	0.88	87.5 (Mn) 12.5 (Sn)	$sd^{15.35}$ (Mn) p (Sn)		Sn	0.84
σ(Sn–C1)	0.96	24.4 (Sn) 75.6 (C1)	$sp^{1.30}$(Sn) $sp^{2.99}$ (C1)	0.91	21.2 (Sn) 78.8 (C1)	$sp^{1.16}$ (Sn) $sp^{2.98}$ (C1)	0.59	C1	−0.50
n(Sn)	0.65		p	-	-	-			

[a]: occ. = occupancy, pol. = polarization, hyb. = hybridization, WBI = Wiberg bond index. NPA = natural population analysis.

Therefore, the single-crystal X-ray diffraction study, ESR spectroscopy and the quantum chemical calculations of **43** are all in support of a stannylidyne radical that comprises the unpaired electron at the tin center. Conspicuously, compound **43** represents the first example of an open-shell stannylidyne complex that features a tin-centered unpaired electron. Notably, the open-shell tetrylidyne complexes containing a tetrel-centered unpaired electron are very unstable and prone to decomposition at ambient temperature. For instance, the germylidyne radical anion **18-Mo**, which is the only other example of this class isolated so far, is only stable in solution below –40 °C. Therefore, the isolation of this room temperature stable stannylidyne radical represents a significant achievement in this field.

2.6. μ-Ylido complexes

Thus far, the synthesis and comprehensive studies on closed- and open-shell group 6 and 7 transition metal tetrylidyne complexes were discussed. In all these complexes, the tetrel atoms are bonded to a bulky organyl group, such as C_6H_3-2,6-Mes_2, $N(SiMe_3)(C_6H_2$-2,4,6-tBu$_3)$ etc., which are necessary to stabilize the highly reactive tetrylidyne complexes. In this chapter, we will focus on the synthesis of heavier analogues of the μ_2-carbido complexes featuring heavier tetrel atoms, that are bonded only two metal fragments. Furthermore, the reactivity of this interesting class of compounds will be discussed in detail.

2.6.1 Access to the first metallasilylidyne complexes

It was already shown in previous chapters that the scorpionate metalate salts **3-Mo** and **3-W** are very powerful, metal-centered nucleophiles, which react with a broad range of aryltetrel(II) halides, E(R)X (E = Ge – Pb; R = C_6H_3-2,6-Mes_2, C_6H_3-2,6-$Trip_2$, $N(SiMe_3)(C_6H_2$-2,4,6-tBu$_3)$; X = Cl – I), to afford after metathetical halide exchange and PMe_3 elimination the heavier tetrylidyne complexes [Tp'$(CO)_2$M≡E−R]. On the other hand, recent studies have shown that $SiBr_2$(SIdipp) (SIdipp = C[N(C_6H_3-2,6-iPr$_2$)CH_2]$_2$) is a very suitable synthon for the synthesis of multiply bonded low-valent silicon complexes and enabled the preparation of silylidene complexes,[33, 176] cationic silylidyne complexes[33, 176] and metallosilanones.[35] Keeping this in mind, we envisaged to combine these tailor-made metal precursors with $SiBr_2$(SIdipp) in a 2:1 ratio.

Indeed, addition of a solution of $SiBr_2$(SIdipp) in fluorobenzene to a fluorobenzene suspension of two equivalents of **3-Mo** or **3-W** at ambient temperature resulted in a color change from yellow to reddish-brown (Mo) or brown (W) within 2 – 3 hours. IR-spectroscopic inspection of the reaction mixtures revealed the formation of the corresponding metallasilylidyne complexes [Tp'$(CO)_2$M≡Si–M$(CO)_2(PMe_3)$Tp'] (**21-Mo**, M = Mo; **21-W**, M = W) together with a small amount of the 17VE radicals [Tp'M$(CO)_2(PMe_3)$] (**2-Mo**, M = Mo; **2-W**, M = W) (Scheme 17). The 17VE radicals were formed probably due to a competing one-electron oxidation of **3-Mo** and **3-W** by $SiBr_2$(SIdipp). This side reaction was also observed during the reactions of **3-M** with the aryltetrel(II) halides EX(R) (E = Si – Pb). Compounds **21-Mo** and **21-W** were isolated after workup as air-sensitive, red-brown (**21-Mo**) and brown (**21-W**) solids in 43 and 51% yields, respectively. Both metallasilylidyne complexes are thermally robust solids and decompose at a

very high temperature of 280 – 283 °C (**21-Mo**) and 268 – 270 °C (**21-W**), without melting. Compounds **21-Mo** and **21-W** are moderately soluble in fluorobenzene, THF and DME, poorly soluble in benzene, toluene and diethyl ether, and insoluble in aliphatic solvents. Both compounds decompose very fast in CH_2Cl_2, but slowly in THF.

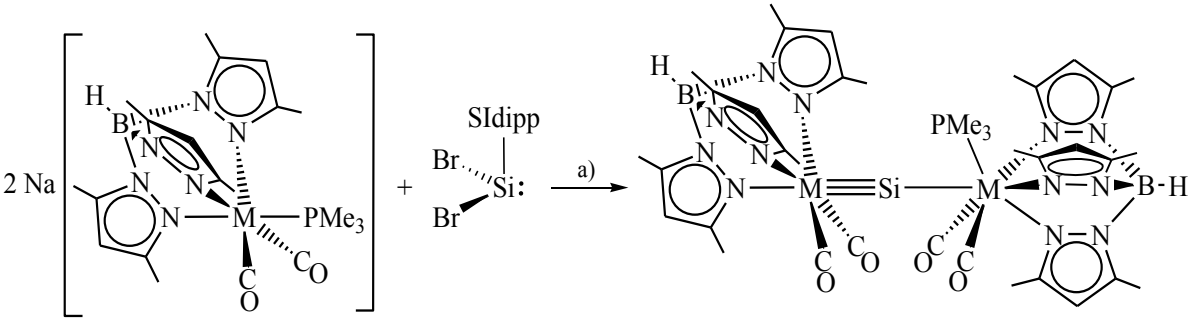

21-Mo, red-brown solid, 43%

21-W, brown solid, 51%

Scheme 17. Synthesis of metallasilylidyne complexes **21-Mo** and **21-W**; a) –SIdipp, –PMe_3, –2NaBr, fluorobenzene, r.t.; formal charges are omitted for clarity.

The molecular structures of **21-Mo** and **21-W** were determined by single-crystal X-ray diffraction analysis. Red blocks of **21-Mo**·0.5(*n*-C_5H_{12}) and **21-W**·2(1,2-$C_6H_4F_2$) were obtained by diffusion of *n*-pentane into a THF solution of **21-Mo** at room temperature, and slow evaporation of a saturated 1,2-$C_6H_4F_2$ solution of **21-W** at ambient temperature, respectively. Compounds **21-Mo** and **21-W** are isostructural and represent the first examples of heavier analogues of metallacarbyne complexes. The molecular structures confirmed the presence of a central M-Si-M (M = Mo, W) core with two structurally different metal sites and distinctly different M–Si (M = Mo, W) bond lengths (Figure 55). The M1–Si bond lengths of **21-Mo** (2.287(2) Å) and **21-W** (2.283(5) Å) suggest the presence of a M–Si triple bond and are slightly larger than the M–Si triple bond length of the three-legged piano-stool silylidyne complexes [$Cp(CO)_2Mo{\equiv}Si(C_6H_3$-2,6-$Trip_2)$] (2.2241(7) Å)[30, 33] and [$Cp^*(CO)_2W{\equiv}Si(C(SiMe_3)_3)$] (2.2297(9) Å),[49] but compare well with the M–Si triple bond lengths of the Tp'-substituted octahedral silylidyne complex **7-Mo** (Mo–Si 2.2614(9) Å) and **7-W** (W–Si 2.2706(8) Å). The M2–Si bond lengths in **21-Mo** (2.438(2) Å) and **21-W** (2.429(5) Å) are markedly longer than the M1–Si bonds (6 – 6.6 %) and appear in the reported range of M–Si single bond lengths (Mo–Si

2.413(1) – 2.7140(8) Å; W–Si 2.388(6) – 2.712(1) Å),[19] thus indicating the presence of a M–Si single bond between the Si atom and the heptacoordinated metal centers (Mo2/W2). Thus, both M–Si bond lengths fully corroborate the description of **21-Mo** and **21-W** as first examples of metallasilylidyne complexes.

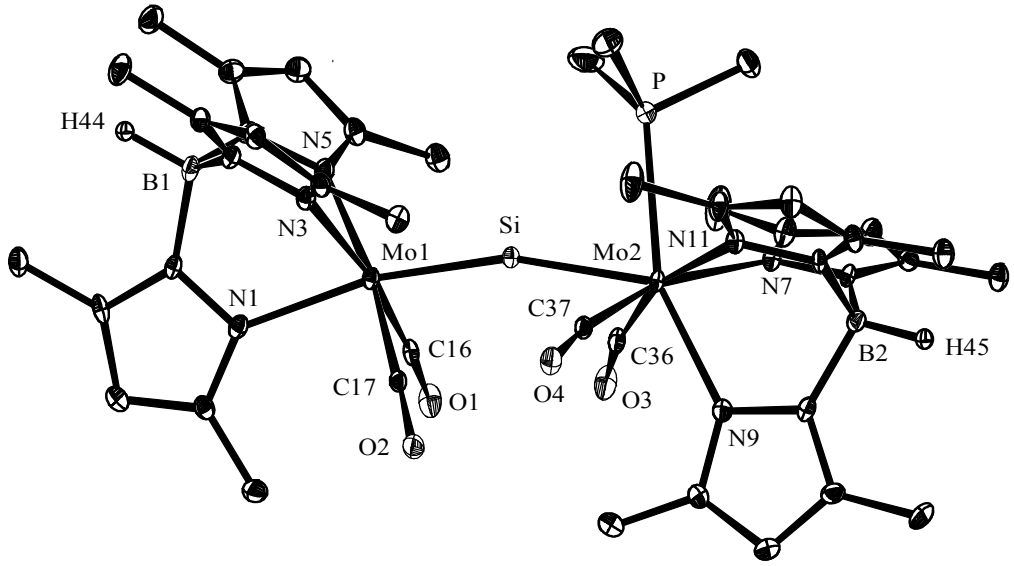

Figure 55. DIAMOND plot of the molecular structure of compound **21-Mo** in the crystal lattice of **21-Mo**·0.5(*n*-C_5H_{12}) at 123(2) K. Thermal ellipsoids are set at 30% probability. Hydrogen atoms (except the B-bonded H atoms) were omitted for clarity. Selected bond lengths [Å] and bond angles [°] of **21-Mo**·(*n*-C_5H_{12}) (bond lengths and angles of **21-W**·2(1,2-$C_6H_4F_2$) are given in square brackets): Mo1-Si 2.287(2) [2.283(5)], Mo2-Si 2.438(2) [2.429(5)], Mo2-P 2.568(2) [2.556(4)], Mo1-N1 2.272(5) [2.24(1)], Mo1-N3 2.271(4) [2.23(1)], Mo1-N5 2.256(4) [2.26(1)], Mo2-N7 2.252(4) [2.27(1)], Mo2-N9 2.227(5) [2.23(1)], Mo2-N11 2.254(4) (2.25(1)), Mo1-C16 1.946(6) [1.94(1)], Mo1-C17 1.953(5) [1.95(2)], Mo2-C36 1.957(6) [1.98(1)], Mo2-C37 1.963(6) [1.95(1)]; Mo1-Si-Mo2 162.93(7) [171.3(2)], N1-Mo1-Si 169.3(1) [176.6(4)], N3-Mo1-Si 104.2(1) [100.8(4)], N5-Mo1-Si 108.9(1) [102.1 (4)], N7-Mo2-Si 131.3(1) [131.4(4)], N9-Mo2-Si 128.1(1) [129.3(4)], N11-Mo2-Si 130.3(1) [130.5(3)], C16-Mo1-Si 84.2(2) [84.1(5)], C17-Mo1-Si 78.5(2) [84.3(5)], C36-Mo2-Si 65.9(2) [64.2(4)], C37-Mo2-Si 66.7(2) [65.6(4)], P-Mo2-Si 75.93(5) [75.1(2)].

The Mo1/W1 centers adopt an octahedral geometry with the Si atom in a *trans*-orientation to one of the pyrazolyl groups of the Tp' ligand (N1-Mo1-Si angle = 169.3(1)°, N1-W1-Si angle =

19 A CSD Survey (11.05.2016) gave 85 compounds with Mo–Si single bonds and 79 compounds with W–Si single bonds, leading to a median/mean Mo–Si and W–Si bond lengths of 2.564/2.559 Å and 2.569/2.568 Å, respectively.

176.6(4)°), whereas the Mo2/W2 centers reside in a distorted face-capped octahedral geometry, in which the Si atom caps the octahedron face built from the PMe_3 and two CO ligands. In both complexes, the *cis*-oriented CO ligands of each metal fragment adopt an overall syn-orientation along the M-Si-M unit. Remarkably, the Mo1-Si-Mo2 atom array (162.93(7)°) deviates more from linearity than the W1-Si-W2 atom array (171.3(2)°). Such deviation from linearity was also found in the silylidyne complexes **7-Mo** (160.8(1)°) and **7-W** (161.7(1)°). In fact, quantum chemical calculations of a relaxed potential energy profile scan for an in-plane bending of the Mo-Si-Mo atom array in **21-Mo** toward the CO ligands, suggest a very flat progression of the energy profile, which leads to a very small bending energy difference in the margin of 8.8 kJ mol^{-1} within a bending angle range of 160 – 180°.

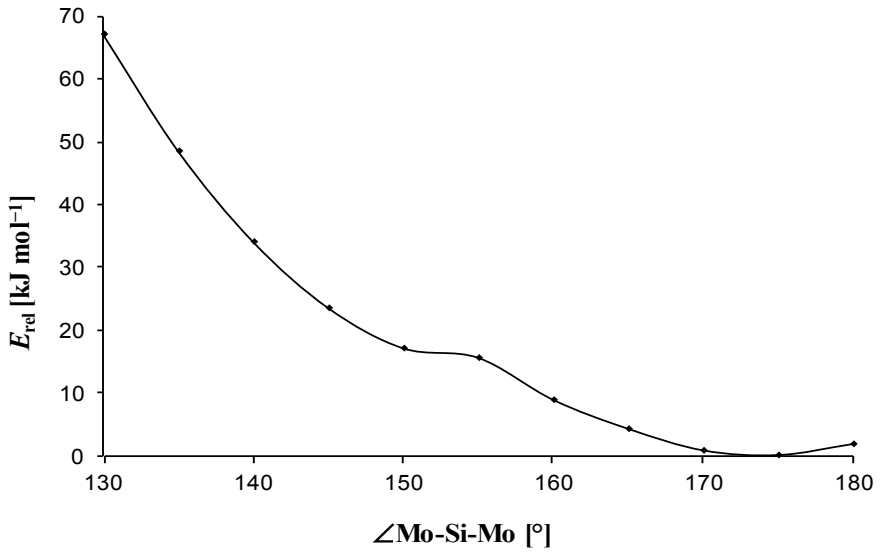

Figure 56. Relaxed potential energy scan at the RI-JCOSX/B97-D3/def2-TZVP/COSMO(THF) level of theory of the in-plane bending of the Mo-Si-Mo angle of **(21-Mo)$_{calc}$** toward the CO ligands. E_{rel} is the energy of the optimized structure at the respective angles relative to **(21-Mo)$_{calc}$**.

The solution NMR and IR spectra of **21-Mo** and **21-W** corroborate very well with the solid state structures. The solid state IR spectrum of **21-Mo** displays three ν_{CO} absorption bands at 1928 (s), 1861 (vs) and 1791 (s) cm^{-1}, whereas that of **21-W** displays five ν_{CO} absorption bands at 1903 (m), 1843 (s), 1833 (s), 1824 (vs), 1768 (s) cm^{-1}. In THF, the IR spectrum of **21-Mo** displays five partially overlapping ν_{CO} absorption bands at 1933 (s), 1870 (vs), 1857 (s, sh), 1806 (m), 1794 (m, sh) (Figure 57), and six absorption bands for **21-W** at 1920 (m), 1915 (m) 1854 (vs), 1841 (s), 1792 (w) and 1778 (m).

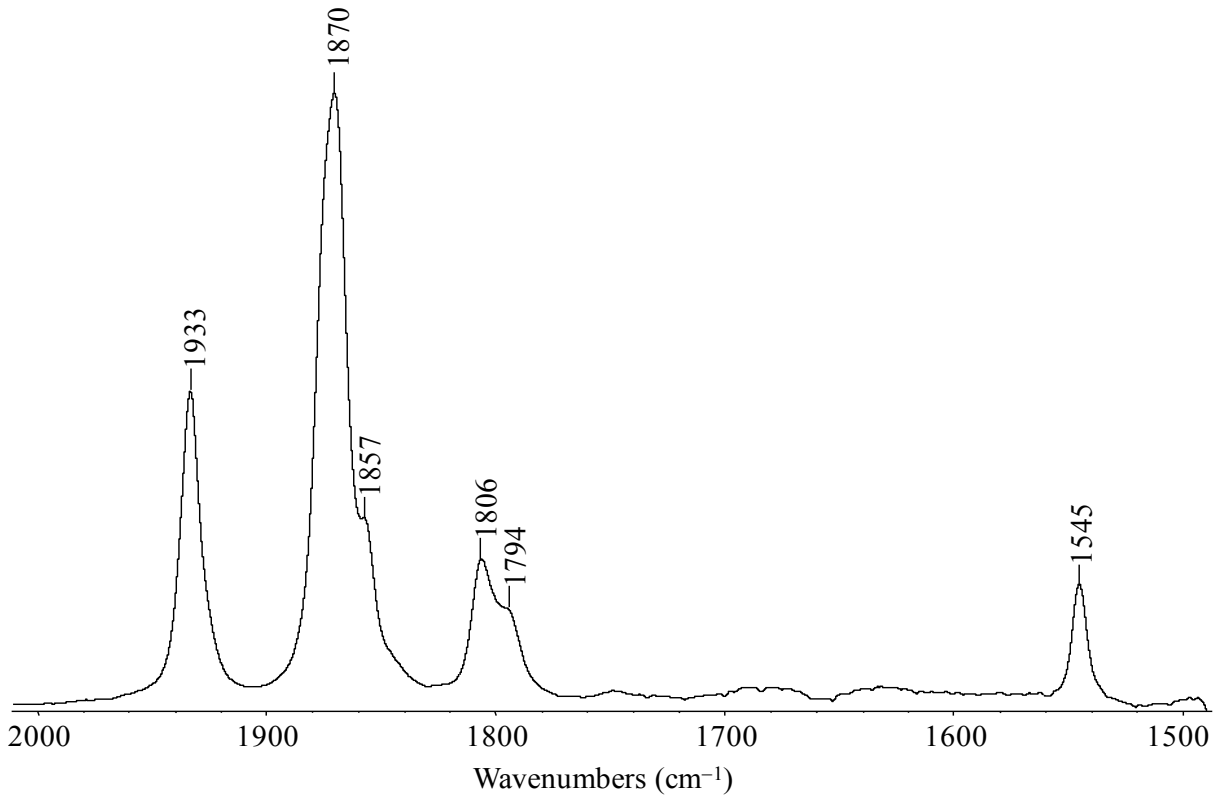

Figure 57. FT-IR spectrum (2000 – 1500 cm^{-1}) of **21-Mo** in THF showing the characteristic ν_{CO} and $\nu_{C\text{-}C\text{-}N}$ absorption bands.

The presence of more than four ν_{CO} absorption bands for the tetracarbonyl complexes suggest the coexistence of at least two different rotamers with respect to a rotation of the two metal fragments about the M-Si-M (M = Mo, W) array on the IR timescale. This was supported by quantum chemical calculations[20] carried out on **21-Mo**, which revealed the presence of three almost isoenergetic rotamers as local minimum structures on the potential energy surface (PES), which differ in the relative orientation of the CO ligands (Figure 58). Thus, the rotamer **(21-Mo)$_{calc}$** adopts a C_s-symmetric structure with two carbonyl units in a *syn*-orientation, whereas the rotamers **(21-Mo)'$_{calc}$** and **(21-Mo)''$_{calc}$** adopt C_1-symmetric structures with two carbonyl units in an *anticlinal*-orientation. The calculated ν_{CO} absorption bands reveal a close proximity for three rotamers, rendering it impossible to assign the absorption bands to a specific rotamer in the experimental spectrum, but the individual positions compare very well with the observed experimental spectrum (Table 27, Figure 59). A close look at the different stretching modes of the calculated ν_{CO} absorption bands reveal that the rotamers **(21-Mo)$_{calc}$** and **(21-Mo)'$_{calc}$** show

20 The quantum chemical calculations were performed by Dr. G. Schnakenburg.

coupled vibration between two carbonyls unit in each molecule, whereas the rotamer **(21-Mo)''$_{calc}$** show very weakly coupled vibration between the two carbonyl units (Figure 59).

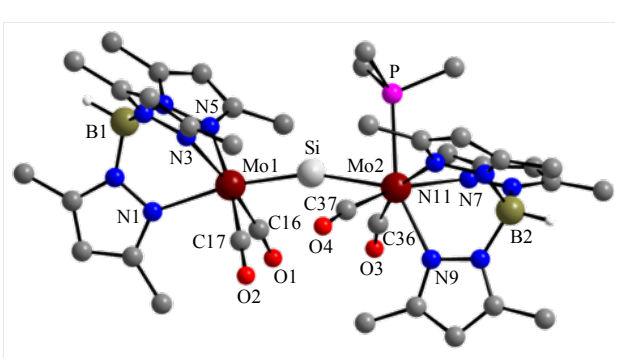

21-Mo

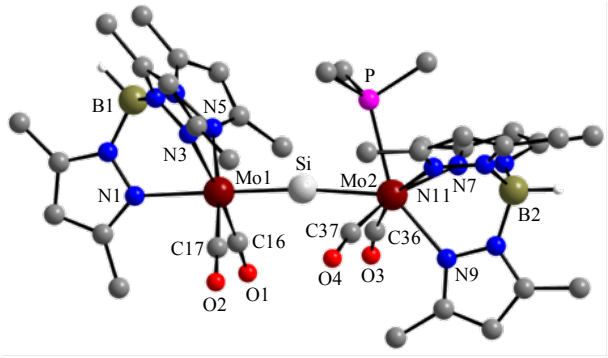

(21-Mo)$_{calc}$, 0.0 kJ mol^{-1}

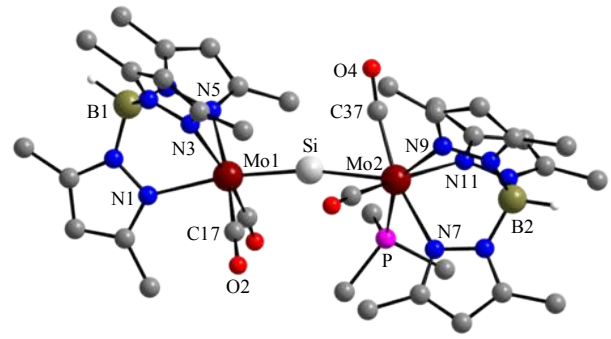

(21-Mo)'$_{calc}$, 1.2 kJ mol^{-1}

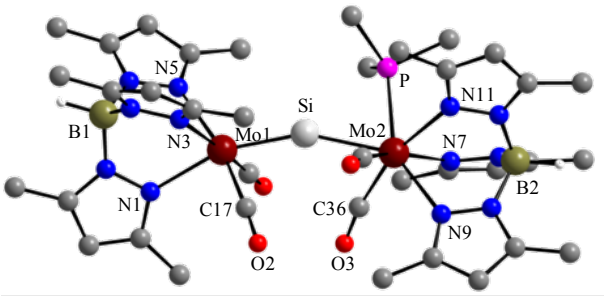

(21-Mo)''$_{calc}$, 9.1 kJ mol^{-1}

Figure 58. Experimental (**21-Mo**) and calculated structures ((**21-Mo)$_{calc}$**, **(21-Mo)'$_{calc}$**, **(21-Mo)''$_{calc}$**) with their corresponding relative Gibbs energies. The calculation was carried out at the RI-JCOSX/B97-D3/def2-TZVP/COSMO(THF) level of theory. The H atoms, except those bonded to B, were omitted for clarity. Atom numbering of the experimental structure was taken over in the calculated structure.

Table 27. Calculated ν_{CO} frequencies [cm^{-1}] (unscaled) of the isomers **(21-Mo)$_{calc}$**, **(21-Mo)'$_{calc}$** and **(21-Mo)''$_{calc}$** at the RI-JCOSX-B97-D3/def2-TZVP/COSMO(THF) level of theory and comparison with experimental values of **21-Mo**.

	IR-1 (sym, sym)	IR-2 (sym, sym)	IR-3 (asym, asym)	IR-4 (asym, asym)	IR-5 (-, sym)	IR-6 (-, asym)	IR-7 (sym, -)	IR-8 (asym, -)
(21-Mo)$_{calc}$	1916	1855	1850	1788				
(21-Mo)'$_{calc}$	1914	1850	1843	1781				
(21-Mo)''$_{calc}$					1921	1857	1846	1782
21-Mo[a]	1933	1870	1867	1806	1794			

[a]: In THF (Figure 57).

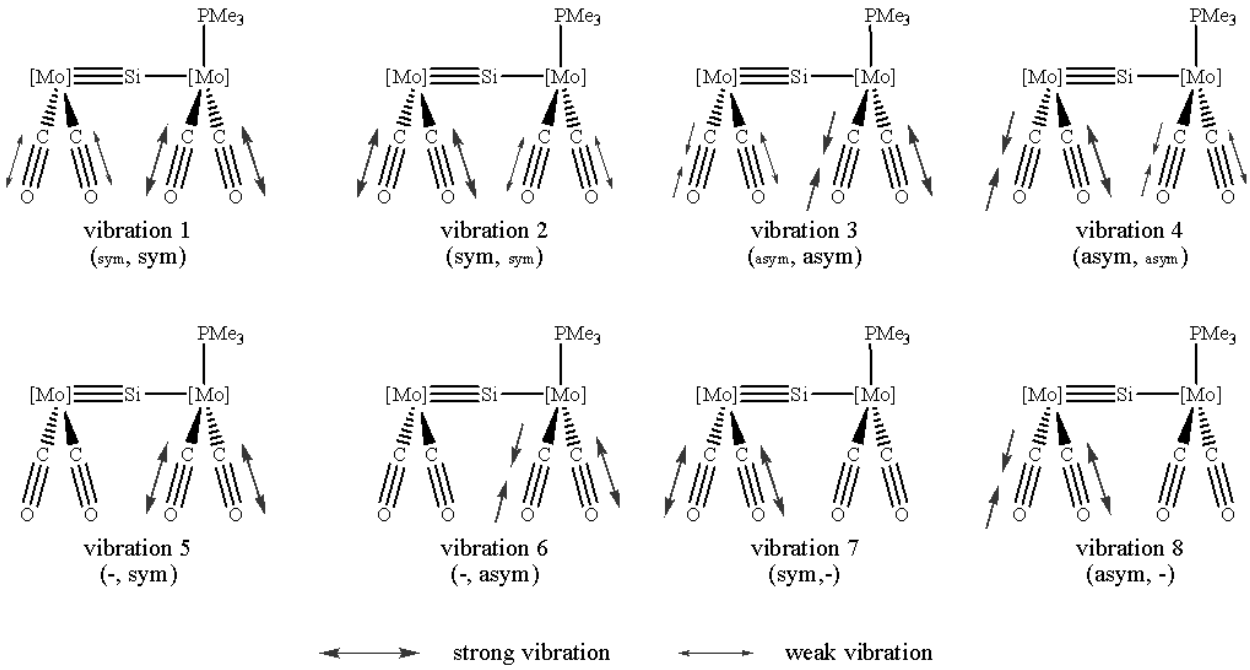

Figure 59. Schematic presentation of the ν_{CO} stretching modes of different symmetry of complex **21-Mo**; [Mo] = Tp'$(CO)_2$Mo.

The ^{29}Si{^{1}H} NMR spectra of **21-Mo** and **21-W** in THF-d_8 display a doublet signal at 438.9 ppm (d, $^2J(^{31}P, ^{29}Si)$ = 56.6 Hz) and 395.6 ppm (d, $^2J(^{31}P, ^{29}Si)$ = 39 Hz), respectively, which appear at a considerably lower field compared to those of the aryl or alkyl substituted silylidyne complexes [Cp$(CO)_2$Mo≡Si(C_6H_3-2,6-Trip$_2$)] (δ = 320.1 ppm, C_6D_6),[30, 33] **7-Mo** (δ = 258.5 ppm, C_6D_6), [Cp*$(CO)_2$W≡Si{C$(SiMe_3)_3$}] (δ = 339.1 ppm, $^1J(^{183}W, ^{29}Si)$ = 316.2 Hz, C_6D_6),[49] **7-W** (δ = 259.8 ppm, $^1J(^{183}W, ^{29}Si)$ = 272 Hz, C_6D_6). This is in agreement with the stronger paramagnetic contribution to the ^{29}Si shielding tensor provoked by the second metal center in **21-Mo** and **21-W**. The ^{29}Si{^{1}H} NMR spectrum of a concentrated solution of **21-W** in 1,2-$C_6H_4F_2$ displays an intense signal accompanied by two different sets of ^{183}W satellites at 397.5 ppm (d, $^2J(^{31}P, ^{29}Si)$ = 41 Hz, $^1J(^{183}W1, ^{29}Si)$ = 250 Hz, $^1J(^{183}W2, ^{29}Si)$ = 20 Hz) (Figure 60), which is in accordance with the description of **21-W** as a metallasilylidyne complex. The large $^1J_{WSi}$ coupling constant between Si and W1 ($^1J(^{183}W1, ^{29}Si)$ = 250 Hz) compares very well with that of the silylidyne complex **7-W** ($^1J(^{183}W, ^{29}Si)$ = 272 Hz), and is indicative of a W-Si triple bond, whereas the low $^1J_{WSi}$ coupling constant between Si and W2 ($^1J(^{183}W2, ^{29}Si)$ = 20 Hz) is representative for a W–Si single bond. The large $^1J_{WSi}$ coupling constant between Si and W1 compared to Si and W2 is also indicative for a higher s-character of the orbital used by Si atom in the W1≡Si bond compared to the W2–Si bond.

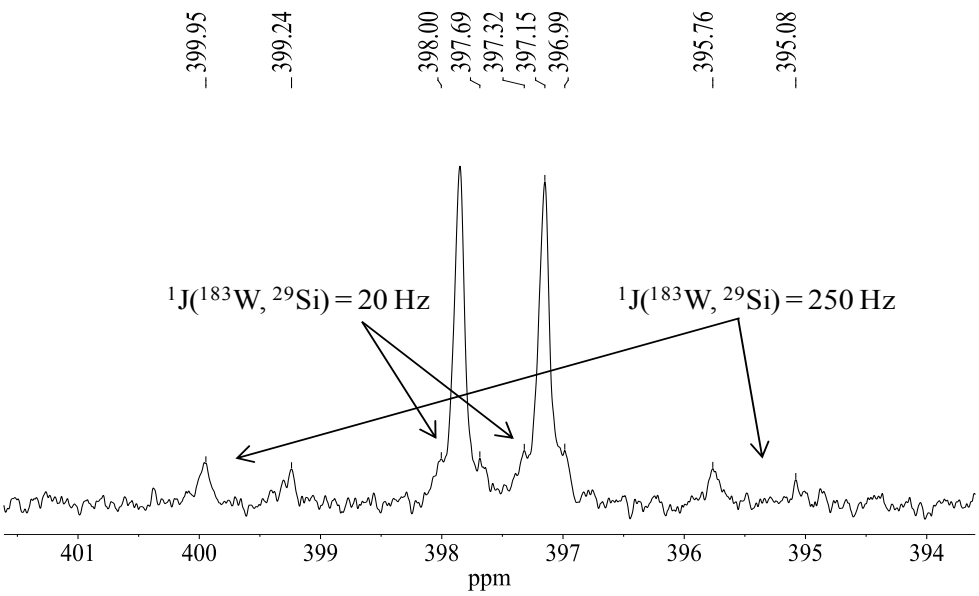

Figure 60. $^{29}Si\{^{1}H\}$ NMR spectrum (59.63 MHz) of **21-W** in 1,2-$C_6H_4F_2$ showing the two different ^{183}W satellites of the ^{29}Si NMR signal.

Although, the solution IR spectra of both metallasilylidyne complexes suggest the presence of more than one rotamer in solution, the ^{1}H, $^{13}C\{^{1}H\}$ and $^{31}P\{^{1}H\}$ NMR spectra in THF-d_8 at 298 K suggest a time-averaged C_s-symmetric structure in solution, which indicates a very fast rotation of the seven-coordinated metal fragments about the M–Si single bonds on the comparatively slower NMR time scale. Even at 193 K, signals in the ^{1}H and ^{31}P NMR spectra of both complexes showed no signs of coalescence behavior, suggesting a quite low energy barrier for the rotational process. The $^{31}P\{^{1}H\}$ NMR spectrum of **21-Mo** in THF-d_8 displays a singlet at –4.4 ppm that is accompanied by a set of silicon satellites with a $^{2}J_{SiP}$ of 56.6 Hz, whereas, the $^{31}P\{^{1}H\}$ NMR signal of **21-W** in the same solvent appears at slightly higher field (–19.8 ppm) and is accompanied by a silicon ($^{2}J_{SiP}$ = 38 Hz) and two sets of tungsten satellites ($^{1}J_{WP}$ = 257 Hz, $^{3}J_{WP}$ = 7 Hz). The ^{1}H NMR spectra of both complexes shows two different sets of signals for the two Tp' ligands on two different metal centers and the methyl groups of each Tp' ligand appear as singlets in the integral ratio of 6:6:3:3 (Figure 61), suggesting an overall C_s-symmetric structure in solution. The most characteristic signals in the $^{13}C\{^{1}H\}$ NMR spectra of **21-Mo** and **21-W** are the two doublet signals with different coupling constants observed for the two different sets of carbonyl ligands. The carbonyl ligands attached to the M1 atom appear at slightly higher field with a lower coupling constant (**21-Mo**: δ = 229.3 ppm (d, $^{4}J(^{13}C, ^{31}P)$ = 1.3 Hz); **21-W**: δ = 225.0 ppm (d, ^{4}J(C,P) = 1.4 Hz)) than the carbonyl ligands attached to the M2 atom (**21-Mo**: δ =

231.6 ppm (d, $^{2}J(^{13}C, ^{31}P)$ = 5.5 Hz); **21-W**: δ = 231.2 ppm (d, ^{2}J(C,P) = 2.5 Hz)). Notably, the C^5-methyl carbon and the C^5 ring carbon atoms of the pyrazolyl groups appear at a slightly higher field compared to the C^3-methyl carbon and the C^3 ring carbon atoms of the pyrazolyl groups, as assigned by ^{1}H NOE experiments in combination with ^{1}H–^{13}C HMBC and HMQC correlation spectroscopy.

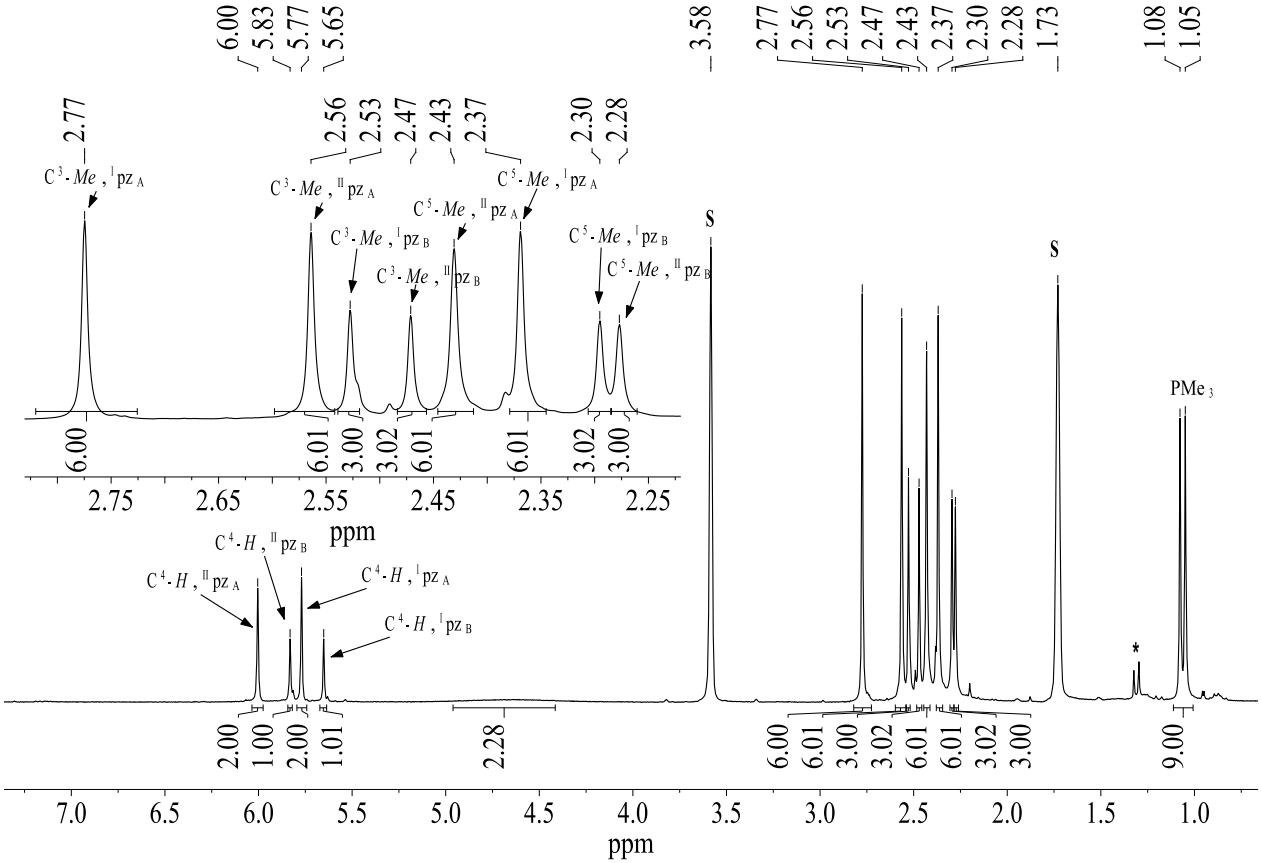

Figure 61. ^{1}H NMR spectrum (300.1 MHz) of **21-Mo** in THF-d_8. The character S denotes the residual proton signals of the deuterated solvent and the asterisk (*) denotes some unknown impurities.

Quantum chemical calculations fully support the description of **21-Mo** as a metallasilylidyne complex. Structural parameters of the optimized minimum structure **(21-Mo)$_{calc}$** at the RI-JCOSX/B97-D3/def2-TZVP/COSMO(THF) level of theory are in good agreement with the experimental values obtained by the single-crystal X-ray diffraction study. Analysis of the electron localization function (ELF) of **(21-Mo)$_{calc}$** reveals that the electron density between Mo1 and Si has a toroidal shape (Figure 62), which is characteristic for a triple bond.[43] The disynaptic

basin population between Mo1 and Si amounts to 5.13e, whereas the basin population between Mo2 and Si of 1.91e is in agreement with a Mo2–Si single bond.

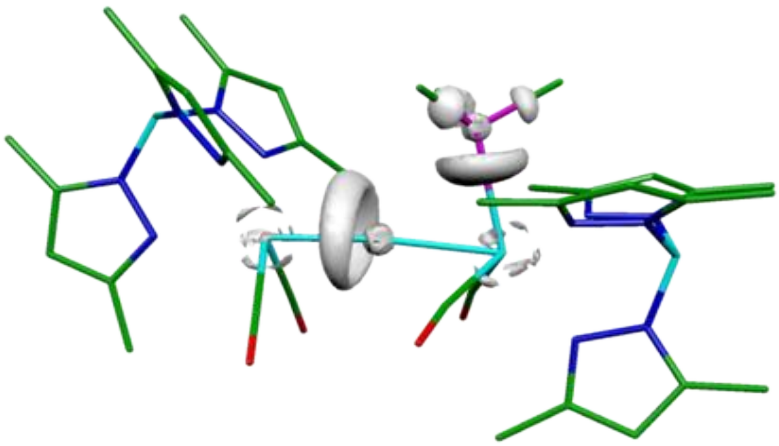

Figure 62. A 3D representation of the electron localization function (ELF) of **21-Mo** with an isosurface plot corresponds to an ELF value of 0.80.

The presence of a triple bond between Mo1 and Si and a single bond between Mo2 and Si in **21-Mo** is further supported by the natural bond orbital (NBO) analysis of **(21-Mo)$_{calc}$** (Table 28), which shows one σ and two π NBOs for the Mo1–Si bond that is characteristic for triple bonds, whereas only one σ NBO was found for the Mo2–Si bond. Furthermore, the different Wiberg bond index for the Mo1–Si and Mo2–Si bond of 1.18 and 0.58 (Table 28), respectively, clearly supports the description of **21-Mo** as a metallasilylidyne complex. In addition, the high polarities of the Mo–Si bonds are reflected in the high opposite NPA charges of Mo (Mo1 –0.59, Mo2 –0.50) and Si (+0.76).

Table 28. Selected results of the natural bond orbital (NBO) analysis of **(21-Mo)$_{calc}$** at the RI-JCOSX/B97-D3/def2-TZVP/COSMO(THF) level of theory. Atom numbering of the experimental structure was taken over in the calculated structure **(21-Mo)$_{calc}$**.[a]

	NBO analysis				NPA partial charges[b]	
	occ.	pol. [%]	hyb.	WBI		
σ(Mo1–Si)	1.75	42.0 (Mo1) 58.0 (Si)	$sd^{2.35}$ (Mo1) $sp^{1.26}$ (Si)	1.18	Mo1	−0.59
π(Mo1–Si)	1.65	78.9 (Mo1) 21.1 (Si)	d (Mo1) p (Si)		Mo2 Si	−0.50 0.76
π(Mo1–Si)	1.53	76.0 (Mo1) 24.0 (Si)	$sd^{6.77}$ (Mo1) $sp^{13.12}$ (Si)		Σ(2 Tp')	–0.36
σ(Mo2–Si)	1.49	51.7 (Mo2) 48.3 (Si)	$sd^{1.33}$ (Mo2) $sp^{1.05}$ (Si)	0.58	Σ(4 CO)	0.15

[a]: occ. = occupancy, pol. = polarization, hyb. = hybridization, WBI = Wiberg bond index. [b]: Partial charges obtained by natural population analysis (NPA).

2.6.2 Access to the first metallagermylidyne complexes

Following the successful isolation of the metallasilylidyne complexes of Mo and W, the same strategy was employed for the synthesis of analogous metallagermylidyne complexes. To obtain the metallagermylidyne complexes, $GeCl_2$(1,4-dioxane) instead of $GeCl_2$(NHC) (NHC = N-heterocyclic carbene) was employed as a suitable ‘‘$GeCl_2$’’ source, as $GeCl_2$(NHC) was found to undergo with **3-Mo** a selective redox reaction leading to the 17VE radical **2-Mo**. Akin to the metallasilylidyne synthesis, the addition of a THF solution of $GeCl_2$(1,4-dioxane) to a solution containing two equiv. of **3-Mo** or **3-W** at ambient temperature leads to a color change from yellowish-brown (**3-Mo**) and yellow (**3-W**) to dark red-brown. Monitoring of the reaction by IR spectroscopy revealed the complete consumption of the starting materials within 15 minutes and formation of the corresponding metallagermylidyne complexes [Tp’$(CO)_2$M≡Ge–M$(CO)_2(PMe_3)$Tp’] (**22-Mo**, M = Mo; **22-W**, M = W), together with a small amount of the 17VE radicals Tp’M$(CO)_2(PMe_3)$ (**2-Mo**, M = Mo; **2-W**, M = W). The metallagermylidyne complexes **22-Mo** and **22-W** were isolated after workup as moderately air-sensitive, brown to dark brown solids in moderate yields (Scheme 18). The metallagermylidyne complexes are thermally robust solids. Compound **22-Mo** melts with decomposition at 287 °C to give a black mass, and compound **22-W** decomposes at 253 – 255 °C to give a black mass. Both complexes are moderately soluble in fluorobenzene, THF and DME, poorly soluble in benzene, toluene and diethyl ether, and insoluble in aliphatic solvents. Unlike to the metallasilylidyne complexes, the metallagermylidyne complexes are stable in THF but decompose rapidly in CH_2Cl_2.

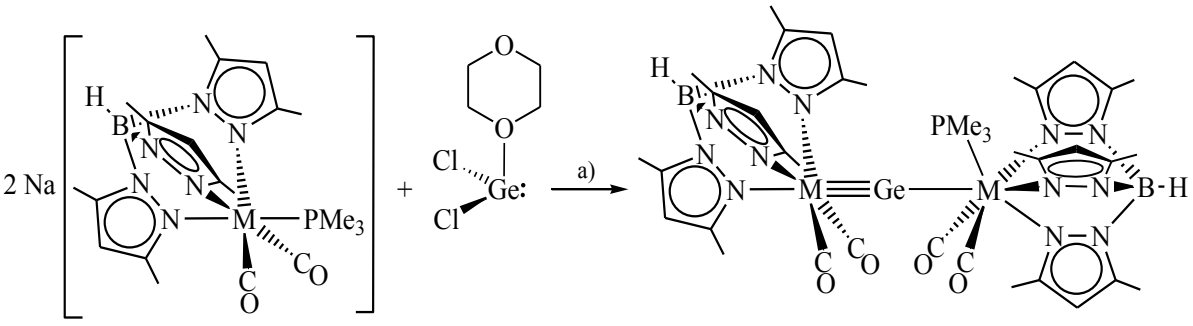

Scheme 18. Synthesis of metallagermylidyne complexes; a) –1,4-dioxane, –PMe_3, –2NaCl, THF, r.t.; formal charges are omitted for clarity.

The solid-state structures of complexes **22-Mo** and **22-W** were obtained by single-crystal X-ray diffraction studies. Suitable red single crystals of **22-Mo**·4(C_7H_8) and **22-W**·4(1,2-$C_6H_4F_2$) were obtained upon cooling a saturated toluene solution of **22-Mo** at –60 °C and a 1,2-diflurobenzene solution of **22-W** at +5 °C, respectively. Compounds **22-Mo** and **22-W** represent the first examples of metallagermylidyne complexes. Interestingly, in the solid state, compounds **22-Mo** and **22-W** feature a slightly different geometry from each other. Thus, akin to the silicon analogues, compound **22-Mo** adopts an approximate C_s-symmetric structure with two carbonyl units in a *syn*-orientation (Figure 63), whereas, compound **22-W** adopts a C_1-symmetric structure with two carbonyl units in an *anticlinal*-orientation (Figure 64). Similar to the silicon analogues, the solid-state structures of **22-Mo**·4(C_7H_8) and **22-W**·4(1,2-$C_6H_4F_2$) show an almost linear central M-Ge-M (M = Mo, W) core with two structurally different metal sites and distinctly different M–Ge (M = Mo, W) bond lengths (Figure 63 and Figure 64).

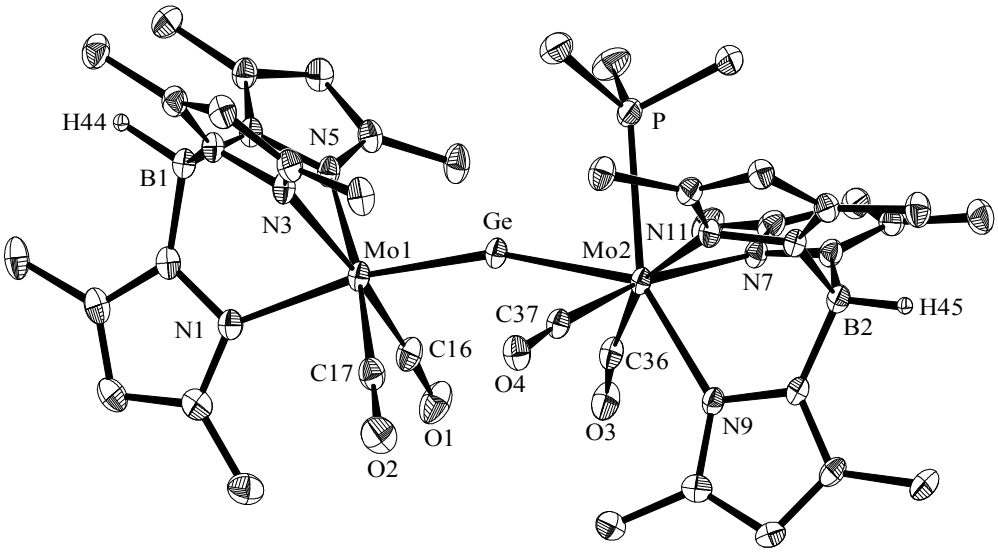

Figure 63. DIAMOND plot of the molecular structure of compound **22-Mo** in the crystal lattice of **22-Mo**·4(C_7H_8) at 123(2) K. Thermal ellipsoids are set at 30% probability. Hydrogen atoms (except the B-bonded H atoms) were omitted for clarity. Selected bond lengths [Å] and bond angles [°]: Mo1-Ge 2.3399(6), Mo2-Ge 2.5163(6), Mo2-P 2.558(1), Mo1-N1 2.255(4), Mo1-N3 2.253(4), Mo1-N5 2.255(4), Mo2-N7 2.262(49, Mo2-N9 2.218(4), Mo2-N11 2.271(4), Mo1- C16 1.958(5), Mo1-C17 1.952(5), Mo2-C36 1.977(5), Mo2-C37 1.969(5); Mo1-Ge-Mo2 161.66(3), N1-Mo1-Ge 169.4(1), N3-Mo1-Ge 103.3(1), N5-Mo1-Ge 107.9(1), N7-Mo2-Ge 122.3(1), N9-Mo2-Ge 134.6(1), N11-Mo2-Ge 132.8(1), C16-Mo1-Ge 84.5(2), C17-Mo1-Ge 79.3(2), C36-Mo2-Ge 66.1(1), C37-Mo2-Ge 70.4(1), P-Mo2-Ge 74.1(1).

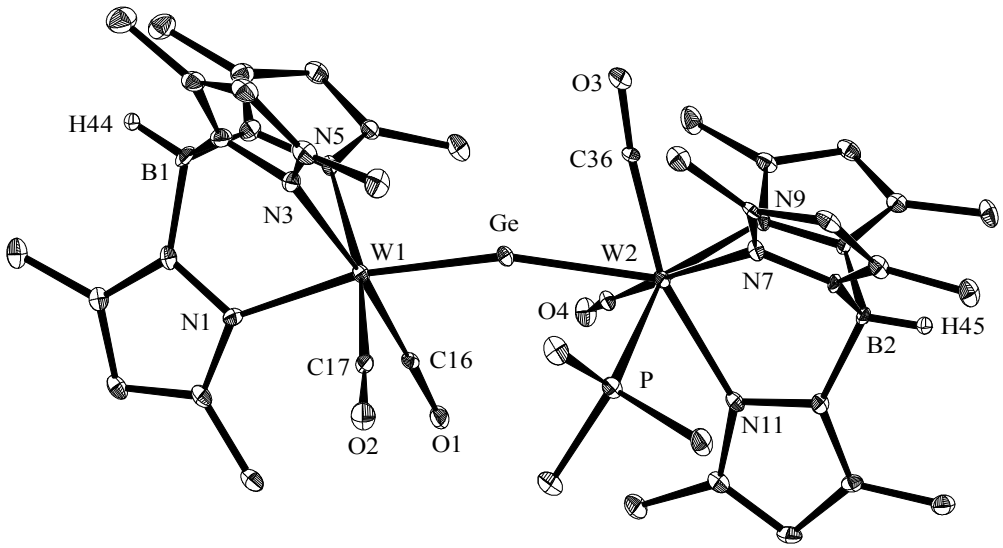

Figure 64. DIAMOND plot of the molecular structure of compound **22-W** in the crystal lattice of **22-W**·4(1,2-$C_6H_4F_2$) at 100 K. Thermal ellipsoids are set at 30% probability. Hydrogen atoms (except the B-bonded H atoms) were omitted for clarity. Selected bond lengths [Å] and bond angles [°]: W1-Ge 2.3542(8), W2-Ge 2.5454(8), W2-P 2.536(2), W1-N1 2.231(6), W1-N3 2.237(6), W1-N5 2.270(5), W2-N7 2.257(5), W2-N9 2.219(5), W2-N11 2.251(6), W1-C16 1.943(7), W1-C17 1.969(7), W2-C36 1.962(7), W2-C37 1.955(7); W1-Ge-W2 161.81(3), N1-W1-Ge 166.7(2), N3-W1-Ge 110.0(1), N5-W1-Ge 102.9(1), N7-W2-Ge 126.4(2), N9-W2-Ge 134.5(1), N11-W2-Ge 130.1(1), C16-W1-Ge 75.8(2), C17-W1-Ge 87.3(2), C36-W2-Ge 67.0(2), C37-W2-Ge 68.6(2), P-W2-Ge 74.75(5).

The M1–Ge (M = Mo, W) bond lengths of **22-Mo** (2.3399(6) Å) and **22-W** (2.3542(8) Å) clearly indicate the presence of a M–Ge triple bond between the Ge and hexacoordinated metal centers (Mo1/W1). The M1–Ge bonds are slightly longer than those of the Cp/Cp*-substituted three-legged piano-stool germylidyne complexes (*d*(Mo≡Ge): 2.271(1) – 2.2837(3) Å; *d*(W≡Ge): 2.277(1) – 2.2938(5) Å),[27, 28, 34, 37, 38, 48] or those of octahedral germylidyne complexes (Mo≡Ge 2.2798(5) – 2.3185(6) Å; W≡Ge 2.293(1) – 2.338(1) Å).[39, 40, 46, 59] The M1≡Ge bond lengths are also very similar to that of the Tp'-substituted octahedral germylidyne complexes **8-Mo** (2.3117(9) [2.3121(9)] Å) and **8-W** (2.3133(3) [2.3084(3)] Å). In contrast, the M2–Ge (M = Mo, W) distances in **22-Mo** (2.5163(6) Å) and **22-W** (2.5454(8) Å) are markedly longer than those of the M1–Ge (M = Mo, W) bonds (7 – 7.5%) and appear in the reported range of M–Ge single

bonds (*d*(Mo–Ge): 2.4990(2) – 2.875(1) Å; *d*(W–Ge): 2.4984(3) – 2.852(1) Å).[177, 178]21 Furthermore, the Mo2–Ge bond length also compare very well with the Mo–Ge single bond length of the heptacoordinated complex [Tp'Mo(CO)$_2$(PMe$_3$)GeCl$_3$] **20-Mo** (2.519(8) Å) (Figure 65), which was prepared for comparison reasons upon reaction of **1-Mo** with a slight excess of GeCl$_2$(1,4-dioxane) in CH$_2$Cl$_2$, and isolated after workup as a bright orange solid. The M1 center of both metallagermylidyne complexes adopts an octahedral geometry with the Ge atom being in a *trans*-orientation to one of the pyrazolyl groups of the Tp' ligand as evidenced by the N1-M1-Ge bond angles of 169.4(1)° (**22-Mo**) and 166.7(2)° (**22-W**), whereas the M2 center resides in a distorted face-capped octahedral geometry, in which the Ge center caps the octahedron face built up from the PMe$_3$ and two CO ligands. Finally, akin to the silicon analogues, the M1-Ge-M2 bond angles of 161.66(3)° (**22-Mo**) and 161.81(3)° (**22-W**) show a slight bending at the tetrel center, but compare very well with those of the Tp'-substituted germylidyne complexes **8-Mo** (159.4(2) [160.6(2)]°) and **8-W** (165.73(9) [159.66(9)]°). The almost linear M1-Ge-M2 atom arrays, together with two unsymmetrical M–Ge bonds fully support the description of **22-Mo** and **22-W** as metallagermylidyne complexes.

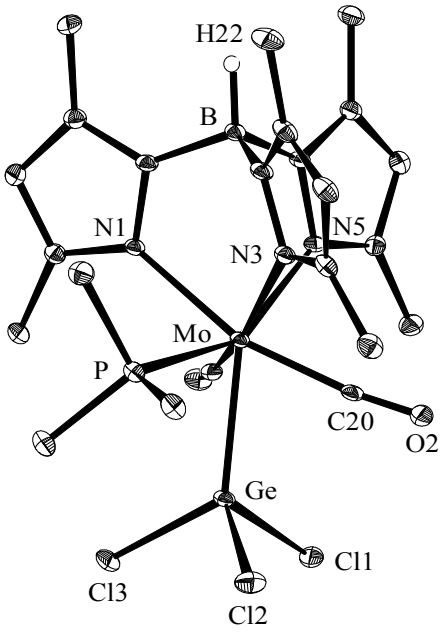

Figure 65. DIAMOND plot of the molecular structure of compound **20-Mo** at 100(2) K. Thermal ellipsoids are set at 30% probability. Hydrogen atoms (except the B-bonded H atoms) were omitted for

21 A CSD Survey (17.05.2016) gave 34 compounds with Mo–Ge single bonds and 90 compounds with W–Ge single bonds, leading to a median/mean Mo–Ge and W–Ge bond lengths of 2.625/2.587 Å and 2.605/2.584 Å, respectively.

clarity. Selected bond lengths [Å] and bond angles [°]: Mo–Ge 2.5188(4), Mo–P 2.5938(7), Mo–C19 1.984(3), Mo–C20 1.975(3), Ge–Cl1 2.2121(7), Ge–Cl2 2.2060(8), Ge–Cl3 2.2047(7), Mo–N1 2.266(2), Mo–N3 2.250(2), Mo–N5 2.221(2); Ge-Mo-P 78.46(2), C19-Mo-Ge 69.64(7), C20-Mo-Ge 71.28(7), N1-Mo-Ge 123.59(5), N3-Mo-Ge 132.81(6), N5-Mo-Ge 133.68(6).

The solid-state structures of **22-Mo** and **22-W** were further supported by multinuclear NMR and IR spectroscopy. The solid-state IR spectrum of **22-Mo** displays three ν_{CO} absorption bands at 1928 (s), 1859 (vs) and 1795 (s) cm^{-1} and that of **22-W** shows four ν_{CO} absorption bands at 1910 (m), 1847 (sh), 1834 (vs) and 1769 (s) cm^{-1}, which clearly supports the tetracarbonyls structures. Akin to the silicon analogues, the metallagermylidyne complexes **22-Mo** and **22-W** also display more than four ν_{CO} absorption bands in THF, indicating the existence of more than one rotamer in solution. Thus, the IR spectrum of **22-Mo** and **22-W** displays six ν_{CO} absorption bands each at 1932 (s), 1923 (sh), 1868 (vs), 1854 (s), 1806 (m), 1798 (sh), and 1921 (sh), 1910 (m), 1853 (vs), 1838 (s), 1780 (m), 1771 (m) cm^{-1}, respectively. The ν_{CO} bands appear almost at the same position as those of their silicon analogues **21-Mo** (ν_{CO}: 1933 (s), 1870 (vs), 1857 (m, sh), 1806 (m) and 1794 (m, sh) cm^{-1}), and **21-W** (ν_{CO}: 1920 (m), 1915 (m), 1854 (vs), 1841 (s), 1792 (w) and 1778 (m) cm^{-1}). The ^{1}H, $^{13}C\{^{1}H\}$ and $^{31}P\{^{1}H\}$ NMR spectra of **22-Mo** and **22-W** show a similar signal pattern to that observed for the corresponding metallasilylidyne complexes and suggest a time averaged C_s-symmetric structure in solution. The spectra indicate clearly a rapid rotation of the seven-coordinated metal fragments about the M2–Ge single bonds on the NMR time scale. The $^{31}P\{^{1}H\}$ NMR spectrum of **22-Mo** displays a singlet signal at –3.7 ppm and that of **22-W** a singlet at –21.1 ppm, which is accompanied by two pair of tungsten satellites with $^{1}J_{WP}$ and $^{3}J_{WP}$ of 252 Hz and 18 Hz, respectively.

Notably, attempts to prepare the corresponding metallastannylidyne or metallaplumbylidyne complexes by the reaction of **3-Mo** and **3-W** with 0.5 equivalent of $SnCl_2$ and $PbCl_2$ led only to the selective formation of the 17VE radical [Tp'M(CO)$_2$(PMe$_3$)] (**2-Mo**, M = Mo; **2-W**, M = W), and elemental tin and lead, respectively.

2.7. Chemistry of the metallatetrylidyne complexes

Following the successful synthesis and characterization of the metallasilylidyne and metallagermylidyne complexes, I subsequently decided to explore the reactivity of this interesting class of compounds. Owing to the high polarity of the metal-tetrel bonds, as observed by quantum chemical calculations, it was assumed that the metallatetrylidyne complexes would be very reactive towards nucleophiles and electrophiles. Furthermore, the presence of triple bonds in these complexes might lead to interesting reactions towards alkynes or heteroalkynes, as it has been reported for the silylidyne complex $[Cp(CO)_2Mo{\equiv}Si(C_6H_3\text{-}2,6\text{-}Trip_2)]$[33] and $[(Cp^*)(i Pr_3P)(H)Os{\equiv}Si(Trip)][HB(C_6F_5)_3]$.[58] Thus, in the following chapters, reactions of these metallatetrylidyne complexes towards nucleophiles, electrophiles, alkynes, heteroalkynes as well as their reduction will be discussed.

2.7.1 Reactivity of metallatetrylidyne complexes towards neutral nucleophiles

The presence of an electrophilic tetrel center together with the easily displaceable trimethylphosphane (PMe_3) ligand prompted me to study the reactivity of these metallatetrylidyne complexes towards the neutral and moderately nucleophilic two-electron donor mesityl isocyanide (MesNC) ligand. Treatment of a mixture of **21-Mo** or **22-Mo** with one equivalent of MesNC in toluene at ambient temperature and subsequent heating of the mixture for 15 minutes at 60 °C and 75 °C, respectively, led to the corresponding MesNC substituted metallatetrylidyne complexes $[Tp'(CO)_2Mo{\equiv}E{-}Mo(CO)_2(MesNC)Tp']$ (**23-Mo**, E = Si; **24-Mo**, E = Ge) via elimination of the PMe_3 ligand (Scheme 19). Monitoring of the reaction by IR and $^{31}P\{^1H\}$ NMR spectroscopy revealed a selective conversion of the starting materials into the products. Compounds **23-Mo** and **24-Mo** were isolated after workup as air-sensitive, red-brown solids in 69 and 91 % yields, respectively. Interestingly, MesNC does not attack the electrophilic tetrel centers even after prolonged heating or in the presence of excess MesNC. Similar to the PMe_3 substituted metallatetrylidyne complexes, **23-Mo** and **24-Mo** are also quite thermally stable solids and only decompose upon melting at 224 – 226 ° and 280 – 283 °C to a brown to dark brown liquid, respectively. Compounds **23-Mo** and **24-Mo** show very similar properties as their precursors. Both compounds are moderately soluble in fluorobenzene, THF and DME, poorly soluble in toluene and diethyl ether, and insoluble in aliphatic solvents.

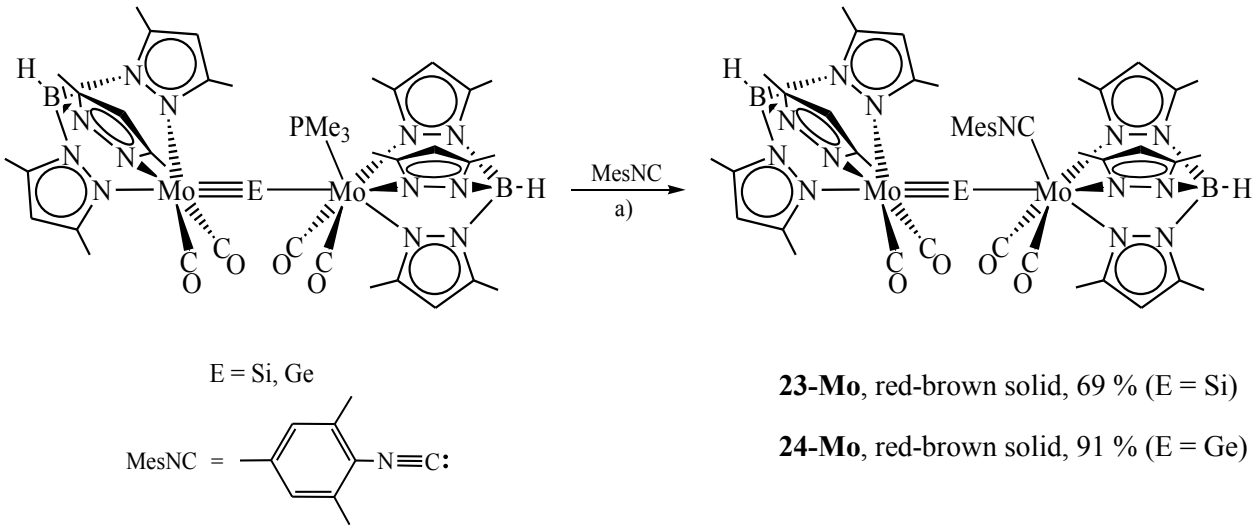

23-Mo, red-brown solid, 69 % (E = Si)

24-Mo, red-brown solid, 91 % (E = Ge)

Scheme 19. Reaction of the metallatetrylidyne complexes towards mesityl isocyanide (MesNC). a) –PMe_3, toluene, 60 – 75 °C.

Compounds **23-Mo** and **24-Mo** were fully characterized by single-crystal X-ray diffraction, multinuclear NMR and IR spectroscopy, and their compositions confirmed by elemental analysis. Orange plates of **23-Mo**·(1,2-$C_6H_4F_2$) and **24-Mo**·2.5(C_7H_8), suitable for X-ray diffraction analysis, were grown upon cooling a saturated solution of **23-Mo** in a 1,2-diflurobenzene/*n*-pentane mixture at +5 °C, and storage of a saturated solution of **24-Mo** in toluene at ambient temperature, respectively. Compounds **23-Mo** and **24-Mo** are isostructural and exhibit similar bonding features as those of the precursors **21-Mo** and **22-Mo**, respectively (Figure 66, Table 29). In the solid-state, both complexes adopt approximately not crystallographic imposed C_s-symmetric structures, and feature an almost linear central Mo-E-Mo (E = Si, Ge) core with two structurally different Mo sites and distinctly different Mo–E bond lengths (Figure 66). The very short Mo1–Si bond length of 2.266(1) Å in **23-Mo** and the Mo1–Ge bond length of 2.3230(3) Å in **24-Mo** clearly show the presence of triple bonds between the hexacoordinated Mo and the tetrel atoms. Notably, in both complexes the Mo1–E bond lengths compare favourably with those of the silylidyne complex **7-Mo** (2.2614(9) Å) and the germylidyne complex **8-Mo** (2.3117(9) [2.3121(9)] Å), but are slightly shorter than the Mo1–E bond lengths (Mo1–Si 2.287(2) Å; Mo1–Ge 2.3399(6) Å) of the PMe_3 substituted metatllatetrylidyne complexes **21-Mo** and **22-Mo** (Table 29). The slight shortening of the Mo1–E triple bonds could be explained by the better π-acception properties of the MesNC ligand compared to the PMe_3 ligand. The π-backdonation from the heptacoordinated metal centers to the tetrel atoms, that is present to a small extent in all metallatetrylidyne complexes, is diminished by the MesNC ligand due to the better withdrawal of

electron density from the heptacoordinated metal d-orbitals to the π^*-antibonding orbitals of the isonitrile group. This is also evidenced by the slight elongation of the C33–N12 bond of the isonitrile groups (**23-Mo** 1.166(4) Å; **24-Mo** 1.171(3) Å) compared to the N≡C bond (1.158(3) Å) of non-coordinated MesNC.[179]

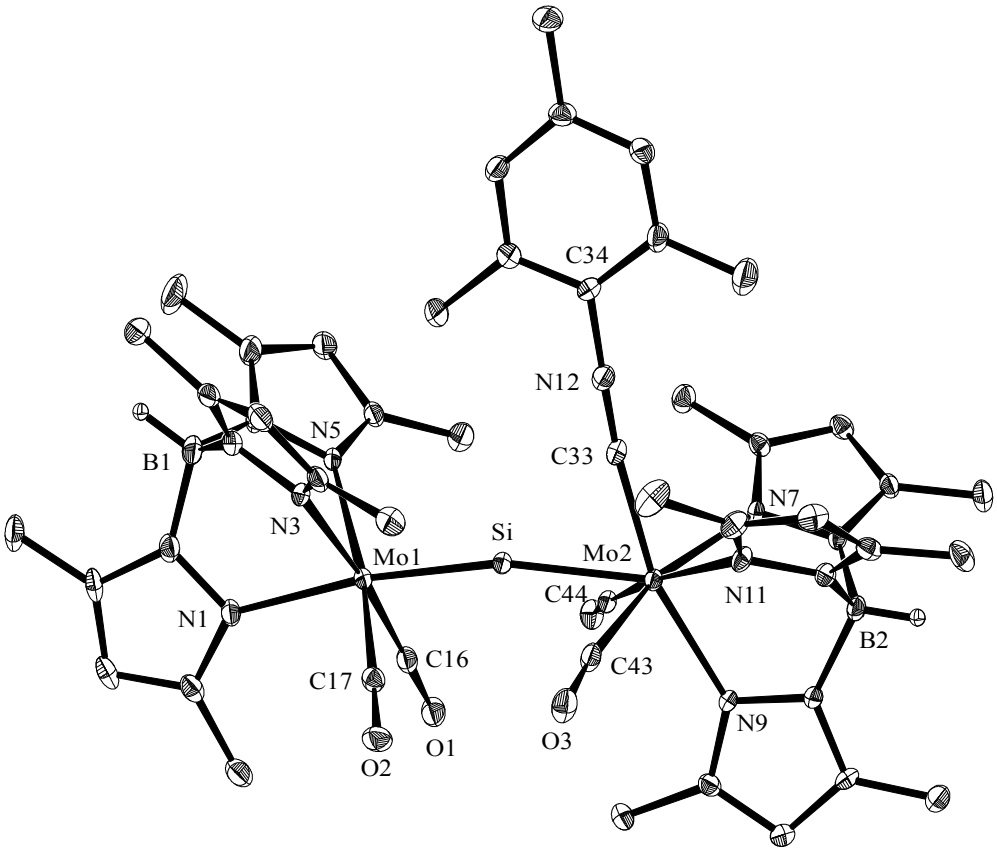

Figure 66. DIAMOND plot of the molecular structure of compound **23-Mo** in the crystal lattice of **23-Mo**·(1,2-$C_6H_4F_2$) at 123(2) K. Thermal ellipsoids are set at 30% probability. Hydrogen atoms (except the B-bonded H atoms) were omitted for clarity. Selected bond lengths [Å] and bond angles [°] of **23-Mo**·(1,2-$C_6H_4F_2$) (corresponding bond lengths and bond angles of **24-Mo**·2.5(C_7H_8) are given in square brackets): Mo1-Si 2.266(1) [2.3230(3)], Mo2-Si 2.440(1) [2.5247(3)], Mo1-N1 2.243(3) [2.235(2)], Mo1-N3 2.251(3) [2.251(2)], Mo1-N5 2.267(3) [2.275(2)], Mo2-N7 2.246(3) [2.235(2)], Mo2-N9 2.209(3) [2.220(2)], Mo2-N11 2.234(3) [2.241(2)], Mo1-C16 1.956(4) [1.955(3)], Mo1-C17 1.958(4) [1.956(3)], Mo2-C43 1.985(4) [1.981(3)], Mo2-C44 1.977(4) [1.987(2)], Mo2-C33 2.058(4) [2.060(3)], C33-N12 1.166(4) [1.171(3)], N12-C34 1.397(5) [1.399(4)]; Mo1-Si-Mo2 166.61(5) [163.92(1)], N1-Mo1-Si 170.65(9) [168.74(5)], N3-Mo1-Si 106.45(8) [108.03(5)], N5-Mo1-Si 102.11(7) [100.82(5)], N7-Mo2-Si 131.77(7) [132.74(5)], N9-Mo2-Si 128.20(7) [129.21(5)], N11-Mo2-Si 129.71(8) [127.91(5)], Mo2-C33-N12 173.7(3) [175.0(2)], C33-Mo2-Si 64.94(9) [67.42(7)], C16-Mo1-Si 78.7(1) [78.46(7)], C17-Mo1-Si 84.8(1) [85.00(8)], C43-Mo2-Si 64.9(1) [65.53(7)], C44-Mo2-Si 64.5(1) [69.04(7)].

The Mo2–E bonds (**23-Mo** 2.440(1) Å; **24-Mo** 2.5247(3) Å) are considerably longer than the corresponding Mo1–E bonds but compare well with the Mo2–E bonds of the precursors **21-Mo** and **22-Mo** (Table 29), confirming the presence of Mo–E single bonds between the heptacoordinated Mo and tetrel atoms. In both complexes, the Mo1 centers adopt an octahedral geometry with the tetrel atoms in *trans*-orientation to one of the pyrazolyl groups of the Tp' ligand (N1-Mo1-Si 170.65(9)°; N1-Mo1-Ge 168.74(5)°). In contrast, the Mo2 centers adopt a face-capped octahedral geometry, in which the tetrel atoms cap the octahedron's face made up by MesNC and two CO ligands. Akin to the PMe_3 substituted metallatetrylidyne complexes, the Mo1-E-Mo2 bond angles in **23-Mo** (166.61(5)°) and **24-Mo** (163.92(1)°) indicate a slight bending at the tetrel atoms (Table 29), but the almost linear Mo-E-Mo atom arrays together with the two unsymmetric Mo–E bonds in complexes **23-Mo** and **24-Mo** confirm their description as metallatetrylidyne complexes.

Table 29. Comparison of selected bonding parameters of the metallatetrylidyne complexes **21-Mo**, **21-W**, **22-Mo**, **22-W**, **23-Mo** and **24-Mo**, with the tetrylidyne complexes **7-Mo**, **7-W**, **8-Mo** and **8-W**.

Complex	M1≡E [Å]	M2–E [Å]	M1-E-M2/C1 [°]	N1-M1-E [°]
[Tp'$(CO)_2$Mo1≡Si–Mo2$(CO)_2$$(PMe_3)$Tp'] (**21-Mo**)	2.287(2)	2.438(2)	162.93(7)	169.3(1)
[Tp'$(CO)_2$W1≡Si–W2$(CO)_2$$(PMe_3)$Tp'] (**21-W**)	2.283(5)	2.429(5)	171.3(2)	176.6(4)
[Tp'$(CO)_2$Mo1≡Ge–Mo2$(CO)_2$$(PMe_3)$Tp'] (**22-Mo**)	2.3399(6)	2.5163(6)	161.66(3)	169.4(1)
[Tp'$(CO)_2$W1≡Ge–W2$(CO)_2$$(PMe_3)$Tp'] (**22-W**)	2.3542(8)	2.5454(8)	161.81(3)	166.7(2)
[Tp'$(CO)_2$Mo1≡Si–Mo2$(CO)_2$(MesNC)Tp'] (**23-Mo**)	2.266(1)	2.440(1)	166.61(5)	170.65(9)
[Tp'$(CO)_2$Mo1≡Ge–Mo2$(CO)_2$(MesNC)Tp'] (**24-Mo**)	2.3230(3)	2.5247(3)	163.92(1)	168.74(5)
[Tp'$(CO)_2$Mo≡Si–Tbb] (**7-Mo**)	2.2614(9)	–	160.8(1)	167.19(7)
[Tp'$(CO)_2$W≡Si–Tbb] (**7-W**)	2.2706(8)	–	161.7(1)	168.27(7)
[Tp'$(CO)_2$Mo≡Ge(C_6H_3-2,6-Mes_2)][a]	2.3117(9)	–	159.4(2)	167.0(1)
(**8-Mo**)	2.3121(9)		160.6(2)	164.8(1)
[Tp'$(CO)_2$W≡Ge(C_6H_3-2,6-Mes_2)][a]	2.3133(3)	–	165.73(9)	169.17(6)
(**8-W**)	2.3084(3)		159.66(9)	165.96(6)

[a]: Two independent molecules in the unit cell.

The spectroscopic data of **23-Mo** and **24-Mo** corroborate very well with their solid-state structures. Interestingly, in contrast to the PMe_3 substituted metallatetrylidyne complexes, the solution IR spectrum of the MesNC substituted metallatetrylidyne complexes in THF shows only four ν_{CO} absorption bands (**23-Mo**: 1942 (s), 1894 (vs), 1880 (m), 1810 (m) cm^{-1}, (Figure 67); **24-Mo**: 1938 (s), 1888 (vs), 1879 (sh), 1814 (m) cm^{-1}), suggesting the presence of only one rotamer in solution. Notably, the ν_{CO} absorption bands of **23-Mo** and **24-Mo** appear at slightly higher wavenumbers compared to those of the complexes **21-Mo** and **22-Mo** (Table 30), indicating the smaller σ-donor/π-acceptor ratio of the MesNC ligand compared to the PMe_3 ligand. Furthermore, the solution IR spectrum of **23-Mo** and **24-Mo** in THF shows an intense ν_{NC} absorption band at 2077 (Figure 67) and 2075 cm^{-1}, respectively, which appears at considerably lower wavenumbers compared to that of the free MesNC (ν_{NC} (in THF) = 2114 cm^{-1}).

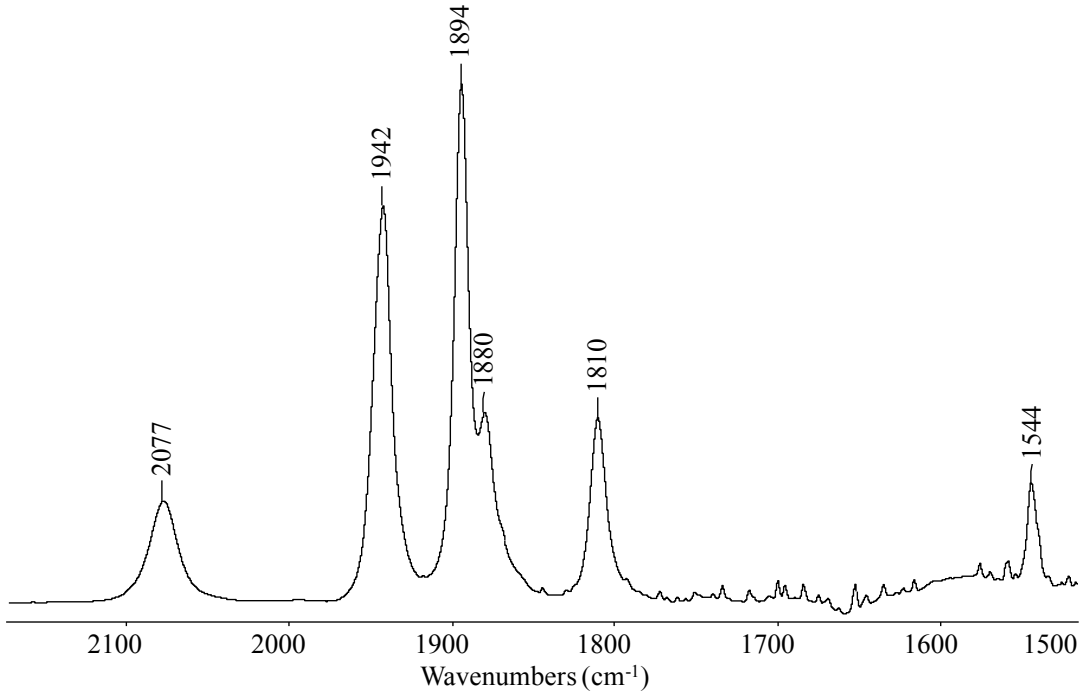

Figure 67. FT-IR spectrum (2180 – 1500 cm^{-1}) of **23-Mo** in THF showing the characteristic ν_{CO}, $\nu_{C\text{-}C\text{-}N}$ and ν_{NC} absorption bands.

The ^1H and $^{13}C\{^1H\}$ NMR spectra of both complexes reveal a C_s-symmetric structure in solution. The most characteristic signal in the $^{13}C\{^1H\}$ NMR spectrum of **24-Mo** is that of the MesN*C* ligand at δ = 182.7 ppm, which in case of **23-Mo** is not observed, probably due to signal broadening. In contrast to **21-Mo**, the $^{29}Si\{^1H\}$ NMR spectrum of **23-Mo** in THF-d_8 displays a

singlet signal at δ = 369.7 ppm, which is considerably high-field shifted compared to that of the starting material **21-Mo** (δ = 438.9 (d, $^2J_{SiP}$ = 56.6 Hz)).

Table 30. Summary of the properties of the metallatetrylidyne complexes.

Complex	Color	Yield %	IR[a], ν(CO) cm^{-1}	^{31}P NMR[b] ppm	^{29}Si NMR[b] ppm
21-Mo	Red brown	43	1933 (s), 1870 (vs), 1857 (sh), 1806 (m), 1794 (sh)	–4.4 (s, $^2J_{SiP}$ = 56.6 Hz)	438.9 (d, $^2J_{SiP}$ = 56.6 Hz)
21-W	Brown	51	1920 (m), 1915 (m), 1854 (vs), 1841 (s), 1792 (w), 1778 (m)	–19.8 (s, $^2J_{SiP}$ = 38 Hz)	395.6 (d, $^2J_{SiP}$ = 39 Hz)
22-Mo	Brown	49	1932 (s), 1923 (sh), 1868 (vs), 1854 (s), 1806 (m), 1798 (sh)	–3.7 (s)	–
22-W	Dark brown	63	1921 (sh), 1910 (m), 1853 (vs), 1838 (s), 1780 (m), 1771 (m)	–21.1 (s)	–
23-Mo	Red brown	69	1942 (s), 1894 (vs), 1880 (m), 1810 (m)	–	369.7 (s)
24-Mo	Red brown	91	1938 (s), 1888 (vs), 1879 (sh), 1814 (m)	–	–

[a]: IR spectrum in THF; [b]: ^{31}P{^{1}H} and ^{29}Si{^{1}H} NMR spectra in THF-d_8.

2.7.2 Reactivity of metallatetrylidyne complexes towards electrophiles

The metallatetrylidyne complexes are highly reactive toward small electrophiles. For instance, they react with Brookhart's acid, $[H(OEt_2)_2][B\{C_6H_3\text{-}3,5\text{-}(CF_3)_2\}_4]$ even at –60 °C. The reaction of **21-Mo**, **21-W**, and **22-Mo** with one equivalent of $[H(OEt_2)_2][B\{C_6H_3\text{-}3,5\text{-}(CF_3)_2\}_4]$ resulted in a color change from red-brown to bright red, reddish orange or yellowish brown, respectively. Monitoring of the reactions by IR spectroscopy revealed a selective conversion of the starting materials into the corresponding protonated complexes $[Tp'(CO)_2M(H)EM(CO)_2(PMe_3)Tp'][B\{C_6H_3\text{-}3,5\text{-}(CF_3)_2\}_4]$ (**25-Mo**, M = Mo, E = Si; **25-W**, M = W, E = Si; **26-Mo**, M = Mo, E = Ge). Compounds **25-Mo**, **25-W** and **26-Mo** were isolated after workup as analytically pure, very air-sensitive, orange to dark brown solids in good yields (Scheme 20, Table 31). All complexes are thermally quite stable but melt at relatively lower temperatures compared to their neutral precursors. For instance, complex **25-Mo** melts to a reddish brown liquid at 116 – 117 °C without any decomposition. All these complexes are well soluble in Et_2O, THF, fluorobenzene and CH_2Cl_2, but insoluble in toluene and aliphatic solvents.

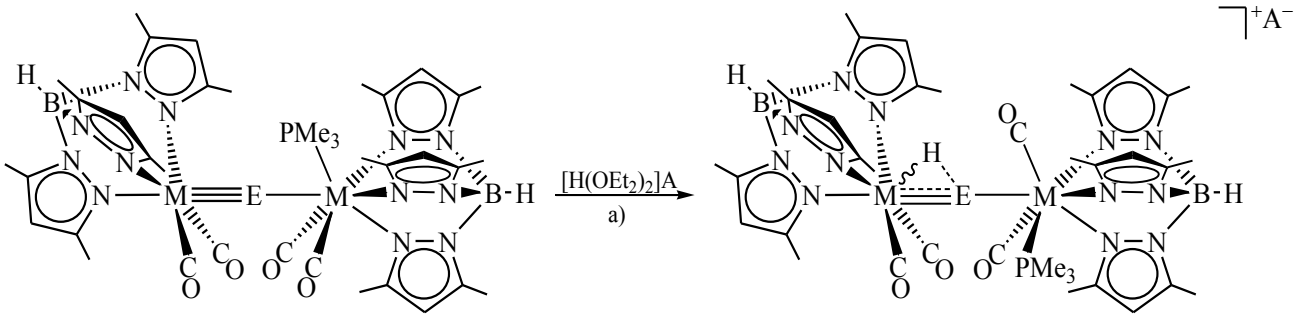

Scheme 20. Addition of $[H^+]$ to the metallatetrylidyne complexes.

Table 31. Selected properties of the protonated compounds of the metallatetrylidyne complexes.

Complex	Color	Yield %	IR[a], ν(CO) cm^{-1}	^{31}P NMR[b] ppm	^{29}Si NMR[b] ppm
25-Mo	Orange	64	1982 (w), 1952 (s), 1916 (vs), 1887 (m)	0.9 (s, $^2J_{SiP}$ = 87.2 Hz)	460.7 (d, $^2J_{SiP}$ = 87.5 Hz)
25-W	Orange	60	1967 (w), 1936 (s), 1897 (vs), 1867 (m)	–22.2 (s, $^2J_{SiP}$ = 70.5 Hz)	417.0 (d, $^2J_{SiP}$ = 70.5 Hz)
26-Mo	Dark brown	72	1984 (w), 1954 (s), 1917 (vs), 1891 (m)	–2.9 (s)	–

[a]: IR spectrum in Et_2O; [b]: $^{31}P\{^1H\}$ and $^{29}Si\{^1H\}$ NMR spectra in CD_2Cl_2.

All complexes were fully characterized by single crystal X-ray diffraction, NMR and IR spectroscopy, and elemental analysis. Suitable red plate-like single crystals of **25-Mo**·($C_4H_{10}O$) and **25-W** were grown upon cooling a saturated Et_2O solution of **25-Mo** at −30 °C, and storage of a saturated solution of **25-W** in Et_2O/*n*-hexane mixture at ambient temperature, respectively, whereas, reddish brown block-like single crystals of **26-Mo**·0.5($C_4H_{10}O$) were grown upon cooling a saturated solution of **25-W** in Et_2O/*n*-hexane mixture at +5 °C. All the complexes are almost isostructural except for the relative orientation of the CO substituents on two metal centers (Figure 68, Figure 69).

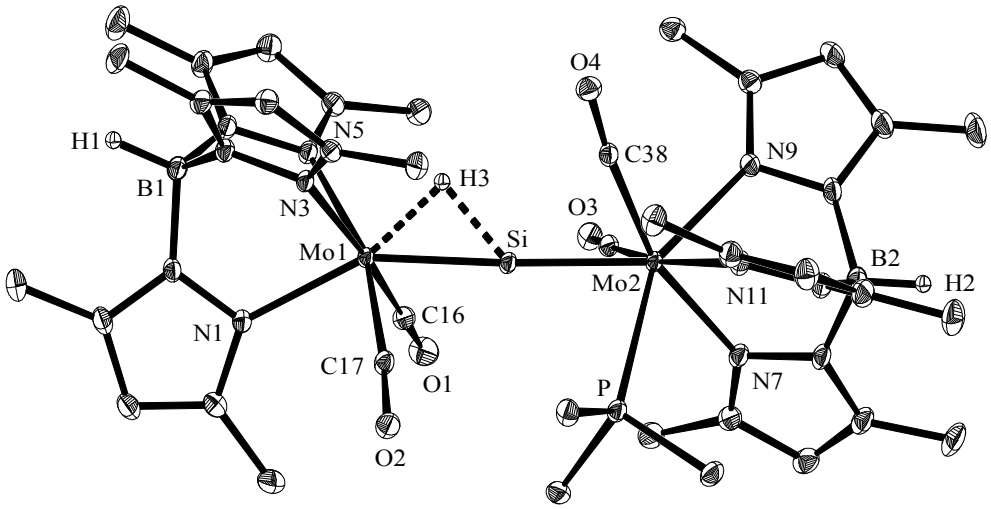

Figure 68. DIAMOND plot of the molecular structure of compound **25-Mo** in the crystal lattice of **25-Mo**·($C_4H_{10}O$) at 123(2) K. Thermal ellipsoids are set at 30% probability. Hydrogen atoms (except the B-bonded H and MoHSi atoms) and the $[B\{C_6H_3\text{-}3,5\text{-}(CF_3)_2\}_4]^-$ were omitted for clarity. Selected bond lengths [Å] and bond angles [°] of **25-Mo**·($C_4H_{10}O$): Mo1-Si 2.2916(8), Mo2-Si 2.3519(8), Mo2-P 2.5644(8), Mo1-H3 1.69(3), Si-H3 1.59(3), Mo1-N1 2.224(2), Mo1 N3 2.235(2), Mo1-N5 2.221(2), Mo2-N7 2.261(2), Mo2-N9 2.219(2), Mo2-N11 2.237(2), Mo1-C16 1.987(3), Mo1-C17 1.981(3), Mo2-C37 1.981(3), Mo2-C38 1.995(3); Mo1-Si-Mo2 173.72(3), Mo1-Si-H3 47.5(11), Mo2-Si-H3 130.1(11), N1-Mo1-Si 152.30(6), N3-Mo1-Si 111.25(6), N5-Mo1-Si 120.52(6), N7-Mo2-Si 125.95(6), N9-Mo2-Si 133.88(6), N11-Mo2-Si 129.08(6), N1-Mo1-H3 163.6(11), P-Mo2-Si 76.76(3), C16-Mo1-Si 77.07(9), C17-Mo1-Si 75.99(8), C37-Mo2-Si 67.52(8), C38-Mo2-Si 69.40(8).

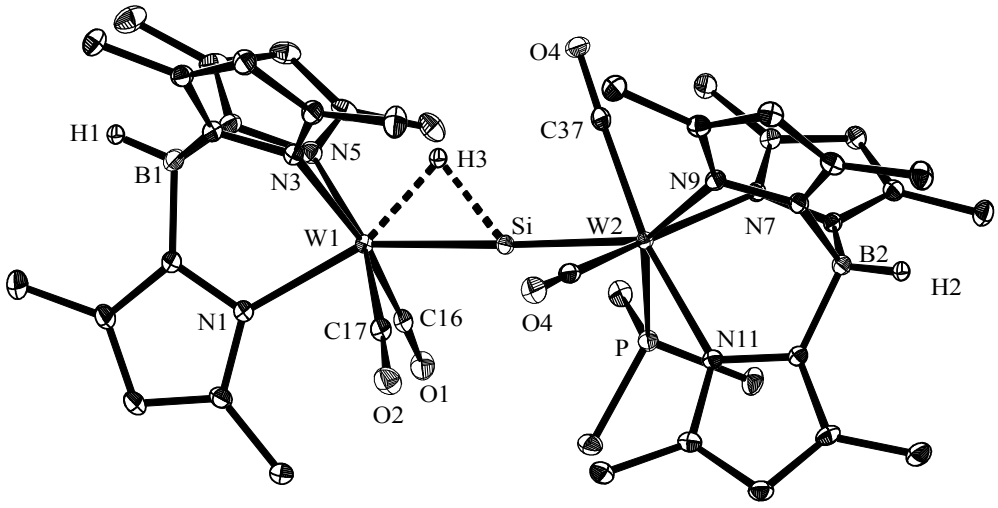

Figure 69. DIAMOND plot of the molecular structure of compound **25-W** at 100(2) K. Thermal ellipsoids are set at 30% probability. Hydrogen atoms (except the B-bonded H and WHSi atoms) and the $[B\{C_6H_3\text{-}3,5\text{-}(CF_3)_2\}_4]^-$ were omitted for clarity. Selected bond lengths [Å] and bond angles [°] of **25-W**: W1-Si 2.3018(7), W2-Si 2.3598(7), W2-P 2.5521(7); W1-Si-W2 172.90(4), N1-W1-Si 151.92(6). Selected bond lengths [Å] and bond angles [°] of **26-Mo**: Mo1-Ge 2.3424(6), Mo2-Ge 2.4217(6), Mo2-P 2.581(1); Mo1-Ge-Mo2 171.35(3), N1-Mo1-Ge 153.5(1).

In the solid-state, all complexes adopt a C_1-symmetric structure and feature an almost linear M-E-M (M = Mo, W; E = Si, Ge) core with two distinctly different M–E bond lengths. The protonation leads to an elongation of the M1–E bonds (Mo1–Si 2.2916(8) Å (**25-Mo**), W1–Si 2.3018(7) Å (**25-W**), Mo1–Ge 2.3424(6) Å (**26-Mo**)), and a shortening of the M2–E bonds (Mo2–Si 2.3519(8) Å (**25-Mo**), W2–Si 2.3598(7) Å (**25-W**), Mo2–Ge 2.4217(6) Å (**26-Mo**)) compared to that of the metallatetrylidyne complexes, which could be explained by the decreased electron density on the tetrel atoms upon protonation leading to the increased back donation from the M2 centers to the tetrel atoms. Notably, both M1–E and M2–E bond lengths appear within the M–E double bond range (Mo=Si 2.287 (1) – 2.3872(7) Å;[112, 113] W=Si 2.354(3) [2.358(2)] – 2.436(1) Å;[114, 180] Mo=Ge 2.3921(5) – 2.4142(7) Å).[34] On the other hand, protonation leads to a decrease of the bending of the central M1-E-M2 core (Mo1-Si-Mo2 173.72(3)° (**25-Mo**), W1-Si-W2 172.90(4)° (**25-W**), Mo1-Ge-Mo2 171.35(3)° (**26-Mo**)). In contrast to the metallatetrylidyne complexes, both metal ceneters in the protonated complexes adopt a distorted face-capped octahedral geometry, in which the tetrel atoms cap the octahedron faces, where one face is built up from the proton and two CO ligands, whereas the other face is build up from a PMe_3 and two CO ligands. The position of the hydrogen atom was ascertained from the

difference Fourier synthesis map and was further supported by the different orientation of the two carbonyl ligands and the pyrazolyl groups of the Tp' ligand at the M1 centers. For example, in compound **25-Mo**, the C16-Mo1-Si angle decreased from 84.2(2)° (**21-Mo**) to 77.07(9)°, whereas the N3-Mo1-Si and N5-Mo1-Si angles increased from 104.2(1)° and 108.9(1)° to 111.25(6)° and 120.52(6)°, respectively (Figure 68). Furthermore, the hydrogen atom is in *trans*-orientation to one of the pyrazolyl groups of the Tp' ligand, as evidenced by the N1-Mo1-H bond angle of 163.6(11)°. Notably, upon protonation the N1-M1-E angles (N1-Mo1-Si 152.30(6)° (**25-Mo**), N1-W1-Si 151.92(6)° (**25-W**) and N1-Mo1-Ge 153.5(1)° (**26-Mo**)) become smaller compared to those observed in the corresponding metallatetrylidyne complexes (N1-Mo1-Si 169.3(1) (**21-Mo**), N1-W1-Si 176.6(4)° (**21-W**) and N1-Mo1-Ge 169.4(1)° (**22-Mo**)).

Compounds **25-Mo**, **25-W** and **26-Mo** were further characterized by multinuclear NMR and IR spectroscopy. Although the solid-state structures of these complexes do not contain a mirror plane, the ^{1}H and ^{13}C{^{1}H} NMR spectra reveal a time-averaged C_s-symmetric structure in solution as evidenced by the presence of only two sets of signals for the methyl groups of each Tp' ligand in a 2:1 ratio, indicating a very fast rotation of the M2 fragments about the M2–E bonds in the NMR time scale. The most characteristic signal in the ^{1}H NMR spectrum is that of the hydride ligand, which is bridged between M1 and the tetrel atoms. For example, the ^{1}H NMR spectrum of **25-Mo** in CD_2Cl_2 displays a doublet signal for the hydride ligand at $\delta = -1.96$ (J_{PH} = 2.1 Hz) ppm, which is flanked by a pair of silicon satellites with a coupling constant of 43.3 Hz. This signal is significantly downfield shifted compared to that observed for the complex [Cp*(dmpe)(H)MoSiMes][B(C_6F_5)$_4$] (δ = –9.78 (t, J_{PH} = 20 Hz, J_{SiH} = 15 Hz)).[29] The J_{SiH} coupling constant of 43.3 Hz is within the range suggested for nonclassical η^2-Si–H bonds (J_{SiH} = 20 – 98 Hz).[181] The Si-H coupling constant together with the relatively downfield-shifted signal clearly indicate the hydride as a bridging ligand between the Mo1 and Si atoms. Notably, the corresponding hydride signal in compound **25-W** at 0.0 ppm with a small J_{WH} coupling constant of 29.2 Hz also supports a bridging mode for this ligand. The ^{29}Si{^{1}H} NMR spectra of **25-Mo**, **25-W** in CD_2Cl_2 display a doublet signal at 460.7 ppm (^{2}J(^{31}P, ^{29}Si) = 87.5 Hz) and 417.0 ppm (^{2}J(^{31}P, ^{29}Si) = 70.5 Hz)), respectively, which appears at a significantly lower field compared to that of the corresponding metallasilylidyne complex **21-Mo** (438.9 ppm (^{2}J(^{31}P, ^{29}Si) = 56.6 Hz)) and **21-W** (395.6 ppm (^{2}J(^{31}P, ^{29}Si) = 39 Hz)) (Table 30, Table 31). The ^{31}P{^{1}H} NMR spectra of **25-Mo**, **25-W** and **26-Mo** in CD_2Cl_2 display a singlet at δ = 0.9 ppm (^{2}J(^{31}P, ^{29}Si) = 87.2 Hz),

–22.2 ppm ($^2J(^{31}P, ^{29}Si)$ = 70.5 Hz) and –2.9 ppm, respectively. These signals appear at a close position of that of the corresponding metallatetrylidyne complexes (Table 30, Table 31).

The ATR FT-IR spectra of solid samples of all complexes display four ν_{CO} absorption bands (**25-Mo**: 1980 (w), 1952 (m), 1909 (s), 1873 (s) cm^{-1} (Figure 70); **25-W**: 1968(w), 1935(m), 1892(s), 1860(m) cm^{-1}; **26-Mo**: 1992 (w), 1950 (m), 1902 (s), 1879 (s) cm^{-1}). The ν_{CO} bands are shifted towards higher wavenumbers compared to those of the starting materials, indicating decreased back donation from the metal centers to the carbonyl ligands in the protonated products. Despite the generally informative nature of IR spectroscopy for a differentiation between a terminal and a bridging hydride ligand, the detection of a signal for the hydride ligand in the spectra of the aforementioned complexes was not possible, probably due to overlapping with the carbonyl absorption bands. Akin to the solid-state IR spectrum, the solution IR spectrum also displays four ν_{CO} absorption bands, which are shifted to higher wavenumbers compared to those of the corresponding metallatetrylidyne starting materials. For instance, the IR spectrum of **25-Mo** in Et_2O shows four absorption bands at 1982 (w), 1952 (s), 1916 (vs) and 1887 (m) cm^{-1}.

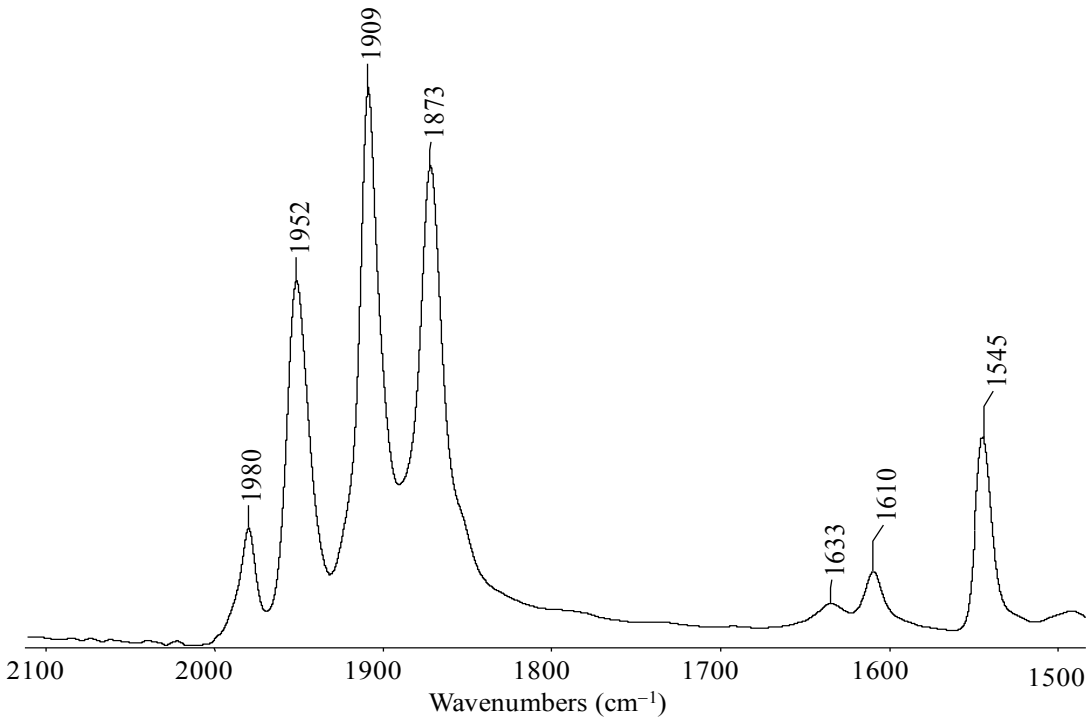

Figure 70. ATR FT-IR spectrum (2100 – 1500 cm^{-1}) of the solid sample of **25-Mo**.

2.7.3 Reactivity of metallatetrylidyne complexes towards polar reagents

The successful reactivity studies of the metallatetrylidyne complexes towards electrophiles or nucleophilic two-electron donor ligands have shown that the electrophile occupies a bridging position between the M1 and tetrel atoms, whereas, the nucleophile attacks the M2 center (*vide supra*). Accordingly, my next target was to check the reactivity pattern of these complexes towards polar reagents, such as [(PMe_3)AuCl]. Interestingly, despite the electrophilic nature of the tetrel atoms and the nucleophilic nature of the metal centers, the $[Au(PMe_3)]^+$ strongly coordinates to the tetrel atoms displaying a weak interaction with the M1 center, whereas the chloride anion binds at the M2 centers. Thus, treatment of the metallatetrylidyne complexes **21-Mo** and **22-Mo** with one equivalent of [(PMe_3)AuCl] in toluene at ambient temperature resulted in a color change from red-brown (**21-Mo**) or brown (**22-Mo**) to orange and light red-brown, respectively, leading to the formation of the addition products [Tp'$(CO)_2$Mo(η^3-AuPMe_3)EMo$(CO)_2$(Cl)Tp'] (**27-Mo**, E = Si; **28-Mo**, E = Ge) (Scheme 21). Compounds **27-Mo** and **28-Mo** were isolated after workup as analytically pure yellowish orange (**27-Mo**) and reddish orange (**28-Mo**) microcrystalline solids in 64 and 72% yields, respectively. Both compounds are moderately air-sensitive, quite thermally stable solids, which decompose at 313 – 315 °C (**27-Mo**) and 198 – 210 °C (**28-Mo**) to a brown to black mass. The solids are well soluble in CH_2Cl_2, fluorobenzene and THF, moderately soluble in toluene and Et_2O and insoluble in common aliphatic solvents. Akin to the metallasilylidyne complexes, compounds **27-Mo** and **28-Mo** slowly decomposes in THF, leading to the formation of a mixture of unspecified compounds.

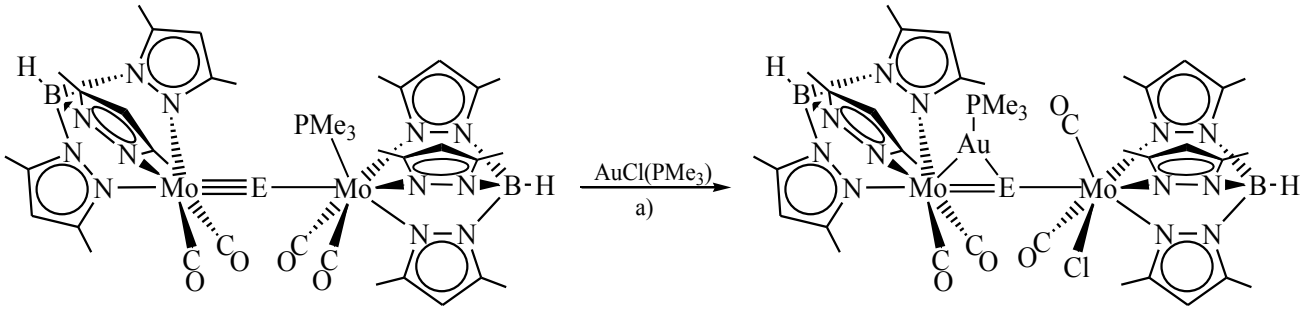

E = Si, Ge

27-Mo, yellowish orange solid, 64% (E = Si)

28-Mo, reddish orange solid, 72% (E = Ge)

Scheme 21. Addition of [(PMe_3)AuCl] to the metallatetrylidyne complexes **21-Mo** and **22-Mo**. a) –PMe_3, toluene, r.t..

The solid-state structures of **27-Mo** and **28-Mo** were determined by single crystal X-ray diffraction. Suitable orange block-shaped single crystals of **27-Mo**·4(CH_2Cl_2) were obtained upon slow evaporation of a solution of **27-Mo** at ambient temperature, whereas the orange plate-like single crystals of **28-Mo**·3.5(C_6H_5F) were grown upon cooling a saturated solution of **28-Mo** in a fluorobenzene/*n*-pentane mixture at –35 °C. Compounds **27-Mo** and **28-Mo** are isostructural and adopt a C_1-symmetric structure in the solid-state. The structure of the silicon analogue **27-Mo** is depicted in Figure 71.

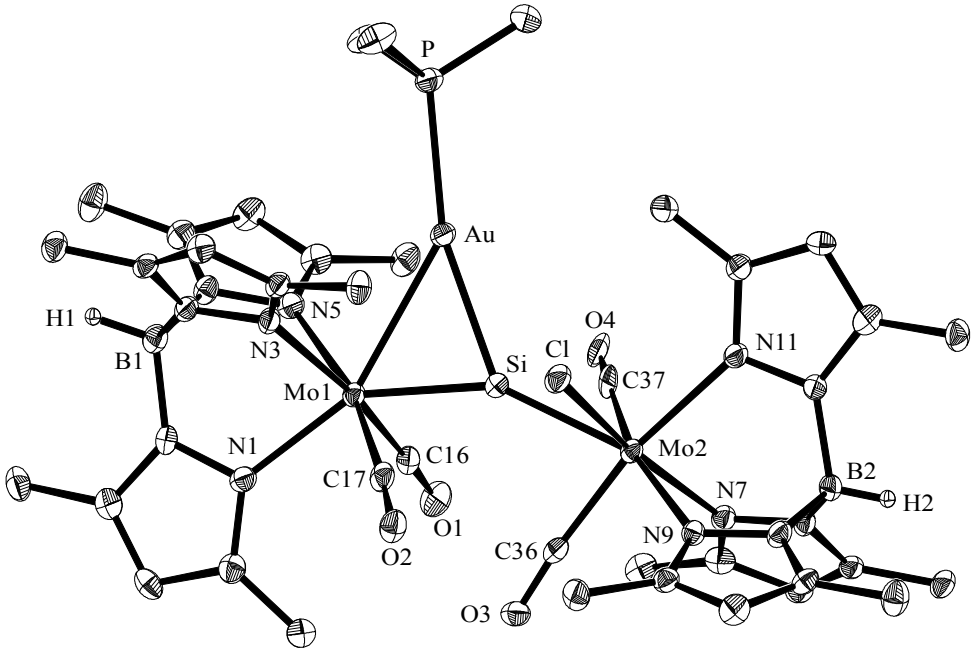

Figure 71. DIAMOND plot of the molecular structure of compound **27-Mo** in the crystal lattice of **27-Mo**·4(CH_2Cl_2) at 123(2) K. Thermal ellipsoids are set at 30% probability. Hydrogen atoms (except the B-bonded H atoms) were omitted for clarity. Selected bond lengths [Å] and bond angles [°] of **27-Mo**·4(CH_2Cl_2) (corresponding bond lengths and bond angles of **28-Mo**·3.5(C_6H_5F) are given in square brackets): Mo1-Si 2.323(2) [2.394(1)], Mo2-Si 2.400(2) [2.462(1)], Mo1-Au 2.8164(5) [2.8121(8)], Au-Si 2.423(2) [2.497(1)], Au-P 2.329(2) [2.299(2)], Mo1-N1 2.210(5) [2.207(7)], Mo1-N3 2.245(5) [2.262(7)], Mo1-N5 2.274(5) [2.288(7)], Mo2-N7 2.208(5) [2.217(7)], Mo2-N9 2.223(5) [2.220(7)], Mo2-N11 2.242(5) [2.265(7)], Mo1-C16 1.945(6) [1.931(9)], Mo1-C17 1.955(7) [1.95(1)], Mo2-C36 1.949(6) [1.958(9),], Mo2-C37 1.96(2) [1.93(3)], Mo2-Cl 2.567(7) [2.535(8)]; Mo1-Si-Mo2 152.19(8) [160.32(5)], N1-Mo1-Si 148.4(1) [157.1(2)], N1-Mo1-Au 156.4(1) [146.2(2)], N3-Mo1-Si 117.8(1) [116.8(2)], N5-Mo1-Si 120.6(1) [113.0(2)], Mo1-Au-P 143.45(4) [149.89(7)], Si-Au-P 164.56(6) [155.88(7)], Mo1-Si-Au 72.76(5) [70.15(3)], Mo2-Si-Au 135.04(8) [129.51(4)].

So far, no examples of structurally characterized μ_3-silicido complexes have been reported, and indeed **27-Mo** is the first example of this class of compounds. Furthermore, **28-Mo** is also one of the rare examples of μ_3-germido complexes.[86, 182, 183] Recently, a similar reaction has been reported for the anionic μ-borido complex $[Li(DME)_3][\{(\eta^5\text{-}C_5H_4Me)(CO)_2Mn\}_2B]$ with [(ITol)AuCl] (ITol = *N,N'*-bis(4-methylphenyl)imidazol-2-ylidene), which leads to the formation of the neutral trimetallic gold boride complex $[\{(\eta^5\text{-}C_5H_4Me)(CO)_2Mn\}_2B(AuITol)]$.[184]The most striking structural features of **27-Mo** and **28-Mo** are the two inequivalent Mo–E (E = Si, Ge) bonds (2.323(2) and 2.400(2) Å (**27-Mo**); 2.394(1) and 2.462(1) Å (**28-Mo**)), with the shorter one being that bridged by the $[(PMe_3)Au]$ fragment, and the trigonal planar coordination of the tetrel atoms, as evidenced by the sum of the angles around the tetrel centers of 359.99° (**27-Mo**) and 359.98° (**28-Mo**). The addition leads to an elongation of the Mo1–E bonds and to a shortening of the Mo2–E bonds compared to the corresponding bonds of the metallatetrylidyne complex precursors (Table 32). In both compounds, the Mo1–E bonds appear within the reported range for Mo–E double bonds with tri-coordinated tetrel atoms (Mo=Si 2.2853(8) – 2.3872(7) Å: Mo=Ge 2.3921(5) – 2.4142(7) Å).[29, 30, 33, 34, 111-113] On the other side, the Mo2–E bond lengths appear slightly shorter than corresponding Mo–E single bond lengths (Mo–Si 2.413(1) – 2.7140(8) Å; Mo–Ge 2.4990(2) – 2.875(1) Å),[22] indicating the presence of multiple bond character. In both complexes, the $[Au(PMe_3)]^+$ fragment is bonded as a bridging ligand between the Mo1 and tetrel atoms as suggested by the Mo1–Au and Au–E bond lengths. Thus, the Au–E bond lengths (Au-Si 2.423(2) Å, Au-Ge 2.497(1) Å**)** appear within the reported range for Au–E single bonds ($(Au–Si)_{Mean}$ = 2.419 Å, $(Au–Ge)_{Mean}$ = 2.465 Å)[23], suggesting a strong bonding between Au and the tetrel atoms, while the Mo1–Au bond lengths of 2.8164(5) (**27-Mo**) and 2.8121(8) Å **(28-Mo)** are also within the reported range for Mo–Au single bonds ($(Mo–Au)_{Mean}$ = 2.824 Å),[24] indicating a considerable bonding interaction between Mo1 and Au. Remarkably, the addition of the gold fragment to the Mo1–Si bond leads to a significant bending of the Mo1-Si-

22 A CSD survey (11.05.2016) gave 85 compounds with Mo–Si single bonds and 34 compounds with Mo–Ge single bonds, leading to a median/mean Mo–Si and Mo–Ge bond lengths of 2.564/2.559 Å and 2.625/2.587 Å, respectively.

23 A CSD survey (26.05.2016) gave 18 compounds with Au–Si single bonds and 32 compounds with Au–Ge single bonds, leading to a median/mean Au–Si and Au–Ge bond length of 2.388/2.419 Å and 2.438/2.465 Å, respectively.

24 A CSD survey (26.05.2016) gave 50 compounds with Mo–Au single bonds leading to a median/mean Mo–Au bond lengths of 2.804/2.824 Å.

Mo2 atom array (152.19(8)°) in compound **27-Mo**, but surprisingly does not lead to a noticeable change in the Mo1-Ge-Mo2 atom array (160.32(5)°) of compound **28-Mo** as shows a comparison with the corresponding angles in the precursors **21-Mo** and **22-Mo** (Table 32). On the other hand, the Si-Au-P angle (164.56(6)°) in **27-Mo** is much more widened compared to the Ge-Au-P angle (155.88(7)°) in **28-Mo**, which together with the Mo1-E-Mo2 bond angle gives a good indication of the interaction of the [(PMe_3)Au] fragment with the Mo1 and the tetrel atoms. Thus, upon going from Si to Ge, the interaction of the [(PMe_3)Au] fragment becomes weaker with the tetrel center but relatively stronger with the Mo1 center.

Table 32. Comparison of selected bonding parameters of the metallatetrylidyne complexes **21-Mo** and **22-Mo** with compounds **27-Mo** and **28-Mo**.

Complex	M1≡E [Å]	M2–E [Å]	M1-E-M2 [°]	N1-M1-E [°]
[Tp'$(CO)_2$Mo1≡Si–Mo2$(CO)_2$(PMe_3)Tp'] (**21-Mo**)	2.287(2)	2.438(2)	162.93(7)	169.3(1)
[Tp'$(CO)_2$Mo1≡Ge–Mo2$(CO)_2$(PMe_3)Tp'] (**22-Mo**)	2.3399(6)	2.5163(6)	161.66(3)	169.4(1)
[Tp'$(CO)_2$Mo1(η^3-AuPMe_3)SiMo2$(CO)_2$(Cl)Tp'] (**27-Mo**)	2.323(2)	2.400(2)	152.19(8)	148.4(1)
[Tp'$(CO)_2$Mo1(η^3-AuPMe_3)GeMo2$(CO)_2$(Cl)Tp'] (**28-Mo**)	2.394(1)	2.462(1)	160.32(5)	157.1(2)

The spectroscopic data of **27-Mo** and **28-Mo** are consistent with the solid-state structures. Akin to the metallatetrylidyne complexes, the ^{1}H and ^{13}C{^{1}H} NMR spectra also revealed a C_s-symmetric structure in solution, suggesting a very fast rotation of the Mo2 fragments about the Mo2–E bond on the NMR time scale. The ^{31}P{^{1}H} NMR spectrum of **27-Mo** in CD_2Cl_2 displays a singlet signal at δ = 25.7 ppm which is accompanied by a pair of silicon satellites with a $^2J_{SiP}$ of 89 Hz, whereas the ^{31}P{^{1}H} NMR signal of **28-Mo** appears slightly upfield-shifted (δ = 19.4 ppm). The ^{29}Si{^{1}H} NMR spectrum of **27-Mo** in CD_2Cl_2 displays a doublet signal at δ = 265.7 ppm with a $^2J_{SiP}$ of 89 Hz. The signal appears significantly upfield-shifted compared to that observed for the metallasilylidyne complex **21-Mo** (δ = 438.9 ppm (d, ^2J(^{31}P, ^{29}Si) = 56.6 Hz)).

The IR spectra of compounds **27-Mo** and **28-Mo** show only four ν_{CO} absorption bands at 1921(s), 1885(m), 1835(vs) cm^{-1} and 1821(m), and 1925(s), 1887(s), 1837(vs), 1827(sh) cm^{-1}, respectively, suggesting the presence of only one rotamer in solution. As expected, the solid-state IR spectra also display a similar ν_{CO} absorption bands pattern as that observed in solution.

Surprisingly, the reaction of the metallasilylidyne complex **21-Mo** with MeI takes a different course than that observed with [(PMe_3)AuCl], and affords an addition product, where the methylium (Me^+) binds to the molybdenum center and the iodide (I^-) to the silicon center. Thus, heating of a mixture of compound **21-Mo** with an excess of MeI in chlorobenzene at 110 °C leads to a selective conversion of the starting material into the addition product [Tp'$(CO)_2$Mo=Si(I)–Mo$(CO)_2$(Me)Tp'] (**29-Mo**) upon elimination of the PMe_3 ligand (Scheme 22). Compound **29-Mo** could be isolated after workup as a moderately air-sensitive, yellow solid in 69% yield. It is moderately soluble in CH_2Cl_2, sparingly soluble in THF or fluorobenzene and insoluble in toluene, Et_2O or any aliphatic solvents. Compound **29-Mo** is an extremely thermally stable solid, which decomposes at 292 – 294 °C to give a brown mass.

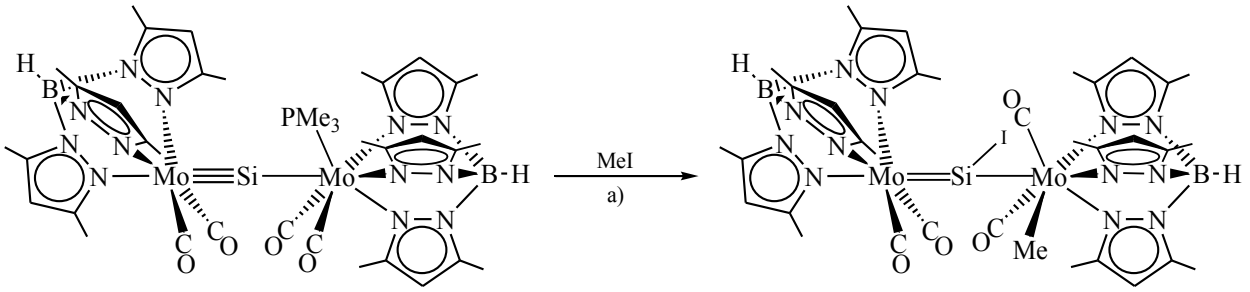

29-Mo, yellow solid, 69%

Scheme 22. Addition of MeI to the metallasilylidyne complex, **21-Mo**. a) –PMe_3, chlorobenzene, 110 °C.

Several attempts to obtain single crystals of compound **29-Mo** suitable for X-ray diffraction analysis failed, and afforded only crystals of low quality from which the structural motif could be seen. Therefore, the structural parameters of the compound **29-Mo** will not be discussed. However, compound **29-Mo** was characterized by multinuclear NMR and IR spectroscopy and the composition was confirmed by elemental analysis. Akin to the compound **27-Mo**, the ^1H and $^{13}C\{^1H\}$ NMR spectra of **29-Mo** in CD_2Cl_2 at ambient temperature also revealed a C_s-symmetric structure in solution, as evidenced by the appearance of the methyl group signals of each Tp' ligand in a 2:1 ratio. Thus, a very fast rotation of the seven-coordinated molybdenum fragment about the Mo2–Si bond in NMR time scale is indicated. In the ^1H NMR spectrum, the Mo-*Me* group appeares as a singlet resonance at $\delta = 0.57$ ppm, whereas in the $^{13}C\{^1H\}$ NMR spectrum the corresponding methyl carbon appears as a singlet resonance at very high field ($\delta = -34.0$ ppm). This is a characteristic feature of metal-alkyl complexes.[185-189] The $^{29}Si\{^1H\}$ NMR spectrum of **29-Mo** in CD_2Cl_2 displays a singlet resonance at 222.0 ppm, which is significantly

upfield-shifted compared to that of the metallasilylidyne complex **21-Mo** (δ = 438.9 ppm (d, $^{2}J(^{31}P, ^{29}Si)$ = 56.6 Hz)), and appears in the expected region for a silylidene-type complex.[33, 113]

The IR spectrum of compound **29-Mo** in CH_2Cl_2 displays four ν_{CO} absorption bands at 1936(s), 1906(m), 1848(vs), 1836(sh) cm^{-1} (Figure 72). The ν_{CO} bands are slightly shifted towards higher frequencies compared with those of the corresponding metallasilylidyne complex **21-Mo** (Table 30), suggesting an overall decrease of the electron density upon substitution of the electron donating PMe_3 ligand by MeI.

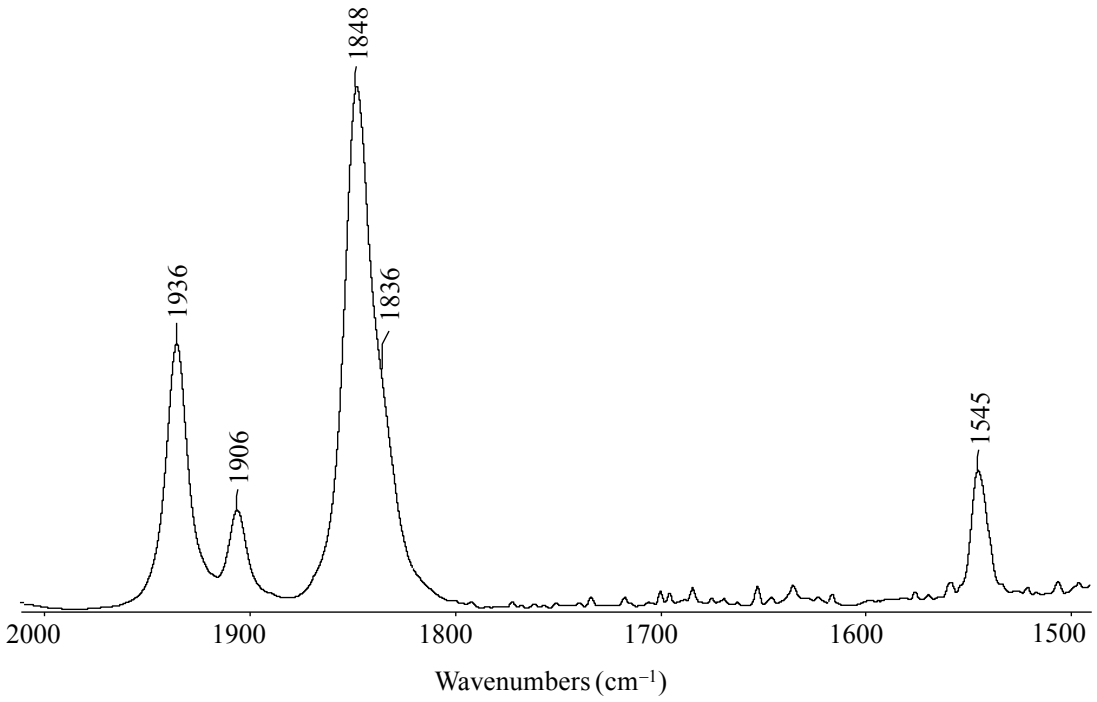

Figure 72. FT-IR spectrum (2000 – 1500 cm^{-1}) of **29-Mo** in CH_2Cl_2 solution.

2.7.4 Reduction of a metallasilylidyne complex: First example featuring a 1,3-dimetalla-2-silaallene structure

The neutral metallasilylidyne complex **21-Mo** undergoes two-electron reduction at ambient temperature by KC_8 in DME leading to the formation of the μ-silicido complex dianion $[K(diglyme)]_2[(\mu\text{-Si})\{Mo(CO)_2Tp'\}_2]$ (**30-Mo**) with concomitant elimination of the PMe_3 ligand. Monitoring of the reaction progress by IR spectroscopy revealed an almost selective conversion of the starting material into the complex salt **30-Mo**, which was isolated after workup as an extremely air-sensitive, yellow solid in 59 % yield (Scheme 23). The yellow solid is thermally remarkably robust and decomposes at 328 – 329 °C to a gray mass. The salt **30-Mo** is stable and moderately soluble in diglyme, sparingly soluble in DME, but rapidly decomposes in THF, fluorobenzene or CH_2Cl_2, thus excluding the analysis of the complex salt by NMR spectroscopy. The identity of **30-Mo** was unequivocally confirmed by single-crystal X-ray diffraction analysis and solid-state IR spectroscopy, while the composition was further confirmed by elemental analysis.

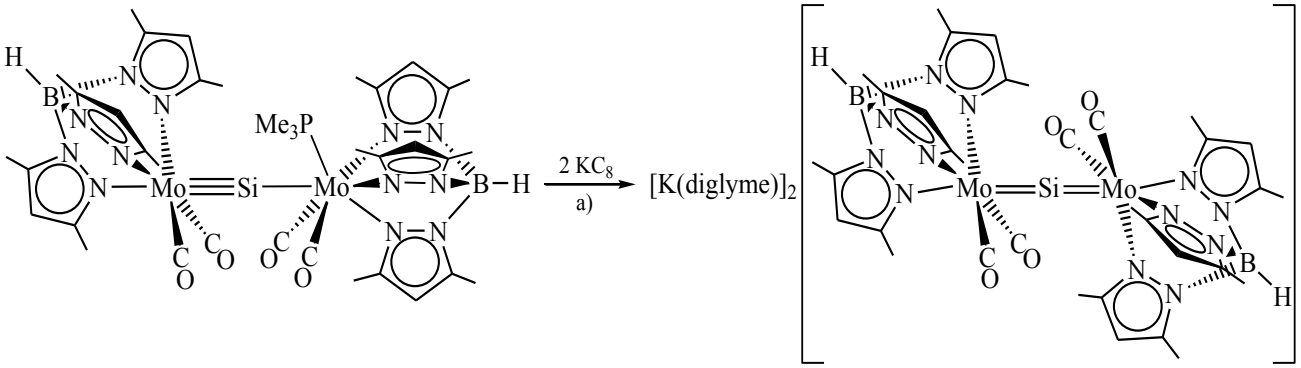

30-Mo, yellow solid, 59%

Scheme 23. Synthesis of the complex salt $[K(diglyme)]_2[(\mu\text{-Si})\{Mo(CO)_2Tp'\}_2]$ (**30-Mo**) upon two-electron reduction of **21-Mo**; a) $-PMe_3$, DME/diglyme, r.t.; formal charges are omitted for clarity.

Orange-yellow blocks of **30-Mo**·$4(C_6H_{14}O_3)$, suitable for X-ray diffraction analysis, were grown upon cooling a saturated diglyme solution of **30-Mo** at –35 °C. Single crystal X-ray diffraction analysis reveals the presence of C_{2h}-symmetric $[(\mu\text{-Si})\{Mo(CO)_2Tp'\}_2]^{2-}$ dianions in **30-Mo** (Figure 73), which are well separated from the $[K(diglyme)_2]^+$ cations as evidenced by the shortest Si···O and Si···K distances of 5.1381(1) Å and 7.6889(2) Å (cf. $\Sigma r(Si\cdots O)_{vdW}$ = 3.7 Å, $\Sigma r(Si\cdots K)_{vdW}$ = 4.9 Å), respectively.[190] Remarkably, the Mo-Si-Mo# core of the $[(\mu$-

Si){Mo(CO)$_2$Tp'}$_2$]$^{2-}$ dianions is perfectly linear with a Mo-Si-Mo# angle of 180.0 °. Conspicuously, this is the first example of a compound featuring a perfectly linear two coordinated silicon atom. Furthermore, in contrast to the metallasilylidyne complex **21-Mo**, the Mo–Si bond lengths are equal within the error margin (Mo–Si 2.3493(2) Å, Mo#–Si 2.3494(2) Å) and within the reported range for Mo=Si bond lengths in silylidene complexes (2.287(1) – 2.3872(7) Å),[25] suggesting the presence of a 1,3-dimetalla-2-silaallene structure in the dianions. Complex **30-Mo** represents the first example of a silicon analogue of the metallacumulene class of μ-carbido complexes and fills the missing link between the μ-carbido and their heavier analogues of this class.[72, 86, 89, 164] The CO ligands at the metal fragments adopt an antiperiplanar conformation along the Mo-Si-Mo vector as evidenced by the dihedral angle of 0.00° between the least-square planes of the atoms O1-C16-Mo-Si and O1#-C16#-Mo#-Si.

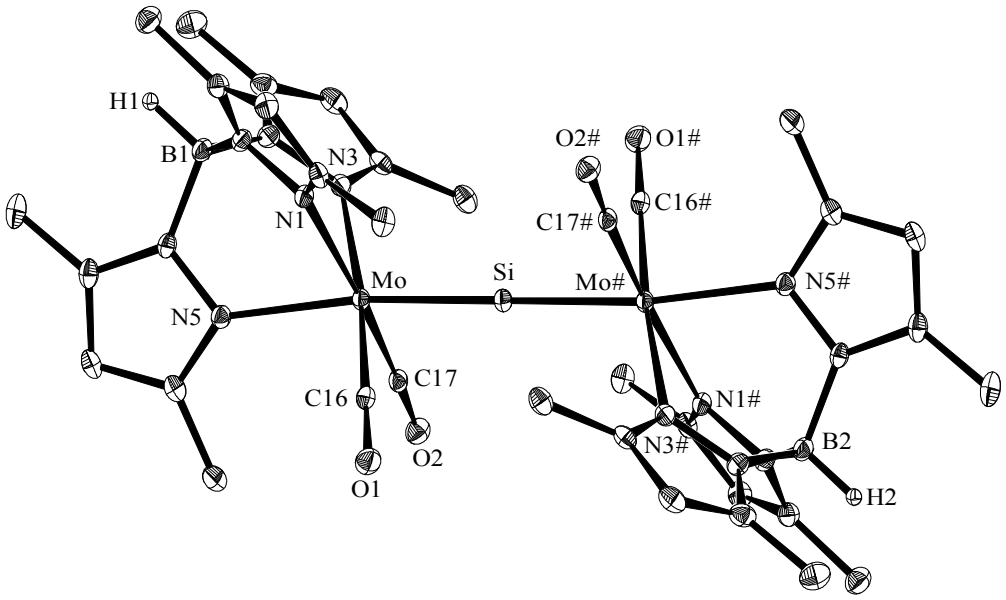

Figure 73. DIAMOND plot of the molecular structure of the dianion [(μ-Si){MoTp'(CO)$_2$}$_2$]$^{2-}$ in the crystal lattice of **30-Mo**·4($C_6H_{14}O_3$) at 123(2) K. Thermal ellipsoids are set at 30% probability. Hydrogen atoms (except the B-bonded H atoms), solvent molecules and the potassium cations are omitted for clarity. Selected bond lengths [Å] and bond angles [°]: Mo-Si 2.3493(2), Mo(#)-Si 2.3494(2), Mo-N1 2.296(2), Mo-N3 2.303(2), Mo-N5 2.326(2), Mo-C16 1.918(2), Mo-C17 1.916(2); Mo-Si-Mo 180.0, N1-Mo-Si 103.61(4), N3-Mo-Si 107.73(4), N5-Mo-Si 173.00(4), C16-Mo-Si 78.47(6), C17-Mo-Si 82.42(6).

25 A CSD survey (28.05.2016) gave 7 compounds with Mo=Si bonds, leading to a median and mean Mo–Si bond lengths of 2.317 Å and 2.323 Å, respectively.

The solid state ATR-IR spectrum of **30-Mo** is in agreement with the solid state structure and displays two ν_{CO} absorption bands for the four carbonyl groups at 1765 (s) and 1696 (vs) cm^{-1}, which emerge at remarkably lower frequency compared to those of the metallasilylidyne complex **21-Mo** (ν(CO): 1928 (s), 1861 (vs), 1791 (s) cm^{-1}). This indicates an increase of the Mo→CO backbonding resulting from the increased electron density on the Mo centers, which is also reflected in the *ca*. 3 pm shorter Mo-C_{CO} bonds of **30-Mo** compared to those of **21-Mo** in the solid state. The experimentally observed ν_{CO} absorption bands are in good agreement with the calculated four ν_{CO} absorption bands at 1784, 1743, 1686 and 1683 cm^{-1} for the C_{2h}-symmetric isomer of the dianion $[(\mu\text{-Si})\{Mo(CO)_2Tp'\}_2]^{2-}$ (*vide infra*), of which two pairs are closely separated giving rise to two broad bands in the experimental ATR-IR spectrum.

The experimental results of compound **30-Mo** were further supported by quantum chemical calculations, which reveal the presence of two almost isoenergetic minimum structures of either C_1 (**{(30-Mo)$^{2-}$}$_{calc}$**) or C_{2h} (**{(30-Mo)$^{2-}$}'$_{calc}$**) symmetry on the potential energy hypersurface (Figure 74). Interestingly, in contrast to the C_{2h}-symmetric structure, the C_1-symmetric structure, which is the lowest energy structure, does not feature a linear Mo-So-Mo angle. The calculated bonding parameters of the C_{2h}-symmetric structures (**{(30-Mo)$^{2-}$}'$_{calc}$**) are in very good agreement with the experimental bonding parameters of **(30-Mo)$^{2-}$** (Table 33). Strikingly, the calculations suggest a quite different bonding situation for **(30-Mo)$^{2-}$** in contrast to the carbon-based allenes ($R_2C{=}C{=}CR_2$) or heavier allenes ($R_2Si{=}Si{=}SiR_2$),[191, 192] which is however remarkably similar to that of the μ-carbido and μ-germido complexes [(μ-C){$ReCp(CO)_2$}$_2$] and [(μ-Ge){$MnCp(CO)_2$}$_2$],[83, 88] and also to the related μ-borido complex cation in $[(\mu\text{-B})\{FeCp(CO)_2\}_2][B(C_6H_3\text{-}3,5\text{-}(CF_3)_2)_4]$.[193] The Mo-Si-Mo σ-bonding spine, which consists of the HOMO–27 and HOMO–4 (Figure 76) in **(30-Mo)$^{2-}$**, could be best described as a 3-center–4-electron (3c-4e) bond, resulting from an overlap of the 3s(Si) and $3p_z$(Si) orbitals with a combination of the σ-accepting LUMOs (mainly d_z^2 orbitals) of the anionic $[Mo(CO)_2Tp']^-$ fragments (Figure 75 and Figure 76). The orbital interaction of the residing p_x(Si) and p_y(Si) orbitals with the HOMOs (mainly d_{xz} orbitals), HOMOs–1 (mainly d_{yz} orbitals) and HOMOs–2 (mainly d_{xy} orbitals) of the $[Mo(CO)_2Tp']^-$ fragments gives rise to the four further delocalized Mo=So=Mo bonding orbitals in **(30-Mo)$^{2-}$** (e.g. HOMO–5, Figure 76), which build up the π-core of the compound as well as two non-bonding metal-centered orbitals (e.g. HOMO, Figure 76). This ultimately leads to a 3-center–12-electron bonding interation between silicon and the two

metal fragments, which differs from the 3-center–8-electron bond in allenes or heavier allenes and leads to a symmetric distribution of the π-electron density along the Mo-Si-Mo vector as well as partial triple-bond character of the Mo–Si bonds in **(30-Mo)$^{2-}$**.

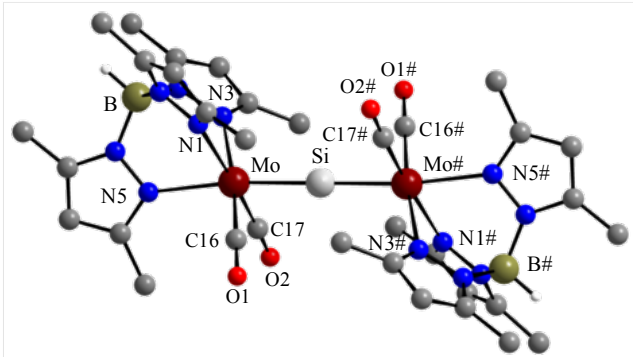

(30-Mo)$^{2-}$

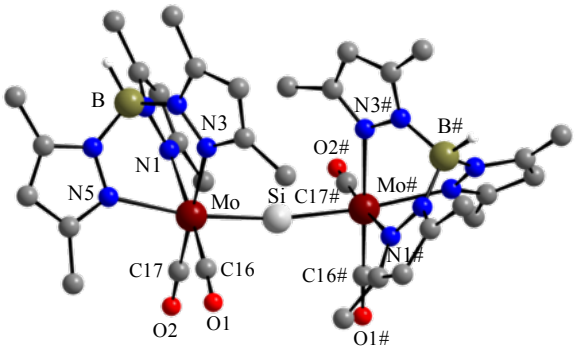

{(30-Mo)$^{2-}$}$_{calc}$, 0.0 kJ mol^{-1}

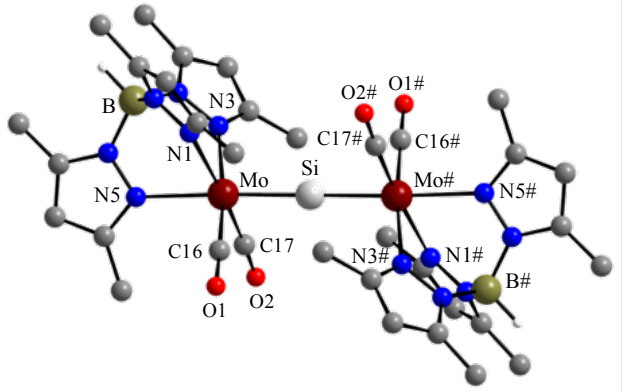

{(30-Mo)$^{2-}$}'$_{calc}$, 10.2 kJ mol^{-1}

Figure 74. Experimental **(30-Mo)$^{2-}$** and calculated (**{(30-Mo)$^{2-}$}$_{calc}$** and **{(30-Mo)$^{2-}$}'$_{calc}$**) structures of the dianion [(μ-Si){Mo(CO)$_2$Tp'}$_2$]$^{2-}$at the RI-JCOSX/B97-D3/def2-TZVP/COSMO(THF) level of theory with their corresponding relative Gibbs energies. The H atoms (except B-H) were omitted for clarity. Atom numbering of the experimental structure was taken over in the calculated structure.

Table 33. Comparison of selected experimental and calculated bonding parameters of **30-Mo**·4($C_6H_{14}O_3$), **{(30-Mo)$^{2-}$}$_{calc}$** and **{(30-Mo)$^{2-}$}'$_{calc}$**.

	Mo–Si [Å]	Mo#–Si [Å]	Mo–C16 [Å]	Mo–C17 [Å]	Mo–N1 [Å]	Mo–N3 [Å]	Mo–N5 [Å]
30-Mo·4($C_6H_{14}O_3$)	2.3493(2)	2.3494(2)	1.918(2)	1.916(2)	2.296(2)	2.303(2)	2.326(2)
{(30-Mo)$^{2-}$}$_{calc}$	2.332	2.332	1.931	1.934	2.340	2.325	2.344
{(30-Mo)$^{2-}$}'$_{calc}$	2.351	2.350	1.928	1.929	2.335	2.330	2.363
	Mo-Si-Mo# [°]	C16-Mo-Si [°]	C17-Mo-Si [°]	N1-Mo-Si [°]	N3-Mo-Si [°]	N5-Mo-Si [°]	C16-Mo-C17 [°]
30-Mo·4($C_6H_{14}O_3$)	180.0	78.47(6)	82.42(6)	103.61(4)	107.73(4)	173.00(4)	86.42(8)
{(30-Mo)$^{2-}$}$_{calc}$	170.05	87.92	87.94	91.69	95.63	169.53	85.86
{(30-Mo)$^{2-}$}'$_{calc}$	179.96	83.09	83.28	102.44	102.63	177.84	86.15

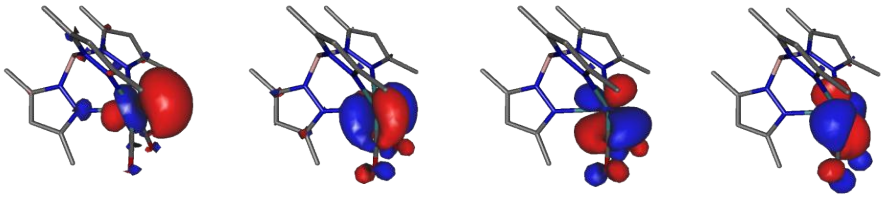

Figure 75. Selected Kohn-Sham orbitals of the anionic $[Mo(CO)_2Tp']^-$ fragments; isosurface value corresponds to 0.04 e bohr^{-3}.

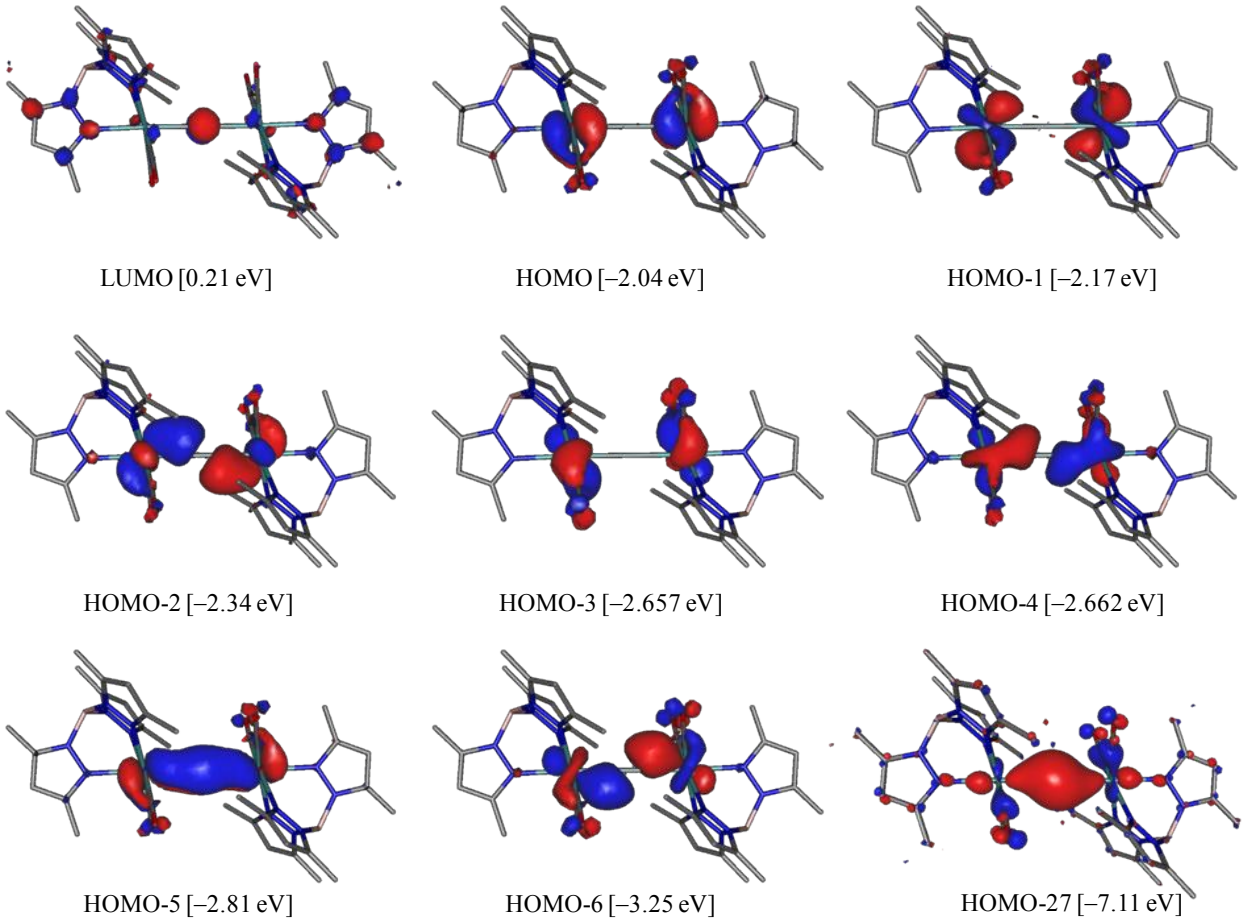

Figure 76. Selected Kohn-Sham orbitals of the anionic $\{\mathbf{(30\text{-}Mo)^{2-}}\}'_{calc}$ fragments; the isosurface value corresponds to 0.04 e bohr^{-3}.

The partial triple bond character of the Mo–Si bonds in $\mathbf{(30\text{-}Mo)^{2-}}$ is also reflected by the ELF analyses of $\{\mathbf{(30\text{-}Mo)^{2-}}\}_{calc}$ and $\{\mathbf{(30\text{-}Mo)^{2-}}\}'_{calc}$ (Figure 77), which display a toroidal and a crescent shape of the electron density between the Mo and Si atoms, respectively, with a disynaptic basin population of each bond of 3.28e.

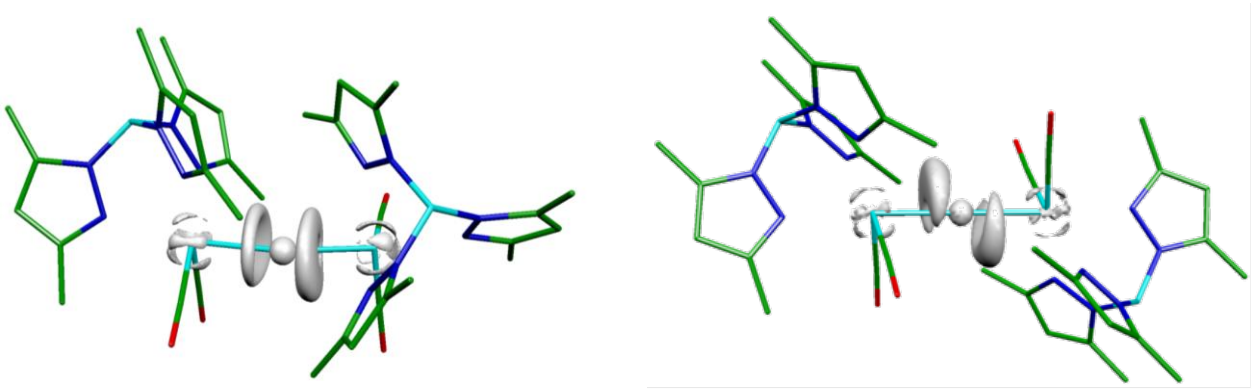

{(30-Mo)$^{2-}$}$_{calc}$ **{(30-Mo)$^{2-}$}'$_{calc}$**

Figure 77. 3D representation of the electron localization function (ELF) in **{(30-Mo)$^{2-}$}$_{calc}$** and **{(30-Mo)$^{2-}$}'$_{calc}$** with an ELF value of 0.80.

The partial triple bond character of the Mo–Si bonds in complex **30-Mo** was further supported by the NRT analysis on the model system C_{2h}-symmetric $[(\mu\text{-Si})\{Mo(CO)_2Tp\}_2]^{2-}$, which revealed an averaged resonance weight of 13 % of Mo–Si, 70 % of Mo=Si and 10 % of Mo≡Si bond-containing structures and an averaged NRT bond order for the Mo–Si bonds of 1.85.

2.7.5 Reactivity of metallasilylidyne complexes towards alkynes: First examples containing planar tetracoordinated silicon (ptSi)

Alkyne metathesis is a very well established and important class of reactions in organic synthesis, which led to a Nobel Prize in chemistry for Y. Chauvin, R. H. Grubbs and R. R. Schrock in 2005.[26] Recent studies have shown that metal silylidyne complexes also undergo 2+2 cycloadditions with alkynes to afford metallasilacyclobutadienes, which may become key intermediates in silyne metathesis.[33, 58] These results prompted us to investigate the reaction of the metallasilylidyne complexes towards alkynes. Indeed, the metallasilylidyne complexes **21-Mo** and **21-W** react very fast with different alkynes R^1-C≡C-R^2 (R^1 = H, Me, R^2 = Me, TMS, Ph) at elevated temperature (100 – 110 °C), but surprisingly, in contrast to the normal silylidyne complexes, the metallasilylidyne complexes afforded the very interesting tricyclic complexes [Tp'$(CO)_2$MSiC(R^1)C(R^2)M$(CO)_2$Tp'] (**31-Mo**: M = Mo, R^1, R^2 = Me; **31-W**: M = W, R^1, R^2 = Me; **32-Mo**: M = Mo, R^1 = H, R^2 = TMS; **32-W**: M = W, R^1 = H, R^2 = TMS; **33-Mo**: M = Mo, R^1 = H, R^2 = Ph) (Scheme 24). Monitoring of the reactions by IR spectroscopy revealed an almost selective conversion of the starting materials into the products, which were isolated after workup and crystallization as moderately air-sensitive, yellow to bright yellow solids in very good yields (Table 34). All compounds are thermally robust solids, which decomposes at very high temperature (Table 34) and are well soluble in THF, fluorobenzene, and toluene, and moderate to sparingly soluble in Et_2O and aliphatic solvents.

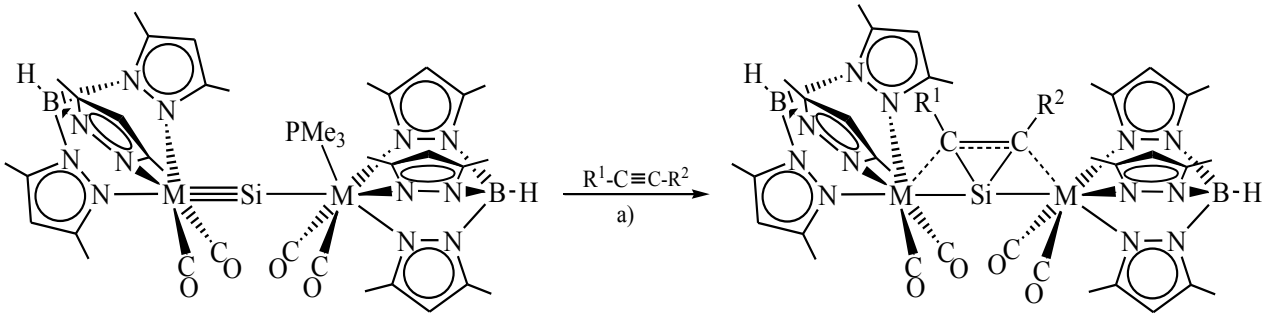

M = Mo, W R^1 = H, Me; R^2 = Me, TMS, Ph **31-Mo**, **32-Mo**, **33-Mo**, **31-W**, **32-W**

Scheme 24. Addition of alkynes to the metallasilylidyne complexes **21-Mo** and **21-W**.

26 The Nobel Prize in Chemistry, **2005**. Y. Chauvin, R. H. Grubbs, R. R. Schrock. http://www.nobelprize.org/nobel_prizes/chemistry/laureates/2005/

Table 34. Selected properties of the alkyne cyclization products **31-Mo**, **31-W**, **32-Mo**, **32-W** and **33-Mo**

Complex	Color	Yield %	M.P. °C	IR[a], ν(CO) cm^{-1}	^{29}Si NMR[b] ppm
[Tp'(CO)$_2$MoSiC(Me)C(Me)Mo(CO)$_2$Tp'] (**31-Mo**)	Yellow	87	285 – 287	1943 (s), 1898 (w), 1869 (vs), 1828 (w)	204.3 (s)
[Tp'(CO)$_2$WSiC(Me)C(Me)W(CO)$_2$Tp'] (**31-W**)	Yellow	84	277 – 279	1930 (s), 1884 (w), 1855 (vs), 1813 (w)	198.8 (s, $^1J_{Wsi}$ = 22 Hz)
[Tp'(CO)$_2$MoSiC(H)C(TMS)Mo(CO)$_2$Tp'] (**32-Mo**)	Yellow	81	313 – 314	1946 (s), 1900 (w), 1873 (vs), 1833 (w)	200.4 (s)
[Tp'(CO)$_2$WsiC(H)C(TMS)W(CO)$_2$Tp'] (**32-W**)	Yellow	76	353 – 354	1933 (s), 1885 (w), 1857 (vs), 1817 (w)	186.1 (s$^1J_{Wsi}$ = 22 &15 Hz)
[Tp'(CO)$_2$MoSiC(H)C(Ph)Mo(CO)$_2$Tp'] (**33-Mo**)	Bright yellow	67	223 – 225	1944 (s), 1902 (w), 1869 (vs), 1836 (vw)	216.9 (s)

[a]: IR spectrum in THF; [b]: ^{29}Si{^{1}H} NMR spectrum in C_6D_6.

Notably, the reactivity of the alkynes depends on the electron richness as well as on the steric crowding around the C≡C bond. For example, unlike to 2-butyne, the reaction of 3-hexyne with **21-Mo** in chlorobenzene is very slow and takes several hours at 110 °C, leading finally to the formation of several byproducts along with the targeted [3,3,3]-tricyclic complex [Tp'(CO)$_2$MoSiC(Et)C(Et)Mo(CO)$_2$Tp'].[27] Furthermore, the reaction with an electron-rich alkyne, such as Me_2N–C≡C–NMe_2 resulted in an unselective reaction and a rather complicated mixture of products.

The solid-state structures of all complexes, except for **31-W**, were determined by single-crystal X-ray diffraction analyses. All complexes exhibit very similar structural features, and therefore, only the structures of **31-Mo** and **32-Mo** will be discussed here, while selected bonding parameters of all complexes are given in Table 35. Clear yellow plates of **31-Mo**·1.5(C_7H_8) and **32-Mo**·(C_6H_6) were obtained by slow evaporation of a toluene solution of **31-Mo** at ambient temperature, and storage of a benzene solution of **32-Mo** at ambient temperature, respectively. In the solid-state **31-Mo** adopts an approximate, but not crystallographically imposed, C_{2v}-symmetric structure, whereas **32-Mo** adopts a C_s-symmetric structure (Figure 78, Figure 79). The most striking structural features of both complexes is that the silicon center is planar besides being tetracoordinated, as evidenced by the sum of angles around the silicon center (Σ(∠Si) = 360.1° [359.8°] (**31-Mo**), 359.4° (**32-Mo**)). This observation is against the van't Hoff/Le Bel

27 ^{1}H NMR (300.1 MHz, 298 K) data of [Tp'(CO)$_2$MoSiC(Et)C(Et)Mo(CO)$_2$Tp'] in C_6D_6 are as follows: 0.57 (t, ^3J(H,H) = 7.5 Hz, 6H, CH_2CH_3), 2.10, 2.67 (s, 6H each, $C^{3/5}$-*Me*, pz_B), 2.20, 2.59 (s, 12 each, $C^{3/5}$-*Me*, pz_A), 2.39 (q, ^3J(H,H) = 7.5 Hz, 4H, CH_2CH_3), 5.40 (s, 2H, C4-*H*, pz_B), 5.61 (s, 2H, C4-*H*, pz_A).

rule, which suggests a tetrahedral geometry for tetracoordinated tetrel elements.[194, 195] Thus, these silicon atoms could be considered as anti-van't Hoff/Le Bel silicon and remarkably these compounds are the first examples incorporating an anti-van't Hoff/Le Bel silicon isolated at room temperature. Notably, an X-ray crystal structure featuring a planar tetracoordinated silicon atom was reported in a phthalocyanine environment, but latter on the structure of this compound was doubted by Boldyrev, Schleyer, and Kesse, and was suggested to have a formal divalent silicon in the phthalocyanine rather than a tetravalent silicon atom.[196, 197] So far, a planar tetracoordinated silicon has been only observed in $SiAl_4^-$ ions produced through a laser vaporization cluster source in helium carrier gas by photoelectron spectroscopy.[198] Surprisingly, the calculated structure of $SiAl_4^-$ ions resembles quite well with the planar core of both compounds, which consists of the atoms Mo1, Mo2, Si1, C16 and C17 atoms (Figure 78, Figure 79).

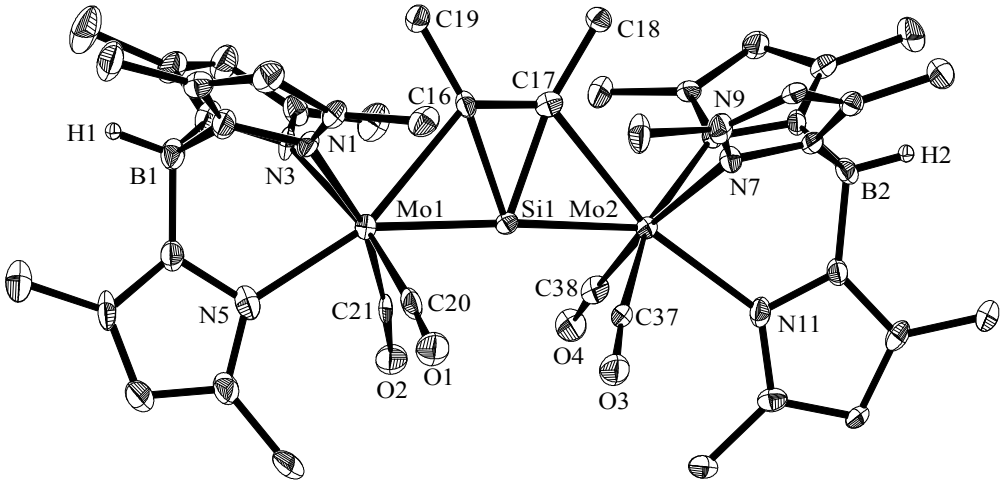

Figure 78. DIAMOND plot of the molecular structure of **31-Mo** in the crystal lattice of **31-Mo**·1.5(C_7H_8) at 123(2) K. Thermal ellipsoids are set at 30% probability. Hydrogen atoms (except the B-bonded H atoms) are omitted for clarity. Selected bond lengths [Å] and bond angles [°] (the bond lengths and angles in the square brackets are for the second independent molecule found in the unit cell): Mo1-Si1 2.278(3) [2.290(3)], Mo2-Si1 2.275(3) [2.281(3)], Si1-C16, 1.91(1) [1.91(1)], Si1-C17 1.89(1) [1.91(1)], C16-C17 1.37(1) [1.35(1)], Mo1-C16 2.44(1) [2.45(1)], Mo2-C17 2.45(1) [2.46(1)]; Mo1-Si1-Mo2 175.9(1) [176.7(1)], Mo1-Si1-C16 70.7(3) [70.7(3)], Mo2-Si-C17 71.3(3) [71.1(3)], C16-Si1-C17 42.2(4) [41.3(4)], Si1-Mo1-C16 47.5(2) [47.3(2)], Si1-Mo2-C17 47.1(3) [47.4(3)], Mo1-C16-C19 108.6(7) [107.4(7)], C17-C16-C19 121.6(8) [121.2(9)], C16-C17-C18 122.1(9) [121.9(9)], Si1-C16-C17 68.4(6) [69.4(6)], Si1-C17-C16 69.4(6) [69.3(6)], Mo2-C17-C18 107.3(7) [107.4(7)], Mo1-C16-Si1 61.8(3) [62.0(3)], Mo2-C17-Si1 61.6(3) [61.5(3)], N5-Mo1-Si1 148.7(2) [150.5(2)], N5-Mo1-C16 163.5(3) [162.2(3)], N11-Mo2-Si1 150.4(3) [147.5(2)], N11-Mo2-C17 162.5(3) [165.1(3)].

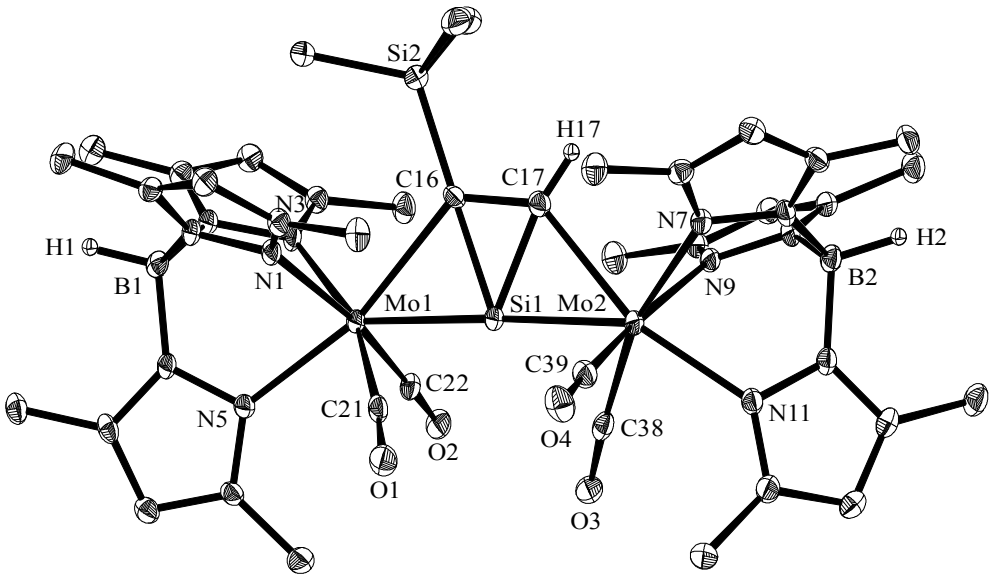

Figure 79. DIAMOND plot of the molecular structure of **32-Mo** in the crystal lattice of **32-Mo**·(C_6H_6) at 123(2) K. Thermal ellipsoids are set at 30% probability. Hydrogen atoms (except the B-bonded H atoms) are omitted for clarity. Selected bond lengths [Å] and bond angles [°]: Mo1-Si1 2.272(1), Mo2-Si1 2.287(1), Si1-C16 1.946(4), Si1-C17 1.870(4), C16-C17 1.382(5), Mo1-C16 2.468(3), Mo2-C17 2.383(4); Mo1-Si1-Mo2 176.80(5), Mo1-Si1-C16 71.1(1), Mo2-Si1-C17 69.1(1), C16-Si1-C17 42.4(2), Mo1-C16-Si1 60.6(1), Si1-Mo1-C16 48.27(9), Mo1-C16-Si2 120.5(2), Si2-C16-C17 113.3(3), Si1-C16-C17 65.8(2), Si1-C17-C16 71.8(2), Mo2-C17-Si1 63.7(1), Mo2-C17-H17 103.68(1), C16-C17-H17 120.68(1), Si1-Mo2-C17 47.14(9), N5-Mo1-C16 165.6(1), N5-Mo1-Si1 146.14(8), N11-Mo2-C17 162.6(1), N11-Mo2-Si1 150.10(8).

Furthermore, in all the aforementioned complexes the C16 and C17 atoms are both tetracoordinated and planar as evidenced by the sum of the angles around these atoms (Table 35). The addition of alkynes leads to a remarkable change of the Mo-Si-Mo unit in both compounds. Thus, in contrast to the metallasilylidyne **21-Mo**, the two Mo–Si bond lengths in **31-Mo** (*d*(Mo1–Si) = 2.278(3) [2.290(3)] Å, *d*(Mo2–Si) = 2.275(3) [2.281(3)] Å) and **32-Mo** (*d*(Mo1–Si) = 2.272(1) Å, *d*(Mo2–Si) = 2.287(1) Å) are almost equal, and surprisingly fall within the region observed for the Mo–Si triple bonds of metallasilylidyne complexes (*d*(Mo1–Si) = 2.287(2) Å (**21-Mo**), 2.266(1) Å (**23-Mo**)) (Table 29, Table 35). Such a shortening of both Mo–Si bonds could be rationalized on the basis of the high ring strain of the tricycles. Another striking structural change of the Mo-Si-Mo unit is the Mo-Si-Mo angle that becomes more widened upon alkyne addition compared to that in the metallasilylidyne complex **21-Mo** (Table 29, Table 35). For instance, the Mo1-Si1-Mo2 angle (176.80(5)**°**) in **32-Mo** is *ca*. 15 **°** wider than that of the metallasilylidyne complex **21-Mo** (162.93(7) **°**). The C16–C17 bond of compounds **31-Mo**

(1.37(1) [1.35(1)] Å) and **32-Mo** (1.382(5) Å) appears slightly longer than a $C(sp^2)$–$C(sp^2)$ double bond (1.34 Å) but significantly shorter than a $C(sp^3)$–$C(sp^3)$ single bond (1.54 Å), thus indicating considerable multiple bond character. The Si–C bond lengths in both complexes (**31-Mo**: Si1–C16 1.91(1) [1.91(1)] Å, Si1–C17 1.89(1) [1.91(1)] Å; **32-Mo**: Si1-C16 1.946(4) Å, Si1–C17 1.870(4) Å) are longer than the mean Si–$C(sp^2)$ bond lengths (1.818 Å) in silacyclopropenes, but compare very well with the mean Si–$C(sp^3)$ bond length (1.908 Å) in silacyclopropanes.[28] Interestingly, the symmetric alkyne, such as 2-butyne in compound **31-Mo** is also symmetrically bonded to both metal centers as evidenced by the almost equal Mo–C bond lengths (Mo1–C16 2.44(1) [2.45(1)] Å; Mo2–C17 2.45(1) [2.46(1)] Å), whereas in the case of unsymmetric alkynes, such as trimethylsilylacetylene in compound **32-Mo**, the terminal carbon is bonded more strongly to the molybdenum center than the internal carbon as evidenced by the shorter Mo2–C17 bond (2.383(4) Å) compared to the Mo1–C16 bond (2.468(3) Å).

Table 35. Selected bonding parameters of compounds **31-Mo**, **32-Mo**, **32-W** and **33-Mo**

Complex	M1-Si1 [Å]	M2-Si1 [Å]	C16-C17 [Å]	Si1-C16 [Å]	Si1-C17 [Å]	Mo1-C16 [Å]
[Tp'$(CO)_2$Mo1SiC(Me)C(Me)Mo2$(CO)_2$Tp'][a]	2.278(3)	2.275(3)	1.37(1)	1.91(1)	1.89(1)	2.44(1)
(**31-Mo**)	2.290(3)	2.281(3)	1.35(1)	1.91(1)	1.91(1)	2.45(1)
[Tp'$(CO)_2$Mo1SiC(H)C(TMS)Mo2$(CO)_2$Tp']	2.272(1)	2.287(1)	1.382(5)	1.946(4)	1.870(4)	2.468(3)
(**32-Mo**)						
[Tp'$(CO)_2$W1SiC(H)C(TMS)Mo2$(CO)_2$Tp']	2.283(1)	2.291(1)	1.395(5)	1.959(4)	1.889(4)	2.422(4)
(**32-W**)						
[Tp'$(CO)_2$Mo1SiC(H)C(Ph)Mo2$(CO)_2$Tp']	2.281(1)	2.287(1)	1.370(6)	1.968(4)	1.882(5)	2.472(4)
(**33-Mo**)	2.290(1)	2.289(1)	1.380(6)	1.968(4)	1.876(5)	2.476(4)

	Mo2-C17 [Å]	M1-Si1-M2 [°]	Σ(∠Si) [°]	Σ(∠C16) [°]	Σ(∠C17) [°]
[Tp'$(CO)_2$Mo1SiC(Me)C(Me)Mo2$(CO)_2$Tp']	2.45(1)	175.9(1)	360.1	360.4	360.4
(**31-Mo**)	2.46(1)	176.7(1)	359.8	360.0	360.1
[Tp'$(CO)_2$Mo1SiC(H)C(TMS)Mo2$(CO)_2$Tp']	2.383(4)	176.80(5)	359.4	360.2	359.86
(**32-Mo**)					
[Tp'$(CO)_2$W1SiC(H)C(TMS)Mo2$(CO)_2$Tp']	2.362(4)	179.58(5)	359.22	360.02	359.95
(**32-W**)					
[Tp'$(CO)_2$Mo1SiC(H)C(Ph)Mo2$(CO)_2$Tp']	2.351(4)	179.25(7)	359.46	359.76	359.92
(**33-Mo**)	2.330(4)	179.23(6)	359.02	359.57	359.6

[a]: Two independent molecules were found in the asymmetric unit.

28 A CSD survey (04.06.2016) gave 36 hits of silacyclopropenes with a Si–C mean and median bond length of 1.818 and 1.819 Å, respectively, and 41 hits for silacyclopropanes with a Si–C mean and median bond length of 1.908 and 1.879 Å, respectively.

Notably, the Mo–C bond lengths in all complexes are significantly longer than that of molybdenum alkyl complexes ($d(L_nMo–CX_3)_{Mean}$ = 2.218 Å; X = any non metal),[29] thus suggesting a very weak interaction between the molybdenum and carbon atoms of the alkyne fragments.

The solution NMR and IR spectra of all complexes corroborate well with the solid-state structures. The ^1H and $^{13}C\{^1H\}$ NMR spectra of **31-Mo** and **31-W** in C_6D_6 at ambient temperature reveal a C_{2v}-symmetric structure in solution as indicated by the appearance of only one set of signals for the two Tp' ligands, whereas those of **32-Mo**, **32-W** and **33-Mo** display a C_s-symmetric structure as suggested by the two sets of signals for two Tp' ligands in the molecules (Figure 80). The ^1H NMR spectrum of **32-Mo**, **32-W** and **33-Mo** displays a downfield-shifted signal for the C-H of the terminal alkyne fragment at δ = 10.36, 10.64 and 9.26 ppm, respectively, which is characteristic for a vinylic proton of a silirene ring.[199-202] These proton signals are accompanied by a pair of silicon satellites with a coupling constant of 10 – 14 Hz, which is typical for a classical $^2J_{SiH}$ coupling.[181, 203] The $^{13}C\{^1H\}$ NMR spectrum of all complexes exhibit downfield-shifted signals for the alkenic carbon of the SiC_2 rings which are very characteristic for well-known silirenes.[199, 200, 202, 204] For example, the $^{13}C\{^1H\}$ NMR spectrum of **33-Mo** displays two singlet signals at 154.0 ppm (PhC=*C*H) and 169.2 ppm (Ph*C*=CH) ppm, which compare very well with those of the silirene $(SiMe_3)_3SiSi(PhCCH)N(SiMe_3)Dipp$ (δ = 149.4 ppm (PhC=*C*H) and 169.7 ppm (Ph*C*=CH)).[202] Notably, a strong interaction of the alkyne fragment with the metal centers, along with the strong bonding to the silicon center, would have lead to the formation of a silacyclopropane type structure, and that would have given very high field-shifted signals for the C-*H* as well as for the *C*-R carbon atoms. The observed downfield-shifted signals for the corresponding C-*H* and *C*-R carbon atoms are clearly indicating of a silacyclopropene-type structure with a very weak interaction with the metal centers. The $^{29}Si\{^1H\}$ NMR spectrum of all complexes in C_6D_6 displays a singlet signal (δ = 204.3 ppm (**31-Mo**), 198.8 ppm ($^1J_{WSi}$ = 22 Hz) (**31-W**), 200.4 ppm (**32-Mo**), 186.1 ppm ($^1J_{WSi}$ = 24 & 15 Hz) (**32-W**) and 216.9 ppm (**33-Mo**)) (Table 34) for the planar tetracoordinated silicon atom, which appears significantly upfield-shifted compared to that of the corresponding metallasilylidyne complexes (Table 30).

29 A CSD survey (04.06.2016) gave 365 hits for the Mo–C single bond in a $L_nMo–CX_3$ environment with a mean and median Mo–C bond length of 2.218 and 2.205 Å, respectively.

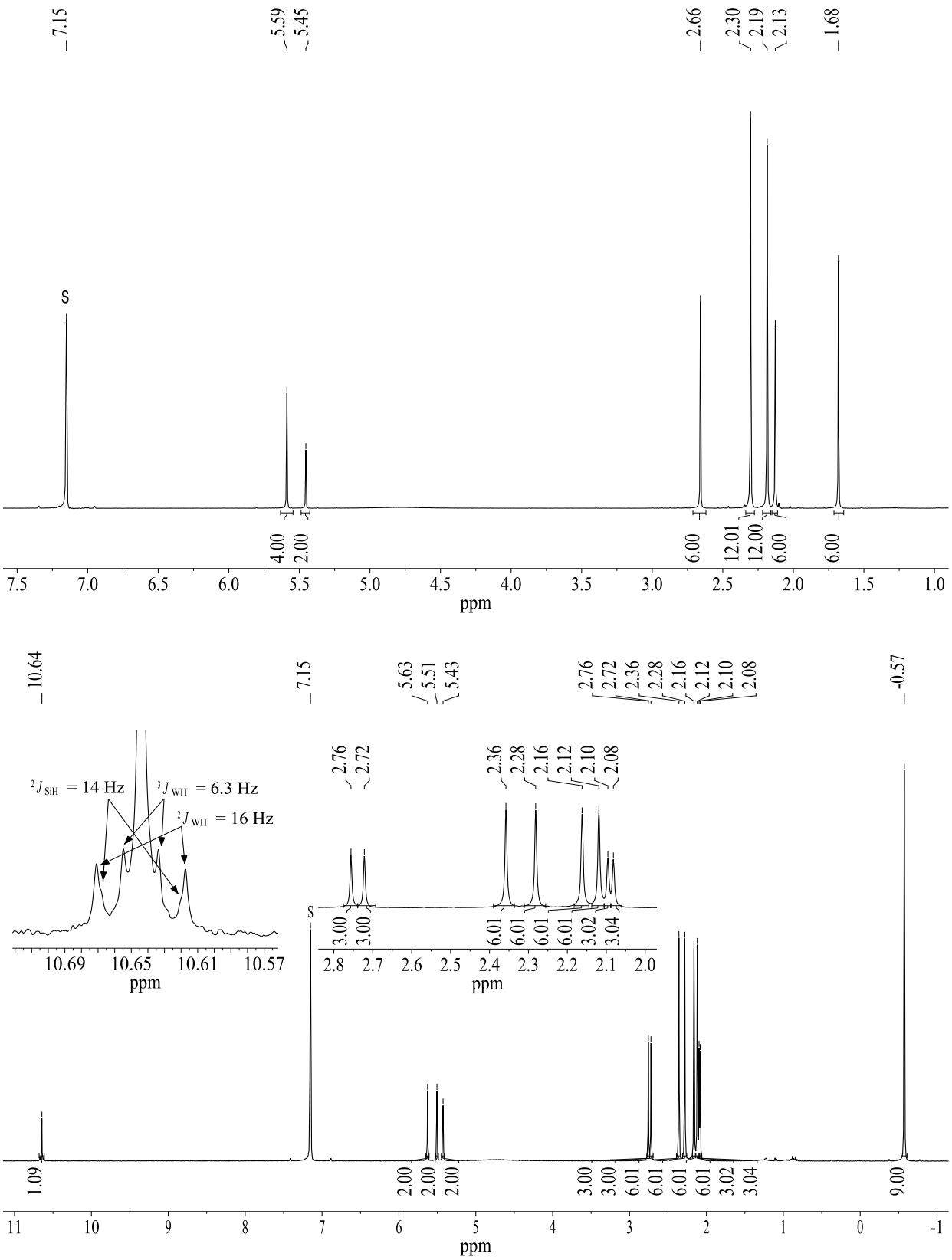

Figure 80. ^{1}H NMR spectrum (300.1 MHz) of **31-Mo** (top) and **32-W** (bottom) in C_6D_6. The character S denotes the residual proton signal of the deuterated solvent.

Interestingly, although the W–Si bonds in **32-W** are short and compare very well with the W≡Si triple bond of the metallasilylidyne **21-W**, the $^{1}J_{WSi}$ coupling constant of **32-W** is considerably lowere (15 – 24 Hz) than that in **21-W** ($^{1}J(W^{1},Si)$ = 250 Hz). However, the $^{1}J(W^{1},Si)$ coupling constant of **32-W** compares very well with the $^{1}J(W^{2},Si)$ coupling constant in **21-W** (20 Hz), thus indicating a very low s-character in both W-Si bonds.

The solution IR spectra of all cycloaddition products show a similar pattern with four ν_{CO} absorption bands, that are slightly shifted towards higher wavenumbers compared to their corresponding metallasilylidyne complexes (Table 34). For instance, the IR spectrum of **31-Mo** in THF solution displays four ν_{CO} absorption bands at 1943 (s), 1898 (w), 1869 (vs) and 1828 (w) cm^{-1} (Figure 81), which are shifted to higher frequency compared to those observed for the metallasilylidyne **21-Mo** (ν_{CO}: 1933 (s), 1870 (vs), 1857 (s, sh), 1806 (m), 1794 (m, sh) cm^{-1}; Figure 57, *vide supra*). Interestingly, the aforementioned spectra display two ν_{CO} absorption bands that are significantly weaker in intensity compared to the other two. This phenomenon could not be rationalized yet.

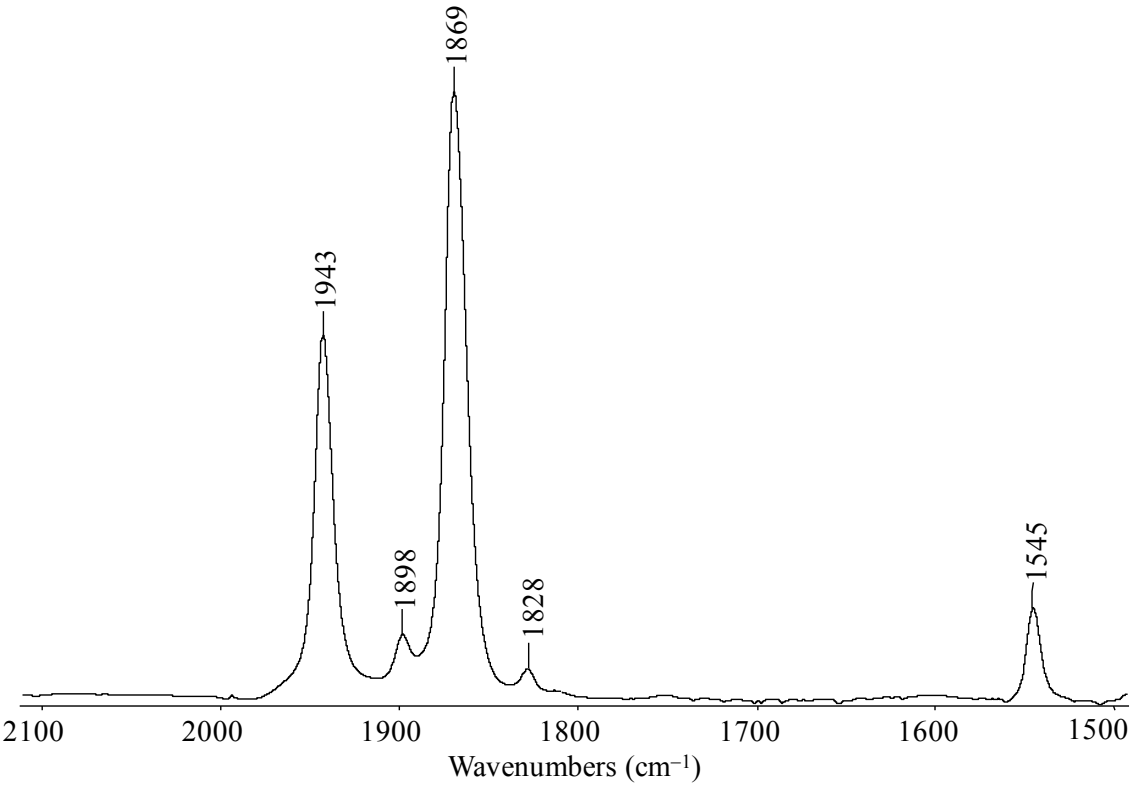

Figure 81. FT-IR spectrum (2100 – 1500 cm^{-1}) of **31-Mo** in THF.

In an attempt to delineate the bonding of these new cycloaddition products more clearly, detailed quantum chemical calculations were carried out on **31-Mo** at the RI-JCOSX/B97-D3/def2-TZVP level of theory. Geometric optimization of **31-Mo** afforded a minimum structure with an excellent agreement between the calculated bonding parameters and the experimental values obtained by single-crystal X-ray diffraction studies (Figure 82, Table 36). The optimized structure indeed affirms the presence of the planar tetracoordinated silicon (ptSi) with significant bonding interaction with the two molybdenum and two carbon (C16 and C17) centers as indicated by the very short Mo–Si (Mo1–Si1 2.290 Å, Mo2–Si1 2.291 Å) and Si–C (Si1–C16 1.915 Å, Si1–C17 1.910 Å) bonds.

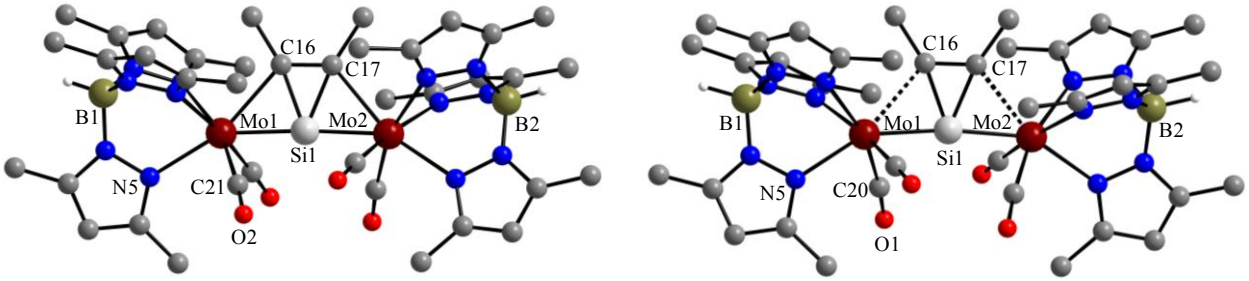

31-Mo **(31-Mo)$_{calc}$**

Figure 82. Experimental (left) and calculated (right) structures of compound **31-Mo**. The calculation was carried out at the RI-JCOSX/B97-D3/def2-TZVP level of theory. The H atoms, except those bonded to B, were omitted for clarity. Atom numbering of the experimental structure was taken over in the calculated structure.

Table 36. Comparison of selected experimental and calculated bonding parameters of **31-Mo** and **(31-Mo)$_{calc}$**

Complex	M1-Si1 [Å]	M2-Si1 [Å]	C16-C17 [Å]	Si1-C16 [Å]	Si1-C17 [Å]	Mo1-C16 [Å]
31-Mo[a]	2.278(3)	2.275(3)	1.37(1)	1.91(1)	1.89(1)	2.44(1)
	2.290(3)	2-281(3)	1.35(1)	1.91(1)	1.91(1)	2.45(1)
(31-Mo)$_{calc}$	2.290	2.291	1.375	1.915	1.910	2.510

	Mo2-C17 [Å]	M1-Si1-M2 [°]	Σ(∠Si) [°]	Σ(∠C16) [°]	Σ(∠C17) [°]
31-Mo	2.45(1)	175.9(1)	360.1	360.4	360.4
	2.46(1)	176.7(1)	359.8	360.0	360.1
(31-Mo)$_{calc}$	2.537	172.25	360.74	360.78	360.66

[a]: Two independent molecules were found in the asymmetric unit.

The structure was further supported by the natural bond orbital (NBO) analysis. Thus, one σ NBO was found for each Mo–Si bond being highly polarized towards the molybdenum atoms,

with an occupancy of 1.59e (Mo1–Si1) and 1.34e (Mo2–Si1) leading to a Wiberg bond index (WBI) of 0.69 for each bond (Table 37). Similarly, one σ NBO was also found for each Si–C bond being also highly polarized towards the carbon atoms with an occupancy of 1.60e (Si1–C16) and 1.63e (Si1–C17). This leads to a Wiberg bond index (WBI) of 0.45 and 0.46 for the Si1–C16 and Si1–C17 bond, respectively (Table 37). Furthermore, one σ NBO and one π NBO, which are almost unpolarized, were found for the C16–C17 bond having a population of 1.95e and 1.87e, respectively, clearly supporting the silacyclopropene-type structure (Table 37). This was also reflected by the Wiberg bond index of 1.76 for the C16–C17 bond. As expected, no NBO was found for the Mo1–C16 and Mo2–C17 bonds, thus indicating a very weak or no interaction between the Mo and C16/C17 atoms. Finally, the charge distribution in **31-Mo** was studied by natural population analysis (NPA), which revealed that the addition of an alkyne leads to a significant increase of the partial positive charge of the silicon atom from +0.76 in **21-Mo** to +1.29 in **31-Mo**. Similarly, the partial negative charge of both molybdenum atoms also decreases from –0.59 (Mo1) and –0.50 (Mo2) in **21-Mo** to –0.38 for both atoms in **31-Mo**.

Table 37. Selected results of the natural bond orbital (NBO) analysis of **(31-Mo)$_{calc}$** at the RI-JCOSX/B97-D3/def2-TZVP level of theory. Atom numbering of the experimental structure was taken over in the calculated structure **(31-Mo)$_{calc}$**.[a]

	NBO analysis				NPA partial charges[b]	
	occ.	pol. [%]	hyb.	WBI		
σ(Mo1–Si1)	1.59	60.9 (Mo1) 39.1 (Si1)	$sd^{4.21}$ (Mo1) $sp^{0.91}$ (Si1)	0.69	Mo1	−0.38
σ(Mo2–Si1)	1.34	88.2 (Mo2) 11.8 (Si1)	$sd^{12.12}$ (Mo2) p (Si1)	0.69	Mo2	−0.38
σ(Si1–C16)	1.60	23.2 (Si1) 76.8 (C16)	$sp^{5.63}$ (Si1) $sp^{2.85}$ (C16)	0.45	Si1	1.29
σ(Si1–C17)	1.63	26.9 (Si1) 73.1 (C17)	$sp^{2.01}$ (Si1) $sp^{2.90}$ (C17)	0.46	C16	–0.31
σ(C16–C17)	1.95	49.9 (C16) 50.1 (C17)	$sp^{1.85}$ (C16) $sp^{1.83}$ (C17)	1.76	C17	–0.32
π(C16–C17)	1.87	49.9 (C16) 50.2 (C17)	p (C16) p (C17)			

[a]: occ. = occupancy, pol. = polarization, hyb. = hybridization, WBI = Wiberg bond index. [b]: Partial charges obtained by natural population analysis (NPA).p

2.7.6 Reactivity of metallasilylidyne complexes towards phosphaalkyne

Similarly to alkynes, the metallasilylidyne **21-Mo** also reacts with the phosphaalkyne ^{t}BuC≡P at elevated temperature. However, in contrast to the alkynes, which afford a silacyclopropene type structure with a weak interaction of the alkyne with the metal centers, the reaction with ^{t}BuC≡P leads to the metallaphosphasilacyclobutadiene [Tp'(CO)$_2$Mo(PC^{t}Bu)SiMo(CO)$_2$Tp'] (**34-Mo**) (Scheme 25). The reaction of **21-Mo** with an excess of ^{t}BuC≡P in chlorobenzene leads to the formation of **34-Mo** along with a small amount of radical **2-Mo** as observed by *in situ* IR spectroscopy. Compound **34-Mo** was isolated after workup as an air-sensitive, dark-brown solid in 42% yield (Scheme 25). The dark-brown solid is moderately soluble in CH_2Cl_2, sparingly soluble in THF or chlorobenzene and insoluble in toluene, Et_2O, and aliphatic solvents. It slowly decomposes in CH_2Cl_2 to form Tp'Mo(CO)$_2$(PMe$_3$)Cl and a mixture of unknown compounds.

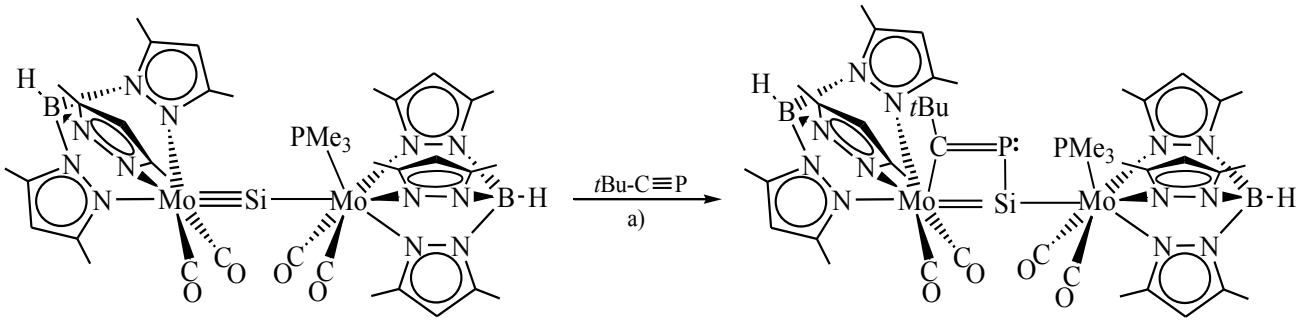

34-Mo, dark-brown solid, 42%

Scheme 25. Addition of ^{t}BuC≡P to the metallasilylidyne complex **21-Mo**. a) chlorobenzene, 100 °C.

Compound **34-Mo** was characterized by multinuclear NMR and IR spectroscopy, and the composition was confirmed by elemental analysis. Several attempts to crystallize the compound from THF or fluorobenzene failed due to the low solubility in these solvents, whereas insufficient stability of **34-Mo** for prolonged time in CH_2Cl_2 hindered the formation of suitable single crystals. The solid state IR spectrum displays three ν_{CO} absorption bands at 1895 (s), 1810 (vs) and 1761 (vs) cm^{-1}, which appear at significantly lower wavenumbers than those of the metallasilylidyne **21-Mo** (ν_{CO}: 1928 (s), 1861 (vs) and 1791 (s) cm^{-1}), suggesting an overall increase of the electron density in the molecule resulting from the addition of the ^{t}BuC≡P. Interestingly, akin to the metallasilylidyne **21-Mo**, the solution IR spectrum of **34-Mo** in CH_2Cl_2 also exhibits five ν_{CO} absorption bands at 1899 (s), 1839 (s), 1816 (vs), 1774 (m) and 1770 (m) cm^{-1}, indicating the presence of more than one rotamer in solution with respect to the Mo–Si

single bond. The ^{1}H and $^{13}C\{^{1}H\}$ NMR spectra of the compound in CD_2Cl_2 at ambient temperature reveal a time-averaged C_s-symmetric structure in solution, suggesting a very fast rotation of the PMe_3 bearing molybdenum fragment about the Mo–Si single bond on the NMR time scale. The $^{13}C\{^{1}H\}$ NMR spectrum in CD_2Cl_2 displays a characteristic downfield-shifted doublet signal at δ = 194.2 ppm for the P=*C* carbon atom with a $^{1}J_{CP}$ coupling constant of 41.5 Hz. In addition, the $^{13}C\{^{1}H\}$ NMR spectrum also reveals two very lowfield-shifted doublet signals at δ = 230.1 and 240.3 ppm with a J_{CP} coupling constant of 5.3 Hz and 16.3 Hz, respectively. The signal at 230.1 ppm with the J_{CP} coupling constant of 5.3 Hz compares very well with that observed for the carbonyl ligands of the seven-coordinated molybdenum fragment of **21-Mo** (δ = 231.6 ppm (d, $^{2}J_{CP}$ = 5.5 Hz)), and thus can be assigned to the carbonyl ligands bonded to the PMe_3 containing molybdenum fragment. The other carbonyl signal, which appears at lower field than the corresponding CO resonance of the metallasilylidyne **21-Mo** (δ = 229.3 ppm (d, $^{4}J_{CP}$ = 1.3 Hz)), displays a remarkably stronger coupling ($^{3}J_{CP}$ = 16.3 Hz) with the phosphorus nucleus of the metallaphosphasilacyclobutadiene ring than that expected for a $^{3}J_{CP}$ coupling (<10 Hz). The latter observation suggests the presence of a transannular interaction from the phosphorus center to the molybdenum center. Attempts to detect the $^{29}Si\{^{1}H\}$NMR resonance signal of **34-Mo** failed due to the low solubility of the compound in common organic solvents. The $^{31}P\{^{1}H\}$NMR spectrum shows a characteristic strongly lowfield-shifted doublet signal at δ = 461.4 ppm with a J_{PP} coupling constant of 46.5 Hz for the phosphorus atom of the metallaphosphasilacyclobutadiene ring, together with an another doublet signal for the PMe_3 ligand at –8.2 ppm with the same coupling constant (Figure 83). Interestingly, the J_{PP} coupling constant of 46.5 Hz is markedly larger than a P,P three-bond coupling and can only be rationalized by the well-known through-space coupling.[205, 206] Notably, a through-space coupling would be favourable only when the phosphorus atom of the metallaphosphasilacyclobutadiene ring is located in close proximity to the PMe_3 ligand. Accordingly, this would justify the postulated structure, although it would be contradictory to the outcome of the known reaction between $^{t}BuC{\equiv}P$ and the osmium silylidyne complex $[(Cp^*)(^{i}Pr_3P)(H)Os{\equiv}Si(Trip)][HB(C_6F_5)_3]$ which gives the [2+2] cycloaddition product $[(Cp^*)(^{i}Pr_3P)(H)Os{=}Si(Trip)(P{=}C^{t}Bu)][HB(C_6F_5)_3]$ containing a osmium phosphinidene moiety.[58] Notably, this osmium phosphinidene complex also displays a very lowfield-shifted $^{31}P\{^{1}H\}$NMR signal at 516 ppm in bromobenzene-d_5 for the phosphinidene phosphorus atom (Os=*P*).

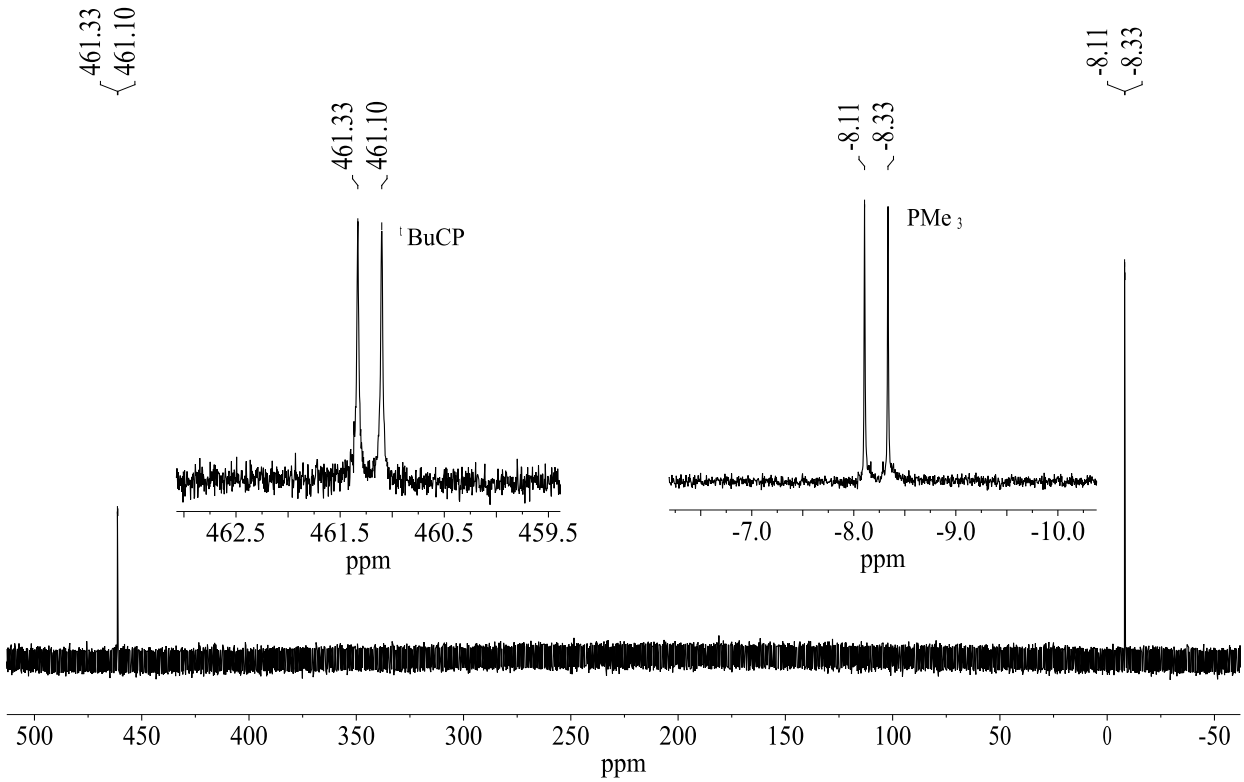

Figure 83. $^{31}P\{^{1}H\}$ NMR spectrum (202.5 MHz) of **34-Mo** in CH_2Cl_2 showing the two doublet resonance signals for the two different phosphorus nuclei.

2.8. Plumbylidyne transfer reaction

The chemistry of complete intermetallic transfer of a triply bonded ligand system of main group elements is a very important class of reactions for both biological and synthetic chemistry, and has surprisingly developed for mostly group 15 and 16 elements.[207-210] Comparatively, this class of reactions are far less developed in case of group 14 elements. After the first report by E. O. Fischer in 1975 of a carbyne ligand transfer reaction from chromium to cobalt,[211] only very few examples have been reported for a complete transfer of a carbyne ligand from one metal center to another.[212, 213] In sharp contrast, this important class of transfer reactions are almost unexplored in the case of the recently emerged heavier analogues of carbyne complexes [$L_nM{\equiv}ER$] (E = Si – Pb). Only very recently, a germylidyne ligand transfer reaction was shown by Filippou and co-workers, where a germylidyne ligand was transferred from a rhenium to a molybdenum center (Scheme 26).[55] Apart from this, no example is known for a tetrylidyne ligand transfer reaction.

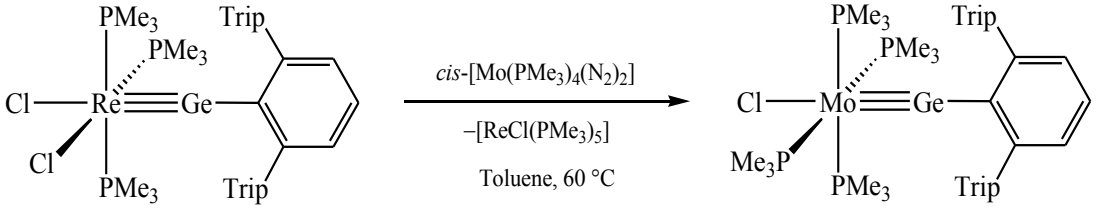

Scheme 26. Germylidyne ligand transfer reaction from a rhenium germylidyne to a Mo-center.

Recent theoretical studies on transition metal ylidyne complexes have shown that the bond dissociation energy of the M≡E bond gradually decreases from C to Pb, and this energy decreases further upon moving from 3rd- to 2nd-row transition metals.[214] These results indicate that 1st-row transition metal plumbylidyne complexes would have much lower M≡Pb bond dissociation energies and might undergo intermetallic plumbylidyne ligand (RPb^+) transfer in the presence of a suitable metal precursor. In fact, recent studies by Filippou and co-workers have shown that the manganese plumbylidyne complex [(η^5-C_5H_4Me)$(CO)_2$Mn≡Pb(C_6H_3-2,6-$Trip_2$)][B(C_6H_3-3,5-$(CF_3)_2)_4$], which was obtained by the reaction of PPN[MnCl(η^5-C_5H_4Me)$(CO)_2$] (**3-Mn**) with one equivalent of PbI(C_6H_3-2,6-$Trip_2$), and subsequent chloride abstraction from the intermediate choloroplumbylidene complex [(η^5-C_5H_4Me)$(CO)_2$Mn=Pb(Cl)(C_6H_3-2,6-$Trip_2$)] with one equivalent of Na[B(C_6H_3-3,5-$(CF_3)_2)_4$] (Scheme 27), is highly reactive towards polar coordinating solvents, such as THF or Et_2O.[54]

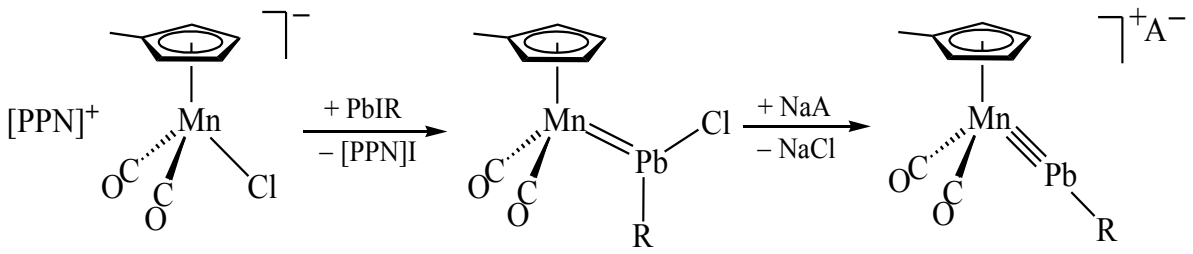

R = C_6H_3-2,6-$Trip_2$, $A^- = [B(C_6H_3\text{-}3,5\text{-}(CF_3)_2)_4]^-$

Scheme 27. Reported synthesis of the manganese plumbylidyne from **3-Mn**.

It was also observed that this plumbylidyne complex reacts with NaCl forming back the corresponding chloroplumbylidene complex [(η^5-C_5H_4Me)$(CO)_2$Mn=Pb(Cl)(C_6H_3-2,6-$Trip_2$)]. Furthermore, the reaction of this plumbylidyne complex with an excess of PMe_3 resulted in the formation of [(η^5-C_5H_4Me)Mn$(CO)_2(PMe_3)$] and presumably [Pb$(PMe_3)_2$(C_6H_3-2,6-$Trip_2$)][B{C_6H_3-3,5-$(CF_3)_2$}$_4$],[30] analogous to the lead cation [Pb$(py)_2$(C_6H_3-2,6-$Trip_2$)][B$(C_6F_5)_3$(Me)] (py = pyridine), reported by Power et al., in 2004,[215] upon cleavage of the Mn≡Pb bond (Scheme 28).

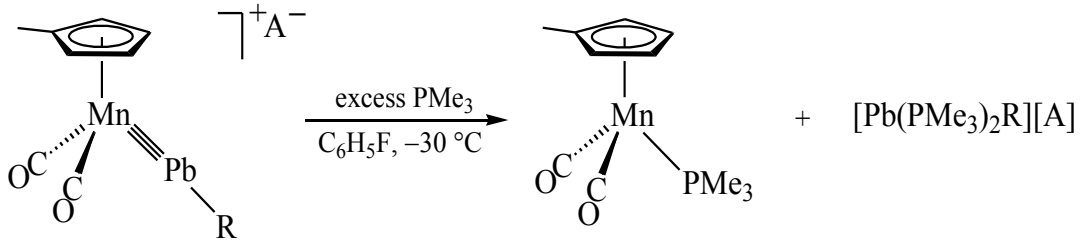

R = C_6H_3-2,6-$Trip_2$; A = $B(C_6H_3\text{-}3,5\text{-}(CF_3)_2)_4$

Scheme 28. Reaction of the manganese plumbylidyne with free PMe_3.

As shown earlier, the metalate salt Na[Tp'Mo$(CO)_2(PMe_3)$] (**3-Mo**) is a very strong metal-centered nucleophile, which reacts with Pb(X)R (X = Cl – I; R = C_6H_3-2,6-Mes_2, C_6H_3-2,6-$Trip_2$) to afford selectively after metathetical halide exchange and PMe_3 elimination the corresponding plumbylidyne complexes [Tp'$(CO)_2$Mo≡Pb–R]. Both complexes are thermally stable, but are light sensitive and compared to the C_6H_3-2,6-Mes_2 substituted compound, the C_6H_3-2,6-$Trip_2$ substituted compound is much more light sensitive, thus preventing the isolation of the later compound in an analytically pure form. Following these observations, my goal was to develop

30 Several attempts to isolate this lead cation were unsuccessful due to its extremely high light and air-sensitivity.

the synthesis of a manganese plumbylidyne complex bearing the C_6H_3-2,6-Mes_2 substituent, following a similar approach to that used for the corresponding C_6H_3-2,6-$Trip_2$ substituted plumbylidyne complex, and subsequently to investigate its reactivity towards the metalate **3-Mo** for a potential plumbylidyne ligand transfer between the manganese and the molybdenum centers.

2.8.1 Manganese plumbylidene complexes

In order to obtain the C_6H_3-2,6-Mes_2 substituted manganese plumbylidene complex, **3-Mn** was reacted with PbX(C_6H_3-2,6-Mes_2) (X = Cl – I) following the same approach used for the C_6H_3-2,6-$Trip_2$ substituted plumbylidene complex [(η^5-C_5H_4Me)$(CO)_2$Mn=Pb(Cl)(C_6H_3-2,6-$Trip_2$)].[54] Surprisingly, in this case, the reaction proceeds via the manganese dihaloplumbyl complexes. Notably, similar results were also observed earlier during the synthesis of the manganese stannylidene complexes [(η^5-C_5H_4R)$(CO)_2$Mn=Sn(Cl)(C_6H_3-2,6-$Trip_2$)] (R = H, Me) (Scheme 29).[54]

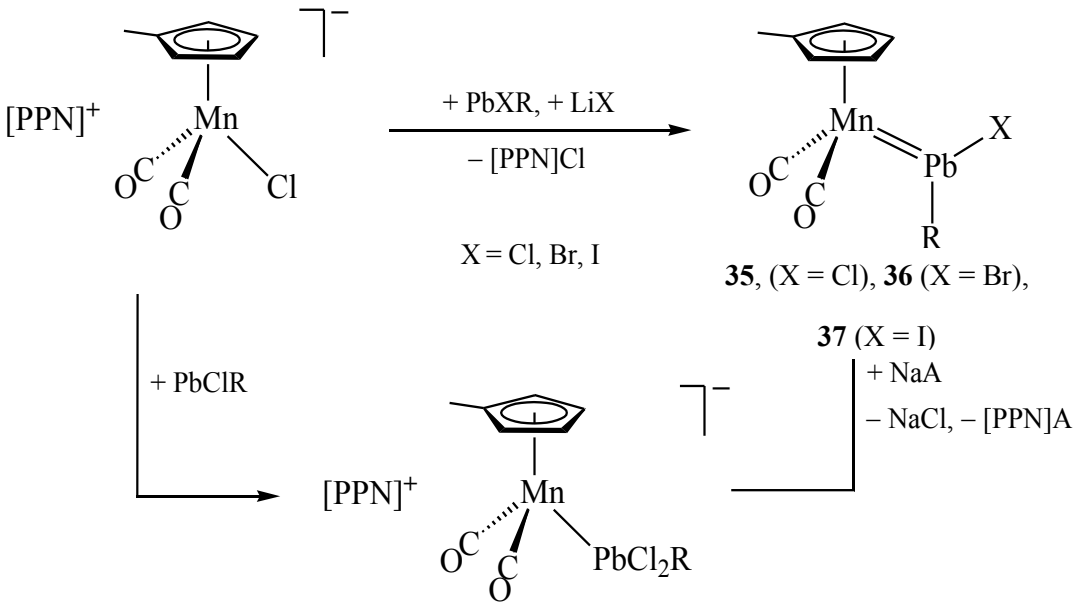

R = C_6H_3-2,6-Mes_2; A = $B(C_6H_3$-3,5-$(CF_3)_2)_4$

Scheme 29. Syntheses of the manganese plumbylidene complexes.

Unfortunately, in this case using PbX(C_6H_3-2,6-Mes_2) (X = Cl – I) the reactions did not selectively lead to the respective anionic dihaloplumbyl complexes [PPN][(η^5-C_5H_4Me)$(CO)_2$Mn–PbX_2(C_6H_3-2,6-Mes_2)]. An IR spectroscopic inspection of the reaction mixtures in all cases revealed a mixture of a haloplumbylidene complex, an anionic

dihaloplumbyl complex, and unreacted starting material along with a very small amount of [(η^5-C_5H_4Me)$Mn(CO)_3$] (Figure 84). Nevertheless, the reactions with $PbBr(C_6H_3$-2,6-$Mes_2)$ in the presence of LiBr or $PbI(C_6H_3$-2,6-$Mes_2)$ in the presence of LiI in a mixture of THF/*n*-hexane solvent directly affords the desired bromoplumbylidene complex [(η^5-C_5H_4Me)$(CO)_2Mn$=$Pb(Br)(C_6H_3$-2,6-$Mes_2)$] (**36**) and the iodoplumbylidene complex [(η^5-C_5H_4Me)$(CO)_2Mn$=$Pb(I)(C_6H_3$-2,6-$Mes_2)$] (**37**), respectively, which were isolated after workup as air-sensitive, brown solids in moderate yields (40 – 47%). In contrast, the attempt for the direct synthesis of the chloroplumbylidene complex [(η^5-C_5H_4Me)$(CO)_2Mn$=$Pb(Cl)(C_6H_3$-2,6-$Mes_2)$] (**35**) by the addition of LiCl and $PbCl(C_6H_3$-2,6-$Mes_2)$ did not work. However, addition of one equivalent of a nonoxidizing halide abstracting agent such as $Na[B\{C_6H_3$-3,5-$(CF_3)_2\}_4]$ in fluorobenzene afforded selectively the chloroplumbylidene complex **35** (Figure 84), which was isolated after workup as an air-sensitive, red-brown solid in 58% yield (Scheme 29).

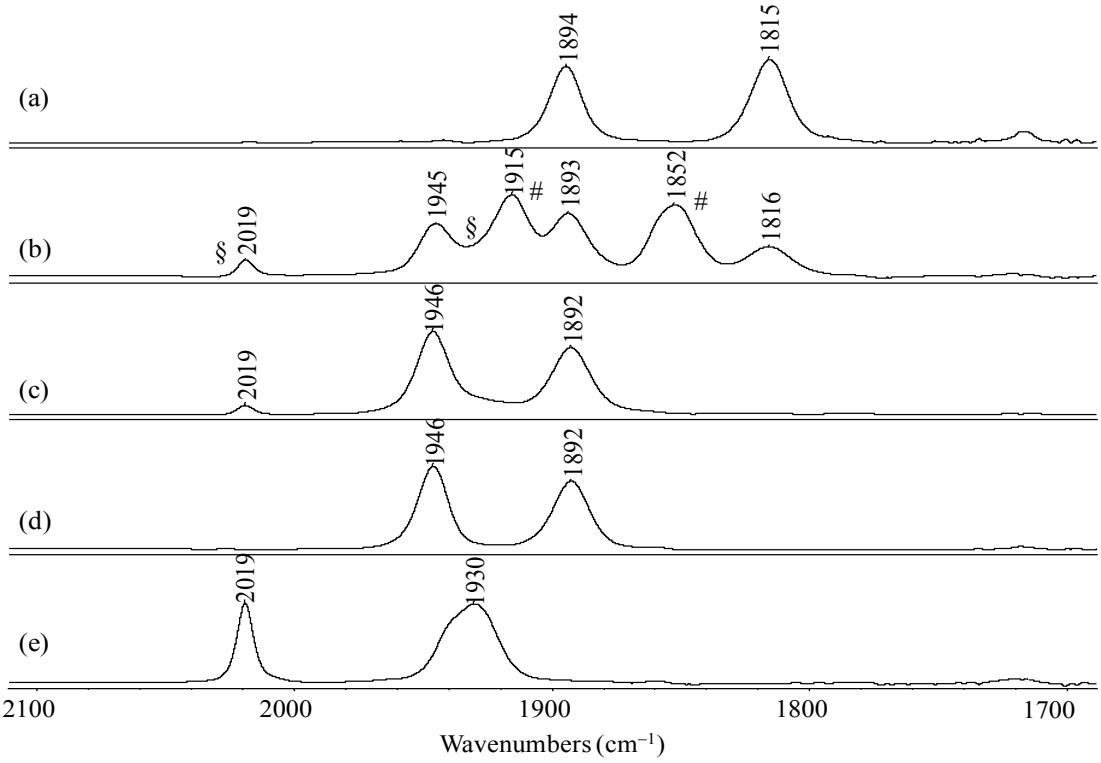

Figure 84. FT-IR spectra (in fluorobenzene) in the region of 2100 – 1700 cm^{-1}: (a) of pure complex **3-Mn**; (b) of the reaction of **3-Mn** with $PbCl(C_6H_3$-2,6-$Mes_2)$ in fluorobenzene after 3 hours of stirring (the ν_{CO} bands of the dichloroplumbyl complex PPN[(η^5-C_5H_4Me)$(CO)_2Mn\{PbCl_2(C_6H_3$-2,6-$Mes_2)\}$] and those of [(η^5-C_5H_4Me)$Mn(CO)_3$] are marked with the characters # and §, respectively); (c) of the reaction

of **3-Mn** with $PbCl(C_6H_3\text{-}2,6\text{-}Mes_2)$ in fluorobenzene after 3 hours of stirring and addition of one equivalent of $Na[B\{C_6H_3\text{-}3,5\text{-}(CF_3)_2\}_4]$; (d) of pure complex **35**; (e) of $[(\eta^5\text{-}C_5H_4Me)Mn(CO)_3]$.

All plumbylidene complexes are light sensitive and hence their synthesis was carried out under exclusion of light using brown glass Schlenck tubes. The haloplumbylidene complexes are quite thermally stable solids. The chloroplumbylidene complex **35** starts to decompose at 144 – 145 °C to give a dark brown solid, which melts to a black liquid at 152 – 154 °C.

Due to the similar structural and spectroscopic properties of compounds **35** – **37**, only compound **35** will be discussed in detail. To determine the molecular structure of **35**, suitable red-brown single crystals were grown by slow cooling of a *n*-pentane solution of **35** at +5 °C, and analysed by single crystal X-ray diffraction analysis. The molecular structure of the three-legged piano-stool complex exhibits a very short Mn–Pb bond (d(Mn–Pb) = 2.4699(9) Å) with a trigonal planer Pb atom ($\Sigma\angle$Pb = 359.96°) (Figure 85). The Mn–Pb bond length in **35** is comparable with that observed in the C_6H_3-2,6-$Trip_2$ substituted chloroplumbylidene complex $[(\eta^5\text{-}C_5H_4Me)(CO)_2Mn{=}Pb(Cl)(C_6H_3\text{-}2,6\text{-}Trip_2)]$ (d(Mn–Pb) = 2.492(1) Å), which has been earlier reported by Filippou and co-workers,[54] and also with those of literature known Mn=Pb bonded complexes such as $[\{(C_5H_4Me)(CO)_2Mn\}_3Pb]$ (d(Mn–Pb) = 2.490(1)Å)[86, 91] and $[(\mu\text{-}Pb)\{(CpMn(CO)_2\}_2]$ (d(Mn–Pb) = 2.463(1) Å).[86, 89] The Mn–Pb bond length of **35** is however much shorter than the average Mn–Pb single bond lengths (2.511 – 2.703 Å).[31] The Pb–Cl bond length in **35** (2.605(1) Å) is in the range observed for base-stabilized lead chlorides (d(Pb–Cl): 2.565 – 2.647 Å).[32] Notably, in compound **35**, one of the CO ligands is coplanar with the plumbylidene ligand plane with the *m*-terphenyl substituent pointing towards the CO ligand and the chloride located between the Cp' ring and the other CO ligand (Figure 85). This situation is best illustrated by the torsion angles of C(31)-Mn-Pb-C(1) 7.5(4)°, C(32)-Mn-Pb-C(1) 100.9(4)° and C(32)-Mn-Pb-Cl 80.0(3)°. The Mn-Pb-C_{aryl} angle in complex **35** is widened up to 149.9(1)°, probably owing to the large steric demand of the *m*-terphenyl substituent and/or the partial triple bond character of the Mn–Pb bond. The C_{aryl}-Pb-Cl angle is lowered to 96.5(1)°, which indicates the low tendency of the lead atom to undergo sp^2-hybridization. These structural features fit well

31 A CSD search (07.03.2016) has shown only 5 structurally characterized complexes having Mn-Pb single bond with a four-coordinated lead atom. d(Mn–Pb): 2.511 – 2.703 Å, Mean: 2.612, Median: 2.616.

32 A CSD search (07.03.2016) has shown only 10 structurally characterized compounds having a three-coordinated lead atom bonded to chloride. d(Pb–Cl): 2.534 – 2.846 Å, Mean: 2.644, Median: 2.647.

with those of previously isolated chlorogermylidene and chlorostannylidene complexes of electron-rich transition metals.[55, 56, 136] Notably, the Pb–C_{aryl} bond length in the plumbylidene complex **35** (2.206(5) Å) is shorter than that observed in the metalloplumbylene complexes [$Cp(CO)_3M$–$Pb(C_6H_3$-2,6-$Trip_2)$] (M = Cr, Mo, W) (2.278(9) – 2.294(4) Å),[32] or in the dimeric bromoplumbylene [$PbBr(C_6H_3$-2,6-$Trip_2)]_2$ (2.329(11) Å).[216]

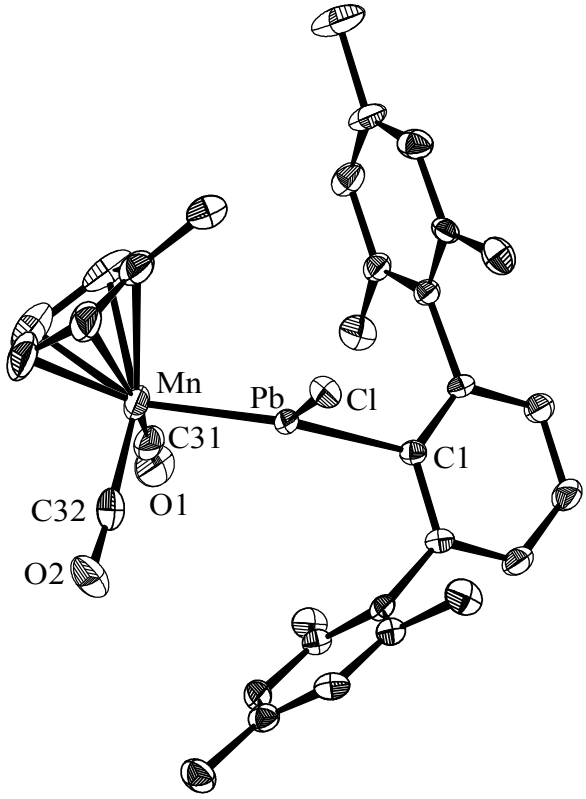

Figure 85. DIAMOND plot of the molecular structure of complex **35**. The thermal ellipsoids represent 30 % of the electronic probability at 123(2) K. Hydrogen atoms are omitted for clarity. Selected bond lengths [Å] and bond angles [°]: Mn-Pb 2.4699(9), Pb-C(1) 2.206(5), Pb-Cl 2.605(1), Mn-C(31) 1.772(8); Mn-C(32) 1.781(8), Mn-Pb-C(1) 149.9(1), Mn-Pb-Cl 113.56(4), C(1)-Pb-Cl 96.5(1), C(31)-Mn-C(32) 93.3(3), Pb-Mn-C(31) 91.7(2), Pb-Mn-C(32) 93.1(2).

The solution IR and NMR spectra of the compound **35** corroborate well with the solid-state structure. The IR spectrum in fluorobenzene displays two strong ν_{CO} absorption bands of almost equal intensity at 1946 and 1892 cm^{-1}, which appear at higher wavenumbers than those of the metalate PPN[$MnCl(\eta^5$-$C_5H_4Me)(CO)_2$] (**3-Mn**) (ν_{CO} in fluorobenzene: 1894 (vs) and 1815 (vs) cm^{-1}), or the complexes [$(\eta^5$-$C_5H_4Me)Mn(CO)_2(PMe_3)$] (ν_{CO} in C_6H_5F 1924, 1856 cm^{-1}), [$CpMn(CO)_2$(Pyridine)] (ν_{CO} in hexane 1935, 1869 cm^{-1}).[217] In fact, the ν_{CO} absorption bands

appear at higher wavenumbers than those of the indium(I) complex [Cp(CO)$_2$MnIn(C$_6$H$_3$-2,6-Trip$_2$)] (ν_{CO} in nujol 1940, 1864 cm^{-1})[218] but lower than those of the borylene complex [Cp(CO)$_2$Mn=B(Bu^t)] (ν_{CO} in C$_6$H$_6$ 1968, 1912 cm^{-1}),[219] or the alkylidene complex [Cp(CO)$_2$Mn=C(C$_6$H$_5$)Cl] (ν_{CO} in CH$_2$Cl$_2$: 1995, 1935 cm^{-1}).[220] This suggests that the σ-donor/π-acceptor ratio of the ligands decreases in the series C(Ph)Cl < BR < PbRCl < Py < PMe$_3$.

The ^{1}H and ^{13}C{^{1}H} NMR spectra of compound **35** reveal an overall C_s-symmetric structure in solution at room temperature and display a single set of signals for the *ortho* H and C nuclei of the terphenyl substituent. The variable temperature ^{1}H and ^{13}C{^{1}H} NMR spectroscopy for compound **35** in CD$_2$Cl$_2$ show a double set of resonances for the *ortho*-CH$_3$ nuclei below −70 °C (Figure 86), suggesting a hindered rotation around the Pb-C$_{aryl}$ bond of the molecule in which the *m*-terphenyl substituent is fixed in the orthogonal conformation. Notably, the exchange of the halide substituents on the lead atom affects the rotation of the terphenyl substituent as evidenced by the line broadening of the *ortho*-Me signals of the mesityl substituents. The peak width at half height ($\Delta\nu_{1/2}$) of the *ortho*-CH$_3$ signals of the mesityl groups increases upon going from the chloroplumbylidene complex (**35**) to the iodoplumbylidene complex (**37**) (**35**: 3.4 Hz; **36**: 8.7 Hz; **37**: 18.4 Hz) (Figure 86). This increasing line broadening can be rationalized by the increasing size of the halide substituent, which prevents the fast rotation of the *m*-terphenyl group around the Pb-C$_{aryl}$ bond. In the ^{13}C{^{1}H} NMR spectrum of **35** the characteristic downfield shifted resonance for the lead-bonded C$_{aryl}$ atom appears at 242.7 ppm.

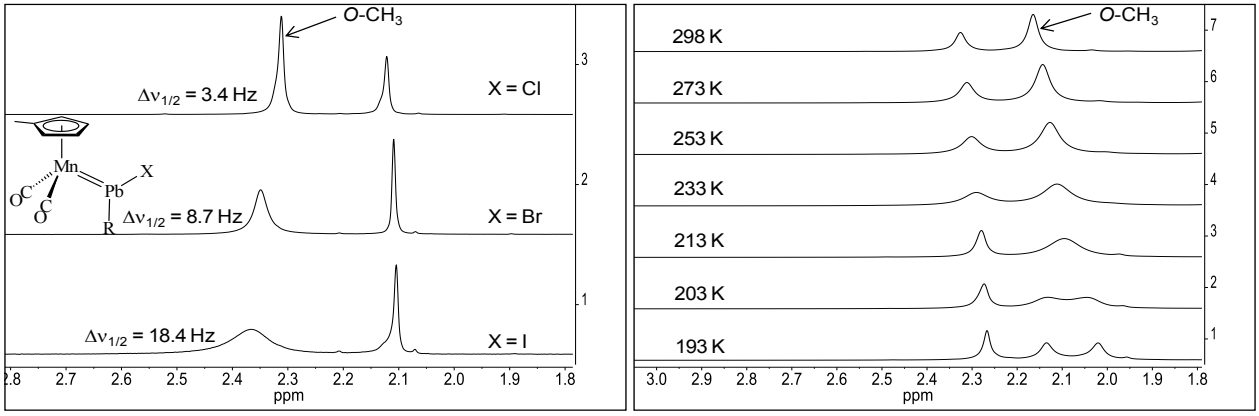

Figure 86. Stacked ^{1}H NMR spectra of **35**, **36** and **37** in C$_6$D$_6$ at 298 K showing the increasing line width of the *ortho*-CH$_3$ group of the mesityl ring (left). Stacked variable temperature ^{1}H NMR spectra of **35** in CD$_2$Cl$_2$ showing the splitting of the *ortho*-CH$_3$ groups of the mesityl ring at a lower temperature (right).

2.8.2 A cationic manganese plumbylidyne complex

Having in hand all the haloplumbylidene complexes of the type [(η^5-C_5H_4Me)$(CO)_2$Mn=Pb(X)(C_6H_3-2,6-Mes_2)] (X = Cl – I), my next target was to synthesize the cationic plumbylidyne complex by halide abstraction using a suitable nonoxidizing halide abstracting agent. The reaction of the chloroplumbylidene complex **35** with one equivalent of Na[B{C_6H_3-3,5-$(CF_3)_2$}$_4$] in *n*-pentane was accompanied by a slow color change of the insoluble solid from colorless to dark-brown within 18 hours affording selectively the manganese plumbylidyne complex [(η^5-C_5H_4Me)$(CO)_2$Mn≡Pb(C_6H_3-2,6-Mes_2)][B(C_6H_3-2,6-$(CF_3)_2$)$_4$] (**39**) (Scheme 30). ATR-IR monitoring of the insoluble solid after 30 minutes of stirring showed three ν(CO) absorption bands at 1914, 1925 and 1967 cm^{-1} for an intermediate suggested to be chloro-bridged manganese complex [{(η^5-C_5H_4Me)$(CO)_2$MnPbR}$_2$(μ-Cl)][B{C_6H_3-2,6-$(CF_3)_2$}$_4$] (R = C_6H_3-2,6-Mes_2), which gradually converts to **39** upon further reaction with Na[B{C_6H_3-3,5-$(CF_3)_2$}$_4$] (Scheme 30). Complex **39** was isolated as an air-sensitive, thermally robust (M.P. 170 – 171 °C (dec.)), brown solid, which is moderately light sensitive in solution, stable in fluorobenzene and CH_2Cl_2 but decomposes in THF.

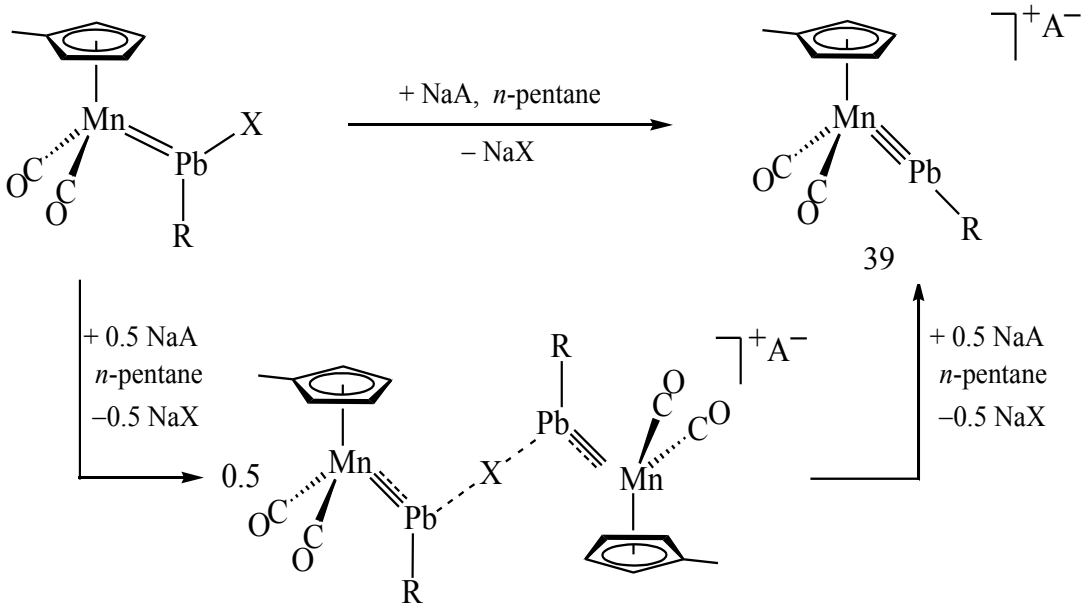

R = C_6H_3-2,6-Mes_2; X = Cl, Br, I

A^- = $[B\{C_6H_3\text{-}3,5\text{-}(CF_3)_2\}_4]^-$

Scheme 30. Synthesis of the manganese plumbylidyne complex.

Brown plates of **39** suitable for single crystal X-ray diffraction analysis were grown upon cooling a saturated solution of **39** in a CH_2Cl_2/*n*-pentane mixture at –30 °C. The three-legged piano-stool complex features a very short Mn–Pb bond (2.3829(4) Å) and an almost linearly coordinated plumbylidyne ligand (Mn-Pb-C_{aryl} = 174.82(7)°) (Figure 87). The Mn–Pb bond in complex **39** is shortened by *ca*. 0.09 Å and the Mn-Pb-C_{aryl} angle is widened by *ca*. 25° compared to that in the chloroplumbylidene complex **35**. In fact, this Mn–Pb bond is the shortest Mn–Pb triple bond reported to date and being slightly shorter than that previously reported for the manganese plumbylidyne complex $[(\eta^5\text{-}C_5H_4Me)(CO)_2Mn{\equiv}Pb(C_6H_3\text{-}2,6\text{-}Trip_2)][B\{C_6H_3\text{-}2,6\text{-}(CF_3)_2\}_4]$ (Mn–Pb 2.3963(9) Å).[54] The Mn-Pb bond length of **39** compares well with that reported for Mn–Pb triple bond [*d*(Mn≡Pb) = 2.40 Å] using the theoretically calculated triple bond covalent radii for Mn (1.03 Å) and Pb (1.37 Å) atoms.[173]

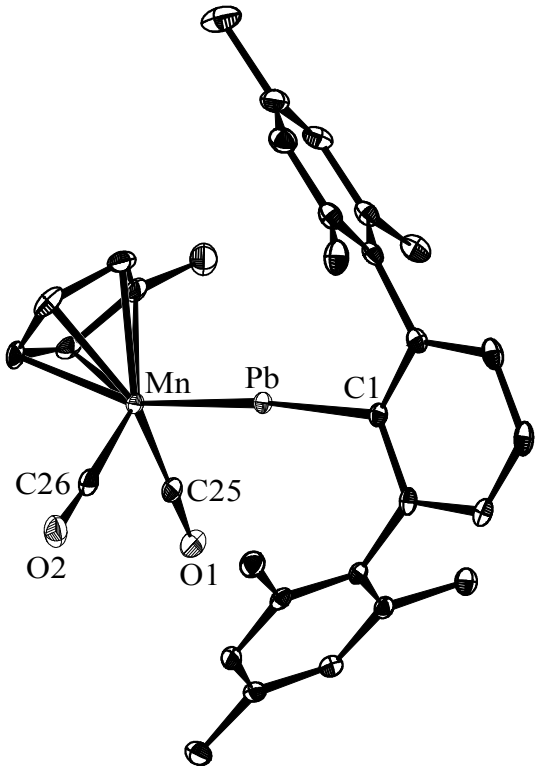

Figure 87. DIAMOND plot of the molecular structure of complex **39**. The thermal ellipsoids represent 30% of the electronic probability at 100(2)K. Hydrogen atoms are omitted for clarity. Selected bond lengths [Å] and bond angles [°]: Mn-Pb 2.3829(4), Pb-C(1) 2.165(3), Mn-C(25) 1.808 (3), Mn-C(26) 1.807(3); Mn-Pb-C(1) 174.82(7), C(25)-Mn-C(26) 92.6(1), Pb-Mn-C(25) 91.85(9), Pb-Mn-C(26) 92.04(9).

The IR and NMR spectra corroborate well with the solid-state structure of complex **39**. The ν_{CO} absorption bands of the plumbylidyne complex **39** (ATR-Solid: 1992 (s) and 1952 (s) cm^{-1}) appear at higher wavenumbers than those of the plumbylidene complex **35** (ATR-Solid: 1941 (vs) and 1886 (vs) cm^{-1}), but lower in comparison to those of the alkylidyne complex [(η^5-C_5H_4Me)$(CO)_2$Mn≡C(Ph)]BPh_4 (CH_2Cl_2: 2084, 2047 cm^{-1}).[221] This suggests that the σ-donor/π-acceptor ratio of the plumbylidyne ligand (Pb-R) in **39** is considerably lower than that of the plumbylidene ligand in **35** but higher than that of the alkylidyne ligand (C-Ph). The ^1H and $^{13}C\{^1H\}$ NMR spectra of **39** confirm an overall C_s-symmetric structure of the complex in solution, showing one set of sharp signals for the *ortho* H and C nuclei of the mesityl goups of the *m*-terphenyl substituent at room temperature. This suggests that the rotation of the *m*-terphenyl substituent in complex **39** is fast at room temperature on the NMR time scale. The most distinctive signal of the plumbylidyne complex in the $^{13}C\{^1H\}$ NMR spectrum is that of the lead-bound C_{aryl} atom, which appears at considerably lower field (δ = 268.5 ppm) than that of the plumbylidene complex **35** (δ = 242.7 ppm), but at a close position to that of the molybdenum plumbylidyne complex *trans*-[Br$(PMe_3)_4$Mo≡Pb(C_6H_3-2,6-$Trip_2$)] (δ = 280.6 ppm).[43]

Interestingly, bromide or iodide abstraction from the complexes **36** and **37** afforded only the corresponding bromo-bridged [{(η^5-C_5H_4Me)$(CO)_2$MnPbR}$_2$(μ-Br)][B{C_6H_3-2,6-$(CF_3)_2$}$_4$] (**38**) or iodo-bridged [{(η^5-C_5H_4Me)$(CO)_2$MnPbR}$_2$(μ-I)][B{C_6H_3-2,6-$(CF_3)_2$}$_4$] complexes, respectively, irrespective of the reaction stoichiometry, solvent, reaction time or temperature. The halo-bridged complexes are presumably formed via trapping of the highly electrophilic plumbylidyne complex by a second equivalent of the corresponding halo-plumbylidene complex. Formation of a bromo-bridged or iodo-bridged complex compared to the chloro-bridged complex, which readily converts to the plumbylidyne complex upon further reaction with Na[B{C_6H_3-3,5-$(CF_3)_2$}$_4$], can be rationalized with the larger size of the halide group, which helps the two bulky *m*-terphenyl groups away from each other in the bridged complexes. This also explains why during the formation of the plumbylidyne complex [(η^5-C_5H_4Me)$(CO)_2$Mn≡Pb(C_6H_3-2,6-$Trip_2$)][B{C_6H_3-2,6-$(CF_3)_2$}$_4$] bearing the bulkier C_6H_3-2,6-$Trip_2$ substituent at the lead atom, the corresponding iodo-bridged intermediate is not observed.[54] Notably, formation of a similar halide-bridged dinuclear species [{CpFe$(CO)_2$E(Mes*)}$_2$(μ-X)][B{C_6H_3-3,5-$(CF_3)_2$}$_4$] (E = Ga, In; X = Cl, Br) was also observed

during the halide abstraction from halogallyl and –indyl complexes towards the preparation of corresponding cationic gallanediyl and indanediyl complexes.[222]

To establish the structure of the intermediate, the bromo-bridged complex **38** was isolated in 38% yield as a red-brown solid and characterized by single crystal X-ray diffraction and multi-nuclear NMR and IR spectroscopy. The molecular structure indeed reveals a bromo-bridged structure with Mn–Pb bond lengths (Mn1–Pb1 2.437(1) Å, Mn2–Pb2 2.4406(9) Å) and Mn-Pb-C_{aryl} angles (Mn1-Pb1-C1 167.4(2)°, Mn2-Pb2-C33 156.9(2)°) that lie between the values observed in the chloroplumbylidene complex **35** (Mn–Pb 2.4699(9) Å, Mn-Pb-C_{aryl} 149.9(1)°) and the plumbylidyne complex **39** (Mn–Pb 2.3829(4) Å, Mn-Pb-C_{aryl} 174.82(7)°) (Figure 88). The Pb–Br bond lengths (Pb1–Br 2.9110(6) Å, Pb2–Br 2.8976(6) Å) compare well with those of the bromo-bridged dimeric plumbylene $((Pb(\mu\text{-}Br)(C_6H_3\text{-}2,6\text{-}Ar_2))_2$, Ar = C_6H_2-2,6-*i*Pr_2-4-*t*Bu, $(Pb–Br)_{av}$ 2.913 Å).[223]

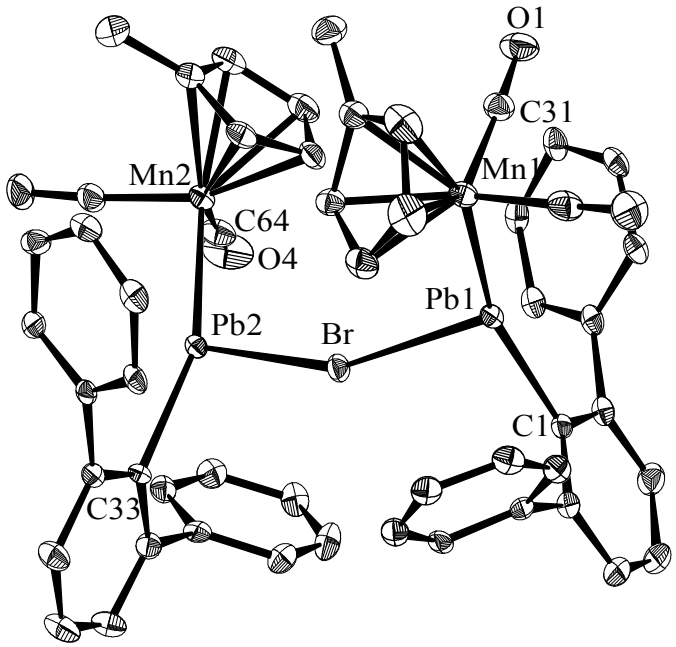

Figure 88. DIAMOND plot of the molecular structure of the complex cation in the bromo-bridged complex **38**. The thermal ellipsoids represent 30% of the electronic probability at 123(2)K. Hydrogen atoms and CH_3 groups of the mesityl rings are omitted for clarity. Selected bond lengths [Å] and bond angles [°]: Mn1-Pb1 2.437(1), Mn2-Pb2 2.4406(9), Pb1-C1 2.203(6), Pb2-C33 2.200(5), Pb1-Br 2.9110(6), Pb2-Br 2.8976(6), Mn1-C31 1.804(8), Mn1-C32 1.796(9), Mn2-C63 1.789(7), Mn2-C64 1.795(9); Mn1-Pb1-C1 157.4(2), Mn2-Pb2-C33 156.9(2), Mn1-Pb1-Br 109.58(3), Mn2-Pb2-Br 108.26(3), C1-Pb1-Br 92.3(1), C33-Pb2-Br 93.9(2), C31-Mn-C32 91.5(3), C63-Mn2-C64 91.1(4).

The NMR and IR spectra are consistent with the structure observed in the solid-state. Thus, the ^{1}H and $^{13}C\{^{1}H\}$ NMR spectra revealed a 2:1 ratio of the C_6H_3-2,6-Mes_2 and [B{C_6H_3-2,6-$(CF_3)_2$}$_4$]$^-$ moieties. In the $^{13}C\{^{1}H\}$ NMR spectrum the characteristic lead-bonded C_{aryl} atom gives rise to a resonance signal at δ = 258.7 ppm, which appears in between to that of the plumbylidene complex **35** (δ = 242.7 ppm) and the plumbylidyne complex **39** (δ = 268.5 ppm). The solid state IR spectrum exhibits three ν_{CO} absorption bands (ATR-Solid: 1964 (s), 1922 (s), and 1914 (s) cm^{-1}), which also appear in between those of the chloroplumbylidene complex **35** (ATR-solid: 1941 (vs) and 1886 (vs) cm^{-1}), and the plumbylidyne complex **39** (ATR-Solid: 1992 (s) and 1952 (s) cm^{-1}).

2.8.3 Plumbylidyne ligand transfer between a manganese and a molybdenum center

After the successful isolation of the manganese plumbylidyne complex **39**, which is also very reactive towards two electron donor ligands – such as THF and PMe_3, I studdied its reaction towards the metalate salt Na[Tp'Mo(CO)$_2$(PMe$_3$)] (**3-Mo**) in order to check the viability of a plumbylidyne ligand transfer. Indeed, treatment of **39** with the metalate salt **3-Mo**·DME in *n*-hexane or C_6D_6 at ambient temperature lead to the transfer of the plumbylidyne ligand (PbR, R = C_6H_3-2,6-Mes_2) to the molybdenum center, resulting in the formation of the molybdenum plumbylidyne complex [Tp´(CO)$_2$Mo≡Pb(C_6H_3-2,6-Mes_2)] (**10-Mo**) upon elimination of [(η^5-C_5H_4Me)Mn(CO)$_2$(PMe$_3$)] (Scheme 31). This represents the first example of an intermetallic transfer reaction of a plumbylidyne ligand.

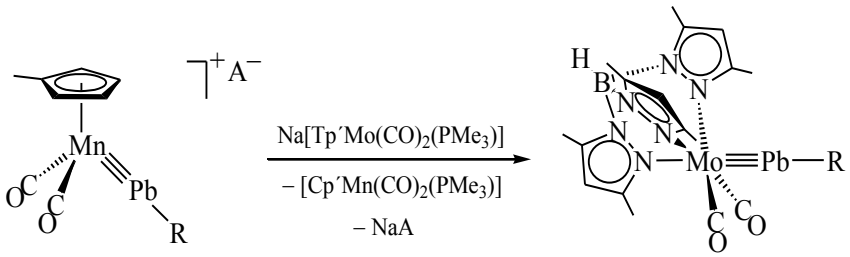

39 **10-Mo**

Scheme 31. Plumbylidyne ligand transfer between manganese and molybdenum.

The transfer reaction was followed by IR and NMR spectroscopy, and the formation of the final products was confirmed by comparing the spectroscopic data with those of authentic samples. The reaction in *n*-hexane was monitored by IR spectroscopy, revealing the immediate formation of the new plumbylidyne complex **10-Mo** (ν_{CO}: 1899, 1832 cm^{-1}) and [(η^5-

$C_5H_4Me)Mn(CO)_2(PMe_3)]$ (ν_{CO}: 1935, 1873 cm^{-1}) along with a very small amount of the radical complex [Tp'Mo$(CO)_2(PMe_3)$] (**2-Mo**) (ν_{CO}: 1903, 1770 cm^{-1}) as a side product (Figure 89).

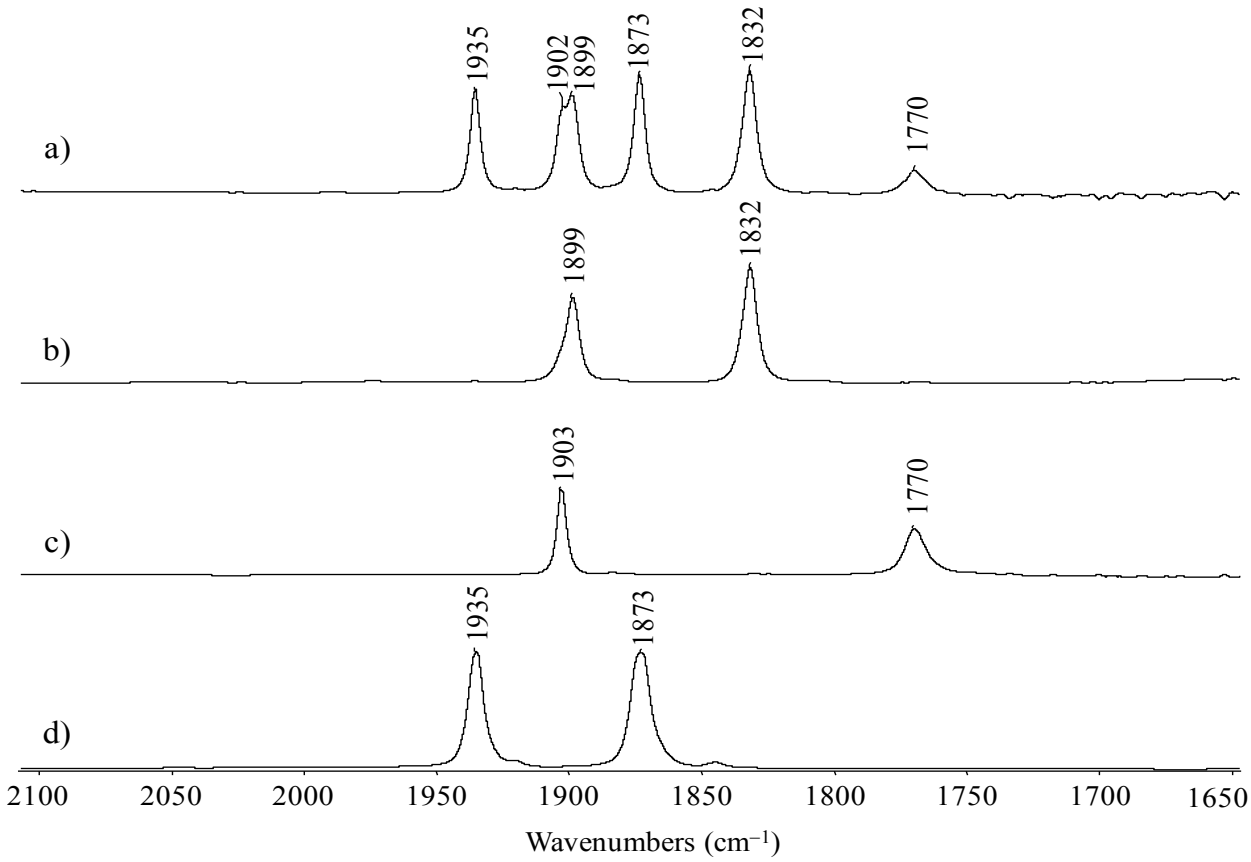

Figure 89. a) IR spectrum of the mixture obtained from the reaction between complex **39** and **3-Mo**·DME in *n*-hexane; b) IR spectrum of the complex **10-Mo** isolated from the reaction of **3-Mo** with PbBr(C_6H_3-2,6-Mes_2); c) IR spectrum of the pure metalloradical [Tp´Mo$(CO)_2(PMe_3)$] (**2-Mo**); d) IR spectrum of pure [(η^5-$C_5H_4Me)Mn(CO)_2(PMe_3)$]. All spectra were recorded in *n*-hexane.

The transfer reaction, which was carried out in C_6D_6, was followed by ^1H and $^{31}P\{^1H\}$ NMR spectroscopy. The ^1H NMR spectrum revealed an almost selective reaction and formation of the molybdenum plumbylidyne **10-Mo** and [(η^5-$C_5H_4Me)Mn(CO)_2(PMe_3)$]. The ^1H NMR spectrum in C_6D_6 compares well with those of the respective pure samples (Figure 90). Furthermore, the $^{31}P\{^1H\}$ NMR spectrum shows only one broad signal at δ = 48.1 ppm, which fits very well with that observed for [(η^5-$C_5H_4Me)Mn(CO)_2(PMe_3)$].

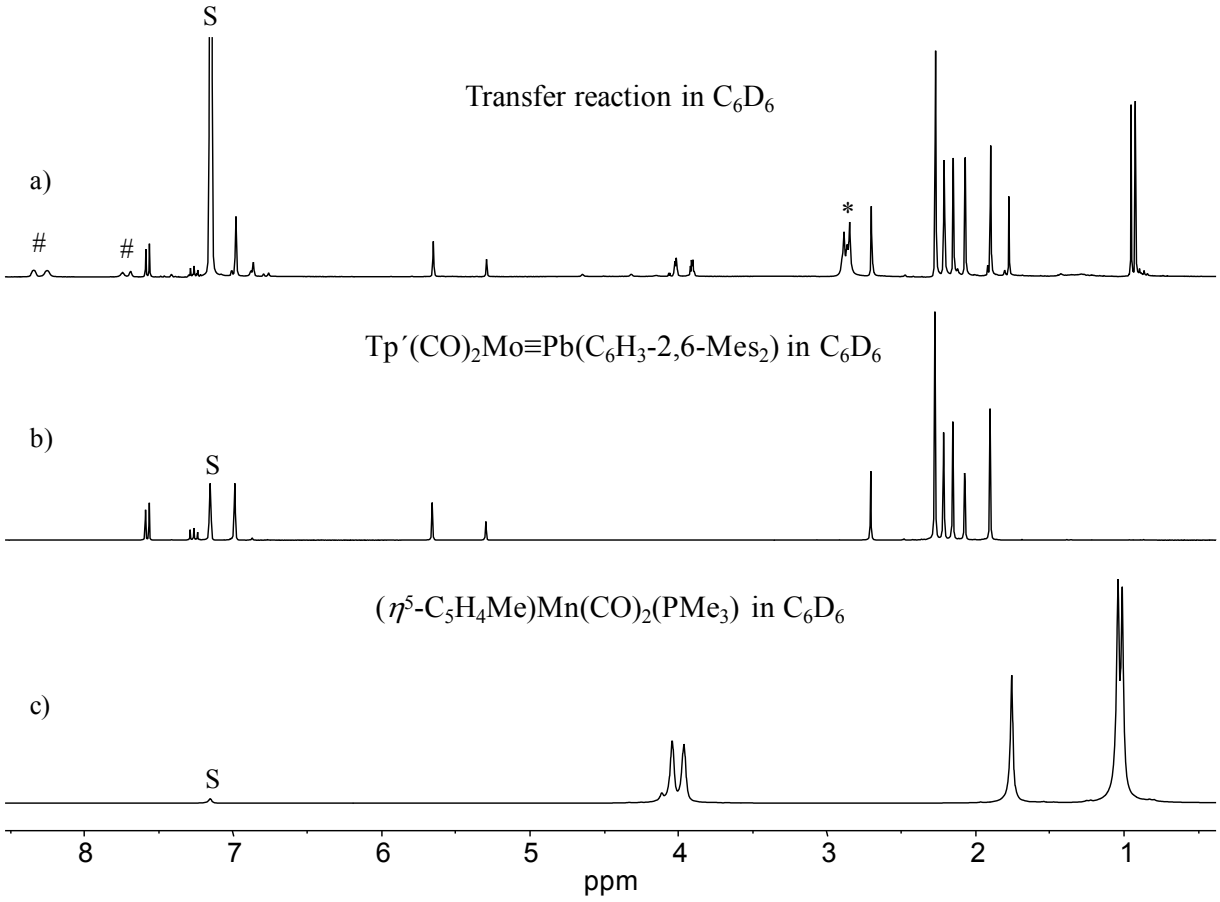

Figure 90. a) ^{1}H NMR spectrum (300.1 MHz, C_6D_6, 298 K) of the reaction between **39** and **3-Mo**·DME indicating the formation of complexes **10-Mo**, [(η^5-C_5H_4Me)$Mn(CO)_2(PMe_3)$], and Na[B{C_6H_3-3,5-$(CF_3)_2$}$_4$]. The residual proton signal of the deuterated solvent is indicated by the symbol S and the signals of Na[B{C_6H_3-3,5-$(CF_3)_2$}$_4$] and free DME by the symbol # and ∗, respectively; b) ^{1}H NMR spectrum (300.1 MHz, C_6D_6, 298 K) of complex **10-Mo** isolated from the reaction of **3-Mo** with PbBr(C_6H_3-2,6-Mes_2); c) ^{1}H NMR spectrum (300.1 MHz, C_6D_6, 298 K) of complex [(η^5-C_5H_4Me)$Mn(CO)_2(PMe_3)$].

2.9. Access to the first NHC-stabilized disilavinylidene

The chemistry of low valent group 14 elements is an important research topic in modern inorganic chemistry, and it experienced a renaissance in the last two decades. Most importantly, compounds featuring multiple bonds between heavier group 14 elements find growing interest due to their surprisingly different properties and structural behavior than those of their lighter congeners. For example, the potential energy surface (PES) of C_2H_2 shows the vinylidene $H_2C{=}C$: as the only higher energy-minimum structure, which rapidly isomerizes by quantum-mechanical tunneling to the global energy minimum acetylene HC≡CH.[224] In contrast, the PES of Si_2H_2 reveals that the energetic minima in order of increasing energy are a structure bridged by two hydrogen atoms, a structure bridged by one hydrogen atom, a disilavinylidene, and a *trans*-bent disilyne structure (Figure 91).[225, 226]

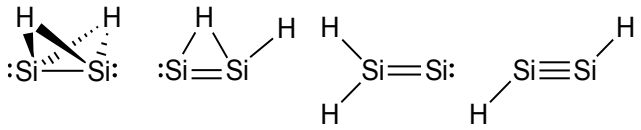

Figure 91: Calculated minimum structures of Si_2H_2. The relative energy increases for the structures from left to right. The bonds to the bridged H atoms correspond to three-center two-electron bonds, and two dots represent a lone pair of electrons.

The mono- and dihydrogen-bridged structures were already detected by rotational spectroscopy in low-temperature matrices.[227, 228] The *trans*-bent disilyne derivatives Si_2R_2 were also isolated using bulky substituents (R = silyl[10, 13, 229], aryl[12], alkyl[14]) and their chemistry is still flourishing since the isolation of the first stable derivative.[230] But so far an experimental proof for the existence of disilavinylidenes has not been reported in the literature.

In recent years, N-heterocyclic carbenes (NHCs) proved to be very useful bases for stabilizing low-valent main group elements, and in fact, this approach lead to a renaissance in low-valent silicon chemistry.[231-234] Some remarkable examples of the thermodynamic stabilization provided by the N-heterocyclic carbenens are the Si(0) compounds $Si_2(Idipp)_2$[235] and Si(bNHC) (bNHC = chelating bis-N-heterocyclic carbene),[236] the NHC adducts of the Si(II) compounds SiX_2 (X = Cl, Br, I),[176, 237-239] Si(X)R (X = Cl, Br; R = aryl, amino),[107, 110, 240, 241] and $SiR(Si{=}SiR_2)$,[242] the NHC-stabilized 1-silacyclopenta-2,4-dienylidenes $(RC)_4Si$,[243, 244] or the NHC trapped $[SiR]^+$,[110, 239, 245] and Si^{2+} ions.[239] Recently the same concept was employed to isolate the room temperature stable silagermenylidene ($R_2Si{=}Ge$)[246] and phosphasilenylidene (RP=Si).[247]

Notably, an NHC-stabilized disilavinylidene was recently presumed to be one of the intermediates during the formation of an NHC-stabilized trisilacycloprop-1-ylidene, but no experimental evidence was provided.[248] Recent theoretical work by Frenking and co-workers has predicted that NHC-stabilized silavinylidenes and their heavier homologues should be stable and isolable molecules.[249] I set out to combine the well-known Lewis base character of $ECl_2(LB)$ (E = Si, Ge; LB = NHC, $C(PPh_3)_2$, PPh_3CMe_2)[232, 250-255] with the electrophilicity of multiply bonded low valent silicon compounds, such as 1,2 dihalodisilenes,[12, 108-110, 256] and envisaged that this approach might lead to new interesting silicon chemistry. Herein, the realization of this approach is reported including the synthesis and full characterization of an unprecedented NHC-stabilized bromo(silyl)silylene and its reduction product, an NHC-stabilized disilavinylidene.[121]

$SiBr_2$(SIdipp)[176] and (*E*)-Tbb(Br)Si=Si(Br)Tbb[110] were chosen as the starting material to test our concept. Heating of a 2:1 mixture of $SiBr_2$(SIdipp) and (*E*)-Tbb(Br)Si=Si(Br)Tbb in toluene at 100 °C for 5 hours lead to a color change from yellow to light orange. Monitoring of the reaction by ^{1}H NMR spectroscopy revealed a selective but incomplete conversion (~90 %) of the starting materials into the NHC-stabilized bromo(silyl)silylene $SiBr(SiBr_2Tbb)$(SIdipp) (**45**). Further heating of the reaction mixture only leads to a slow decomposition of the resulted product.[33] Compound **45** was isolated after workup as a yellow, extremely air-sensitive solid in 61 % yield (Scheme 32). Compound **45** decomposes upon melting at 122 – 125 °C and is moderately soluble in aliphatic solvents and well soluble in toluene and THF.

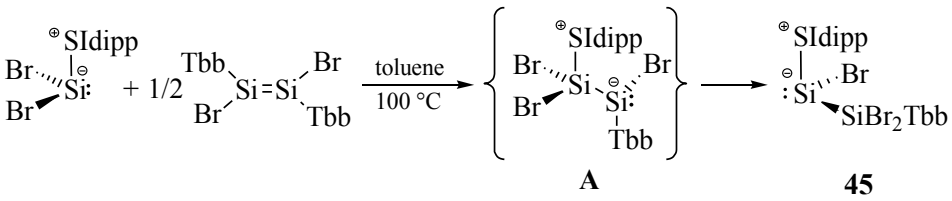

Scheme 32: Synthesis of **45** via the putative intermediate (SIdipp)Br_2SiSi(Br)Tbb (**A**).

A two-step reaction mechanism can be suggested for the formation of **45**, given the Lewis basic character of $SiBr_2$(SIdipp)[176] and the propensity of 1,2-dibromodisilenes (*E*)-

[33] To check the thermal stability of **45**, variable temperature ^{1}H NMR spectra were recorded , which revealed that at elevated temperatures (>80 °C) **45** slowly dissociates into $SiBr_2$(SIdipp) and (*E*)-Tbb(Br)Si=Si(Br)Tbb, together with a very small amount of some unknown Tbb-containing byproducts . The byproducts presumably form during the dimerisation of the expected monomeric silylene [TbbSiBr] intermediate.

R(Br)Si=Si(Br)R to act as precursors for bromosilylenes Si(Br)R.[108, 109] In the first step, the base-stabilized silylene intermediate **A** is slowly formed, which then rapidly rearranges via a 1,2-migration of bromine from the four- to the three-coordinate silicon center to give the final product **45** (Scheme 32). The reaction of $SiBr_2$(SIdipp) with Ge(Br)R (R = C_6H_3-2,6-Mes_2) was found to stop at the base-stabilized aryl(bromo)germylene (SIdipp)Br_2SiGe(Br)R, similar to the intermediate **A**, thus providing an indirect evidence for the suggested mechanism.[34]

Compound **45** is the first NHC-stabilized bromo(silyl)silylene to be reported and was characterized by single crystal X-ray diffraction, multinuclear NMR spectroscopy and elemental analysis. In general, silylsilylenes are an interesting class of very reactive Si(II) compounds, which have been suggested as transient intermediates in silylsilylene-disilene rearrangement reactions.[12, 257, 258] Only recently one stable amido(silyl)silylene Si[Si($SiMe_3$)$_3$][N($SiMe_3$)(dipp)] (dipp = C_6H_3-2,6-*i*Pr_2) was reported.[259] Base-stabilized silylsilylenes are also very rare and only three examples have been reported. These are the amidinato-stabilized derivative Si[SiX{N*t*Bu)$_2$CHPh}][(N*t*Bu)$_2$CPh] (X = H, Cl),[260, 261] the NHC-stabilized disilylsilylene Si(Si*t*Bu$_3$)$_2$(IMe_4)[262] and the NHC-stabilized hydrido(silyl)silylene SiH(Si*t*Bu$_3$)(IMe_4).[263]

The molecular structure of **45** features a trigonal-pyramidal geometry at the Si2 center, indicating the presence of a stereochemically active lone pair of electrons at Si2, and tetrahedral geometry at the Si1 atom, as expected for silyl substituents (Figure 92). The sum of angles at Si2 (287.4°) compares well with that of $SiBr_2$(SIdipp) ($\Sigma\angle$Si = 290°)[176] and corresponds to a pyramidalization degree of 81%.[35] The bulky SIdipp and Tbb substituents as well as the bromine atoms (Br1 and Br3) adopt an almost antiperiplanar conformation along the Si1–Si2 single bond ,as evidenced by the torsion angles $C1_{(Tbb)}$-Si1-Si2-$C25_{(NHC)}$ and Br1-Si1-Si2-Br3, which have the values of −159.5(2)° and 179.48(5)°, respectively. The Si1–Si2 bond length is 2.391(1) Å, which compares well with that of the amido(silyl)silylene Si[Si($SiMe_3$)$_3$][N($SiMe_3$)(dipp)] ((*d*(Si–Si) = 2.386(1) Å)[259] or with that of the amidinato-stabilized silylsilylene

[34] The molecular structure of (SIdipp)Br_2SiGe(Br)R; was determined by single crystal X-ray diffraction analysis. The molecular structure revealed an elongated Si–Ge single bond (*d*(Si–Ge) = 2.5076 (9) Å): D. Hoffmann, personal communication.

[35] The degree of pyramidalization ranges between 0% for a trigonal-planar-coordinated central atom and 100%, which corresponds to a sum of angles of 270°.

Si[SiX{N*t*Bu)$_2$CHPh}][(N*t*Bu)$_2$CPh] (X = H, *d*(Si–Si) = 2.377(5)Å; X = Cl, *d*(Si–Si) = 2.381(7) Å),[260, 261] but is slightly longer than the Si–Si single bond length in α-Si (2.352 Å).[264]

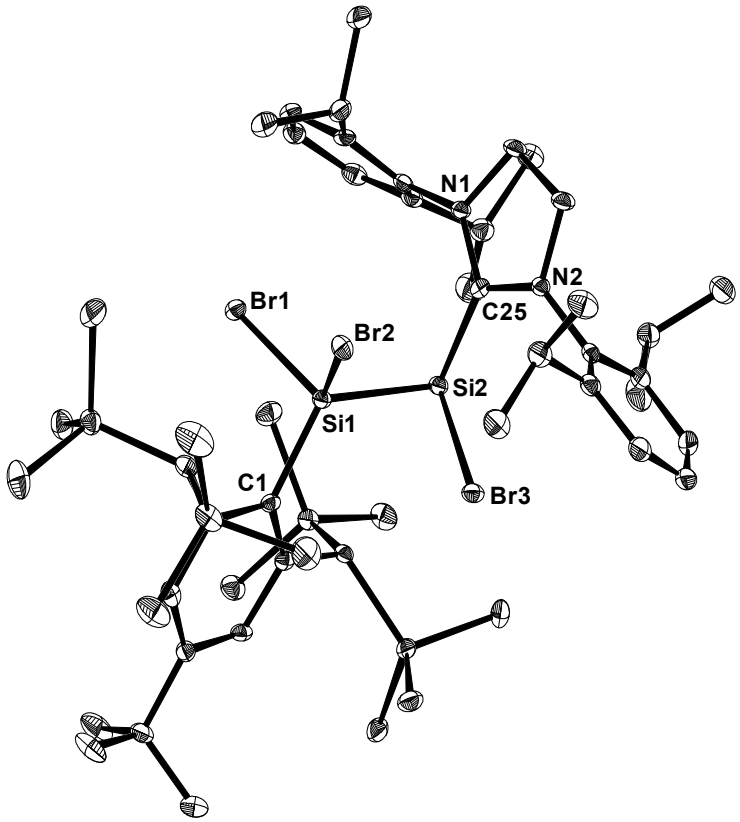

Figure 92. DIAMOND plot of the molecular structure of compound **45** in the crystal lattice of the *n*-pentane solvate **45**·(*n*-C_5H_{12}). The thermal ellipsoids represent 30 % of the electronic probability at 123(2) K. Hydrogen atoms and the solvent molecule are not depicted for clarity. Selected bond lengths [Å], bond angles [°] and torsion angles [°]: Si1–Si2 2.391(1), Si1–C1 1.921(3), Si2–C25 1.978(3), Si1–Br1 2.2634(9), Si1–Br2 2.286(1), Si2–Br3 2.342(1); C1-Si1-Si2 119.7(1), C1-Si1-Br1 101.24(9), C1-Si1-Br2 116.1(1), C25-Si2-Si1 102.1(1), C25-Si2-Br3 100.7(1), Si1-Si2-Br3 84.59(4), Si2-Si1-Br1 114.94(5), Si2-Si1-Br2 102.68(4); C1-Si1-Si2-C25 −159.5(2), C1-Si1-Si2-Br3 −59.6(1), C25-Si2-Si1-Br1 79.7(1), C25-Si2-Si1-Br2 −29.0(1), Br1-Si1-Si2-Br3 179.48(5).

The Si–C_{NHC} bond length (*d*(Si2–C25) = 1.978(3) Å) compares well with those of other NHC-stabilized Si^{II} bromides, such as $SiBr_2$(SIdipp) (*d*(Si–C_{NHC}) = 2.007(5) Å)[36][176] or $SiBr_2$(Idipp) (*d*(Si–C_{NHC}) = 1.989(3) Å).[238] Similarly, the Si^{II}–Br bond length of **45** (*d*(Si2–Br3) = 2.342(1) Å) is found in the range reported for other Si^{II} bromides (2.3201(7)-2.3607(8) Å),[176, 238] whereas

[36] Two independent molecules were found in the single crystals of $SiBr_2$(SIdipp) by X-ray diffraction studies. The mean value of the corresponding bonding parameter is given.

the Si1–Br1 (2.2634(9) Å) and Si1–Br2 (2.286(1) Å) bonds are considerably shortened and close in value to the mean Si–Br bond length of bromosilanes (2.243).[37]

Further structural information of **45** was provided by the solution NMR spectra. The ^{29}Si NMR spectrum displays four singlets at δ = 2.45, 2.64, –11.3 and –1.9 ppm. The two most downfield-shifted signals correspond to the $SiMe_3$ substituents of the Tbb group, indicating the presence of a stereogenic trigonal-pyramidal Si2 center with a high racemization barrier, which is known for three-coordinate Si^{II} compounds.[107] The other two signals at –11.3 and –1.9 ppm were assigned by ^{1}H-^{29}Si correlation spectroscopy to the *Si*Br_2 and *Si*Br nuclei, respectively. The silylene (*Si*Br) resonance signal (δ = –1.9 ppm) in the NMR spectrum appears at a slightly higher field than that of $SiBr_2$(SIdipp) (δ = 10.8 ppm).[176] The carbene carbon (*C*25) signal in the ^{13}C NMR spectrum appears at δ = 190.9 ppm. It compares well with that of $SiBr_2$(SIdipp) (δ = 188.7 ppm)[176] and is indicative of a donor-acceptor character of the Si–C_{NHC} bond.

Compound **45** contains many reactive sites and could be used for the synthesis of new low-valent silicon compounds. For example, the bromido substituent could be substituted by different nucleophiles towards the generation of new NHC-stabilized silylsilylenes. The silylene center could be employed in coordination chemistry towards electrophiles, or it could be reduced to get new low-valent silicon compounds.

Indeed, reduction of **45** by two-electrons leads to the formation of the first example of an NHC-stabilized disilavinylidene (*Z*)-(SIdipp)Si=Si(Br)Tbb (**46**). Thus, treatment of **45** with two equivalents of KC_8 in benzene at ambient temperature leads to a color change from orange to red and proceeds smoothly and selectively, as evidenced by ^{1}H NMR spectroscopy, to afford compound **46**.[38] The NHC-stabilized disilavinylidene was isolated after workup and crystallization from *n*-pentane as a bright red, microcrystalline solid in 60 % yield. Compound **46** can also be crystallized very easily from a saturated benzene solution, and it is well soluble in all common organic solvents. The red solid is extremely air-sensitive and instantaneously looses its

[37] The mean Si–Br bond length of all structurally characterized bromosilanes featuring a four-coordinated silicon center is given according to a Cambridge Structural Database survey (12.05.2015). The Si–Br bonds of bromosilanes range from 2.153–2.326 Å.

[38] Reduction of **45** by two equivalents of sodium naphthalenide solution in THF was also carried out. This reduction was less selctive and purification of the desired product was difficult due to its high lipophilicity.

color upon exposure to air. It shows remarkable thermal stability and only starts to decompose upon melting at 237 – 238 °C.

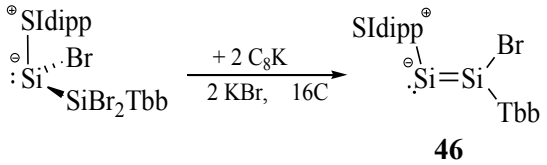

46

Scheme 33: Synthesis of the NHC-stabilized disilavinylidene **46** upon two-electron reduction of **45**.

Compound **46** was fully characterized by single crystal X-ray diffraction, elemental analysis, and multinuclear NMR spectroscopy. The molecular structure reveals an almost planar core made out of the atoms C1, Si1, Br, Si2 and C25 (Σ∠Si = 360.1 (1)°; Figure 93). The Si1–Si2 double bond length of **46** is 2.167(2) Å, which is ~ 22 pm shorter than that of compound **45**. Interestingly, this Si1–Si2 bond in **46** is significantly shorter that that observed in $Si_2(Idipp)_2$ (2.229(1) Å)[235] and $Si_2(SIdipp)_2$ (2.2323(8) Å)[33] and also shorter than that of (*E*)-Tbb(Br)Si=Si(Br)Tbb (2.216 Å)[110]. This shortening can be explained by the fact that the hybrid orbital of Si1 employed in the Si1–Si2 *σ*-bonding of **46** has a high s character (50 %) (Table 39). The bulky Tbb and SIdipp groups are *trans*-oriented around the Si1=Si2 double bond, as evidenced by the torsion angle $C1_{(Tbb)}$-Si1-Si2-$C25_{(NHC)}$ of 177.3(2)°, and also the two central rings of the two bulky ligands are orthogonally oriented as demonstrated by the dihedral angle between the Tbb and NHC central ring least-square planes and the least-square plane passing through the atoms C1, Si1, Si2, Br and C25, which have values of 83.8(1)° and 92.9(1)°, respectively. Another interesting structural feature of **46** is the almost orthogonal arrangement of the NHC (C25-Si2-Si1 97.6(1)°) with respect to the Si1-Si2 bond vector, akin to that observed in the silagermenylidene Tip_2Si=Ge(NHC) (C_{NHC}-Ge-Si 98.90(5)°)[246] or in the phosphasilenylidene (IDipp)Si=PMes* (C_{NHC}-Si-P 96.90(6)°).[247] A reason for the orthogonal arrangement of the NHC is provided by the natural bond orbital (NBO) analysis of the model compound (*Z*)-(NHC)Si=Si(Br)R ((*Z*)-**46**'$_{calc}$; NHC = $C[N(C_6H_3\text{-}2,6\text{-}Me_2)CH_2]_2$, R = C_6H_3-2,6-$[CH(SiH_3)_2]_2$; Figure 95, *vide infra*),[121] which revealed a stereochemically active lone pair of electrons of high s character (77%) at Si2, while hybrid orbitals of Si2 with a high p character are used for the *σ*-bonding to the Si1 and the C_{NHC} atoms (89% and 90%, respectively). The Si2–$C25_{(NHC)}$ bond length in **46** (1.937(4) Å) compares well to that in $Si_2(SIdipp)_2$ (1.924(2) Å)[33] or $Si_2(Idipp)_2$ (1.927(2) Å)[235] but appears slightly longer than the Si1–$C1_{(Tbb)}$ bond (1.882(4) Å).

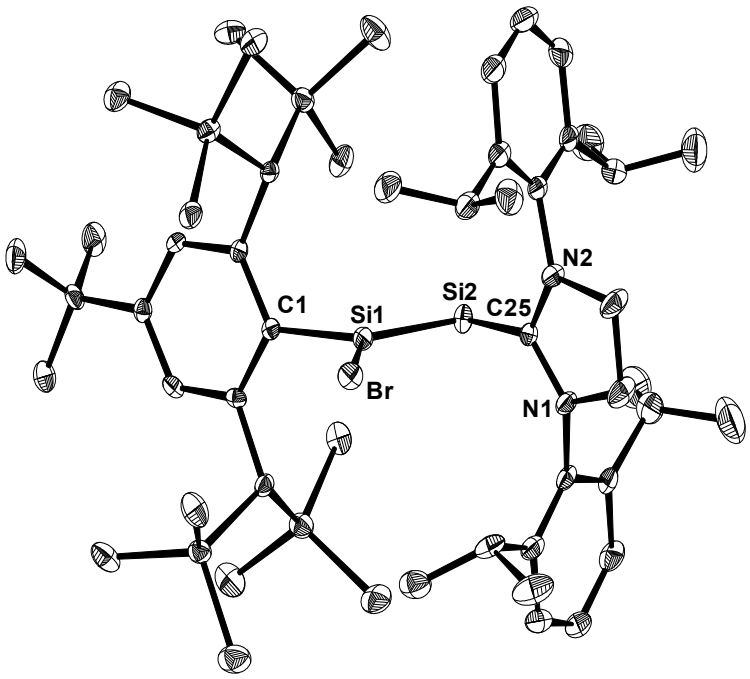

Figure 93. DIAMOND plot of the molecular structure of **46** in the crystal lattice of the *n*-pentane solvate **46**·(*n*-C_5H_{12}). The thermal ellipsoids are set at 30 % probability level. Hydrogen atoms and the solvent molecule are not depicted for clarity. Selected bond lengths [Å], bond angles [°] and torsion angles [°]: Si1–Si2 2.167(2), Si1–C1 1.882(4), Si2–C25 1.937(4), Si1–Br 2.286(1); C1-Si1-Si2 123.4(1), C1-Si1-Br 109.5(1), C25-Si2-Si1 97.6(1), Si2-Si1-Br 127.16(5); C1-Si1-Si2-C25 177.3(2), C25-Si2-Si1-Br −4.0(2).

The solution NMR spectra of **46** indicate an overall C_s-symmetric structure in solution. In contrast to **45**, two $SiMe_3$ groups of the Tbb substituent, as well as the C^2/C^6 and C^3/C^5 positions of the peripheral dipp substituents of the SIdipp group in **46** become equivalent as a consequence of a rapid rotation of the bulky Tbb and SIdipp groups around the respective Si-C bonds. In the $^{29}Si\{^1H\}$ NMR spectrum of **46** two distinctive signals were observed at δ = 86.0 and 34.6 ppm which were assigned to the three-coordinate and two-coordinate silicon atoms of the Si=Si core, respectively, using ^1H-^{29}Si correlation spectroscopy. Interestingly, though the chemical shift of the three-coordinate silicon atom (δ(Si1) = 86.0 ppm) compares well with that of (*E*)-Tbb(Br)Si=Si(Br)Tbb (δ = 84.12 ppm in C_6D_6),[110] the chemical shift for the two-coordinate Si atom (δ(Si2) = 34.6 ppm) appears at a much higher field than that for Si_2(SIdipp)$_2$ (δ(Si) = 215.2 ppm in C_6D_6 at 348 K),[33] Si_2(Idipp)$_2$ (δ(Si) = 224.5 ppm in C_6D_6),[235] or (Idipp)Si=PMes* (δ(Si) = 267.3 ppm in C_6D_6).[247]

The experimental results were further supported by detailed density functional theory (DFT) analysis. The minimum structure obtained by geometric optimization at the RIJ-B97-D3/TZVP

level of theory shows an excellent agreement between experimental and calculated bonding parameters (Figure 94; Table 38).

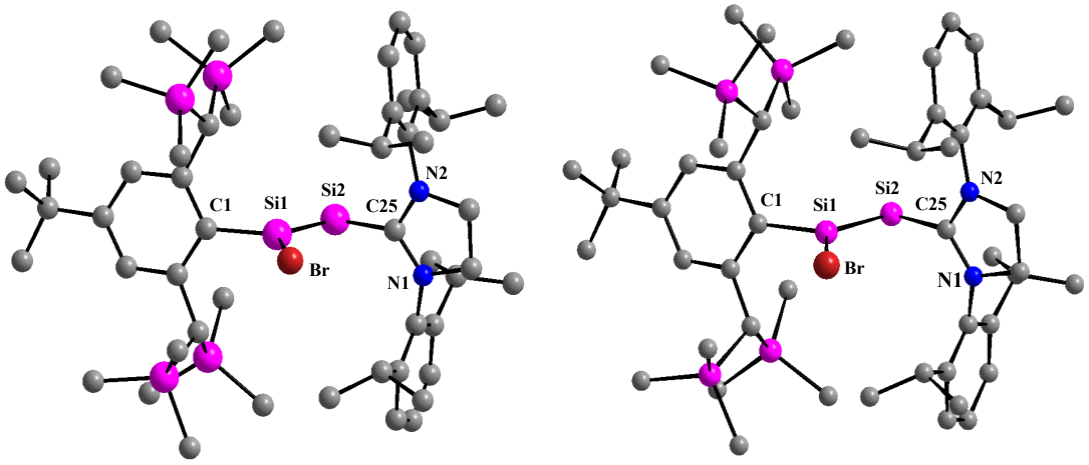

46 **46**$_{calc}$

Figure 94: Experimental (**46**, left) and calculated (**46**$_{calc}$, RIJ-B97-D3/TZVP, right) structures of (*Z*)-(SIdipp)Si=Si(Br)Tbb. The H atoms are omitted for clarity. Atom numbering of the experimental structure was taken over in the calculated structure.

Table 38: Comparison of selected experimental bond lengths and angles of **46** with the calculated bond lengths and angles of **46**$_{calc}$, (*Z*)-**46**'$_{calc}$, (*E*)-**46**'$_{calc}$ and (*Z*)-**46**''$_{calc}$.

	Si1–Si2 [Å]	Si1–C1 [Å]	Si2–C25 [Å]	Si–Br [Å]	C1-Si1-Si2 [°]	C1-Si1-Br [°]	C25-Si2-Si1 [°]	Si-Si-Br [°]	φ_{aryl}[a] [°]	φ_{NHC}[b] [°]
46	2.167(2)	1.882(4)	1.937(4)	2.286(1)	123.4(1)	109.5(1)	97.6(1)	127.16(5)	83.9(1)	92.9(1)
46$_{calc}$	2.176	1.896	1.950	2.309	121.54	109.87	98.84	128.58	100.12	88.46
(*Z*)-**46'**$_{calc}$	2.211	1.923	1.974	2.345	119.41	105.81	104.14	132.67	86.81	105.20
(*E*)-**46'**$_{calc}$	2.251	1.942	1.978	2.337	151.85	103.17	111.96	100.28	73.07	128.64
(*Z*)-**46''**$_{calc}$	2.246	1.959	1.926	2.328	103.94	107.71[c]	116.42	135.61	92.05	35.79

[a]: The dihedral angle φ_{aryl} is the angle between the least-square plane of the aryl ring atoms and the least-square plane of the atoms C1, Si1, Si2, Br and C25. [b]: The dihedral angle φ_{NHC} is the angle between the least-square plane of the NHC ring atoms and the least-square plane of the atoms C1, Si1, Si2, Br and C25. [c]: The C25-Si2-Br angle is given.

Calculations on the small model system (*Z*)-(NHC)Si=Si(Br)R ((*Z*)-**46**'$_{calc}$; NHC = C[N(C$_6$H$_3$-2,6-Me$_2$)CH$_2$]$_2$, R = C$_6$H$_3$-2,6-[CH(SiH$_3$)$_2$]$_2$; Figure 95) at the same level of theory revealed two additional minimum structures on the potential energy hypersurface. The one corresponding to the (*E*)-diastereomer ((*E*)-**46**'$_{calc}$, and the other corresponding to the structural isomer (*Z*)-**46**''$_{calc}$, an NHC-stabilized bromodisilyne (Figure 95) were found to be less stable than (*Z*)-**46**'$_{calc}$ by 43.4 and 33.0 KJmol^{-1}, respectively. The bonding parameters obtained for all three isomers are given in Table 38. The bonding parameters obtained for the model system (*Z*)-46'$_{calc}$ deviate slightly

from the experimental results, and this could be the consequence of a lower steric crowding around the Si1–Si2 double bonds.

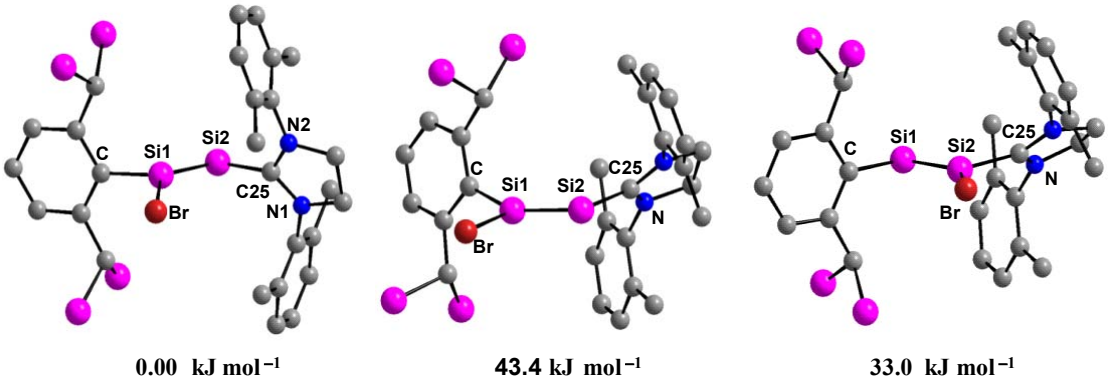

Figure 95:. Calculated (RIJ-B97-D3/TZVP) structures of the model compound (*Z*)-(NHC)Si=Si(Br)R ((*Z*)-**46**'$_{calc}$, left), its (*E*)-isomer (*E*)-**46**'$_{calc}$ (middle) and its constitutional isomer (*Z*)-Br(NHC)Si=SiR ((*Z*)-**46**''$_{calc}$, right) with their corresponding relative Gibbs energies (NHC = C[N(C_6H_3-2,6-Me_2)CH_2]$_2$; R = C_6H_3-2,6-{$CH(SiH_3)_2$}$_2$). The H atoms are omitted for clarity. Atom numbering of the experimental structure was taken over in the calculated structures.

A close look at the Kohn-Sham frontier orbitals shows that the HOMO is the Si1=Si2 π-bonding orbital, while the rather low in energy HOMO–1 orbital is the lone pair on Si2 (Figure 96). Furthermore, the LUMO is the orbital that is mainly C_{NHC}-centered and the LUMO+1 is the Si1=Si2 π^* orbital (Figure 96).

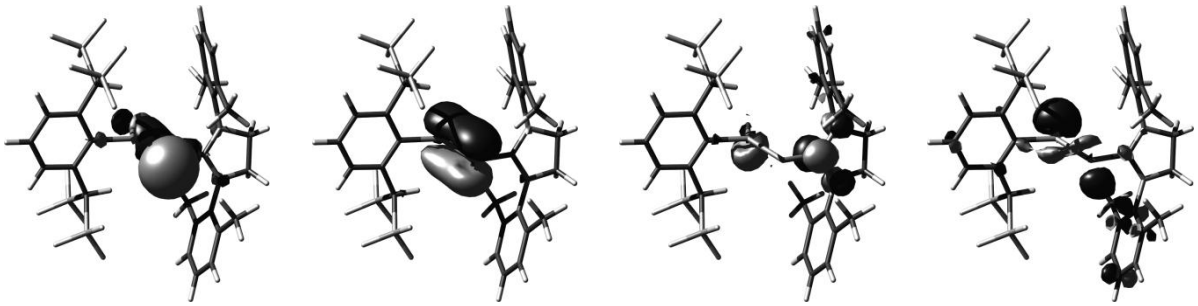

Figure 96: Selected Kohn-Sham frontiers orbitals of (*Z*)-**46**'$_{calc}$ and their corresponding energy eigenvalues; isosurface value 0.05 e bohr^{-3}.

The natural bond orbital (NBO) and natural resonance theory (NRT) analysis corroborates well with the observed solid state structure. The NBO analysis represents highly localised Si=Si, Si–C_{NHC}, Si–C_{aryl}, and Si–Br bonds (Table 39). For example, the Si–Si σ bond NBO is occupied

with 1.92 electrons and the Si–Si π bond NBO with 1.84 electrons. Whereas the Si–Si σ bond is slightly polarised towards the Si1 atom, the Si–Si π bond is not polarised and it is formed with almost pure Si p orbitals. This localized electron density leads to a high Wiberg bond index (WBI) of 1.79 indicating the presence of a quite covalent Si=Si bond. This was further supported by the NRT analysis, which shows an overall Si–Si bond order of 1.91 (Table 39). The natural population analysis (NPA) of (*Z*)-**46**'$_{calc}$ revealed a substantial charge flow from the NHC to the disilavinylidene fragment as evidenced by the overall NPA charge of the NHC (q(Σ(NHC)) = 0.42). Interestingly, the two-coordinate Si1 is almost electroneutral (q = 0.03), whereas the three-coordinate Si2 atom bears a positive partial charge (q = 0.52), and the negative charge is mostly localized on the Br atom (q = –0.36) and aryl group (q(Σ(aryl)) = –0.62) (Table 39).

Table 39: Selected results of the natural bond orbital (NBO) and natural resonance theory (NRT) analyses of (*Z*)-**46**'$_{calc}$. Atom numbering of the experimental structure was taken over in the calculated structure (*Z*)-**46**'$_{calc}$.[a]

NBO analysis					NPA partial charges[b]		NRT analysis[c]	
	occ.	pol. [%]	hyb.	WBI				tot / cov / ionic
σ(Si1–Si2)	1.92	60.8 (Si1) 39.2 (Si2)	$sp^{1.01}$ (Si1) $sp^{8.27}$ (Si2)	1.79	Si1	0.52	Si1–Si2	1.91 / 1.61 / 0.30
π(Si1–Si2)	1.84	51.1 (Si1) 48.9 (Si2)	$sp^{26.11}$(Si1) $sp^{38.59}$(Si2)		Si2	0.03		
σ(Si1–C_{aryl})	1.94	29.4 (Si1) 70.6 (C_{aryl})	$sp^{2.36}$ (Si1) $sp^{2.53}$ (C_{aryl})	0.78	C_{aryl} Σ(aryl)	−0.46 −0.62	Si1–C_{aryl}	0.96 / 0.57 / 0.40
σ(Si2–C_{NHC})	1.93	22.6 (Si2) 77.4 (C_{NHC})	$sp^{9.05}$ (Si2) $sp^{1.38}$ (C_{NHC})	0.84	C_{NHC} Σ(NHC)	0.17 0.42	Si2–C_{NHC}	1.13 / 0.47 / 0.66
σ(Si1–Br)	1.97	26.6 (Si1) 73.4 (Br)	$sp^{4.75}$ (Si1) $sp^{4.48}$ (Br)	0.79	Br	−0.36	Si1–Br	0.94 / 0.49 / 0.45
n(Si2)	1.78		$sp^{0.3}$		Σ(Si_2Br)	0.19		

[a]: occ.: occupancy, pol.: polarization, hyb.: hybridization, WBI: Wiberg bond index, tot / cov / ionic: total bond order / covalent bord order / ionic bond order. [b]: Partial charges obtained by natural population analysis (NPA). [c]: A local NRT analysis was carried out including the Br, Si1, Si2, N, C_{aryl} and C_{NHC} atoms.

3 Summary and Outlook

3.1. Summary

The work presented in this thesis is predominantly focused on the development of unprecedented open-shell tetrylidyne complexes of group 6 and 7 transition metals comprising of a tetrel-centered unpaired electron, and the heavier analogues of metallacarbyne complexes featuring a multiply-bonded tetrel element between two metal fragments. In addition, an unique intermetallic plumbylidyne ligand transfer reaction was discovered and an NHC-stabilized disilavinylidene was isolated for the first time under normal experimental conditions.

Chapter 2.1.1 presents the synthesis and the characterization of novel electron-rich scorpionate metalate salts Na[Tp'M(CO)$_2$(PMe$_3$)] (**3-Mo**, M = Mo; **3-W**, M = W), those were employed as very efficient nucleophiles for the synthesis of metal–tetrel multiply-bonded complexes. The metalate salts **3-Mo** and **3-W** were prepared upon two-electron reduction of the corresponding M(II)-precursors [Tp'M(CO)$_2$(PMe$_3$)Cl] (**1-Mo**, M = Mo; **1-W**, M = W) (Scheme 34). The reductions were shown to proceed via the 17VE radical intermediates [Tp'M(CO)$_2$(PMe$_3$)] (**2-Mo**, M = Mo; **2-W**, M = W). For comparison reason, the radical **2-Mo** was separately prepared by one-electron reduction of **1-Mo** and fully characterized.

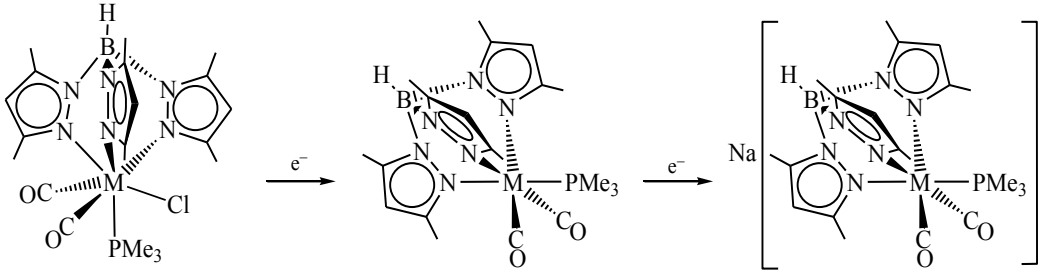

1-Mo (M = Mo) **2-Mo** (M = Mo) **3-Mo** (M = Mo)
1-W (M = W) **2-W** (M = W) **3-W** (M = W)

Scheme 34. Synthesis of the scorpionate metalate salts **3-Mo** and **3-W** via the 17VE radical intermediates **2-Mo** and **2-W** by the two-electron reduction of **1-Mo** and **1-W**, respectively.

The reactivity of the scorpionate metalate salts **3-Mo** and **3-W** was first investigated towards 1,2-dibromodisilene (*E*)-Tbb(Br)Si=Si(Br)Tbb, both in the presence and absence of 4-dmap (Scheme 35) (Chapter 2.1.2 and 2.1.3). The reaction in the presence of 4-dmap led to the zwitterionic silylidene complexes [Tp'(CO)$_2$M=Si(4-dmap)Tbb] (**6-Mo**, M = Mo; **6-W**, M = W), whereas that in the absence of 4-dmap directly afforded the silylidyne complexes

[Tp'(CO)$_2$M≡Si(Tbb)] (**7-Mo**, M = Mo; **7-W**, M = W). The silylidene and silylidyne complexes were isolated and fully spectroscopically and structurally characterized. The silylidene complexes **6-Mo** and **6-W** display an interesting dynamic behavior in solution, which was thoroughly investigated by NMR and IR spectroscopy, in which the 4-dmap substituent dissociates and forms the corresponding silylidyne complexes. Thereafter, it was also shown that treatment of the silylidene complexes with the Lewis acid $B(C_6F_5)_3$ yielded the corresponding silylidyne complexes **7-Mo** and **7-W**.

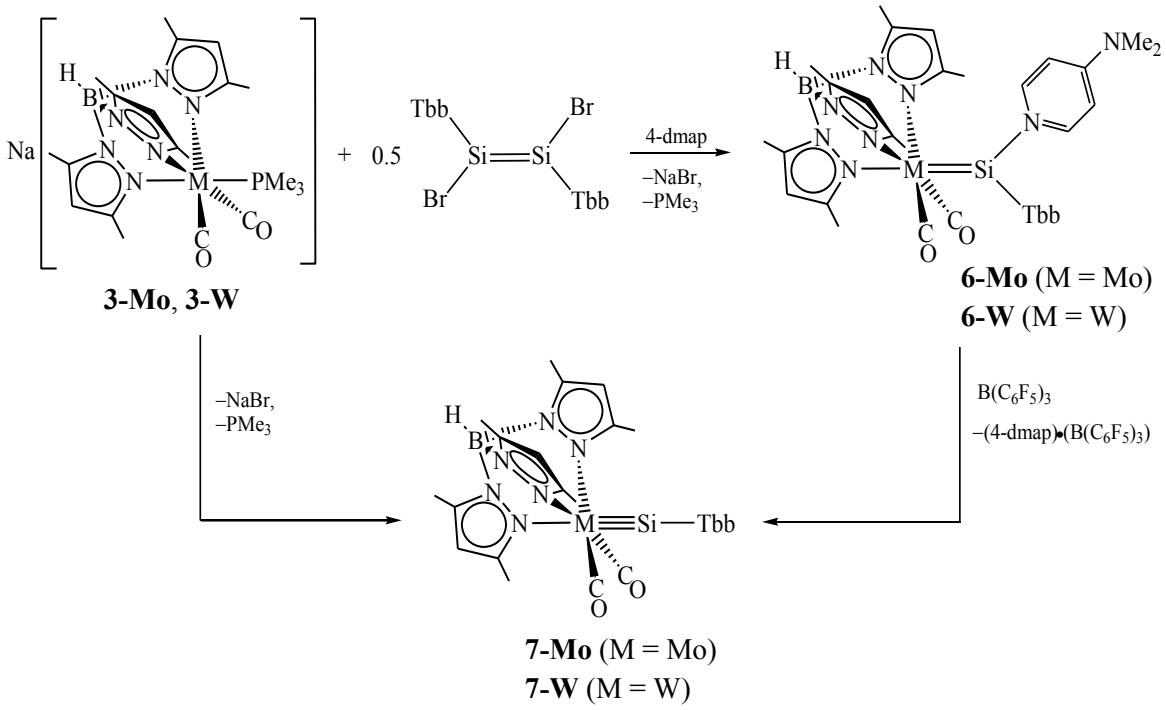

Scheme 35. Synthesis of silylidene and silylidyne complexes from 1,2-dibromodisilene.

In the quest for structurally diverse silylidyne complexes, the metalate salt **3-Mo** was also reacted with the Si(II) cation salt [(Cp*)Si][$B(C_6F_5)_4$], which afforded the unprecedented silylidyne complex [Tp'(CO)$_2$Mo≡Si(Cp*)] (**5-Mo**) (Scheme 36) (Chapter 2.1.3). The solid-state structure of the silylidyne **5-Mo** revealed an η^3-coordination of the Cp* substituent to the Si atom. Interestingly, compound **5-Mo** represents the first example of a heavier tetrylidyne complex, which features a π-bound substituent at the tetrel atom.

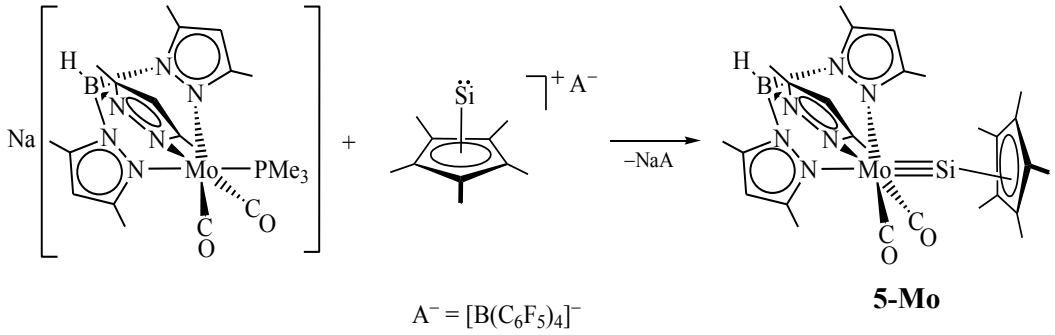

Scheme 36. Facile access to the silylidyne complex **5-Mo** upon reaction of **3-Mo** with [(Cp*)Si][$B(C_6F_5)_4$].

In chapter 2.1.4 the synthesis and full characterization of a series of closed-shell tetrylidyne complexes of the general formula [$Tp^x(CO)_2M{\equiv}E–R$] (Tp^x = Tp', R = C_6H_3-2,6-Mes_2: **8-Mo** (M = Mo, E = Ge), **8-W** (M = W, E = Ge), **9-Mo** (M = Mo, E = Sn), **9-W** (M = W, E = Sn), **10-Mo** (M = Mo, E = Pb), **10-W** (M = W, E = Pb); Tp^x = Tp', R = N(TMS)Mes*: **11-Mo** (M = Mo, E = Ge), **11-W** (M = W, E = Ge), **16-Mo** (M = Mo, E = Sn); Tp^x = Tp, R = C_6H_3-2,6-Mes_2: **12-Mo** (M = Mo, E = Ge); Tp^x = Tp', R = C_6H_3-2,6-$Trip_2$: **13-Mo** (M = Mo, E = Ge), **17-Mo** (M = Mo, E = Pb); Tp^x = Tp', R = Mes*: **14-Mo** (M = Mo, E = Ge); Tp^x = Tp', R = Eind: **15-Mo** (M = Mo, E = Ge) is described. The tetrylidyne complexes, except **8-W**, **12-Mo** and **13-Mo**, which were prepared from the triscarbonyl metalates K[Tp'M$(CO)_3$] (M = Mo, W), were mainly prepared from the scorpionate metalate salts **3-Mo** and **3-W** by metathetical halide exchange with the corresponding halotetrylenes E(X)R (X = Cl – I). Compounds **9-Mo**, **9-W**, **10-Mo**, **10-W**, **16-Mo** and **17-Mo** are the first examples of group 6 metals stannylidyne and plumbylidyne complexes obtained by salt metathesis. All the tetrylidyne complexes featuring a C_6H_3-2,6-Mes_2 substituent were thoroughly investigated by cyclic voltammetry, which revealed a reversible one-electron reduction for all complexes in the potential range of (–2.038) – (–1.729) V, thus suggesting them to be very promising precursors for open-shell tetrylidyne complexes.

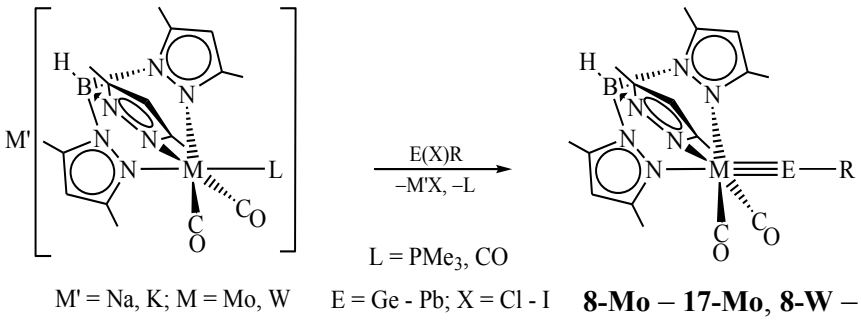

Scheme 37. Facile access to group 6 metals tetrylidyne complexes bearing a Tp' ligand by salt metathesis.

In chapter 2.2 the synthesis and characterization of an unprecedented open-shell germylidyne radical anion salt $K(THF)_3[Tp'(CO)_2MoGe(C_6H_3\text{-}2,6\text{-}Mes_2)]$ (**18-Mo**) is presented. Compound was obtained upon one-electron reduction of the closed-shell precursor **8-Mo** using KC_8 (Scheme 38). Compound **18-Mo** is the first example of an open-shell ylidyne complex in which the spin density is centered on a heavier p-block element. Compound **8-Mo** also undergoes an interesting reaction with *i*PrNC (Chapter 2.3) involving a Mo–Ge complete bond cleavage and an isocyanide-isocyanide C-C coupling affording an unprecedented N-heterocyclic germylene **19-Mo** (Scheme 38).

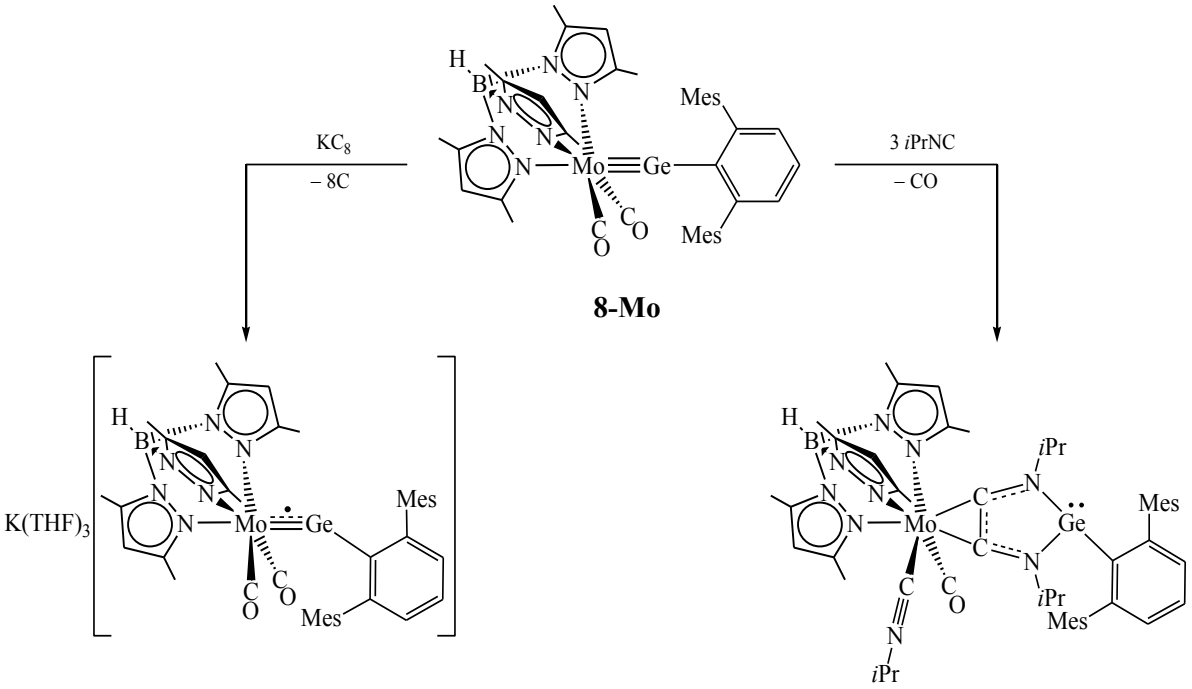

Scheme 38. Synthesis of the unprecedented open-shell germylidyne radical anion salt **18-Mo** and the N-heterocyclic germylene **19-Mo** from **8-Mo**.

Chapter 2.4 dealt with the synthesis and full characterization of the manganese stannylidene and stannylidyne complexes. The manganese chlorostannylidene complex *trans*-$[H(dmpe)_2Mn{=}Sn(Cl)(C_6H_3\text{-}2,6\text{-}Mes_2)]$ (**40**) was obtained starting from $[MnH(\eta^2\text{-}H_2)(dmpe)_2]$ (**1-Mn**) and $SnCl(C_6H_3\text{-}2,6\text{-}Mes_2)$ following a new method involving dihydrogen elimination (Chapter 2.4.1) (Scheme 39). The chloride abtraction from the intermediate chlorostannylidene complex **40** afforded the stannylidyne complexes *trans*-$[H(dmpe)_2Mn{\equiv}Sn(C_6H_3\text{-}2,6\text{-}Mes_2)][B\{C_6H_3\text{-}3,5\text{-}(CF_3)_2\}_4]$ (**41**) and *trans*-$[H(dmpe)_2Mn{\equiv}Sn(C_6H_3\text{-}2,6\text{-}$

Mes_2)][Al{$OC(CF_3)_3$}$_4$] (**42**) (Scheme 39). Compounds **41** and **42** represent the first examples of structurally characterized manganese stannylidyne complexes (Chapter 2.4.2).

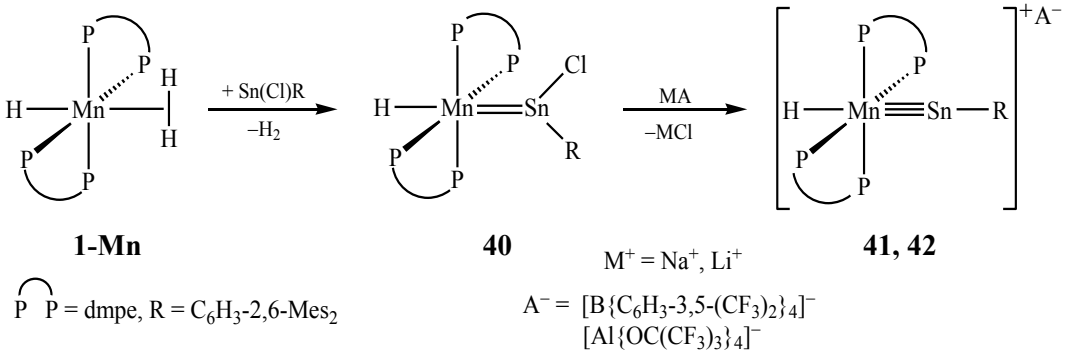

Scheme 39. Facile access to the stannylidyne complexes **41** and **42** by the dihydrogen elimination at the Mn center followed by the chloride abstraction from the intermediate chlorostannylidene complex **40**.

The reaction of the stannylidyne complex **41** with KH led to the first manganese hydridostannylidene complex *trans*-[H(dmpe)$_2$Mn=SnH(C_6H_3-2,6-Mes_2)] (**44**) (Chapter 2.4.3) (Scheme 40). Chapter 2.5 includes the synthesis and full characterization of the first open-shell stannylidyne complex *trans*-[H(dmpe)$_2$MnSnC_6H_3-2,6-Mes_2)] (**43**) featuring a Sn-centered unpaired electron.

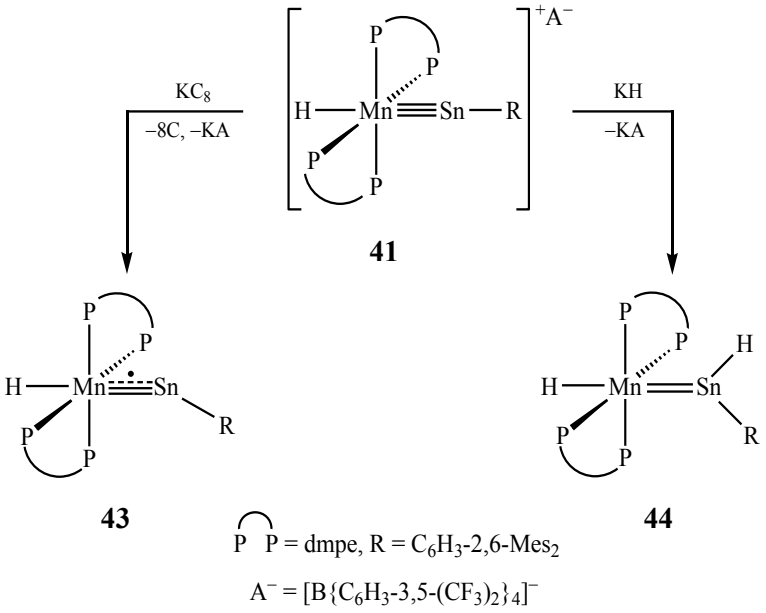

Scheme 40. One-electron reduction and hydride addition of the manganese stannylidyne complex **41**.

The scorpionate metalate salts **3-Mo** and **3-W** were not only very useful precursors for the synthesis of the tetrylidyne complexes of the general formula [Tp'$(CO)_2$M≡E–R], but also were

found to be very convenient metal precursors for the synthesis of the unprecedented metallatetrylidyne complexes [Tp'$(CO)_2$M≡E–M$(CO)_2$$(PMe_3)$Tp'] (M = Mo, W; E = Si, Ge) (Chapter 2.6). Thus, reactions of **3-Mo** and **3-W** with $SiBr_2$(SIdipp) or $GeCl_2$(1,4-dioxane) in a 2:1 ratio at ambient temperature led to the formation of the first metallasilylidyne (**21-Mo**, **21-W**) and metallagermylidyne (**22-Mo**, **22-W**) complexes (Scheme 41).

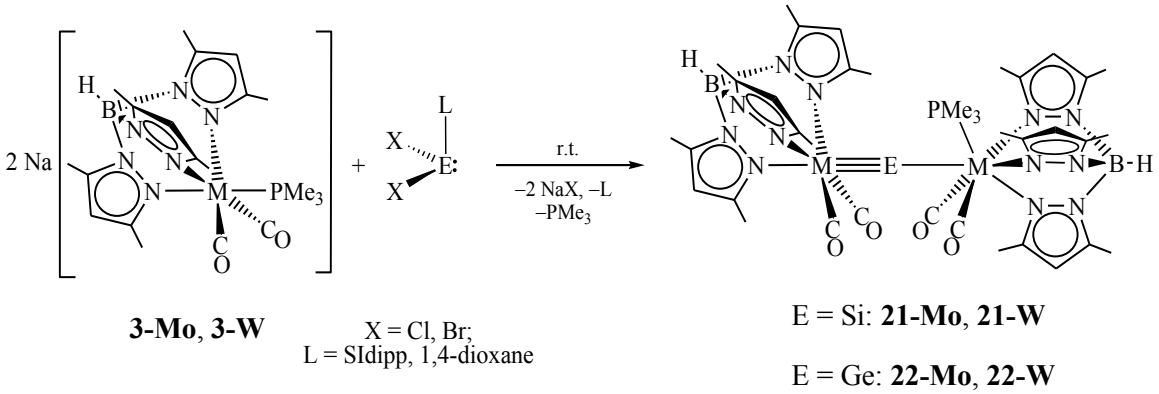

3-Mo, **3-W** X = Cl, Br; L = SIdipp, 1,4-dioxane

E = Si: **21-Mo**, **21-W**

E = Ge: **22-Mo**, **22-W**

Scheme 41. Facile access to the first examples of metallasilylidyne and metallagermylidyne complexes.

The success in isolating these novel metallasilylidyne (**21-Mo**, **21-W**) and the metallagermylidyne (**22-Mo**) complexes prompted us to study their reactivity, which provided access to many unprecedented complexes (Chapter 2.7). For example, the reactions of **21-Mo** and **22-Mo** with MesNC afforded after substitution of the PMe_3 ligand the MesNC substituted metallatetrylidyne complexes [Tp'$(CO)_2$Mo≡E–Mo$(CO)_2$(MesNC)Tp'] (**23-Mo**, E = Si; **24-Mo**, E = Ge) (Scheme 42). Compounds **23-Mo** and **24-Mo** display similar structural and spectroscopic properties to their PMe_3 substituted precursors. Treatment of Brookhart's acid, $[H(OEt_2)_2][B\{C_6H_3\text{-}3,5\text{-}(CF_3)_2\}_4]$ with **21-Mo**, **21-W** and **22-Mo** resulted in the formation of the protonated complexes [Tp'$(CO)_2$M(H)EM$(CO)_2$$(PMe_3)$Tp'][B{$C_6H_3$-3,5-$(CF_3)_2$}$_4$] (**25-Mo**, M = Mo, E = Si; **25-W**, M = W, E = Si; **26-Mo**, M = Mo, E = Ge) (Scheme 42). The spectroscopic and structural parameters of **25-M** and **26-M** suggest that the added proton is located in a bridging position between the hexacoordinated metal centers and the tetrel atoms. Interestingly, the addition of polar reagents such as [(PMe_3)AuCl] and MeI to the metallatetrylidyne complexes follows two different paths. In the case of [(PMe_3)AuCl], the electrophilic $[Au(PMe_3)]^+$ occupies a bridging position between the hexacoordinated Mo-center and the tetrel atoms, and the chloride anion binds to the heptacoordinated Mo-center yielding the unprecedented μ_3-ylido complexes [Tp'$(CO)_2$Mo(η^3-AuPMe_3)EMo$(CO)_2$(Cl)Tp'] (**27-Mo**, E = Si; **28-Mo**, E = Ge) (Scheme 42). Notably, compound **27-Mo** represents the first example of a μ_3-silicido complex. In contrast, the

reaction of **21-Mo** with MeI led to the formation of [Tp'(CO)$_2$Mo=Si(I)–Mo(CO)$_2$(Me)Tp'] (**29-Mo**), in which the methylium (Me^+) ion substituted the PMe_3 ligand and the iodide ion was attached to the silicon center. The two reactions indicate the ambiphilic character of the tetrel atoms in μ-ylido complexes.

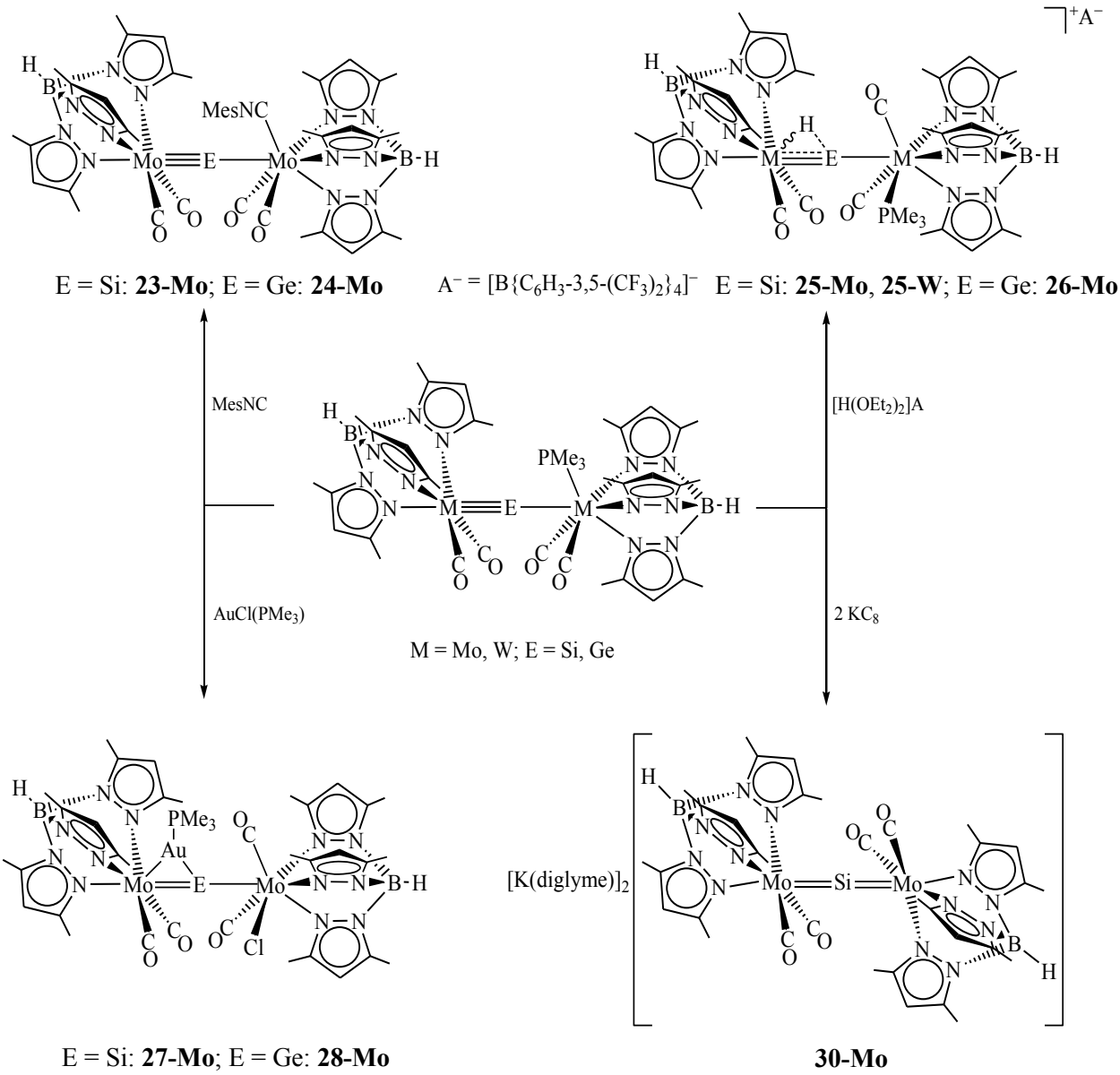

Scheme 42. Reactivity of the metallatetrylidyne complexes.

Reduction of the metallasilylidyne complex **21-Mo** afforded the *μ*-silicido complex dianion [K(diglyme)]$_2$[(μ-Si){Mo(CO)$_2$Tp'}$_2$] (**30-Mo**) with concomitant elimination of the PMe_3 ligand (Scheme 42). Compound **30-Mo** is the first silicon analogue of a metallacumulene and also

represents the first example of a compound featuring a perfectly linear-coordinated doubly-bonded silicon atom.

Addition of alkynes to the metallasilylidyne complexes **21-Mo** and **21-W** afforded the very interesting tricyclic complexes [Tp'$(CO)_2$MSiC(R^1)C(R^2)M$(CO)_2$Tp'] (**31-Mo**: M = Mo, R^1,R^2 = Me; **31-W**: M = W, R^1,R^2 = Me; **32-Mo**: M = Mo, R^1 = H, R^2 = TMS; **32-W**: M = W, R^1 = H, R^2 = TMS; **33-Mo**: M = Mo, R^1 = H, R^2 = Ph) instead of [2+2]-cycloaddition products (Scheme 43). Auspiciously, the addition products are the first compounds featuring planar tetracoordinated silicon centers (ptSi).

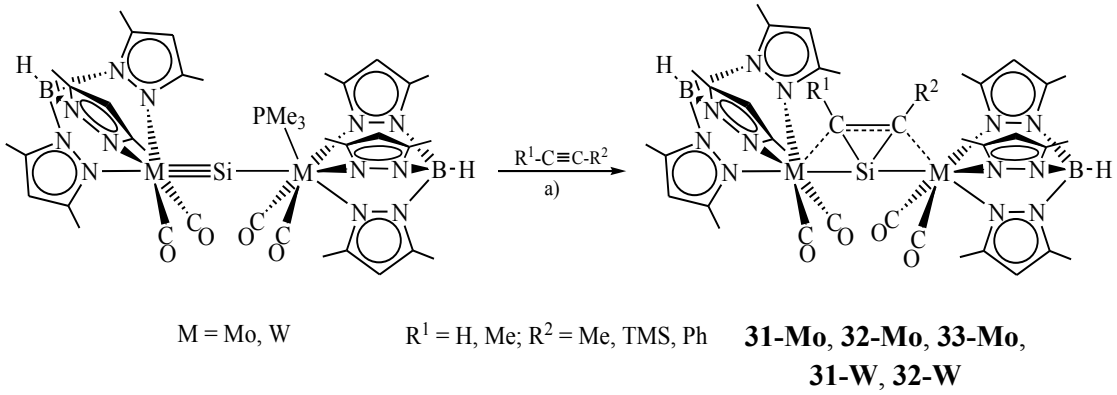

Scheme 43. Addition of alkynes to metallasilylidyne complexes **21-Mo** and **21-W**.

The chapter 2.8 describes the synthesis and charcterization of manganese plumbylidene and plumbylidyne complexes, and an unprecedented intermetallic plumbylidyne ligand transfer reaction. The manganese metalate salt PPN[MnCl(η^5-C_5H_4Me)$(CO)_2$] (**3-Mn**) was reacted with different haloplumbylenes Pb(X)(C_6H_3-2,6-Mes_2) (X = Cl – I) to obtain a series of haloplumbylidene complexes [(η^5-C_5H_4Me)$(CO)_2$Mn=Pb(X)(C_6H_3-2,6-Mes_2)] (**35**, X = Cl; **36**, X = Br; **37**, X = I). Chloride abstraction from the chloroplumbylidene complex **35** using Na[B{C_6H_3-3,5-$(CF_3)_2$}$_4$] resulted in the plumbylidyne complex [(η^5-C_5H_4Me)$(CO)_2$Mn≡Pb(C_6H_3-2,6-Mes_2)][B{C_6H_3-3,5-$(CF_3)_2$}$_4$] (**39**), which was fully characterized. Finally, treatment of the manganese plumbylidyne complex **39** with the scorpionate metalate salt Na[Tp'Mo$(CO)_2(PMe_3)$] (**3-Mo**) yielded the plumbylidyne complex **10-Mo** after plumbylidyne ligand transfer from the Mn to the Mo center. The transfer reactions were investigated throughly by NMR and IR spectroscopy.

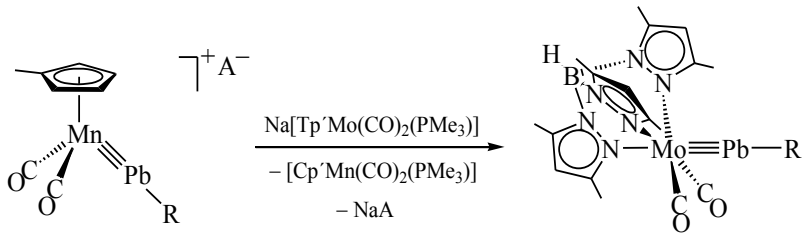

39 **10-Mo**

Scheme 44. Unprecedented plumbylidyne ligand transfer reaction from Mn to Mo center.

Chapter 2.9 delt with the synthesis and characterization of a novel NHC-stabilized disilavinylidene (*Z*)-(SIdipp)Si=Si(Br)Tbb (**46**) obtained via two-electron reduction of the NHC-stabilized bromo(silyl)silylene $SiBr(SiBr_2Tbb)(SIdipp)$ (**45**) (Scheme 45). The unprecedented NHC-stabilized bromo(silyl)silylene **45** was successfully prepared by heating of a 2:1 mixture of $SiBr_2(SIdipp)$ and (*E*)-Tbb(Br)Si=Si(Br)Tbb in toluene at elevated temperature. Compound **46** is the first example of a bottlable disilavinylidene isolated under normal experimental conditions.

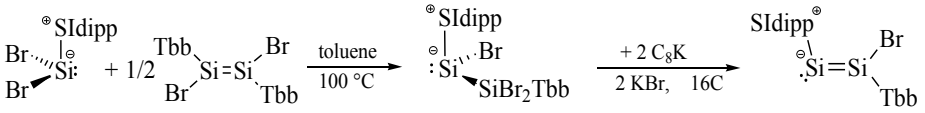

45 **46**

Scheme 45. Facile access to the NHC-stabilized bromo(silyl)silylene **45** and disilavinylidene **46**.

3.2. Outlook

The present work has demonstrated that open-shell tetrylidyne complexes featuring a tetrel-centered unpaired electron can be obtained by one-electron reduction of corresponding closed-shell tetrylidyne complexes. Examples included the first germylidyne radical anion salt $K(THF)_3[Tp'(CO)_2MoGe(C_6H_3\text{-}2,6\text{-}Mes_2)]$ (**18-Mo**) and the neutral metal stannylidyne radical *trans*-$[H(dmpe)_2MnSn(C_6H_3\text{-}2,6\text{-}Mes_2)]$ (**43**). Since the cyclic voltammograms of all the Tp'-substituted group 6 metal tetrylidyne complexes $[Tp'(CO)_2M{\equiv}E(C_6H_3\text{-}2,6\text{-}Mes_2)]$ (M = Mo, W; E = Ge – Pb) display a reversible one-electron electrochemical reduction, chemical reduction of these compounds by one-electron might lead to open-shell ylidyne radical anions of Sn and Pb (Figure 97). Furthermore the silylidyne complexes $[Tp'(CO)_2M{\equiv}Si–Tbb]$ (M = Mo, W) displayed an electrochemically reversible one-electron oxidation. Thus, preparation of open-shell metal silylidyne radical cations $[Tp'(CO)_2M{\equiv}Si–Tbb]^+$ (Figure 97) could also be tried in future using a suitable one-electron oxidizing agent.

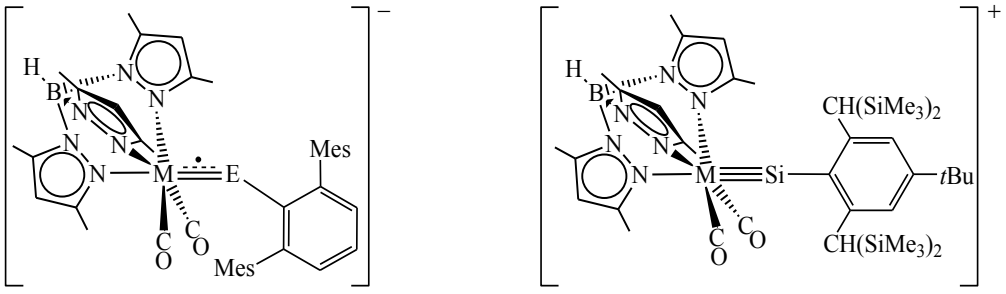

Figure 97. Feasible tetrylidyne radical anions and radical cations.

Formation of the μ-ylido complexes [Tp'$(CO)_2$M≡E–M$(CO)_2$$(PMe_3)$Tp'] (M = Mo, W; E = Si, Ge) upon reaction of Tp'-substituted metalate salts **3-Mo**/**3-W** with $SiBr_2$(SIdipp) or $GeCl_2$(1,4-dioxane) in a 2:1 ratio presumably proceeds either through the intermediate halotetrylidyne complexes [Tp'$(CO)_2$M≡E–X] (M = Mo, W; E = Si, Ge; X = Cl, Br) or the base-stabilized halotetrylidyne complexes [Tp'$(CO)_2$M=E(X)L] (L = SIdipp, 1,4-dioxane). Especially appealing would be the haloylidyne complexes (Figure 98), which might be accessible using a sterically more bulky scorpionate ligand, such as Tp^{iPr2}.

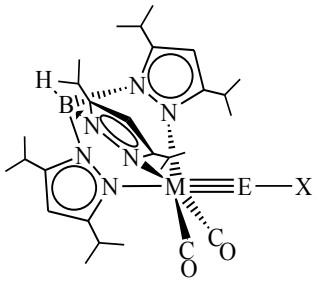

Figure 98. Feasible haloylidyne complexes using sterically more bulky Tp^{iPr2} ligand.

The present work demonstrated the superiority of the scorpionate ligands over Cp/Cp* ligand in the isolation of highly ractive ylidyne or μ-ylido complexes. Therefore, it is conceivable that scorpionate ligands would be also interesting to make ylidyne or μ-ylido complexes of other transition metals. For example, the well known titanium metalate salt Et_4N[TpTi$(CO)_4$] could be employed for the synthesis of ylidyne or μ-ylido complexes of titanium (Figure 99). Furthermore, the Ir(I) complex [TpIr$(C_2H_4)_2$] is known to lose one ethylene ligand to form the reactive 16VE intermediate [TpIr(C_2H_4)]. The intermediate [TpIr(C_2H_4)] could be trapped with a variety of halotetrylenes EX$(C_6H_3$-2,6-$Mes_2)$ (E = Ge – Pb; X = Cl – I) to form the Tp-substituted tetrylidene complexes of the general formula [Tp(C_2H_4)Ir=E(X)$(C_6H_3$-2,6-$Mes_2)$], which after

halide abstraction might lead to unprecedented iridium tetrylidyne complex cations $[Tp(C_2H_4)Ir{\equiv}E(C_6H_3\text{-}2,6\text{-}Mes_2)]^+$ (Figure 99). Moreover, preparation of neutral tetrahedral tetrylidyne complexes of group 10 transition metals of the general formula $[Tp'M{\equiv}E(C_6H_3\text{-}2,6\text{-}Mes_2)]$ (M = Ni, Pt, Pd; E = Si – Pb) could be also accessible starting from KTp', $M(COD)_2$ and a suitable halotetrylene (Figure 99).

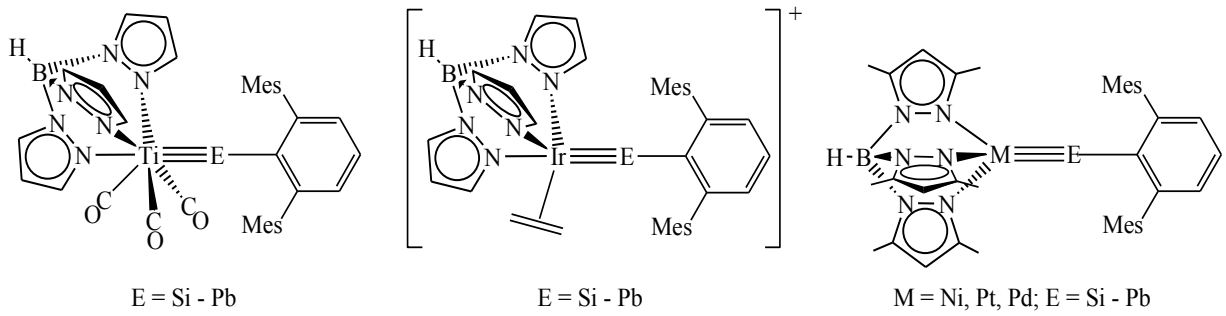

Figure 99. Feasible tetrylidyne complexes of group 4, 9, 10 transition metals using Tp/Tp' ligands.

Preliminary reactivity studies of the ylidyne and μ-ylido complexes resulted in many unprecedented complexes with unexpected bonding features. Thus, it would be very interesting to investigate further the reactivity of these complexes and to understand better the electronic structure of these compounds.

4 Experimental Section

4.1. General Part

All experiments were carried out in an argon atmosphere under strict exclusion of oxygen and moisture using Schlenk or glove box techniques.[265] The glove-box (MBRAUN) was maintained under an argon atmosphere with typically +1.5 mbar pressure (H_2O content <0.1 ppm; O_2 content <0.1 ppm). Argon was commercially received with a purity of ≥ 99.999 % and passed through a gas purification system composed of two consecutive columns to remove traces of water and oxygen. The first column was filled with BTS copper catalyst R3-11G from BASF and heated at ~80 °C and the second column with 4 Å molecular sieves. Regeneration of the internal glove-box catalyst at regular intervals was also carried out (typically every six - twelve months) using 5 % H_2 doped argon regeneration gas and the automatic regeneration routine of the glove-box.The solvents were refluxed for ~3 days over the corresponding drying agents, flushed several times with argon during reflux and distilled under argon. For very air-sensitive compounds solvents were used from the glove box which was additionally degassed before storage. For large scale experiments solvents stored over 4 Å molecular sieves were used.

Solvent	Pre-drying agent	Drying agent
n-pentane, *n*-heptane, petrol ether	---	Na-wire
C_6H_5F, C_6H_5Cl, 1,2-$C_6H_4F_2$	---	CaH_2
CH_3CN, CH_3CH_2CN	---	CaH_2
n-hexane	Na-wire	Na/Benzophenone/tetraglyme
benzene, Et_2O, THF, DME	Na-wire	Na/Benzophenone
diglyme		Na-wire
toluene	---	K
CH_2Cl_2	Sicapent	Na/Pb alloy

For extremely sensitive compounds solvents were freshly recondenced from the corresponding drying agent: *n*-pentane, *n*-hexane, benzene from KC_8; Et_2O, THF and DME from K/benzophenone or KC_8. For air-stable compounds commercially available solvents were used without further purification.

For transfer of solvents or solutions during reaction, stainless steel cannulas were used, which were dried before use in the oven at 110 °C. The transfer was facilitated by the vessel of origin being left under a positive pressure of argon gas, and the receptable vessel closed with a pressure release valve. Filtrations of the reaction mixture were done using stainless steel cannulas containing a filter-head at one end of the cannulas. Whatmann® (GF/B 25) filter paper was used for such filtration which was fixed with Teflon tape on the filter-head of the cannulas and store for few minutes in the oven at 110 °C prior to use. After use, cannulas were cleaned by through rinsing with acetone, followed by dilute HCl, distilled water and again acetone.

All glassware was cleaned by storage in a KOH/isopropanol bath for 2 – 3 days, followed by thoroughly washing with tap water, then storage in the dilute HCl bath for 1 – 2 hours and finally cleaned with tap water, acetone and distilled water. The clean glassware was then dried in the oven at ~110 °C for overnight. The glassware was baked before use at 650 °C and allowed to cool to ambient temperatures under active vacuum. All glass joints were greased with Glisseal® HV laboratory grease, or in the case of higher temperature reactions, involving refluxing solvents, Teflon grease was used. For low temperature reactions, isopropanol or petrol ether together with dry ice or liquid N_2 was used on Dewar vessels.

4.2. Analytical Methods

4.2.1 IR spectroscopy

IR spectra of solutions were recorded on a Nicolet 380 FT-IR spectrometer in the range of 2200 – 1500 cm^{-1} using a cell of NaCl windows. IR spectra of the pure solids were recorded on a Bruker Alpha FT-IR spectrometer in the range of $4000 - 400$ cm^{-1} in the glove using the platinum single reflection diamond ATR module. The following abbreviations were used for the intensities of absorption bands: vs = very strong, s = strong, m = medium, w = weak, vw = very weak, sh = shoulder.

4.2.2 NMR spectroscopy

NMR spectra were recorded on a Bruker Avance DMX-300, DPX-300, DPX-400 or DMX-500 NMR spectrometer. The samples were normally prepared either in screw-cap 5 mm NMR sample tubes or Young type NMR tubes with rotaflo gas-tight Teflon stoppers, latter one being preferred method for highly sensitive compounds. The deuterated solvents for samples were dried over the corresponding drying agent (Table 40), degassed and trap-to-trap recondensed and stored

over 4 Å molecular sieves. The ^{1}H and $^{13}C\{^{1}H\}$-NMR spectra were calibrated against the residual proton and natural abundance ^{13}C resonances of the deuterated solvent relative to tetramethylsilane (Table 40). Heteronuclear spectra were calibrated as followes: $^{19}F\{^{1}H\}$: external $CFCl_3$; $^{31}P\{^{1}H\}$: external 85 % H_3PO_4; $^{119}Sn\{^{1}H\}$: external $SnMe_4$; The standard was filled in a capillary, which was sealed-off and introduced in a 5 mm NMR tube containing the corresponding deuterated solvent. The NMR tube was finally vacuum-sealed and used for the calibration.

Table 40. Deuterated solvents drying agent and calibrations (multiplicity of the signals in brackets)

Solvent	Drying agent	^{1}H NMR, δ, ppm	^{13}C NMR, δ, ppm
C_6D_6	Na	7.15 (br)	128.0 (3)
Toluene-d_8	Na	2.09 (5)	20.4 (7)
THF-d_8	Na	1.73 (br)	25.3 (5)
CD_3CN	CaH_2	1.93 (br)	1.3 (7)
CD_2Cl_2	CaH_2	5.32 (3)	53.8 (5)
$CDCl_3$	CaH_2	7.24 (1)	77.0 (3)

The following abbreviations were used for the forms and multiplicities of the NMR signals: s = singlet, d = doublet, t = triplet, q = quartet, sept = septet, m = multiplet, br = broad. The ^{1}H and ^{13}C NMR signals of all compounds were assigned by a combination of HMQC, HMBC and DEPT experiments. In addition, the selective 1D transient (DPFGSE) NOE experiments were carried out for some Tp' containing complexes to assign the C^3- and C^5-bonded methyl protons. These experiments allowed in combination with the HMQC and HMBC experiments to assign unequivocally the C^3 and C^5 resonances of the 3,5-dimethylpyrazolyl groups. For Tp' containing complexes, the abbreviation pz_A was used to denote the two symmetry-equivalent (enantiotopic) 3,5-dimethylpyrazolyl groups of the Tp' ligand and the subscript pz_B for the third (diastereotopic) 3,5-dimethylpyrazolyl arm of the Tp' ligand lying in the symmetry plane of the overall pseudo-C_s symmetric complexes. For complexes comprising two chemically different (constitutionally heterotopic) Tp' ligands, the subscript characters I and II were used to denote two different Tp' ligands.

4.2.3 X-ray Crystallography

Generally, suitable crystals for the X-ray diffraction analysis were separated from the supernatant solution at the temperature of crystallization and covered with Fomblin® Y lubricant to protect from air and moisture. A crystal suitable for measurement was selected on a microscope and transferred to the diffractometers. The data were collected on a STOE IPDS IIT diffractometer equipped with an Oxford Cryostream 700er series low-temperature cooling device or a Brucker X8-KappaApexII equipped with a Kryoflex, Brucker AXS low-temperature cooling device or on a Nonius Kappa CCD diffractometer equipped with an Oxford Cryostream 600er series low-temperature cooling device or on a Bruker D8-Venture diffractometer equipped with an Oxford Cryostream 800er series low-temperature cooling device. For all experiments, except for those measure on Bruker D8-Venture, Mo-*K*α graphite-monochromated radiation (λ = 0.71073 Å) was used. For experiments on Bruker D8-Venture, Cu-*K*α graphite-monochromated radiation (λ = 1.54178 Å) was used. Intensities were measured using the rotation method and upon complete data collection were corrected for background, polarization and Lorentz effects. The absorption correction (numerical or semi-empirical from equivalents), structure solution (direct or Patterson methods), and structure refinement, using full-matrix least squares on F^2, were carried out using the SHELX-97 programs.[39] All atoms with the exception of hydrogen were anisotropically refined. The hydrogen atoms were included isotropically using the riding model on the bound carbon atoms. Metal hydride hydrogen atoms were located by the difference in the Fourier synthesis map, isotropically refined and normalized. The graphical representation of the molecular structures was carried out using DIAMOND version 2.1c. The details for the individual structure solutions included in this dissertation are available in the appendix.

4.2.4 Elemental analysis

The elemental analysis samples were prepared in ‘‘tin-boats’’ in the glove box and was sealed off very tightly before bringing out of the glove box to minimized any contact with the atmosphere. The C, H, N analyses of all compounds were carried out three times on an Elementar Vario Micro elemental analyser or a Leco CHNS-932 analyser. The individual C, H, N values did not differ by more than 0.3% (absolute). The mean values of the measurements are given for each compound.

39 G. M. Sheldrick, SHELXS97 and SHELXL97, University of Göttingen, Germany, 1997.

4.2.5 Melting point determination

The melting points were determined in duplicate for each sample using M-560 or B-545 Büchi melting point apparatus. The samples were sealed in capillary tubes under vacuum and rapidly heated to a temperature approximately 20 K lower than that at which melting or decomposition started. Heating was then continued with a rate of approximately 2 K min^{-1} until the sample melted or decomposed. Afterwards the samples were allowed to cool to room temperature and investigated by NMR or solution IR spectroscopy to confirm whether decomposition had occurred upon thermal treatment.

4.2.6 Cyclic voltametry

Cyclic voltammetric studies were performed with an Autolab Eco electrochemical work station composed of an Autolab PGSTAT 20 potentiostat/galvanostat. The results were analyzed with the Autolab software version 4.9. Experiments were carried out in a glove box or outside under arogon in a gas-tight specially designed full-glass three-electrode cell. A glass carbon disk electrode (d = 2 mm) was used as working electrode, a Pt wire of 1 mm diameter as counter electrode and a $Fe(C_5Me_5)_2/Fe(C_5Me_5)_2^+$ solution (4 mM in THF/0.1 M [*n*-Bu_4N]PF_6) as reference electrode, which was separated from the substrate/electrolyte solution by a Luggin capillary fitted with a Vycor Diaphragm (4 mm). For all experiments *iR*-drop compensation was used. [*n*-Bu_4N]PF_6 was used as supporting electrolyte and THF, fluorobenzene or 1,2-diflurobenzene as solvent.

4.2.7 EPR Spectroscopy

The EPR spectra were recorded on an ELEXSYS E580 EPR spectrometer from Bruker equipped with an ER 4122 Super High Sensitivity (SHQ) resonator for the X-band, an EN5107D2 for the Q-band, and an ER 4118S-MS5 for S-band measurements. The temperature was controlled with an Oxford ESR900 cryostat for the X-band resonator and a CF935 cryostat for the Q-band and S-band measurements, both in the combination with a temperature controlling unit ITC503S. Determination of the *g*-values were done with Mn^{2+}/MgO as standard and the line positions were corrected as detailed in the literature.[266] All spectra were background corrected and the simulations were carried out using the program *EasySpin*.[267]

4.2.8 UV-Vis Spectroscopy

UV-Vis spectrophotometric investigations were carried out on an Evolution 300 spectrophotometer from the Thermo electron corporation. Normally samples were prepared inside the glove box using pure samples and extremely dry and degassed solvents. The spectra of several concentrations were measured and the extinction coefficient (ε) were determined by plotting absorbance to concentration of the appropriate absorbance band, and determining the gradient of the linear regressed line through the data points using Microsoft Excel 2007 programme.

4.3. Starting materials prepared according to literature procedures

Reagent	References	Experimentator
KTp'	[268]	Ghana/Bogner/Portius
KTp	[269]	–
K[Tp'Mo(CO)$_3$]	[103]	Ghana
K[Tp'W(CO)$_3$]	[103]	Ghana
Tp'Mo(CO)$_2$Cl	[104]	Ghana
Tp'W(CO)$_2$(PMe$_3$)Cl	[103]	Ghana
MnH(η^2-H$_2$)(dmpe)$_2$]	[162]	Ghana
PPN[(η^5-C$_5$H$_4$Me)Mn(CO)$_2$Cl]	[217]	Ghana
C$_6$H$_3$I-2,6-Mes$_2$	[270]	Hofer/Kühlmorgen
C$_6$H$_3$I-2,6-Trip$_2$	[271]	Hofer
LiC$_6$H$_3$-2,6-Mes$_2$	[272]	Ghana
(Et$_2$O)LiC$_6$H$_3$-2,6-Trip$_2$	[273]	Ghana
PMe$_3$	[274]	Ghana/Kühlmorgen/Papazoglou
dmpe	[275]	Kühlmorgen/Ghana
SIdipp	[176]	Kühlmorgen/Bogner
IMe$_4$	[33]	Kühlmorgen
SiBr$_4$	[33]	Kühlmorgen
GeCl$_4$	[276]	Kühlmorgen
GeCl$_2$·1,4-dioxane	[277]	Ghana

$SiBr_2$(SIdipp)	[33]	Ghana
$(C_6H_3$-2,6-$Mes_2)SiCl(IMe_4)$	[107]	Chernov
$(C_6H_3$-2,6-$Mes_2)GeCl$	[144]	Ghana
$(C_6H_3$-2,6-$Trip_2)GeCl$	[278]	Ghana
$(C_6H_3$-2,6-$Mes_2)SnCl$	[144]	Ghana
$(C_6H_3$-2,6-$Mes_2)PbCl$	[60]	Ghana
$(C_6H_3$-2,6-$Mes_2)PbBr$	[216]	Ghana
$(C_6H_3$-2,6-$Mes_2)PbI$	[279]	Ghana
$(C_6H_3$-2,6-$Trip_2)PbBr$	[216]	Ghana
GeCl{N(TMS)Mes*}	[38]	Ghana
SnCl{N(TMS)Mes*}	[38]	Ghana
E-(Tbb)BrSi=SiBr(Tbb)	[110]	Ghana/ Papazoglou/Hoffmann
Mes*GeCl	[280]	Ghana
(*E*)-Eind(Cl)Ge=Ge(Cl)Eind	-	Wienkenhöver
$[(PMe_3)AuCl]$	[281]	Ghana
$B(C_6F_5)_3$	[282]	Chernov
$Na[B\{C_6H_3$-3,5-$(CF_3)_2\}_4]$	[283]	Ghana
$Li[Al\{OC(CF_3)_3\}_4]$	[284]	Chakraborty
HCl/Et_2O	-	Ghana/Kühnel-Lysek
$H(OEt_2)[B\{C_6H_3$-3,5-$(CF_3)_2\}_4]$	[285]	Ghana
KC_8	[286]	Ghana
*t*BuC≡P	[287]	Puffler
[PPN]Cl	[288]	-

4.4. Commercially available starting materials

Reagent	Supplier	Pre-Purification
4-dmap	Fluka	
LiCl	Alfa Aesar	
LiBr	Sigma Aldrich	
LiI	Fluka	
MesNC	-	
*i*PrNC	-	
$CH_3C{\equiv}CCH_3$	ABCR	Dried over CaH_2 and recondensed
PhC≡CH	Fluka	
TMSC≡CH	–	
$C_2H_5C{\equiv}CC_2H_5$	Merck	

4.5. Syntheses

4.5.1 [Tp'Mo(CO)$_2$(PMe$_3$)Cl] (1-Mo)

PMe_3 (0.44 mL, ρ = 0.735 g/mL, 4.25 mmol, 1.2 equiv.), that was pre-cooled to −30°C, was added to a stirred solution of Tp'Mo(CO)$_2$Cl (1.726 g, 3.562 mmol) in *ca*. 50 mL of CH_2Cl_2 at −35°C. Upon addition, the color of the solution immediately changed from yellowish brown to light reddish brown. The solution was allowed to warm slowly to ambient temperature. An IR spectrum of the solution was recorded after 15 minutes of stirring and revealed that the ν_{CO} absorption bands of the starting material at 2013 and 1928 cm^{-1} had been replaced by those of the product at 1940 and 1841 cm^{-1}. The solvent was removed under reduced pressure and the residue transformed into a powder by grinding during a freeze-pump-thaw cycle. The resulting bright yellow powder was washed once with *n*-pentane/diethyl ether mixture (5:1, *ca*. 20 mL) and dried under vacuum for 1 hour at ambient temperature to afford complex **1-Mo** as a bright yellow solid. Yield: 1.841 g (3.283 mmol, 92%). Bright yellow single crystals suitable for X-ray crystallographic analysis were grown from a concentrated THF solution by cooling at −60 °C.

Properties: It is very well soluble in CH_2Cl_2 and THF, moderately soluble in toluene and Et_2O and insoluble in *n*-hexane. The compound is moderately air sensitive.

Melting Points: The solid slowly turns brown above 184 °C and decomposes upon melting at 221 – 222 °C to give a black oily mass.

Elemental analysis: calcd. (%) for $C_{20}H_{31}BClMoN_6O_2P$ (560.68 g/mol): C 42.84, H 5.57, N 14.99; found: C 42.55, H 5.71, N 15.52.

Spectroscopic Data:

IR (CH_2Cl_2): $\tilde{\nu}$ (cm^{-1}) = 1940 (s) and 1841 (vs) [ν(CO)], 1546 (m) [$\nu(C\text{-}C\text{-}N)_{pz}$].

IR (THF): $\tilde{\nu}$ (cm^{-1}) = 1936 (s) and 1840 (vs) [ν(CO)], 1547 (m) [$\nu(C\text{-}C\text{-}N)_{pz}$].

IR (toluene): $\tilde{\nu}$ (cm^{-1}) = 1936 (s) and 1839 (vs) [ν(CO)], 1547 (m) [$\nu(C\text{-}C\text{-}N)_{pz}$].

ATR-IR (solid): $\tilde{\nu}$ (cm^{-1}) = 2978 (vw), 2961 (vw), 2924 (vw), 2527 (vw) [ν(BH)], 1930 (s) [ν(CO)], 1825 (vs) [ν(CO)], 1546 (m) [$\nu(C\text{-}C\text{-}N)_{pz}$], 1492 (vw), 1441 (m), 1414 (m), 1381 (w, sh), 1371 (m), 1353 (w, sh), 1304 (vw), 1285 (vw, sh), 1278 (w), 1209 (m), 1194 (m), 1150 (vw), 1122 (vw), 1100 (vw, sh), 1064 (m), 1046 (w),

1036 (vw, sh), 983 (vw), 951 (m), 940 (m), 873 (vw), 854 (w), 810 (w), 796 (m, sh), 787 (m), 773 (m), 721 (w), 692 (m), 669 (w), 644 (m), 611 (w), 593 (vw), 572 (w), 560 (vw, sh), 512 (w), 473 (vw), 451 (m), 400 (vw).

^{1}H NMR: (300.1 MHz, CD_2Cl_2, 298 K): δ (ppm) = 2.03 (s, 3H, 1 × C^3-*Me*, pz_B), 2.10 (d, ^{2}J(P,H) = 10.5 Hz, 9H, P*Me*$_3$), 2.33 (s, 6H, 2 × C^3-*Me*, pz_A), 2.43 (s, 9H, 2 × C^5-*Me*, pz_A and 1 × C^5-*Me*, pz_B), 4.78 (br, $\Delta\nu_{1/2}$ = ~ 200 Hz, 1H, B*H*); this signal appears as a very broad hump over the base line in a strongly enlarged version of the spectrum), 5.90 (s, 3H, 3 × C^4-*H*, pz_A and pz_B).

^{13}C{^{1}H} NMR: (75.47 MHz, CD_2Cl_2, 298 K): δ (ppm) = 12.8 (s, 2C, 2 × C^5-*Me*, pz_A), 13.4 (s, 1C, 1 × C^5-*Me*, pz_B), 15.1 (s, 1C, 1 × C^3-*Me*, pz_B), 15.2 (s, 2C, 2 × C^3-*Me*, pz_A), 19.4 (d, ^{1}J(C,P) = 40.7 Hz, 3C, P*Me*$_3$), 107.1 (s, 2C, 2 × *C*^{4}-H, pz_A), 107.9 (s, 1C, 1 × *C*^{4}-H, pz_B), 144.7 (s, 2C, 2 × *C*^{5}-Me, pz_A), 147.3 (s, 1C, 1 × *C*^{5}-Me, pz_B), 151.8 (d, ^{3}J(C,P) = 1.9 Hz, 1C, 1 × *C*^{3}-Me, pz_B), 152.0 (s, 2C, 2 × *C*^{3}-Me, pz_A), 252.9 (d, ^{2}J(C,P) = 51.1 Hz, 2C, 2 × *C*O).

^{31}P{^{1}H} NMR: (121.5 MHz, CD_2Cl_2, 298 K): δ (ppm) = 33.6 (s).

4.5.2 [Tp´W(CO)$_2$(PMe$_3$)Cl] (1-W)

PMe_3 (0.52 mL, ρ = 0.735 g/mL, 5.02 mmol, 1.2 equiv.), that was pre-cooled to 0°C, was added to a stirred suspension of Tp´W(CO)$_3$Cl (2.5 g, 4.16 mmol) in 60 mL of THF at 0 °C. The suspension was slowly warmed to ambient temperature and stirred it for 40 hours at this temperature. Upon stirring the color of the suspension gradually changed from light brown to bright orange. The progress of the reaction was monitored by IR spectroscopy, which revealed a slow but selective conversion of the starting material (ν_{CO} = 2022, 1934 and 1906 cm^{-1}) into the product (ν_{CO} = 1916 and 1841 cm^{-1}). After completion of the reaction, the bright orange solution was evaporated to dryness and the residue transformed into a powder by grinding during a freeze-pump-thaw cycle. The resulting yellowish orange powder was washed once with petrol-ether (50 mL) and finally dried under reduced pressure for 30 minutes at ambient temperature to afford a very fine yellowish orange powder. Yield: 2.5 g (3.85 mmol, 93%).

Properties: It is very well soluble in CH_2Cl_2 and THF, moderately soluble in toluene and Et_2O and insoluble in aliphatic solvents. Compound **1-W** is moderately sensitive towards the air.

Melting Points: The solid decomposes upon melting at 199–202 °C to give a dark brown oily mass.

Elemental analysis: calcd. (%) for $C_{20}H_{31}BClN_6O_2PW$ (648.58 g/mol): C 37.04, H 4.82, N 12.96; found: C 37.04, H 4.92, N 12.96.

Spectroscopic Data:

IR (CH_2Cl_2): $\tilde{\nu}$ (cm^{-1}) = 1923 (s) and 1820 (vs) [ν(CO)], 1547 (m) [ν(C-C-N)$_{pz}$].

IR (THF): $\tilde{\nu}$ (cm^{-1}) = 1921 (s) and 1819 (vs) [ν(CO)], 1547 (m) [ν(C-C-N)$_{pz}$].

IR (toluene): $\tilde{\nu}$ (cm^{-1}) = 1922 (s) and 1820 (vs) [ν(CO)], 1549 (m) [ν(C-C-N)$_{pz}$].

ATR-IR (solid): $\tilde{\nu}$ (cm^{-1}) = 2979 (vw), 2961 (vw), 2925 (vw, sh), 2915 (vw), 2857 (vw), 2543 (vw, sh) [ν(BH)], 2525 (vw) [ν(BH)], 1915 (s) [ν(CO)], 1807 (vs) [ν(CO)], 1548 (m) [ν(C-C-N)$_{pz}$], 1493 (vw), 1446 (m), 1437 (w, sh), 1414 (m), 1381 (w), 1371 (m), 1350 (w, sh), 1303 (w), 1277 (w), 1209 (m), 1200 (m, sh), 1153 (vw), 1144 (vw), 1131 (vw), 1120 (vw), 1098 (vw), 1065 (m), 1048 (w), 1037 (vw), 981 (vw), 951 (s), 939 (m), 876 (vw), 858 (w), 812 (w), 786 (m), 774 (m), 724 (w), 691 (m), 672 (m), 645 (m), 604 (vw), 579 (w), 517 (vw), 478 (w, sh), 463 (m), 441 (vw), 417 (vw).

^{1}H NMR: (300.1 MHz, CD_2Cl_2, 298 K): δ (ppm) = 2.13 (s, 3H, 1 × C^3-*Me*, pz$_B$), 2.17 (d, ^2J(P,H) = 10.3 Hz, 9H, P*Me*$_3$), 2.39 (s, 6H, 2 × C^3-*Me*, pz$_A$), 2.42 (s, 6H, 2 × C^5-*Me*, pz$_A$), 2.44 (s, 3H, 1 × C^5-*Me*, pz$_B$), 4.70 (br q, $\Delta\nu_{1/2}$ = ~ 250 Hz, 1H, B*H*); this signal appears as a very broad hump over the base line in a strongly enlarged version of the spectrum), 5.91 (s, 1H, 1 × C^4-*H*, pz$_B$), 5.93 (s, 2H, 2 × C^4-*H*, pz$_A$).

^{13}C{^{1}H} NMR: (75.47 MHz, CD_2Cl_2, 298 K): δ (ppm) = 12.7 (s, 2C, 2 × C^5-*Me*, pz$_A$), 13.3 (s, 1C, 1 × C^5-*Me*, pz$_B$), 15.6 (s, 2C, 2 × C^3-*Me*, pz$_A$), 15.8 (s, 1C, 1 × C^3-*Me*, pz$_B$), 18.6 (d, ^1J(C,P) = 42.4 Hz, 3C, P*Me*$_3$), 107.4 (s, 2C, 2 × *C*^{4}-H, pz$_A$), 107.9 (s, 1C, 1 × *C*^{4}-H, pz$_B$), 144.5 (s, 2C, 2 × *C*^{5}-Me, pz$_A$), 146.5 (s, 1C, 1 × *C*^{5}-Me, pz$_B$), 151.3 (d, ^3J(C,P) = 2.2 Hz, 1C, 1 × *C*^{3}-Me, pz$_B$), 152.1 (s, 2C, 2 × *C*^{3}-Me, pz$_A$), 251.7 (d, ^2J(C,P) = 41.5 Hz, ^1J(W,C) = 149.3 Hz, 2C, 2 × *C*O).

$^{31}P\{^{1}H\}$ NMR: (121.5 MHz, CD_2Cl_2, 298 K): δ (ppm) = –1.93 (s, ^{1}J(W,P) = 63 Hz).

4.5.3 [Tp'Mo(CO)$_2$(PMe$_3$)] (2-Mo)

A mixture of **1-Mo** (300 mg, 0.535 mmol) and sodium sand (12.3 mg, 0.535 mmol) was treated with 10 mL of THF in the presence of a catalytic amount of naphthalene and the obtained yellowish brown mixture was stirred for 10 days at ambient temperature. During this time, the color of the solution slowly changed from yellowish brown to light yellow. Completion of the reaction was confirmed by IR spectroscopy. The solution was evaporated to dryness *in vacuo* to give a dirty yellow, slightly oily residue, which was transformed into a powder by grinding during a freeze-pump-thaw cycle. The powder was extracted with toluene (2 × 10 mL), and the combined extracts were concentrated to *ca*. 5 mL in *vacuo*, treated with 10 mL of *n*-pentane, and stored at –60 °C for 48 hours. The obtained light yellow precipitate was collected by filtration at –60 °C and dried in *vacuo* for 1 hour at ambient temperature to afford complex **2-Mo** as an analytically pure, air-sensitive solid. Yield: 158 mg (0.301 mmol, 56%).

Properties: It is well soluble in THF, toluene and Et_2O, and moderately soluble in *n*-hexane.

Melting Points: The soid decomposes upon melting at 226–227 °C to a dark brown liquid.

Elemental analysis: calcd. (%) for $C_{20}H_{31}BMoN_6O_2P{\cdot}0.75C_7H_8$ (594.33 g/mol): C 51.03, H 6.27, N 14.14; found: C 51.40 , H 6.47, N 14.11.

Spectroscopic Data:

IR (THF): $\tilde{\nu}$ (cm^{-1}) = 1893 (vs) and 1756 (s) [ν(CO)], 1544 (w) [ν(C-C-N)$_{pz}$].

IR (toluene): $\tilde{\nu}$ (cm^{-1}) = 1894 (vs) and 1757 (s) [ν(CO)], 1544 (w) [ν(C-C-N)$_{pz}$].

IR (*n*-hexane): $\tilde{\nu}$ (cm^{-1}) = 1903 (vs) and 1770 (s) [ν(CO)], 1545 (w) [ν(C-C-N)$_{pz}$].

IR (Et_2O): $\tilde{\nu}$ (cm^{-1}) = 1898 (vs) and 1764 (s) [ν(CO)], 1545 (w) [ν(C-C-N)$_{pz}$].

ATR-IR (solid): $\tilde{\nu}$ (cm^{-1}) = 2968 (vw), 2925 (vw), 2531 (vw) [ν(BH)], 1883 (s) [ν(CO)], 1737 (s) [ν(CO)], 1544 (m) [ν(C-C-N)$_{pz}$], 1491 (vw), 1444 (m), 1424 (w, sh), 1415 (m), 1381 (m), 1369 (m), 1348 (w), 1305 (vw), 1285 (w), 1205 (m), 1192 (m), 1145 (vw), 1064 (m), 1043 (w), 977 (vw, sh), 957 (m), 940 (w), 868 (vw), 851

(w), 816 (w), 782 (m), 728 (w), 718 (vw), 694 (w), 668 (w), 645 (m), 594 (vw), 558 (vw), 529 (vw), 509 (vw), 471 (vw), 452 (m), 424 (vw), 408 (vw).

4.5.4 Na[Tp'Mo(CO)$_2$(PMe$_3$)] (3-Mo)

A dark green THF solution of sodium naphthalenide (0.38 M, 16.7 mL, 6.35 mmol, 2.0 equiv.)[40] was slowly added via a syringe to a solution of **1-Mo** (1.784 g, 3.18 mmol) in 30 mL of THF at ambient temperature. Upon addition, the color of the solution changed from dark yellowish brown to light yellowish brown. Complex **1-Mo** was very rapidly converted to the product **3-Mo** as evidenced by IR spectroscopy.[41] The obtained solution was concentrated under reduced pressure to *ca*. 10 mL and treated with 10 mL of *n*-hexane. The resulting suspension was filtered from a tiny amount of a light brown residue. The yellowish brown filtrate was evaporated to dryness in *vacuo*, and the residue transformed into powder by grinding during a freeze-pump-thaw cycle. The resulting dirty yellow powder was washed with *n*-hexane/benzene mixture (3:1, 3 × 15 mL) and dried under vacuum for 2 hours at 50 °C to afford the metalate **3-Mo** as an extremely air sensitive, yellow solid. Yield: 1.66 g (3.03 mmol, 95%).

Properties: Complex **3-Mo** is well soluble in THF and DME, sparingly soluble in C_6H_5F, and insoluble in toluene, Et_2O and *n*-hexane. It is extremely sensitive towards the air.

Melting Points: Yellow solid slowly turns gray above 271 °C and decomposes upon melting at 288 °C to give a black liquid.

Spectroscopic Data:

IR (THF): $\tilde{\nu}$ (cm^{-1}) = 1766 (m), 1726 (vs), 1644 (m), 1620 (s) and 1596 (s) [ν(CO)], 1546 (w) [ν(C-C-N)$_{pz}$].

IR (DME): $\tilde{\nu}$ (cm^{-1}) = 1762 (vs), 1727 (vs), 1645 (s) and 1623 (s) [ν(CO)], 1546 (w) [ν(C-C-N)$_{pz}$].

---

[40] The preparation of sodium naphthalenide solution in THF from sodium and naphthalene has been reported: H. C. Wang, G. Levin, M. Szwarc, *J. Am. Chem. Soc*. **1978**, *100*, 3969.

[41] A very small amount of Tp'Mo(CO)$_2$PMe$_3$ (**2-Mo**) was always observed as an intermediate during addition. After addition was completed, the IR spectrum of the solution showed only ν(CO) bands of the metalate **3-Mo**.

IR (acetonitrile): $\tilde{\nu}$ (cm^{-1}) = 1755 (vs) and 1663 (vs) [ν(CO)], 1545 (w) [ν(C-C-N)$_{pz}$].

ATR-IR (solid): $\tilde{\nu}$ (cm^{-1}) = 2968 (vw), 2952 (vw, sh), 2922 (vw, sh), 2903 (vw), 2860 (vw), 2810 (vw), 2510 (vw) [ν(BH)], 1676 (vs) [ν(CO)], 1576 (s) [ν(CO)], 1545 (m) [ν(C-C-N)$_{pz}$], 1535 (m, sh), 1491 (vw), 1459 (vw, sh), 1440 (w), 1414 (m), 1379 (w), 1370 (m), 1348 (w), 1296 (vw), 1276 (vw), 1204 (m), 1194 (m), 1158 (vw), 1146 (vw), 1105 (vw, sh), 1092 (vw), 1063 (w), 1041 (w), 979 (vw), 947 (m), 931 (w, sh), 867 (vw), 848 (w), 817 (w), 806 (w), 778 (m), 767 (w, sh), 717 (vw, sh), 696 (w), 664 (w), 639 (w), 614 (vw), 578 (w), 539 (vw), 512 (vw), 499 (vw), 483 (vw), 461 (w), 438 (vw), 422 (vw), 401 (vw).

^{1}H NMR: (300.1 MHz, THF-d_8, 298 K): δ (ppm) = 1.27 (d, ^{2}J(P,H) = 5.8 Hz, 9H, P*Me*$_3$), 2.22 (s, 3H, 1 × C^5-*Me*, pz$_B$), 2.34 (s, 6H, 2 × C^5-*Me*, pz$_A$), 2.43 (s, 3H, 1 × C^3-*Me*, pz$_B$), 2.53 (s, 6H, 2 × C^3-*Me*, pz$_A$), 4.6 (br, $\Delta\nu_{1/2}$ = ~ 200 Hz, 1H, B*H*); this signal appears as a very broad hump over the base line in a strongly enlarged version of the spectrum), 5.47 (s, 1H, 1 × C^4-*H*, pz$_B$), 5.63 (s, 2H, 2 × C^4-*H*, pz$_A$).

^{13}C{^{1}H} NMR: (75.47 MHz, THF-d_8, 298 K): δ (ppm) = 12.9 (s, 1C, 1 × C^5-*Me*, pz$_B$), 13.1 (s, 2C, 2 × C^5-*Me*, pz$_A$), 16.2 (s, 1C, 1 × C^3-*Me*, pz$_B$), 17.0 (s, 2C, 2 × C^3-*Me*, pz$_A$), 23.0 (d, ^{1}J(C,P) = 16.8 Hz, 3C, P*Me*$_3$), 104.6 (s, 1C, 1 × *C*^{4}-H, pz$_B$), 105.4 (s, 2C, 2 × *C*^{4}-H, pz$_A$), 141.8 (s, 1C, 1 × *C*^{5}-Me, pz$_B$), 143.3 (s, 2C, 2 × *C*^{5}-Me, pz$_A$), 150.1 (s, 1C, 1 × *C*^{3}-Me, pz$_B$), 151.0 (s, 2C, 2 × *C*^{3}-Me, pz$_A$), 234.4 (d, ^{2}J(C,P) = 12.6 Hz, 2 × *C*O).

^{31}P{^{1}H} NMR: (121.5 MHz, THF-d_8, 298 K): δ (ppm) = 15.8 (s).

4.5.5 Na[Tp'W(CO)$_2$(PMe$_3$)] (3-W)

A dark green solution of sodium naphthalenide in THF (0.44 M, 19.1 mL, 8.49 mmol, 2.3 equiv.) was slowly added via syringe to a suspension of **1-W** (2.495 g, 3.69 mmol) in 60 mL of THF at ambient temperature. Upon addition the color of the suspension changed from dark yellowish orange to brownish yellow and complex **1-W** was very rapidly converted to the product **3-W**, as evidenced by IR spectroscopy. After complete addition, the reaction mixture was stirred for 1 hour at ambient temperature and treated with ~20 mL of *n*-hexane to precipitate out

the NaCl. The brownish yellow suspension was then filtered through celite using a filtration frit. Resulting filtrate was evaporated to dryness and pulverised once by a freeze-pump-thaw cycle. Major part of the naphthalene was sublimed out from the mixture using a sublimation apparatus. After sublimation, the yellow solid was washed with *n*-hexane/benzene mixture (3:1, 3 × 50 mL) at ambient tempearture and finally dried for 15 hours at 75 °C to obtain as a spectroscopically pure, extremely air-sensitive, yellow solid. Yield: 2.23 g (3.51 mmol, 95%).

Properties: Complex **3-W** is well soluble in THF and DME, sparingly soluble in C_6H_5F, and insoluble in toluene, Et_2O and *n*-hexane. It is extremely sensitive towards air.

Spectroscopic Data:

IR (THF): $\tilde{\nu}$ (cm^{-1}) = 1756 (m), 1715 (vs), 1639 (m), 1614 (s) and 1594 (s) [ν(CO)], 1546 (w) [ν(C-C-N)$_{pz}$].

IR (DME): $\tilde{\nu}$ (cm^{-1}) = 1753 (vs), 1716 (vs), 1639 (s) and 1619 (s) [ν(CO)], 1546 (w) [ν(C-C-N)$_{pz}$].

IR (acetonitrile): $\tilde{\nu}$ (cm^{-1}) = 1743 (vs) and 1654 (vs) [ν(CO)], 1545 (w) [ν(C-C-N)$_{pz}$].

ATR-IR (solid): $\tilde{\nu}$ (cm^{-1}) = 2973 (vw, sh), 2956 (vw), 2922 (vw, sh), 2904 (vw), 2859 (vw), 2807 (vw), 2513 (vw) [ν(BH)], 1709 (w, sh) [ν(CO)], 1671 (s) [ν(CO)], 1586 (w) [ν(CO)], 1545 (m) [ν(C-C-N)$_{pz}$], 1528 (vs) [ν(CO)], 1439 (w), 1414 (m), 1380 (w), 1370 (m), 1346 (w), 1294 (vw), 1274 (vw), 1200 (m), 1190 (m, sh), 1179 (w, sh), 1145 (vw), 1066 (sh), 1058 (w), 1042 (w), 979 (vw), 943 (m), 923 (w, sh), 869 (vw), 849 (w), 817 (w), 804 (vw), 779 (m), 766 (w, sh), 718 (vw), 701 (w, sh), 695 (w), 681 (w), 663 (m), 644 (w), 635 (w), 573 (w), 556 (w), 505 (vw), 463 (w), 438 (vw), 425 (vw), 417 (vw), 402 (vw).

^{1}H NMR: (300.1 MHz, THF-d_8, 298 K): δ (ppm) = 1.38 (d, ^2J(P,H) = 6.3 Hz, 9H, P*Me*$_3$), 2.22 (s, 3H, 1 × C^5-*Me*, pz$_B$), 2.35 (s, 6H, 2 × C^5-*Me*, pz$_A$), 2.44 (s, 3H, 1 × C^3-*Me*, pz$_B$), 2.55 (s, 6H, 2 × C^3-*Me*, pz$_A$), 4.6 (br, $\Delta\nu_{1/2}$ = ~ 200 Hz, 1H, B*H*); this signal appears as a very broad hump over the base line in a strongly enlarged version of the spectrum), 5.53 (s, 1H, 1 × C^4-*H*, pz$_B$), 5.68 (s, 2H, 2 × C^4-*H*, pz$_A$).

$^{13}C\{^1H\}$ NMR: (75.47 MHz, THF-d_8, 298 K): δ (ppm) = 12.8 (s, 1C, 1 × C^5-*Me*, pz_B), 13.0 (s, 2C, 2 × C^5-*Me*, pz_A), 17.1 (s, 1C, 1 × C^3-*Me*, pz_B), 17.8 (s, 2C, 2 × C^3-*Me*, pz_A), 23.7 (d, ^1J(C,P) = 22.0 Hz, 3C, P*Me*$_3$), 104.8 (s, 1C, 1 × C^4-H, pz_B), 105.8 (s, 2C, 2 × C^4-H, pz_A), 141.7 (s, 1C, 1 × C^5-Me, pz_B), 143.3 (s, 2C, 2 × C^5-Me, pz_A), 150.4 (s, 1C, 1 × C^3-Me, pz_B), 151.9 (s, 2C, 2 × C^3-Me, pz_A), 229.8 (br s, $\Delta\nu_{1/2}$ = 12.3 Hz, 2 × *C*O).

$^{31}P\{^1H\}$ NMR: (121.5 MHz, THF-d_8, 298 K): δ (ppm) = −11.0 (s, ^1J(W,P) = 397.5 Hz).

4.5.6 [Tp'Mo(CO)$_2$(PMe$_3$)H] (4-Mo)

To a yellow suspension of Na[Tp'Mo(CO)$_2$(PMe$_3$)] (**3-Mo**) (200 mg, 0.365 mmol) in 5 mL of Et_2O, a stock solution of HCl (1 mL, 0.41 mmol, 1.12 equiv.) in Et_2O was added dropwisely at 0 °C. Immediate after addition, the color of the suspension changed from yellow to light brown. The suspension was slowly brought to ambient temperature and checked by solution IR spectrum, which revealed the formation of a new compound along with a very small amount of Tp'Mo(CO)$_2$(PMe$_3$) radical (**2-Mo**). All the volatiles were removed under reduced pressure and the residue was extracted with benzene/*n*-pentane mixture (1:1, 10 mL). The off white extract was dried under reduced pressure to obtain the targeted compound as benzene solvate (**4-Mo**·0.6(C_6H_6).

Properties: It is well soluble in all common organic solvent and moderately sensitive towards air.

Elemental analysis: calcd. (%) for $C_{20}H_{32}BMoN_6O_2P$·0.6(C_6H_6) (573.10 g/mol): C 49.46, H 6.26, N 14.66; found: C 49.17 , H 6.20, N 14.24.

Spectroscopic Data:

IR (Et_2O): $\tilde{\nu}$ (cm^{-1}) = 1917 (s) and 1814 (vs) [ν(CO)], 1546 (m) [ν(C-C-N)$_{pz}$].

^1H NMR: (300.1 MHz, C_6D_6, 298 K): δ (ppm) = −3.49 (d, ^2J(P,H) = 68.3 Hz, 1H, Mo-*H*), 0.96 (d, ^2J(P,H) = 8.0 Hz, 9H, P*Me*$_3$), 2.02 (s, 3H, 1 × C^5-*Me*, pz_B), 2.20 (s, 6H, 2 × C^5-*Me*, pz_A), 2.48 (s, 6H, 2 × C^3-*Me*, pz_A), 2.84 (s, 3H, 1 × C^3-*Me*, pz_B), ~ 4.62 (br, $\Delta\nu_{1/2}$ = ~ 250 Hz, 1H, B*H*); this signal appears as a very broad hump over the base line in a strongly enlarged version of the spectrum), 5.39 (s, 1H, 1 × C^4-*H*, pz_B), 5.60 (s, 2H, 2 × C^4-*H*, pz_A).

$^{13}C\{^1H\}$ NMR: (75.47 MHz, C_6D_6, 298 K): δ (ppm) = 12.7 (s, 1C, 1 × C^5-*Me*, pz_B), 12.8 (s, 2C, 2 × C^5-*Me*, pz_A), 15.8 (s, 1C, 1 × C^3-*Me*, pz_B), 16.6 (s, 2C, 2 × C^3-*Me*, pz_A), 20.7 (d, ^1J(C,P) = 26.2 Hz, 3C, P*Me*$_3$), 106.4 (s, 1C, 1 × C^4-H, pz_B), 107.3 (s, 2C, 2 × C^4-H, pz_A), 143.6 (s, 1C, 1 × C^5-Me, pz_B), 144.7 (s, 2C, 2 × C^5-Me, pz_A), 152.3 (s, 1C, 1 × C^3-Me, pz_B), 152.7 (s, 2C, 2 × C^3-Me, pz_A), 225.8 (d, ^2J(C,P) = 11.9 Hz, 2C, 2 × *C*O).

$^{31}P\{^1H\}$ NMR: (121.5 MHz, C_6D_6, 298 K): δ (ppm) = 8.6 (s).

4.5.7 [Tp'(CO)$_2$Mo≡Si(C$_5$Me$_5$)] (5-Mo)

To a yellow solution of **3-Mo** (163 mg, 0.30 mmol) in 15 mL of THF, a colorless solution of $[(C_5Me_5)Si][B(C_6F_5)_4]$ (270 mg, 0.32 mmol, 1.08 equiv.) in 10 mL of THF was dropwisely added via syringe at ambient temperature. Upon addition the color of the solution immediately changed from yellow to orange. An IR spectrum after 20 minutes of the crude reaction mixture revealed the complete consumption of the metalate and the formation of a new compound (ν_{CO}: 1849 (s) and 1971 (vs) cm^{-1}) along with very small amount of **2-Mo** radical. All volatiles were removed under reduced pressure and the residue was extracted with toluene (3 × 15 mL) at ambient temperature. The combine orange extract was concentrated to ~10 mL and then was treated with 20 mL of *n*-pentane. The amorphous orange solid that precipitated out from the solution was isolated by filtration of the light yellow supernatant. The solid was crystallized from Et_2O solution at −30 °C to obtain analytically pure, orange solid in moderate yield. Yield: 90 mg (0.15 mmol, 49 %).

Properties: Compound **5-Mo** is well soluble in THF and fluorobenzene, sparingly soluble in Et_2O and benzene and insoluble in all common aliphatic solvents. It is highly sensitive towards air.

Melting Points: Orange solid decomposes upon melting to a black liquid at 319 – 322 °C.

Elemental analysis: calcd. (%) for $C_{27}H_{37}BMoN_6O_2Si$ (612.46 g/mol): C 52.95, H 6.09, N 13.72; found: C 52.70, H 6.08, N 13.20.

Spectroscopic Data:

IR (THF): $\tilde{\nu}$ (cm^{-1}) = 1849 (s) and 1772 (vs) [ν(CO)], 1544 (w) [ν(C-C-N)$_{pz}$].

IR (Fluorobenzene): $\tilde{\nu}$ (cm^{-1}) = 1847 (s) and 1767 (vs) [ν(CO)], 1544 (w) [ν(C-C-N)$_{pz}$].

ATR-IR (solid): $\tilde{\nu}$ (cm^{-1}) = 2981 (vw), 2918 (vw), 2862 (vw), 2525 (vw) [ν(BH)], 1846 (s) [ν(CO)], 1761 (vs) [ν(CO)], 1544 (w) [ν(C-C-N)$_{pz}$], 1479 (vw), 1447 (w), 1415 (m), 1383 (m), 1367 (w, sh), 1204 (m), 1189 (w), 1145 (vw), 1120 (vw), 1066 (w), 1045 (w), 982 (vw), 931 (vw), 872 (vw), 854 (vw), 812 (w), 795 (w), 776 (m), 696 (w), 665 (vw), 650 (w), 609 (w), 591 (m), 583 (m), 559 (m), 546 (m), 522 (w), 494 (w), 462 (w), 433 (vw), 417 (vw), 407 (vw).

^{1}H NMR: (300.1 MHz, C_6D_6, 298 K): δ (ppm) = 1.90 (s, 15H, C_5Me_5), 2.17, 2.89 (s, 3H each, pz_B), 2.21, 2.45 (s, 6H each, pz_A), ~ 4.8 (br, $\Delta\nu_{1/2}$ = ~ 200 Hz, 1H, B*H*); this signal is visible as a very broad hump over the base line in a strongly enlarged version of the spectrum), 5.47 (s, 1H, C^4-*H*, pz_B), 5.66 (s, 2H, C^4-*H*, pz_A).

^{1}H NMR: (300.1 MHz, THF-d_8, 298 K): δ (ppm) = 2.298 (s, 3H, 1 × C^5-*Me*, pz_B), 2.304 (s, 6H, 2 × C^5-*Me*, pz_A), 2.32 (s, 21H (15H + 6H), (C_5Me_5) + (2 × C^3-*Me*, pz_A)), 2.46 (s, 3H, 1 × C^3-*Me*, pz_B), 4.63 (br, $\Delta\nu_{1/2}$ = ~ 250 Hz, 1H, B*H*); this signal is visible as a very broad hump over the base line in a strongly enlarged version of the spectrum), 5.65 (s, 3H, C^4-*H*, pz_A and pz_B).

^{13}C{^{1}H} NMR: (75.47 MHz, C_6D_6, 298 K): δ (ppm) = 10.0 (s, 5C, C_5Me_5), 12.6 (s, 2C, 2 × C^5-*Me*, pz_A), 12.8 (s, 1C, 1 × C^5-*Me*, pz_B), 15.5 (s, 1C, 1 × C^3-*Me*, pz_B), 17.5 (s, 2C, 2 × C^3-*Me*, pz_A), 105.7 (s, 2C, 2 × C^4-H, pz_A), 106.2 (s, 1C, 1 × C^4- H, pz_B), 122.5 (s, ^{1}J(Si,C) = 13.4 Hz, 5C, C_5Me_5), 143.0 (s, 1C, 1 × C^5-Me, pz_B), 143.5 (s, 2C, 2 × C^5-Me, pz_A), 149.6 (s, 2C, 2 × C^3-Me, pz_A), 153.0 (s, 1C, 1 × C^3-Me, pz_B), 227.3 (s, 2C, 2 × *C*O).

^{29}Si{^{1}H} NMR: (99.34 MHz, THF-d_8, 298 K): δ (ppm) = – 272.4 (s).

4.5.8 [Tp'(CO)$_2$Mo=Si(4-dmap)Tbb] (6-Mo)

An orange solution of *E*-(Tbb)BrSi=SiBr(Tbb) (763 mg, 0.68 mmol, 0.5 equiv.) and 4-dimethylaminopyridine (4-dmap) (167 mg, 1.37 mmol, 1.0 equiv.) in 20 mL of toluene was dropwisely added at ambient temperature to a yellow suspension of **3-Mo** (750 mg, 1.37 mmol, 1.0 equiv.) in 30 mL of toluene. The orange suspension was then heated to 80 °C for 1 hour.

During this time, the color of the suspension changed to brown, and the metalate converted selectively into complex **6-Mo** as evidenced by IR spectroscopy. The brown suspension was filtered into another schlenck tube and the brown filtrate was evaporated to dryness and the residue obtained was washed with *n*-hexane (2 × 10 mL) and dried shortly *in vacuo*. The resulting brown solid was suspended in 30 mL of diethyl ether and stored at –60 °C for 18 hours. A microcrystalline brown solid was isolated after filtration of the light brown supernatant at –60 °C and dried *in vacuo* at ambient temperature for 4 hours. Yield: 1.03 g (0.98 mmol, 72%).

Properties: Compound **6-Mo** is very good soluble in THF and fluorobenzene, and moderately soluble in toluene and diethyl ether.

Melting Points: Upon heating to *ca*. 170 °C the brown complex **6-Mo** releases 4-dmap to give the red silylidyne complex **7-Mo**, which upon further heating decomposes into a brown liquid at 265 – 267 °C.

Elemental analysis: calcd. (%) for $C_{48}H_{81}BMoN_8O_2Si_5$ (1049.39 g/mol): C 50.94, H 7.78, N 10.68; found: C 54.70, H 7.73, N 10.64.

Spectroscopic Data:

IR (THF): $\tilde{\nu}$ (cm^{-1}) = 1862 (s) and 1779 (vs) [ν(CO)], 1545 (w) [ν(C-C-N)$_{pz}$].

IR (toluene): $\tilde{\nu}$ (cm^{-1}) = 1865 (s) and 1782 (vs) [ν(CO)], 1544 (w) [ν(C-C-N)$_{pz}$].

ATR-IR (solid): $\tilde{\nu}$ (cm^{-1}) = 3071 (vw), 2962 (sh), 2952 (w), 2922 (vw), 2903 (vw), 2867 (vw), 2811 (vw), 2518 (vw) [ν(BH)], 1852 (s) [ν(CO)], 1766 (s) [ν(CO)], 1622 (m), 1587 (vw), 1543 (m) [ν(C-C-N)$_{pz}$], 1523 (w), 1477 (vw), 1441 (m), 1414 (w), 1391 (m), 1381 (w), 1375 (w), 1343 (vw), 1301 (vw), 1258 (sh), 1247 (m), 1221 (m), 1206 (m), 1198 (sh), 1188 (sh), 1171 (vw), 1152 (vw), 1134 (vw), 1118 (vw), 1063 (w), 1051 (w), 1041 (w), 1013 (m), 997 (sh), 983 (sh), 939 (w), 879 (w), 855 (sh), 835 (vs), 817 (m), 784 (m), 771 (m), 763 (m), 745 (w), 726 (vw), 722 (sh), 687 (m), 662 (w), 642 (w), 625 (vw), 602 (w), 589 (vw), 559 (w), 550 (sh), 524 (w), 507 (vw), 492 (vw), 479 (m), 462 (vw), 435 (m), 425 (w), 400 (vw).

^{1}H NMR: (300.1 MHz, THF-d_8, 298 K): δ (ppm) = −0.04 (s, 18H, $C^{2,6}$-CH(SiMe_3)$_A$(SiMe$_3$)$_B$, Tbb)[S42], 0.19 (s, 18H, $C^{2,6}$-CH(SiMe$_3$)$_A$(SiMe_3)$_B$, Tbb),[S8] 1.35 (s, 9H, C^4-CMe_3, Tbb), 2.20 (s, 6H, 2 × C^3-*Me*, pz$_A$), 2.30 (s, 3H, C^5-*Me*, pz$_B$), 2.45 (s, 6H, 2 × C^5-*Me*, pz$_A$), 2.63 (s, 3H, C^3-*Me*, pz$_B$), 2.94 (s, 6H, C^4-NMe_2, 4-dmap), 3.10 (s, ^2J(Si,H) = 9 Hz, 2H, $C^{2,6}$-C*H*(SiMe$_3$)$_2$, Tbb), 4.8 (br, $\Delta\nu_{1/2}$ = ~ 200 Hz, 1H, B*H*); this signal is visible as a very broad hump over the base line in a strongly enlarged version of the spectrum), 5.59 (s, 2H, 2 × C^4-*H*, pz$_A$), 5.63 (s, 1H, C^4-*H*, pz$_B$), 6.20 (br d, ^3J(H,H) = 4 Hz, 2H, $C^{3,5}$-*H*, 4-dmap), 6.78 (s, 2H, $C^{3,5}$-*H*, Tbb), 7.28 (br, $\Delta\nu_{½}$ = ~ 170 Hz , 2H, $C^{2,6}$-*H*, 4-dmap).

^{13}C{^{1}H} NMR: (75.47 MHz, THF-d_8, 298 K): δ (ppm) = 1.78 (br s, $\Delta\nu_{½}$ = 44 Hz, 12C, $C^{2,6}$-CH(SiMe_3)$_2$, Tbb), 12.7 (s, 1C, C^5-*Me*, pz$_B$), 13.1 (s, 2C, 2 × C^5-*Me*, pz$_A$), 15.6 (s, 1C, C^3-*Me*, pz$_B$), 18.7 (s, 2C, 2 × C^3-*Me*, pz$_A$), 29.3 (s, ^1J(Si,C) = 42 Hz, 2C, $C^{2,6}$-*C*H(SiMe$_3$)$_2$, Tbb), 31.6 (s, 3C, C^4-CMe_3, Tbb), 35.0 (s, 1C, C^4-*C*Me$_3$, Tbb), 39.3 (s, 2C, C^4-NMe_2, 4-dmap), 105.7 (s, 2C, 2 × C^4-H, pz$_A$), 106.17 (s, 2C, $C^{3,5}$-H, 4-dmap)[S43], 106.21 (s, 1C, C^4-H, pz$_B$), 123.8 (s, 2C, $C^{3,5}$-H, Tbb), 143.4 (s, 1C, C^5-Me, pz$_B$), 143.7 (s, 2C, 2 × C^5-Me, pz$_A$), 146.8 (br s, 1C, C^1-Si), 150.0 (s, 2C, $C^{2,6}$-CH(SiMe$_3$)$_2$, Tbb), 150.1 (br s, 1C, C^4-CMe$_3$, Tbb), 151.2 (s, 2C, 2 × C^3-Me, pz$_A$), 153.5 (s, 1C, C^3-Me, pz$_B$), 155.7 (s, 1C, C^4-NMe$_2$, 4-dmap), 237.9 (br, 2C, 2 × *C*O).

^{29}Si{^{1}H} NMR: (59.63 MHz, THF-d_8, 298 K): δ (ppm) = 1.67 (s, 4Si, $C^{2,6}$-CH(*Si*Me$_3$)$_A$(*Si*Me$_3$)$_B$, Tbb), 212.1 (s, 1Si, Mo=*Si*).

---

[42] Complex **6-Mo** is overall C_s-symmetric in solution. The coordination plane of the zwitterionic silylidene ligand defined by the atoms W, Si, C_{Tbb} and $N_{4\text{-dmap}}$ lies in the symmetry plane of the molecule, which also contains the pyridine ring plane of 4-dmap, whereas the aryl ring plane of the Tbb substituent lies orthogonal to the symmetry plane. This renders the two *ortho* CH(TMS)$_2$ groups enantiotopic. Due to hindered rotation of the Tbb substituent about the Si-C_{Tbb} bond the two TMS groups in each CH(TMS)$_2$ group are diastereotopic and give rise to two separate signals in the NMR spectra at low temperature. The most shielded TMS group in the ^{1}H NMR spectrum was labeled with the character A and the other TMS group with the character B. The corresponding ^{13}C signals were assigned by an HMQC experiment.

[S43] The $C^{2,6}$-H signal of 4-dmap could not be detected at 298 K due to broadening.

4.5.9 [Tp'(CO)$_2$W=Si(4-dmap)Tbb] (6-W)

An orange solution of *E*-(Tbb)BrSi=SiBr(Tbb) (658 mg, 0.59 mmol, 0.5 equiv.) and 4-dimethylaminopyridine (144 mg, 1.18 mmol, 1.0 equiv.) in 20 mL of toluene was dropwisely added at ambient temperature to a yellow suspension of **3-W** (750 mg, 1.18 mmol, 1.0 equiv.) in 40 mL of toluene. The orange suspension was then heated to 100 °C for 45 minutes. During this time, the color of the suspension changed to brown, and the metalate converted selectively into complex **6-W** as evidenced by IR spectroscopy. The brown suspension was treated with *n*-hexane (10 mL), stirred for 5 minutes at ambient temperature and then filtered. The brown filtrate was evaporated to dryness, and the residue obtained was washed with *n*-pentane (2 × 10 mL) and dried shortly *in vacuo*. The resulting red brown solid was suspended in 30 mL of diethyl ether and stored at −30 °C for 18 hours. A microcrystalline brown solid was isolated after filtration of the light brown supernatant at −30 °C and dried *in vacuo* at ambient temperature for 30 minutes. Yield: 998 mg (0.88 mmol, 74%).

Properties: Complex **6-W** is very good soluble in THF and fluorobenzene, and moderately soluble in toluene and diethyl ether.

Melting Points: Upon heating to *ca*. 161 – 163 °C the brown complex **6-W** releases 4-dmap to give the red silylidyne complex **7-W**, which upon further heating decomposes into a brown liquid at 262 – 265 °C.

Elemental analysis: calcd. (%) for $C_{48}H_{81}BN_8O_2Si_5W$ (1137.29 g/mol): C 50.69, H 7.18, N 9.85; found: C 48.72, H 7.01, N 9.94.

Spectroscopic Data:

IR (THF): $\tilde{\nu}$ (cm^{-1}) = 1855 (s) and 1772 (vs) [ν(CO)], 1546 (w) [ν(C-C-N)$_{pz}$].

IR (toluene): $\tilde{\nu}$ (cm^{-1}) = 1855 (s) and 1772 (vs) [ν(CO)], 1545 (w) [ν(C-C-N)$_{pz}$].

ATR-IR (solid): $\tilde{\nu}$ (cm^{-1}) = 2951 (w), 2901 (vw), 2865 (vw), 2519 (vw) [ν(BH)], 1842 (s) [ν(CO)], 1755 (s) [ν(CO)], 1621 (m), 1587 (vw), 1543 (m) [ν(C-C-N)$_{pz}$], 1523 (w), 1477 (vw), 1441 (w), 1413 (w), 1390 (m), 1374 (w), 1342 (vw), 1300 (vw), 1246 (m), 1220 (m), 1207 (m), 1172 (vw), 1152 (vw), 1134 (vw), 1118 (vw), 1061 (w), 1050 (w), 1013 (m), 939 (w), 880 (w), 835 (vs), 813 (sh), 784 (m), 770 (m), 762 (m), 745 (vw), 726 (vw), 719 (vw), 686 (m), 662 (w), 655

(vw), 639 (w), 625 (vw), 608 (w), 602 (w), 583 (vw), 559 (w), 536 (vw), 524 (w), 508 (vw), 495 (w), 481 (w), 466 (vw), 434 (m), 427 (sh).

^{1}H NMR: (300.1 MHz, THF-d_8, 298 K): δ (ppm) = 0.07 (br s, $\Delta\nu_{½}$ = ~ 40 Hz, 36H, $C^{2,6}$-CH(Si*Me*$_3$)$_2$, Tbb), 1.34 (s, 9H, C^4-C*Me*$_3$, Tbb), 2.28 (s, 6H, 2 × C^3-*Me*, pz$_A$), 2.32 (s, 3H, C^5-*Me*, pz$_B$), 2.46 (s, 6H, 2 × C^5-*Me*, pz$_A$), 2.65 (s, 3H, C^3-*Me*, pz$_B$), 2.94 (s, 6H, C^4-N*Me*$_2$, 4-dmap), 3.21 (s, ^2J(Si,H) = 9 Hz, 2H, $C^{2,6}$-C*H*(SiMe$_3$)$_2$, Tbb), 4.8 (br, $\Delta\nu_{1/2}$ = ~ 200 Hz, 1H, B*H*); this signal is visible as a very broad hump over the base line in a strongly enlarged version of the spectrum), 5.65 (s, 2H, 2 × C^4-*H*, pz$_A$), 5.68 (s, 1H, C^4-*H*, pz$_B$), 6.22 (br d, ^3J(H,H) = 5 Hz, 2H, $C^{3,5}$-*H*, 4-dmap), 6.77 (s, 2H, $C^{3,5}$-*H*, Tbb), 7.27 (br, $\Delta\nu_{½}$ = ~ 100 Hz , 2H, $C^{2,6}$-*H*, 4-dmap).

^{1}H NMR: (300.1 MHz, THF-d_8, 208 K): δ (ppm) = −0.08 (s, 18H, $C^{2,6}$-CH(Si*Me*$_3$)$_A$(SiMe$_3$)$_B$, Tbb)[S44], 0.18 (s, 18H, $C^{2,6}$-CH(SiMe$_3$)$_A$(Si*Me*$_3$)$_B$, Tbb),[S8] 1.33 (s, 9H, C^4-C*Me*$_3$, Tbb), 2.21 (s, 6H, 2 × C^3-*Me*, pz$_A$), 2.32 (s, 3H, C^5-*Me*, pz$_B$), 2.46 (s, 6H, 2 × C^5-*Me*, pz$_A$), 2.64 (s, 3H, C^3-*Me*, pz$_B$), 2.92 (s, 3H, C^4-N*Me*$_A$Me$_B$, 4-dmap), 2.99 (s, 3H, C^4-NMe$_A$*Me*$_B$, 4-dmap), 3.17 (s, ^2J(Si,H) = 9 Hz, 2H, $C^{2,6}$-C*H*(SiMe$_3$)$_2$, Tbb), 4.8 (br, $\Delta\nu_{1/2}$ = ~ 60 Hz, 1H, B*H*), 5.67 (s, 2H, 2 × C^4-*H*, pz$_A$), 5.71 (s, 1H, C^4-*H*, pz$_B$), 6.17 (dd, ^3J(H,H) = 7.2 Hz, ^4J(H,H) = 2.4 Hz, 1H, C^3-*H*, 4-dmap),[S8] 6.45 (dd, ^3J(H,H) = 7.2 Hz, ^4J(H,H) = 2.4 Hz, 1H, C^5-*H*, 4-dmap),[S8] 6.50 (d, ^3J(H,H) = 7.2 Hz, 1H each, C^6-*H*, 4-dmap),[S8] 6.72 (s, 2H, $C^{3,5}$-*H*, Tbb), 7.65 (d, ^3J(H,H) = 7.2 Hz, 1H, C^2-*H*, 4-dmap).

---

[44] Complex **6-W** is overall C_s-symmetric in solution. The coordination plane of the zwitterionic silylidene ligand defined by the atoms W, Si, C_{Tbb} and $N_{4\text{-dmap}}$ lies in the symmetry plane of the molecule, which also contains the pyridine ring plane of 4-dmap, whereas the aryl ring plane of the Tbb substituent lies orthogonal to the symmetry plane. This renders the two *ortho* CH(TMS)$_2$ groups enantiotopic. Due to hindered rotation of the Tbb substituent about the Si-C_{Tbb} bond the two TMS groups in each CH(TMS)$_2$ group are diastereotopic and give rise to two separate signals in the NMR spectra at low temperature. The most shielded TMS group in the ^{1}H NMR spectrum was labeled with the character A and the other TMS group with the character B. The corresponding ^{13}C signals were assigned by an HMQC experiment. Similarly, hindered rotation of the 4-dmap group about the Si-N bond renders the C^2 and C^6, and the C^3 and C^5 positions of the pyridine ring chemically inequivalent and gives rise to four ^{1}H and ^{13}C NMR signals at low temperature. Using HMQC and HMBC experiments all signals could be unequivocally assigned. The most shielded signal in the ^{1}H NMR spectrum at δ = 6.17 ppm was taken as the C^3-H group.

$^{13}C\{^1H\}$ NMR: (75.47 MHz, THF-d_8, 298 K): δ (ppm) = 1.70 (br s,$\Delta\nu_{½}$ = 9 Hz, 12C, $C^{2,6}$-CH(Si*Me*$_3$)$_2$, Tbb), 12.6 (s, 1C, C^5-*Me*, pz_B), 12.9 (s, 2C, 2 × C^5-*Me*, pz_A), 16.2 (s, 1C, C^3-*Me*, pz_B), 19.6 (s, 2C, 2 × C^3-*Me*, pz_A), 28.9 (br s, ^1J(Si,C) = 42 Hz, 2C, $C^{2,6}$-*C*H(SiMe$_3$)$_2$, Tbb), 31.5 (s, 3C, C^4-C*Me*$_3$, Tbb), 35.0 (s, 1C, C^4-*C*Me$_3$, Tbb), 39.3 (s, 2C, C^4-N*Me*$_2$, 4-dmap), 105.9 (s, 2C, 2 × *C*^{4}-H, pz_A), 106.3 (s, 2C, *C*^{3,5}-H, 4-dmap)[S45], 106.5 (s, 1C, *C*^{4}-H, pz_B), 123.9 (s, 2C, *C*^{3,5}-H, Tbb), 143.6 (s, 1C, *C*^{5}-Me, pz_B), 143.7 (s, 2C, 2 × *C*^{5}-Me, pz_A), 146.8 (br s, 1C, *C*^{1}-Si), 149.4 (s, 2C, *C*^{2,6}-CH(SiMe$_3$)$_2$, Tbb), 150.0 (br s, 1C, *C*^{4}-CMe$_3$, Tbb), 152.0 (s, ^2J(W,C) = 4 Hz, 2C, 2 × *C*^{3}-Me, pz_A), 154.6 (s, ^2J(W,C) = 5 Hz, 1C, *C*^{3}-Me, pz_B), 155.6 (s, 1C, *C*^{4}-NMe$_2$, 4-dmap), 232.0 (br, 2C, 2 × *C*O).

$^{13}C\{^1H\}$ NMR: (75.47 MHz, THF-d_8, 208 K): δ (ppm) = 1.31 (s, ^1J(Si,C) = 51 Hz, 6C, $C^{2,6}$-CH(SiMe$_3$)$_A$(Si*Me*$_3$)$_B$, Tbb),[S8] 1.87 (s, ^1J(Si,C) = 51 Hz, 6C, $C^{2,6}$-CH(Si*Me*$_3$)$_A$(SiMe$_3$)$_B$, Tbb),[S8] 12.7 (s, 1C, C^5-*Me*, pz_B), 13.1 (s, 2C, 2 × C^5-*Me*, pz_A), 16.3 (s, 1C, C^3-*Me*, pz_B), 19.5 (s, 2C, 2 × C^3-*Me*, pz_A), 28.0 (s, 2C, $C^{2,6}$-*C*H(SiMe$_3$)$_2$, Tbb), 31.5 (s, 3C, C^4-C*Me*$_3$, Tbb), 34.9 (s, 1C, C^4-*C*Me$_3$, Tbb), 39.5 (s, 2C, C^4-N*Me*$_A$*Me*$_B$, 4-dmap), 105.86 (s, 2C, 2 × *C*^{4}-H, pz_A), 105.92 (s, 1C, *C*^{5}-H, 4-dmap),[S8] 106.35 (s, 1C, *C*^{3}-H, 4-dmap),[S8] 106.41 (s, 1C, *C*^{4}-H, pz_B), 123.6 (s, 2C, *C*^{3,5}-H, Tbb), 141.4 (s, 1C, *C*^{6}-H, 4-dmap),[S8] 143.4 (s, 1C, *C*^{5}-Me, pz_B), 143.6 (s, 2C, 2 × *C*^{5}-Me, pz_A), 145.9 (s, 1C, *C*^{1}-Si), 148.9 (s, 2C, *C*^{2,6}-CH(SiMe$_3$)$_2$, Tbb), 149.4 (s, 1C, *C*^{4}-CMe$_3$, Tbb), 151.2 (s, 1C, *C*^{2}-H, 4-dmap),[S8] 151.6 (s, 2C, 2 × *C*^{3}-Me, pz_A), 154.2 (s, 1C, *C*^{3}-Me, pz_B), 155.4 (s, 1C, *C*^{4}-NMe$_A$Me$_B$, 4-dmap), 232.6 (s, 2C, 2 × *C*O).

$^{29}Si\{^1H\}$ NMR: (59.63 MHz, THF-d_8, 298 K): δ (ppm) = 2.02 (s, 4Si, $C^{2,6}$-CH(*Si*Me$_3$)$_A$(*Si*Me$_3$)$_B$, Tbb), 201.5 (br s, $\Delta\nu_{1/2}$ = 58.6 Hz, 1Si, W=*Si*).

$^{29}Si\{^1H\}$ NMR: (59.63 MHz, THF-d_8, 208 K): δ (ppm) = −1.24 and 1.65 (s each, 2Si each, $C^{2,6}$-CH(*Si*Me$_3$)$_A$(*Si*Me$_3$)$_B$, Tbb), 202.6 (s, ^1J(W,Si) = 298 Hz, 1Si, W=*Si*).

[45] The *C*^{2,6}-H signal of 4-dmap could not be detected at 298 K due to broadening.

4.5.10 [Tp'(CO)$_2$Mo≡Si–Tbb] (7-Mo)

4.5.10.1. Synthesis of 7-Mo from 3-Mo and *E*-(Tbb)BrSi=SiBr(Tbb)

A mixture of *E*-(Tbb)BrSi=SiBr(Tbb) (407 mg, 0.365 mmol, 0.5 equiv.) and **3-Mo** (400 mg, 0.73 mmol, 1.0 equiv.) was treated with 30 mL of toluene. The resulting yellow suspension was then heated at 110 °C for 30 minutes. During this time, the color of the suspension changed to red brown, and the metalate was converted selectively into the silylidyne complex **7-Mo** as confirmed by IR spectroscopy. All volatiles were removed under reduced pressure, and the red brown solid was extracted with 100 mL of *n*-pentane at ambient temperature. The red extract was concentrated in *vacuo* to 20 mL upon which a voluminus red solid was precipitated out from the sloution. The amorphous red solid was collected by filtration of the supernatant at ambient temperature, washed with 5 mL of *n*-pentane and dried under reduced pressure for 15 minutes at ambient temperature. Yield: 451 mg (0.49 mmol, 67%). The solid was shown by IR and ^{1}H NMR spectroscopy to be pure.

4.5.10.2. Synthesis of 7-Mo from [Tp'(CO)$_2$Mo=Si(4-dmap)Tbb] (6-Mo) and B(C$_6$F$_5$)$_3$

A colorless solution of B(C$_6$F$_5$)$_3$ (171 mg, 0.33 mmol, 1.00 equiv.) in 10 mL of diethyl ether was added slowly via a syringe to a stirred suspension of complex **6-Mo** (350 mg, 0.33 mmol, 1.00 equiv.) in 10 mL of diethyl ether. The red brown suspension turned instantly into a red solution. Selective formation of the silylidyne complex **7-Mo** was confirmed by IR spectroscopy. All volatiles were removed under vacuum, and the reddish-orange solid was extracted with *n*-hexane (3 × 30 mL) at ambient temperature. The combined extracts were evaporated to dryness *in vacuo*, and the resulting residue dissolved in 10 mL of diethyl ether. The red solution was stored at +5 °C for 24 hours. An amorphous reddish-orange solid was isolated by filtration at 0 °C. The amorphous reddish-orange solid was recrystallized from 15 mL of Et$_2$O at +5 °C and finally dried *in vacuo* for 1 hour at ambient temperature to afford analytically pure reddish-orange solid. Yield: 182 mg (0.20 mmol, 59%).

Properties: Complex **7-Mo** is very good soluble in toluene, THF and fluorobenzene, and moderately soluble in aliphatic solvent.

Melting Points: The reddish-orange solid compound shows extremely high thermal stability and only starts changing colour very slowly from reddish-orange to red at above

253 °C and completely decomposes upon melting to a dark brown liquid at 283 – 285 °C.

Elemental analysis: calcd. (%) for $C_{41}H_{71}BMoN_6O_2Si_5$ (927.22): C 53.11, H 7.72, N 9.06; found: C 52.56, H 7.70, N 8.99.

Spectroscopic Data:

IR (THF): $\tilde{\nu}$ (cm^{-1}) = 1912 (s) and 1835 (vs) [ν(CO)], 1545 (w) [$\nu(C\text{-}C\text{-}N)_{pz}$].

IR (toluene): $\tilde{\nu}$ (cm^{-1}) = 1912 (s) and 1836 (vs) [ν(CO)], 1544 (w) [$\nu(C\text{-}C\text{-}N)_{pz}$].

IR (*n*-pentane): $\tilde{\nu}$ (cm^{-1}) = 1918 (s) and 1844 (vs) [ν(CO)], 1546 (w) [$\nu(C\text{-}C\text{-}N)_{pz}$].

ATR-IR (solid): $\tilde{\nu}$ (cm^{-1}) = 2953 (w), 2928 (vw), 2903 (vw), 2871 (vw), 2765 (vw), 2530 (vw) [ν(BH)], 1904 (s) [ν(CO)], 1829 (vs) [ν(CO)], 1586 (w), 1543 (m) [$\nu(C\text{-}C\text{-}N)_{pz}$], 1525 (w), 1477 (vw), 1447 (m), 1414 (m), 1397 (m), 1382 (m), 1373 (m), 1348 (sh), 1260 (m), 1248 (m), 1203 (m), 1169 (w), 1160 (w), 1134 (w), 1064 (w), 1045 (w), 1008 (w), 984 (vw), 955 (m), 939 (w), 889 (m), 856 (sh), 837 (vs), 801 (m), 791 (m), 772 (m), 763 (m), 744 (w), 723 (w), 692 (m), 662 (w), 657 (sh), 646 (m), 627 (vw), 607 (w), 580 (vw), 563 (vw), 553 (sh), 514 (vw), 502 (w), 480 (w), 459 (m), 420 (m).

^{1}H NMR: (300.1 MHz, C_6D_6, 298 K): δ (ppm) = 0.27 (s, ^2J(Si,H) = 6 Hz, 36H, $C^{2,6}$-CH(Si*Me*$_3$)$_2$, Tbb), 1.24 (s, 9H, C^4-C*Me*$_3$, Tbb), 2.06 (s, 3H, C^5-*Me*, pz_B), 2.11 (s, 6H, 2 × C^5-*Me*, pz_A), 2.77 (s, 3H, C^3-*Me*, pz_B), 2.83 (s, 6H, 2 × C^3-*Me*, pz_A), 3.43 (s, ^2J(Si,H) = 9 Hz, 2H, $C^{2,6}$-C*H*(SiMe$_3$)$_2$, Tbb), 4.6 (br, $\Delta\nu_{1/2}$ = ~ 200 Hz, 1H, B*H*); this signal is visible as a very broad hump over the base line in a strongly enlarged version of the spectrum), 5.39 (s, 1H, C^4-*H*, pz_B), 5.67 (s, 2H, 2 × C^4-*H*, pz_A), 6.87 (s, 2H, $C^{3,5}$-*H*, Tbb).

^{13}C{^{1}H} NMR: (75.47 MHz, C_6D_6, 298 K): δ (ppm) = 0.72 (s, ^1J(Si,C) = 52 Hz, 12C, $C^{2,6}$-CH(Si*Me*$_3$)$_2$, Tbb), 12.6 (s, 2C, 2 × C^5-*Me*, pz_A), 12.7 (s, 1C, C^5-*Me*, pz_B), 15.4 (s, 1C, C^3-*Me*, pz_B), 18.9 (s, 2C, 2 × C^3-*Me*, pz_A), 30.9 (s, 3C, C^4-C*Me*$_3$, Tbb), 31.0 (s, ^1J(Si,C) = 41 Hz, 2C, $C^{2,6}$-*C*H(SiMe$_3$)$_2$, Tbb), 34.9 (s, 1C, C^4-*C*Me$_3$, Tbb), 106.4 (s, 2C, 2 × *C*^{4}-H, pz_A), 107.2 (s, 1C, *C*^{4}-H, pz_B), 122.2 (s, 2C, *C*^{3,5}-H, Tbb), 143.97 (s, 1C, *C*^{5}-Me, pz_B), 143.99 (s, 2C, 2 × *C*^{5}-Me, pz_A), 148.6 (s,

1C, C^{1}-Si), 150.4 (s, 2C, $C^{2,6}$-CH($SiMe_3$)$_2$, Tbb), 150.7 (s, 2C, 2 × C^{3}-Me, pz_A), 152.8 (s, 1C, C^{3}-Me, pz_B), 154.1 (s, 1C, C^{4}-CMe_3, Tbb), 229.0 (s, 2C, 2 × *C*O).

$^{29}Si\{^{1}H\}$ NMR: (59.63 MHz, C_6D_6, 298 K): δ (ppm) = 2.2 (s, 4Si, $C^{2,6}$-CH(*Si*Me_3)$_2$, Tbb), 258.5 (s, 1Si, Mo≡*Si*).

4.5.11 [Tp'(CO)$_2$W≡Si–Tbb] (7-W)

4.5.11.1. Synthesis of 7-W from 3-W and *E*-(Tbb)BrSi=SiBr(Tbb)

A mixture mixture of *E*-(Tbb)BrSi=SiBr(Tbb) (439 mg, 0.39 mmol, 0.5 equiv.) and **3-W** (500 mg, 0.79 mmol, 1.0 equiv.) was treated with 30 mL of toluene. The resulting yellow suspension was then heated at 110 °C for 30 minutes. During this time, the color of the suspension changed to red, and the metalate was converted selectively into the silylidyne complex **7-W** as confirmed by IR spectroscopy. All volatiles were removed under vacuum, and the red solid was extracted with *n*-pentane (3 × 40 mL) at ambient temperature. The combined extracts were concentrated in *vacuo* to 25 mL and the resulting suspension was stored at 0 °C for 10 minutes. An amorphous red solid was collected by filtration of the supernatant at 0 °C and dried under reduced pressure for 15 minutes at 60 °C. Yield: 527 mg (0.52 mmol, 66%). The solid was shown by IR and ^{1}H NMR spectroscopy to be pure.

4.5.11.2. Synthesis of 7-W from [Tp'(CO)$_2$W=Si(4-dmap)Tbb] (6-W) and B(C_6F_5)$_3$

A colorless solution of B(C_6F_5)$_3$ (293 mg, 0.57 mmol, 1.00 equiv.) in 10 mL of diethyl ether was added slowly via a syringe to a stirred suspension of complex **6-W** (650 mg, 0.57 mmol, 1.00 equiv.) in 20 mL of diethyl ether. The brown suspension turned instantly into a red solution. Selective formation of the silylidyne complex **7-W** was confirmed by IR spectroscopy. All volatiles were removed under vacuum, and the red solid was extracted with *n*-hexane (3 × 40 mL) at 0 °C. The combined extracts were evaporated to dryness *in vacuo*, and the resulting residue dissolved in 20 mL of diethyl ether. The red solution was stored at +5 °C for 15 hours. An amorphous red solid was isolated by filtration at 0 °C and dried *in vacuo* for 2 hours at ambient temperature. Yield: 386 mg (0.38 mmol, 67%).

Properties: Complex **7-W** is very good soluble in toluene, THF and fluorobenzene, and moderately soluble in aliphatic solvent.

Melting Points: Red solid decomposes upon melting at 252 – 253 °C to a brown liquid.

Elemental analysis: calcd. (%) for $C_{41}H_{71}BN_6O_2Si_5W$ (1015.12): C 48.51, H 7.05, N 8.28; found: C 48.33, H 7.11, N 8.36.

Spectroscopic Data:

IR (THF): $\tilde{\nu}$ (cm^{-1}) = 1901 (s) and 1822 (vs) [ν(CO)], 1545 (w) [ν(C-C-N)$_{pz}$].

IR (toluene): $\tilde{\nu}$ (cm^{-1}) = 1901 (s) and 1823 (vs) [ν(CO)], 1545 (w) [ν(C-C-N)$_{pz}$].

IR (*n*-pentane): $\tilde{\nu}$ (cm^{-1}) = 1907 (s) and 1831 (vs) [ν(CO)], 1546 (w) [ν(C-C-N)$_{pz}$].

ATR-IR (solid): $\tilde{\nu}$ (cm^{-1}) = 2952 (m), 2925 (vw), 2902 (w), 2767 (vw), 2544 (vw) [ν(BH)], 1928 (vw), 1897 (s) [ν(CO)], 1818 (vs) [ν(CO)], 1587 (w), 1543 (m) [ν(C-C-N)$_{pz}$], 1527 (w), 1476 (vw), 1447 (w), 1414 (m), 1397 (w), 1382 (w), 1371 (m), 1260 (w), 1247 (m), 1204 (m), 1170 (vw), 1160 (vw), 1135 (vw), 1065 (w), 1046 (vw), 1017 (vw), 1009 (vw), 981 (vw), 955 (w), 940 (vw), 890 (m), 836 (vs), 792 (m), 776 (m), 764 (sh), 745 (w), 723 (vw), 692 (m), 684 (sh), 646 (m), 620 (vw), 609 (w), 577 (vw), 565 (vw), 522 (vw), 507 (w), 484 (w), 462 (m), 421 (m).

^{1}H NMR: (300.1 MHz, C_6D_6, 298 K): δ (ppm) = 0.28 (s, ^2J(Si,H) = 6 Hz, 36H, C^{2,6}-CH(Si*Me*$_3$)$_2$, Tbb), 1.25 (s, 9H, C^4-C*Me*$_3$, Tbb), 2.00 (s, 3H, C^5-*Me*, pz$_B$), 2.06 (s, 6H, 2 × C^5-*Me*, pz$_A$), 2.82 (s, 3H, C^3-*Me*, pz$_B$), 2.88 (s, 6H, 2 × C^3-*Me*, pz$_A$), 3.46 (s, ^2J(Si,H) = 9 Hz, 2H, C^{2,6}-C*H*(SiMe$_3$)$_2$, Tbb), 4.6 (br, $\Delta\nu_{1/2}$ = ~ 200 Hz, 1H, B*H*); this signal is visible as a very broad hump over the base line in a strongly enlarged version of the spectrum), 5.32 (s, 1H, C^4-*H*, pz$_B$), 5.66 (s, 2H, 2 × C^4-*H*, pz$_A$), 6.93 (s, 2H, C^{3,5}-*H*, Tbb).

^{13}C{^{1}H} NMR: (75.47 MHz, C_6D_6, 298 K): δ (ppm) = 0.71 (s, ^1J(Si,C) = 52 Hz, 12C, C^{2,6}-CH(Si*Me*$_3$)$_2$, Tbb), 12.5 (s, 3C, (2 × C^5-*Me*, pz$_A$) + (C^5-*Me*, pz$_B$)), 15.9 (s, 1C, C^3-*Me*, pz$_B$), 20.1 (s, 2C, 2 × C^3-*Me*, pz$_A$), 30.9 (s, 3C, C^4-C*Me*$_3$, Tbb), 31.1 (s, ^1J(Si,C) = 41 Hz, 2C, C^{2,6}-*C*H(SiMe$_3$)$_2$, Tbb), 34.9 (s, 1C, C^4-*C*Me$_3$, Tbb), 106.6 (s, 2C, 2 × *C*^{4}-H, pz$_A$), 107.4 (s, 1C, *C*^{4}-H, pz$_B$), 122.5 (s, 2C, *C*^{3,5}-H, Tbb), 143.8 (s, 1C, *C*^{5}-Me, pz$_B$), 143.9 (s, 2C, 2 × *C*^{5}-Me, pz$_A$), 150.6 (s, 2C, *C*^{2,6}-CH(SiMe$_3$)$_2$, Tbb), 150.7 (s, 1C, *C*^{1}-Si), 151.3 (s, ^2J(W,C) = 4 Hz, 2C, 2 ×

C^3-Me, pz_A), 153.67 (s, ^2J(W,C) = 5 Hz, 1C, C^3-Me, pz_B), 153.74 (s, 1C, C^4-CMe_3, Tbb), 223.8 (s, ^1J(W,C) = 159 Hz, 2C, 2 × *C*O).

$^{29}Si\{^1H\}$ NMR: (59.63 MHz, C_6D_6, 298 K): δ (ppm) = 2.1 (s, ^1J(Si,C) = 52 Hz, 4 × *Si*Me_3, Tbb), 259.8 (s, ^1J(W,Si) = 272 Hz, 1Si, W≡*Si*).

4.5.12 [Tp'(CO)$_2$Mo≡Ge(C$_6$H$_3$-2,6-Mes$_2$)] (8-Mo)

4.5.12.1. Synthesis from K[Tp'Mo(CO)$_3$]·2THF

A mixture of K[Tp'Mo(CO)$_3$]·2THF (136 mg, 0.206 mmol) and (GeCl(C$_6$H$_3$-2,6-Mes$_2$))$_2$ (87 mg, 0.103 mmol) was treated with ~ 10 mL of toluene. The resulting orange suspension was immersed in an ultrasonic bath for 5 minutes and then heated at 110 °C for 1 hour with rapid stirring. The color of the suspension changed from orange to yellowish-brown. Complete conversion of the starting material into the product was confirmed by IR spectroscopy, which revealed the selective formation of the product (ν(CO): 1924 (s) and 1850 (vs) cm^{-1}). The resulting yellowish-brown suspension was concentrated under *vacuo* to *ca*. 5 mL and treated with 5 mL of *n*-hexane. The obtained suspension was filtered and the filtrate was pumped down and pulverised once by a freeze-pump-thaw cycle. Obtained yellowish-brown powder was dried in *vacuo* at 60 °C for 3 hours to afford compound **8-Mo**, as an extremely air-sensitive, analytically pure solid. Yield: 157 mg (0.188 mmol, 91%).

4.5.12.2. Synthesis from Na[Tp'Mo(CO)$_2$(PMe$_3$)] (3-Mo)

A yellow solution of (GeCl(C$_6$H$_3$-2,6-Mes$_2$))$_2$, (154 mg, 0.183 mmol) in 5 mL of THF was slowly added to a stirred solution of **3-Mo** (200 mg, 0.365 mmol) in 15 mL of THF at ambient temperature. The color of the solution immediately changed from yellow to yellowish-brown. An IR spectrum after 5 min confirmed the complete consumption of the starting material and formation of the product (1919 and 1842 cm^{-1} in Bruker Alpha as THF film) along with ~ 5% of the **2-Mo** radical (1891 and 1753 cm^{-1}). The resulting yellowish brown solution was dried under reduced pressure and pulverised once by freeze-pump-thaw cycle and then extracted with *n*-pentane (2 × 10 mL). The extract was concentrated to *ca*. 5 mL and stored at −60 °C for 48 hrs. A microcrystalline yellowish brown solid was isolated by filtration at −60 °C and dried under *vacuo* for 2 hrs at 80 °C. Yield: 262 mg (0.317 mmol, 86%).

Properties: Complex **8-Mo** is very good soluble in all common organic solvent. It is extremely sensitive towards air.

Melting Points: The compound exhibit very high thermal stability and does not melt or decomposes up to 240 °C.

Elemental analysis: calcd (%) for $C_{41}H_{47}BGeMoN_6O_2$ (835.21 g/mol): C 58.96, H 5.67, N 10.06; found: C 58.66, H 5.93, N 9.98%.

Spectroscopic Data:

IR (THF): $\tilde{\nu}$ (cm^{-1}) = 1924 (s) and 1850 (vs) [ν(CO)], 1544 (w) [ν(C-C-N)$_{pz}$].

IR (toluene): $\tilde{\nu}$ (cm^{-1}) = 1925 (s) and 1850 (vs) [ν(CO)], 1545 (w) [ν(C-C-N)$_{pz}$].

IR (*n*-hexane): $\tilde{\nu}$ (cm^{-1}) = 1929 (s) and 1858 (vs) [ν(CO)], 1545 (w) [ν(C-C-N)$_{pz}$].

ATR-IR (solid): $\tilde{\nu}$ (cm^{-1}) = 2952 (vw), 2918 (w), 2856 (w), 2523 (w) [ν(BH)], 1914 (s) [ν(CO)], 1842 (vs) [ν(CO)], 1612 (w), 1574 (vw), 1546 (m) [ν(C-C-N)$_{pz}$], 1486 (vw), 1447 (m), 1412 (m), 1373 (m), 1348 (w, sh), 1306 (vw), 1202 (m), 1187 (w), 1152 (vw), 1129 (vw), 1106 (vw), 1086 (vw), 1064 (m), 1046 (w), 1035 (w), 1011 (vw, sh), 982 (w), 913 (vw), 888 (vw), 873 (vw), 850 (m), 808 (m), 782 (m), 742 (m), 709 (vw), 693 (m), 663 (vw), 646 (m), 622 (w), 588 (vw), 574 (w), 549 (vw), 509 (w), 478 (vw), 470 (w, sh), 458 (m), 424 (vw), 402 (vw), 393 (w).

^{1}H NMR: (300.1 MHz, C_6D_6, 298 K): δ (ppm) = 1.99 (s, 3H, C^5-*Me*, pz$_B$), 2.03 (s, 6H, 2 × C^5-*Me*, pz$_A$), 2.13 (s, 6H, 2 × C^4-*Me*, Mes), 2.24 (s, 6H, 2 × C^3-*Me*, pz$_A$), 2.31 (s, 12H, 2 × C^{2,6}-*Me*, Mes), 2.55 (s, 3H, C^3-*Me*, pz$_B$), 4.6 (br, $\Delta\nu_{1/2}$ = ~ 220 Hz, 1H, B*H*); this signal is visible as a very broad hump over the base line in a strongly enlarged version of the spectrum), 5.35 (s, 1H, C^4-*H*, pz$_B$), 5.56 (s, 2H, 2 × C^4-*H*, pz$_A$), 6.87 (d, ^3J(H,H) = 7.5 Hz, 2H, C^{3,5}- *H,* C_6H_3), 6.92 (s, 4H, C^{3,5}-*H*, Mes), 7.14 (t, ^3J(H,H) = 7.5 Hz, 1H, C^4-*H*, C_6H_3).

^{13}C{^{1}H} NMR: (75.47 MHz, C_6D_6, 298 K): δ (ppm) = 12.5 (s, 2C, 2 × C^5-*Me*, pz$_A$), 12.6 (s, 1C, C^5-*Me*, pz$_B$), 15.1 (s, 1C, C^3-*Me*, pz$_B$), 17.5 (s, 2C, 2 × C^3-*Me*, pz$_A$), 21.1 (s, 2C, 2 × *C*^{4}-*Me*, Mes), 21.5 (s, 4C, 2 × *C*^{2,6}-*Me*, Mes), 106.2 (s, 2C, 2 × *C*^{4}-H, pz$_A$),

107.2 (s, 1C, C^4-H, pz_B), 129.0 (s, 2C, $C^{3,5}$, C_6H_3), 129.6 (s, 4C, 2 × $C^{3,5}$, Mes), 131.2 (s, 1C, C^4, C_6H_3), 136.6 (s, 4C, 2 × $C^{2,6}$, Mes), 137.6 (s, 2C, 2 × C^1, Mes), 137.7 (s, 2C, 2 × C^4, Mes), 143.5 (s, 2C, 2 × C^5-Me, pz_A), 143.7 (s, 1C, C^5-Me, pz_B), 145.6 (s, 2C, $C^{2,6}$, C_6H_3), 150.0 (s, 2C, 2 × C^3-Me, pz_A), 153.1 (s, 1C, C^3-Me, pz_B), 164.3 (s, 1C, C^1, C_6H_3), 228.1 (s, 2C, 2 × *C*O).

4.5.13 [Tp'(CO)$_2$W≡Ge(C$_6$H$_3$-2,6-Mes$_2$)] (8-W)

A mixture of K[Tp'W(CO)$_3$]·THF (500 mg, 0.67 mmol) and (GeCl(C$_6$H$_3$-2,6-Mes$_2$))$_2$ (282 mg, 0.33 mmol, 0.5 equiv.) was treated with 25 mL of toluene at ambient temperature. The resulting orange suspension was heated to 110 °C for 1 hour. Upon heating the color of the suspension changed to yellowish-brown. An inspection of the reaction mixture after 1 hour by IR spectroscopy revealed a clean and complete conversion of the starting material into the product. All volatiles were removed under reduced pressure and the residue was treated with 30 mL of 1:1 mixture of *n*-hexane/Et$_2$O mixture. The yellowish-brown suspension was filtered and the filtrate was concentrated to ~ 8 mL, upon which a light purple color microcrystalline solid precipitated out from the solution. The precipitate was isolated, by filtration of the light yellowish-brown supernatant, washed with *n*-hexane (2 × 5 mL) at ambient temperature and finally dried under reduced pressure for 1 hour at ambient temperature. All the filtrate were collected and concentrated to ~ 5 mL and stored at 0 °C for 1 hour and that resulted in the precipitation of a light purple color, microcrystalline solid, which was isolated by filtration of the supernatant at 0 °C. The isolated solid was washed with 2 mL of *n*-hexane at 0 °C and dried for 2 hours under reduced pressure at ambient temperature. Combined yield: 518 mg (0.56 mmol, 84 %).

Properties: Compound **8-W** is very good soluble in all common organic solvent.

Melting Points: The light purple solid decomposes upon heating to a shiny light yellow solid at 221 – 224 °C.

Elemental analysis: calcd (%) for $C_{41}H_{47}BGeN_6O_2W$ (823.11 g/mol): C 53.35, H 5.13, N 9.10; found: C 53.25, H 5.55, N 8.96%.

Spectroscopic Data:

IR (THF): $\tilde{\nu}$ (cm^{-1}) = 1913 (s) and 1836 (vs) [ν(CO)], 1545 (w) [ν(C-C-N)$_{pz}$].

IR (toluene): $\tilde{\nu}$ (cm^{-1}) = 1913 (s) and 1836 (vs) [ν(CO)], 1545 (w) [ν(C-C-N)$_{pz}$].

IR (*n*-hexane): $\tilde{\nu}$ (cm^{-1}) = 1919 (s) and 1844 (vs) [ν(CO)], 1547 (w) [$\nu(C\text{-}C\text{-}N)_{pz}$].

ATR-IR (solid): $\tilde{\nu}$ (cm^{-1}) = 2977 (vw), 2951 (vw), 2918 (w), 2855 (vw), 2538 (w) [ν(BH)], 2523 (vw) [ν(BH)], 1901 (s) [ν(CO)], 1827 (vs) [ν(CO)], 1612 (w), 1575 (vw), 1546 (m) [$\nu(C\text{-}C\text{-}N)_{pz}$], 1486 (vw), 1447 (m), 1412 (m), 1377 (m), 1370 (m), 1346 (w, sh), 1305 (vw), 1202 (m) 1184 (w), 1153 (vw), 1128 (vw), 1107 (vw), 1086 (vw), 1063 (m), 1047 (w), 1034 (w), 1010 (vw, sh), 982 (w), 913 (vw), 888 (vw), 875 (vw), 849 (m), 808 (w), 783 (m), 741 (m), 710 (vw), 693 (m), 663 (vw), 646 (m), 617 (w), 588 (vw), 575 (w), 551 (vw), 516 (vw), 505 (vw), 481 (w), 473 (w, sh), 462 (m), 424 (vw), 404 (vw), 393 (w).

^{1}H NMR: (300.1 MHz, C_6D_6, 298 K): δ (ppm) = 1.94 (s, 3H, C^5-*Me*, pz_B), 1.99 (s, 6H, 2 × C^5-*Me*, pz_A), 2.14 (s, 6H, 2 × C^4-*Me*, Mes), 2.28 (s, 6H, 2 × C^3-*Me*, pz_A), 2.31 (s, 12H, 2 × $C^{2,6}$-*Me*, Mes), 2.61 (s, 3H, C^3-*Me*, pz_B), 4.5 (br, $\Delta\nu_{1/2}$ = ~ 220 Hz, 1H, B*H*); this signal is visible as a very broad hump over the base line in a strongly enlarged version of the spectrum), 5.29 (s, 1H, C^4-*H*, pz_B), 5.54 (s, 2H, 2 × C^4-*H*, pz_A), 6.933 (s, 4H, $C^{3,5}$-*H*, Mes), 6.934 (d, ^3J(H,H) = 7.5 Hz, 2H, $C^{3,5}$- *H,* C_6H_3), 7.18 (t, ^3J(H,H) = 7.5 Hz, 1H, C^4-*H*, C_6H_3).

$^{13}C\{^1H\}$ NMR: (75.47 MHz, C_6D_6, 298 K): δ (ppm) = 12.39 (s, 2C, 2 × C^5-*Me*, pz_A), 12.44 (s, 1C, C^5-*Me*, pz_B), 15.6 (s, 1C, C^3-*Me*, pz_B), 18.9 (s, 2C, 2 × C^3-*Me*, pz_A), 21.2 (s, 2C, 2 × C^4-*Me*, Mes), 21.5 (s, 4C, 2 × $C^{2,6}$-*Me*, Mes), 106.3 (s, 2C, 2 × C^4-H, pz_A), 107.4 (s, 1C, C^4-H, pz_B), 129.3 (s, 2C, $C^{3,5}$, C_6H_3), 129.5 (s, 4C, 2 × $C^{3,5}$, Mes), 130.9 (s, 1C, C^4, C_6H_3), 136.6 (s, 4C, 2 × $C^{2,6}$, Mes), 137.5 (s, 2C, 2 × C^4, Mes), 137.9 (s, 2C, 2 × C^1, Mes), 143.4 (s, 2C, 2 × C^5-Me, pz_A), 143.5 (s, 1C, C^5-Me, pz_B), 146.2 (s, 2C, $C^{2,6}$, C_6H_3), 150.8 (s, 2C, 2 × C^3-Me, pz_A), 154.0 (s, 1C, C^3-Me, pz_B), 166.9 (s, 1C, C^1, C_6H_3), 222.7 (s, ^1J(W,C) = 162 Hz, 2C, 2 × *C*O).

4.5.14 [Tp'(CO)$_2$Mo≡Sn(C$_6$H$_3$-2,6-Mes$_2$)] (9-Mo)

To a yellow solution of **3-Mo** (300 mg, 0.547 mmol) in 25 mL of THF, a yellow solution of SnCl(C_6H_3-2,6-Mes_2) (256 mg, 0.547 mmol) in 15 mL of THF was added dropwisely at room temperature. The color turned from yellow to dark greenish-brown. An IR spectrum after 5 minutes revealed the complete conversion of the starting material into the expected product (1892

and 1820 cm^{-1} in Alfa) and ~ 5% of **2-Mo** radical. The solvent was evaporated to dryness and the greenish-brown residue was extracted with *n*-hexane (2 × 15 mL). The greenish brown extract was filtered from a brown insoluble material. The filtrate was evaporated to dryness *in vacuo* and the residue was again dissolved in ~ 20 mL of Et_2O. The clear greenish-brown Et_2O solution was concentrated under reduced pressure to *ca*. 5 mL and stored at −60 °C for 24 hours. The microcrystalline greenish-brown solid that form was isolated by filtration at −60 °C and dried under reduced pressure for 3 hours at 65 °C. Yield: 327 mg (0.371 mmol, 68%).

Properties: Compound **9-Mo** is very good soluble in THF, Et_2O, toluene and moderately soluble in aliphatic solvents.

Melting Points: The compound exhibits very high thermal stability and decomposes upon melting at 231 – 233 °C to give a black mass.

Elemental analysis: calcd (%) for $C_{41}H_{47}BMoN_6O_2Sn$ (881.31 g/mol): C 55.87, H 5.37, N 9.53; found: C 55.85, H 5.41, N 9.18%.

Spectroscopic Data:

IR (THF): $\tilde{\nu}$ (cm^{-1}) = 1897 (s) and 1828 (vs) [ν(CO)], 1545 (w) [$\nu(C\text{-}C\text{-}N)_{pz}$].

IR (toluene): $\tilde{\nu}$ (cm^{-1}) = 1898 (s) and 1828 (vs) [ν(CO)], 1545 (w) [$\nu(C\text{-}C\text{-}N)_{pz}$].

IR (*n*-hexane): $\tilde{\nu}$ (cm^{-1}) = 1903 (s) and 1836 (vs) [ν(CO)], 1545 (w) [$\nu(C\text{-}C\text{-}N)_{pz}$].

ATR-IR (solid): $\tilde{\nu}$ (cm^{-1}) = 3121 (vw), 3026 (vw), 2971 (vw), 2917 (w), 2852 (vw), 2731 (vw), 2520 (w) [ν(BH)], 1880 (s) [ν(CO)], 1809 (vs) [ν(CO)], 1611 (w), 1560 (vw), 1543 (m) [$\nu(C\text{-}C\text{-}N)_{pz}$], 1485 (vw), 1445 (m), 1411 (m), 1372 (m), 1346 (w, sh), 1207 (m), 1192 (m), 1150 (w), 1118 (vw), 1096 (vw), 1087 (vw), 1063 (m), 1045 (m), 1031 (w, sh), 979 (w), 901 (vw), 865 (vw), 850 (m), 805 (m), 789 (w), 780 (m), 738 (m), 692 (m), 660 (vw), 644 (m), 624 (w), 587 (vw), 573 (w), 547 (vw), 517 (w), 482 (w), 461 (m).

^{1}H NMR: (300.1 MHz, C_6D_6, 298 K): δ (ppm) = 1.96 (s, 6H, 2 × C^3-*Me*, pz_A), 2.03 (s, 3H, C^5-*Me*, pz_B), 2.12 (s, 6H, 2 × C^5-*Me*, pz_A), 2.21 (s, 6H, 2 × C^4-*Me*, Mes), 2.27 (s, 12H, 2 × $C^{2,6}$-*Me*, Mes), 2.65 (s, 3H, C^3-*Me*, pz_B), 4.6 (br, $\Delta\nu_{1/2}$ = ~ 200 Hz, 1H, B*H*); this signal is visible as a very broad hump over the base line in an

strongly enlarged version of the spectrum), 5.37 (s, 1H, C^4-*H*, pz_B), 5.61 (s, 2H, 2 × C^4-*H*, pz_A), 6.965 (d, ^3J(H,H) = 7.5 Hz, 2H, $C^{3,5}$-*H,* C_6H_3), 6.972 (s, 4H, 2 × $C^{3,5}$-*H*, Mes), 7.16 (t, ^3J(H,H) = 7.5 Hz, 1H, C^4-*H*, C_6H_3).

$^{13}C\{^1H\}$ NMR: (75.47 MHz, C_6D_6, 298 K): δ (ppm) = 12.6 (s, 2C, 2 × C^5-*Me*, pz_A), 12.8 (s, 1C, C^5-*Me*, pz_B), 15.3 (s, 1C, C^3-*Me*, pz_B), 18.0 (s, 2C, 2 × C^3-*Me*, pz_A), 21.26 (s, 2C, 2 × C^4-*Me*, Mes), 21.29 (s, 4C, 2 × $C^{2,6}$-*Me*, Mes), 106.4 (s, 2C, 2 × C^4-H, pz_A), 107.3 (s, 1C, 1 × C^4-H, pz_B), 129.5 (s, 2C, $C^{3,5}$-H, C_6H_3), 129.8 (s, 4C, 2 × $C^{3,5}$-H, Mes), 130.5 (s, 1C, C^4-H, C_6H_3), 136.7 (s, 4C, 2 × $C^{2,6}$, Mes), 137.9 (s, 2C, 2 × C^4, Mes), 138.3 (s, 2C, 2 × C^1, Mes), 143.5 (s, 2C, 2 × C^5-Me, pz_A), 144.0 (s, 1C, C^5-Me, pz_B), 145.9 (s, 2C, $C^{2,6}$, C_6H_3), 150.0 (s, 2C, 2 × C^3-Me, pz_A), 153.8 (s, 1C, C^3-Me, pz_B), 182.9 (s, 1C, Sn-C^1, C_6H_3), 227.9 (s, 2C, 2 × *C*O).

$^{119}Sn\{^1H\}$ NMR: (111.9 MHz, C_6D_6, 298 K) δ (ppm) = 642.4 (br s, $\Delta\nu_{1/2}$ = 70 Hz).

4.5.15 [Tp'(CO)$_2$W≡Sn(C$_6$H$_3$-2,6-Mes$_2$)] (9-W)

To a yellow solution of **3-W** (500 mg, 0.79 mmol) in 20 mL of THF, a yellow solution of SnCl(C_6H_3-2,6-Mes_2) (368 mg, 0.79 mmol, 1 equiv.) in 10 mL of THF was slowly added at ambient temperature and stirred for 1 hour. Immediate after addition, the color of the solution changed to brown. Monitoring of the reaction by IR spectroscopy revealed a selective conversion of the starting material into the product. After stirring for 1 hour, all volatiles were removed under reduced pressure and the sticky residue was pulverized by freeze-pump-thaw cycle. Obtain brown powder was extracted with 2:1 Et_2O/*n*-hexane mixture (2 × 15 mL) and the combined extract was concentrated to ~15 mL upon which an amorphous brown solid precipitated out from the solution. The suspension was stored at 0 °C for 30 minutes and afterwards the light brown supernatant was filtered off to obtain a brown solid which was washed with *n*-pentane (2 × 10 mL) and dried for 2 hours at ambient temperature. Yield: 548 mg (0.57 mmol, 72 %).

Properties: Complex **9-W** is very good soluble in THF, Et_2O, toluene and moderately soluble in aliphatic solvent.

Melting Points: The compound starts to decompose at 205 – 208 °C to a shiny greyish-brown solid, which melts to a black liquid at 228 – 231 °C.

Elemental analysis: calcd (%) for $C_{41}H_{47}BN_6O_2SnW$ (969.21 g/mol): C 50.81, H 4.89, N 8.67; found: C 50.42, H 5.15, N 8.50%.

Spectroscopic Data:

IR (THF): $\tilde{\nu}$ (cm^{-1}) = 1886 (s) and 1814(vs) [ν(CO)], 1545 (w) [ν(C-C-N)$_{pz}$].

IR (toluene): $\tilde{\nu}$ (cm^{-1}) = 1886 (s) and 1815 (vs) [ν(CO)], 1545 (w) [ν(C-C-N)$_{pz}$].

ATR-IR (solid): $\tilde{\nu}$ (cm^{-1}) = 3033 (vw), 2981 (vw), 2955 (vw), 2916 (w), 2855 (vw), 2731 (vw), 2545 (vs) [ν(BH)], 2527 (vw) [ν(BH)], 1883 (s) [ν(CO)], 1806 (vs) [ν(CO)], 1612 (w), 1563 (vw), 1544 (m) [ν(C-C-N)$_{pz}$], 1489 (vw), 1447 (m), 1413 (m), 1378 (sh), 1371 (m), 1348 (sh), 1210 (m), 1197 (m), 1175 (vw), 1158 (vw), 1148 (vw), 1120 (vw), 1094 (vw), 1066 (m), 1048 (w), 1031 (w), 982 (vw), 953 (vw), 892 (vw), 874 (vw), 856 (m), 818 (w), 801 (m), 776 (w), 738 (w), 694 (w), 664 (vw), 645 (w), 618 (vw), 589 (vw), 573 (vw), 547 (vw), 522 (w), 507 (vw), 484 (w), 470 (w), 463 (w), 425 (vw), 412 (vw), 402 (w).

^{1}H NMR: (300.1 MHz, C_6D_6, 298 K): δ (ppm) = 1.97 (s, 3H, C^5-*Me*, pz_B), 1.98 (s, 6H, 2 × C^3-*Me*, pz_A), 2.07 (s, 6H, 2 × C^5-*Me*, pz_A), 2.22 (s, 6H, 2 × C^4-*Me*, Mes), 2.27 (s, 12H, 2 × $C^{2,6}$-*Me*, Mes), 2.71 (s, 3H, C^3-*Me*, pz_B), 4.6 (br, $\Delta\nu_{1/2}$ = ~ 180 Hz, 1H, B*H*); this signal is visible as a very broad hump over the base line in an strongly enlarged version of the spectrum), 5.32 (s, 1H, C^4-*H*, pz_B), 5.59 (s, 2H, 2 × C^4-*H*, pz_A), 6.99 (s, 4H, 2 × $C^{3,5}$-*H*, Mes), 7.02 (d, ^3J(H,H) = 7.5 Hz, 2H, $C^{3,5}$-*H,* C_6H_3), 7.19 (t, ^3J(H,H) = 7.5 Hz, 1H, C^4-*H*, C_6H_3).

^{13}C{^{1}H} NMR: (75.47 MHz, C_6D_6, 298 K): δ (ppm) = 12.4 (s, 1C, C^5-*Me*, pz_B), 12.7 (s, 2C, 2 × C^5-*Me*, pz_A), 15.8 (s, 1C, C^3-*Me*, pz_B), 19.7 (s, 2C, 2 × C^3-*Me*, pz_A), 21.23 (s, 4C, 2 × $C^{2,6}$-*Me*, Mes), 21.26 (s, 2C, 2 × C^4-*Me*, Mes), 106.5 (s, 2C, 2 × C^4-H, pz_A), 107.6 (s, 1C, 1 × C^4-H, pz_B), 129.7 (s, 2C, $C^{3,5}$-H, C_6H_3), 129.8 (s, 4C, 2 × $C^{3,5}$-H, Mes), 130.4 (s, 1C, C^4-H, C_6H_3), 136.7 (s, 4C, 2 × $C^{2,6}$, Mes), 137.7 (s, 2C, 2 × C^4, Mes), 138.6 (s, 2C, 2 × C^1, Mes), 143.4 (s, 2C, 2 × C^5-Me, pz_A), 143.6 (s, 1C, C^5-Me, pz_B), 146.6 (s, 2C, $C^{2,6}$, C_6H_3), 150.7 (s, 2C, 2 × C^3-Me, pz_A), 154.6 (s, 1C, C^3-Me, pz_B), 183.3 (s, ^2J(W,C) = 39 Hz, 1C, Sn-C^1, C_6H_3), 222.3 (s, ^1J(W,C) = 164 Hz, 2C, 2 × *C*O).

^{119}Sn{^{1}H} NMR: (111.9 MHz, C_6D_6, 298 K) δ (ppm) = 616.9 (br s, $\Delta\nu_{1/2}$ = 124 Hz, ^{1}J(W,Sn) = 1740 Hz).

4.5.16 [Tp'(CO)$_2$Mo≡Pb(C$_6$H$_3$-2,6-Mes$_2$)] (10-Mo)

A yellow solution of PbBr(C$_6$H$_3$-2,6-Mes$_2$) (219 mg, 0.365 mmol) in 5 mL of THF was added drop wise over 5 minutes to a stirred solution of **3-Mo** (200 mg, 0.365 mmol) in 15 mL of THF in a brown glass Schlenk tube at room temperature. The color of the solution immediately changed from yellow to dark green. After 10 minutes an IR spectrum was recorded, which revealed a complete conversion of **3-Mo** into product **10-Mo** (ν(CO) = 1890 and 1818 cm^{-1}) . A ν(CO) band of lower intensity at 1751 cm^{-1} was also observed suggesting the formation of some radical **2-Mo** (the second ν(CO) band of **2-Mo** was obscured by the ν(CO) band of **10-Mo** at 1890 cm^{-1}). Then the solvent was removed *in vacuo*. The residue was extracted with *n*-hexane (3 × 10 mL) and the green extract was evaporated to dryness *in vacuo*. The green solid was dissolved in roughly 15 mL of Et$_2$O, the solution concentrated under reduced pressure to ca. 5 mL and stored at –60 °C for 48 hours. The microcrystalline, dark green solid was isolated by filtration at –60 °C and was dried *in vacuo* for 4 hours at 80 °C. Yield: 255 mg (0.263 mmol, 72 %).

Properties: Complex **10-Mo** is very good soluble in THF, Et$_2$O, toluene and moderately soluble in aliphatic solvent.

Melting Points: Upon heating complex **10-Mo** starts to decompose above 210 °C and turns to a greenish brown liquid at 240 – 241 °C. It is very light sensitive in solution, and should be stored in the dark.

Elemental analysis: calcd (%) for $C_{41}H_{47}BMoN_6O_2Pb$ (969.8 g/mol): C 50.78, H 4.88, N 8.67; found: C 50.55, H 5.13, N 8.76%.

Spectroscopic Data:

IR (THF): $\tilde{\nu}$ (cm^{-1}) = 1890 (s) and 1818 (vs) [ν(CO)], 1545 (w) [ν(C-C-N)$_{pz}$].

IR (toluene): $\tilde{\nu}$ (cm^{-1}) = 1893 (s) and 1823 (vs) [ν(CO)], 1545 (w) [ν(C-C-N)$_{pz}$].

IR (*n*-hexane): $\tilde{\nu}$ (cm^{-1}) = 1899 (s) and 1832 (vs) [ν(CO)], 1546 (w) [ν(C-C-N)$_{pz}$].

ATR-IR (solid): $\tilde{\nu}$ (cm^{-1}) = 3025 (vw), 2972 (w), 2954 (vw), 2919 (w), 2856 (w), 2527 (vw) [ν(BH)], 1887 (s) [ν(CO)], 1815 (vs) [ν(CO)], 1611 (w), 1565 (vw), 1543 (m)

[ν(C-C-N)$_{pz}$], 1485 (w), 1446 (m), 1414 (m), 1374 (m), 1349 (w, sh), 1303 (vw), 1285 (vw), 1205 (m), 1149 (vw), 1089 (vw, sh), 1066 (m), 1046 (w), 1032 (w, sh), 1012 (vw), 983 (vw), 908 (vw), 871 (vw), 853 (w), 812 (w), 802 (w), 776 (w), 735 (w), 694 (w), 648 (w), 623 (vw), 587 (vw), 572 (vw), 546 (vw), 516 (vw), 480 (vw), 460 (w), 421 (vw), 409 (vw).

^{1}H NMR: (300.1 MHz, C_6D_6, 298 K): δ (ppm) = 1.90 (s, 6H, 2 × C^{3}-*Me*, pz$_A$), 2.07 (s, 3H, C^{5}-*Me*, pz$_B$), 2.15 (s, 6H, 2 × C^{5}-*Me*, pz$_A$), 2.21 (s, 6H, 2 × C^{4}-*Me*, Mes), 2.27 (s, 12H, 2 × C^{2,6}-*Me*, Mes), 2.70 (s, 3H, C^{3}-*Me*, pz$_B$), 4.6 (br, $\Delta\nu_{1/2}$ = ~ 205 Hz, 1H, B*H*); this signal is visible as a very broad hump over the base line in an strongly enlarged version of the spectrum), 5.30 (s, 1H, C^{4}-*H*, pz$_B$), 5.66 (s, 2H, 2 × C^{4}-*H*, pz$_A$), 6.99 (s, 4H, 2 × C^{3,5}-*H*, Mes), 7.26 (t, ^{3}J(H,H) = 7.5 Hz, 1H, C^{4}-*H*, C_6H_3), 7.57 (d, ^{3}J(H,H) = 7.5 Hz, 2H, C^{3,5}-*H,* C_6H_3).

^{13}C{^{1}H} NMR: (75.47 MHz, C_6D_6, 298 K): δ (ppm) = 12.5 (s, 2C, 2 × C^{5}-*Me*, pz$_A$), 12.9 (s, 1C, C^{5}-*Me*, pz$_B$), 15.1 (s, 1C, C^{3}-*Me*, pz$_B$), 16.4 (s, 2C, 2 × C^{3}-*Me*, pz$_A$), 21.0 (s, 4C, 2 × *C*^{2,6}-*Me*, Mes), 21.3 (s, 2C, 2 × *C*^{4}-*Me*, Mes), 106.4 (s, 2C, 2 × *C*^{4}-H, pz$_A$), 107.0 (s, 1C, 1 × *C*^{4}-H, pz$_B$), 128.5 (s, 1C, *C*^{4}-H, C_6H_3), 129.9 (s, 4C, 2 × *C*^{3,5}-H, Mes), 135.5 (s, 2C, *C*^{3,5}-H, C_6H_3), 136.1 (s, 4C, 2 × *C*^{2,6}, Mes), 137.6 (s, 2C, 2 × *C*^{4}, Mes), 139.4 (s, 2C, 2 × *C*^{1}, Mes), 143.6 (s, 2C, 2 × *C*^{5}-Me, pz$_A$), 145.1 (s, 1C, *C*^{5}-Me, pz$_B$), 145.3 (s, 2C, *C*^{2,6}, C_6H_3), 151.1 (s, 2C, 2 × *C*^{3}-Me, pz$_A$), 154.5 (s, 1C, *C*^{3}-Me, pz$_B$), 222.7 (s, 2C, 2 × *C*O), 266.8 (s, 1C, Pb-*C*^{1}, C_6H_3).

4.5.17 [Tp'(CO)$_2$W≡Pb(C$_6$H$_3$-2,6-Mes$_2$)] (10-W)

To a yellow suspension of **3-W** (458 mg, 0.72 mmol) in 25 mL of THF, a yellow solution of PbCl(C_6H_3-2,6-Mes_2) (400 mg, 0.72 mmol, 1 equiv.) in 15 mL of THF was slowly added at ambient temperature under complete exclusion of light using a brown glass schlenck tube. Immediate after addition the color of the suspension changed to dark green. An IR spectrum after 5 minutes of a aliquot of the green reaction mixture revealed a complete consumption of the starting material and formation of the plumbylidyne complex along with very small amount of **2-W** radical. After stirring for 15 minutes all the volatiles were removed under reduced pressure and the residue was extracted with 2:1 Et_2O/*n*-pentane mixture (40 mL). The dark green extract was concentrated to ~10 mL and the resulting green suspension was stored at +5 °C for 3 hours.

The microcrystalline green solid that form upon cooling was isolated by the filtration of the light green supernatant at 0 °C and the isolated solid was washed with 5 mL of *n*-pentane and dried under reduced pressure for 3 hours at ambient temperature to obtain the complex as an Et_2O solvate (0.5 equiv) . Yield: 480 mg (0.44 mmol, 61%).

Properties: Complex **10-W** is very good soluble in THF, Et_2O, toluene and moderately soluble in aliphatic solvent.

Melting Points: Compound decomposes to a shiny gray solid at 215 – 218 °C.

Elemental analysis: calcd (%) for $C_{41}H_{47}BN_6O_2PbW \cdot 0.5\ (C_4H_{10}O)$ (1094.76 g/mol): C 47.18, H 4.79, N 7.68; found: C 45.66, H 4.59, N 7.62%.

Spectroscopic Data:

IR (THF): $\tilde{\nu}$ (cm^{-1}) = 1880 (s) and 1809 (vs) [ν(CO)], 1545 (w) [$\nu(C\text{-}C\text{-}N)_{pz}$].

IR (toluene): $\tilde{\nu}$ (cm^{-1}) = 1881 (s) and 1809 (vs) [ν(CO)], 1545 (w) [$\nu(C\text{-}C\text{-}N)_{pz}$].

IR (*n*-pentane): $\tilde{\nu}$ (cm^{-1}) = 1889 (s) and 1820 (vs) [ν(CO)], 1547 (w) [$\nu(C\text{-}C\text{-}N)_{pz}$].

ATR-IR (solid): $\tilde{\nu}$ (cm^{-1}) = 3031 (vw), 2981 (vw), 2958 (vw), 2913 (w), 2854 (w), 2728 (vw), 2538 (vw) [ν(BH)], 2524 (vw) [ν(BH)], 1874 (s) [ν(CO)], 1802 (vs) [ν(CO)], 1610 (w), 1568 (vw), 1543 (m) [$\nu(C\text{-}C\text{-}N)_{pz}$], 1486 (vw), 1444 (m), 1411 (m), 1371 (m), 1348 (w, sh), 1303 (vw), 1198 (m), 1183 (w), 1149 (vw), 1114 (w), 1088 (vw), 1063 (m), 1046 (w), 1027 (w), 1013 (w), 981 (w), 934 (vw), 890 (vw), 873 (vw), 850 (m), 812 (w), 792 (m), 774 (m), 733 (w), 692 (w), 663 (vw), 645 (w), 617 (vw), 585 (vw), 570 (w), 546 (vw), 523 (vw), 508 (vw), 482 (vw), 472 (sh), 462 (w), 442 (vw), 429 (vw), 403 (vw).

^{1}H NMR: (300.1 MHz, C_6D_6, 298 K): δ (ppm) = 1.91 (s, 6H, 2 × C^3-*Me*, pz_A), 2.02 (s, 3H, C^5-*Me*, pz_B), 2.10 (s, 6H, 2 × C^5-*Me*, pz_A), 2.22 (s, 6H, 2 × C^4-*Me*, Mes), 2.28 (s, 12H, 2 × $C^{2,6}$-*Me*, Mes), 2.75 (s, 3H, C^3-*Me*, pz_B), 4.6 (br, $\Delta\nu_{1/2}$ = ~ 205 Hz, 1H, B*H*); this signal is visible as a very broad hump over the base line in an strongly enlarged version of the spectrum), 5.26 (s, 1H, C^4-*H*, pz_B), 5.63 (s, 2H, 2 × C^4-*H*, pz_A), 7.00 (s, 4H, 2 × $C^{3,5}$-*H*, Mes), 7.29 (t, ^3J(H,H) = 7.5 Hz, 1H, C^4-*H*, C_6H_3), 7.56 (d, ^3J(H,H) = 7.5 Hz, 2H, $C^{3,5}$-*H,* C_6H_3).

^{13}C{^{1}H} NMR: (75.47 MHz, C_6D_6, 298 K): δ (ppm) = 12.4 (s, 2C, 2 × C^5-*Me*, pz_A), 12.8 (s, 1C, C^5-*Me*, pz_B), 15.6 (s, 1C, C^3-*Me*, pz_B), 18.0 (s, 2C, 2 × C^3-*Me*, pz_A), 20.9 (s, 4C, 2 × $C^{2,6}$-*Me*, Mes), 21.3 (s, 2C, 2 × C^4-*Me*, Mes), 106.5 (s, 2C, 2 × C^4-H, pz_A), 107.3 (s, 1C, 1 × C^4-H, pz_B), 128.4 (s, 1C, C^4-H, C_6H_3), 129.9 (s, 4C, 2 × $C^{3,5}$-H, Mes), 135.2 (s, 2C, $C^{3,5}$-H, C_6H_3), 136.1 (s, 4C, 2 × $C^{2,6}$, Mes), 137.5 (s, 2C, 2 × C^4, Mes), 139.6 (s, 2C, 2 × C^1, Mes), 143.5 (s, 2C, 2 × C^5-Me, pz_A), 144.6 (s, 1C, C^5-Me, pz_B), 145.9 (s, 2C, $C^{2,6}$, C_6H_3), 151.6 (s, 2C, 2 × C^3-Me, pz_A), 155.6 (s, 1C, C^3-Me, pz_B), 218.3 (s, ^1J(W,C) = 170 Hz, 2C, 2 × *C*O), 255.9 (s, 1C, Pb-C^1, C_6H_3).

4.5.18 [Tp'(CO)$_2$Mo≡Ge{N(TMS)Mes*}] (11-Mo)

To a yellow solution of **3-Mo** (300 mg, 0.547 mmol) in 20 mL of THF, a colorless solution of GeCl{N(TMS)Mes*} (241 mg, 0.547 mmol) in 10 mL of THF was added dropwise at ambient temperature. Upon addition, the color of the solution immediately changed to red orange. An IR spectrum after 5 min revealed complete conversion of the starting material into the product (1911 and 1835 cm^{-1} in Alfa) along with a small amount (~ 5%) of the radical **2-Mo**. All volatiles were removed under vaccum and the residue was extracted with toluene (2 × 10 mL). The red orange extract was evaporated to dryness *in vacuo* and the product crystallised from a *n*-hexane/Et_2O mixture (3:1, 20 mL) by cooling at – 30 °C. A microcrystalline orange solid was isolated by filtration at –30 °C and dried under vaccum for 2 hours at 60 °C. Yield: 270 mg (0.32 mmol, 58 %).

Properties: Complex **11-Mo** is very good soluble in THF, fluorobenzene, moderately soluble in toluene and Et_2O and sparingly soluble in aliphatic solvents.

Melting Points: The compound exhibit very high thermal stability and does not melt or decompose up to 240 °C.

Elemental analysis: calcd (%) for $C_{38}H_{60}BGeMoN_7O_2Si$ (854.37 g/mol): C 53.42, H 7.08, N 11.48; found: C 51.98, H 6.81, N 10.77%.

Spectroscopic Data:

IR (THF): $\tilde{\nu}$ (cm^{-1}) = 1913 (s) and 1838 (vs) [ν(CO)], 1546 (w) [ν(C-C-N)$_{pz}$].

IR (toluene): $\tilde{\nu}$ (cm^{-1}) = 1913 (s) and 1838 (vs) [ν(CO)], 1545 (w) [ν(C-C-N)$_{pz}$].

ATR-IR (solid): $\tilde{\nu}$ (cm^{-1}) = 2957(w), 2905 (vw), 2865 (vw), 2538 (vw) [ν(BH)], 1901 (s) [ν(CO)], 1826 (vs) [ν(CO)], 1601 (vw), 1542 (m) [ν(C-C-N)$_{pz}$], 1477 (vw), 1447 (m), 1413 (m), 1373 (m), 1361 (m), 1265 (vw), 1253 (w), 1240 (vw), 1205 (m), 1197 (m), 1177 (m), 1143 (vw), 1103 (m), 1072 (w), 1062 (w), 1045 (w), 981 (vw), 910 (vw), 885 (w), 850 (s), 833 (m), 817 (w, sh), 787 (m), 771 (m), 742 (m), 695 (m), 643 (m), 629 (w), 597 (w), 575 (w), 550 (w), 519 (w), 481 (m), 458 (m).

^{1}H NMR: (300.1 MHz, C_6D_6, 298 K): δ (ppm) = 0.52 (s, 9H, Si*Me*$_3$), 1.26 (s, 9H, C^4-C(C*H*$_3$)$_3$, Mes*), 1.69 (s, 18H, C^{2,6}-C(C*H*$_3$)$_3$, Mes*), 2.06, 2.77 (s each, 3H, C$^{3/5}$-*Me*, pz$_B$), 2.12, 2.49 (s each, 6H, 2 × C$^{3/5}$-*Me*, pz$_A$), 5.39 (s, 1H, C^4-*H*, pz$_B$), 5.59 (s, 2H, 2 × C^4-*H*, pz$_A$), 7.55 (s, 2H, C^{3,5}-*H*, Mes*).

^{1}H NMR: (300.1 MHz, THF-d_8, 298 K): δ (ppm) = 0.42 (s, 9H, Si*Me*$_3$), 1.32 (s, 9H, C^4-C(C*H*$_3$)$_3$, Mes*), 1.69 (s, 18H, C^{2,6}-C(C*H*$_3$)$_3$, Mes*), 2.33 (s, 6H, 2 × C^3-*Me*, pz$_A$), 2.34 (s, 3H, C^5-*Me*, pz$_B$), 2.36 (s, 6H, 2 × C^5-*Me*, pz$_A$), 2.54 (s, 3H, C^3-*Me*, pz$_B$), 4.7 (br, $\Delta\nu_{1/2}$ = ~ 220 Hz, 1H, B*H*); this signal is visible as a very broad hump over the base line in a strongly enlarged version of the spectrum), 5.77 (s, 2H, 2 × C^4-*H*, pz$_A$), 5.79 (s, 1H, C^4-*H*, pz$_B$), 7.51 (s, 2H, C^{3,5}-*H*, Mes*).

^{13}C{^{1}H} NMR: (75.47 MHz, THF-d_8, 298 K): δ (ppm) = 4.04 (s, 3C, Si*Me*$_3$), 12.7 (s, 2C, 2 × C^5-*Me*, pz$_A$), 12.9 (s, 1C, C^5-*Me*, pz$_B$), 15.4 (s, 1C, C^3-*Me*, pz$_B$), 18.2 (s, 2C, 2 × C^3-*Me*, pz$_A$), 31.6 (s, 3C, C^4-C(*C*H$_3$)$_3$, Mes*), 35.2 (s, 1C, C^4-*C*(CH$_3$)$_3$, Mes*), 36.4 (s, 6C, C^{2,6}-C(*C*H$_3$)$_3$, Mes*), 38.9 (s, 2C, C^{2,6}-*C*(CH$_3$)$_3$, Mes*), 106.6 (s,

2C, 2 × C^4-H, pz_A), 107.4 (s, 1C, C^4-H, pz_B), 126.2 (s, 2C, $C^{3,5}$, Mes*), 138.0 (s, 1C, C^1, Mes*), 144.6 (s, 2C, 2 × C^5-Me, pz_A), 144.8 (s, 1C, C^5-Me, pz_B), 147.0 (s, 1C, C^4, Mes*), 148.6 (s, 2C, $C^{2,6}$, Mes*), 151.0 (s, 2C, 2 × C^3-Me, pz_A), 153.6 (s, 1C, C^3-Me, pz_B), 228.0 (s, 2C, 2 × *C*O).

$^{29}Si\{^1H\}$ NMR: (59.63 MHz, THF-d_8, 298 K): δ (ppm) = 9.64 (s, ^1J(Si,C) = 58 Hz, *Si*Me_3).

4.5.19 [Tp'(CO)$_2$W≡Ge{N(TMS)Mes*}] (11-W)

To a suspension of **3-W** (250 mg, 0.39 mmol) in 30 mL of toluene, a clear solution of GeCl{N(TMS)Mes*} (173 mg, 0.39 mmol, 1 equiv.) in 10 mL of toluene was dropwisely added at ambient temperature and stirred for 1 hour. Immediate after addition the color of the suspension started to change from yellow to yellowish orange and finally reddish orange. An IR spectrum of an aliquot of the suspension after 5 minutes revealed complete consumption of the starting material and formation of the desired product along with very small amount of **2-W** radical. The reddish orange suspension was treated with 10 mL of petrol-ether and then filtered into another schlenck tube. The filtrate was evaporated to dryness under reduced pressure and the slightly sticky residue was pulverized by a freeze-pump-thaw cycle. The orange powder was washed with 20 mL of *n*-hexane and then the solid was dried under reduced pressure for 3 hours at ambient temperature. Yield: 183 mg (0.19 mmol, 49 %).

Properties: Complex **11-W** is very good soluble in THF, fluorobenzene, moderately soluble in toluene and Et_2O and sparingly soluble in aliphatic solvents.

Melting Points: The orange solid decomposes to a brown solid at 280 –282 °C

Elemental analysis: calcd (%) for $C_{38}H_{60}BN_7O_2GeSiW$ (942.27 g/mol): C 48.44, H 6.42, N 10.41; found: C 49.37, H 6.50, N 10.47%.

Spectroscopic Data:

IR (THF): $\tilde{\nu}$ (cm^{-1}) = 1902 (s) and 1824 (vs) [ν(CO)], 1545 (w) [ν(C-C-N)$_{pz}$].

IR (toluene): $\tilde{\nu}$ (cm^{-1}) = 1902 (s) and 1824 (vs) [ν(CO)], 1545 (w) [ν(C-C-N)$_{pz}$].

ATR-IR (solid): $\tilde{\nu}$ (cm^{-1}) = 2959(w), 2935 (sh), 2924 (sh), 2908 (vw), 2868 (vw), 2549 (vw) [ν(BH)], 1889 (s) [ν(CO)], 1812 (vs) [ν(CO)], 1600 (vw), 1543 (m) [ν(C-C-N)$_{pz}$], 1477 (vw), 1447 (m), 1413 (m), 1389 (w), 1372 (m), 1362 (w), 1285

(vw), 1266 (vw), 1253 (w), 1242 (vw), 1208 (m), 1197 (m), 1178 (m), 1144 (vw), 1105 (m), 1071 (w), 1063 (w), 1047 (w), 983 (vw), 950 (vw), 936 (vw), 911 (vw), 885 (w), 853 (s), 834 (m), 819 (w, sh), 789 (m), 772 (m), 744 (m), 730 (w), 695 (m), 677 (vw), 655 (vw), 643 (m), 626 (vw), 596 (vw), 573 (w), 549 (vw), 527 (vw), 484 (m), 463 (m), 418 (vw), 401 (vw).

^{1}H NMR: (300.1 MHz, C_6D_6, 298 K): δ (ppm) = 0.53 (s, 9H, Si*Me*$_3$), 1.26 (s, 9H, C^4-C(C*H*$_3$)$_3$, Mes*), 1.72 (s, 18H, C^{2,6}-C(C*H*$_3$)$_3$, Mes*), 2.00, 2.82 (s each, 3H, C$^{3/5}$-*Me*, pz$_B$), 2.07, 2.53 (s each, 6H, 2 × C$^{3/5}$-*Me*, pz$_A$), 5.33 (s, 1H, C^4-*H*, pz$_B$), 5.57 (s, 2H, 2 × C^4-*H*, pz$_A$), 7.56 (s, 2H, C^{3,5}-*H*, Mes*).

^{1}H NMR: (300.1 MHz, THF-d_8, 298 K): δ (ppm) = 0.41 (s, 9H, Si*Me*$_3$), 1.32 (s, 9H, C^4-C(C*H*$_3$)$_3$, Mes*), 1.68 (s, 18H, C^{2,6}-C(C*H*$_3$)$_3$, Mes*), 2.33 (s, 3H, C^5-*Me*, pz$_B$), 2.34 (s, 6H, 2 × C^3-*Me*, pz$_A$), 2.36 (s, 6H, 2 × C^5-*Me*, pz$_A$), 2.58 (s, 3H, C^3-*Me*, pz$_B$), 4.7 (br, $\Delta\nu_{1/2}$ = ~ 200 Hz, 1H, B*H*); this signal is visible as a very broad hump over the base line in a strongly enlarged version of the spectrum), 5.82 (s, 3H, 3 × C^4-*H*, (pz$_A$ + pz$_B$), 7.50 (s, 2H, C^{3,5}-*H*, Mes*).

^{13}C{^{1}H} NMR: (75.47 MHz, THF-d_8, 298 K): δ (ppm) = 3.86 (s, 3C, Si*Me*$_3$), 12.6 (s, 2C, 2 × C^5-*Me*, pz$_A$), 12.7 (s, 1C, C^5-*Me*, pz$_B$), 15.9 (s, 1C, C^3-*Me*, pz$_B$), 19.5 (s, 2C, 2 × C^3-*Me*, pz$_A$), 31.6 (s, 3C, C^4-C(*C*H$_3$)$_3$, Mes*), 35.2 (s, 1C, C^4-*C*(CH$_3$)$_3$, Mes*), 36.3 (s, 6C, C^{2,6}-C(*C*H$_3$)$_3$, Mes*), 38.9 (s, 2C, C^{2,6}-*C*(CH$_3$)$_3$, Mes*), 106.8 (s, 2C, 2 × *C*^{4}-H, pz$_A$), 107.6 (s, 1C, *C*^{4}-H, pz$_B$), 126.2 (s, 2C, *C*^{3,5}, Mes*), 138.5 (s, 1C, *C*^{1}, Mes*), 144.6 (s, 2C, 2 × *C*^{5}-Me, pz$_A$), 144.7 (s, 1C, *C*^{5}-Me, pz$_B$), 146.9 (s, 1C, *C*^{4}, Mes*), 148.6 (s, 2C, *C*^{2,6}, Mes*), 151.7 (s, 2C, 2 × *C*^{3}-Me, pz$_A$), 154.4 (s, 1C, *C*^{3}-Me, pz$_B$), 221.6 (s, 2C, 2 × *C*O).

^{29}Si{^{1}H} NMR: (59.63 MHz, THF-d_8, 298 K): δ (ppm) = 8.54 (s, *Si*Me$_3$).

4.5.20 [Tp(CO)$_2$Mo≡Ge(C$_6$H$_3$-2,6-Mes$_2$)] (12-Mo)

A mixture of K[TpMo(CO)$_3$]·0.8 THF (100 mg, 0.23 mmol) and (GeCl(C$_6$H$_3$-2,6-Mes$_2$))$_2$ (95 mg, 0.11 mmol) was treated with 10 mL of toluene at ambient temperature. The orange suspension was heated to 110 °C for 4 hours, upon which the color of the suspension changed to brown. The progress of the reaction was monitored by IR spectroscopy, which revealed a

complete and selective conversion of the starting material into the product. After completion of the reaction, the brown suspension was concentrated to ~5 mL under reduce pressure and then was treated with 5 mL of *n*-pentane. The resulting suspension was filtered into another schlenck tube. The brown filtrate was evaporated to dryness, pulverized once by a freeze-pump-thaw cycle and washed with 2 mL of *n*-pentane at ambient temperature. Analytically pure compound was obtained upon crystallization from 2:1 Et_2O/*n*-hexane mixture at –60 °C. Yield: 124 mg (0.17 mmol, 73%).

Properties: Complex **12-Mo** is very good soluble in THF, toluene, Et_2O and moderately soluble in aliphatic solvent.

Melting Points: Above 185 °C the brown solid slowly turns dark brown and at 233 – 235 °C melts to a dark brown liquid. Melting was further confirmed by IR spectroscopy.

Elemental analysis: calcd (%) for $C_{35}H_{35}BGeMoN_6O_2$ (751.05 g/mol): C 55.97, H 4.70, N 11.19; found: C 56.40, H 5.33, N 10.57%.

Spectroscopic Data:

IR (THF): $\tilde{\nu}$ (cm^{-1}) = 1930 (s) and 1857 (vs) [ν(CO)].

IR (toluene): $\tilde{\nu}$ (cm^{-1}) = 1931 (s) and 1858 (vs) [ν(CO)].

IR (*n*-hexane): $\tilde{\nu}$ (cm^{-1}) = 1937(s) and 1867 (vs) [ν(CO)].

ATR-IR (solid): $\tilde{\nu}$ (cm^{-1}) = 3145 (vw), 3118 (vw), 2953 (vw), 2919 (w), 2869 (vw), 2855 (vw), 2732 (vw), 2475 (w) [ν(BH)], 1920 (s) [ν(CO)], 1842 (vs) [ν(CO)], 1609 (w), 1558 (vw), 1511 (vw), 1499 (w), 1465 (vw), 1446 (w), 1428 (vw), 1418 (vw), 1405 (m), 1394 (w), 1376 (w), 1306 (m), 1206 (m) 1174 (vw), 1158 (vw), 1114 (m), 1095 (w), 1072 (w), 1046 (s), 1010 (sh), 980 (w), 927 (vw), 878 (vw), 849 (w), 812 (vw), 804 (w), 787 (w), 774 (m), 755 (s), 743 (m), 727 (m), 714 (s), 662 (w), 620 (sh), 613 (w), 587 (vw), 566 (w), 545 (vw), 538 (vw), 502 (w), 463 (w), 451 (m), 427 (vw), 401 (vw).

^{1}H NMR: (300.1 MHz, C_6D_6, 298 K): δ (ppm) = 2.21 (s, 12H, 2 × $C^{2,6}$-*Me*, Mes), 2.30 (s, 6H, 2 × C^4-*Me*, Mes), 5.57 (t, ^3J(H,H) = 2.2 Hz, 1H, C^4-*H*, pz_B), 5.83 (t,

^{3}J(H,H) = 2.1 Hz, 2H, C^{4}-*H*, pz_A), 6.89 (d, ^{3}J(H,H) = 7.5 Hz, 2H, $C^{3,5}$- *H,* C_6H_3), 7.07 (s, 4H, $C^{3,5}$-*H*, Mes), 7.11 (t, ^{3}J(H,H) = 7.5 Hz, 1H, C^{4}-*H*, C_6H_3), 7.14 (d, signal overlaps with the signal of residual deuterated solvent; 1H, C^{5}-*H*, pz_B), 7.25 (dd, ^{3}J(H,H) = 2.3 Hz, ^{4}J(H,H) = 0.6 Hz, 2H, 2 × C^{5}-*H*, pz_A), 7.30 (d, ^{3}J(H,H) = 2.0 Hz, 2H, 2 × C^{3}-*H*, pz_A), 7.64 (d, ^{3}J(H,H) = 1.8 Hz, 1H, 1 × C^{3}-*H*, pz_B).

$^{13}C\{^{1}H\}$ NMR: (75.47 MHz, C_6D_6, 298 K): δ (ppm) = 21.23 (s, 2C, 2 × C^{4}-*Me*, Mes), 21.25 (s, 4C, 2 × $C^{2,6}$-*Me*, Mes), 104.9 (s, 2C, 2 × C^{4}-H, pz_A), 105.8 (s, 1C, C^{4}-H, pz_B), 128.2 (s, 2C, $C^{3,5}$, C_6H_3), 129.4 (s, 4C, 2 × $C^{3,5}$, Mes), 131.5 (s, 1C, C^{4}, C_6H_3),134.69 (s, 2C, 2 × C^{5}-H, pz_A), 134.73 (s, 1C, C^{5}-H, pz_B), 137.1 (s, 2C, 2 × C^{1}, Mes), 137.3 (s, 4C, 2 × $C^{2,6}$, Mes), 138.0 (s, 2C, 2 × C^{4}, Mes), 144.9 (s, 1C, C^{3}-H, pz_B), 145.3 (s, 2C, $C^{2,6}$, C_6H_3), 146.1 (s, 2C, 2 × C^{3}-H, pz_A), 164.3 (s, 1C, C^{1}, C_6H_3), 226.7 (s, 2C, 2 × *C*O).

4.5.21 [Tp'(CO)$_2$Mo≡Ge(C_6H_3-2,6-Trip$_2$)] (13-Mo)

A mixture of K[Tp'Mo(CO)$_3$]·2THF (200mg, 0.30 mmol) and GeCl(C_6H_3-2,6-Trip$_2$) (179 mg, 0.30 mmol) was treated with ~ 20 mL of toluene. The resulting yellow suspension was immersed in an ultrasonic bath for 7 minutes and then heated at 110 °C for 2 hours. The color of the suspension changed from yellow to yellowish brown and the progress of the reaction was followed by IR spectroscopy, which revealed ~98% consumption of the metalate (100% metalate did not consumed even after longer heating at 130 °C), with the selective formation of the product (1927 (s) and 1853 (vs) cm^{-1}). The solvent was removed under vaccum and the residue was pulverised once by a freeze-pump-thaw cycle and extracted with *n*-hexane (3 × 15 mL). The brown residue was discarded and the yellowish brown extract was evaporated to dryness and pulverised once by a freeze-pump-thaw cycle. The yellowish brown powder obtained was again dissolved in *n*-hexane (30 mL) and the *n*-hexane solution was concentrated to *ca*. 10 mL and stored at –60 °C for 24 hours. The yellowish brown precipitates that form upon cooling, was isolated by filtration at –60 °C and dried *in vacuo* at 60 °C for 3 hours. Yield: 216 mg (0.215 mmol, 71%).

Properties: Complex **13-Mo** is very good soluble in all common organic solvent.

Melting Points: The yellowish-brown solid slowly decomposes above 260 °C and changes color to dark reddish-brown, which then melt at 281 – 283 °C to a brown liquid.

Elemental analysis: calcd (%) for $C_{53}H_{71}BGeMoN_6O_2$ (1003.53 g/mol): C 63.43, H 7.13, N 8.37; found: C 63.08, H 6.86, N 8.33%.

Spectroscopic Data:

IR (THF): $\tilde{\nu}$ (cm^{-1}) = 1926 (s) and 1852 (vs) [ν(CO)], 1545 (w) [ν(C-C-N)$_{pz}$].

IR (toluene): $\tilde{\nu}$ (cm^{-1}) = 1927 (s) and 1853 (vs) [ν(CO)], 1545 (w) [ν(C-C-N)$_{pz}$].

IR (*n*-hexane): $\tilde{\nu}$ (cm^{-1}) = 1932 (s) and 1860 (vs) [ν(CO)], 1546 (w) [ν(C-C-N)$_{pz}$].

ATR-IR (solid): $\tilde{\nu}$ (cm^{-1}) = 3050 (vw), 2960 (m), 2925 (w), 2866 (w), 2528 (w) [ν(BH)], 1927 (vs) [ν(CO)], 1850 (vs) [ν(CO)], 1606 (w), 1567 (vw), 1544 (m) [ν(C-C-N)$_{pz}$], 1458 (w, sh), 1445 (m), 1431 (m), 1414 (m), 1382 (m), 1375 (m), 1362 (m), 1316 (w), 1238 (vw), 1205 (m), 1169 (w), 1145 (vw), 1130 (vw), 1100 (w), 1066 (m), 1045 (w), 980 (w), 941 (w), 922 (vw), 879 (w), 854 (w), 815 (w), 805 (m), 781 (m), 772 (m), 746 (w), 695 (m), 650 (m), 619 (w), 582 (vw), 566 (w), 536 (w), 512 (w), 477 (w), 460 (m), 450 (m).

^{1}H NMR: (300.1 MHz, C_6D_6, 298 K): δ (ppm) = 1.12 (d, ^3J(H,H) = 6.8 Hz, 12H, 2×C^{2,6}-CH*Me*$_A$Me$_B$, Trip), 1.34 (d, ^3J(H,H) = 7.0 Hz, 12H, 2×C^4-CH*Me*$_2$, Trip), 1.47 (d, ^3J(H,H) = 6.9 Hz, 12H, 2×C^{2,6}-CHMe$_A$*Me*$_B$, Trip), 1.99 (s, 3H, C^5-*Me*, pz$_B$), 2.06 (s, 6H, 2 × C^5-*Me*, pz$_A$), 2.18 (s, 6H, 2 × C^3-*Me*, pz$_A$), 2.55 (s, 3H, C^3-*Me*, pz$_B$), 2.90 (sept, ^3J(H,H) = 6.9 Hz, 2H, 2×C^4-C*H*Me$_2$, Trip), 3.21 (sept, ^3J(H,H) = 6.8 Hz, 4H, 2×C^{2,6}-C*H*Me$_A$Me$_B$), 4.6 (br, $\Delta\nu_{1/2}$ = ~ 220 Hz, 1H, B*H*); this signal is visible as a very broad hump over the base line in a strongly enlarged version of the spectrum), 5.30 (s, 1H, C^4-*H*, pz$_B$), 5.61 (s, 2H, 2 × C^4-*H*, pz$_A$), 7.02-7.13 (m, 3H, C^{3,5}-*H* and C^4-*H*, C_6H_3], 7.23 [s, 4H, 2×C^{3,5}-*H*, Trip].

^{13}C{^{1}H} NMR: (75.47 MHz, C_6D_6, 298 K): δ (ppm) = 12.6 (s, 1C, C^5-*Me*, pz$_B$), 12.7 (s, 2C, 2 × C^5-*Me*, pz$_A$), 15.2 (s, 1C, C^3-*Me*, pz$_B$), 18.6 (s, 2C, 2 × C^3-*Me*, pz$_A$), 23.6 (s, 4C, 2×C^{2,6}-CHMe$_A$*Me*$_B$, Trip), 24.3 (s, 4C, 2×C^4-CH*Me*$_2$, Trip), 31.5 (s, 4C, 2×C^{2,6}-*C*HMe$_A$Me$_B$, Trip), 35.0 (s, 2C, 2×C^4-*C*HMe$_2$, Trip), 106.0 (s, 2C, 2 × *C*^{4}-H, pz$_A$), 107.2 (s, 1C, *C*^{4}-H, pz$_B$), 122.1 (s, 4C, 2×*C*^{3,5}, Trip), 129.0 (s, 1C, *C*^{4},

C_6H_3), 131.2 (s, 2C, $C^{3,5}$, C_6H_3), 136.0 (s, 2C, 2×C^1, Trip), 143.6 (s, 2C, 2 × C^5-Me, pz_A), 143.7 (s, 1C, C^5-Me, pz_B), 144.0 (s, 2C, $C^{2,6}$, C_6H_3), 147.4 (s, 4C, 2×$C^{2,6}$, Trip), 149.5 (s, 2C, 2×C^4, Trip), 150.3 (s, 2C, 2 × C^3-Me, pz_A), 153.0 (s, 1C, C^3-Me, pz_B), 166.9 (s, 1C, C^1, C_6H_3), 228.9 (s, 2C, 2 × CO).

4.5.22 [Tp'(CO)$_2$Mo≡GeMes*] (14-Mo)

A colorless solution of Mes*Li·2THF (300 mg, 0.76 mmol) in 5 mL of THF was slowly added to a colorless solution of $GeCl_2$·1,4-dioxane (175 mg, 0.76 mmol) in 5 mL of THF at −78 °C. Upon addition the color of the solution immediately changed to orange. After stirring for 45 minutes at −78 °C, a yellow solution of **3-Mo** (415 mg, 0.76 mmol, 1 equiv.) in 15 mL of THF was added into it. Immediate after addition the color of the solution changed to brown. The brown solution was slowly brought to room temperature and an aliquot of the solution was checked by IR spectroscopy, which revealed complete consumption of the starting material and almost selective formation of the desired product. All volatiles were removed and the sticky residue was pulverized by freeze-pump-thaw cycle. The brown solid was extracted with 2:1 *n*-hexane/Et_2O mixture (2 × 15 mL) at ambient temperature and the brown extracts were concentrated to ~ 8 mL. The resulting suspension was stored at −60 °C for 15 minutes, upon which a brown solid precipitated out, which was isolated by filtration of the supernatant at −60 °C. The brown solid obtained was re-extracted with 2:1 *n*-hexane/Et_2O mixture (2 × 20 mL) at ambient temperature and the combine extract was concentrated to ~ 15 mL, upon which a brown solid precipitated out. The precipitate was isolated by filtration of the light brown supernatant and dried for 2 hours at ambient temperature and 2 hours at 60 °C. Yield: 199 mg (0.26 mmol, 34 %).

Properties: Complex **14-Mo** is very good soluble in toluene, THF and moderately soluble in aliphatic solvent.

Melting Points: The compound exhibit very high thermal stability and decomposes upon melting at 253 – 256 °C to give dark brown liquid.

Elemental analysis: calcd (%) for $C_{35}H_{51}BGeMoN_6O_2$ (767.18 g/mol): C 54.79, H 6.70, N 10.95; found: C 53.89, H 6.79, N 11.14%.

Spectroscopic Data:

IR (THF): $\tilde{\nu}$ (cm^{-1}) = 1913 (s) and 1837 (vs) [ν(CO)], 1544 (w) [ν(C-C-N)$_{pz}$].

IR (toluene): $\tilde{\nu}$ (cm^{-1}) = 1913 (s) and 1838 (vs) [ν(CO)], 1544 (w) [$\nu(C\text{-}C\text{-}N)_{pz}$].

IR (*n*-pentane): $\tilde{\nu}$ (cm^{-1}) = 1922 (s) and 1849 (vs) [ν(CO)], 1544 (w) [$\nu(C\text{-}C\text{-}N)_{pz}$].

ATR-IR (solid): $\tilde{\nu}$ (cm^{-1}) = 3016 (vw), 2990 (vw), 2959 (w), 2929 (vw), 2907 (vw), 2868 (vw), 2547 (vw) [ν(BH)], 2528 (vw) [ν(BH)], 1908 (s) [ν(CO)], 1830 (vs) [ν(CO)], 1593 (w), 1542 (m) [$\nu(C\text{-}C\text{-}N)_{pz}$], 1476 (vw), 1445 (m), 1411 (m), 1381 (sh), 1374 (m), 1365 (sh), 1348 (sh), 1305 (vw), 1281 (vw), 1243 (w), 1204 (m), 1194 (w), 1143 (w), 1128 (w), 1066 (m), 1044 (w), 1028 (w), 982 (w), 950 (vw), 939 (vw), 927 (vw), 906 (vw), 879 (w), 853 (w), 814 (w), 809 (w), 799 (w), 775 (w), 767 (m), 744 (vw), 722 (vw), 693 (w), 663 (vw), 652 (w), 642 (w), 623 (vw), 595 (vw), 580 (w), 569 (vw), 534 (vw), 518 (w), 496 (vw), 477 (w), 463 (m), 452 (w), 429 (vw), 413 (vw).

^{1}H NMR: (300.1 MHz, C_6D_6, 298 K): δ (ppm) = 1.22 (s, 9H, C^4-C(CH_3)$_3$, Mes*), 1.72 (s, 18H, $C^{2,6}$-C(CH_3)$_3$, Mes*), 2.09 (s, 3H, C^5-*Me*, pz_B), 2.23 (s, 6H, 2 × C^5-*Me*, pz_A), 2.58 (s, 6H, 2 × C^3-*Me*, pz_A), 2.78 (s, 3H, C^3-*Me*, pz_B), 4.8 (br, $\Delta\nu_{1/2}$ = ~ 220 Hz, 1H, B*H*); this signal is visible as a very broad hump over the base line in a strongly enlarged version of the spectrum), 5.38 (s, 1H, C^4-*H*, pz_B), 5.68 (s, 2H, 2 × C^4-*H*, pz_A), 7.47 (s, 2H, $C^{3,5}$-*H*, Mes*).

^{13}C{^{1}H} NMR: (75.47 MHz, C_6D_6, 298 K): δ (ppm) = 12.7 (s, 1C, C^5-*Me*, pz_B), 12.9 (s, 2C, 2 × C^5-*Me*, pz_A), 15.3 (s, 1C, C^3-*Me*, pz_B), 17.8 (s, 2C, 2 × C^3-*Me*, pz_A), 31.2 (s, 3C, C^4-C(CH_3)$_3$, Mes*), 35.2 (s, 6C, $C^{2,6}$-C(CH_3)$_3$, Mes*), 35.5 (s, 1C, C^4-*C*(CH_3)$_3$, Mes*), 37.9 (s, 2C, $C^{2,6}$-*C*(CH_3)$_3$, Mes*), 106.7 (s, 2C, 2 × *C*^{4}-H, pz_A), 106.9 (s, 1C, *C*^{4}-H, pz_B), 121.2 (s, 2C, *C*^{3,5}, Mes*), 143.9 (s, 2C, 2 × *C*^{5}-Me, pz_A), 144.1 (s, 1C, *C*^{5}-Me, pz_B), 151.1 (s, 2C, 2 × *C*^{3}-Me, pz_A), 152.3 (s, 1C, *C*^{4}, Mes*), 152.7 (s, 1C, *C*^{3}-Me, pz_B), 157.6 (s, 2C, *C*^{2,6}, Mes*), 161.0 (s, 1C, *C*^{1}, Mes*), 230.7 (s, 2C, 2 × *C*O).

4.5.23 [Tp'(CO)$_2$Mo≡GeEind] (15-Mo)

To a yellow suspension of **3-Mo** (150 mg, 0.27 mmol) in 8 mL of benzene, a yellow solution of (*E*)-Eind(Cl)Ge=Ge(Cl)Eind (134 mg, 0.14 mmol, 0.5 equiv.) in 4 mL of benzene was slowly added at ambient temperature. Immediate after addition the color of the suspension changed from yellow to red-brown. An IR spectrum after 10 minutes of an aliquot of the brown suspension

indicates the formation of the germylidyne complex along with a small amount of **2-Mo** radical. After stirring for 15 minutes the suspension was treated with 4 mL of *n*-pentane and filtered into another schlenck tube. The red-brown filtrate was evaporated to dryness and the sticky solid was pulverized by a freeze-pump-thaw cycle. The red-brown powder was extracted with 10 mL of *n*-pentane at ambient temperature. The extract was concentrated to ~3 mL and stored at −60 °C for 48 hours. The microcrystalline precipitate that forms upon cooling was isolated by filtration of a light red-orange supernatant at −60 °C. The obtained red-brown solid was re-crystallized from *n*-pentane at −60 °C to obtain analytically pure solid in moderate yield. Yield: 131 mg (0.15 mmol, 53%).

Properties: Complex **15-Mo** is very good soluble in all common organic solvent.

Melting Points: The compound exhibit very high thermal stability and only melts to a red-brown liquid at 230 – 234 °C.

Elemental analysis: calcd (%) for $C_{45}H_{67}BGeMoN_6O_2$ (903.41 g/mol): C 59.83, H 7.48, N 9.30; found: C 59.56, H 7.17, N 9.36%.

Spectroscopic Data:

IR (THF): $\tilde{\nu}$ (cm^{-1}) = 1916 (s) and 1841 (vs) [ν(CO)], 1544 (w) [ν(C-C-N)$_{pz}$].

IR (toluene): $\tilde{\nu}$ (cm^{-1}) = 1916 (s) and 1842 (vs) [ν(CO)], 1544 (w) [ν(C-C-N)$_{pz}$].

IR (*n*-hexane): $\tilde{\nu}$ (cm^{-1}) = 1924 (s) and 1852 (vs) [ν(CO)], 1545 (w) [ν(C-C-N)$_{pz}$].

ATR-IR (solid): $\tilde{\nu}$ (cm^{-1}) = 2959 (m), 2932 (w), 2920 (w), 2874 (w), 2851 (vw), 2838 (vw), 2733 (vw), 2544 (sh) [ν(BH)], 2526 (vw) [ν(BH)], 1911 (s) [ν(CO)], 1835 (vs) [ν(CO)], 1578 (vw), 1542 (m) [ν(C-C-N)$_{pz}$], 1488 (vw), 1463 (sh), 1445 (m), 1413 (m), 1395 (w), 1374 (m), 1349 (sh), 1331 (w), 1306 (vw), 1290 (vw), 1277 (vw), 1260 (vw), 1247 (vw), 1206 (m), 1192 (m), 1157 (vw), 1147 (vw), 1125 (vw), 1116 (vw), 1065 (m), 1044 (w), 1032 (sh), 978 (w), 971 (w), 950 (w), 929 (vw), 919 (sh), 899 (sh), 889 (vw), 871 (vw), 853 (w), 815 (w), 809 (sh), 794 (m), 777 (m), 702 (sh), 693 (m), 667 (vw), 654 (sh), 644 (m), 622 (w), 593 (vw), 561 (w), 534 (vw), 526 (vw), 516 (w), 478 (w), 461 (m), 449 (m), 404 (vw).

^{1}H NMR: (300.1 MHz, C_6D_6, 298 K): δ (ppm) = 0.80 (t, ^{3}J(H,H) = 7.2 Hz 12H, $C^{1,7}$-(CH_2CH_3)$_2$), 0.93 (t, ^{3}J(H,H) = 7.2 Hz, 12H, $C^{3,5}$-(CH_2CH_3)$_2$), 1.54 (m, ^{3}J(H,H) = 7.2 Hz, 8H, $C^{1,7}$-($CH_AH_BCH_3$)$_2$), 1.64 (s, 4H, $C^{2,6}H_2$), 2.06 (s, 3H, C^{5}-*Me*, pz_B), 2.21 (s, 6H, 2 × C^{5}-*Me*, pz_A), 2.33 (m, ^{3}J(H,H) = 7.2 Hz, 8H, $C^{3,5}$-($CH_AH_BCH_3$)$_2$), 2.718 (s, 6H, 2 × C^{3}-*Me*, pz_A), 2.723 (s, 3H, C^{3}-*Me*, pz_B), 4.8 (br, $\Delta\nu_{1/2}$ = ~ 160 Hz, 1H, B*H*); this signal is visible as a very broad hump over the base line in a strongly enlarged version of the spectrum), 5.35 (s, 1H, C^{4}-*H*, pz_B), 5.70 (s, 2H, 2 × C^{4}-*H*, pz_A), 6.83 (s, 1H, C^{8}-*H*).

^{13}C{^{1}H} NMR: (75.47 MHz, C_6D_6, 298 K): δ (ppm) = 9.3 (s, 4C, $C^{1,7}$-(CH_2CH_3)$_2$), 10.1 (s, 4C, $C^{3,5}$-(CH_2CH_3)$_2$), 12.7 (s, 1C, C^{5}-*Me*, pz_B), 12.8 (s, 2C, 2 × C^{5}-*Me*, pz_A), 15.3 (s, 1C, C^{3}-*Me*, pz_B), 17.9 (s, 2C, 2 × C^{3}-*Me*, pz_A), 33.4 (s, 4C, $C^{1,7}$-(CH_2CH_3)$_2$), 38.3 (s, 4C, $C^{3,5}$-(CH_2CH_3)$_2$), 41.5 (s, 2C, $C^{2,6}H_2$), 49.5 (s, 2C, $C^{1,7}$), 52.8 (s, 2C, $C^{3,5}$), 106.5 (s, 2C, 2 × C^{4}-H, pz_A), 106.9 (s, 1C, C^{4}-H, pz_B), 122.5 (s, 1C, C^{8}-H), 143.9 (s, 2C, 2 × C^{5}-Me, pz_A), 144.2 (s, 1C, C^{5}-Me, pz_B), 149.2 (s, 2C, $C^{7a,8a}$), 151.2 (s, 2C, 2 × C^{3}-Me, pz_A), 152.6 (s, 1C, C^{3}-Me, pz_B), 154.6 (s, 2C, $C^{3a,4a}$), 160.2 (s, 1C, C^{4}-Ge), 230.5 (s, 2C, 2 × *C*O).

4.5.24 [Tp'(CO)$_2$Mo≡Sn{N(TMS)Mes*}] (16-Mo)

A mixture of **3-Mo** (100 mg, 0.18 mmol) and SnCl{N(TMS)Mes*} (89 mg, 0.18 mmol, 1 equiv.) was treated with 10 mL of benzene at ambient temperature under complete exclusion of light using brown glass schlenck tube. Immediately after addition the color of the suspension changed to brown. An IR spectrum after 5 minutes of an aliquot of the reaction mixture revealed the formation of amino-stannylidyne complex along with a small amount of **2-Mo** radical. The brown suspension was treated with 4 mL of *n*-pentane and then filtered into another brown glass schlenck tube. The filtrate was evaporated to dryness under reduce pressure and the residue was treated to with 4 mL of Et_2O and stored at −60 °C. A black solid, which precipitated out, was separated by filtration. The filtrate was treated with 2 mL of *n*-hexane, then concentrated to ~4 mL and stored at −30 °C for 18 hours. Brown microcrystalline precipitate was isolated by filtration at −30 °C and dried shortly under reduced pressure. Yield: 27 mg (0.03 mmol, 16%). Extremely high light sensitivity leads to the rapid decomposion during work up which results to a very low isolated yield.

Properties: Complex **16-Mo** is very good soluble in THF, fluorobenzene, moderately soluble in toluene and Et_2O and sparingly soluble in aliphatic solvents.

Spectroscopic Data:

IR (THF): $\tilde{\nu}$ (cm^{-1}) = 1893 (s) and 1828 (vs) [ν(CO)], 1546 (w) [ν(C-C-N)$_{pz}$].

IR (benzene): $\tilde{\nu}$ (cm^{-1}) = 1892 (s) and 1824 (vs) [ν(CO)], 1545 (w) [ν(C-C-N)$_{pz}$].

ATR-IR (solid): $\tilde{\nu}$ (cm^{-1}) = 2949 (w), 2910 (w), 2865 (w), 2548 (vw) [ν(BH)], 2530 (vw) [ν(BH)], 1884 (s) [ν(CO)], 1814 (vs) [ν(CO)], 1601(vw), 1544 (w) [ν(C-C-N)$_{pz}$], 1489 (vw), 1446 (m), 1411 (m), 1391 (w), 1381 (m), 1372 (m), 1360 (m), 1351 (sh), 1266 (vw), 1254 (m), 1217 (sh), 1208 (sh), 1200 (m), 1184 (m), 1147 (w), 1108 (w), 1065 (w), 1045 (w), 983 (vw), 952 (vw), 926 (sh), 913 (vw), 879 (m), 846 (sh), 833 (m), 814 (m), 799 (m), 787 (w), 774 (m), 756 (w), 693 (m), 677 (m), 644 (m), 628 (w), 595 (vw), 587 (vw), 557 (vw), 545 (vw), 516 (w), 485 (vw), 468 (sh), 454 (m), 434 (sh), 407 (vw).

^{1}H NMR: (300.1 MHz, C_6D_6, 298 K): δ (ppm) = 0.59 (s, 9H, Si*Me*$_3$), 1.30 (s, 9H, C^4-C(C*H*$_3$)$_3$, Mes*), 1.76 (s, 18H, C^{2,6}-C(C*H*$_3$)$_3$, Mes*), 2.08 (s, 3H, C^5-*Me*, pz$_B$), 2.17 (s, 6H, 2 × C^5-*Me*, pz$_A$), 2.47 (s, 6H, 2 × C^3-*Me*, pz$_A$), 2.72 (s, 3H, C^3-*Me*, pz$_B$), 4.7 (br, $\Delta\nu_{1/2}$ = ~ 220 Hz, 1H, B*H*); this signal is visible as a very broad hump over the base line in a strongly enlarged version of the spectrum), 5.40 (s, 1H, C^4-*H*, pz$_B$), 5.61 (s, 2H, 2 × C^4-*H*, pz$_A$), 7.60 (s, 2H, C^{3,5}-*H*, Mes*).

^{13}C{^{1}H} NMR: (75.47 MHz, C_6D_6, 298 K): δ (ppm) = 4.61 (s, 3C, Si*Me*$_3$), 12.6 (s, 2C, 2 × C^5-*Me*, pz$_A$), 13.0 (s, 1C, C^5-*Me*, pz$_B$), 15.5 (s, 1C, C^3-*Me*, pz$_B$), 18.1 (s, 2C, 2 × C^3-*Me*, pz$_A$), 31.6 (s, 3C, C^4-C(*C*H$_3$)$_3$, Mes*), 34.6 (s, 1C, C^4-*C*(CH$_3$)$_3$, Mes*), 36.0 (s, 6C, C^{2,6}-C(*C*H$_3$)$_3$, Mes*), 38.2 (s, 2C, C^{2,6}-*C*(CH$_3$)$_3$, Mes*), 106.7 (s, 2C, 2 × *C*^{4}-H, pz$_A$), 107.5 (s, 1C, *C*^{4}-H, pz$_B$), 125.0 (s, 2C, *C*^{3,5}, Mes*), 141.8 (s, 1C, *C*^{1}, Mes*), 144.0 (s, 2C, 2 × *C*^{5}-Me, pz$_A$), 144.4 (s, 1C, *C*^{5}-Me, pz$_B$), 145.5 (s, 1C, *C*^{4}, Mes*), 148.1 (s, 2C, *C*^{2,6}, Mes*), 150.7 (s, 2C, 2 × *C*^{3}-Me, pz$_A$), 154.2 (s, 1C, *C*^{3}-Me, pz$_B$), 227.3 (s, 2C, 2 × *C*O).

^{29}Si{^{1}H} NMR: (59.63 MHz, THF-d_8, 298 K): δ (ppm) = 6.95 (s, *Si*Me$_3$).

4.5.25 [Tp'(CO)$_2$Mo≡Pb(C$_6$H$_3$-2,6-Trip$_2$)] (17-Mo)

A yellow solution of PbBr(C$_6$H$_3$-2,6-Trip$_2$) (241 mg, 0.313 mmol) in 4 mL of THF was added drop wise via a syringe to a stirred solution of **3-Mo**·DME (200 mg, 0.313 mmol) in 16 mL of THF in a brown glass Schlenk tube at room temperature. The color of the solution changed immediately from yellowish brown to green. After 5 minutes an IR spectrum of the solution was recorded, which revealed that **3-Mo** was consumed to give the plumbylidyne complex **17-Mo** (ν(CO) = 1896 and 1827 cm^{-1}) and another dicarbonyl complex (ν(CO) = 1910 and 1808 cm^{-1}), which is suggested to be the metalloplumbylene [Tp'(CO)$_2$(PMe$_3$)Mo–Pb(C$_6$H$_3$-2,6-Trip$_2$)]. The radical **2-Mo** was also formed to a minor extent as evidenced by its characteristic ν(CO) band at 1756 cm^{-1} (the second ν(CO) band of **2-Mo** was obscured by the ν(CO) band of **17-Mo** at 1896 cm^{-1}). Stirring was continued under exclusion of day light. Monitoring of the reaction by IR spectroscopy revealed a gradual increase in the intensity of the ν(CO) bands of the product **17-Mo** at the expense of those of the intermediate [Tp'(CO)$_2$(PMe$_3$)Mo–Pb(C$_6$H$_3$-2,6-Trip$_2$)]. After 3,5 hours of stirring the reaction was completed, and the reaction mixture was evaporated to dryness *in vacuo*. The obtained oily residue was pulverised by a freeze-pump-thaw cycle. The green solid was extracted with *n*-pentane (2 × 20 mL) and the extract was evaporated to dryness *in vacuo*. The obtained solid was dissolved in 15 mL of Et$_2$O, the solution was concentrated *in vacuo* to *ca*. 10 mL and stored at –60 °C for 48 hours. A green microcrystalline precipitate was formed, which was isolated by filtration at –60 °C and dried under vaccum for 4.5 hours at ambient temperature to afford complex **17-Mo** as a green solid, which was shown by NMR spectroscopy to be contaminated with 5% of C$_6$H$_3$-1,3-Trip$_2$. Yield: 87 mg (0.076 mmol, 24 %).

Complex **17-Mo** is extremely light sensitive especially in solution. This prevented the isolation of complex **17-Mo** in analytically pure form, despite vigorous protection from daylight during work-up and isolation. In fact, upon exposure of a green solution of **17-Mo** in C$_6$D$_6$ to daylight, a rapid decomposition of **17-Mo** was observed leading to precipitation of a black solid (presumbly elementary lead) and discoloration of the solution to pale yellow. An ^{1}H NMR spectrum of the pale yellow solution showed that C$_6$H$_4$-1,3-Trip$_2$ had formed upon decomposition.

Properties: Complex **17-Mo** is very good soluble in THF, Et$_2$O, toluene and moderately soluble in aliphatic solvent.

Spectroscopic Data:

IR (THF): $\tilde{\nu}$ (cm^{-1}) = 1896 (s) and 1827 (vs) [ν(CO)], 1545 (w) [ν(C-C-N)$_{pz}$].

IR (toluene): $\tilde{\nu}$ (cm^{-1}) = 1898 (s) and 1828 (vs) [ν(CO)], 1545 (w) [ν(C-C-N)$_{pz}$].

^{1}H NMR: (300.1 MHz, C_6D_6, 298 K): δ (ppm) = 1.14 (d, ^3J(H,H) = 6.9 Hz, 12H, 2 × $C^{2,6}$-CH*Me*$_A$Me$_B$, Trip), 1.35 (d, ^3J(H,H) = 6.9 Hz, 12H, 2 × C^4-CH*Me*$_2$, Trip), 1.50 (d, ^3J(H,H) = 6.9 Hz, 12H, 2 × $C^{2,6}$-CHMe$_A$*Me*$_B$, Trip), 2.04 (s, 3H, C^3-*Me* or C^5-*Me*, pz$_B$), 2.10 (s, 6H, 2 × C^3-*Me* or 2 × C^5-*Me*, pz$_A$), 2.15 (s, 6H, 2 × C^3-*Me* or 2 × C^5-*Me*, pz$_A$), 2.67 (s, 3H, C^3-*Me* or C^5-*Me*, pz$_B$), 2.91 (sept, ^3J(H,H) = 6.9 Hz, 2H, 2 × C^4-C*H*Me$_2$, Trip), 3.19 (sept, ^3J(H,H) = 6.9 Hz, 4H, 2 × $C^{2,6}$-C*H*Me$_A$Me$_B$), 4.6 (br, 1H, B*H*; this signal is visible as a very broad hump over the base line in an strongly enlarged version of the spectrum), 5.23 (s, 1H, C^4-*H*, pz$_B$), 5.66 (s, 2H, 2 × C^4-*H*, pz$_A$), 7.25 (t, ^3J(H,H) = 7.5 Hz, 1H, C^4-*H*, C_6H_3), 7.27 (s, 4H, 2 × $C^{3,5}$-*H*, Trip), 7.84 (d, ^3J(H,H) = 7.5 Hz, 2H, $C^{3,5}$-*H*, C_6H_3).

^{13}C{^{1}H} NMR: (75.47 MHz, C_6D_6, 298 K): δ (ppm) = 12.5 (s, 2C, 2 × C^3-*Me* or 2 × C^5-*Me*, pz$_A$), 12.8 (s, 1C, C^3-*Me* or C^5-*Me*, pz$_B$), 15.0 (s, 1C, C^3-*Me* or C^5-*Me*, pz$_B$), 17.6 (s, 2C, 2 × C^3-*Me* or 2 × C^5-*Me*, pz$_A$), 24.1 (s, 4C, 2 × $C^{2,6}$-CHMe$_A$*Me*$_B$, Trip), 24.2 (s, 4C, 2 × C^4-CH*Me*$_2$, Trip), 25.5 (s, 4C, 2 × $C^{2,6}$-CH*Me*$_A$Me$_B$, Trip), 31.2 (s, 4C, 2 × $C^{2,6}$-*C*HMe$_A$Me$_B$, Trip), 34.9 (s, 2C, 2 × C^4-*C*HMe$_2$, Trip), 106.3 (s, 2C, 2 × C^4-H, pz$_A$), 107.0 (s, 1C, 1 × C^4-H, pz$_B$), 122.5 (s, 4C, 2 × $C^{3,5}$-H, Trip), 126.5 (s, 1C, C^4-H, C_6H_3), 137.3 (s, 2C, $C^{3,5}$-H, C_6H_3), 137.5 (s, 2C, 2 × C^1, Trip), 143.8 (s, 2C, 2 × C^3-Me or 2 × C^5-Me, pz$_A$), 144.1 (s, 2C, $C^{2,6}$, C_6H_3), 144.8 (s, 1C, C^3-Me or C^5-Me, pz$_B$), 147.0 (s, 4C, 2 × $C^{2,6}$-CHMe$_A$Me$_B$, Trip), 149.3 (s, 2C, 2 × C^4-CHMe$_2$, Trip), 151.1 (s, 2C, 2 × C^3-Me or 2 × C^5-Me, pz$_A$), 154.2 (s, 1C, C^3-Me or C^5-Me, pz$_B$), 224.7 (s, 2C, 2 × *C*O), 272.5 (s, 1C, Pb-C^1, C_6H_3).

4.5.26 K(THF)$_3$[Tp'(CO)$_2$MoGe(C$_6$H$_3$-2,6-Mes$_2$)] (18-Mo)

To a mixture of **8-Mo** (500 mg, 0.60 mmol) and KC_8 (81 mg, 0.60 mmol, 1 equiv.) ~15 mL of THF was condensed from a schlenck tube containing THF over KC_8 using liq. N_2 cooling bath. The schlenck tube was then placed into a −78 °C cooling bath and then slowly allowed to warm until −50 °C upon which the color of the suspension changed from yellowish brown to dark green. The reaction mixture was stirred for 1 hour at this temperature and then again cooled down

to −68 °C. The resulting dark green suspension was filtered very carefully into another schlenck tube via a filtration cannula keeping the solution temperature always bellow −60 °C. The filtrate was treated with pre-cold (−70 °C) *n*-pentane (20 mL) and stored at −60 °C for 3 hours. The microcrystalline green precipitate, which forms upon cooling was isolated by filtration of the green supernatant at −78 °C. Obtained green solid was washed with *n*-pentane (2 × 5 mL) at −78 °C and then dried under reduced pressure for 2 hours at −70 °C. Yield: 172 mg (0.16 mmol, 26.3%).

Properties: Complex **18-Mo** is very well soluble in THF, insoluble in toluene and *n*-pentane. It is extremely air and thermally sensitive, decomposes in solution above −40 °C turning into a brown solution. Complex **18-Mo** also decomposes in solid state at room temperature and the green color changes to brown.

Spectroscopic Data:

ATR-IR (solid): $\widetilde{\nu}$ (cm^{-1}) = 1794 (vs) and 1723 (vs) [ν(CO)], 1543 (m) [$\nu(C\text{-}C\text{-}N)_{pz}$].

4.5.27 [Tp'(CO)(*i*PrNC)Mo(CN*i*Pr$_2$)$_2$Ge(C$_6$H$_3$-2,6-Mes$_2$)] (19-Mo)

To a yellowish brown solution of **8-Mo** (400 mg, 0.48 mmol) in 25 mL of *n*-heptane 0.2 mL (147 mg, 2.12 mmol, 4.4 equiv.) of *i*PrNC was added at 0 °C. The mixture was heated to 100 °C for 6 hours, upon which the clear solution become turbid and the color of the solution changed to dark brown. Monitoring of the reaction by IR spectroscopy revealed complete consumption of the starting material after 6 hours and formation of a new product. The suspension was filtered into another schlenck tube leaving behind an off white solid. The brown filtrate was concentrated to ~10 mL and stored at −60 °C for 2 hours. Upon cooling, a yellowish brown microcrystalline solid was precipitated out from the solution which was isolated by filtration of the brown supernatant at −60 °C. The isolated solid was washed with *n*-pentane (2 × 2 mL) at −60 °C and then dried for 30 minutes under reduced pressure to obtain a yellowish brown solid in pure form. Yield: 291 mg (0.29 mmol, 60%).

Properties: Complex **19-Mo** is very good soluble in all common organic solvent.

Melting Points: Compound decomposes upon melting at 155 – 158 °C to a reddish-brown liquid.

Elemental analysis: calcd (%) for $C_{52}H_{68}BGeMoN_9O$ (1014.52 g/mol): C 61.56, H 6.76, N 12.43; found: C 58.54, H 6.63, N 13.66%.

Spectroscopic Data:

IR (THF): $\tilde{\nu}$ (cm^{-1}) = 2131 (m) [ν(N≡C)], 1903 (w), 1870 (vs) [ν(CO)], 1782 (m) 1544 (m) [$\nu(C\text{-}C\text{-}N)_{pz}$].

ATR-IR (solid): $\tilde{\nu}$ (cm^{-1}) = 3018 (vw), 2973 (sh), 2957 (vw), 2920 (w), 2861 (vw), 2729 (vw), 2522 (vw) [ν(BH)], 2115 (m) [ν(N≡C)], 2078 (sh) [ν(N≡C)], 1900 (vw), 1863 (vs) [ν(CO)], 1774 (s), 1610 (vw), 1570 (vw), 1542 (m) [$\nu(C\text{-}C\text{-}N)_{pz}$], 1497 (m), 1444 (s), 1414 (s), 1374 (s), 1327 (s), 1308 (sh), 1195 (s) 1165 (w), 1120 (w), 1064 (m), 1044 (w), 1032 (sh), 1016 (vw), 981 (vw), 957 (vw), 921 (vw), 871 (vw), 849 (m), 832 (vw), 806 (m), 775 (m), 737 (w), 695 (m), 664 (vw), 650 (sh), 642 (w), 608 (vw), 591 (vw), 576 (w), 549 (vw), 536 (vw), 502 (w), 461 (m), 433 (w), 411 (vw), 402 (vw).

^{1}H NMR: (300.1 MHz, C_6D_6, 298 K): δ (ppm) = 0.57, 0.60, 0.71, 0.92, 1.48 and 1.60 (each d, ^3J(H, H) = ~6.5 Hz, each 3H, (CHMe_AMe_B)NC), 1.85, 2.50 and 2.53 (each s, each 3H, C^3-*Me*, pz), 2.02, 2.07 and 2.17 (each s, each 3H, C^5-*Me*, pz), 2.29 (s, 6H, 2 × C^4-*Me*, Mes), 2.37 and 2.44 (each s, each 6H, 2 × $C^{2,6}$-*Me*, Mes), 3.19, 3.75 and 4.21 (each sept, ^3J(H, H) = ~6.5 Hz, each 1H, (C*H*Me_AMe_B)NC), 4.6 (br, $\Delta\nu_{1/2}$ = ~ 220 Hz, 1H, B*H*); this signal is visible as a very broad hump over the base line in a strongly enlarged version of the spectrum), 5.50, 5.51 and 5.69 (each s, each 1H, C^4-*H*, pz), 6.95 and 6.99 (each s, each 2H, $C^{3,5}$-*H*, Mes), 6.99 (d, ^3J(H,H) = 7.3 Hz, 2H, $C^{3,5}$- *H,* C_6H_3), 7.25 (t, ^3J(H,H) = 7.3 Hz, 1H, C^4-*H*, C_6H_3).

^{13}C{^{1}H} NMR: (75.47 MHz, C_6D_6, 298 K): δ (ppm) = 12.6, 12.8 and 12.9 (each s, each 1C, C^5-*Me*, pz), 14.9, 16.0 and 18.0 (each s, each 1C, C^3-*Me*, pz), 21.4 (s, 2C, 2 × C^4-*Me*, Mes), 22.2, 22.5, 23.3, 24.2, 26.1 nad 26.7 (each s, each 1C, (CHMe_AMe_B)NC), 22.3 and 22.7 (each s, each 2C, 2 × $C^{2,6}$-*Me*, Mes), 48.6, 49.7 and 51.2 (each s, each 1C, (*C*HMe_AMe_B)NC), 106.5, 106.66 and 106.73 (each s, each 1C, C^4-H, pz), 128.0 (s, 1C, C^4, C_6H_3, signal overlap with the signal of deuterated solvent), 128.6 and 128.7 (each s, each 2C, 2 × $C^{3,5}$, Mes),

129.8 (s, 2C, $C^{3,5}$, C_6H_3), 135.6 (s, 2C, 2 × C^4, Mes), 136.2 and 136.3 (each s, each 2C, 2 × $C^{2,6}$, Mes), 142.3 (s, 2C, 2 × C^1, Mes), 143.1, 143.9 and 144.6 (each s, each 1C, C^5-Me, pz), 147.9 (s, 2C, $C^{2,6}$, C_6H_3), 151.2, 151.9 and 152.6 (each s, each 1C, C^3-Me, pz), 160.4 (s, 1C, C^1, C_6H_3), 176.5 (s, 1C, *i*PrN≡*C*), 209.4 and 222.0 (s, 1C each, $(CHMe_AMe_B)NC$), 232.7 (s, 1C, *C*O).

4.5.28 [Tp'Mo(CO)$_2$(PMe$_3$)GeCl$_3$] (20-Mo)

A reddish orange solution of **1-Mo** (300 mg, 0.54 mmol) in 15 mL of CH_2Cl_2 was slowly added to another schlenck tube containing $GeCl_2$·(1,4-dioxane) (124 mg, 0.54 mmol, 1 equiv.) via a transferring cannula at −30 °C. After addition the color of the suspension slowly changed to dark red. Monitoring of the reaction by IR spectroscopy revealed an incomplete conversion of the starting material into the product even after 1 hour. After 1 hour, the suspension was filtered into another schlenck tube containing $GeCl_2$·(1,4-dioxane) (62 mg, 0.27 mmol, 0.5 equiv.). After stirring for 1 hour at ambient temperature, an IR spectrum of the aliquot of the suspension indicate complete consumption of **1-Mo** and almost selective formation of the targeted complex. The suspension was filtered into another schlenck tube and all volatiles were removed under reduced pressure. The residue was washed with Et_2O (5 mL) and then crystallized from 8 mL of CH_2Cl_2 at −60 °C to afford **24-Mo** as a bright orange microcrystalline solid. Yield: 182 mg (0.26 mmol, 48%).

Properties: It is well soluble in CH_2Cl_2 and THF, sparingly soluble in toluene and Et_2O and insoluble in *n*-hexane.

Spectroscopic Data:

IR (CH_2Cl_2): $\tilde{\nu}$ (cm^{-1}) = 1969 (s) and 1891 (vs) [ν(CO)], 1546 (m) [ν(C-C-N)$_{pz}$].

IR (THF): $\tilde{\nu}$ (cm^{-1}) = 1969 (s) and 1893 (vs) [ν(CO)], 1545 (m) [ν(C-C-N)$_{pz}$].

^{1}H NMR: (300.1 MHz, CD_2Cl_2, 298 K): δ (ppm) = 0.94 (d, ^2J(P,H) = 9.1 Hz, 9H, P*Me*$_3$), 2.21 (s, 3H, 1 × C^3-*Me*, pz$_B$), 2.33 (s, 3H, 1 × C^5-*Me* pz$_B$), 2.38 (s, 6H, 2 × C^3-*Me*, pz$_A$), 2.46 (s, 6H, 2 × C^5-*Me*, pz$_A$) 4.64 (br, $\Delta\nu_{1/2}$ = ~ 280 Hz, 1H, B*H*); this signal appears as a very broad hump over the base line in a strongly enlarged version of the spectrum), 5.87 (s, 1H, 1 × C^4-*H*, pz$_B$), 6.03 (s, 2H, 2 × C^4-*H*, pz$_A$).

$^{13}C\{^1H\}$ NMR: (75.47 MHz, CD_2Cl_2, 298 K): δ (ppm) = 13.2 (s, 2C, 2 × C^5-*Me*, pz_A), 13.4 (s, 1C, 1 × C^5-*Me*, pz_B), 15.3 (s, 1C, 1 × C^3-*Me*, pz_B), 17.8 (s, 2C, 2 × C^3-*Me*, pz_A), 18.0 (d, ^1J(C,P) = 27 Hz, 3C, P*Me*$_3$), 107.9 (s, 1C, 1 × *C*^{4}-H, pz_B), 108.8 (s, 2C, 2 × *C*^{4}-H, pz_A), 147.7 (d, ^3J(C,P) = 0.9 Hz, 1C, 1 × *C*^{5}-Me, pz_B), 148.1 (s, 2C, 2 × *C*^{5}-Me, pz_A), 152.7 (d, ^3J(C,P) = 1.0 Hz, 1C, 1 × *C*^{3}-Me, pz_B), 154.1 (d, ^3J(C,P) = 1.5 Hz, 2C, 2 × *C*^{3}-Me, pz_A), 238.0 (d, ^2J(C,P) = 6.7 Hz, 2C, 2 × *C*O).

$^{31}P\{^1H\}$ NMR: (121.5 MHz, CD_2Cl_2, 298 K): δ (ppm) = 1.19 (s).

4.5.29 [Tp'(CO)$_2$Mo≡Si-Mo(CO)$_2$(PMe$_3$)Tp'] (21-Mo)

A yellow solution of $SiBr_2$(SIdipp) (791 mg, 1.37 mmol) in 20 mL of fluorobenzene was added via a syringe to a yellow suspension of **3-Mo** (1.50 g, 2.74 mmol, 2.0 equiv.) in 60 mL of fluorobenzene at ambient temperature. The reaction mixture was stirred for 2.5 hours. During this time, the color of the suspension changed to red brown. An aliquot of the solution was taken, the solvent removed in vacuo, and an IR spectrum of the residue was recorded in THF. The IR spectrum revealed the formation of complex **21-Mo** (ν(CO) = 1933, 1870, 1857, 1806 and 1794 cm^{-1}) along with radical **2-Mo** (ν (CO) = 1893 and 1755 cm^{-1}). The red brown suspension was evaporated to dryness *in vacuo*. ^1H NMR and $^{31}P\{^1H\}$ NMR spectra of the resulting red brown solid was recorded in benzene-d_6, which revealed only the presence of complex **21-Mo,** free SIdipp and traces of free PMe_3. The solid was treated with 30 mL of *n*-pentane, and the suspension was ultrasonicated for 10 minutes. The red brown insoluble solid was isolated after filtration of the light red supernatant, and extracted with toluene (4 × 50 mL). The combined extracts were concentrated to *ca.* 40 mL *in vacuo* and stored at –60 °C for 72 hours. The resulting red brown precipitate was isolated by filtration at –60 °C and washed with *n*-pentane (40 mL) at ambient temperature. The obtained solid was suspended in 50 mL of Et_2O and the suspension was concentrated to *ca.* 20 mL *in vacuo* and stored at –60 °C for 24 hours. The insoluble microcrystalline solid was isolated by filtration at –60 °C, washed with *n*-pentane (30 mL) at ambient temperature and dried *in vacuo* for a short period of time to afford complex **21-Mo**·0.6Et_2O as an air-sensitive, red brown solid. Complex **21-Mo** could be isolated in diethyl ether free form upon drying over 4 - 5 days at 100 °C. Yield: 614 mg (0.586 mmol, 43%).

Properties: Complex **21-Mo** is well soluble in THF and fluorobenzene, moderately soluble in toluene and insoluble in Et_2O and aliphatic solvent.

Melting Points: The solid decomposes at 280-283 °C to give a black mass.

Elemental analysis: calcd (%) for $C_{37}H_{53}B_2Mo_2N_{12}O_4PSi \cdot 0.6Et_2O$[46] (1046.94 g/mol): C 45.20, H 5.68, N 16.06; found: C 45.27, H 5.63, N 16.01.

Spectroscopic Data:

IR (THF): $\tilde{\nu}$ (cm^{-1}) = 1933 (s), 1870 (vs), 1857 (m, sh), 1806 (m) and 1794 (m, sh) [ν(CO)], 1545 (m) [$\nu(C\text{-}C\text{-}N)_{pz}$].

IR (toluene): $\tilde{\nu}$ (cm^{-1}) = 1934 (s), 1871 (vs), 1857 (m, sh), 1809 (m) and 1792 (m) [ν(CO)], 1545 (m) [$\nu(C\text{-}C\text{-}N)_{pz}$].

IR (fluorobenzene): $\tilde{\nu}$ (cm^{-1}) = 1932 (s), 1869 (vs), 1800 (m) [ν(CO)], 1545 (m) [$\nu(C\text{-}C\text{-}N)_{pz}$].

ATR-IR (solid): $\tilde{\nu}$ (cm^{-1}) = 2965 (w), 2927 (w), 2893 (vw), 2878 (vw), 2549 (vw) and 2529 (vw, sh) [ν(BH)], 1928 (s), 1861 (vs) and 1791 (s) [ν(CO)], 1541 (m) [$\nu(C\text{-}C\text{-}N)_{pz}$], 1488 (vw), 1441 (m), 1413 (m), 1377 (m), 1368 (m), 1348 (w), 1307 (vw), 1286 (vw), 1197 (m), 1151 (vw), 1119 (w), 1071 (sh), 1063 (m), 1042 (m), 980 (vw), 955 (m), 941 (sh), 870 (vw), 854 (w), 816 (sh), 808 (m), 799 (sh), 772 (m), 726 (vw), 695 (m), 671 (vw), 655 (vw), 640 (m), 609 (w), 591 (w), 564 (w), 524 (vw), 505 (w), 491 (m), 474 (w), 452 (w), 440 (m), 412 (vw), 400 (vw).

^{1}H NMR: (300.1 MHz, C_6D_6, 298 K): δ (ppm) = 0.74 (d, ^2J(P,H) = 8.4 Hz, 9H, P*Me*$_3$), 1.91, 2.18, 2.72, 2.93 (s, 3H each, pz_B), 2.06, 2.26, 2.47, 3.14 (s, 6H each, pz_A), ~ 4.5 (br, $\Delta\nu_{1/2}$ = ~ 150 Hz, 2H, B*H*); this signal is visible as a very broad hump over the base line in a strongly enlarged version of the spectrum), 5.30 (s, 1H, C^4-*H*), 5.45 (s, 3H, C^4-*H*), 5.80 (s, 2H, C^4-*H*).

^{1}H NMR: (300.1 MHz, THF-d_8, 298 K): δ (ppm) = 1.06 (d, ^2J(P,H) = 8.5 Hz, 9H, P*Me*$_3$), 2.28 (s, 3H, 1 × C^5-*Me*, $^{II}pz_B$), 2.30 (s, 3H, 1 × C^5-*Me*, $^{I}pz_B$), 2.37 (s, 6H, 2 × C^5-*Me*, $^{I}pz_A$), 2.43 (s, 6H, 2 × C^5-*Me*, $^{II}pz_A$), 2.47 (s, 3H, 1 × C^3-*Me*, $^{II}pz_B$), 2.53 (s, 3H, 1 × C^3-*Me*, $^{I}pz_B$), 2.56 (s, 6H, 2 × C^3-*Me*, $^{II}pz_A$), 2.77 (s, 6H, 2 × C^3-*Me*,

[46] The composition of the diethylether solvate of **21-Mo** was determined by ^{1}H NMR spectroscopy.

$^{I}pz_A$), 4.67 (br, $\Delta\nu_{1/2}$ = ~ 155 Hz, 2H, B*H*); this signal is visible as a very broad hump over the base line in a strongly enlarged version of the spectrum), 5.65 (s, 1H, 1 × C^4-*H*, $^{I}pz_B$), 5.77 (s, 2H, 2 × C^4-*H*, $^{I}pz_A$), 5.83 (s, 1H, 1 × C^4-*H*, $^{II}pz_B$), 6.00 (s, 2H, 2 × C^4-*H*, $^{II}pz_A$).

$^{13}C\{^1H\}$ NMR: (75.47 MHz, THF-d_8, 298 K): δ (ppm) = 12.7 (s, 1C, 1 × C^5-*Me*, $^{I}pz_B$), 12.89 (s, 2C, 2 × C^5-*Me*, $^{II}pz_A$), 12.91 (s, 2C, 2 × C^5-*Me*, $^{I}pz_A$), 13.0 (s, 1C, 1 × C^5-*Me*, $^{II}pz_B$), 15.47 (s, 1C, 1 × C^3-*Me*, $^{I}pz_B$), 15.53 (s, 1C, 1 × C^3-*Me*, $^{II}pz_B$), 17.8 (s, 2C, 2 × C^3-*Me*, $^{II}pz_A$), 18.27 (s, 2C, 2 × C^3-*Me*, $^{I}pz_A$), 18.3 (d, ^1J(C,P) = 28.1Hz, 3C, P*Me*$_3$), 106.1 (s, 2C, 2 × *C*^{4}-H, $^{I}pz_A$), 106.6 (s, 1C, 1 × *C*^{4}-H, $^{I}pz_B$), 107.9 (s, 1C, 1 × *C*^{4}-H, $^{II}pz_B$), 108.7 (s, 2C, 2 × *C*^{4}-H, $^{II}pz_A$), 143.8 (s, 2C, 2 × *C*^{5}-Me, $^{I}pz_A$), 144.2 (s, 1C, 1 × *C*^{5}-Me, $^{I}pz_B$), 146.3 (d, ^4J(C,P) = 1.3 Hz, 1C, 1 × *C*^{5}-Me, $^{II}pz_B$), 147.4 (s, 2C, 2 × *C*^{5}-Me, $^{II}pz_A$), 150.8 (s, 2C, 2 × *C*^{3}-Me, $^{I}pz_A$), 152.7 (d, ^3J(C,P) = 1.0 Hz, 1C, 1 × *C*^{3}-Me, $^{II}pz_B$), 152.9 (d, ^3J(C,P) = 1.3 Hz, 2C, 2 × *C*^{3}-Me, $^{II}pz_A$), 153.0 (s, 1C, 1 × *C*^{3}-Me, $^{I}pz_B$), 229.3 (d, ^4J(C,P) = 1.3 Hz, 2C, 2 × ^{I}*C*O), 231.6 (d, ^2J(C,P) = 5.5 Hz, 2C, 2 × ^{II}*C*O).

$^{31}P\{^1H\}$ NMR: (121.5 MHz, C_6D_6, 298 K): δ (ppm) = – 5.5 (s, ^2J(Si,P) = 58.4 Hz).

$^{31}P\{^1H\}$ NMR: (121.5 MHz, THF-d_8, 298 K): δ (ppm) = – 4.4 (s, ^2J(Si,P) = 56.6 Hz).

$^{29}Si\{^1H\}$ NMR: (59.63 MHz, THF-d_8, 298 K): δ (ppm) = 438.9 (d, ^2J(Si, P) = 56.6 Hz).

4.5.30 [Tp'(CO)$_2$W≡Si-W(CO)$_2$(PMe$_3$)Tp'] (21-W)

A yellow suspension of $SiBr_2$(SIdipp) (1.36 g, 2.35 mmol) in 20 mL of fluorobenzene was slowly added via a syringe to a stirred yellow suspension of **3-W** (3.00 g, 4.72 mmol, 2 equiv.) in 60 mL of fluorobenzene at ambient temperature. Immediate after addition, the color of the suspension changed from yellow to brown. The suspension was stirred for 3 hours at ambient temperature. An IR spectrum of the brown solution was recorded after three hours of stirring, which showed that starting material was consumed and formed complex **21-W** (ν(CO) in fluorobenzene = 1918 (m), 1852 (vs), 1839 (s, sh), 1784 (m, sh), 1773 (m)) in addition to a small amount of the 17VE radical **2-W** (ν(CO) in fluorobenzene = 1871 (s), 1743 (s)). All volatiles were removed under reduced pressure, and the sticky brown solid was grinded during a freeze-pump-thaw cycle. The brown powder obtained was washed with 20 mL of *n*-pentane at ambient

temperature and then extracted with toluene (3 × 100 mL) at 60 °C. The combined brown extracts were evaporated to dryness under reduced pressure. The brown solid obtained was washed with Et_2O (2 × 30 mL) at ambient temperature to remove SIdipp and **2-W** and dried under reduced pressure for four hours at 60 °C. Yield: 1.43 g (1.21 mmol, 51%).

Properties: The brown solid is well soluble in THF, moderately soluble in toluene and sparingly soluble in Et_2O.

Melting Points: The brown solid decomposes upon heating to a greyish-brown solid at 268 – 270 °C.

Elemental analysis: calcd (%) for $C_{37}H_{53}B_2N_{12}O_4PSiW_2$ (1178.26 g/mol): C 37.72, H 4.53, N 14.27; found: C 37.63, H 4.57, N 13.87.

Spectroscopic Data:

IR (THF): $\tilde{\nu}$ (cm^{-1}) = 1920 (m), 1915 (m) 1854 (vs), 1841 (s), 1792 (w) and 1778 (m) [ν(CO)], 1546 (m) [$\nu(C\text{-}C\text{-}N)_{pz}$].

ATR-IR (solid): $\tilde{\nu}$ (cm^{-1}) = 3128 (vw), 2959 (vw), 2924 (vw), 2555 (vw) [ν(BH)], 2527 (vw) [ν(BH)], 1903 (m) [ν(CO)], 1843 (s) [ν(CO)], 1833 (s) [ν(CO)], 1824 (vs) [ν(CO)], 1768 (s) [ν(CO)], 1543 (m) [$\nu(C\text{-}C\text{-}N)_{pz}$], 1490 (vw), 1444 (m), 1413 (m), 1380 (m), 1371 (m), 1349 (w), 1309 (vw), 1288 (vw), 1257 (vw), 1205 (s), 1184 (sh), 1152 (vw), 1065 (m), 1044 (m), 984 (w), 953 (m), 940 (sh), 910 (w), 873 (vw), 855 (w), 813 (m), 801 (m), 783 (m), 774 (m), 728 (vw), 717 (vw), 695 (m), 667 (w), 647 (m), 638 (sh), 590 (w), 569 (vw), 526 (m), 500 (w), 463 (m), 453 (m), 423 (vw), 413 (vw).

^{1}H NMR: (300.1 MHz, C_6D_6, 298 K): δ (ppm) = 1.01 (d, ^2J(P,H) = 8.7 Hz, 9H, P*Me*$_3$), 1.90, 2.17, 2.65, 3.04 (s, 3H each, pz_B), 2.03, 2.23, 2.53, 3.18 (s, 6H each, pz_A), ~ 4.6 (br, $\Delta\nu_{1/2}$ = ~ 180 Hz, 2H, B*H*); this signal is visible as a very broad hump over the base line in a strongly enlarged version of the spectrum), 5.31, 5.48 (s, 1H each, C^4-*H*), 5.43, 5.74 (s, 2H each, C^4-*H*).

^{1}H NMR: (300.1 MHz, THF-d_8, 298 K): δ (ppm) = 1.19 (d, ^2J(P,H) = 8.9 Hz, 9H, P*Me*$_3$), 2.30 (s, 3H, 1 × C^5-*Me*, $^{II}pz_B$), 2.32 (s, 3H, 1 × C^5-*Me*, $^{I}pz_B$), 2.36 (s, 6H, 2 ×

C^5-*Me*, $^{I}pz_A$), 2.45 (s, 9H(2 × C^5-*Me*, $^{II}pz_A$) + (C^3-*Me*, $^{II}pz_B$)), 2.57 (s, 6H, 2 × C^3-*Me*, $^{II}pz_A$), 2.59 (s, 3H, 1 × C^3-*Me*, $^{I}pz_B$), 2.75 (s, 6H, 2 × C^3-*Me*, $^{I}pz_A$), ~ 4.7 ((br, $\Delta\nu_{1/2}$ = ~ 160 Hz, 2H, B*H*); this signal is visible as a very broad hump over the base line in a strongly enlarged version of the spectrum), 5.71 (s, 1H, 1 × C^4-*H*, $^{I}pz_B$), 5.79 (s, 2H, 2 × C^4-*H*, $^{I}pz_A$), 5.87 (s, 1H, 1 × C^4-*H*, $^{II}pz_B$), 6.07 (s, 2H, 2 × C^4-*H*, $^{II}pz_A$).

$^{13}C\{^1H\}$ NMR: (75.47 MHz, THF-d_8, 298 K): δ (ppm) = 12.6 (s, 1C, 1 × C^5-*Me*, $^{I}pz_B$), 12.78 (s, 2C, 2 × C^5-*Me*, $^{II}pz_A$), 12.81 (s, 2C, 2 × C^5-*Me*, $^{I}pz_A$), 12.9 (s, 1C, 1 × C^5-*Me*, $^{II}pz_B$), 15.9 (s, 1C, 1 × C^3-*Me*, $^{II}pz_B$), 16.2 (s, 1C, 1 × C^3-*Me*, $^{I}pz_B$), 18.6 (s, 2C, 2 × C^3-*Me*, $^{II}pz_A$), 19.0 (d, ^1J(C,P) = 31.4 Hz, 3C, P*Me*$_3$), 19.5 (s, 2C, 2 × C^3-*Me*, $^{I}pz_A$), 106.2 (s, 2C, 2 × *C*^{4}-H, $^{I}pz_A$), 106.9 (s, 1C, 1 × *C*^{4}-H, $^{I}pz_B$), 108.0 (s, 1C, 1 × *C*^{4}-H, $^{II}pz_B$), 109.1 (s, 2C, 2 × *C*^{4}-H, $^{II}pz_A$), 143.5 (s, 2C, 2 × *C*^{5}-Me, $^{I}pz_A$), 143.9 (s, 1C, 1 × *C*^{5}-Me, $^{I}pz_B$), 146.0 (d, ^4J(C,P) = 1.0 Hz, 1C, 1 × *C*^{5}-Me, $^{II}pz_B$), 147.4 (s, 2C, 2 × *C*^{5}-Me, $^{II}pz_A$), 151.6 (s, 2C, 2 × *C*^{3}-Me, $^{I}pz_A$), 152.4 (d, ^3J(C,P) = 1.0 Hz, 1C, 1 × *C*^{3}-Me, $^{II}pz_B$), 153.6 (d, ^3J(C,P) = 1.4 Hz, 2C, 2 × *C*^{3}-Me, $^{II}pz_A$), 153.9 (s, 1C, 1 × *C*^{3}-Me, $^{I}pz_B$), 225.0 (d, ^4J(C,P) = 1.4 Hz, 2C, 2 × ^{I}*C*O), 231.2 (d, ^2J(C,P) = 2.5 Hz, 2C, 2 × ^{II}*C*O).

$^{31}P\{^1H\}$ NMR: (121.5 MHz, C_6D_6, 298 K): δ (ppm) = – 21.1 (s, ^1J(W,P) = 260 Hz, ^2J(Si,P) = 39 Hz).

$^{31}P\{^1H\}$ NMR: (121.5 MHz, THF-d_8, 298 K): δ (ppm) = – 19.8 (s,^1J(W,P) = 257 Hz, ^3J(W,P) = 7.0 Hz, ^2J(Si,P) = 38 Hz).

$^{29}Si\{^1H\}$ NMR: (59.63 MHz, THF-d_8, 298 K): δ (ppm) = 395.6 (d, ^2J(Si,P) = 39 Hz).

$^{29}Si\{^1H\}$ NMR: (59.63 MHz, 1,2-$C_6H_4F_2$, 298 K): δ (ppm) = 397.5 (d, ^1J(W^1,Si) = 250 Hz, ^1J(W^2,Si) = 20 Hz, ^2J(Si,P) = 41 Hz).

4.5.31 [Tp'(CO)$_2$Mo≡Ge-Mo(CO)$_2$(PMe$_3$)Tp'] (22-Mo)

A solution of $GeCl_2$·1,4-dioxane (106 mg, 0.456 mmol) in 10 mL of THF was added via a syringe to a solution of **3-Mo** (500 mg, 0.912 mmol) in 30 mL of THF and the mixture was stirred for 15 minutes at ambient temperature. The color of the solution changed from yellowish brown to dark red brown. Completion of the reaction was confirmed by IR spectroscopy, which revealed the formation of complex **22-Mo**, together with small amount of radical **2-Mo**. The red

brown solution was evaporated to dryness in *vacuo* and pulverised by a freeze-pump-thaw cycle. The resulting solid was extracted with a toluene/hexane (2:1) mixture (4 × 20 mL). The combined extracts were concentrated to *ca.* 5 mL in *vacuo*, treated with 8 mL of *n*-pentane and stored at –30 °C for 24 hours to obtain brown microcrystalline solid. The solid was isolated by filtration at –30 °C and subsequently washed with *n*-hexane (20 mL) and dried *in vacuo* at ambient temperature. The resulting brown powder was redissolved in THF (15 mL) and concentrated to *ca.* 3 mL *in vacuo* to obtain a brown suspension which was treated with 10 mL of *n*-pentane and stored at –60 °C for 48 hours. The obtained microcrystalline solid was isolated by filtration at –60 °C and dried *in vacuo* for 3 hours at 100 °C to afford complex **22-Mo** as an air-sensitive, brown solid. Yield: 232 mg (0.222 mmol, 49%).

Properties: Complex **22-Mo** is well soluble in THF and fluorobenzene, moderately soluble in toluene and insoluble in Et_2O and aliphatic solvents.

Melting Points: The solid melts with decomposition at 287 °C to give a black mass.

Elemental analysis: calcd (%) for $C_{37}H_{53}B_2GeMo_2N_{12}O_4P$ (1046.98 g/mol): C 42.44, H 5.10, N 16.06; found: C 41.29, H 5.07, N 15.31.

Spectroscopic Data:

IR (THF): $\widetilde{\nu}$ (cm^{-1}) = 1932 (s), 1923 (sh), 1868 (vs), 1854 (s), 1806 (m), 1798 (sh) [ν(CO)], 1545 (m) [$\nu(C\text{-}C\text{-}N)_{pz}$].

IR (toluene): $\widetilde{\nu}$ (cm^{-1}) = 1933 (s), 1924 (sh), 1868 (vs), 1855 (s), 1809 (m), 1798 (sh) [ν(CO)], 1545 (m) [$\nu(C\text{-}C\text{-}N)_{pz}$].

ATR-IR (solid): $\widetilde{\nu}$ (cm^{-1}) = 2955 (vw), 2926 (vw), 2549 (vw) and 2530 (vw, sh) [ν(BH)], 1928 (s), 1859 (vs) and 1795 (s) [ν(CO)], 1543 (m) [$\nu(C\text{-}C\text{-}N)_{pz}$], 1488 (vw), 1444 (m), 1415 (m), 1382 (w), 1375 (w), 1369 (m), 1347 (w), 1307 (vw), 1287 (vw), 1198 (m), 1146 (sh), 1065 (m), 1043 (w), 981 (w), 954 (m), 941 (sh), 903 (w), 871 (sh), 854 (w), 810 (m), 797 (m), 775 (m), 728 (vw), 695 (m), 671 (vw), 655 (sh), 642 (m), 608 (w), 586 (vw), 563 (w), 523 (vw), 511 (vw), 494 (w), 467 (w), 459 (w), 450 (w), 426 (vw), 406 (vw).

^{1}H NMR: (300.1 MHz, C_6D_6, 298 K): δ (ppm) = 0.77 (d, ^{2}J(P,H) = 8.1 Hz, 9H, P*Me*$_3$), 1.92, 2.16, 2.71, 2.92 (s, 3H each, pz_B), 2.07, 2.25, 2.49, 3.11 (s, 6H each, pz_A), ~ 4.6 (br, $\Delta\nu_{1/2}$ = ~ 180 Hz, 2H, B*H*); this signal is visible as a very broad hump over the base line in a strongly enlarged version of the spectrum), 5.33 (s, 1H, C^4-*H*), 5.46 (s, 3H, C^4-*H*), 5.78 (s, 2H, C^4-*H*).

^{1}H NMR: (300.1 MHz, THF-d_8, 298 K): δ (ppm) = 1.07 (d, ^{2}J(P,H) = 8.1 Hz, 9H, P*Me*$_3$), 2.28 (s, 3H, 1 × C^5-*Me*, $^{II}pz_B$), 2.30 (s, 3H, 1 × C^5-*Me*, $^{I}pz_B$), 2.37 (s, 6H, 2 × C^5-*Me*, $^{I}pz_A$), 2.43 (s, 6H, 2 × C^5-*Me*, $^{II}pz_A$), 2.46 (s, 3H, 1 × C^3-*Me*, $^{II}pz_B$), 2.53 (s, 3H, 1 × C^3-*Me*, $^{I}pz_B$), 2.56 (s, 6H, 2 × C^3-*Me*, $^{II}pz_A$), 2.74 (s, 6H, 2 × C^3-*Me*, $^{I}pz_A$), 4.6 (br, $\Delta\nu_{1/2}$ = ~ 155 Hz, 2H, B*H*); this signal is visible as a very broad hump over the base line in a strongly enlarged version of the spectrum), 5.68 (s, 1H, 1 × C^4-*H*, $^{I}pz_B$), 5.79 (s, 2H, 2 × C^4-*H*, $^{I}pz_A$), 5.83 (s, 1H, 1 × C^4-*H*, $^{II}pz_B$), 6.00 (s, 2H, 2 × C^4-*H*, $^{II}pz_A$).

^{13}C{^{1}H} NMR: (75.47 MHz, THF-d_8, 298 K): δ (ppm) = 12.81 (s, 1C, 1 × C^5-*Me*, $^{I}pz_B$), 12.84 (s, 2C, 2 × C^5-*Me*, $^{I}pz_A$), 12.87 (s, 2C, 2 × C^5-*Me*, $^{II}pz_A$), 13.1 (s, 1C, 1 × C^5-*Me*, $^{II}pz_B$), 15.55 (s, 1C, 1 × C^3-*Me*, $^{II}pz_B$), 15.60 (s, 1C, 1 × C^3-*Me*, $^{I}pz_B$), 17.9 (s, 2C, 2 × C^3-*Me*, $^{II}pz_A$), 18.3 (s, 2C, 2 × C^3-*Me*, $^{I}pz_A$), 18.7 (d, ^{1}J(C,P) = 27.1Hz, 3C, P*Me*$_3$), 106.2 (s, 2C, 2 × *C*^{4}-H, $^{I}pz_A$), 106.9 (s, 1C, 1 × *C*^{4}-H, $^{I}pz_B$), 107.9 (s, 1C, 1 × *C*^{4}-H, $^{II}pz_B$), 108.7 (s, 2C, 2 × *C*^{4}-H, $^{II}pz_A$), 143.8 (s, 2C, 2 × *C*^{5}-Me, $^{I}pz_A$), 144.5 (s, 1C, 1 × *C*^{5}-Me, $^{I}pz_B$), 146.3 (d, ^{4}J(C,P) = 0.7 Hz, 1C, 1 × *C*^{5}-Me, $^{II}pz_B$), 147.3 (s, 2C, 2 × *C*^{5}-Me, $^{II}pz_A$), 150.8 (s, 2C, 2 × *C*^{3}-Me, $^{I}pz_A$), 152.8 (d, ^{3}J(C,P) = 1.4 Hz, 1C, 1 × *C*^{3}-Me, $^{II}pz_B$), 153.1 (d, ^{3}J(C,P) = 1.4 Hz, 2C, 2 × *C*^{3}-Me, $^{II}pz_A$), 153.6 (s, 1C, 1 × *C*^{3}-Me, $^{I}pz_B$), 230.3 (d, ^{4}J(C,P) = 1.4 Hz, 2C, 2 × ^{I}*C*O), 234.9 (d, ^{2}J(C,P) = 4.9 Hz, 2C, 2 × ^{II}*C*O).

^{31}P{^{1}H} NMR: (121.5 MHz, C_6D_6, 298 K): δ (ppm) = – 4.5 (s).

^{31}P{^{1}H} NMR: (121.5 MHz, THF-d_8, 298 K): δ (ppm) = – 3.7 (s).

4.5.32 [Tp'(CO)$_2$W≡Ge-W(CO)$_2$(PMe$_3$)Tp'] (22-W)

A solution of $GeCl_2$·1,4-dioxane (182 mg, 0.79 mmol) in 5 mL of THF was slowly added via a syringe to a yellow solution of **3-W** (1 g, 1.57 mmol) in 40 mL of THF and the mixture was

stirred for 15 minutes at ambient temperature. The color of the solution immediately changed from yellow to dark red brown. Completion of the reaction was confirmed by IR spectroscopy revealing formation of complex **22-W** and small amount of radical **2-W**. The dark red-brown solution was evaporated to dryness and the resulting solid was washed with 15 mL of *n*-hexane. The brown solid was extracted with toluene/fluorobenzene mixture (3:1; 3 × 60 mL) at ambient temperature. The combined extract was dried under reduce pressure, washed with 30 mL of Et_2O and finally dried again for 3 hours at ambient temperature to obtain compound **22-W** as a moderately air-sensitive, dark brown solid. Yield: 608 mg (0.50 mmol, 63%).

Properties: Complex **22-W** is moderately soluble in THF and fluorobenzene, sparingly soluble in toluene and insoluble in Et_2O and aliphatic solvents.

Melting Points: The solid decomposes to a very dark brown solid at 253 – 255 °C.

Elemental analysis: calcd (%) for $C_{37}H_{53}B_2GeN_{12}O_4PW_2$ (1222.78 g/mol): C 36.34, H 4.37, N 13.75; found: C 36.59, H 4.55, N 13.42.

Spectroscopic Data:

IR (THF): $\tilde{\nu}$ (cm^{-1}) = 1921 (sh), 1910 (m), 1853 (vs), 1838 (s), 1780 (m), 1771 (m) [ν(CO)], 1546 (m) [$\nu(C\text{-}C\text{-}N)_{pz}$].

IR (toluene): $\tilde{\nu}$ (cm^{-1}) = 1912 (sh), 1909 (m), 1853 (vs), 1839 (s), 1778 (m) [ν(CO)], 1545 (m) [$\nu(C\text{-}C\text{-}N)_{pz}$].

ATR-IR (solid): $\tilde{\nu}$ (cm^{-1}) = 3126 (vw), 3063 (vw), 2980 (sh), 2963 (vw), 2927 (vw), 2913 (vw), 2861 (vw), 2815 (vw), 2551 (vw) and 2523 (vw) [ν(BH)], 1910 (m), 1847 (sh), 1834 (vs), and 1769 (s) [ν(CO)], 1546 (m) [$\nu(C\text{-}C\text{-}N)_{pz}$], 1491 (vw), 1444 (m), 1413 (m), 1382 (sh), 1374 (m), 1367 (sh), 1348 (w), 1308 (vw), 1289 (vw), 1200 (m), 1150 (vw), 1127 (sh), 1117 (vw), 1064 (m), 1045 (w), 982 (w), 957 (m), 941 (sh), 909 (vw), 873 (vw), 856 (w), 817 (sh), 810 (w), 785 (m), 775 (w), 731 (vw), 719 (vw), 702 (sh), 694 (w), 670 (w), 652 (sh), 644 (m), 629 (sh), 598 (w), 586 (w), 568 (w), 526 (vw), 497 (w), 487 (vw), 456 (w).

^{1}H NMR: (300.1 MHz, C_6D_6, 298 K): δ (ppm) = 1.07 (d, ^2J(P,H) = 8.5 Hz, 9H, PMe_3), 1.91, 2.14, 2.61 and 3.02 (each s, 3H each, pz_B), 2.04, 2.252, 2.56 and 3.15

(each s, 6H each, pz_A), ~ 4.5 (br, $\Delta\nu_{1/2}$ = ~ 180 Hz, 2H, B*H*); this signal is visible as a very broad hump over the base line in a strongly enlarged version of the spectrum), 5.33 and 5.47 (each s, each 1H, C^4-*H*, pz_B), 5.43and 5.71 (each s, each 2H, C^4-*H*, pz_A).

^{1}H NMR: (300.1 MHz, THF-d_8, 298 K): δ (ppm) = 1.19 (d, ^2J(P,H) = 8.7 Hz, 9H, P*Me*$_3$), 2.30 (s, 3H, 1 × C^5-*Me*, $^{II}pz_B$), 2.32 (s, 3H, 1 × C^5-*Me*, $^{I}pz_B$), 2.37 (s, 6H, 2 × C^5-*Me*, $^{I}pz_A$), 2.43 (s, 3H, 1 × C^3-*Me*, $^{II}pz_B$), 2.45 (s, 6H, 2 × C^5-*Me*, $^{II}pz_A$), 2.58 (s, 6H, 2 × C^3-*Me*, $^{II}pz_A$), 2.59 (s, 3H, 1 × C^3-*Me*, $^{I}pz_B$), 2.72 (s, 6H, 2 × C^3-*Me*, $^{I}pz_A$), 4.6 (br, $\Delta\nu_{1/2}$ = ~ 165 Hz, 2H, B*H*); this signal is visible as a very broad hump over the base line in a strongly enlarged version of the spectrum), 5.73 (s, 1H, 1 × C^4-*H*, $^{I}pz_B$), 5.81 (s, 2H, 2 × C^4-*H*, $^{I}pz_A$), 5.86 (s, 1H, 1 × C^4-*H*, $^{II}pz_B$), 6.07 (s, 2H, 2 × C^4-*H*, $^{II}pz_A$).

^{13}C{^{1}H} NMR: (75.47 MHz, THF-d_8, 298 K): δ (ppm) = 12.6 (s, 1C, 1 × C^5-*Me*, $^{I}pz_B$), 12.74 (s, 2C, 2 × C^5-*Me*, $^{I}pz_A$), 12.75 (s, 2C, 2 × C^5-*Me*, $^{II}pz_A$), 12.9 (s, 1C, 1 × C^5-*Me*, $^{II}pz_B$), 15.9 (s, 1C, 1 × C^3-*Me*, $^{II}pz_B$), 16.2 (s, 1C, 1 × C^3-*Me*, $^{I}pz_B$), 18.7 (s, 2C, 2 × C^3-*Me*, $^{II}pz_A$), 19.2 (d, ^1J(C,P) = 30.7 Hz, 3C, P*Me*$_3$), 19.7 (s, 2C, 2 × C^3-*Me*, $^{I}pz_A$), 106.3 (s, 2C, 2 × *C*^{4}-H, $^{I}pz_A$), 107.2 (s, 1C, 1 × *C*^{4}-H, $^{I}pz_B$), 108.0 (s, 1C, 1 × *C*^{4}-H, $^{II}pz_B$), 109.1 (s, 2C, 2 × *C*^{4}-H, $^{II}pz_A$), 143.6 (s, 2C, 2 × *C*^{5}-Me, $^{I}pz_A$), 144.2 (s, 1C, 1 × *C*^{5}-Me, $^{I}pz_B$), 146.0 (d, ^4J(C,P) = 0.7 Hz, 1C, 1 × *C*^{5}-Me, $^{II}pz_B$), 147.2 (s, 2C, 2 × *C*^{5}-Me, $^{II}pz_A$), 151.6 (s, 2C, 2 × *C*^{3}-Me, $^{I}pz_A$), 152.5 (d, ^3J(C,P) = 1.0 Hz, 1C, 1 × *C*^{3}-Me, $^{II}pz_B$), 153.8 (d, ^3J(C,P) = 1.5 Hz, 2C, 2 × *C*^{3}-Me, $^{II}pz_A$), 154.3 (s, 1C, 1 × *C*^{3}-Me, $^{I}pz_B$), 225.8 (d, ^4J(C,P) = 1.6 Hz, 2C, 2 × ^{I}*C*O), 234.1 (d, ^2J(C,P) = 1.8 Hz, 2C, 2 × ^{II}*C*O).

^{31}P{^{1}H} NMR: (121.5 MHz, C_6D_6, 298 K): δ (ppm) = – 21.9 (s, ^1J(W,P) = 255 Hz, ^3J(W,P) = 17 Hz).

^{31}P{^{1}H} NMR: (121.5 MHz, THF-d_8, 298 K): δ (ppm) = – 21.1 (s, ^1J(W,P) = 252 Hz, ^3J(W,P) = 18 Hz).

4.5.33 [Tp'(CO)$_2$Mo≡Si-Mo(CO)$_2$(MesNC)Tp'] (23-Mo)

A mixture of compound **21-Mo** (400 mg, 0.40 mmol) and MesNC (58 mg, 0.40 mmol, 1 equiv.) was treated with 30 mL of toluene at ambient temperature. The resulting red-brown

solution was stirred at ambient temperature for 3 hours and the progress of the reaction was followed by IR spectroscopy, which revealed a selective but very slow conversion of compound **21-Mo** into **23-Mo**. So the reaction mixture was heated to 60 °C for 1 hour and the completion of the reaction was confirmed by IR spectroscopy. During the course of the reaction the color of the reaction mixture did not change. The obtained red brown solution was concentrated to ~10 mL and then treated with 20 mL of *n*-pentane. The resulting red brown precipitate was isolated by filtration of a light brown supernatant, washed with *n*-pentane (2 × 10 mL) and dried under reduced pressure for 16 hours at 75 °C. The compound **23-Mo** was isolated as a red brown, air-sensitive solid. Yield: 293 mg (0.27 mmol, 69%).

Properties: Complex **23-Mo** is well soluble in THF and fluorobenzene, moderately soluble in toluene and insoluble in Et_2O and aliphatic solvent.

Melting Points: The red brown solid decomposes upon melting to a brown liquid at 224 – 226 °C.

Elemental analysis: calcd (%) for $C_{44}H_{55}B_2Mo_2N_{13}O_4Si$ (1071.58): C 49.31, H 5.17, N 16.99; found: C 48.31, H 5.33, N 16.56 %.

Spectroscopic Data:

IR (THF): $\tilde{\nu}$ (cm^{-1}) = 2077 (m) [ν(NC)], 1942 (s), 1894 (vs), 1880 (m) and 1810 (m) [ν(CO)], 1544 (m) [$\nu(C\text{-}C\text{-}N)_{pz}$].

ATR-IR (solid): $\tilde{\nu}$ (cm^{-1}) = 3016 (vw), 2924 (vw), 2854 (vw), 2548 (vw, sh), 2521 (w), 2071 (m) [*ν*(NC)], 1949 (s) [*ν*(CO)], 1899 (vs) [*ν*(CO)], 1870 (s) [*ν*(CO)], 1802 (s) [*ν*(CO)], 1542 (m) [$\nu(C\text{-}C\text{-}N)_{pz}$], 1445 (m), 1414 (m), 1380 (w), 1372 (m), 1351 (w, sh), 1306 (vw), 1203 (m), 1187 (m, sh), 1147 (vw), 1066 (m), 1044 (w), 981 (w), 907 (vw), 872 (vw), 853 (w), 811 (w), 790 (w), 775 (m), 744 (w), 711 (vw), 695 (w), 646 (w), 595 (w), 588 (w), 565 (w), 522 (w), 479 (m), 462 (w), 442 (vw), 422 (w).

^{1}H NMR: (300.1 MHz, C_6D_6, 298 K): *δ* (ppm) = 1.53 (s, 6H, $C^{2,6}$-*Me*, Mes), 1.70 (s, 3H, C^4-*Me*, Mes), 2.00, 2.22, 2.79, 2.96 (s, 3H each, $C^{3,5}$-*Me*, pz_B), 2.05, 2.34, 2.42, 3.01 (s, 6H each, $C^{3,5}$-*Me*, pz_A), 4.7 (br, $\Delta\nu_{1/2}$ = ~ 155 Hz, 2H, B*H*); this signal

is visible as a very broad hump over the base line in a strongly enlarged version of the spectrum), 5.43, 5.51 (s, 1H each, C^4-*H*, pz_B), 5.49, 5.68 (s, 2H each, C^4-*H*, pz_A), 6.14 (s, 2H, $C^{3,5}$-*H*, Mes).

^{1}H NMR: (300.1 MHz, THF-d_8, 298 K): δ (ppm) = 1.36 (s, 6H, $C^{2,6}$-*Me*, Mes), 2.15 (s, 3H, C^4-*Me*, Mes), 2.33 (s, 3H, C^5-*Me*, pz_B), 2.40 (s, 21H, ($C^{3,5}$-*Me*, pz_A) + (C5-Me, pz_A) + (C^5-*Me*, pz_B), 4 singlet signals overlap with each other), 2.56, 2.57 (s, 3H each, C^3-*Me*, pz_B), 2.69 (s, 6H, C^3-*Me*, pz_A), 4.6 ((br, $\Delta\nu_{1/2}$ = ~ 200 Hz, 1H, B*H*); this signal appears as a very broad hump over the base line in a strongly enlarged version of the spectrum), 5.71, 5.98 (s, 1H each, C^4-*H*, pz_B), 5.74, 5.90 (s, 2H each, pz_A), 6.67 (s, 2H, $C^{3,5}$-*H*, Mes).

^{13}C{^{1}H} NMR: (75.47 MHz, THF-d_8, 298 K): δ (ppm) = 12.7, 12.81 (s, 2C each, C^5-*Me*, pz_A), 12.77, 12.9 (s, 1C each, C^3-*Me*, pz_B), 15.4, 18.1 (s, 2C each, C^3-*Me*, pz_A), 15.5 (s, 2C (1 + 1), C^3-*Me*, pz_B, 2 singlet signal overlap with each other), 17.3 (s, 2C, $C^{2,6}$-*Me*, Mes) 21.0 (s, 1C, C^4-*Me*, Mes), 105.9, 107.6 (s, 2C each, *C*^{4}-H, pz_A), 106.7, 108.1 (s, 1C each, *C*^{4}-H, pz_B), 125.7 (s, 1C, *C*^{1}, Mes), 129.3 (s, 2C, *C*^{3,5}-H, Mes), 135.6 (s, 2C, *C*^{2,6}-Me, Mes), 139.6 (s, 1C, *C*^{4}-Me, Mes), 143.5, 146.1 (s, 2C each, *C*^{5}-Me, pz_A), 144.5, 146.4 (s, 1C each, *C*^{5}-Me, pz_B), 150.5, 151.4 (s, 2C each, *C*^{3}-Me, pz_A), 152.5, 153.3 (s, 1C each, *C*^{3}-Me, pz_B), 226.6, 228.1 (s, 2C each, *CO*).[47]

^{29}Si{^{1}H} NMR: (59.63 MHz, THF-d_8, 298 K): δ (ppm) = 369.7 (s).

4.5.34 [Tp'(CO)$_2$Mo≡Ge-Mo(CO)$_2$(MesNC)Tp'] (24-Mo)

A schlenck tube was charged with **22-Mo** (100 mg, 0.10 mmol) and MesNC (14 mg, 0.10 mmol, 1 equiv.). Toluene (10 mL) was added to this mixture at room temperature and stirred for 15 minutes, followed by heating to 75 °C for another 15 minutes. Upon heating, the color of the solution changed from dark red brown to bright red brown. Progress of the reaction was followed by IR and ^{31}P{^{1}H} NMR spectroscopy, which revealed a selective and complete conversion of the starting material into the product after 15 minutes of heating. Obtained bright red brown solution was concentrated to ~ 4 mL and then it was treated with 6 mL of *n*-pentane upon which a red brown solid precipitate out from the solution. The red brown precipitate was isolated by

[47] The signal of MesN*C* was not observed in the ^{13}C{^{1}H} NMR spectrum.

filtration of the light brown supernatant at room temperature. Isolated solid was dried *in vacuo* for 3 hours at ambient temperature and then 3 hours at 75 °C to obtain **24-Mo** as an analytically pure, air-sensitive, red brown solid. Yield: 97 mg (0.087 mmol, 91 %).

Properties: Complex **24-Mo** is well soluble in THF and fluorobenzene, moderately soluble in toluene and insoluble in Et_2O and aliphatic solvent.

Melting Points: The red brown solid decomposes upon melting to a dark brown liquid at 280 – 283 °C.

Elemental analysis: calcd (%) for $C_{44}H_{55}B_2GeMo_2N_{13}O_4$ (1046.98 g/mol): C 47.35, H 4.97, N 16.31; found: C 45.94, H 4.86, N 15.69.

Spectroscopic Data:

IR (THF): $\widetilde{\nu}$ (cm^{-1}) = 2075 (m) [ν(NC)], 1938 (s), 1888 (vs), 1879 (s, sh) and 1814 (m) [ν(CO)], 1544 (m) [$\nu(C\text{-}C\text{-}N)_{pz}$].

ATR-IR (solid): $\widetilde{\nu}$ (cm^{-1}) = 2978 (vw), 2962 (vw), 2952 (vw), 2922 (vw), 2912 (sh), 2858 (vw), 2554 (vw) [ν(BH)], 2516 (w) [ν(BH)], 2076 (m) [ν(NC)], 1941 (s) [ν(CO)], 1892 (vs) [ν(CO)], 1874 (vs) [ν(CO)], 1807 (s) [ν(CO)], 1543 (m) [$\nu(C\text{-}C\text{-}N)_{pz}$], 1472 (vw), 1445 (m), 1414 (m), 1381 (w), 1371 (m), 1350 (sh), 1306 (vw), 1247 (vw), 1202 (m), 1189 (m), 1147 (vw), 1066 (m), 1045 (w), 1035 (sh), 982 (vw), 958 (vw), 934 (vw), 906 (vw), 888 (vw), 871 (vw), 853 (w), 809 (m), 798 (sh), 787 (w), 773 (m), 745 (w), 714 (vw), 694 (m), 662 (vw), 647 (w), 631 (sh), 594 (w), 584 (w), 563 (w), 544 (vw), 520 (vw), 511 (vw), 486 (w), 473 (sh), 466 (sh), 462 (w), 449 (w), 429 (vw), 418 (w).

^{1}H NMR: (300.1 MHz, C_6D_6, 298 K): δ (ppm) = 1.55 (s, 6H, $C^{2,6}$-*Me*, Mes), 1.71 (s, 3H, C^4-*Me*, Mes), 2.01, 2.19, 2.77, 2.91 (s, 3H each, $C^{3,5}$-*Me*, pz_B), 2.05, 2.32, 2.43, 3.00 (s, 6H each, $C^{3,5}$-*Me*, pz_A), ~4.6 (br, $\Delta\nu_{1/2}$ = ~ 180 Hz, 2H, B*H*); this signal is visible as a very broad hump over the base line in a strongly enlarged version of the spectrum), 5.45, 5.49 (s, 1H each, C^4-*H*, pz_B), 5.50, 5.69 (s, 2H each, C^4-*H*, pz_A), 6.15 (s, 2H, $C^{3,5}$-*H*, Mes).

^{1}H NMR: (300.1 MHz, THF-d_8, 298 K): δ (ppm) = 1.40 (s, 6H, $C^{2,6}$-*Me*, Mes), 2.16 (s, 2H, C^{4}-*Me*, Mes), 2.33 (s, 3H, C^{5}-*Me*, pz_B), 2.39 (s, 12H, C^{5}-*Me*, pz_A + C^{3}-*Me*, pz_A), 2.40 (s, 3H, C^{5}-*Me*, pz_B), 2.41 (s, 6H, C^{5}-*Me*, pz_A), 2.55 (s, 3H, C^{3}-*Me*, pz_B), 2.56 (s, 3H, C^{3}-*Me*, pz_B), 2.68 (s, 6H, C^{3}-*Me*, pz_A), 5.72 (s, 1H, C^{4}-*H*, pz_B), 5.77 (s, 2H, C^{4}-*H*, pz_A), 5.89 (s, 2H, C^{4}-*H*, pz_A), 5.98 (s, 1H, C^{4}-*H*, pz_B), 6.69 (s, 2H, $C^{3,5}$-*H*, Mes).

^{13}C{^{1}H} NMR: (75.47 MHz, THF-d_8, 298 K): δ (ppm) = 12.7, 12.8 (s each, 2C, C^{5}-*Me*, pz_A), 12.85, 12.88 (s each, 1C, C^{5}-*Me*, pz_B), 15.4, 18.2 (s each, 2C, C^{3}-*Me*, pz_A), 15.5, 15.6 (s each, 1C, C^{3}-*Me*, pz_B), 17.5 (s, 2C, $C^{2,6}$-*Me*, Mes), 21.0 (s, 1C, C^{4}-*Me*, Mes), 106.1, 107.6 (s each, C^{4}-H, pz_A), 107.0, 108.1 (s each, 1C, C^{4}-H, pz_B), 125.9 (s, 1C, C^{1}, Mes), 129.3 (s, 2C, $C^{3,5}$-H, Mes), 135.1 (s, 2C, $C^{2,6}$-Me, Mes), 139.4 (s, 1C, C^{4}-Me, Mes), 143.6, 145.9 (s each, 2C, C^{5}-Me, pz_A), 144.9, 146.3 (s each, 1C, C^{5}-Me, pz_B), 150.5, 151.5 (s each, 2C, C^{3}-Me, pz_A), 152.6, 153.7 (s each, 1C, C^{3}-Me, pz_B), 182.7 (s, 1C, MesN*C*), 229.0, 229.6 (s each, 2C, *CO*).

4.5.35 [Tp'(CO)$_2$Mo(H)SiMo(CO)$_2$(PMe$_3$)Tp'][B{C$_6$H$_3$-3,5-(CF$_3$)$_2$}$_4$] (25-Mo)

A colorless solution of H(OEt$_2$)$_2$[B{C$_6$H$_3$-3,5-(CF$_3$)$_2$}$_4$] (49 mg, 0.048 mmol) in 5 mL of Et$_2$O was added to a stirred red brown suspension of **21-Mo**·0.6Et$_2$O (50 mg, 0.048 mmol) in 10 mL of Et$_2$O at –40 °C. Upon addition the red brown suspension rapidly changed to a bright red solution. An IR spectrum of an aliquot of the bright red solution was recorded after 10 minutes, which revealed that the starting material was completely consumed. The solution was concentrated to ~2.5 mL under reduce pressure at –40 °C, further cooled down to –60 °C and treated with cold (–60 °C) *n*-pentane, resulting the precipitation of the product as red oil. The mixture was frozen in liquid N$_2$ and scratched with spatula before melting. The whole mixture was slowly brought to room temperature and the pale yellow supernatant was filtered off to obtain slightly sticky bright red solid, which was pulverised by grinding it once by a freeze-pump-thaw cycle. The resulting orange powder was dissolved in 10 mL of Et$_2$O and concentrated to ~2 mL under reduced pressure. The obtained solution was treated with 2 mL of *n*-pentane at room temperature, upon which an orange microcrystalline solid precipitated out from the solution. The suspension was stored at –60 °C for 30 minutes and then filtered off the pale yellow supernatant to obtain an orange solid, which was washed with 2 mL of *n*-pentane at –60 °C and dried *in vacuo* for 30

minutes at ambient temperature to afford complex **25-Mo** as an air-sensitive, analytically pure, orange solid. Yield: 57 mg (0.03 mmol, 64%).

Properties: Complex **25-Mo** is well soluble in THF, Et_2O and fluorobenzene, insoluble in toluene and aliphatic solvents.

Melting Points: The solid melts to a reddish brown liquid at 116 – 117 °C.

Elemental analysis: calcd (%) for $C_{69}H_{66}B_3F_{24}Mo_2N_{12}O_4PSi$ (1866.67 g/mol): C 44.40, H 3.56, N 9.00; found C 44.68, H 3.76, N 8.50%.

Spectroscopic Data:

IR (Et_2O): $\tilde{\nu}$ (cm^{-1}) = 1982 (w), 1952 (s), 1916 (vs), 1887 (m) [ν(CO)], 1546 (m) [$\nu(C\text{-}C\text{-}N)_{pz}$].

IR (fluorobenzene): $\tilde{\nu}$ (cm^{-1}) = 1982 (w), 1951 (s), 1914 (vs), 1883 (m) [ν(CO)], 1545 (m) [$\nu(C\text{-}C\text{-}N)_{pz}$].

ATR-IR (solid): $\tilde{\nu}$ (cm^{-1}) = 3016 (vw), 2966 (vw), 2936 (vw), 2879 (vw), 2564 (vw) [ν(BH)], 1980 (w) [ν(CO)], 1952 (m) [ν(CO)], 1909 (s) [ν(CO)], 1873 (s) [ν(CO)], 1633 (vw), 1610 (vw), 1545 (m) [$\nu(C\text{-}C\text{-}N)_{pz}$], 1444 (w), 1417 (m), 1386 (vw), 1354 (s), 1314 (vw), 1275 (vs), 1202 (w), 1182 (w), 1161 (s), 1143 (w, sh), 1118 (vs), 1086 (w, sh), 1069 (m), 1046 (w), 986 (vw), 953 (m), 934 (w), 887 (m), 855 (w), 839 (m), 813 (w), 795 (m), 758 (vw), 745 (vw), 712 (m), 682 (s), 671 (s), 646 (w), 618 (vw), 595 (w), 581 (w), 558 (w), 492 (vw), 442 (m).

^{1}H NMR: (300.1 MHz, CD_2Cl_2, 298 K): δ (ppm) = –1.95 (d, ^3J(P,H) = 1.8 Hz, ^1J(Si,H) = 43.5 Hz, 1H, Si-*H*-Mo), 1.22 (d, ^2J(P,H) = 9.6 Hz, 9H, P*Me*$_3$), 2.25 (s, 3H, 1 × C^3-*Me*, $^{II}pz_B$), 2.35 (s, 3H, 1 × C^5-*Me*, $^{II}pz_B$), 2.42 (s, 6H, 2 × C^3-*Me* or 2 × C^5-*Me*, $^{I}pz_A$), 2.45 (s, 9H (6+3), 2 × C^3-*Me*, $^{II}pz_A$ and 1 × C^3-*Me* or 1 × C^5-*Me*, $^{I}pz_B$), 2.488 (s, 6H, 2 × C^3-*Me* or 2 × C^5-*Me*, $^{I}pz_A$), 2.493 (s, 6H, 2 × C^5-*Me*, $^{II}pz_A$), 2.51 (s, 3H, 1 × C^3-*Me* or 1 × C^5-*Me*, $^{I}pz_B$), 4.74 (br, $\Delta\nu_{1/2}$ = ~ 180 Hz, 2H, B*H*); this signal is visible as a very broad hump over the base line in a strongly enlarged version of the spectrum), 5.96 (s, 1H, 1 × C^4-*H*, $^{II}pz_B$), 5.98 (s, 2H, 2 × C^4-*H*, $^{I}pz_A$), 6.05 (s, 1H, 1 × C^4-*H*, $^{I}pz_B$), 6.14 (s, 2H, 2 × C^4-*H*,

$^{II}pz_A$), 7.58 (s, 4H, 4 × C^4-*H*, $B(C_6H_3$-3,5-$(CF_3)_2)_4$), 7.75 (m, 8H, 4 × $C^{2,6}$-*H*, $B(C_6H_3$-3,5-$(CF_3)_2)_4$).

$^{13}C\{^1H\}$ NMR: (75.47 MHz, CD_2Cl_2, 298 K): δ (ppm) = 12.8 (s, 2C, 2 × C^5-*Me*, $^{I}pz_A$), 13.15 (s, 2C, 2 × C^5-*Me*, $^{II}pz_A$), 13.2 (s, 1C, 1 × C^5-*Me*, $^{I}pz_B$), 13.4 (s, 1C, 1 × C^5-*Me*, $^{II}pz_B$), 15.51 (s, 1C, 1 × C^3-*Me*, $^{I}pz_B$), 15.55 (s, 1C, 1 × C^3-*Me*, $^{II}pz_B$), 16.7 (s, 2C, 2 × C^3-*Me*, $^{I}pz_A$), 18.1 (s, 2C, 2 × C^3-*Me*, $^{II}pz_A$), 20.2 (d, $^1J(^{13}C, ^{31}P)$ = 30.9 Hz, 3C, P*Me*$_3$), 107.2 (s, 2C, 2 × *C*^{4}-H, $^{I}pz_A$), 108.4 (s, 1C, 1 × *C*^{4}-H, $^{II}pz_B$), 108.5 (s, 1C, 1 × *C*^{4}-H, $^{I}pz_B$), 109.8 (s, 2C, 2 × *C*^{4}-H, $^{II}pz_A$), 117.9 (sept, ^3J(C,F) = 3.8 Hz, 4 × *C*^{4}-H, $B(C_6H_3$-3,5-$(CF_3)_2)_4$), 125.0 (q, ^1J(C,F) = 272.4 Hz, 8C, 8 × *C*F_3, $B(C_6H_3$-3,5-$(CF_3)_2)_4$), 129.3 (qq, ^2J(C,F) = 31.6 Hz, ^3J(C,B) = 2.9 Hz, 8C, 4 × *C*^{3,5}-CF_3, Ar^F), 135.2 (s, 8C, 4 × *C*^{2,6}-H, Ar^F), 146.6 (s, 2C, 2 × *C*^{5}-Me, $^{I}pz_A$), 147.1 (s, 1C, 1 × *C*^{5}-Me, $^{I}pz_B$), 148.7 (d, ^4J(C,P) = 1.2 Hz, 1C, 1 × *C*^{5}-Me, $^{II}pz_B$), 149.5 (s, 2C, 2 × *C*^{5}-Me, $^{II}pz_A$), 150.6 (s, 2C, 2 × *C*^{3}-Me, $^{I}pz_A$), 152.0 (d, ^3J(C,P) = 1.2 Hz, 1C, 1 × *C*^{3}-Me, $^{II}pz_B$), 153.0 (d, ^3J(C,P) = 1.4 Hz, 2C, 2 × *C*^{3}-Me, $^{II}pz_A$), 153.4 (s, 1C, 1 × *C*^{3}-Me, $^{I}pz_B$), 162.1 (q, ^1J(C,B) = 49.8 Hz, 4 × *C*^{1}, $B(C_6H_3$-3,5-$(CF_3)_2)_4$), 223.5 (d, ^4J(C,P) = 2.6 Hz, 2C, 2 × ^{I}*C*O), 227.2 (d, ^2J(C,P) = 7.3 Hz, 2C, 2 × ^{II}*C*O).

$^{31}P\{^1H\}$ NMR: (121.5 MHz, CD_2Cl_2, 298 K): δ (ppm) = 0.9 (s, ^2J(Si,P) = 87.2 Hz).

$^{29}Si\{^1H\}$ NMR: (59.63 MHz, CD_2Cl_2, 298 K): δ (ppm) = 460.7 (d, ^2J(Si, P) = 87.5 Hz).

$^{19}F\{^1H\}$ NMR: (282.4 MHz, CD_2Cl_2, 298 K): δ (ppm) = –63.1 (s).

4.5.36 [Tp'(CO)$_2$W(H)SiW(CO)$_2$(PMe$_3$)Tp'][B{C$_6$H$_3$-3,5-(CF$_3$)$_2$}$_4$] (25-W)

A mixture of **21-W** (100 mg, 0.08 mmol) and $H(OEt_2)_2[B\{C_6H_3$-3,5-$(CF_3)_2\}_4]$ (86 mg, 0.08 mmol, 1 equiv.) was treated with 10 mL of pre-cold (–60 °C) diethyl ether at –60 °C and stirred for 1 hour. Upon stirring, the suspension becomes clear and the red-brown color of the suspension turn lighter. After 1 hour, the suspension was treated with 2 mL of pre-cold *n*-hexane at –60 °C and filtered into another schlenck tube. The reddish orange filtrate was treated with 10 mL of *n*-hexane at –60 °C and then it was concentrated to ~ 10 mL at the same temperature, upon which a red oil precipitated out from the solution. The oily precipitate was collected by filtration of the light orange supernatant and pulverized once by a freeze-pump-thaw cycle to get a reddish

orange powder. The powder was redissolved in 5 mL of Et_2O and then ~ 15 mL of *n*-hexane was dropwisely added into this solution at ambient temperature. The addition of *n*-hexane resulted in the precipitation of a microcrystalline orange solid, which was isolated by filtration of the light orange supernatant and finally dried for 2 hours at ambient temperature to afford compound **25-W**·0.5(C_6H_{14}) as an extremely air-sensitive orange solid. Yield: 107 mg (0.05 mmol, 60%).

Properties: Complex **25-W** is well soluble in THF, Et_2O and fluorobenzene, insoluble in toluene and aliphatic solvents.

Melting Points: The orange solid melts to a dark orange liquid at 124 – 126 °C.

Elemental analysis: calcd (%) for $C_{69}H_{66}B_3F_{24}N_{12}O_4PSiW_2 \cdot 0.5C_6H_{14}$ (2085.56 g/mol): C 41.46, H 3.53, N 8.06; found C 41.79, H 3.47, N 7.73%.

Spectroscopic Data:

IR (Et_2O): $\tilde{\nu}$ (cm^{-1}) = 1967 (w), 1936 (s), 1897 (vs), 1867 (m) [ν(CO)], 1546 (m) [$\nu(C\text{-}C\text{-}N)_{pz}$].

IR (fluorobenzene): $\tilde{\nu}$ (cm^{-1}) = 1967 (w), 1934 (s), 1895 (vs), 1863 (m) [ν(CO)], 1546 (m) [$\nu(C\text{-}C\text{-}N)_{pz}$].

ATR-IR (solid): $\tilde{\nu}$ (cm^{-1}) = 2965 (vw), 2931 (vw), 2872 (vw), 2860 (vw, sh), 2564 (vw) [ν(BH)], 1968 (w) [ν(CO)], 1935 (m) [ν(CO)], 1892 (s) [ν(CO)], 1860 (m) [ν(CO)], 1635 (vw), 1609 (vw), 1545 (m) [$\nu(C\text{-}C\text{-}N)_{pz}$], 1494 (vw), 1446 (w), 1417 (m), 1385 (vw), 1352 (s), 1315 (vw), 1273 (vs), 1204 (w), 1180 (w), 1162 (s), 1117 (vs), 1095 (sh), 1068 (m), 1047 (w), 985 (vw), 953 (m), 936 (w), 897 (sh), 886 (m), 857 (w), 838 (m), 807 (w), 790 (m), 756 (vw), 744 (vw), 712 (s), 693 (vw), 681 (s), 669 (s), 646 (w), 638 (sh), 619 (vw), 595 (vw), 568 (m), 556 (w), 519 (vw), 505 (vw), 475 (vw), 446 (m), 401 (vw).

^{1}H NMR: (300.1 MHz, CD_2Cl_2, 298 K): δ (ppm) = 0.00 (d, ^3J(P,H) = 0.7 Hz, ^1J(Si,H) = 27.0 Hz, ^1J(W,H) = 29.2 Hz, ^2J(W,H) = 4.7 Hz, 1H, Si-*H*-W), 1.25 (d, ^2J(P,H) = 9.4 Hz, 9H, P*Me*$_3$), 2.26 (s, 3H, 1 × C^3-*Me*, $^{II}pz_B$), 2.36 (s, 3H, 1 × C^5-*Me*, $^{II}pz_B$), 2.41 (s, 6H, 2 × C^5-*Me*, $^{I}pz_A$), 2.44 (s, 3H, 1 × C^5-*Me*, $^{I}pz_B$), 2.481 (s, 2 × C^5-*Me*, $^{II}pz_A$), 2.484 (s, 6H, 2 × C^3-*Me* $^{II}pz_A$), 2.49 (s, 6H, 2 × C^3-*Me*, $^{I}pz_A$), 2.55 (s, 3H, 1 × C^3-*Me*, $^{I}pz_B$), 4.67 (br, $\Delta\nu_{1/2}$ = ~ 180 Hz, 2H, B*H*); this signal is

visible as a very broad hump over the base line in a strongly enlarged version of the spectrum), 5.98 (s, 1H, 1 × C^4-*H*, $^{II}pz_B$), 6.00 (s, 2H, 2 × C^4-*H*, $^{I}pz_A$), 6.07 (s, 1H, 1 × C^4-*H*, $^{I}pz_B$), 6.17 (s, 2H, 2 × C^4-*H*, $^{II}pz_A$), 7.56 (s, 4H, 4 × C^4-*H*, $B(C_6H_3\text{-}3,5\text{-}(CF_3)_2)_4$), 7.72 (m, 8H, 4 × $C^{2,6}$-*H*, $B(C_6H_3\text{-}3,5\text{-}(CF_3)_2)_4$).

$^{13}C\{^1H\}$ NMR: (75.47 MHz, CD_2Cl_2, 298 K): δ (ppm) = = 12.8 (s, 2C, 2 × C^5-*Me*, $^{I}pz_A$), 13.05 (s, 2C, 2 × C^5-*Me*, $^{II}pz_A$), 13.09 (s, 1C, 1 × C^5-*Me*, $^{I}pz_B$), 13.2 (s, 1C, 1 × C^5-*Me*, $^{II}pz_B$), 15.9 (s, 1C, 1 × C^3-*Me*, $^{II}pz_B$), 16.1 (s, 1C, 1 × C^3-*Me*, $^{I}pz_B$), 17.6 (s, 2C, 2 × C^3-*Me*, $^{I}pz_A$), 18.7 (s, 2C, 2 × C^3-*Me*, $^{II}pz_A$), 20.1 (d, $^1J(^{13}C, ^{31}P)$ = 33.6 Hz, 3C, P*Me*$_3$), 107.4 (s, 2C, 2 × *C*^{4}-H, $^{I}pz_A$), 108.5 (s, 1C, 1 × *C*^{4}-H, $^{II}pz_B$), 108.7 (s, 1C, 1 × *C*^{4}-H, $^{I}pz_B$), 110.0 (s, 2C, 2 × *C*^{4}-H, $^{II}pz_A$), 117.9 (sept, ^3J(C,F) = 3.8 Hz, 4 × *C*^{4}-H, $B(C_6H_3\text{-}3,5\text{-}(CF_3)_2)_4$), 125.0 (q, ^1J(C,F) = 272.4 Hz, 8C, 8 × *C*F$_3$, $B(C_6H_3\text{-}3,5\text{-}(CF_3)_2)_4$), 129.3 (qq, ^2J(C,F) = 31.6 Hz, ^3J(C,B) = 2.9 Hz, 8C, 4 × *C*^{3,5}-CF_3, Ar^F), 135.2 (s, 8C, 4 × *C*^{2,6}-H, Ar^F), 146.4 (s, 2C, 2 × *C*^{5}-Me, $^{I}pz_A$), 146.8 (s, 1C, 1 × *C*^{5}-Me, $^{I}pz_B$), 148.4 (d, ^4J(C,P) = 0.8 Hz, 1C, 1 × *C*^{5}-Me, $^{II}pz_B$), 149.3 (s, 2C, 2 × *C*^{5}-Me, $^{II}pz_A$), 151.0 (s, 2C, 2 × *C*^{3}-Me, $^{I}pz_A$), 152.0 (d, ^3J(C,P) = 1.0 Hz, 1C, 1 × *C*^{3}-Me, $^{II}pz_B$), 153.0 (d, ^3J(C,P) = 1.3 Hz, 2C, 2 × *C*^{3}-Me, $^{II}pz_A$), 153.9 (s, 1C, 1 × *C*^{3}-Me, $^{I}pz_B$), 162.2 (q, ^1J(C,B) = 49.8 Hz, 4 × *C*^{1}, $B(C_6H_3\text{-}3,5\text{-}(CF_3)_2)_4$), 218.9 (d, ^4J(C,P) = 2.1 Hz, 2C, 2 × ^{I}*C*O), 224.2 (d, ^2J(C,P) = 5.2 Hz, 2C, 2 × ^{II}*C*O).

$^{31}P\{^1H\}$ NMR: (121.5 MHz, CD_2Cl_2, 298 K): δ (ppm) = –22.2 (s, ^2J(Si,P) = 70.5 Hz, ^1J(W,P) = 195.3 Hz, ^3J(W,P) = 8.0 Hz).

$^{29}Si\{^1H\}$ NMR: (59.63 MHz, CD_2Cl_2, 298 K): δ (ppm) = 417.0 (d, ^2J(Si, P) = 70.5 Hz).

4.5.37 [Tp'(CO)$_2$Mo(H)GeMo(CO)$_2$(PMe$_3$)Tp'][B{C$_6$H$_3$-3,5-(CF$_3$)$_2$}$_4$] (26-Mo)

Compound **22-Mo** (100 mg, 0.10 mmol) was suspended in 10 mL of Et_2O and to this red-brown suspension a colorless solution of $H(OEt_2)_2[B\{C_6H_3\text{-}3,5\text{-}(CF_3)_2\}_4]$ (97 mg, 0.10 mmol) in 5 mL of Et_2O was added at ambient temperature. Immediate after addition the red-brown suspension changed to a yellowish brown solution. An IR spectrum after 2 minutes revealed a selective conversion of **22-Mo** to **26-Mo**. The solution was treated with 5 mL of *n*-hexane and filtered into another schlenck tube. The yellowish brown filtrate was concentrated to ~10 mL and stored at +5°C for crystallization. A dark brown crystalline solid that forms upon crystallization

was isolated by filtration of a light orange supernatant at 0 °C and was dried for 3 hours at 75 °C. Yield: 131 mg (0.07 mmol, 72%).

Properties: Complex **26-Mo** is well soluble in THF, Et_2O and fluorobenzene, insoluble in toluene and aliphatic solvents.

Melting Points: The solid melts to a red-brown liquid at 167 – 169 °C.

Elemental analysis: calcd (%) for $C_{69}H_{66}B_3F_{24}GeMo_2N_{12}O_4P$ (1911.20 g/mol): C 43.36, H 3.48, N 8.79; found C 42.97, H 3.69, N 8.59%.

Spectroscopic Data:

IR (Et_2O): $\tilde{\nu}$ (cm^{-1}) = 1984 (w), 1954 (s), 1917 (vs), 1891 (m) [ν(CO)], 1546 (m) [$\nu(C\text{-}C\text{-}N)_{pz}$].

ATR-IR (solid): $\tilde{\nu}$ (cm^{-1}) = 3001 (sh), 2981 (vw), 2966 (vw), 2930 (vw), 2869 (vw), 2569 (vw) [ν(BH)], 1992 (w) [ν(CO)], 1950 (m) [ν(CO)], 1902 (s) [ν(CO)], 1879 (s) [ν(CO)], 1608 (vw), 1590 (vw), 1545 (m) [$\nu(C\text{-}C\text{-}N)_{pz}$], 1493 (vw), 1443 (w), 1416 (m), 1387 (sh), 1374 (sh), 1365 (sh), 1352 (s), 1314 (vw), 1272 (vs), 1204 (w), 1182 (m), 1163 (s), 1140 (sh), 1118 (vs), 1094 (sh), 1070 (s), 1046 (w), 1036 (sh), 985 (vw), 951 (w), 936 (w), 898 (w), 887 (w), 855 (w), 839 (w), 813 (w), 799 (m), 783 (sh), 745 (vw), 732 (vw), 712 (m), 693 (w), 681 (m), 670 (m), 646 (w), 637 (sh), 618 (vw), 595 (sh), 586 (w), 562 (w), 550 (sh), 539 (vw), 513 (vw), 489 (vw), 473 (vw), 460 (vw), 448 (w), 437 (w), 427 (w), 401 (vw).

^{1}H NMR: (300.1 MHz, CD_2Cl_2, 298 K): δ (ppm) = –0.52 (d, ^3J(P,H) = 1.6 Hz, 1H, Ge-H-Mo), 1.18 (d, ^2J(P,H) = 9.3 Hz, 9H, P*Me*$_3$), 2.24 (s, 3H, 1 × C^3-*Me*, $^{II}pz_B$), 2.35 (s, 3H, 1 × C^5-*Me*, $^{II}pz_B$), 2.42 (s, 6H, 2 × C^5-*Me*, $^{I}pz_A$), 2.43 (s, 3H, 1 × C^5-*Me*, $^{I}pz_B$), 2.45 (s, 6H, 2 × C^3-*Me*, $^{I}pz_A$), 2.47 (s, 6H, 2 × C^3-*Me*, $^{II}pz_A$), 2.48 (s, 6H, 2 × C^5-*Me*, $^{II}pz_A$), 2.52 (s, 3H, 1 × C^3-*Me*, $^{I}pz_B$), 4.68 (br, $\Delta\nu_{1/2}$ = ~ 180 Hz, 2H, B*H*); this signal is visible as a very broad hump over the base line in a strongly enlarged version of the spectrum), 5.97 (s, 1H, 1 × C^4-*H*, $^{II}pz_B$), 5.98 (s, 2H, 2 × C^4-*H*, $^{I}pz_A$), 6.05 (s, 1H, 1 × C^4-*H*, $^{I}pz_B$), 6.14 (s, 2H, 2 × C^4-*H*, $^{II}pz_A$), 7.57 (s,

4H, 4 × C^4-*H*, $B(C_6H_3$-3,5-$(CF_3)_2)_4$), 7.74 (m, 8H, 4 × $C^{2,6}$-*H*, $B(C_6H_3$-3,5-$(CF_3)_2)_4$).

$^{13}C\{^1H\}$ NMR: (75.47 MHz, CD_2Cl_2, 298 K): δ (ppm) = = 12.8 (s, 2C, 2 × C^5-*Me*, $^{I}pz_A$), 13.1 (s, 2C, 2 × C^5-*Me*, $^{II}pz_A$), 13.2 (s, 1C, 1 × C^5-*Me*, $^{I}pz_B$), 13.3 (s, 1C, 1 × C^3-*Me*, $^{II}pz_B$), 15.6 (s, 1C, 1 × C^3-*Me*, $^{II}pz_B$), 15.7 (s, 1C, 1 × C^5-*Me*, $^{I}pz_B$), 16.9 (s, 2C, 2 × C^3-*Me*, $^{I}pz_A$), 18.2 (s, 2C, 2 × C^3-*Me*, $^{II}pz_A$), 20.3 (d, $^1J(^{13}C, ^{31}P)$ = 30.1 Hz, 3C, P*Me*$_3$), 107.3 (s, 2C, 2 × *C*^{4}-H, $^{I}pz_A$), 108.55 (s, 1C, 1 × *C*^{4}-H, $^{II}pz_B$), 108.62 (s, 1C, 1 × *C*^{4}-H, $^{I}pz_B$), 109.8 (d, $^4J(^{13}C, ^{31}P)$ = 0.6 Hz, 2C, 2 × *C*^{4}-H, $^{II}pz_A$), 117.9 (sept, ^3J(C,F) = 3.8 Hz, 4 × *C*^{4}-H, $B(C_6H_3$-3,5-$(CF_3)_2)_4$), 125.0 (q, ^1J(C,F) = 272.4 Hz, 8C, 8 × *C*F$_3$, $B(C_6H_3$-3,5-$(CF_3)_2)_4$), 129.3 (qq, ^2J(C,F) = 31.6 Hz, ^3J(C,B) = 2.9 Hz, 8C, 4 × *C*^{3,5}-CF_3, Ar^F), 135.2 (s, 8C, 4 × *C*^{2,6}-H, Ar^F), 146.5 (s, 2C, 2 × *C*^{5}-Me, $^{I}pz_A$), 147.2 (s, 1C, 1 × *C*^{5}-Me, $^{I}pz_B$), 148.8 (d, ^4J(C,P) = 1.3 Hz, 1C, 1 × *C*^{5}-Me, $^{II}pz_B$), 149.4 (s, 2C, 2 × *C*^{5}-Me, $^{II}pz_A$), 150.5 (s, 2C, 2 × *C*^{3}-Me, $^{I}pz_A$), 152.1 (d, ^3J(C,P) = 1.2 Hz, 1C, 1 × *C*^{3}-Me, $^{II}pz_B$), 153.2 (d, ^3J(C,P) = 1.6 Hz, 2C, 2 × *C*^{3}-Me, $^{II}pz_A$), 153.3 (s, 1C, 1 × *C*^{3}-Me, $^{I}pz_B$), 162.1 (q, ^1J(C,B) = 49.8 Hz, 4 × *C*^{1}, $B(C_6H_3$-3,5-$(CF_3)_2)_4$), 225.8 (d, ^4J(C,P) = 2.8 Hz, 2C, 2 × ^{I}*C*O), 229.0 (d, ^2J(C,P) = 7.4 Hz, 2C, 2 × ^{II}*C*O).

$^{31}P\{^1H\}$ NMR: (121.5 MHz, CD_2Cl_2, 298 K): δ (ppm) = –2.9 (s).

$^{19}F\{^1H\}$ NMR: (282.4 MHz, CD_2Cl_2, 298 K): δ (ppm) = –63.1 (s).

4.5.38 [Tp'(CO)$_2$Mo(η^3-AuPMe$_3$)SiMo(CO)$_2$(Cl)Tp'] (27-Mo)

A mixture of complex **21-Mo** (200 mg, 0.20 mmol) and [(PMe$_3$)AuCl] (62mg, 0.20 mmol, 1 equiv.) was treated with 10 mL of toluene at ambient temperature. The resulting red-brown suspension was stirred at ambient temperature for 20 hours. Upon stirring the red-brown suspension slowly turn into an orange suspension. Complete consumption of the starting material was confirmed by IR spectroscopy. The resulting suspension was treated with 5 mL of *n*-pentane, upon which a yellowish orange solid precipitated out, which was isolated by filtration. Isolated solid was redissolved in 10 mL of fluorobenzene and was treated with 4 mL of *n*-pentane. The orange suspension was filtered into another schlenck tube and concentrated to ~ 2 mL. The resulting suspension was treated with 4 mL of *n*-pentane and stored at 0 °C for 15 minutes. The yellowish orange solid precipitated out was isolated by filtration of the pale yellow supernatant at

0 °C and was dried shortly under reduced pressure. Finally, the yellowish orange solid was crystallized from 2:1 *n*-pentane/CH_2Cl_2 (10 mL) mixture and the microcrystalline yellowish orange solid obtained, was dried under reduced pressure for 2 hours at ambient temperature to get an analytically pure, moderately air sensitive yellowish orange solid. Yield: 157 mg (0.13 mmol, 64 %).

Properties: Complex **27-Mo** is moderately soluble in THF and fluorobenzene, sparingly soluble in toluene and insoluble in aliphatic solvents.

Melting Points: Compound **27-Mo** shows a very high thermal stability and only decomposes at 313 – 315 °C to a brown solid.

Elemental analysis: calcd (%) for $C_{37}H_{53}AuB_2ClMo_2N_{12}O_4PSi$ (1234.88): C 35.99, H 4.33, N 13.61; found: C 36.30, H 4.54, N 13.28 %.

Spectroscopic Data:

IR (THF): $\tilde{\nu}$ (cm^{-1}) = 1921 (s), 1885 (m), 1835 (vs) and 1821 (m) [ν(CO)], 1545 (m) [$\nu(C\text{-}C\text{-}N)_{pz}$].

ATR-IR (solid): $\tilde{\nu}$ (cm^{-1}) = 2952 (vw), 2922 (vw), 2858 (vw), 2547 (vw, sh) [ν(BH)], 2525 (vw) [ν(BH)], 1916 (s) [ν(CO)], 1882 (s) [ν(CO)], 1827 (vs, sh) [ν(CO)], 1815 (vs) [ν(CO)], 1542 (m) [$\nu(C\text{-}C\text{-}N)_{pz}$], 1492 (vw), 1443 (m), 1412 (s), 1381 (m, sh), 1371 (s), 1351 (w, sh), 1309 (vw), 1290 (w), 1202 (s), 1149 (w), 1128 (vw), 1065 (m), 1044 (w), 981 (w), 955 (s), 871 (vw), 853 (w), 810 (m), 778 (m), 744 (w), 692 (m), 674 (w), 674 (vw), 645 (m), 628 (w), 586 (w), 532 (s), 518 (w), 476 (w), 459 (m), 427 (vw), 412 (vw).

^{1}H NMR: (300.1 MHz, CD_2Cl_2, 298 K): δ (ppm) = 0.92 (d, ^2J(P,H) = 9.7 Hz, 9H, P*Me*$_3$), 2.31 (s, 3H, C^3-*Me*, pz_B)[48], 2.40, 2.43 (s, 6H each, C^5-*Me*, pz_A), 2.41 (s, 3H, C^5-*Me*, pz_B), 2.42 (s, 6H (3H + 3H), C^3-*Me* + C^5-*Me*, pz_B, two signal overlap with each other), 2.47, 2.74 (s, 6H each, C^3-*Me*, pz_A), 4.73 (br, $\Delta\nu_{1/2}$ = ~ 160 Hz, 2H, B*H*); this signal is visible as a very broad hump over the base line in a strongly enlarged version of the spectrum), 5.86, 5.89 (s, 2H each, C^4-*H*, pz_A), 5.88 (s, 2H (1H + 1H), C^4-*H*, pz_B, two signal overlap with each other).

[48] Two different Tp' ligands on two molybdenum center can't be differentiate from correlation spectra.

$^{13}C\{^1H\}$ NMR: (75.47 MHz, CD_2Cl_2, 298 K): δ (ppm) = 12.8, 12.9 (s, 2C each, C^5-*Me*, pz_A), 13.2, 13.5 (s, 1C each, C^5-*Me*, pz_B), 14.5 (d, $^1J(^{13}C, ^{31}P)$ = 28.7 Hz, 3C, P*Me*$_3$), 15.2, 15.3 (s, 1C each, C^3-*Me*, pz_B), 15.5, 17.6 (s, 2C each, C^3-*Me*, pz_A), 106.6, 107.0 (s, 2C each, C^4-H, pz_A), 107.1, 107.6 (s, 1C each, C^4-H, pz_B), 144.8, 144.9 (s, 2C each, C^5-Me, pz_A), 145.8, 146.5 (s, 1C each, C^5-Me, pz_B), 151.6, 152.4 (s, 2C each, C^3-Me, pz_A), 153.6, 153.7 (s, 1C each, C^3-Me, pz_B), 227.7, 233.9 (s, 2C each, *C*O).

$^{31}P\{^1H\}$ NMR: (121.5 MHz, CD_2Cl_2, 298 K): δ (ppm) = 25.7 (s, ^2J(Si,P) = 89 Hz).

$^{29}Si\{^1H\}$ NMR: (59.63 MHz, CD_2Cl_2, 298 K): δ (ppm) = 265.7 (d, ^2J(Si, P) = 89 Hz).

4.5.39 [Tp'(CO)$_2$Mo(η^3-AuPMe$_3$)GeMo(CO)$_2$(Cl)Tp'] (28-Mo)

To a brown solution of **22-Mo** (100 mg, 10 mmol) in 10 mL of toluene, solid [(PMe$_3$)AuCl] (30 mg, 0.10 mmol, 1 equiv.) was added at ambient temperature and stirred for 5 hours. Upon stirring, the brown solution changed to a light red-brown suspension. The progress of the reaction was followed by IR spectroscopy which revealed a selective conversion of the starting material into the product. The suspension was concentrated to ~6 mL, treated with 6 mL of *n*-pentane and stirred for another 30 minutes at ambient temperature. The reddish orange precipitate that formed was isolated by filtration of the light brown supernatant at ambient temperature and dried for 2 hours at 75 °C. Analytically pure, reddish orange solid was obtained by crystallization of the **28-Mo** from Et_2O at –30 °C. Yield: 88 mg (0.07 mmol, 72%).

Properties: Complex **28-Mo** is moderately soluble in THF and fluorobenzene, sparingly soluble in toluene and insoluble in aliphatic solvents.

Melting Points: Compound **28-Mo** shows a quite high thermal stability and only decomposes at 198 – 201 °C to a black mass.

Elemental analysis: calcd (%) for $C_{37}H_{53}AuB_2ClGeMo_2N_{12}O_4P$ (1279.40): C 34.73, H 4.18, N 13.14; found: C 35.13, H 4.20, N 11.87 %.

Spectroscopic Data:

IR (THF): $\tilde{\nu}$ (cm^{-1}) = 1925 (s), 1887 (s), 1837 (vs) and 1827 (s, sh) [ν(CO)], 1545 (m) [$\nu(C\text{-}C\text{-}N)_{pz}$].

ATR-IR (solid): $\tilde{\nu}$ (cm^{-1}) = 3022 (vw), 2974 (vw), 2953 (vw), 2924 (vw), 2908 (sh), 2894 (sh), 2862 (vw), 2814 (vw), 2542 (vw, sh) [ν(BH)], 2522 (vw) [ν(BH)], 1916 (s) [ν(CO)], 1875 (s) [ν(CO)], 1839 (m), 1822 (s, sh) [ν(CO)], 1811 (vs) [ν(CO)], 1542 (m) [$\nu(C\text{-}C\text{-}N)_{pz}$], 1494 (vw), 1443 (m), 1412 (m), 1380 (m, sh), 1370 (m), 1351 (w, sh), 1308 (vw), 1290 (w), 1280 (sh), 1350 (vw), 1199 (s), 1185 (sh), 1153 (vw), 1129 (vw), 1064 (m), 1044 (w), 972 (sh), 956 (s), 869 (vw), 852 (w), 811 (m), 793 (s), 779 (m), 758 (w), 749 (w), 731 (w), 693 (m), 678 (w), 646 (m), 628 (vw), 617 (vw), 590 (sh), 579 (w), 564 (sh), 515 (w), 477 (vw), 462 (m), 432 (vw).

^{1}H NMR: (300.1 MHz, THF-d_8, 298 K): δ (ppm) = 0.98 (d, ^{2}J(P,H) = 10.3 Hz, 9H, P*Me*$_3$), 2.30 and 2.46 (s each, 3H each, C^3-*Me*, pz_B)[49], 2.38 (s, 3H, C^5-*Me*, pz_B), 2.40 (s, 15H, (4 × C^5-*Me*, pz_A) + (C^5-*Me*, pz_B); three signals overlap with each other), 2.47, 2.74 (s, 6H each, C^3-*Me*, pz_A), 4.73 (br, $\Delta\nu_{1/2}$ = ~ 160 Hz, 2H, B*H*); this signal is visible as a very broad hump over the base line in a strongly enlarged version of the spectrum), 5.79, 5.85 (s, 2H each, C^4-*H*, pz_A), 5.81, 5.82 (s, 1H each, C^4-*H*, pz_B).

^{13}C{^{1}H} NMR: (75.47 MHz, CD_2Cl_2, 298 K): δ (ppm) = 12.6, 12.8 (s, 2C each, C^5-*Me*, pz_A), 13.1, 13.3 (s, 1C each, C^5-*Me*, pz_B), 14.2 (d, ^{1}J(^{13}C, ^{31}P) = 30.2 Hz, 3C, P*Me*$_3$), 15.6, 15.7 (s, 1C each, C^3-*Me*, pz_B), 15.8, 17.9 (s, 2C each, C^3-*Me*, pz_A), 106.9, 107.1 (s, 2C each, *C*^{4}-H, pz_A), 107.4, 107.9 (s, 1C each, *C*^{4}-H, pz_B), 144.0, 144.6 (s, 2C each, *C*^{5}-Me, pz_A), 145.2, 146.1 (s, 1C each, *C*^{5}-Me, pz_B), 151.8, 152.9 (s, 2C each, *C*^{3}-Me, pz_A), 153.6, 153.8 (s, 1C each, *C*^{3}-Me, pz_B), 227.5, 237.6 (s, 2C each, *C*O).

^{31}P{^{1}H} NMR: (121.5 MHz, CD_2Cl_2, 298 K): δ (ppm) = 19.4 (s).

4.5.40 [Tp'(CO)$_2$Mo=Si(I)–Mo(CO)$_2$(Me)Tp'] (29-Mo)

To a red-brown solution of **21-Mo** (200 mg, 0.20 mmol) in 10 mL of chlorobenzene, MeI (57 mg, 0.40 mmol, 2 equiv.) was added at ambient temperature and the reaction mixture was heated to 110 °C for 30 minutes. Upon heating, the color of the solution changed from red-brown to

[49] Two different Tp' ligands on two molybdenum center can't be differentiate from correlation spectra.

reddish-orange. Monitoring of the reaction by IR spectroscopy revealed a selective conversion of the starting material into the product. The reddish-orange solution was concentrated to ~5 mL, and the resulting suspension was treated with 10 mL of *n*-pentane and stored at 0 °C for 15 minutes. The yellow amorphous solid that precipitated out was isolated by filtration of the reddish-orange supernatant at 0 °C. The isolated yellow solid was washed with *n*-pentane (2 × 1.5 mL) and dried under reduced pressure for 30 minutes at ambient temperature to afford **29-Mo** as an analytically pure yellow solid. Yield: 147 mg (0.14 mmol, 69%).

Properties: Complex **29-Mo** is moderately soluble in THF and fluorobenzene, sparingly soluble in toluene and insoluble aliphatic solvents.

Melting Points: The yellow solid decomposes at 292 – 294 °C to give a brown mass.

Elemental analysis: calcd (%) for $C_{35}H_{47}B_2IMo_2N_{12}O_4Si$ (1068.32 g/mol): C 39.35, H 4.43, N 15.73; found: C 39.19, H 4.48, N 15.60.

Spectroscopic Data:

IR (THF): $\tilde{\nu}$ (cm^{-1}) = 1936 (s), 1906 (m), 1852 (vs), 1839 (s) [ν(CO)], 1546 (m) [ν(C-C-N)$_{pz}$].

IR (CH_2Cl_2): $\tilde{\nu}$ (cm^{-1}) = 1936 (s), 1906 (m), 1848 (vs), 1836 (sh) [ν(CO)], 1546 (m) [ν(C-C-N)$_{pz}$].

IR (chlorobenzene): $\tilde{\nu}$ (cm^{-1}) = 1934 (s), 1905 (m), 1847 (vs), 1836 (sh) [ν(CO)], 1546 (m) [ν(C-C-N)$_{pz}$].

ATR-IR (solid): $\tilde{\nu}$ (cm^{-1}) = 3126 (vw), 2972 (vw), 2958 (vw), 2927 (vw), 2913 (sh), 2860 (vw), 2820 (vw), 2733 (vw), 2548 (vw) and 2530 (vw) [ν(BH)], 1930 (s), 1905 (m), 1845 (vs) and 1831 (vs) [ν(CO)], 1545 (m) [ν(C-C-N)$_{pz}$], 1487 (vw), 1446 (m), 1414 (m), 1380 (m), 1371 (m), 1352 (sh), 1298 (vw), 1288 (vw), 1252 (w), 1205 (m), 1197 (m), 1146 (vw), 1131 (vw), 1065 (m), 1046 (m), 1036 (sh), 983 (w), 974 (sh), 872 (vw), 855 (w), 812 (m), 785 (m), 776 (sh), 713 (m), 691 (m), 666 (vw), 644 (m), 631 (w), 622 (w), 604 (w), 585 (w), 571 (sh), 516 (w), 473 (w), 459 (m), 433 (m).

^{1}H NMR: (300.1 MHz, CD_2Cl_2, 298 K): δ (ppm) = 0.57 (s, Mo-*Me*), 2.24, 2.39, (s, 3H each, C^3-*Me*, pz_B), 2.36 – 2.48 (two sharp s and two very br signal overlap with each other, 18 H, (2 × C^3-*Me*, pz_A) + (2 × C^5-*Me*, pz_B)), 2.45, 2.48 (s, 6H each, 2 × C^5-*Me*, pz_A), ~ 4.8 (br, $\Delta\nu_{1/2}$ = ~ 180 Hz, 2H, B*H*); this signal is visible as a very broad hump over the base line in a strongly enlarged version of the spectrum), 5.87, 5.90 (s, 1H each, C^4-*H*, pz_B), 5.94 (one sharp s & one br s overlap with each other, 4H, C^4-*H*, pz_A).

^{13}C{^{1}H} NMR: (125.77 MHz, CD_2Cl_2, 298 K): δ (ppm) = –34.0 (s, 1C, Mo-*Me*), 12.88, 12.93 (s, 2C each, 2 × C^5-*Me*, pz_A), 13.5, 13.6 (s, 1C each, 1 × C^5-*Me*, pz_B), 14.84, 17.10 (very br s, 2C, 2 × C^3-*Me*, pz_A), 107.4 (very br s, 2C, 2 × C^4-H, pz_A), 107.6 (s, 2C, 2 × C^4-H, pz_A), 107.8, 107.9 (s, 1C each, C^4-H, pz_B), 145.5, 146.0 (br s, 2C each, 2 × C^5-Me, pz_A), 146.5, 146.9 (s, 1C each, C^5-Me, pz_B), 153.1, 153.8 (very br s, 2C each, 2 × C^3-Me, pz_A), 153.5, 154.6 (s, 1C each, C^3-Me, pz_B), 226.2 (very br s, 2 × *C*O).[50]

^{29}Si{^{1}H} NMR: (59.63 MHz, CD_2Cl_2, 298 K): δ (ppm) = 222.0 (s).

4.5.41 [K(diglyme)]$_2$[Tp'(CO)$_2$Mo=Si=Mo(CO)$_2$Tp'] (30-Mo)

A mixture of **21-Mo** (200mg, 0.20 mmol) and KC_8 (57 mg, 0.42 mmol, 2.1 equiv.) was suspended in 15 mL of DME and the red brown suspension was stirred for 30 minutes at ambient temperature, upon which the color of the suspension changed to blackish yellow. Completion of the reaction was confirmed by IR spectroscopy and the reaction mixture was evaporated to dryness in *vacuo*. The blackish yellow residue was extracted with diglyme (2 × 10 mL). The combined bright yellow extract was concentrated to *ca.* 12 mL, upon which a bright yellow microcrystalline solid precipitated out from the solution. The precipitate was isolated by filtration and dried in *vacuo* for 3 hours at ambient temperature to give 123 mg of complex **30-Mo**. A second crop of the product (26 mg) was obtained upon concentration of the mother liquor to *ca.* 5 mL and subsequent treatment with 5 mL of *n*-pentane and storage at –30 °C for 24 hours. Combined yield: 149 mg (0.117 mmol, 59%).

[50] One set of CO signal is not visible because of very broadness. Some signals appear as a very broad and the $\Delta\nu_{1/2}$ can't be determine because of either overlap with other signals or because of lack of proper shape of the signal.

Properties: The yellow solid is moderately soluble in diglyme, sparingly soluble in DME and insoluble in Et_2O. Immediately react with THF or CH_2Cl_2. Extremely sensitive towards O_2 and moisture.

Melting Points: The complex **30-Mo** shows extremely high thermal stability and only starts changing color from yellow to gray at 318 °C and completely decomposes to a dark black solid at 328 – 329 °C.

Elemental analysis: calcd (%) for $C_{34}H_{44}B_2K_2Mo_2N_{12}O_4Si \cdot 2diglyme$ (1272.92 g/mol): C 43.40, H 5.70, N 13.20; found: C 42.82, H 5.93, N 13.03.

Spectroscopic Data:

ATR-IR (solid): $\tilde{\nu}$ (cm^{-1}) = 2981 (vw) 2954 (vw), 2919 (w), 2878 (vw, sh), 2820 (vw), 2548 (vw) [ν(BH)], 2527 (vw) [ν(BH)], 1765 (s) [ν(CO)], 1696 (vs) [ν(CO)], 1539 (m) [$\nu(C\text{-}C\text{-}N)_{pz}$], 1475 (vw), 1441 (w), 1411 (m), 1372 (m), 1351 (w), 1298 (vw), 1247 (vw), 1198 (m), 1187 (m, sh), 1141 (w, sh), 1128 (w), 1099 (m), 1065 (m), 1037 (m), 1015 (w), 981 (w), 919 (vw), 866 (vw, sh), 849 (m), 809 (m), 797 (w, sh), 767 (m), 695 (m), 665 (vw), 644 (w), 605 (w), 637 (vw, sh), 525 (w), 498 (s), 462 (w), 450 (vw), 431 (vw).

The solution NMR spectra of complex **30-Mo** could not be meassured due to its insolubility and high sensitivity towards common deuterated solvent.

4.5.42 [Tp'(CO)$_2$MoSiC(Me)C(Me)Mo(CO)$_2$Tp'] (31-Mo)

To a stirred red-brown solution of **21-Mo** (200 mg, 0.20 mmol) in 6 mL of chlorobenzene, precooled (0 °C) 2-butyne (0.05 mL, 35 mg, 0.64 mmol, 3.2 equiv.) was added via a syringe at 0 °C. The reaction mixture was warmed to room temperature and stirred for 5 minutes. No reaction was observed at this temperature according to IR spectroscopy. The red-brown solution was then immersed in a preheated oil bath (100 °C). Within 5 minutes the color of the solution changed from red-brown to orange. An IR spectrum was recorded of the orange solution after 10 minutes and revealed the complete consumption of the starting material and selective formation of complex **31-Mo**. The orange solution was cooled to room temperature, treated with 4 mL of *n*-hexane and filtered. The orange filtrate was evaporated to dryness under reduced pressure. The

resulting yellow solid was washed at ambient temperature with an Et_2O/*n*-hexane mixture (2:1, 6 mL) and finally dried at ambient temperature to afford **31-Mo** as an analytically pure yellow powder. Yield: 171 mg (0.174 mmol, 87%).

Properties: The yellow solid is well soluble in THF and toluene, moderately soluble in Et_2O, sparingly soluble in *n*-hexane.

Melting Points: The solid decomposes upon heating to a brown mass at 285 – 287 °C.

Elemental analysis: calcd (%) for $C_{38}H_{50}B_2Mo_2N_{12}O_4Si$·(980.47 g/mol): C 46.55, H 5.14, N 17.14; found: C 46.69, H 5.23, N 17.10.

Spectroscopic Data:

IR (THF): $\tilde{\nu}$ (cm^{-1}) = 1943 (s), 1898 (w), 1869 (vs), 1828 (w) [ν(CO)], 1545 (m) [ν(C-C-N)$_{pz}$].

IR (toluene): $\tilde{\nu}$ (cm^{-1}) = 1944 (s), 1899 (w), 1870 (vs), 1830 (vw) [ν(CO)], 1545 (m) [ν(C-C-N)$_{pz}$].

ATR-IR (solid): $\tilde{\nu}$ (cm^{-1}) = 2981 (vw), 2961 (vw), 2926 (w), 2862 (vw), 2548 (w) [ν(BH)], 2532 (w) [ν(BH)],, 1936 (s) [ν(CO)], 1893 (m) [ν(CO)], 1858 (vs) [ν(CO)], 1822 (m) [ν(CO)], 1543 (m) [ν(C-C-N)$_{pz}$], 1490 (vw), 1448 (m), 1414 (m), 1375 (m), 1350 (m), 1202 (s), 1147 (w), 1114 (w), 1067 (m), 1046 (m), 983 (w), 892 (vw), 872 (vw), 854 (w), 813 (m), 791 (sh), 778 (s), 694 (m), 665 (vw), 640 (s), 628 (sh), 584 (m), 565 (w), 519 (w), 497 (vw), 479 (w), 457 (s).

^{1}H NMR: (300.1 MHz, C_6D_6, 298 K): δ (ppm) = 1.68 (s, 6H, 2 × C-*Me*), 2.13 (s, 6H, 2 × C^5-*Me*, 2 × pz_B), 2.19 (s, 12H, 4 × C^5-*Me*, 4 × pz_A), 2.30 (s, 12H, 4 × C^3-*Me*, 4 × pz_A), 2.66 (s, 6H, 2 × C^3-*Me*, 2 × pz_B), 4.8 ((br, $\Delta\nu_{1/2}$ = ~ 140 Hz, 2H, 2 × B*H*); this signal appears as a very broad hump over the base line in a strongly enlarged version of the spectrum), 5.45 (s, 2H, 2 × C^4-*H*, 2 × pz_B), 5.59 (s, 4H, 4 × C^4-*H*, 4 × pz_A).

^{13}C{^{1}H} NMR: (75.47 MHz, C_6D_6, 298 K): δ (ppm) = 12.7 (s, 4C, 4 × C^5-*Me*, 4 × pz_A), 13.0 (s, 2C, 2 × C^5-*Me*, 2 × pz_B), 15.3 (s, 4C, 4 × C^3-*Me*, 4 × pz_A), 15.6 (s, 2C, 2 × C^3-*Me*, 2 × pz_B), 23.2 (s, 2C, 2 × C-*Me*), 106.6 (s, 4C, 4 × *C*^{4}-H, 4 × pz_A), 107.6 (s,

2C, 2 × C^4-H, 2 × pz_B), 144.45 (s, 4C, 4 × C^5-Me, 4 × pz_A), 144.52 (s, 2C, 2 × C^5-Me, 2 × pz_B), 150.8 (s, 4C, 4 × C^3-Me, 4 × pz_A), 153.0 (s, 2C, 2 × C^3-Me, 2 × pz_B), 159.2 (s, 2C, 2 × *C*-Me), 226.8 (s, 4C, 4 × *C*O).

$^{29}Si\{^1H\}$ NMR: (59.63 MHz, C_6D_6, 298 K): δ (ppm) = 204.3 (s).

4.5.43 [Tp'(CO)$_2$WSiC(Me)C(Me)W(CO)$_2$Tp'] (31-W)

To a stirred brown solution of **21-W** (200 mg, 0.170 mmol) in 10 mL of chlorobenzene, precooled (0 °C) 2-butyne (0.10 mL, 69 mg, 1.28 mmol, 7.5 equiv.) was added via a syringe at 0 °C. The solution was heated in a preheated oil bath at 110 °C for 15 minutes. Upon heating, the color of the solution changed from brown to brownish yellow. Monitoring of the reaction by IR spectroscopy revealed a selective conversion of the starting materials to the product. All volatiles were removed under reduced pressure, and the obtained dirty yellow solid was treated with an Et_2O/*n*-hexane mixture (2:1, 15 mL). The resulting yellow suspension was ultrasonicated shortly, then concentrated to approximately 8 mL, and stored at 0 °C for 30 minutes. The yellow precipitate was collected after filtration of the light yellowish brown supernatant, and dried under vacuum for 2 hours at ambient temperature to yield complex **31-W** as a yellow powder. Analytically pure **31-W** was obtained upon crystallization of the yellow solid from benzene at +5 °C. Yield: 164 mg (0.142 mmol, 84%).

Properties: Complex **31-W** is well soluble in THF and toluene, moderately soluble in Et_2O, sparingly soluble in *n*-hexane.

Melting Points: Complex **31-W** decomposes to a light brown mass at 277 – 279 °C.

Elemental analysis: calcd (%) for $C_{38}H_{50}B_2N_{12}O_4SiW_2$ (1156.27 g/mol): C 39.47, H 4.36, N 14.54; found: C 39.90, H 4.39, N 14.12.

Spectroscopic Data:

IR (THF): $\tilde{\nu}$ (cm^{-1}) = 1930 (s), 1884 (w), 1855 (vs), 1813 (w) [ν(CO)], 1546 (m) [ν(C-C-N)$_{pz}$].

IR (toluene): $\tilde{\nu}$ (cm^{-1}) = 1932 (s), 1886 (w), 1856 (vs), 1815 (vw) [ν(CO)], 1546 (m) [ν(C-C-N)$_{pz}$].

ATR-IR (solid): $\tilde{\nu}$ (cm^{-1}) = 2962 (vw), 2923 (w), 2858 (vw), 2820 (vw), 2547 (w) [ν(BH)], 2530 (w) [ν(BH)], 1925 (s) [ν(CO)], 1882 (m) [ν(CO)], 1841 (vs) [ν(CO)], 1806 (m) [ν(CO)], 1542 (m), 1491 (vw), 1479 vw, 1446 (m), 1414 (m), 1380 (sh), 1371 (m), 1350 (w), 1203 (s), 1142 (w), 1066 (m), 1048 (m), 984 (w), 874 (vw), 857 (m), 813 (m), 779 (s), 692 (m), 679 (m), 641 (s), 621 (vw), 577 (s), 522 (vw), 508 (vw), 482 (m), 462 (s), 418 (vw), 410 (vw), 404 (vw).

^{1}H NMR: (300.1 MHz, C_6D_6, 298 K): δ (ppm) = 1.75 (s, 6H, 2 × C-*Me*), 2.09 (s, 6H, 2 × C^5-*Me*, 2 × pz_B), 2.14 (s, 12H, 4 × C^5-*Me*, 4 × pz_A), 2.32 (s, 12H, 4 × C^3-*Me*, 4 × pz_A), 2.73 (s, 6H, 2 × C^3-*Me*, 2 × pz_B), 4.7 ((br, $\Delta\nu_{1/2}$ = ~ 130 Hz, 2H, 2 × B*H*); this signal appears as a very broad hump over the base line in a strongly enlarged version of the spectrum), 5.43 (s, 2H, 2 × C^4-*H*, 2 × pz_B), 5.56 (s, 4H, 4 × C^4-*H*, 4 × pz_A).

^{13}C{^{1}H} NMR: (75.47 MHz, C_6D_6, 298 K): δ (ppm) = 12.7 (s, 4C, 4 × C^5-*Me*, 4 × pz_A), 12.8 (s, 2C, 2 × C^5-*Me*, 2 × pz_B), 16.1 (s, 6C, (4 × C^3-*Me*, 4 × pz_A) + (2 × C^3-*Me*, 2 × pz_B)), 23.9 (s, 2C, 2 × C-*Me*), 106.8 (s, 4C, 4 × *C*^{4}-H, 4 × pz_A), 107.8 (s, 2C, 2 × *C*^{4}-H, 2 × pz_B), 143.9 (s, 2C, 2 × *C*^{5}-Me, 2 × pz_B), 144.3 (s, 4C, 4 × *C*^{5}-Me, 4 × pz_A), 151.2 (s, 4C, 4 × *C*^{3}-Me, 4 × pz_A), 153.5 (s, 2C, 2 × *C*^{3}-Me, 2 × pz_B), 153.6 (s, 2C, 2 × *C*-Me), 222.3 (s, ^{1}J(W,C) = 156 Hz, 4C, 4 × *C*O).

^{29}Si{^{1}H} NMR: (59.63 MHz, C_6D_6, 298 K): δ (ppm) = 198.8 (s, ^{1}J(W,Si) = 22 Hz).

4.5.44 [Tp'(CO)$_2$MoSiC(H)C(TMS)Mo(CO)$_2$Tp'] (32-Mo)

To a stirred red-brown solution of **21-Mo** (200 mg, 0.20 mmol) in 6 mL of chlorobenzene, precooled (0 °C) trimethylsilylacetylene (0.1 mL, 69 mg, 0.70 mmol, 3.5 equiv.) was added via a syringe at 0 °C. The red-brown solution was immersed in a preheated oil bath (110 °C). Within 10 minutes the color of the solution changed from red-brown to yellow. An IR spectrum of the yellow solution revealed the selective conversion of the starting materials to the product. All volatiles were removed under reduced pressure to give a yellow solid, which was extracted with an Et_2O/*n*-hexane mixture (2:1, 20 mL). The extract was concentrated to approximately 12 mL, leading to a partial precipitation of the product. The suspension was stored at −60 °C for 18 hours. The yellow microcrystalline precipitate was separated from the pale yellow supernatant by

filtration at −60 °C and dried under vacuum for 3 hours at ambient temperature. Yield: 165 mg (0.16 mmol, 81%).

Properties: Complex **32-Mo** is well soluble in THF, fluorobenzene and toluene, moderately soluble in Et_2O and sparingly soluble in *n*-hexane.

Melting Points: The yellow solid slowly turns brown above 230 °C and decomposes to a black liquid at 313 – 314 °C.

Elemental analysis: calcd (%) for $C_{39}H_{54}B_2Mo_2N_{12}O_4Si_2$ (1024.60 g/mol): C 45.72, H 5.31, N 16.40; found: C 45.27, H 5.63, N 16.01.

Spectroscopic Data:

IR (THF): $\tilde{\nu}$ (cm^{-1}) = 1946 (s), 1900 (w), 1873 (vs), 1833 (vw) [ν(CO)], 1545 (m) [ν(C-C-N)$_{pz}$].

IR (toluene): $\tilde{\nu}$ (cm^{-1}) = 1947 (s), 1902 (w), 1873 (vs), 1835 (vw) [ν(CO)], 1545 (m) [ν(C-C-N)$_{pz}$].

ATR-IR (solid): $\tilde{\nu}$ (cm^{-1}) = 3034 (vw), 2948 (vw), 2925 (w), 2860 (vw), 2544 (sh) [ν(BH)], 2520 (w) [ν(BH)], 1940 (s) [ν(CO)], 1895 (m) [ν(CO)], 1858 (vs) [ν(CO)], 1822 (m) [ν(CO)], 1543 (m) [ν(C-C-N)$_{pz}$], 1491 (vw), 1478 (w), 1446 (m), 1415 (m), 1379 (m), 1370 (m), 1350 (sh), 1282 (m), 1262 (vw), 1246 (w), 1207 (sh), 1196 (s), 1184 (sh), 1148 (w), 1116 (vw), 1065 (m), 1046 (w), 1035 (sh), 984 (w), 872 (vw), 841 (s), 815 (m), 794 (m), 778 (w), 760 (m), 743 (w), 693 (m), 674 (s), 642 (m), 623 (w), 589 (m), 565 (sh), 542 (vw), 516 (w), 447 (w), 456 (s), 419 (w), 402 (vw), 384 (w).

^{1}H NMR: (300.1 MHz, C_6D_6, 298 K): δ (ppm) = –0.59 (s, 9H, Si*Me*$_3$), 2.12, 2.15 (s each, 3H each, 1 ×C^5-*Me* each, ^{I}pz$_B$/^{II}pz$_B$), 2.17, 2.21 (s each, 6H each, 2 × C^5-*Me* each, 2 × ^{I}pz$_A$/^{II}pz$_A$), 2.25, 2.32 (s each, 6H each, 2 × C^3-*Me* each, 2 × ^{I}pz$_A$/^{II}pz$_A$), 2.66, 2.68 (s each, 3H each, 1 × C^3-*Me* each, ^{I}pz$_B$/^{II}pz$_B$), 4.8 ((br, $\Delta\nu_{1/2}$ = ~ 140 Hz, 2H, 2 × B*H*); this signal appears as a very broad hump over the base line in a strongly enlarged version of the spectrum), 5.45, 5.47 (s each,

1H each, 1 × C^4-*H* each, $^{I}pz_B/^{II}pz_B$), 5.53, 5.66 (s each, 2H each, 2 × C^4-*H* each, 2 × $^{I}pz_A/^{II}pz_A$), 10.36 (s, ^1J(C,H) = 187 Hz, ^2J(Si,H) = 13 Hz, 1H, Me_3SiCCH).

$^{13}C\{^1H\}$ NMR: (75.47 MHz, C_6D_6, 298 K): δ (ppm) = 0.18 (s, 3C, $SiMe_3$), 12.66, 12.69 (s each, 2C each, 2 × C^5-*Me* each, 2 × $^{I}pz_A/^{II}pz_A$), 12.88, 12.93 (s each, 1C each, 1 × C^5-*Me* each, $^{I}pz_B/^{II}pz_B$), 15.57, 15.62 (s each, 1C each, 1 × C^3-*Me* each, $^{I}pz_B/^{II}pz_B$), 16.0, 16.3 (s each, 2C each, 2 × C^3-*Me* each, 2 × $^{I}pz_A/^{II}pz_A$), 106.9, 107.1 (s each, 2C each, 2 × C^4-H each, 2 × $^{I}pz_A/^{II}pz_A$), 107.7, 107.8 (s each, 1C each, 1 × C^4-H each, $^{I}pz_B/^{II}pz_B$), 144.4, 144.6 (s each, 1C each, 1 × C^5-Me each, $^{I}pz_B/^{II}pz_B$), 144.7, 144.9 (s each, 2C each, 2 × C^5-Me each, 2 × $^{I}pz_A/^{II}pz_A$), 150.8, 150.9 (s each, 2C each, 2 × C^3-Me each, 2 × $^{I}pz_A/^{II}pz_A$), 153.0 (s, 2C, (1 × C^3-Me $^{I}pz_B$) + (1 × C^3-Me,$^{II}pz_B$)), 171.9 (s, 1C, Me_3SiCCH), 179.1 (s, 1C, Me_3SiCCH), 225.5, 227.0 (s each, 2C each, 4 × *C*O).

$^{29}Si\{^1H\}$ NMR: (59.63 MHz, C_6D_6, 298 K): δ (ppm) = –2.1 (s, $SiMe_3$) 200.4 (s, Mo*Si*Mo).

4.5.45 [Tp'(CO)$_2$WSiC(H)C(TMS)W(CO)$_2$Tp'] (32-W)

To a stirred brown solution of **21-W** (100 mg, 0.085 mmol) in 10 mL of chlorobenzene, trimethylsilylacetylene (0.06 mL, 41 mg, 0.42 mmol, 5 equiv.) was added via a syringe at ambient temperature. The reaction mixture was heated at 100 °C for 30 minutes. During this time the color of the solution changed from brown to brownish yellow. Completion of the reaction was confirmed by IR spectroscopy, and then all volatiles were removed under reduced pressure. The residue obtained was extracted with an Et_2O/*n*-hexane mixture (2:1, 3 × 5 mL) at ambient temperature. The combined brownish yellow extracts were concentrated to approximately 8 mL *in vacuo* and stored at –60 °C for 48 hours. A yellow solid precipitated out, which was collected after filtration of the light brown supernatant at –60 °C and was recrystallized from an Et_2O/*n*-hexane mixture (1:1, 10 mL) at –30 °C. The microcrystalline yellow solid was isolated after filtration of the light yellow supernatant at –30 °C, and dried under vacuum for 2 hours at ambient temperature. Yield: 77 mg (0.064 mmol, 76%).

Properties: Complex **32-W** is well soluble in THF, fluorobenzene and toluene, moderately soluble in Et_2O and sparingly soluble in *n*-hexane.

Melting Points: Upon heating the yellow color starts to fade very slowly above 250 °C and the light yellow solid turns to a black mass at 353 – 354 °C (dec.).

Elemental analysis: calcd (%) for $C_{39}H_{54}B_2N_{12}O_4Si_2W_2$ (1200.40 g/mol): C 39.02, H 4.53, N 14.00; found: C 39.38, H 4.61, N 13.95.

Spectroscopic Data:

IR (THF): $\tilde{\nu}$ (cm^{-1}) = 1933 (s), 1885 (w), 1857 (vs), 1817 (vw) [ν(CO)], 1546 (m) [ν(C-C-N)$_{pz}$].

IR (toluene): $\tilde{\nu}$ (cm^{-1}) = 1934 (s), 1886 (w), 1858 (vs), 1818 (vw) [ν(CO)], 1546 (m) [ν(C-C-N)$_{pz}$].

ATR-IR (solid): $\tilde{\nu}$ (cm^{-1}) = 2960 (vw), 2928 (w), 2865 (vw), 2549 (w) [ν(BH)], 2531 (sh) [ν(BH)], 1928 (s) [ν(CO)], 1884 (m) [ν(CO)], 1845 (vs) [ν(CO)], 1815 (m) [ν(CO)], 1544 (m) [ν(C-C-N)$_{pz}$], 1491 (vw), 1446 (m), 1415 (m), 1382 (sh), 1372 (m), 1350 (sh), 1254 (m), 1202 (s), 1148 (w), 1133 (sh), 1065 (m), 1048 (m), 984 (w), 955 (vw), 874 (vw), 845 (s), 817 (m), 780 (m), 760 (m), 732 (w), 694 (m), 669 (m), 653 (sh), 642 (m), 615 (w), 592 (sh), 575 (m), 536 (vw), 521 (vw), 479 (w), 461 (s), 433 (w).

^{1}H NMR: (300.1 MHz, C_6D_6, 298 K): δ (ppm) = –0.57 (s, 9H, Si*Me*$_3$), 2.08, 2.10 (s each, 3H each, 1 × C^5-*Me* each, ^{I}pz$_B$/^{II}pz$_B$), 2.12, 2.16 (s each, 6H each, 2 × C^5-*Me* each, 2 × ^{I}pz$_A$/^{II}pz$_A$), 2.28, 2.36 (s each, 6H each, 2 × C^3-*Me* each, 2 × ^{I}pz$_A$/^{II}pz$_A$), 2.72, 2.76 (seach, 3H each, 1 × C^3-*Me* each, ^{I}pz$_B$/^{II}pz$_B$), 4.7 ((br, $\Delta\nu_{1/2}$ = ~ 140 Hz, 2H, 2 × B*H*); this signal appears as a very broad hump over the base line in a strongly enlarged version of the spectrum), 5.43 (s, 2H, (C^4-*H*, ^{I}pz$_B$) + (C^4-*H*, ^{II}pz$_B$)), 5.51, 5.63 (s each, 2H each, 2 × C^4-*H* each, 2 × ^{I}pz$_A$/^{II}pz$_A$), 10.64 (s, ^2J(W,H) = 16 Hz, ^3J(W,H) = 6.3 Hz, ^2J(Si,H) = 14 Hz, 1H, Me$_3$SiCC*H*).

^{13}C{^{1}H} NMR: (75.47 MHz, C_6D_6, 298 K): δ (ppm) = 0.56 (s, 3C, Si*Me*$_3$),12.59, 12.61 (s each, 2C each, 2 × C^5-*Me* each, 2 × ^{I}pz$_A$/^{II}pz$_A$), 12.70, 12.77 (s each, 1C each, 1 × C^5-*Me* each, ^{I}pz$_B$/^{II}pz$_B$), 16.06, 16.09 (s each, 1C each, 1 × C^3-*Me* each, ^{I}pz$_B$/^{II}pz$_B$), 16.7, 17.1 (s each, 2C each, 2 × C^3-*Me* each, 2 × ^{I}pz$_A$/^{II}pz$_A$), 107.0, 107.3 (s

each, 2C each, 2 × C^4-H each, 2 × $^{I}pz_A/^{II}pz_A$), 107.89, 107.94 (s each, 1C each, 1 × C^4-H each, $^{I}pz_B/^{II}pz_B$), 143.8, 144.2 (s each, 1C each, 1 × C^5-Me each, $^{I}pz_B/^{II}pz_B$), 144.6, 144.7 (s each, 2C each, 2 × C^5-Me each, 2 × $^{I}pz_A/^{II}pz_A$), 151.3, 151.4 (s each, 2C each, 2 × C^3-Me each, 2 × $^{I}pz_A/^{II}pz_A$), 153.4, 153.6 (s each, 1C each, 1 × C^3-Me each, $^{I}pz_B/^{II}pz_B$), 166.8 (s, 1C, Me_3SiCCH), 169.3 (s, 1C, Me_3SiCCH), 220.5 (s, ^1J(W,C) = 157 Hz, 2C, 2 × *C*O), 222.7 (s, ^1J(W,C) = 152 Hz, 2C, 2 × *C*O).

$^{29}Si\{^1H\}$ NMR: (59.63 MHz, C_6D_6, 298 K): δ (ppm) = −1.3 (s, *Si*Me_3) 186.1 (s, ^1J(W,Si) = 24 and 15 Hz, W*Si*W).

4.5.46 [Tp'(CO)$_2$MoSiC(H)C(Ph)Mo(CO)$_2$Tp'] (33-Mo)

To a stirred red-brown solution of **21-Mo** (200 mg, 0.20 mmol) in 8 mL of fluorobenzene, a solution of phenylacetylene (21 mg, 0.21 mmol) in 2 mL of fluorobenzene was added via a syringe at ambient temperature. The red-brown solution was heated for 1 hour at 80 °C. During this time the color of the solution changed to yellowish brown. The complete consumption of the starting material was confirmed by IR spectroscopy and ^{31}P NMR spectroscopy. Afterwards, all volatiles were removed under reduced pressure, and the residue was extracted with an Et_2O/*n*-hexane mixture (2:1, 10 mL). The extract was stored at −60 °C for 72 hours, upon which a bright yellow precipitate was formed. The precipitate was collected by filtration at −60 °C, washed with *n*-pentane (2 × 2 mL) at −60 °C and dried under vacuum for 18 hours at ambient temperature and then for 4 hours at 60 °C to afford complex **33-Mo** as an analytically pure, bright yellow solid. Yield: 137 mg (0.133 mmol, 67%).

Properties: Complex **33-Mo** is well soluble in THF, fluorobenzene and toluene, moderately soluble in Et_2O and sparingly soluble in *n*-hexane.

Melting Points: The yellow solid decomposes to a brown solid at 223 – 225 °C.

Elemental analysis: calcd (%) for $C_{42}H_{50}B_2Mo_2N_{12}O_4Si$ (1028.51 g/mol): C 49.05, H 4.90, N 16.34; found: C 49.58, H 5.20, N 16.00.

Spectroscopic Data:

IR (THF): $\tilde{\nu}$ (cm^{-1}) = 1944 (s), 1902 (w), 1869 (vs), 1836 (vw) [ν(CO)], 1545 (m) [ν(C-C-N)$_{pz}$].

IR (toluene): $\tilde{\nu}$ (cm^{-1}) = 1945 (s), 1903 (w), 1870 (vs), 1837 (vw) [ν(CO)], 1545 (m) [ν(C-C-N)$_{pz}$].

ATR-IR (solid): $\tilde{\nu}$ (cm^{-1}) = 2979 (w), 2959 (w), 2928 (vw), 2869 (w), 2549 (sh) [ν(BH)], 2529 (w) [ν(BH)], 1940 (s) [ν(CO)], 1901 (m) [ν(CO)], 1859 (vs) [ν(CO)], 1835 (s) [ν(CO)], 1618 (vw), 1589 (vw), 1543 (m) [ν(C-C-N)$_{pz}$], 1483 (w), 1445 (m), 1414 (s), 1371 (s), 1350 (sh), 1258 (vw), 1200 (s), 1147 (w), 1131 (sh), 1066 (m), 1046 (m), 983 (w), 872 (vw), 855 (w), 811 (m), 779 (m), 742 (m), 693 (s), 670 (sh), 644 (m), 622 (w), 605 (w), 589 (m), 543 (vw), 526 (w), 513 (w), 486 (w), 475 (w), 456 (m), 414 (vw), 406 (vw), 400 (vw).

^{1}H NMR: (300.1 MHz, C_6D_6, 298 K): δ (ppm) = 2.10, 2.15 (s each, 3H each, 1 ×C^5-*Me* each, $^{I}pz_B/^{II}pz_B$), 2.16, 2.20 (s each, 6H each, 2 × C^5-*Me* each, 2 × $^{I}pz_A/^{II}pz_A$), 2.29, 2.31 (s each, 6H each, 2 × C^3-*Me* each, 2 × $^{I}pz_A/^{II}pz_A$), 2.69, 2.72 (s each, 3H each, 1 × C^3-*Me* each, $^{I}pz_B/^{II}pz_B$), 4.8 ((br, $\Delta\nu_{1/2}$ = ~ 150 Hz, 2H, 2 × B*H*); this signal appears as a very broad hump over the base line in a strongly enlarged version of the spectrum), 5.37, 5.54 (s each, 2H each, 2 × C^4-*H* each, 2 × $^{I}pz_A/^{II}pz_A$), 5.44, 5.51 (s each, 1H each, 1 × C^4-*H* each, $^{I}pz_B/^{II}pz_B$), 6.26 – 6.32 (m, 2H, C^{2,6}-*H*, Ph), 6.46 – 6.54 (m, 2H, C^{3,5}-*H*, Ph), 6.57 – 6.64 (m, 1H, C^4-*H*, Ph), 9.25 (s, ^2J(Si,H) = 10 Hz, 1H, PhCC*H*).

^{13}C{^{1}H} NMR: (75.47 MHz, C_6D_6, 298 K): δ (ppm) = 12.52, 12.62 (s each, 2C each, 2 × C^5-*Me* each, 2 × $^{I}pz_A/^{II}pz_A$), 12.94, 12.96 (s each, 1C each, 1 × C^5-*Me* each, $^{I}pz_B/^{II}pz_B$), 15.52, 16.06 (s each, 2C each, 2 × C^3-*Me* each, 2 × $^{I}pz_A/^{II}pz_A$), 15.53,[51] 15.58 (s each, 1C each, 1 × C^3-*Me* each, $^{I}pz_B/^{II}pz_B$), 106.8, 107.1 (s each, 2C each, 2 × *C*^{4}-H each, 2 × $^{I}pz_A/^{II}pz_A$), 107.67, 107.69 (s each, 1C each, 1 × *C*^{4}-H each, $^{I}pz_B/^{II}pz_B$), 126.1 (s, 1C, *C*^{4}-H, Ph), 126.5 (s, 2C, *C*^{2,6}-H, Ph), 127.1 (s, 2C, *C*^{3,5}-H, Ph), 144.4, 144.5 (s each, 2C each, 2 × *C*^{5}-Me each, 2 × $^{I}pz_A/^{II}pz_A$), 144.7, 144.8 (s each, 1C each, 1 × *C*^{5}-Me each, $^{I}pz_B/^{II}pz_B$), 147.8 (s, 1C, *C*^{1}, Ph), 151.0, 151.3 (s each, 2C each, 2 × *C*^{3}-Me each, 2 × $^{I}pz_A/^{II}pz_A$), 152.93, 152.94

[51] This signal partially overlaps with the signal at 15.52 ppm.

(s each, 1C each, 1 × C^3-Me each, $^{I}pz_B/^{II}pz_B$)), 154.0 (s, 1C, PhC*C*H), 169.2 (s, 1C, Ph*C*CH), 224.9, 225.9 (s each, 2C each, 4 × *C*O).

$^{29}Si\{^1H\}$ NMR: (59.63 MHz, C_6D_6, 298 K): δ (ppm) = 216.9 (s).

4.5.47 [Tp'(CO)$_2$Mo(PC^{t}Bu)SiMo(CO)$_2$Tp'] (34-Mo)

Complex **21-Mo** (100 mg, 0.10 mmol) was dissolved in 8 mL of chlorobenzene and to this red-brown solution, few drops of *t*BuCP (excess) was added at ambient temperature. The resulting solution was heated to 100 °C for 30 minutes followed by 1 hour at 60 °C, upon which the color of the solution changed to dark brown. An IR spectrum of the aliquot of the dark brown suspension revealed complete consumption of the starting material and formation of **34-Mo** and small amount of radical **2-Mo**. The dark brown suspension was filtered into another schlenck tube, and all volatiles were removed under reduced pressure. The residue was treated with 4 mL of *n*-pentane and 10 mL of Et_2O leading to the formation of a dark brown precipitate along with a yellowish brown supernatant. The precipitate was isolated by filtration of the supernatant, washed with *n*-pentane (2 mL) and dried shortly under reduced pressure at ambient temperature. Yield: 46 mg (0.04 mmol, 42%).

Properties: Complex **34-Mo** is moderately soluble in CH_2Cl_2, sparingly soluble in fluorobenzene and insoluble in toluene, Et_2O and aliphatic solvents. It slowly decomposes in CH_2Cl_2, and moderately sensitive towards air.

Elemental analysis: calcd (%) for $C_{42}H_{62}B_2Mo_2N_{12}O_4P_2Si$ (1102.56 g/mol): C 45.75, H 5.67, N 15.24; found: C 45.47, H 5.65, N 14.60.

Spectroscopic Data:

IR (CH_2Cl_2): $\tilde{\nu}$ (cm^{-1}) = 1899 (s), 1839 (s), 1816 (vs), 1774 (m) and 1770 (m) [ν(CO)], 1547 (m) [$\nu(C\text{-}C\text{-}N)_{pz}$].

IR (chlorobenzene): $\tilde{\nu}$ (cm^{-1}) = 1899 (s), 1840 (s), 1820 (vs), 1775 (m) [ν(CO)], 1546 (m) [$\nu(C\text{-}C\text{-}N)_{pz}$].

ATR-IR (solid): $\tilde{\nu}$ (cm^{-1}) = 3016 (vw), 2976 (sh), 2958 (w), 2937 (vw), 2911 (vw), 2894 (vw), 2879 (vw), 2866 (vw), 2532 (vw) [ν(BH)], 2478 (w), 1895 (s), 1810 (vs) and 1761 (s) [ν(CO)], 1583 (vw), 1544 (m) [$\nu(C\text{-}C\text{-}N)_{pz}$], 1508 (vw), 1476 (vw),

1448 (m), 1413 (m), 1374 (m), 1354 (m), 1343 (m), 1306 (vw), 1283 (w), 1251 (vw), 1226 (sh), 1210 (m), 1198 (m), 1183 (w), 1158 (vw), 1144 (vw), 1123 (vw), 1100 (w), 1074 (w), 1060 (w), 1054 (sh), 1042 (w), 1023 (w), 1001 (vw), 985 (vw), 971 (sh), 953 (m), 942 (sh), 873 (m), 863 (sh), 850 (m), 819 (m), 805 (w), 783 (sh), 774 (m), 766 (sh), 740 (w), 723 (w), 696 (w), 685 (w), 673 (w), 656 (vw), 646 (w), 632 (w), 613 (w), 583 (w), 571 (sh), 564 (w), 553 (w), 527 (w), 504 (m), 495 (sh), 480 (vw), 466 (w), 452 (sh), 442 (m), 403 (m), 382 (w).

^{1}H NMR: (500.1 MHz, CD_2Cl_2, 298 K): δ (ppm) = 0.77 (s, 9H, *Me*$_3$CP), 1.77 (d, ^{2}J(P,H) = 7.5 Hz, 9H, P*Me*$_3$), 2.01, 2.88 (s, 3H each, C^3-*Me*, pz$_B$), 2.07, 2.34 (s, 3H each, 1 × C^5-*Me*, pz$_B$), 2.10, 2.77 (s, 6H each, 2 × C^3-*Me*, pz$_A$), 2.38, 2.40 (s, 6H each, 2 × C^5-*Me*, pz$_A$), 4.7 (br, $\Delta\nu_{1/2}$ = ~ 200 Hz, 2H, B*H*); this signal is visible as a very broad hump over the base line in a strongly enlarged version of the spectrum), 5.58, 5.87 (s, 1H each, C^4-*H*, pz$_B$), 5.76, 6.18 (s, 2H each, 2 × C^4-*H*, pz$_A$).

^{13}C{^{1}H} NMR: (125.78 MHz, CD_2Cl_2, 298 K): δ (ppm) = 12.1, 13.2 (s, 1C each, C^5-*Me*, pz$_B$), 13.0, 13.8 (s, 2C each, 2 × C^5-*Me*, pz$_A$) 14.1, 16.9 (s, 1C each, C^3-*Me*, pz$_B$), 16.8 (s, 2C, 2 × C^3-*Me*, pz$_A$), 17.4 (d, ^{4}J(C,P) = 2.4 Hz, 2C, 2 × C^3-*Me*, pz$_A$), 19.4 (d, ^{1}J(C,P) = 20.0 Hz, 3C, P*Me*$_3$), 30.7 (d, ^{3}J(C,P) = 10.6 Hz, 3C, C*Me*$_3$), 106.1 (s, 2C, 2 × *C*^{4}-H, ^{I}pz$_A$), 40.6 (br s, 1C, *C*Me$_3$) 105.7, 107.1 (s, 1C each, *C*^{4}-H, pz$_B$), 105.9, 110.6 (s, 2C each, 2 × *C*^{4}-H, pz$_A$), 142.8, 145.0 (s, 1C each, *C*^{5}-Me, pz$_B$), 144.4, 151.6 (s, 2C each, 2 × *C*^{5}-Me, pz$_B$), 148.8 (s, 1C each, *C*^{3}-Me, pz$_B$), 150.8, 152.4 (s, 2C each, 2 × *C*^{3}-Me, pz$_A$), 194.2 (d, ^{1}J(C,P) = 41.5 Hz, 1C, *t*Bu*C*P), 230.1 (d, ^{3}J(C,P) = 5.3 Hz, 2C, 2 × *C*O), 240.3 (d, ^{2}J(C,P) = 16.3 Hz, 2C, 2 × *C*O).

^{31}P{^{1}H} NMR: (202.5 MHz, CD_2Cl_2, 298 K): δ (ppm) = –8.2 (d, ^{3}J(P,P) = 46.5 Hz), 461.4 (d, ^{3}J(P,P) = 46.5 Hz).

4.5.48 [(η^5-C_5H_4Me)(CO)$_2$Mn=Pb(Cl)(C_6H_3-2,6-Mes_2)] (35)

A mixture of PPN[(η^5-C_5H_4Me)Mn(CO)$_2$Cl] (**3-Mn**) (250 mg, 0.327 mmol) and PbCl(C_6H_3-2,6-Mes_2) (196 mg, 0.352 mmol) was treated with 8 mL of fluorobenzene at room temperature, leading to a red-brown solution with some red-brown oily material. An IR spectrum of the solution was recorded after 5 minutes of stirring and revealed that the starting material had been

consumed to give a new dicarbonyl complex displaying two ν(CO) absorption bands of almost equal intensity at 1916 and 1852 cm^{-1}. This species is suggested to be the manganese dichloroplumbyl complex PPN[(η^5-C_5H_4Me)$(CO)_2$Mn{$PbCl_2(C_6H_3$-2,6-$Mes_2)$}]. Some starting material and the chloroplumbylidene complex **35** were also present in the reaction solution as evidenced by the appearance of three additional ν(CO) bands of lower intensity in the IR spectrum at 1815 cm^{-1} (**3-Mn**), 1893 cm^{-1} (**3-Mn** and **35**) and 1946 cm^{-1} (**35**). The red-brown solution was stirred for 3 hours under exclusion of day-light. No significant change in the composition of the reaction mixture was observed during this time by IR spectroscopy.[52] Then one equivalent of Na[B{C_6H_3-3,5-$(CF_3)_2$}$_4$] (290 mg, 0.327 mmol) was added to the mixture leading to the selective formation of **35** as evidenced by IR spectroscopy. The obtained red-brown suspension was evaporated to dryness under reduced pressure to give a pale brown solid. The solid was extracted with 25 mL of *n*-pentane and the red-brown extract was concentrated in *vacuo* to *ca.* 4 mL, upon which a red brown, microcrystalline solid precipitated. The suspension was stored at – 60 °C for 15 minutes, and the microcrystalline solid was collected by filtration at –60 °C. The solid was washed with *n*-pentane (2 × 1.5 mL) at – 60 °C and dried in *vacuo* for 30 minutes at ambient temperature to afford complex **35** as an analytically pure, red-brown solid. Yield: 141 mg (0.189 mmol, 58%).

Properties: Compound **35** is very good soluble in THF, Et_2O, toluene and moderately soluble in aliphatic solvent.

Melting Points: Upon heating complex **35** starts to decompose at 144 – 145 °C to give a dark brown solid, which then melts to a black liquid at 152 – 154 °C. Complex **35** is light sensitive and should be stored in the dark.

Elemental analysis: calcd (%) for $C_{32}H_{32}ClMnO_2Pb$ (746.19 g/mol): C 51.51, H4.32; found C 51.47, H 4.46%.

Spectroscopic Data:

IR (CH_2Cl_2): $\tilde{\nu}$ (cm^{-1}) = 1947 (vs) and 1892 (vs) [ν(CO)].

IR (fluorobenzene): $\tilde{\nu}$ (cm^{-1}) = 1946 (vs) and 1892 (vs) [ν(CO)].

52 Only some [(η^5-C_5H_4Me)$Mn(CO)_3$] was additionally formed (ν(CO) in fluorobenzene: 2019 (s) and 1930 (vs) cm^{-1}) probably by photodegradation of **35** or the dichloroplumbyl complex.

IR (*n*-pentane): $\tilde{\nu}$ (cm^{-1}) = 1951 (vs) and 1900 (vs) [ν(CO)].

ATR-IR (solid): $\tilde{\nu}$ (cm^{-1}) = 3028 (vw), 2967 (w), 2945 (vw), 2918 (m), 2856 (w), 2734 (vw), 1941 (vs) [ν(CO)], 1886 (vs) [ν(CO)], 1610 (w), 1568 (vw), 1559 (vw), 1480 (w), 1450 (m), 1378 (w), 1353 (vw), 1303 (vw), 1263 (vw), 1247 (vw), 1176 (w), 1164 (vw), 1093 (vw), 1067 (vw), 1038 (w), 1029 (w, sh), 1014 (vw, sh), 1001 (vw), 923 (vw), 914 (vw), 855 (m), 847 (w, sh), 833 (w), 801 (w), 737 (w), 730 (vw, sh), 645 (m), 631 (w, sh), 599 (s), 571 (s), 545 (vw), 516 (w), 456 (vw), 438 (vw), 422 (vw).

^{1}H NMR: (300.1 MHz, C_6D_6, 298 K): δ (ppm) = 1.43 (s, 3H, C_5H_4*Me*), 2.12 (s, 6H, 2 × C^4-*Me*, Mes), 2.31 (s, 12H, $\Delta\nu_{1/2}$ = 3.4 Hz, 2 × $C^{2,6}$-*Me*, Mes), 3.87 (m, 2H, $C^{2,5}$-*H*, C_5H_4Me), 4.07 (m, 2H, $C^{3,4}$-*H*, C_5H_4Me), 6.92 (s, 4H, 2 × $C^{3,5}$-*H*, Mes), 7.27 (t, ^{3}J(H,H) = 7.5 Hz, 1H, C^4-*H*, C_6H_3), 7.60 (d, ^{3}J(H,H) = 7.5 Hz, 2H, $C^{3,5}$-*H*, C_6H_3).

^{1}H NMR: (300.1 MHz, CD_2Cl_2, 193 K): δ (ppm) = 1.68 (s, 3H, C_5H_4*Me*), 2.02 (s, 6H, 2 × C^2-*Me*, Mes), 2.13 (s, 6H, 2 × C^6-*Me*, Mes), 2.27 (s, 6H, 2 × C^4-*Me*, Mes), 4.05 (s, 2H, $C^{2,5}$-*H*, C_5H_4Me), 4.30 (s, 2H, $C^{3,4}$-*H*, C_5H_4Me), 7.00 (s, 4H, 2 × $C^{3,5}$-*H*, Mes), 7.62 (t, ^{3}J(H,H) = 7.5 Hz, 1H, C^4-*H*, C_6H_3), 7.92 (d, ^{3}J(H,H) = 7.5 Hz, 2H, $C^{3,5}$-*H*, C_6H_3).

^{13}C{^{1}H} NMR: (75.47 MHz, C_6D_6, 298 K): δ (ppm) = 13.6 (s, 1C, C_5H_4*Me*), 21.2 (s, 2C, 2 × C^4-*Me*, Mes), 21.4 (br s, 4C, 2 × $C^{2,6}$-*Me*, Mes), 79.4 (s, 2C, *C*^{2,5}-H, C_5H_4Me), 80.6 (s, 2C, *C*^{3,4}-H, C_5H_4Me), 99.6 (s, 1C, *C*^{1}-Me, C_5H_4Me), 129.2 (s, 1C, *C*^{4}-H, C_6H_3), 129.8 (s, 4C, 2 × *C*^{3,5}-H, Mes), 135.2 (s, 2C, *C*^{3,5}-H, C_6H_3), 135.5 (s, 2C, 2 × *C*^{1}, Mes), 136.9 (br s, 4C, 2 × *C*^{2,6}, Mes), 138.5 (s, 2C, 2 × *C*^{4}, Mes), 144.7 (s, 2C, *C*^{2,6}, C_6H_3), 227.8 (s, 2C, 2 × *C*O), 242.7 (s, 1C, Pb-*C*^{1}, C_6H_3).

^{13}C{^{1}H} NMR: (75.47 MHz, CD_2Cl_2, 193 K): δ (ppm) = 13.4 (s, 1C, C_5H_4*Me*), 20.6 (br s, 2C, 2 × C^2-*Me*, Mes), 20.7 (s, 2C, 2 × C^4-*Me*, Mes), 21.0 (br s, 2C, 2 × *C*^{6}-*Me*, Mes), 77.1 (s, 2C, *C*^{2,5}-H, C_5H_4Me), 80.7 (s, 2C, *C*^{3,4}-H, C_5H_4Me), 100.8 (s, 1C, *C*^{1}-Me, C_5H_4Me), 128.7 (s, 4C, 2 × *C*^{3,5}-H, Mes), 128.8 (s, 1C, *C*^{4}-H, C_6H_3), 134.1 (s, 2C, 2 × *C*^{1}, Mes), 134.5 (s, 2C, *C*^{3,5}-H, C_6H_3), 134.8 (br s, 2C, 2 × *C*^{2}, Mes),

137.1 (br s, 2C, 2 × C^6, Mes), 138.1 (s, 2C, 2 × C^4, Mes), 142.9 (s, 2C, $C^{2,6}$, C_6H_3), 226.5 (s, 2C, 2 × *C*O), 240.0 (s, 1C, Pb-C^1, C_6H_3).

4.5.49 [(η^5-C_5H_4Me)$(CO)_2$Mn=Pb(Br)(C_6H_3-2,6-Mes_2)] (36)

A mixture of PPN[(η^5-C_5H_4Me)$Mn(CO)_2Cl$] (**3-Mn**) (250 mg, 0.33 mmol), Pb(Br)(C_6H_3-2,6-Mes_2) (197 mg, 0.33 mmol) and LiBr (29 mg, 0.33 mmol) was treated with a mixture of 15 mL of THF and 25 mL of *n*-hexane at ambient temperature and stirred for 3 hours. Upon stirring the color of the suspension changed from brown to red-brown with some white solid. Monitoring of the reaction by IR spectroscopy revealed an almost selective conversion of the starting material into the product along with a very small amount of [(η^5-C_5H_4Me)$Mn(CO)_3$]. The resulting suspension was filtered into another schlenck tube, and the filtrate was evaporated to dryness under reduced pressure. The sticky brown residue was pulverized once by a freeze-pump-thaw cycle and the resulting powder was extracted with *n*-pentane (20 mL). The red-brown extract was concentrated to *ca.* 2 mL, leading to the precipitation of microcrystalline brown solid which was isolated by filtration of the light brown supernatant at ambient temperature and dried under reduced pressure for 15 minutes at ambient temperature. Yield: 98 mg (0.124 mmol, 40 %).

Properties: Complex **36** is very good soluble in THF, Et_2O, toluene and moderately soluble in aliphatic solvent. Complex **36** is light sensitive and should be stored in the dark.

Spectroscopic Data:

^{1}H NMR: (300.1 MHz, C_6D_6, 298 K): δ (ppm) = 1.43 (s, 3H, C_5H_4*Me*), 2.11 (s, 6H, 2 × C^4-*Me*, Mes), 2.35 (br s, $\Delta\nu_{1/2}$ = 8.4 Hz, 12H, 2 × $C^{2,6}$-*Me*, Mes), 3.84 (m, 2H, $C^{2,5}$-*H*, C_5H_4Me), 4.06 (m, 2H, $C^{3,4}$-*H*, C_5H_4Me), 6.91 (s, 4H, 2 × $C^{3,5}$-*H*, Mes), 7.27 (t, ^3J(H,H) = 7.5 Hz, 1H, C^4-*H*, C_6H_3), 7.57 (d, ^3J(H,H) = 7.5 Hz, 2H, $C^{3,5}$-*H*, C_6H_3).

4.5.50 [(η^5-C_5H_4Me)$(CO)_2$Mn=Pb(I)(C_6H_3-2,6-Mes_2)] (37)

A mixture of PPN[(η^5-C_5H_4Me)$Mn(CO)_2Cl$] (**3-Mn**) (350 mg, 0.46 mmol), Pb(Cl)(C_6H_3-2,6-Mes_2) (255 mg, 0.46 mmol) and LiI (61 mg, 0.46 mmol) was treated with a mixture of 15 mL of THF and 25 mL of *n*-hexane at ambient temperature and stirred for 30 minutes. The color of the suspension immediately changed from brown to red-brown with some white precipitate. Monitoring of the reaction by IR spectroscopy revealed an almost selective conversion of the

starting material into the product along with a very small amount of [(η^5-C_5H_4Me)$Mn(CO)_3$]. The red-brown suspension was filtered into another schlenck tube, and the filtrate was evaporated to dryness under reduce pressure. The residue was pulverized by a freeze-pump-thaw cycle, and the resulting red-brown powder was extracted with *n*-pentane (2 × 10 mL) at ambient temperature. The combined extract was concentrated to ~2 – 3 mL and stored at −30 °C for 30 minutes. The microcrystalline brown solid that precipitated out was isolated by filtration of the light brown supernatant at −30 °C. The isolated solid was recrystallised from *n*-pentane at −30 °C and dried under reduced pressure for 30 minutes at ambient temperature to obtain analytically pure, brown solid in moderate yield. Yield: 181 mg (0.22 mmol, 47%).

Properties: Complex **37** is very good soluble in THF, Et_2O, toluene and moderately soluble in aliphatic solvent. Complex **37** is light sensitive and should be stored in the dark.

Elemental analysis: calcd (%) for $C_{32}H_{32}IMnO_2Pb$ (837.64 g/mol): C 45.88, H 3.85; found C 46.20, H 4.00%.

Spectroscopic Data:

IR (THF film, ATR): $\widetilde{\nu}$ (cm^{-1}) = 1942 (vs) and 1889 (vs) [ν(CO)].

^{1}H NMR: (300.1 MHz, C_6D_6, 298 K): δ (ppm) = 1.43 (s, 3H, C_5H_4*Me*), 2.10 (s, 6H, 2 × C^4-*Me*, Mes), 2.36 (br s, $\Delta\nu_{1/2}$ = 18.7 Hz, 12H, 2 × $C^{2,6}$-*Me*, Mes), 3.82 (br s, $\Delta\nu_{1/2}$ = 6.5 Hz, 2H, $C^{2,5}$-*H*, C_5H_4Me), 4.04 (br s, $\Delta\nu_{1/2}$ = 6.2 Hz, 2H, $C^{3,4}$-*H*, C_5H_4Me), 6.91 (s, 4H, 2 × $C^{3,5}$-*H*, Mes), 7.28 (t, ^3J(H,H) = 7.4 Hz, 1H, C^4-*H*, C_6H_3), 7.56 (d, ^3J(H,H) = 7.4 Hz, 2H, $C^{3,5}$-*H*, C_6H_3).

$^{13}C\{^1H\}$ NMR: (75.47 MHz, C_6D_6, 298 K): δ (ppm) = 13.5 (s, 1C, C_5H_4*Me*), 21.2 (s, 2C, 2 × C^4-*Me*, Mes), 21.8 (br s, $\Delta\nu_{1/2}$ = ~48 Hz, 4C, 2 × $C^{2,6}$-*Me*, Mes), 80.3 (s, 2C, $C^{2,5}$-H, C_5H_4Me), 82.4 (s, 2C, $C^{3,4}$-H, C_5H_4Me), 99.8 (s, 1C, C^1-Me, C_5H_4Me), 129.0 (s, 1C, C^4-H, C_6H_3), 130.0 (s, 4C, 2 × $C^{3,5}$-H, Mes), 135.3 (s, 2C, $C^{3,5}$-H, C_6H_3), 135.4 (s, 2C, 2 × C^1, Mes), 136.5 (br s, $\Delta\nu_{1/2}$ = ~70 Hz, 4C, 2 × $C^{2,6}$, Mes), 138.4 (s, 2C, 2 × C^4, Mes), 144.7 (s, 2C, $C^{2,6}$, C_6H_3), 227.8 (s, 2C, 2 × *C*O), 236.8 (s, 1C, Pb-C^1, C_6H_3).

4.5.51 [{(η^5-C_5H_4Me)$(CO)_2$MnPb(C_6H_3-2,6-Mes_2)}$_2$(μ-Br)][B{C_6H_3-2,6-$(CF_3)_2$}$_4$] (38)

A mixture of **36** (98 mg, 0.12 mmol) and Na[B{C_6H_3-3,5-$(CF_3)_2$}$_4$] (110 mg, 0.12 mmol, 1 equiv.)[53] was treated with 10 mL of *n*-pentane at ambient temperature and stirred for 12 hours inside the glove box. Upon stirring the white solid of the suspension transformed into brown solid with almost colorless supernatant. The monitoring of the reaction by solid state IR spectroscopy of the precipitate revealed the formation of title compound **38** in complete expense of **36**. Stirring for a longer period of time does not led to the formation of corresponding plumbylidyne complex. The red-brown precipitate was isolated by filtration of the supernatant and crystallized from 1:1 CH_2Cl_2/*n*-pentane (10 mL) mixture at –60 °C to separate from excess Na[B{C_6H_3-3,5-$(CF_3)_2$}$_4$]. The microcrystalline red-brown solid isolated by filtration of the light brown supernatant at –60 °C and dried shortly under reduced pressure at ambient temperature. Yield: 56 mg (0.024 mmol, 38%).

Properties: Complex **38** is very good soluble in THF, Et_2O, fluorobenzene and insoluble in toluene and aliphatic solvent.

Spectroscopic Data:

ATR-IR (solid): $\tilde{\nu}$ (cm^{-1}) = 1964 (s), 1922 (s), and 1914 (s) [ν(CO)].

^{1}H NMR: (300.1 MHz, CD_2Cl_2, 298 K): δ (ppm) = 1.75 (s, 6H, 2 × C_5H_4*Me*), 2.11 (s, 24H, 4 × $C^{2,6}$-*Me*, Mes), 2.32 (s, 12H, 4 × C^4-*Me*, Mes), 4.16 (s, 4H, 2 × $C^{3,4}$-*H*, C_5H_4Me), 4.19 (s, 4H, 2 × $C^{2,5}$-*H*, C_5H_4Me), 7.08 (s, 8H, 4 × $C^{3,5}$-*H*, Mes), 7.57 (s, 4H, 4 × C^4-*H*, B(C_6H_3-3,5-$(CF_3)_2$)$_4$), 7.74 (s, 8H, 4 × $C^{2,6}$-*H*, B(C_6H_3-3,5-$(CF_3)_2$)$_4$), 7.87 (t, ^3J(H,H) = 7.1 Hz, 2H, 2 × C^4-*H*, C_6H_3), 8.38 (d, ^3J(H,H) = 7.1 Hz, 4H, 2 × $C^{3,5}$-*H*, C_6H_3).

^{13}C{^{1}H} NMR: (75.47 MHz, CD_2Cl_2, 193 K): δ (ppm) = 13.8 (s, 2C, 2 × C_5H_4*Me*), 21.2 (s, 12C, 4 × $C^{2,6}$-*Me* + 4 × C^4-*Me*, Mes), 80.0 (s, 4C, 2 × $C^{2,5}$-H, C_5H_4Me), 80.2 (s, 4C, 2 × $C^{3,4}$-H, C_5H_4Me), 101.9 (s, 2C, 2 × C^1-Me, C_5H_4Me), 117.9 (sept,

[53] 1 equiv. of Na[B(C_6H_3-3,5-$(CF_3)_2$)$_4$] was used to get the corresponding plumbylidyne complex but the reaction leads to the formation of bridging complex **38**. Later on, it was found that this bridging complex **38** very slowly converted to the corresponding plumbylidyne complex upon storing a fluorobenzene/*n*-pentane solution at –30 °C for several months (>2 months).

$^{3}J(^{13}C,^{19}F)$ = 4 Hz, 4 × C^{4}-H, $B(C_6H_3\text{-}3,5\text{-}(CF_3)_2)_4$), 125.0 (q, $^{1}J(^{13}C,^{19}F)$ = 272 Hz, 8C, 8 × CF_3, $B(C_6H_3\text{-}3,5\text{-}(CF_3)_2)_4$), 129.3 (qm, $^{2}J(^{13}C,^{19}F)$ = 31 Hz, 8C, 4 × $C^{3,5}$-CF_3, $B(C_6H_3\text{-}3,5\text{-}(CF_3)_2)_4$), 130.7 (s, 8C, 4 × $C^{3,5}$-H, Mes), 131.4 (s, 2C, 2 × C^{4}-H, C_6H_3), 134.5 (s, 4C, 4 × C^{1}, Mes), 135.2 (br s, 8C, 4 × $C^{2,6}$-H, $B(C_6H_3\text{-}3,5\text{-}(CF_3)_2)_4$), 137.1 (s, 8C, 2 × $C^{2,6}$, Mes), 137.9 (s, 4C, 2 × $C^{3,5}$-H, C_6H_3), 140.4 (s, 4C, 4 × C^{4}, Mes), 143.1 (s, 4C, 2 × $C^{2,6}$, C_6H_3), 162.2 (q, $^{1}J(^{13}C,^{11}B)$ = 50 Hz, 4 × C^{1}, $B(C_6H_3\text{-}3,5\text{-}(CF_3)_2)_4$), 222.3 (s, 4C, 4 × CO), 258.7 (s, 2C, 2 × Pb-C^{1}, C_6H_3).

4.5.52 [(η^5-C_5H_4Me)$(CO)_2Mn{\equiv}Pb(C_6H_3$-2,6-$Mes_2)$][B{$C_6H_3$-3,5-$(CF_3)_2$}$_4$] (39)

A mixture of complex **35** (140 mg, 0.188 mmol) and Na[B{C_6H_3-3,5-$(CF_3)_2$}$_4$] (166 mg, 0.187 mmol) was treated with 10 mL of *n*-pentane in a glove box. Complex **35** dissolved to give a red-brown solution containing insoluble, white Na[B{C_6H_3-3,5-$(CF_3)_2$}$_4$]. The suspension was stirred at ambient temperature for 30 minutes. During this time the color of the solution faded, and the insoluble solid took on a dark brown color. An IR spectrum was recorded from the light brown supernatant solution indicating the presence of some starting material **35** (ν(CO) = 1951 and 1900 cm^{-1}). An ATR-IR spectrum of the insoluble dark brown precipitate showed three ν(CO) absorption bands of an intermediate product at 1967, 1925 and 1914 cm^{-1}, which is suggested to be the chloro-bridged dinuclear plumbylidene complex [{(η^5-C_5H_4Me)$(CO)_2MnPb(C_6H_3$-2,6-$Mes_2)$}$_2$(μ-Cl)][B{C_6H_3-3,5-$(CF_3)_2$}$_4$].[54] Stirring of the suspension was continued for 18 hours to accomplish a full conversion of the intermediate product to the plumbylidyne complex **39**, which was confirmed by ATR-IR spectroscopy. Then the colorless supernatant solution was filtered off, and the dark brown solid was dried in *vacuo* for 15 minutes. The brown solid was suspended in 4 mL of *n*-hexane and treated with 4 mL of CH_2Cl_2. The obtained brown solution was freed from a small amount of a pale brown insoluble material (mostly NaCl) by filtration. The brown filtrate was concentrated under reduced pressure to *ca.* 5 mL leading to a brown suspension, which was stored at –60 °C for one hour. The

[54] The ν(CO) bands of the intermediate product compare well with those of the analogous bromo-bridged complex [{(η^5-C_5H_4Me)$(CO)_2MnPb(C_6H_3$-2,6-$Mes_2)$}$_2$(μ-Br)][B{C_6H_3-3,5-$(CF_3)_2$}$_4$], which is selectively formed in the reaction of [(η^5-C_5H_4Me)$(CO)_2Mn{=}Pb(C_6H_3$-2,6-$Mes_2)$Br] with Na[B{C_6H_3-3,5-$(CF_3)_2$}$_4$]. The latter compound was isolated as an analytically pure brown solid that was characterized by IR spectroscopy, ^{1}H NMR and ^{13}C NMR spectroscopy, and single-crystal X ray-diffraction.

obtained brown, microcrystalline precipitate was collected by filtration at –60 °C and dried in *vacuo* for one hour at ambient temperature to afford complex **39** as an air-sensitive, analytically pure, brown solid. Yield: (221 mg, 0.140 mmol, 75%).

Properties: Complex **39** is very good soluble in THF, Et_2O and fluorobenzene, and insoluble in toluene and aliphatic solvent.

Melting Points: Complex **39** decomposes upon melting at 170 – 171 °C to give a brown liquid. It is more light sensitive in solution than in the solid state, and should be stored in the dark over longer periods of time. Its light sensitivity in solution is less pronounced than that of **35**.

Elemental analysis: calcd (%)for $C_{64}H_{44}BF_{24}MnO_2Pb$ (1573.94 g/mol): C 48.84, H 2.82; found C 48.66, H 3.09%.

Spectroscopic Data:

ATR-IR (solid): $\tilde{\nu}$ (cm^{-1}) = 2965 (w), 2928 (w), 2879 (vw), 1992 (s) [ν(CO)], 1952 (s) [ν(CO)], 1609 (w), 1482 (vw), 1457 (vw), 1381 (vw), 1351 (s), 1299 (w), 1286 (m, sh), 1271 (vs), 1186 (m,sh), 1158 (s), 1113 (vs), 1048 (m, sh), 1033 (m, sh), 1000 (w), 945 (vw), 932 (vw), 921 (vw), 902 (w), 885 (s), 861 (w), 837 (m), 806 (w), 744 (w), 735 (vw,sh), 710 (m), 681 (s), 668 (s), 619 (w), 612 (w, sh), 580 (m), 549 (m), 500 (w), 448 (w), 403 (vw, sh), 395 (vw).

^{1}H NMR: (300.1 MHz, CD_2Cl_2, 298 K): δ (ppm) = 1.73 (s, 3H, C_5H_4*Me*), 2.16 (s, 12H, 2 × $C^{2,6}$-*Me*, Mes), 2.39 (s, 6H, 2 × C^4-*Me*, Mes), 4.40 (m, 2H, $C^{3,4}$-*H*, C_5H_4Me), 4.43 (m, 2H, $C^{2,5}$-*H*, C_5H_4Me), 7.21 (s, 4H, 2 × $C^{3,5}$-*H*, Mes), 7.56 (s, 4H, 4 × C^4-*H*, B(C_6H_3-3,5-(CF_3)$_2$)$_4$), 7.72 (m, 8H, 4 × $C^{2,6}$-*H*, B(C_6H_3-3,5-(CF_3)$_2$)$_4$), 8.02 (t, ^3J(H,H) = 7.5 Hz, 1H, C^4-*H*, C_6H_3), 8.65 (d, ^3J(H,H) = 7.5 Hz, 2H, $C^{3,5}$-*H*, C_6H_3).

^{13}C{^{1}H} NMR: (75.47 MHz, CD_2Cl_2, 193 K): δ (ppm) = 13.8 (s, 1C, C_5H_4*Me*), 20.8 (s, 4C, 2 × $C^{2,6}$-*Me*, Mes), 21.2 (s, 2C, 2 × C^4-*Me*, Mes), 79.5 (s, 2C, $C^{3,4}$-H, C_5H_4Me), 81.1 (s, 2C, $C^{2,5}$-H, C_5H_4Me), 103.8 (s, 1C, C^1-Me, C_5H_4Me), 117.9 (sept, ^3J(^{13}C,^{19}F) = 3 Hz, 4 × C^4-H, B(C_6H_3-3,5-(CF_3)$_2$)$_4$), 125.0 (q, ^1J(^{13}C,^{19}F) = 272 Hz, 8C, 8 × CF_3, B(C_6H_3-3,5-(CF_3)$_2$)$_4$), 129.3 (qm, ^{2}J(^{13}C,^{19}F) = 31 Hz, 8C, 4 ×

$C^{3,5}$-CF_3, B(C_6H_3-3,5-$(CF_3)_2$)$_4$), 131.0 (s, 4C, 2 × $C^{3,5}$-H, Mes), 132.5 (s, 1C, C^4-H, C_6H_3), 134.2 (s, 2C, 2 × C^1, Mes), 135.2 (br s, 8C, 4 × $C^{2,6}$-H, B(C_6H_3-3,5-$(CF_3)_2$)$_4$), 137.4 (s, 4C, 2 × $C^{2,6}$, Mes), 138.5 (s, 2C, $C^{3,5}$-H, C_6H_3), 141.6 (s, 2C, 2 × C^4, Mes), 141.9 (s, 2C, $C^{2,6}$, C_6H_3), 162.1 (q, $^1J(^{13}C,^{11}B)$ = 50 Hz, 4 × C^1, B(C_6H_3-3,5-$(CF_3)_2$)$_4$), 218.2 (s, 2C, 2 × *C*O), 268.5 (s, 1C, Pb-C^1, C_6H_3).

4.5.53 Plumbylidyne ligand transfer reaction of 39 with 3-Mo·DME

4.5.53.1. Monitoring by NMR spectroscopy

A mixture of brown colored **39** (10 mg, 0.006 mmol) and yellow colored **3-Mo**·DME (8 mg, 0.012 mmol) was suspended in 0.5 mL of C_6D_6 in a brown glass vial (2 mL). The suspension was stirred for 5 minutes inside a glove box. During this time the initially colorless supernatant benzene solution took on a greenish yellow and then a brownish green color. The solution was filtered through a filter syringe into a screw-cap brown NMR tube under exclusion of light. The ^{1}H and ^{31}P{^{1}H} NMR spectra of the solution were recorded indicating the formation of complexes **10-Mo** and [(η^5-C_5H_4Me)Mn(CO)$_2$(PMe_3)]. The products were identified upon a comparison of their spectra with those of authentic samples.

4.5.53.2. Monitoring by IR spectroscopy

In a glove box, a brown glass vial (2 mL) was charged with a mixture of **39** (13 mg, 0.008 mmol) and **3-Mo**·DME (7 mg, 0.011 mmol). The mixture was suspended in 1 mL of *n*-hexane under exclusion of light, and the suspension stirred for two hours at ambient temperature. During this time the initially colorless supernatant solution gradually took on a brownish-green color. After 2 hours of stirring an IR spectrum of the supernatant solution was recorded revealing the formation of complex **10-Mo** (ν(CO) in *n*-hexane: 1899 and 1832 cm^{-1}), complex [(η^5-C_5H_4Me)Mn(CO)$_2$(PMe_3)] (ν(CO) in *n*-hexane: 1935 and 1873 cm^{-1}) and of complex **2-Mo** to a minor extent (ν(CO) in *n*-hexane: 1903 and 1770 cm^{-1}). The ν_{CO} bands of the products were identified upon comparison with those of the pure complexes.

4.5.54 *trans*-[H(dmpe)$_2$Mn=Sn(Cl)(C_6H_3-2,6-Mes_2)] (40)

A mixture of [MnH(η^2-H_2)(dmpe)$_2$] (100 mg, 0.279 mmol) and SnCl(C_6H_3-2,6-Mes_2) (131 mg, 0.280 mmol, 1 equiv.) was treated with 15 mL of toluene at room temperature in the glove box. The color of the solution immediately changed from yellow to dark red-brown with gas

evolution (H_2). The reaction solution was stirred for 4 hours. An aliquot of the solution was transferred via a syringe into an NMR tube and a ^{31}P NMR spectrum was recorded, which revealed a complete and selective conversion of the starting material into the stannylidene complex **40**. The red-brown solution was concentrated in *vacuo* to *ca.* 10 mL and treated with 15 mL of petrol ether. The resulting suspension was stored at –60 °C for 18 hours, and the microcrystalline precipitate was separated from the mother liquor by filtration at –60 °C. The red-brown solid was washed once with 10 mL of *n*-pentane at –30 °C and dried in *vacuo* at ambient temperature for 2 hours to give 168 mg of complex **40**. A second crop of the product (47 mg) was obtained upon concentration of the mother liquor to *ca.* 3 mL and storage at –60 °C for 18 hours. Combined yield: 215 mg (0.261 mmol, 93%).

Properties: It is very well soluble in THF and fluorobenzene, moderately soluble in toluene and Et_2O and sparingly soluble in *n*-hexane. Compound is moderately air-sensitive.

Melting Points: Complex **40** is thermally very stable and does not melt or decompose upon heating to 240 °C.

Elemental analysis: calcd. (%) for $C_{36}H_{58}ClMnP_4Sn$ (823.78 g/mol): C 52.48, H 7.10; found C 52.00, H 6.98.

Spectroscopic Data:

ATR-IR (solid): $\tilde{\nu}$ (cm^{-1}) = 1760 [ν(Mn-H)].

^{1}H NMR: (300.1 MHz, C_6D_6, 298 K): δ (ppm) = –13.73 (quint, ^2J(P,H) = 59 Hz, 1H, Mn-*H*), 0.99 (br s, $\Delta\nu_{1/2}$ = 10 Hz, 12H, 4 × P(*Me*^{A})(Me^B)), 1.24 (br s, $\Delta\nu_{1/2}$ =10 Hz, 12H, 4 × P(Me^A)(*Me*^{B})), 1.58 (br s, $\Delta\nu_{1/2}$ = 24 Hz, 4H, 4 × PC*H*^{A}H^B), 1.81 (br s, $\Delta\nu_{1/2}$ = 24 Hz, 4H, 4 × PCH^A*H*^{B}), 2.11 (s, 6H, 2 × *Me*, Mes), 2.24 (s, 6H, 2 × *Me*, Mes), 2.70 (s, 6H, 2 × *Me*, Mes), 6.75 (br s, $\Delta\nu_{1/2}$ = 8 Hz, 2H, 2 ×C^3-*H*, Mes), 6.90 (s, $\Delta\nu_{1/2}$ = 8 Hz, 2H, 2 × C^5-*H*, Mes), 6.94 (d, ^3J(H,H) = 7.4 Hz, 2H, C^{3,5}-*H,* C_6H_3), 7.19 (t, ^3J(H,H) = 7.4 Hz, 1H, C^4-*H*, C_6H_3; the signal overlaps with that of the deuterated solvent at δ = 7.15 ppm).

^{1}H NMR: (300.1 MHz, THF-d_8, 298 K): δ (ppm) = –13.70 (quint, ^2J(P,H) = 59 Hz, 1H, Mn-*H*), 1.11 (br s, $\Delta\nu_{1/2}$ = 7 Hz, 12H, 4 × P(*Me*^{A})(Me^B)), 1.20 (br s, $\Delta\nu_{1/2}$ = 7 Hz, 12H, 4 × P(Me^A)(*Me*^{B})), 1.97 (s, 6H, 2 × C^2-*Me*, Mes), 2.27 (s, 6H, 2 × C^4-

Me, Mes), 2.31 (s, 6H, 2 × C^6-*Me*, Mes), 6.78 (br s, $\Delta\nu_{1/2}$ = 6 Hz, 2H, 2 ×$C^{3,}$-*H*, Mes), 6.81 (d, ^3J(H,H) = 7.4 Hz, 2H, $C^{3,5}$-*H,* C_6H_3), 6.84 (br s, $\Delta\nu_{1/2}$ = 6 Hz, 2H, 2 × C^5-*H*, Mes), 7.21 (t, ^3J(H,H) = 7.4 Hz, 1H, C^4-*H*, C_6H_3); the signals of the methylene protons of the dmpe ligands are obscured by that of the deuterated solvent at δ = 1.73 ppm.

$^{13}C\{^1H\}$ NMR: (75.5 MHz, THF-d_8, 298 K): δ (ppm) = 21.3 (s, 2C, 2 × C^4-*Me*, Mes), 22.7 (s, 2C, 2 × C^6-*Me*, Mes), 22.8 (s, 2C, 2 × C^2-*Me*, Mes), 28.1 (m, 4C, 4 × P(Me^A)(Me^B)), 29.5 (m, 4C, 4 × P(Me^A)(Me^B)), 35.0 (m, 4C, 4 × P*C*H_2), 128.0 (s, 1C, C^4-H, C_6H_3), 129.37 (s, 2C, 2 × C^3-H, Mes), 129.45 (s, 2C, 2 × C^5-H, Mes), 130.1 (s, 2C, $C^{3,5}$-H, C_6H_3), 136.7 (s, 2C, 2 × C^2-Me, Mes), 137.2 (s, 2C, 2 × C^4-Me, Mes), 138.6 (s, 2C, 2 × C^6-Me, Mes), 142.0 (s, 2C, 2 × C^1, Mes), 146.1 (s, 2C, $C^{2,6}$, C_6H_3), 184.7 (s, 1C, Sn-C^1, C_6H_3).

$^{31}P\{^1H\}$ NMR: (121.5 MHz, C_6D_6, 298 K): δ (ppm) = 79.1 (s, $^2J(^{119}Sn,^{31}P)$ = 210 Hz).

$^{31}P\{^1H\}$ NMR: (121.5 MHz, THF-d_8, 298 K): δ (ppm) = 79.5 (s, $^2J(^{119}Sn,^{31}P)$ = 210 Hz).

$^{119}Sn\{^1H\}$ NMR: (111.9 MHz, THF-d_8, 298 K): δ (ppm) = *ca*. 540 (br, $\Delta\nu_{1/2}$ = 7100 Hz).

4.5.55 *trans*-[H(dmpe)$_2$Mn≡Sn(C$_6$H$_3$-2,6-Mes$_2$)][B{C$_6$H$_3$-3,5-(CF$_3$)$_2$}$_4$] (41)

A mixture of complex **40** (100 mg, 0.121 mmol) and Na[B{C_6H_3-3,5-$(CF_3)_2$}$_4$] (108 mg, 0.122 mmol, 1 equiv.) was treated with 10 mL of fluorobenzene at room temperature in the glove box. The color of the solution immediately changed from red-brown to purple. Stirring was continued for 4 hours, and before workup a ^{31}P NMR spectrum was recorded to confirm the complete conversion of **40** into the stannylidyne complex salt **41**. The purple colored solution was concentrated in *vacuo* to *ca.* 8 mL and treated with 2 mL of *n*-hexane. The suspension was filtered from NaCl. The filtrate was concentrated in *vacuo* to *ca.* 5 mL, treated with 4 mL of *n*-hexane and stored at –30 °C for 24 hours. The purple colored crystalline precipitate was isolated by filtration at –30 °C, and after short drying at ambient temperature was ground into a powder by using one freeze-pump-thaw cycle and finally dried in *vacuo* for 3 hours at ambient temperature to afford complex **41** as an analytically pure, purple solid. Yield: 179 mg (0.108 mmol, 89%).

Properties: It is very well soluble in THF and fluorobenzene, insoluble in toluene and *n*-hexane. Compound is extremely air sensitive.

Melting Points: Complex **41** melts at ~ 195 °C to form a purple colored liquid.

Elemental analysis: calcd. (%) for $C_{68}H_{70}BF_{24}MnP_4Sn$ (1651.6 g/mol): C 49.45, H 4.27; found C 49.22, H 4.61%.

Spectroscopic Data:

ATR-IR (solid): $\tilde{\nu}$ (cm^{-1}) = 1792 [ν(Mn-H)].

^{1}H NMR: (400.1 MHz, CD_2Cl_2, 298 K): δ (ppm) = –14.59 (quint, ^2J(P,H) = 66 Hz, 1H, Mn-*H*), 1.15 (br, 4H, 4 × PC*H*^{A}H^B; the signal is partially obscured by that of the methyl protons at δ = 1.17 ppm), 1.17 (br s, $\Delta\nu_{1/2}$ = 9 Hz, 12H, 4 × P(*Me*^{A})(Me^B)), 1.48 (br s, $\Delta\nu_{1/2}$ = 9 Hz, 12H, 4 × P(Me^A)(*Me*^{B})), 1.74 (br m, $\Delta\nu_{1/2}$ = 23 Hz, 4H, 4 × PCH^A*H*^{B}), 2.07 (s, 12H, 2 × C^{2,6}-*Me*, Mes), 2.39 (s, 6H, 2 × C^4-*Me*, Mes), 7.02 (s, 4H, 2 ×C^{3,5}-*H*, Mes), 7.12 (d, ^3J(H,H) = 7.6 Hz, 2H, C^{3,5}-*H,* C_6H_3), 7.50 (t, ^3J(H,H) = 7.6 Hz, 1H, C^4-*H*, C_6H_3), 7.58 (br s, $\Delta\nu_{1/2}$ = 6 Hz, 4H, 4 × C^4-*H*, B(C_6H_3-3,5-$(CF_3)_2$)$_4$), 7.75 (br s, $\Delta\nu_{1/2}$ = 11 Hz, 8H, 4 × C^{2,6}-*H*, B(C_6H_3-3,5-$(CF_3)_2$)$_4$).

^{13}C{^{1}H} NMR: (100.6 MHz, CD_2Cl_2, 298 K): δ (ppm) = 21.3 (s, 2C, 2 × C^4-*Me*, Mes), 21.5 (s, 4C, 2 × C^{2,6}-*Me*, Mes), 24.7 (m, 4C, 4 × P(*Me*^{A})(Me^B)), 33.2 (m, 4C, 4 × P(Me^A)(*Me*^{B})), 34.6 (m, 4C, 4 × P*C*H$_2$), 117.9 (unresolved septet, 4C, 4 × *C*^{4}-H, B(C_6H_3-3,5-$(CF_3)_2$)$_4$), 125.0 (q, ^1J(^{19}F,^{13}C) = 272 Hz, 8C, 4 × C^{3,5}-*C*F_3, B(C_6H_3-3,5-$(CF_3)_2$)$_4$), 129.3 (q, ^2J(^{19}F,^{13}C) = 33 Hz, 8C, 4 × *C*^{3,5}-CF_3, B(C_6H_3-3,5-$(CF_3)_2$)$_4$), 129.9 (s, 4C, *C*^{3,5}-H, Mes), 130.4 (s, 2C, *C*^{3,5}-H, C_6H_3), 131.0 (s, 1C, *C*^{4}-H, C_6H_3), 135.2 (br s, $\Delta\nu_{1/2}$ = 10 Hz, 8C, 4 × *C*^{2,6}-H, B(C_6H_3-3,5-$(CF_3)_2$)$_4$), 137.0 (s, 4C, 2 × *C*^{2,6}-Me, Mes), 138.5 (s, 2C, 2 × *C*^{1}, Mes), 139.3 (s, 2C, 2 × *C*^{4}-Me, Mes), 143.7 (s, 2C, *C*^{2,6}, C_6H_3), 162.2 (q, ^1J(^{13}C,^{11}B) = 49.8 Hz, 4C, 4 × *C*^{1}, B(C_6H_3-3,5-$(CF_3)_2$)$_4$), 188.2 (s, 1C, Sn-*C*^{1}, C_6H_3).

^{31}P{^{1}H} NMR: (162.0 MHz, CD_2Cl_2, 298 K): δ (ppm) = 71.0 (^2J($^{119/117}$Sn,^{31}P) = 200 Hz).

^{119}Sn{^{1}H} NMR: (111.9 MHz, THF-d_8, 298 K): δ (ppm) = 761 (br, $\Delta\nu_{1/2}$ = 1600 Hz).

4.5.56 *trans*-[H(dmpe)$_2$Mn≡Sn(C$_6$H$_3$-2,6-Mes$_2$)][Al(OC(CF$_3$)$_3$)$_4$] (42)

A mixture of complex **40** (100 mg, 0.121 mmol) and Li[Al(OC(CF$_3$)$_3$)$_4$] (119 mg, 0.122 mmol, one equiv.) was treated with 15 mL of fluorobenzene at room temperature The color of the reaction mixture immediately changed from dark red-brown to dark purple. The reaction mixture was stirred for 3 hours. Completion of the reaction was confirmed by ^{31}P NMR spectroscopy. Petrol ether (5 mL) was added, and the suspension was filtered. The clear filtrate was stored at –60 °C for 24 hours. The purple, microcrystalline precipitate was separated from the mother liquor by filtration and dried under vacuum for 3 hours at 60 °C to give a first crop (149 mg) of complex **42**. The mother liquor was concentrated to approximately 8 mL, treated with 5 mL of petrol ether and stored for 1 week at –30 °C to give after filtration and drying of the precipitated solid a second crop (42 mg) of the product. Combined yield: 191 mg (0.109 mmol, 90%).

Properties: It is very well soluble in THF and fluorobenzene, insoluble in toluene and *n*-hexane. The compound is extremely air-sensitive.

Melting Points: Complex **42** is thermally very stable and does not melt or decompose upon heating to 240 °C.

Elemental analysis: calcd. (%) for $C_{52}H_{58}AlF_{36}MnO_4P_4Sn$ (1755.47 g/mol): C 35.58, H 3.33; found C 35.68, H 3.51%.

Spectroscopic Data:

ATR-IR (solid): $\tilde{\nu}$ (cm^{-1}) = 1778 [ν(Mn-H)].

^{1}H NMR: (300.1 MHz, CD_2Cl_2, 298 K): δ (ppm) = –14.58 (quint, ^2J(P,H) = 66 Hz, 1H, Mn-*H*), 1.14 (br, 4H, 4 × PC*H*^{A}H^B; the signal is partially obscured by that of the methyl protons at δ = 1.17 ppm), 1.19 (br s, $\Delta\nu_{1/2}$ = 9 Hz, 12H, 4 × P(*Me*^{A})(Me^B)), 1.49 (br s, $\Delta\nu_{1/2}$ = 9 Hz, 12H, 4 × P(Me^A)(*Me*^{B})), 1.74 (br m, $\Delta\nu_{1/2}$ = 26 Hz, 4H, 4 × PCH^A*H*^{B}), 2.07 (s, 12H, 2 × C^{2,6}-*Me*, Mes), 2.40 (s, 6H, 2 × C^4-*Me*, Mes), 7.02 (s, 4H, 2 × C^{3,5}-*H*, Mes), 7.11 (d, ^3J(H,H) = 7.5 Hz, 2H, C^{3,5}-*H,* C$_6$H$_3$), 7.50 (t, ^3J(H,H) = 7.5 Hz, 1H, C^4-*H*, C$_6$H$_3$).

^{13}C{^{1}H} NMR: (75.47 MHz, CD_2Cl_2, 298 K): δ (ppm) = 21.3 (s, 2C, 2 × C^4-*Me*, Mes), 21.5 (s, 4C, 2 × C^{2,6}-*Me*, Mes), 24.7 (m, 4C, 4 × P(*Me*^{A})(Me^B)), 33.2 (m, 4C, 4 × P(Me^A)(*Me*^{B})), 34.6 (m, 4C, 4 × P*C*H$_2$), 79.4 (m, 4C, 4 × O*C*(CF$_3$)$_3$; this signal

was of very low intensity and appeared as a hump over the base line), 121.6 [q, $^{1}J(^{19}F,^{13}C)$ = 292 Hz, 12C, 4 × OC(CF$_3$)$_3$), 129.9 (s, 4C, $C^{3,5}$-H, Mes), 130.4 (s, 2C, $C^{3,5}$-H, C$_6$H$_3$), 131.0 (s, 1C, C^{4}-H, C$_6$H$_3$), 137.0 (s, 4C, 2 × $C^{2,6}$-Me, Mes), 138.5 (s, 2C, 2 × C^{1}, Mes), 139.3 (s, 2C, 2 × C^{4}-Me, Mes), 143.7 (s, 2C, $C^{2,6}$, C$_6$H$_3$), 188.2 (s, 1C, Sn-C^{1}, C$_6$H$_3$).

^{31}P{^{1}H} NMR: (162.0 MHz, CD_2Cl_2, 298 K): δ (ppm) = 71.0 ($^{2}J(^{119/117}Sn,^{31}P)$ = 215 Hz).

4.5.57 *trans*-[H(dmpe)$_2$Mn=Sn(C$_6$H$_3$-2,6-Mes$_2$)] (43)

To a solid mixture of **41** (600 mg, 0.36 mmol) and C_8K (49 mg, 0.36 mmol, 1 equiv.) ~30 mL of THF was condensed from a schlenck tube containing THF over C_8K. The reaction mixture was slowly brought to −78 °C and stirred for 2 hrs at this temperature. Upon stirring, the color of the suspension changed from purple to dark brown. The brown suspension was slowly brought to 0 °C and stirred for another 1 hr, and afterward, all volatiles were removed under reduced pressure at 0 °C. The brown residue was extracted with *n*-pentane (3 × 20 mL) at 0 °C, and the combined extract was concentrated to ~ 15 mL and stored at −60 °C. A microcrystalline brown solid that precipitated out from the solution was isolated by filtration of the brown supernatant at −60 °C and dried under reduced pressure at 0 °C for 2 hrs. Yield: 140 mg (0.18 mmol, 49%).

Properties: It is very well soluble in THF, fluorobenzene and toluene and moderately soluble in aliphatic solvent. Compound **43** is extremely air-sensitive.

Melting Points: Brown solid decomposes to a very dark brown (almost black) solid upon heating to 152 °C.

Elemental analysis: calcd. (%) for $C_{36}H_{58}MnP_4Sn$ (788.39 g/mol): C 54.84, H 7.42; found C 54.25, H 7.42%.

Spectroscopic Data:

ATR-IR (solid): $\tilde{\nu}$ (cm^{-1}) = 1747 [ν(Mn-H)].

4.5.58 *trans*-[H(dmpe)$_2$Mn=Sn(H)(C$_6$H$_3$-2,6-Mes$_2$)] (44)

A mixture of **41** (600 mg, 0.36 mmol) and KH (20 mg, 0.50 mmol, 1.4 equiv.) was treated with 25 mL of THF at ambient temperature and the purple suspension was stirred at ambient

temperature for 18 hours. Upon stirring, the color of the suspension changed to dark red. Completion of the reaction after 18 hours was confirmed by *in situ* ^{31}P NMR spectroscopy, which revealed a complete conversion of the cationic stannylidyne complex **41** to neutral hydridostannylidene **44,** along with some unknown minor impurities and free dmpe. All volatiles were removed under reduced pressure and pulverized once by freeze-pump-thaw cycle. The resulting dark red powder was extracted with 30 mL of *n*-hexane at ambient temperature. The dark red extract was evaporated to dryness and the residue was redissolved in 10 mL of *n*-hexane. The obtain suspension was concentrated to ~5 mL and stored at –30 °C for 2 hours. The dark red powder that precipitated out upon cooling was isolated by filtration of the dark red supernatant and dried for 1 hour at ambient temperature. Obtained dark red powder was recrystalized from *n*-hexane at –30 °C to afford **44** as an analytically pure dark red solid in moderate yield. Yield: 123 mg (0.16 mmol, 43%).

Properties: It is very well soluble in all common organic solvents. Compound **44** is very sensitive towards air both in solid state and solution. Upon exposure to air, the dark red solution decolorises within 5 minutes.

Melting Points: Compound starts to decompose upon melting at 185 – 188 °C. Melting leads to a dark red liquid.

Elemental analysis: calcd. (%) for $C_{36}H_{59}MnP_4Sn$ (789.4 g/mol): C 54.77, H 7.53; found C 54.23, H 7.36.

Spectroscopic Data:

ATR-IR (solid): $\tilde{\nu}$ (cm^{-1}) = 1743 [*v*(Mn-H)], 1627 [*v*(Sn-H)].

^{1}H NMR: (300.1 MHz, C_6D_6, 298 K): δ (ppm) = –11.93 (quint, ^2J(P,H) = 57 Hz, 1H, Mn-*H*), 1.11 (br s, $\Delta\nu_{1/2}$ = 8 Hz, 12H, 4 × P(*Me*^{A})(Me^B)), 1.24 (br s, $\Delta\nu_{1/2}$ = 8 Hz, 12H, 4 × P(Me^A)(*Me*^{B})), 1.28 (br s, $\Delta\nu_{1/2}$ = 23 Hz, 4H, 4 × PC*H*^{A}H^B; the signal overlaps with the signal at δ = 1.24 ppm), 1.44 (br s, $\Delta\nu_{1/2}$ = 23 Hz, 4H, 4 × PCH^A*H*^{B}), 2.22 (s, 6H, 2 × C^4-*Me*, Mes), 2.32 (s, 12H, 2 × C^{2,6}-*Me*, Mes), 2.70 (s, 6H, 2 × *Me*, Mes), 6.78 (s, 4H, 2 ×C^{3,5}-*H*, Mes), 6.98 (d, ^3J(H,H) = 7.5 Hz, 2H, C^{3,5}-*H,* C_6H_3), 7.25 (t, ^3J(H,H) = 7.5 Hz, 1H, C^4-*H*, C_6H_3), 18.46 (quint, ^1J(Sn,H) = 425 Hz, ^3J(P,H) = 4.9 Hz, 1H, Sn-*H*).

$^{13}C\{^1H\}$ NMR: (75.5 MHz, C_6D_6, 298 K): δ (ppm) = 21.2 (s, 2C, 2 × C^4-*Me*, Mes), 22.0 (s, 4C, 2 × $C^{2,6}$-*Me*, Mes), 28.7 (m, 4C, 4 × P(Me^A)(Me^B)), 29.0 (m, 4C, 4 × P(Me^A)(Me^B)), 34.6 (m, 4C, 4 × P*C*H_2), 127.0 (s, 1C, C^4-H, C_6H_3), 128.75 (s, 2C, $C^{3,5}$-H, C_6H_3), 128.9 (s, 4C, 2 × $C^{3,5}$-H, Mes), 136.0 (s, 2C, 2 × C^4-Me, Mes), 136.7 (s, 2C, 2 × $C^{2,6}$-Me, Mes), 142.2 (s, 2C, 2 × C^1, Mes), 147.3 (s, 2C, $C^{2,6}$, C_6H_3), 173.4 (s, 1C, Sn-C^1, C_6H_3).

$^{31}P\{^1H\}$ NMR (121.5 MHz, C_6D_6, 298 K): δ (ppm) = 78.9 (s, $^2J(^{119}Sn,^{31}P)$ = 248 Hz).

$^{119}Sn\{^1H\}$ NMR: (186.52 MHz, C_6D_6, 298 K): δ (ppm) = 531.7 (br, $\Delta\nu_{1/2}$ = 1322 Hz).

4.5.59 SiBr(SiBr$_2$Tbb)(SIdipp) (45)

A mixture of (*E*)-Tbb(Br)Si=Si(Br)Tbb (300 mg, 0.27 mmol, 0.5 equiv.) and $SiBr_2$(SIdipp) (311 mg, 0.54 mmol) was treated with 20 mL of toluene. The resulting yellow suspension was heated to 100 °C for 5 hours. Upon heating all solids dissolved, and the color of the solution changed gradually to dark orange. Monitoring of the reaction progress by ^1H NMR spectroscopy revealed the selective formation of **45** and furthermore showed that the reaction stopped after *ca.* 90 % of conversion. Prolonged heating did not lead to further conversion. All volatiles were removed under vacuum, and the yellow solid was extracted with 30 mL of *n*-hexane at ambient temperature. The dark orange *n*-hexane extract was evaporated to dryness under vacuum to yield a yellow solid. The solid was dissolved in 10 mL of *n*-hexane, and the orange solution was kept at 0 °C for 15 minutes under slow stirring, whereupon a yellow solid precipitated. The amorphous yellow solid was collected by filtration of the pale orange supernatant at 0 °C and dried under vacuum for 30 minutes at 60 °C. Yield: 372 mg (0.33 mmol, 61 %).

Properties: It is well soluble in all common organic solvent. Compound is extremely sensitive towards air.

Melting Points: Yellow solid starts to decompose upon melting at 122 – 125 °C. Melting leads to an orange liquid.

Elemental analysis: $C_{51}H_{87}Br_3N_2Si_6$ (1136.47): C 53.90, H 7.72, N 2.47; found: C 53.82, H 7.60, 2.55 %.

Spectroscopic Data:

^{1}H NMR: (500.1 MHz, C_6D_6, 298 K): δ (ppm) = 0.27 (s, 18H, $C^{2,6}$-CH(SiMe_3)$_A$(SiMe$_3$)$_B$, Tbb), 0.32 (s, 18H, $C^{2,6}$-CH(SiMe$_3$)$_A$(SiMe_3)$_B$, Tbb), 1.10 (d, ^{3}J(H,H) = 6.7 Hz, 12H, 2 × C^{2}-CHMe_AMe$_B$ + 2 × C^{6}-CHMe_AMe$_B$, dipp), 1.26 (s, 9H, C^{4}-CMe_3, Tbb), 1.67 (d, ^{3}J(H,H) = 6.7 Hz, 6H, 2 × C^{2}-CHMe$_A$$Me_B$, dipp), 1.69 (d, ^{3}J(H,H) = 6.7 Hz, 6H, 2 × C^{6}-CHMe$_A$$Me_B$, dipp), 3.10 (br s, $\Delta\nu_{1/2}$ = 8 Hz, 2H, $C^{2,6}$-CH(SiMe$_3$)$_A$(SiMe$_3$)$_B$, Tbb), 3.41 – 3.53 (m, 6H, 2 × NCH_2 + 2 × C^{2}-CHMe$_A$Me$_B$, dipp), 3.57 (sept, ^{3}J(H,H) = 6.7 Hz, 2H, 2 × C^{6}-CHMe$_A$Me$_B$, dipp), 6.82 (s, 2H, $C^{3,5}$-H, Tbb), 7.05 – 7.09 (m, 4H, 2 × C^{3}-H + 2 × C^{5}-H, dipp), 7.15 (t, ^{3}J(H,H) = 7.7 Hz, 2H, 2 × C^{4}-H, dipp; this signal overlaps with that of the deuterated solvent).

^{13}C{^{1}H} NMR: (125.8 MHz, C_6D_6, 298 K): δ (ppm) = 2.09, 2.11 (s each, ^{1}J(Si,C) = 51 Hz each, 6C each, $C^{2,6}$-CH(SiMe_3)$_A$(SiMe$_3$)$_B$ + $C^{2,6}$-CH(SiMe$_3$)$_A$(SiMe_3)$_B$, Tbb), 23.77, 23.78 (s each, 2C each, 2 × C^{2}-CHMe$_A$$Me_B$ + 2 × C^{6}-CHMe$_A$$Me_B$), 26.7 (s, 2C, 2 × C^{6}-CHMe_AMe$_B$, dipp), 26.8 (s, 2C, 2 × C^{2}-CHMe_AMe$_B$, dipp), 29.4 (s, 4C, $C^{2,6}$-CH(SiMe$_3$)$_A$(SiMe$_3$)$_B$, Tbb + 2 × C^{2}-CHMe$_A$Me$_B$, dipp), 29.5 (s, 2C, 2 × C^{6}-CHMe$_A$Me$_B$, dipp), 31.1 (s, 3C, C^{4}-CMe_3, Tbb), 34.2 (s, 1C, C^{4}-CMe$_3$, Tbb), 55.2 (s, 2C, 2 × NCH$_2$), 123.3 (s, 2C, $C^{3,5}$-H, Tbb), 125.1 (s, 2C, 2 × C^{5}-H, dipp), 125.4 (s, 2C, 2 × C^{3}-H, dipp), 129.2 (s, 1C, C^{1}-Si, Tbb), 130.4 (s, 2C, 2 × C^{4}-H, dipp), 135.5 (s, 2C, 2 × C^{1}, dipp), 146.3 (s, 2C, 2 × C^{6}-CHMe$_A$Me$_B$, dipp), 146.9 (s, 2C each, 2 × C^{2}-CHMe$_A$Me$_B$, dipp), 150.7 (s, 1C, C^{4}-CMe$_3$, Tbb), 151.4 (s, 2C, $C^{2,6}$-CH(SiMe$_3$)$_A$(SiMe$_3$)$_B$, Tbb), 190.9 (s, 1C, NCN).

^{29}Si{^{1}H} NMR: (59.63 MHz, C_6D_6, 298 K): δ (ppm) = −11.3 (s, 1Si, SiBr$_2$), −1.9 (s, 1Si,SiBr), 2.45, 2.64 (s each, 2Si each, $C^{2,6}$-CH(SiMe$_3$)$_A$(SiMe$_3$)$_B$ + $C^{2,6}$-CH(SiMe$_3$)$_A$(SiMe$_3$)$_B$, Tbb).

4.5.60 (*Z*)-(SIdipp)Si═Si(Br)Tbb (46)

A mixture of compound **45** (1.50 g, 1.32 mmol) and KC_8 (0.49 g, 3.62 mmol, 2.75 equiv.) was treated with 40 mL of benzene at ambient temperature. The resulting orange suspension was stirred for 65 hours. During this time the color of the reaction mixture changed to dark red, and monitoring of the reaction progress by ^{1}H NMR spectroscopy revealed a selective and complete conversion of **45** into **46**. The suspension was filtered, and the dark red filtrate was evaporated to dryness under vacuum. The resulting dark red residue was digested with 20 mL of *n*-pentane. The

bright red suspension was concentrated under vacuum to *ca.* 10 mL and stored at −60 °C for 1 hour, whereupon a bright red, microcrystalline solid was obtained. The solid was isolated by filtration of the dark red supernatant at −30 °C and dried under vacuum for 4 hours at 80 °C. The compound **46** was isolated as a bright red, extremely air-sensitive solid. Yield: 0.777 g (0.80 mmol, 60 %).

Properties: It is well soluble in all common organic solvent. Compound is extremely sensitive towards air.

Melting Points: Compound **46** starts to decompose upon melting at 237 – 238 °C. Melting leads to a red liquid.

Elemental analysis: calcd (%) for $C_{51}H_{87}BrN_2Si_6$ (976.67): C 62.71, H 8.98, N 2.87; found: C 62.19, H 9.15, N 2.78 %.

Spectroscopic Data:

^{1}H NMR: (300.1 MHz, C_6D_6, 298 K): δ (ppm) = 0.17 (s, ^1J(C,H) = 119 Hz, 36H, $C^{2,6}$-CH(SiMe_3)$_2$, Tbb), 1.12 (d, ^3J(H,H) = 6.8 Hz, 12H, 2 × $C^{2,6}$-CHMe_AMe$_B$, dipp), 1.29 (s, 9H, C^4-CMe_3, Tbb), 1.61 (d, ^3J(H,H) = 6.8 Hz, 12H, 2 × $C^{2,6}$-CHMe$_A$$Me_B$, dipp), 3.12 (s, ^2J(Si,H) = 9.5 Hz, 2H, $C^{2,6}$-CH(SiMe$_3$)$_2$, Tbb), 3.41 (sept, ^3J(H,H) = 6.8 Hz, 4H, 2 × $C^{2,6}$-CHMe$_A$Me$_B$, dipp), 3.52 (s, 4H, 2 × NCH_2), 6.90 (s, 2H, $C^{3,5}$-*H*, Tbb), 7.10* (d, ^3J(H,H) = 7.8 Hz, 4H, 2 × $C^{3,5}$-*H*, dipp), 7.21* (t, ^3J(H,H) = 7.8 Hz, 2H, 2 × C^4-*H*, dipp).[55]

^{13}C{^{1}H} NMR: (75.47 MHz, C_6D_6, 298 K): δ (ppm) = 1.4 (s, ^1J(Si,C) = 51 Hz, 12C, $C^{2,6}$-CH(SiMe_3)$_2$, Tbb), 25.2 (s, 4C, 2 × $C^{2,6}$-CHMe$_A$$Me_B$, dipp), 26.2 (s, 4C, 2 × $C^{2,6}$-CHMe_AMe$_B$, dipp), 29.1 (s, 4C, 2 × $C^{2,6}$-CHMe$_A$Me$_B$, dipp), 31.3 (s, 3C, C^4-CMe_3, Tbb), 32.9 (s, ^1J(Si,C) = 43 Hz, 2C, $C^{2,6}$-CH(SiMe$_3$)$_2$, Tbb), 34.4 (s, 1C, C^4-CMe$_3$, Tbb), 53.8 (s, 2C, 2 × NCH$_2$), 120.5 (s, 2C, $C^{3,5}$-H, Tbb), 125.3 (s, 4C, 2 × $C^{3,5}$-H, dipp), 130.0 (s, 2C, 2 × C^4-H, dipp), 136.0 (s, 2C, 2 × C^1,

[55] The signals marked with an asterisk correspond to an AB_2 spin system showing a small second-order splitting of the doublet and the triplet signal, respectively. The given ^3J(H,H) coupling constant of 7.8 Hz was confirmed by simulation with the program gNMR (*gNMR*, Version 5.0.6.0, P. H. M. Budzelaar, IvorySoft, Centennial, USA, **2006**).

dipp), 137.9 (s, 1C, C^1-Si, Tbb), 146.7 (s, 4C, 2 × $C^{2,6}$-CHMe$_A$Me$_B$, dipp), 150.9 (s, 2C, $C^{2,6}$-CH(SiMe$_3$)$_2$, Tbb), 151.0 (s, 1C, C^4-CMe$_3$, Tbb), 204.6 (s, 1C, N*C*N).

^{29}Si{^{1}H} NMR: (59.63 MHz, C_6D_6, 298 K*)*: δ (ppm) = 1.6 (s, 4 × *Si*Me$_3$, Tbb), 34.6 (s, 1Si, *Si*=SiBr), 86.0 (s, 1Si, Si=*Si*Br).

5 Appendices

5.1. List of Compounds

Compounds No.	Compounds
1-Mo	[Tp'Mo(CO)$_2$(PMe$_3$)Cl]
1-W	[Tp'W(CO)$_2$(PMe$_3$)Cl]
2-Mo	[Tp'Mo(CO)$_2$(PMe$_3$)]
2-W	[Tp'W(CO)$_2$(PMe$_3$)]
3-Mo	Na[Tp'Mo(CO)$_2$(PMe$_3$)]
3-W	Na[Tp'W(CO)$_2$(PMe$_3$)]
4-Mo	[Tp'Mo(CO)$_2$(PMe$_3$)H]
5-Mo	[Tp'(CO)$_2$Mo≡SiCp*]
6-Mo	[Tp'(CO)$_2$Mo=Si(4-dmap)Tbb]
6-W	[Tp'(CO)$_2$W=Si(4-dmap)Tbb]
7-Mo	[Tp'(CO)$_2$Mo≡Si-Tbb]
7-W	[Tp'(CO)$_2$Mo≡Si-Tbb]
8-Mo	[Tp'(CO)$_2$Mo≡Ge(C$_6$H$_3$-2,6-Mes$_2$)]
8-W	[Tp'(CO)$_2$W≡Ge(C$_6$H$_3$-2,6-Mes$_2$)]
9-Mo	[Tp'(CO)$_2$Mo≡Sn(C$_6$H$_3$-2,6-Mes$_2$)]
9-W	[Tp'(CO)$_2$W≡Sn(C$_6$H$_3$-2,6-Mes$_2$)]
10-Mo	[Tp'(CO)$_2$Mo≡Pb(C$_6$H$_3$-2,6-Mes$_2$)]
10-W	[Tp'(CO)$_2$W≡Pb(C$_6$H$_3$-2,6-Mes$_2$)]
11-Mo	[Tp'(CO)$_2$Mo≡Ge{N(TMS)Mes*}]
11-W	[Tp'(CO)$_2$W≡Ge{N(TMS)Mes*}]
12-Mo	[Tp(CO)$_2$Mo≡Ge(C$_6$H$_3$-2,6-Mes$_2$)]
13-Mo	[Tp'(CO)$_2$Mo≡Ge(C$_6$H$_3$-2,6-Trip$_2$)]
14-Mo	[Tp'(CO)$_2$Mo≡Ge-Mes*]
15-Mo	[Tp'(CO)$_2$Mo≡Ge-Eind]
16-Mo	[Tp'(CO)$_2$Mo≡Sn{N(TMS)Mes*}]
17-Mo	[Tp'(CO)$_2$Mo≡Pb(C$_6$H$_3$-2,6-Trip$_2$)]
18-Mo	K[Tp'(CO)$_2$Mo=Ge(C$_6$H$_3$-2,6-Mes$_2$)]
19-Mo	[Tp'(CO)(^{i}PrNC)Mo(CN^{i}Pr$_2$)$_2$Ge(C$_6$H$_3$-2,6-Mes$_2$)]
20-Mo	[Tp'Mo(CO)$_2$(PMe$_3$)GeCl$_3$]

21-Mo	$[Tp'(CO)_2Mo{\equiv}Si\text{-}Mo(CO)_2(PMe_3)Tp']$
21-W	$[Tp'(CO)_2W{\equiv}Si\text{-}W(CO)_2(PMe_3)Tp']$
22-Mo	$[Tp'(CO)_2Mo{\equiv}Ge\text{-}Mo(CO)_2(PMe_3)Tp']$
22-W	$[Tp'(CO)_2W{\equiv}Ge\text{-}W(CO)_2(PMe_3)Tp']$
23-Mo	$[Tp'(CO)_2Mo{\equiv}Si\text{-}Mo(CO)_2(MesNC)Tp']$
24-Mo	$[Tp'(CO)_2Mo{\equiv}Ge\text{-}Mo(CO)_2(MesNC)Tp']$
25-Mo	$[Tp'(CO)_2MoSi(H)Mo(CO)_2(PMe_3)Tp'][B(C_6H_3\text{-}3,5\text{-}(CF_3)_2)_4]$
25-W	$[Tp'(CO)_2WSi(H)W(CO)_2(PMe_3)Tp'][B(C_6H_3\text{-}3,5\text{-}(CF_3)_2)_4]$
26-Mo	$[Tp'(CO)_2MoGe(H)Mo(CO)_2(PMe_3)Tp'][B(C_6H_3\text{-}3,5\text{-}(CF_3)_2)_4]$
27-Mo	$[Tp'(CO)_2MoSi(\eta^3\text{-}AuPMe_3)Mo(CO)_2(Cl)Tp']$
28-Mo	$[Tp'(CO)_2MoGe(\eta^3\text{-}AuPMe_3)Mo(CO)_2(Cl)Tp']$
29-Mo	$[Tp'(CO)_2MoSi(Me)Mo(CO)_2(I)Tp'$
30-Mo	$[K(diglyme)]_2[(\mu\text{-}Si)\{Mo(CO)_2Tp'\}_2]$
31-Mo	$[Tp'(CO)_2MoSiMo(CO)_2Tp'C(Me)C(Me)]$
31-W	$[Tp'(CO)_2WSiW(CO)_2Tp'C(Me)C(Me)]$
32-Mo	$[Tp'(CO)_2MoSiMo(CO)_2Tp'C(H)C(TMS)]$
32-W	$[Tp'(CO)_2WSiW(CO)_2Tp'C(H)C(TMS)]$
33-Mo	$[Tp'(CO)_2MoSiMo(CO)_2Tp'C(H)C(Ph)]$
34-Mo	$[Tp'(CO)_2MoSiMo(CO)_2Tp'PC^tBu]$
35	$[(C_5H_4Me)(CO)_2Mn{=}Pb(Cl)(C_6H_3\text{-}2,6\text{-}Mes_2)]$
36	$[(C_5H_4Me)(CO)_2Mn{=}Pb(Br)(C_6H_3\text{-}2,6\text{-}Mes_2)]$
37	$[(C_5H_4Me)(CO)_2Mn{=}Pb(I)(C_6H_3\text{-}2,6\text{-}Mes_2)]$
38	$[\{(C_5H_4Me)(CO)_2MnPbC_6H_3\text{-}2,6\text{-}Mes_2)\}_2(\mu\text{-}Br)][B(C_6H_3\text{-}3,5\text{-}(CF_3)_2)_4]$
39	$[(C_5H_4Me)(CO)_2Mn{\equiv}Pb(C_6H_3\text{-}2,6\text{-}Mes_2)][B(C_6H_3\text{-}3,5\text{-}(CF_3)_2)_4]$
40	*trans*-$[H(dmpe)_2Mn{=}Sn(Cl)(C_6H_3\text{-}2,6\text{-}Mes_2)]$
41	*trans*- $[H(dmpe)_2Mn{\equiv}Sn(C_6H_3\text{-}2,6\text{-}Mes_2)][B(C_6H_3\text{-}3,5\text{-}(CF_3)_2)_4]$
42	*trans*- $[H(dmpe)_2Mn{\equiv}Sn(C_6H_3\text{-}2,6\text{-}Mes_2)][Al(OC(CF_3)_3)_4]$
43	*trans*-$[H(dmpe)_2Mn{=}Sn(C_6H_3\text{-}2,6\text{-}Mes_2)]$
44	*trans*-$[H(dmpe)_2Mn{=}Sn(H)(C_6H_3\text{-}2,6\text{-}Mes_2)]$
45	$SiBr(SiBr_2Tbb)(SIdipp)$
46	(*Z*)-(SIdipp)Si═Si(Br)Tbb
1-Mn	$[MnH(\eta^2\text{-}H_2)(dmpe)_2]$
2-Mn	$[MnH(dmpe)_2]_2(\mu\text{-}dmpe)$

5.2. Crystal data and structure refinement

5.2.1 [Tp'Mo(CO)$_2$(PMe$_3$)Cl] (1-Mo)

Device Type	Bruker X8-KappaApexII
Empirical formula	$C_{28}H_{47}BClMoN_6O_4P$
Moiety formula	$C_{20}H_{31}BClMoN_6O_2P$, 2(C_4H_8O)
Formula weight	704.89
Temperature	100(2) K
Crystal system	monoclinic
Space group	$P2_1/c$
Unit cell dimensions	a = 13.9014(13) Å α = 90°
	b = 11.8934(12) Å β = 91.068(5)°
	c = 20.261(2) Å γ = 90°
Volume	3349.3(6) Å^3
Z, ρ_{calc}	4, 1.398 g/cm^3
μ	0.561 mm^{-1}
F(000)	1472
Crystal size	0.60 × 0.40 × 0.30 mm^3
Absorption correction	Empirical
Tmin; Tmax	0.7297; 0.8499
Radiation	MoKα (λ = 0.71073)
Θ range for data collection	2.46 to 28°
Completeness to theta	0.997
Index ranges	$-17 \le h \le 18$, $-15 \le k \le 15$, $-26 \le l \le 26$
Reflections collected	92324
Independent reflections	8066 [R_{int} = 0.0525]
Data/restraints/parameters	8066/34/415
Goodness-of-fit on F^2	1.101
Final R indexes [I>=2σ (I)]	R_1 = 0.0507, wR_2 = 0.1244
Final R indexes [all data]	R_1 = 0.0653, wR_2 = 0.1333
Largest diff. peak/hole	1.611/-0.894 e Å^{-3}

5.2.2 [Tp'Mo(CO)$_2$(PMe$_3$)] (2-Mo)

Device Type	STOE IPDS2T
Empirical formula	$C_{27}H_{39}BMoN_6O_2P$
Moiety formula	$C_{20}H_{31}BMoN_6O_2P$, C_7H_8
Formula weight	616.36
Temperature	123(2) K
Crystal system	triclinic
Space group	P-1
Unit cell dimensions	a = 13.5487(4) Å α = 109.370(2)°

	b = 14.7499(5) Å β = 93.449(3)°
	c = 16.1417(5) Å γ = 98.756(3)°
Volume	2986.48(16) $Å^3$
Z, ρ_{calc}	4, 1.373 g/cm^3
μ	0.527 mm^{-1}
F(000)	1284
Crystal size	0.18 × 0.09 × 0.06 mm^3
Absorption correction	Integration
Tmin; Tmax	0.9111; 0.9691
Radiation	MoKα (λ = 0.71073)
Θ range for data collection	2.94 to 28°
Completeness to theta	0.985
Index ranges	$-17 \le h \le 17, -19 \le k \le 19, -19 \le l \le 21$
Reflections collected	28355
Independent reflections	14213 [R_{int} = 0.0569]
Data/restraints/parameters	14213/100/711
Goodness-of-fit on F^2	0.997
Final R indexes [I>=2σ (I)]	R_1 = 0.0591, wR_2 = 0.1535
Final R indexes [all data]	R_1 = 0.0819, wR_2 = 0.1640
Largest diff. peak/hole	1.833/-1.310 e $Å^{-3}$

5.2.3 Na[Tp'Mo(CO)$_2$(PMe$_3$)] (3-Mo)

Device Type	STOE IPDS2T
Empirical formula	$C_{30}H_{56}BMoN_6NaO_7P$
Moiety formula	$C_{28}H_{51}BMoN_6NaO_6P$, 0. 5($C_4H_{10}O_2$)
Formula weight	773.52
Temperature	123(2) K
Crystal system	monoclinic
Space group	$P2_1/c$
Unit cell dimensions	a = 17.2762(7) Å α = 90°
	b = 14.4377(4) Å β = 114.912(3)°
	c = 16.8995(7) Å γ = 90°
Volume	3823.0(2) $Å^3$
Z, ρ_{calc}	4, 1.344 g/cm^3
μ	0.445 mm^{-1}
F(000)	1628
Crystal size	0.18 × 0.12 × 0.03 mm^3
Absorption correction	Integration
Tmin; Tmax	0.9241; 0.9868
Radiation	MoKα (λ = 0.71073)
Θ range for data collection	2.82 to 28°
Completeness to theta	0.998
Index ranges	$-22 \le h \le 22, -18 \le k \le 19, -22 \le l \le 22$
Reflections collected	31781
Independent reflections	9212 [R_{int} = 0.0707]
Data/restraints/parameters	9212/57/469

Goodness-of-fit on F^2	1.027
Final R indexes [I>=2σ (I)]	$R_1 = 0.0586$, $wR_2 = 0.1324$
Final R indexes [all data]	$R_1 = 0.0913$, $wR_2 = 0.1454$
Largest diff. peak/hole	2.152/-1.332 e $Å^{-3}$

5.2.4 [Tp'Mo(CO)$_2$(PMe$_3$)H] (4-Mo)

Device Type	STOE IPDS2T
Empirical formula	$C_{26}H_{38}BMoN_6O_2P$
Moiety formula	$C_{26}H_{38}BMoN_6O_2P$
Formula weight	604.34
Temperature	123(2) K
Crystal system	triclinic
Space group	P-1
Unit cell dimensions	a = 13.5471(4) Å α = 109.005(2)°
	b = 14.2491(4) Å β = 95.885(2)°
	c = 16.2990(5) Å γ = 95.334(2)°
Volume	2932.26(15) $Å^3$
Z, ρ_{calc}	4, 1.369 g/cm^3
μ	0.535 mm^{-1}
F(000)	1256
Crystal size	0.21 × 0.15 × 0.12 mm^3
Radiation	MoKα (λ = 0.71073)
2Θ range for data collection	5.34 to 53.988°
Completeness to theta	0.976
Index ranges	$-17 \le h \le 16$, $-18 \le k \le 18$, $-20 \le l \le 20$
Reflections collected	22851
Independent reflections	12473 [$R_{int} = 0.0225$]
Data/restraints/parameters	12473/1/693
Goodness-of-fit on F^2	0.993
Final R indexes [I>=2σ (I)]	$R_1 = 0.0260$, $wR_2 = 0.0632$
Final R indexes [all data]	$R_1 = 0.0345$, $wR_2 = 0.0651$
Largest diff. peak/hole	0.71/-0.45 e $Å^{-3}$

5.2.5 [Tp'(CO)$_2$Mo≡Si(C$_5$Me$_5$)] (5-Mo)

Device Type	STOE IPDS2T
Empirical formula	$C_{27}H_{37}BMoN_6O_2Si$
Moiety formula	$C_{27}H_{37}BMoN_6O_2Si$
Formula weight	612.46
Temperature	123(2) K
Crystal system	monoclinic
Space group	$P2_1/c$
Unit cell dimensions	a = 12.0512(2) Å α = 90°
	b = 18.3946(5) Å β = 90.0420(10)°
	c = 13.0909(2) Å γ = 90°
Volume	2901.95(10) $Å^3$

Z, ρ_{calc}	4, 1.402 g/cm^3
μ	0.528 mm^{-1}
F(000)	1272
Crystal size	0.18 × 0.12 × 0.09 mm^3
Absorption correction	Integration
Tmin; Tmax	0.8564; 0.9786
Radiation	MoKα (λ = 0.71073)
2Θ range for data collection	5.414 to 53.994°
Completeness to theta	0.999
Index ranges	-13 ≤ h ≤ 15, -23 ≤ k ≤ 23, -16 ≤ l ≤ 16
Reflections collected	38375
Independent reflections	6333 [R_{int} = 0.0285]
Data/restraints/parameters	6333/0/355
Goodness-of-fit on F^2	0.939
Final R indexes [I>=2σ (I)]	R_1 = 0.0168, wR_2 = 0.0388
Final R indexes [all data]	R_1 = 0.0200, wR_2 = 0.0391
Largest diff. peak/hole	0.23/-0.24 e Å^{-3}

5.2.6 [Tp'(CO)$_2$Mo=Si(4-dmap)Tbb] (6-Mo)

Device Type	STOE IPDS2T
Empirical formula	$C_{48}H_{81}BMoN_8O_2Si_5$
Moiety formula	$C_{48}H_{81}BMoN_8O_2Si_5$
Formula weight	1049.40
Temperature	123(2) K
Crystal system	triclinic
Space group	P-1
Unit cell dimensions	a = 13.5102(9) Å α = 68.295(6)°
	b = 21.4466(16) Å β = 84.656(6)°
	c = 22.157(2) Å γ = 84.404(6)°
Volume	5925.0(8) Å^3
Z, ρ_{calc}	4, 1.176 g/cm^3
μ	0.363 mm^{-1}
F(000)	2232.0
Crystal size	0.25 × 0.1 × 0.06 mm^3
Absorption correction	Integration
Tmin; Tmax	0.7348; 0.9557
Radiation	MoKα (λ = 0.71073)
2Θ range for data collection	5.264 to 56°
Completeness to theta	0.988
Index ranges	-17 ≤ h ≤ 17, -28 ≤ k ≤ 28, -29 ≤ l ≤ 29
Reflections collected	63619
Independent reflections	63619 [R_{sigma} = 0.1668]
Data/restraints/parameters	63619/14/1217
Goodness-of-fit on F^2	0.967
Final R indexes [I>=2σ (I)]	R_1 = 0.1057, wR_2 = 0.2413
Final R indexes [all data]	R_1 = 0.1666, wR_2 = 0.2738

Largest diff. peak/hole	2.65/-1.30 e $Å^{-3}$

5.2.7 [Tp'(CO)$_2$W=Si(4-dmap)Tbb] (6-W)

Device Type	Bruker X8-KappaApexII
Empirical formula	$C_{68}H_{121}BN_8O_7Si_5W$
Moiety formula	$C_{48}H_{81}BN_8O_2Si_5W$, $5(C_4H_8O)$
Formula weight	1497.83
Temperature	100(2) K
Crystal system	monoclinic
Space group	$P2_1/c$
Unit cell dimensions	a = 17.1211(10) Å α = 90°
	b = 20.4411(11) Å β = 107.591(2)°
	c = 23.4450(13) Å γ = 90°
Volume	7821.5(8) $Å^3$
Z, ρ_{calc}	4, 1.272 g/cm^3
μ	1.606 mm^{-1}
F(000)	3160.0
Crystal size	0.4 × 0.16 × 0.16 mm^3
Absorption correction	Empirical
Tmin; Tmax	0.5830; 0.7458
Radiation	MoKα (λ = 0.71073)
2Θ range for data collection	3.744 to 50.498°
Completeness to theta	0.920
Index ranges	$-20 \le h \le 20$, $-24 \le k \le 24$, $-28 \le l \le 28$
Reflections collected	56672
Independent reflections	14131 [R_{int} = 0.0677]
Data/restraints/parameters	14131/52/863
Goodness-of-fit on F^2	1.037
Final R indexes [I>=2σ (I)]	R_1 = 0.0485, wR_2 = 0.1100
Final R indexes [all data]	R_1 = 0.0869, wR_2 = 0.1302
Largest diff. peak/hole	1.62/-1.38 e $Å^{-3}$

5.2.8 [Tp'(CO)$_2$Mo≡Si–Tbb] (7-Mo)

Device Type	Bruker X8-KappaApexII
Empirical formula	$C_{100}H_{160}B_2Mo_2N_{12}O_4Si_{10}$
Moiety formula	$2(C_{41}H_{71}BMoN_6O_2Si_5)\cdot 3(C_6H_6)$
Formula weight	2088.79
Temperature	100(2) K
Crystal system	triclinic
Space group	P-1
Unit cell dimensions	a = 13.3366(8) Å α = 103.244(2)°
	b = 16.7705(11) Å β = 93.358(2)°
	c = 26.6283(18) Å γ = 93.082(2)°
Volume	5773.5(6) $Å^3$
Z, ρ_{calc}	2, 1.202 g/cm^3

μ	0.372 mm^{-1}
F(000)	2220.0
Crystal size	0.16 × 0.12 × 0.02 mm^3
Absorption correction	Empirical
Tmin; Tmax	0.6516; 0.7460
Radiation	MoKα (λ = 0.71073)
2Θ range for data collection	4.806 to 54°
Completeness to theta	0.986
Index ranges	-17≤ h ≤ 11, -21 ≤ k ≤ 21, -34 ≤ l ≤ 34
Reflections collected	68029
Independent reflections	24773 [R_{int} = 0.0766]
Data/restraints/parameters	24773/32/1244
Goodness-of-fit on F^2	0.940
Final R indexes [I>=2σ (I)]	R_1 = 0.0491, wR_2 = 0.0883
Final R indexes [all data]	R_1 = 0.0980, wR_2 = 0.1019
Largest diff. peak/hole	1.19/-0.74 e $Å^{-3}$

5.2.9 [Tp'(CO)$_2$W≡Si–Tbb] (7-W)

Device Type	Bruker X8-KappaApexII
Empirical formula	$C_{100}H_{160}B_2N_{12}O_4Si_{10}W_2$
Moiety formula	$2(C_{41}H_{71}BN_6O_2Si_5W)\cdot 3(C_6H_6)$
Formula weight	2264.61
Temperature	100(2) K
Crystal system	triclinic
Space group	P-1
Unit cell dimensions	a = 13.3378(6) Å α = 103.153(2)°
	b = 16.7530(7) Å β = 93.389(2)°
	c = 26.6221(12) Å γ = 93.252(2)°
Volume	5767.4(4) $Å^3$
Z, ρ_{calc}	2, 1.304 g/cm^3
μ	2.148 mm^{-1}
F(000)	2348.0
Crystal size	0.1 × 0.06 × 0.03 mm^3
Absorption correction	Empirical
Tmin; Tmax	0.6135; 0.7458
Radiation	MoKα (λ = 0.71073)
2Θ range for data collection	4.888 to 54°
Completeness to theta	0.996
Index ranges	-17≤ h ≤ 17, -21 ≤ k ≤ 21, -34 ≤ l ≤ 34
Reflections collected	181082
Independent reflections	25077 [R_{int} = 0.0709]
Data/restraints/parameters	25077/60/1209
Goodness-of-fit on F^2	1.007
Final R indexes [I>=2σ (I)]	R_1 = 0.0301, wR_2 = 0.0572
Final R indexes [all data]	R_1 = 0.0589, wR_2 = 0.0649

Largest diff. peak/hole	2.64/-1.12 e $Å^{-3}$

5.2.10 [Tp'(CO)$_2$Mo≡Ge(C$_6$H$_3$-2,6-Mes$_2$)] (8-Mo)

Device Type	STOE IPDS2T
Empirical formula	$C_{176}H_{218}B_4Ge_4Mo_4N_{24}O_{11}$
Moiety formula	$4(C_{41}H_{47}BGeMoN_6O_2)\cdot 3(C_4H_{10}O)$
Formula weight	3563.10
Temperature	123(2) K
Crystal system	triclinic
Space group	P-1
Unit cell dimensions	a = 13.6228(6) Å α = 95.767(3)°
	b = 18.1668(7) Å β = 101.898(3)°
	c = 18.2993(7) Å γ = 96.136(3)°
Volume	4371.0(3) $Å^3$
Z, ρ_{calc}	1, 1.354 g/cm^3
μ	1.019 mm^{-1}
F(000)	1846.0
Crystal size	0.15 × 0.12 × 0.06 mm^3
Absorption correction	Integration
Tmin; Tmax	0.8622; 0.9414
Radiation	MoKα (λ = 0.71073)
Θ range for data collection	2.84 to 28°
Completeness to theta	0.984
Index ranges	$-17\leq h\leq 17$, $-21\leq k\leq 23$, $-24\leq l\leq 24$
Reflections collected	39338
Independent reflections	20741[R_{int} = 0.0866]
Data/restraints/parameters	20741/253/1061
Goodness-of-fit on F^2	0.807
Final R indexes [I>=2σ (I)]	R_1 = 0.0587, wR_2 = 0.1159
Final R indexes [all data]	R_1 = 0.1486, wR_2 = 0.1388
Largest diff. peak/hole	1.509/-0.841 e $Å^{-3}$

5.2.11 [Tp'(CO)$_2$W≡Ge(C$_6$H$_3$-2,6-Mes$_2$)] (8-W)

Device Type	STOE IPDS2T
Empirical formula	$C_{86}H_{104}B_2Ge_2N_{12}O_5W_2$
Moiety formula	$2(C_{41}H_{47}BGeN_6O_2W)\cdot(C_4H_{10}O)$
Formula weight	1920.31
Temperature	123(2) K
Crystal system	triclinic
Space group	P-1
Unit cell dimensions	a = 13.2244(3) Å α = 76.357(2)°
	b = 13.7613(3) Å β = 86.886(2)°
	c = 24.0578(6) Å γ = 81.115(2)°
Volume	4202.84(17) $Å^3$
Z, ρ_{calc}	2, 1.517 g/cm^3

μ	3.494 mm^{-1}
F(000)	1932.0
Crystal size	0.18 × 0.12 × 0.03 mm^3
Absorption correction	Integration
Tmin; Tmax	0.4079; 0.8230
Radiation	MoKα (λ = 0.71073)
2Θ range for data collection	5.226 to 55.998°
Completeness to theta	0.999
Index ranges	-17≤ h ≤ 17, -18 ≤ k ≤ 18, -31 ≤ l ≤ 31
Reflections collected	86187
Independent reflections	20270[R_{int} = 0.0569]
Data/restraints/parameters	20270/0/1008
Goodness-of-fit on F^2	1.019
Final R indexes [I>=2σ (I)]	R_1 = 0.0298, wR_2 = 0.0617
Final R indexes [all data]	R_1 = 0.0402, wR_2 = 0.0640
Largest diff. peak/hole	1.88/-0.88 e $Å^{-3}$

5.2.12 [Tp'$(CO)_2$Mo≡Sn(C_6H_3-2,6-Mes_2)] (9-Mo)

Device Type	STOE IPDS2T
Empirical formula	$C_{45}H_{57}BMoN_6O_3Sn$
Moiety formula	$C_{41}H_{47}BMoN_6O_2Sn,·(C_4H_{10}O)$
Formula weight	955.41
Temperature	123(2) K
Crystal system	triclinic
Space group	P-1
Unit cell dimensions	a = 11.9425(5) Å α = 114.622(3)°
	b = 14.7040(7) Å β = 100.886(3)°
	c = 15.1179(6) Å γ = 103.595(3)°
Volume	2218.75(19) $Å^3$
Z, ρ_{calc}	2, 1.430 g/cm^3
μ	0.891 mm^{-1}
F(000)	980.0
Crystal size	0.18 × 0.10 × 0.04 mm^3
Absorption correction	Integration
Tmin; Tmax	0.8561; 0.9652
Radiation	MoKα (λ = 0.71073)
Θ range for data collection	2.87 to 28°
Completeness to theta	0.984
Index ranges	-15≤ h ≤ 15, -19 ≤ k ≤ 19, -19 ≤ l ≤ 19
Reflections collected	20941
Independent reflections	10505[R_{int} = 0.0980]
Data/restraints/parameters	10505/0/532
Goodness-of-fit on F^2	1.005
Final R indexes [I>=2σ (I)]	R_1 = 0.0571, wR_2 = 0.1389
Final R indexes [all data]	R_1 = 0.0941, wR_2 = 0.1487

Largest diff. peak/hole	2.373/-1.728 e $Å^{-3}$

5.2.13 [Tp'(CO)$_2$W≡Sn(C$_6$H$_3$-2,6-Mes$_2$)] (9-W)

Device Type	Bruker X8-KappaApexII
Empirical formula	$C_{45}H_{57}BN_6O_3SnW$
Moiety formula	$C_{41}H_{47}BN_6O_2SnW\cdot(C_4H_{10}O)$
Formula weight	1043.31
Temperature	123(2) K
Crystal system	triclinic
Space group	P-1
Unit cell dimensions	a = 11.9498(6) Å α = 114.694(2)°
	b = 14.7137(7) Å β = 100.872(2)°
	c = 15.0710(12) Å γ = 103.6710(10)°
Volume	2211.9(2) $Å^3$
Z, ρ_{calc}	2, 1.566 g/cm^3
μ	3.208 mm^{-1}
F(000)	1044.0
Crystal size	0.25 × 0.06 × 0.04 mm^3
Absorption correction	Empirical
Tmin; Tmax	0.5010; 0.8824
Radiation	MoKα (λ = 0.71073)
Θ range for data collection	3.71 to 28°
Completeness to theta	0.988
Index ranges	$-15 \le h \le 15$, $-19 \le k \le 17$, $-19 \le l \le 19$
Reflections collected	20414
Independent reflections	10548 [R_{int} = 0.0328]
Data/restraints/parameters	10548/0/531
Goodness-of-fit on F^2	1.037
Final R indexes [I>=2σ (I)]	R_1 = 0.0279, wR_2 = 0.0581
Final R indexes [all data]	R_1 = 0.0325, wR_2 = 0.0610
Largest diff. peak/hole	1.032/-1.150 e $Å^{-3}$

5.2.14 [Tp'(CO)$_2$Mo≡Pb(C$_6$H$_3$-2,6-Mes$_2$)] (10-Mo)

Device Type	STOE IPDS2T
Empirical formula	$C_{45}H_{57}BMoN_6O_3Pb$
Moiety formula	$C_{41}H_{47}BMoN_6O_2Pb,\cdot(C_4H_{10}O)$
Formula weight	1043.91
Temperature	123(2) K
Crystal system	triclinic
Space group	P-1
Unit cell dimensions	a = 11.9419(3) Å α = 114.655(2)°
	b = 14.7713(3) Å β = 100.937(2)°
	c = 15.0626(3) Å γ = 103.332(2)°
Volume	2223.50(11) $Å^3$
Z, ρ_{calc}	2, 1.559 g/cm^3

μ	4.108 mm^{-1}
F(000)	1044.0
Crystal size	0.12 × 0.06 × 0.03 mm^3
Absorption correction	Integration
Tmin; Tmax	0.6384; 0.8867
Radiation	MoKα (λ = 0.71073)
Θ range for data collection	2.85 to 28°
Completeness to theta	0.998
Index ranges	-15≤ h ≤ 14, -19 ≤ k ≤ 19, -19 ≤ l ≤ 19
Reflections collected	46722
Independent reflections	10720[R_{int} = 0.0469]
Data/restraints/parameters	10720/33/531
Goodness-of-fit on F^2	0.968
Final R indexes [I>=2σ (I)]	R_1 = 0.0182, wR_2 = 0.0372
Final R indexes [all data]	R_1 = 0.0221, wR_2 = 0.378
Largest diff. peak/hole	0.745/-0.952 e $Å^{-3}$

5.2.15 [Tp'$(CO)_2$W≡Pb(C_6H_3-2,6-Mes_2)] (10-W)

Device Type	STOE IPDS2T
Empirical formula	$C_{102}H_{144}B_2N_{12}O_9Pb_2W_2$
Moiety formula	$2(C_{41}H_{47}BN_6O_2PbW),·5(C_4H_{10}O)$
Formula weight	2485.98
Temperature	123(2) K
Crystal system	monoclinic
Space group	$P2_1/c$
Unit cell dimensions	a = 15.877(8) Å α = 90°
	b = 15.130(4) Å β = 106.69(6)°
	c = 22.86(2) Å γ = 90°
Volume	5261(6) $Å^3$
Z, ρ_{calc}	2, 1.569 g/cm^3
μ	5.429 mm^{-1}
F(000)	2468.0
Crystal size	0.21 × 0.12 × 0.06 mm^3
Absorption correction	Integration
Tmin; Tmax	0.3249; 0.5819
Radiation	MoKα (λ = 0.71073)
2Θ range for data collection	5.576 to 55.998°
Completeness to theta	0.944
Index ranges	-20 ≤ h ≤ 17, -19 ≤ k ≤ 17, -30 ≤ l ≤ 30
Reflections collected	28107
Independent reflections	12069[R_{int} = 0.1202]
Data/restraints/parameters	12069/106/584
Goodness-of-fit on F^2	0.866
Final R indexes [I>=2σ (I)]	R_1 = 0.0658, wR_2 = 0.1490
Final R indexes [all data]	R_1 = 0.1164, wR_2 = 0.1647

Largest diff. peak/hole	2.74/-4.75 e $Å^{-3}$

5.2.16 [Tp'(CO)$_2$Mo≡Ge{N(TMS)Mes*}] (11-Mo)

Device Type	Bruker X8-KappaApexII
Empirical formula	$C_{38}H_{60}BGeMoN_7O_2Si$
Moiety formula	$C_{38}H_{60}BGeMoN_7O_2Si$
Formula weight	854.36
Temperature	100(2) K
Crystal system	monoclinic
Space group	$P2_1/c$
Unit cell dimensions	a = 9.9412(3) Å α = 90°
	b = 21.4800(5) Å β = 90.6650(10)°
	c = 19.6093(5) Å γ = 90°
Volume	4187.03(19) $Å^3$
Z, ρ_{calc}	4, 1.355 g/cm^3
μ	1.087 mm^{-1}
F(000)	1784.0
Crystal size	0.21 × 0.16 × 0.06 mm^3
Absorption correction	Empirical
Tmin; Tmax	0.8040; 0.9377
Radiation	MoKα (λ = 0.71073)
Θ range for data collection	2.81 to 28°
Completeness to theta	0.999
Index ranges	$-12 \le h \le 13$, $-25 \le k \le 28$, $-25 \le l \le 23$
Reflections collected	75874
Independent reflections	10099 [R_{int} = 0.0396]
Data/restraints/parameters	10099/7/481
Goodness-of-fit on F^2	1.067
Final R indexes [I>=2σ (I)]	R_1 = 0.0228, wR_2 = 0.0553
Final R indexes [all data]	R_1 = 0.0283, wR_2 = 0.0569
Largest diff. peak/hole	0.355/-0.421 e $Å^{-3}$

5.2.17 [Tp'(CO)$_2$Mo≡Ge{N(TMS)Mes*}] (11-W)

Device Type	STOE IPDS2T
Empirical formula	$C_{38}H_{60}BGeN_7O_2SiW$
Moiety formula	$C_{38}H_{60}BGeN_7O_2SiW$
Formula weight	942.27
Temperature	123(2) K
Crystal system	monoclinic
Space group	$P2_1/c$
Unit cell dimensions	a = 9.936(2) Å α = 90°
	b = 21.537(4) Å β = 90.404(17)°
	c = 19.570(5) Å γ = 90°
Volume	4187.7(15) $Å^3$
Z, ρ_{calc}	4, 1.495 g/cm^3

μ	3.532 mm^{-1}
F(000)	1912.0
Crystal size	0.25 × 0.10 × 0.04 mm^3
Absorption correction	Integration
Tmin; Tmax	0.4722; 0.8716
Radiation	MoKα (λ = 0.71073)
Θ range for data collection	2.93 to 28°
Completeness to theta	0.989
Index ranges	-12 ≤ h ≤ 13, -28 ≤ k ≤ 24, -25 ≤ l ≤ 23
Reflections collected	21599
Independent reflections	9993 [R_{int} = 0.0575]
Data/restraints/parameters	9993/0/481
Goodness-of-fit on F^2	1.011
Final R indexes [I>=2σ (I)]	R_1 = 0.0393, wR_2 = 0.0798
Final R indexes [all data]	R_1 = 0.0601, wR_2 = 0.0847
Largest diff. peak/hole	1.208/-1.324 e $Å^{-3}$

5.2.18 [Tp(CO)$_2$Mo≡Ge(C$_6$H$_3$-2,6-Mes$_2$)] (12-Mo)

Device Type	Nonius KappaCCD
Empirical formula	$C_{38}H_{42}BGeMoN_6O_2$
Moiety formula	$C_{35}H_{35}BGeMoN_6O_2 \cdot 0.5(C_6H_{14})$
Formula weight	794.12
Temperature	123(2) K
Crystal system	monoclinic
Space group	$P2_1/n$
Unit cell dimensions	a = 8.4305(4) Å α = 90°
	b = 24.1244(1) Å β = 98.140(2)°
	c = 18.5886(7) Å γ = 90°
Volume	3742.5(3) $Å^3$
Z, ρ_{calc}	4, 1.409 g/cm^3
μ	1.179 mm^{-1}
F(000)	1628.0
Crystal size	0.18 × 0.16 × 0.04 mm^3
Absorption correction	Empirical
Tmin; Tmax	0.8158; 0.9543
Radiation	MoKα (λ = 0.71073)
Θ range for data collection	2.58 to 27°
Completeness to theta	0.994
Index ranges	-10 ≤ h ≤ 10, -0 ≤ k ≤ 30, -0 ≤ l ≤ 23
Reflections collected	8134
Independent reflections	8146[R_{int} = 0.0000]
Data/restraints/parameters	8146/2/454
Goodness-of-fit on F^2	1.034
Final R indexes [I>=2σ (I)]	R_1 = 0.0462, wR_2 = 0.1054
Final R indexes [all data]	R_1 = 0.0660, wR_2 = 0.1169

Largest diff. peak/hole	1.799/-1.210 e Å^{-3}

5.2.19 [Tp'(CO)$_2$Mo≡Ge(C$_6$H$_3$-2,6-Trip$_2$)] (13-Mo)

Device Type	Bruker X8-KappaApexII
Empirical formula	$C_{53}H_{71}BGeMoN_6O_2$
Moiety formula	$C_{53}H_{71}BGeMoN_6O_2$
Formula weight	1003.49
Temperature	100(2) K
Crystal system	orthorhombic
Space group	Pbcn
Unit cell dimensions	a = 36.226(4) Å α = 90°
	b = 17.0307(19) Å β = 90°
	c = 16.849(2) Å γ = 90°
Volume	10395(2) Å^3
Z, ρ_{calc}	8, 1.282 g/cm^3
μ	0.864 mm^{-1}
F(000)	4208.0
Crystal size	0.14 × 0.1 × 0.04 mm^3
Absorption correction	Empirical
Tmin; Tmax	0.6696; 0.9683
Radiation	MoKα (λ = 0.71073)
2Θ range for data collection	2.248 to 50.5°
Completeness to theta	0.924
Index ranges	-43 ≤ h ≤ 43, -20 ≤ k ≤ 14, -18 ≤ l ≤ 20
Reflections collected	54691
Independent reflections	9730 [R_{int} = 0.0538]
Data/restraints/parameters	9730/183/596
Goodness-of-fit on F^2	1.255
Final R indexes [I>=2σ (I)]	R_1 = 0.1761, wR_2 = 0.4147
Final R indexes [all data]	R_1 = 0.1909, wR_2 = 0.4219
Largest diff. peak/hole	3.15/-5.72 e Å^{-3}

5.2.20 [Tp'(CO)$_2$Mo≡GeMes*] (14-Mo)

Device Type	Nonius KappaCCD
Empirical formula	$C_{35}H_{51}BGeMoN_6O_2$
Moiety formula	$C_{35}H_{51}BGeMoN_6O_2$
Formula weight	767.15
Temperature	123(2) K
Crystal system	monoclinic
Space group	$P2_1/n$
Unit cell dimensions	a = 8.3996(12) Å α = 90°
	b = 22.490(4) Å β = 96.837(14)°
	c = 19.658(4) Å γ = 90°
Volume	3687.0(12) Å^3
Z, ρ_{calc}	4, 1.382 g/cm^3

μ	1.194 mm^{-1}
F(000)	1592.0
Crystal size	0.3 × 0.12 × 0.1 mm^3
Absorption correction	Empirical
Tmin; Tmax	0.1964; 0.7459
Radiation	MoKα (λ = 0.71073)
2Θ range for data collection	5.21 to 51.998°
Completeness to theta	0.999
Index ranges	$-10 \le h \le 10$, $-27 \le k \le 27$, $-24 \le l \le 24$
Reflections collected	72263
Independent reflections	7245[R_{int} = 0.1895]
Data/restraints/parameters	7245/24/461
Goodness-of-fit on F^2	0.991
Final R indexes [I>=2σ (I)]	R_1 = 0.0572, wR_2 = 0.1178
Final R indexes [all data]	R_1 = 0.1055, wR_2 = 0.1416
Largest diff. peak/hole	1.36/-0.91 e $Å^{-3}$

5.2.21 [Tp'$(CO)_2$Mo≡GeEind] (15-Mo)

Device Type	Nonius KappaCCD
Empirical formula	$C_{45}H_{67}BGeMoN_6O_2$
Moiety formula	$C_{45}H_{67}BGeMoN_6O_2$
Formula weight	903.39
Temperature	123(2) K
Crystal system	triclinic
Space group	P-1
Unit cell dimensions	a = 10.6185(6) Å α = 74.215(2)°
	b = 18.7854(11) Å β = 83.890(2)°
	c = 24.1562(15) Å γ = 77.860(2)°
Volume	4526.9(5) $Å^3$
Z, ρ_{calc}	4, 1.326 g/cm^3
μ	0.983 mm^{-1}
F(000)	1896.0
Crystal size	0.24 × 0.22 × 0.12 mm^3
Absorption correction	Empirical
Tmin; Tmax	0.7982; 0.8911
Radiation	MoKα (λ = 0.71073)
Θ range for data collection	1.83 to 28°
Completeness to theta	0.993
Index ranges	$-14 \le h \le 14$, $-22 \le k \le 24$, $-31 \le l \le 31$
Reflections collected	66258
Independent reflections	21685[R_{int} = 0.0698]
Data/restraints/parameters	21685/24/1043
Goodness-of-fit on F^2	1.046
Final R indexes [I>=2σ (I)]	R_1 = 0.0614, wR_2 = 0.1337
Final R indexes [all data]	R_1 = 0.1061, wR_2 = 0.1503

Largest diff. peak/hole	1.746/-1.765 e Å^{-3}

5.2.22 [Tp'(CO)$_2$Mo≡Pb(C$_6$H$_3$-2,6-Trip$_2$)] (17-Mo)

Device Type	STOE IPDS2T
Empirical formula	$C_{53}H_{71}BMoN_7O_2Pb$
Moiety formula	$C_{53}H_{71}BMoN_7O_2Pb$
Formula weight	1138.10
Temperature	123(2) K
Crystal system	orthorohombic
Space group	$P2_1\,2_1\,2_1$
Unit cell dimensions	a = 13.4421(3) Å α = 90°
	b = 14.2917(2) Å β = 90.404(17)°
	c = 26.3870(4) Å γ = 90°
Volume	5069.22(15) Å^3
Z, ρ_{calc}	4, 1.491 g/cm^3
μ	3.609 mm^{-1}
F(000)	2304.0
Crystal size	0.15 × 0.13 × 0.06 mm^3
Absorption correction	Integration
Tmin; Tmax	0.6135; 0.8126
Radiation	MoKα (λ = 0.71073)
Θ range for data collection	2.72 to 28°
Completeness to theta	0.998
Index ranges	$-17 \le h \le 17$, $-18 \le k \le 18$, $-34 \le l \le 34$
Reflections collected	43823
Independent reflections	12214 [R_{int} = 0.0297]
Data/restraints/parameters	12214/22/599
Goodness-of-fit on F^2	0.903
Final R indexes [I>=2σ (I)]	R_1 = 0.0180, wR_2 = 0.0276
Final R indexes [all data]	R_1 = 0.0218, wR_2 = 0.0281
Largest diff. peak/hole	0.375/-0.670 e Å^{-3}

5.2.23 K(THF)$_3$[Tp'(CO)$_2$MoGe(C$_6$H$_3$-2,6-Mes$_2$)] (18-Mo)

Device Type	Bruker D8-Venture
Empirical formula	$C_{130}H_{190}B_2Ge_2K_2Mo_2N_{12}O_{16}$
Moiety formula	$2(C_{53}H_{71}BGeKMoN_6O_5)\cdot 6(C_4H_8O)$
Formula weight	2613.81
Temperature	99.99 K
Crystal system	monoclinic
Space group	$P2_1/c$
Unit cell dimensions	a = 15.9619(19) Å α = 90°
	b = 16.1215(18) Å β = 106.500(6)°
	c = 26.942(3) Å γ = 90°
Volume	6647.5(14) Å^3
Z, ρ_{calc}	2, 1.306 g/cm^3

μ	3.105 mm^{-1}
F(000)	2756.0
Crystal size	0.24 × 0.2 × 0.08 mm^3
Absorption correction	Empirical
Tmin; Tmax	0.30888; 0.7535
Radiation	CuKα (λ = 1.54178)
2Θ range for data collection	5.774 to 133.188°
Completeness to theta	0.910
Index ranges	-19 ≤ h ≤ 18, -19 ≤ k ≤ 19, -32 ≤ l ≤ 31
Reflections collected	37251
Independent reflections	10940[R_{int} = 0.0871]
Data/restraints/parameters	10940/131/760
Goodness-of-fit on F^2	1.204
Final R indexes [I>=2σ (I)]	R_1 = 0.1504, wR_2 = 0.3131
Final R indexes [all data]	R_1 = 0.1756, wR_2 = 0.3278
Largest diff. peak/hole	2.60/-1.22 e $Å^{-3}$

5.2.24 [Tp'(CO)(^{i}PrNC)Mo(CN^{i}Pr$_2$)$_2$Ge(C$_6$H$_3$-2,6-Mes$_2$)] (19-Mo)

Device Type	Bruker X8-KappaApexII
Empirical formula	$C_{213}H_{284}B_4Ge_4Mo_4N_{36}O_4$
Moiety formula	$4(C_{52}H_{68}BGeMoN_9O)\cdot(C_5H_{12})$
Formula weight	4130.10
Temperature	100(2) K
Crystal system	triclinic
Space group	P-1
Unit cell dimensions	a = 13.7119(8) Å α = 80.983(2)°
	b = 16.2967(9) Å β = 79.103°
	c = 25.8850(15) Å γ = 87.197(2)°
Volume	5608.6(6) $Å^3$
Z, ρ_{calc}	1, 1.223 g/cm^3
μ	0.802 mm^{-1}
F(000)	2162.0
Crystal size	0.18 × 0.1 × 0.02 mm^3
Absorption correction	Empirical
Tmin; Tmax	0.5981; 0.7460
Radiation	MoKα (λ = 0.71073)
2Θ range for data collection	3.686 to 55.998°
Completeness to theta	0.996
Index ranges	-19 ≤ h ≤ 19, -22 ≤ k ≤ 14, -36 ≤ l ≤ 36
Reflections collected	175627
Independent reflections	27020 [R_{int} = 0.0636]
Data/restraints/parameters	27020/32/1254
Goodness-of-fit on F^2	1.085
Final R indexes [I>=2σ (I)]	R_1 = 0.0395, wR_2 = 0.1088
Final R indexes [all data]	R_1 = 0.0665, wR_2 = 0.1170

Largest diff. peak/hole	1.06/-0.77e Å^{-3}

5.2.25 [Tp'Mo(CO)$_2$(PMe$_3$)GeCl$_3$] (20-Mo)

Device Type	Bruker X8-KappaApexII
Empirical formula	$C_{20}H_{31}BCl_3GeMoN_6O_2P$
Moiety formula	$C_{20}H_{31}BCl_3GeMoN_6O_2P$
Formula weight	704.17
Temperature	100(2) K
Crystal system	monoclinic
Space group	$P2_1/c$
Unit cell dimensions	a = 11.2508(13) Å α = 90°
	b = 16.0664(18) Å β = 107.565(5)°
	c = 16.5219(18) Å γ = 90°
Volume	2847.3(6) Å^3
Z, ρ_{calc}	4, 1.643 g/cm^3
μ	1.863 mm^{-1}
F(000)	1416.0
Crystal size	0.50 × 0.12 × 0.10 mm^3
Absorption correction	Empirical
Tmin; Tmax	0.4560; 0.8356
Radiation	MoKα (λ = 0.71073)
Θ range for data collection	2.89 to 28°
Completeness to theta	0.998
Index ranges	$-14 \le h \le 14$, $-21 \le k \le 18$, $-21 \le l \le 20$
Reflections collected	100844
Independent reflections	6858 [R_{int} = 0.04928]
Data/restraints/parameters	6858/1/328
Goodness-of-fit on F^2	1.104
Final R indexes [I>=2σ (I)]	R_1 = 0.0332, wR_2 = 0.0810
Final R indexes [all data]	R_1 = 0.0449, wR_2 = 0.0916
Largest diff. peak/hole	1.289/-0.756 e Å^{-3}

5.2.26 [Tp'(CO)$_2$Mo≡Si–Mo(CO)$_2$(PMe$_3$)Tp'] (21-Mo)

Device Type	Nonius KappaCCD
Empirical formula	$C_{79}H_{118}B_4Mo_4N_{24}O_8P_2Si_2$
Moiety formula	$2(C_{37}H_{53}B_2Mo_2N_{12}O_4PSi)\cdot(C_5H_{12})$
Formula weight	2077.09
Temperature	123(2) K
Crystal system	monoclinic
Space group	$P2_1/n$
Unit cell dimensions	a = 11.9565(16) Å α = 90°
	b = 25.378(4) Å β = 104.783(5)°
	c = 16.080(2) Å γ = 90°
Volume	4717.9(12) Å^3
Z, ρ_{calc}	2, 1.462 g/cm^3

μ	0.643 mm^{-1}
F(000)	2140.0
Crystal size	0.23 × 0.17 × 0.10 mm^3
Absorption correction	Empirical
Tmin; Tmax	0.8661; 0.9384
Radiation	MoKα (λ = 0.71073)
Θ range for data collection	2.45 to 25.25°
Completeness to theta	0.996
Index ranges	-14 ≤ h ≤ 13, 0 ≤ k ≤ 30, 0 ≤ l ≤ 19
Reflections collected	10053
Independent reflections	10059[R_{int} = 0.0000]
Data/restraints/parameters	10059/57/601
Goodness-of-fit on F^2	1.125
Final R indexes [I>=2σ (I)]	R_1 = 0.0563, wR_2 = 0.1176
Final R indexes [all data]	R_1 = 0.0771, wR_2 = 0.1321
Largest diff. peak/hole	1.882/-0.706 e $Å^{-3}$

5.2.27 [Tp'(CO)$_2$W≡Si–W(CO)$_2$(PMe$_3$)Tp'] (21-W)

Device Type	STOE IPDS2T
Empirical formula	$C_{49}H_{61}B_2F_4N_{12}O_4PSiW_2$
Moiety formula	$C_{37}H_{53}B_2N_{12}O_4PSiW_2 \cdot 2(C_6H_4F_2)$
Formula weight	1406.47
Temperature	123(2) K
Crystal system	monoclinic
Space group	$P2_1$
Unit cell dimensions	a = 9.5819(4) Å α = 90°
	b = 33.2390(13) Å β = 118.887(3)°
	c = 9.8020(3) Å γ = 90°
Volume	2733.42(19) $Å^3$
Z, ρ_{calc}	2, 1.709 g/cm^3
μ	4.325 mm^{-1}
F(000)	1388.0
Crystal size	0.21 × 0.09 × 0.08 mm^3
Absorption correction	Integration
Tmin; Tmax	0.2578; 0.6800
Radiation	MoKα (λ = 0.71073)
2Θ range for data collection	5.342 to 55.998°
Completeness to theta	0.994
Index ranges	-12 ≤ h ≤ 12, -43 ≤ k ≤ 43, -12 ≤ l ≤ 12
Reflections collected	11592
Independent reflections	11592 [R_{sigma} = 0.0719]
Data/restraints/parameters	11592/31/694
Goodness-of-fit on F^2	1.035
Final R indexes [I>=2σ (I)]	R_1 = 0.0577, wR_2 = 0.1364
Final R indexes [all data]	R_1 = 0.0675, wR_2 = 0.1405

Largest diff. peak/hole	3.78/-7.82 e Å^{-3}

5.2.28 [Tp'(CO)$_2$Mo≡Ge–Mo(CO)$_2$(PMe$_3$)Tp'] (22-Mo)

Device Type	STOE IPDS2T
Empirical formula	$C_{65}H_{85}B_2GeMo_2N_{12}O_4P$
Moiety formula	$C_{37}H_{53}B_2GeMo_2N_{12}O_4P \cdot 4(C_7H_8)$
Formula weight	1415.51
Temperature	123(2) K
Crystal system	monoclinic
Space group	$P2_1/c$
Unit cell dimensions	a = 13.1889(2) Å α = 90°
	b = 27.9573(5) Å β = 100.4540(10)°
	c = 18.2797(3) Å γ = 90°
Volume	6628.32(19) Å^3
Z, ρ_{calc}	4, 1.418 g/cm^3
μ	0.903 mm^{-1}
F(000)	2928.0
Crystal size	0.21 × 0.08 × 0.04 mm^3
Absorption correction	Integration
Tmin; Tmax	0.8330; 0.9648
Radiation	MoKα (λ = 0.71073)
Θ range for data collection	2.90 to 28°
Completeness to theta	0.998
Index ranges	-17 ≤ h ≤ 17, -36 ≤ k ≤ 36, -24 ≤ l ≤ 23
Reflections collected	64827
Independent reflections	15967 [R_{sigma} = 0.0655]
Data/restraints/parameters	15967/107/809
Goodness-of-fit on F^2	1.022
Final R indexes [I>=2σ (I)]	R_1 = 0.0606, wR_2 = 0.1636
Final R indexes [all data]	R_1 = 0.0868, wR_2 = 0.1770
Largest diff. peak/hole	2.863/-0.852 e Å^{-3}

5.2.29 [Tp'(CO)$_2$W≡Ge–W(CO)$_2$(PMe$_3$)Tp'] (22-W)

Device Type	Bruker X8-KappaApexII
Empirical formula	$C_{61}H_{69}B_2F_8GeN_{12}O_4PW_2$
Moiety formula	$C_{37}H_{53}B_2GeN_{12}O_4PW_2 \cdot 4(C_6H_4F_2)$
Formula weight	1679.16
Temperature	100(2) K
Crystal system	triclinic
Space group	P-1
Unit cell dimensions	a = 11.4798(8) Å α = 77.415(4)°
	b = 14.0996(10) Å β = 76.833(4)°
	c = 21.4184(17) Å γ = 73.944(4)°
Volume	3199.2(4) Å^3
Z, ρ_{calc}	2, 1.743 g/cm^3
μ	4.159 mm^{-1}

F(000)	1656.0
Crystal size	0.2 × 0.09 × 0.02 mm^3
Absorption correction	Empirical
Tmin; Tmax	0.5447; 0.7459
Radiation	MoKα (λ = 0.71073)
2Θ range for data collection	1.98 to 53.998°
Completeness to theta	0.995
Index ranges	-14 ≤ h ≤ 14, -17 ≤ k ≤ 18, -27 ≤ l ≤ 27
Reflections collected	89276
Independent reflections	13872 [R_{int} = 0.0701]
Data/restraints/parameters	13872/270/977
Goodness-of-fit on F^2	1.093
Final R indexes [I>=2σ (I)]	R_1 = 0.0531, wR_2 = 0.0908
Final R indexes [all data]	R_1 = 0.0802, wR_2 = 0.1001
Largest diff. peak/hole	3.27/-2.06 e $Å^{-3}$

5.2.30 [Tp'$(CO)_2$Mo≡Si–Mo$(CO)_2$(MesNC)Tp'] (23-Mo)

Device Type	STOE IPDS2T
Empirical formula	$C_{50}H_{59}B_2F_2Mo_2N_{13}O_4Si$
Moiety formula	$C_{44}H_{55}B_2Mo_2N_{13}O_4Si·(C_6H_4F_2)$
Formula weight	1185.69
Temperature	123(2) K
Crystal system	triclinic
Space group	P-1
Unit cell dimensions	a = 11.9568(5) Å α = 89.141(4)°
	b = 13.3661(6) Å β = 71.679(3)°
	c = 18.5104(8) Å γ = 78.175(3)°
Volume	2744.8(2) $Å^3$
Z, ρ_{calc}	2, 1.435 g/cm^3
μ	0.541mm^{-1}
F(000)	13216.0
Crystal size	0.15 × 0.06 × 0.03 mm^3
Absorption correction	Integration
Tmin; Tmax	0.8117; 0.9753
Radiation	MoKα (λ = 0.71073)
2Θ range for data collection	5.454 to 58.36°
Completeness to theta	0.994
Index ranges	-16 ≤ h ≤ 16, -18 ≤ k ≤ 18, -25 ≤ l ≤ 25
Reflections collected	30913
Independent reflections	14426[R_{int} = 0.0800]
Data/restraints/parameters	14426/6/682
Goodness-of-fit on F^2	0.754
Final R indexes [I>=2σ (I)]	R_1 = 0.0452, wR_2 = 0.0738
Final R indexes [all data]	R_1 = 0.1094, wR_2 = 0.0848
Largest diff. peak/hole	0.68/-1.06 e $Å^{-3}$

5.2.31 [Tp'(CO)$_2$Mo≡Ge–Mo(CO)$_2$(MesNC)Tp'] (24-Mo)

Device Type	Nonius KappaCCD
Empirical formula	$C_{123}H_{150}B_4Ge_4Mo_4N_{26}O_8$
Moiety formula	$2(C_{44}H_{55}B_2GeMo_2N_{13}O_4)\cdot 5(C_7H_8)$
Formula weight	2692.87
Temperature	123(2) K
Crystal system	triclinic
Space group	P-1
Unit cell dimensions	a = 11.7440(2) Å α = 97.4428(8)°
	b = 13.7560(2) Å β = 94.2868(8)°
	c = 20.2542(3) Å γ = 100.5480(7)°
Volume	3173.37(9) Å^3
Z, ρ_{calc}	1, 1.409 g/cm^3
μ	0.916 mm^{-1}
F(000)	1386.0
Crystal size	0.16 × 0.08 × 0.02 mm^3
Absorption correction	Semi-empirical from equivalents
Tmin; Tmax	0.8673; 0.9819
Radiation	MoKα (λ = 0.71073)
Θ range for data collection	1.95 to 28°
Completeness to theta	0.998
Index ranges	$-15 \le h \le 15$, $-18 \le k \le 18$, $-26 \le l \le 26$
Reflections collected	10053
Independent reflections	15306[R_{int} = 0.0000]
Data/restraints/parameters	15306/10/796
Goodness-of-fit on F^2	0.968
Final R indexes [I>=2σ (I)]	R_1 = 0.0374, wR_2 = 0.0840
Final R indexes [all data]	R_1 = 0.0625, wR_2 = 0.0918
Largest diff. peak/hole	1.024/-0.827 e Å^{-3}

5.2.32 [Tp'(CO)$_2$Mo(H)SiMo(CO)$_2$(PMe$_3$)Tp'][B{C$_6$H$_3$-3,5-(CF$_3$)$_2$}$_4$] (25-Mo)

Device Type	STOE IPDS2T
Empirical formula	$C_{73}H_{76}B_3F_{24}Mo_2N_{12}O_5PSi$
Moiety formula	$C_{37}H_{54}B_2Mo_2N_{12}O_4Si$, $C_{32}H_{12}BF_{24}\cdot(C_4H_{10}O)$
Formula weight	1940.83
Temperature	123(2) K
Crystal system	triclinic
Space group	P-1
Unit cell dimensions	a = 16.331(2) Å α = 93.943(14)°
	b = 16.408(3) Å β = 106.025(11)°
	c = 18.051(3) Å γ = 108.813(13)°
Volume	4333.9(13) Å^3
Z, ρ_{calc}	2, 1.487 g/cm^3
μ	0.427mm^{-1}
F(000)	1964.0

Crystal size	0.27 × 0.18 × 0.09 mm^3
Absorption correction	Integration
Tmin; Tmax	0.8934; 0.9626
Radiation	MoKα (λ = 0.71073)
Θ range for data collection	2.93 to 28°
Completeness to theta	0.992
Index ranges	-21 ≤ h ≤ 21, -21 ≤ k ≤ 21, -23 ≤ l ≤ 23
Reflections collected	52225
Independent reflections	20755[R_{int} = 0.0478]
Data/restraints/parameters	20755/286/1225
Goodness-of-fit on F^2	1.018
Final R indexes [I>=2σ (I)]	R_1 = 0.0437, wR_2 = 0.1198
Final R indexes [all data]	R_1 = 0.0568, wR_2 = 0.1248
Largest diff. peak/hole	2.429/-1.225 e $Å^{-3}$

5.2.33 [Tp'(CO)$_2$W(H)SiW(CO)$_2$(PMe$_3$)Tp'][B{C$_6$H$_3$-3,5-(CF$_3$)$_2$}$_4$] (25-W)

Device Type	Bruker X8-KappaApexII
Empirical formula	$C_{69}H_{66}B_3F_{24}N_{12}O_4PSiW_2$
Moiety formula	$C_{37}H_{54}B_2N_{12}O_4SiW_2$, $C_{32}H_{12}BF_{24}$
Formula weight	2042.52
Temperature	100(2) K
Crystal system	triclinic
Space group	P-1
Unit cell dimensions	a = 14.0235(6) Å α = 65.373(2)°
	b = 17.6326(8) Å β = 73.972(2)°
	c = 19.0592(9) Å γ = 68.333(2)°
Volume	3939.5(3) $Å^3$
Z, ρ_{calc}	2, 1.722 g/cm^3
μ	3.065 mm^{-1}
F(000)	2008.0
Crystal size	0.38 × 0.24 × 0.09 mm^3
Absorption correction	Empirical
Tmin; Tmax	0.5910; 0.7460
Radiation	MoKα (λ = 0.71073)
2Θ range for data collection	4.752 to 56°
Completeness to theta	0.996
Index ranges	-18 ≤ h ≤ 18, -23 ≤ k ≤ 23, -25 ≤ l ≤ 25
Reflections collected	182339
Independent reflections	18883[R_{int} = 0.0372]
Data/restraints/parameters	18883/78/1120
Goodness-of-fit on F^2	1.044
Final R indexes [I>=2σ (I)]	R_1 = 0.0251, wR_2 = 0.0514
Final R indexes [all data]	R_1 = 0.0338, wR_2 = 0.0553
Largest diff. peak/hole	1.77/-1.33 e $Å^{-3}$

5.2.34 [Tp'(CO)$_2$Mo(H)GeMo(CO)$_2$(PMe$_3$)Tp'][B{C$_6$H$_3$-3,5-(CF$_3$)$_2$}$_4$] (26-Mo)

Device Type	STOE IPDS2T
Empirical formula	$C_{142}H_{142}B_6F_{48}Ge_2Mo_4N_{24}O_9P_2$
Moiety formula	$2(C_{37}H_{54}B_2GeMo_2N_{12}O_4, C_{32}H_{12}BF_{24})\cdot(C_4H_{10}O)$
Formula weight	3896.53
Temperature	123(2) K
Crystal system	triclinic
Space group	P-1
Unit cell dimensions	a = 11.9588(4) Å α = 91.364(2)°
	b = 17.6465(5) Å β = 92.156(3)°
	c = 21.3321(6) Å γ = 107.167(2)°
Volume	4295.3(2) Å^3
Z, ρ_{calc}	1, 1.506 g/cm^3
μ	0.758 mm^{-1}
F(000)	1958.0
Crystal size	0.21 × 0.15 × 0.12 mm^3
Absorption correction	Integration
Tmin; Tmax	0.8196; 0.9392
Radiation	MoKα (λ = 0.71073)
2Θ range for data collection	5.088 to 55.998°
Completeness to theta	0.982
Index ranges	$-15 \le h \le 15, -22 \le k \le 23, -28 \le l \le 28$
Reflections collected	72484
Independent reflections	72484[R_{sigma} = 0.1605]
Data/restraints/parameters	72484/242/1177
Goodness-of-fit on F^2	0.757
Final R indexes [I>=2σ (I)]	R_1 = 0.0510, wR_2 = 0.1032
Final R indexes [all data]	R_1 = 0.1330, wR_2 = 0.1234
Largest diff. peak/hole	1.37/-1.39 e Å^{-3}

5.2.35 [Tp'(CO)$_2$Mo(η^3-AuPMe$_3$)SiMo(CO)$_2$(Cl)Tp'] (27-Mo)

Device Type	Nonius KappaCCD
Empirical formula	$C_{41}H_{61}AuB_2Cl_9Mo_2N_{12}O_4PSi$
Moiety formula	$C_{37}H_{53}AuB_2ClMo_2N_{12}O_4PSi\cdot4(CH_2Cl_2)$
Formula weight	1574.59
Temperature	123(2) K
Crystal system	monoclinic
Space group	Cc
Unit cell dimensions	a = 15.0312(3) Å α = 90°
	b = 21.1756(5) Å β = 100.0060(14)°
	c = 19.0961(4) Å γ = 90°
Volume	5985.7(2) Å^3
Z, ρ_{calc}	4, 1.747 g/cm^3
μ	3.355 mm^{-1}
F(000)	3112.0

Crystal size	0.40 × 0.08 × 0.06 mm^3
Absorption correction	Semi-empirical from equivalents
Tmin; Tmax	0.3471; 0.8240
Radiation	MoKα (λ = 0.71073)
Θ range for data collection	2.75 to 28°
Completeness to theta	0.999
Index ranges	-19 ≤ h ≤ 19, -27 ≤ k ≤ 27, -25 ≤ l ≤ 25
Reflections collected	87147
Independent reflections	14204[R_{int} = 0.0649]
Data/restraints/parameters	14204/53/702
Goodness-of-fit on F^2	0.976
Final R indexes [I>=2σ (I)]	R_1 = 0.0386, wR_2 = 0.0838
Final R indexes [all data]	R_1 = 0.0570, wR_2 = 0.0894
Largest diff. peak/hole	1.527/-1.055 e $Å^{-3}$

5.2.36 [Tp'$(CO)_2$Mo(η^3-AuPMe_3)GeMo$(CO)_2$(Cl)Tp'] (28-Mo)

Device Type	Nonius KappaCCD
Empirical formula	$C_{116}H_{141}Au_2B_4Cl_2F_7Ge_2Mo_4N_{24}O_8P_2$
Moiety formula	$2(C_{37}H_{53}AuB_2ClGeMo_2N_{12}O_4P)\cdot 7(C_6H_5F)$
Formula weight	3231.48
Temperature	123(2) K
Crystal system	triclinic
Space group	P-1
Unit cell dimensions	a = 11.1248(4) Å α = 81.4743(17)°
	b = 13.7501(5) Å β = 76.2883(15)°
	c = 21.8544(9) Å γ = 88.6660(16)°
Volume	3212.6(2) $Å^3$
Z, ρ_{calc}	1, 1.670 g/cm^3
μ	3.252 mm^{-1}
F(000)	1606.0
Crystal size	0.21 × 0.08 × 0.06 mm^3
Absorption correction	Semi-empirical from equivalents
Tmin; Tmax	0.5483; 0.8288
Radiation	MoKα (λ = 0.71073)
Θ range for data collection	2.66 to 26°
Completeness to theta	0.988
Index ranges	-13 ≤ h ≤ 13, -16 ≤ k ≤ 16, -26 ≤ l ≤ 26
Reflections collected	50565
Independent reflections	12462[R_{int} = 0.1197]
Data/restraints/parameters	12462/89/849
Goodness-of-fit on F^2	0.970
Final R indexes [I>=2σ (I)]	R_1 = 0.0552, wR_2 = 0.1227
Final R indexes [all data]	R_1 = 0.1206, wR_2 = 0.1412
Largest diff. peak/hole	1.441/-2.644 e $Å^{-3}$

5.2.37 [K(diglyme)]$_2$[Tp'(CO)$_2$Mo=Si=Mo(CO)$_2$Tp'] (30-Mo)

Device Type	STOE IPDS2T
Empirical formula	$C_{70}H_{128}B_2K_2Mo_2N_{12}O_{22}Si$
Moiety formula	$C_{34}H_{44}B_2Mo_2N_{12}O_4Si \cdot 2(C_{18}H_{42}KO_9)$
Formula weight	1809.63
Temperature	123(2) K
Crystal system	orthorhombic
Space group	Pbca
Unit cell dimensions	a = 18.5406(5) Å α = 90°
	b = 24.8594(6) Å β = 90°
	c = 19.5832(5) Å γ = 90°
Volume	9026.1(4) Å^3
Z, ρ_{calc}	4, 1.332 g/cm^3
μ	0.455 mm^{-1}
F(000)	3816.0
Crystal size	0.14 × 0.14 × 0.13 mm^3
Absorption correction	Integration
Tmin; Tmax	0.9391; 0.9433
Radiation	MoKα (λ = 0.71073)
Θ range for data collection	2.74 to 26.78°
Completeness to theta	0.992
Index ranges	$-22 \le h \le 23$, $-29 \le k \le 31$, $-24 \le l \le 24$
Reflections collected	58570
Independent reflections	9562 [R_{sigma} = 0.0631]
Data/restraints/parameters	9562/5/517
Goodness-of-fit on F^2	0.830
Final R indexes [I>=2σ (I)]	R_1 = 0.0296, wR_2 = 0.0475
Final R indexes [all data]	R_1 = 0.0611, wR_2 = 0.0515
Largest diff. peak/hole	0.823/-0.385 e Å^{-3}

5.2.38 [Tp'(CO)$_2$MoSiC(Me)C(Me)Mo(CO)$_2$Tp'] (31-Mo)

Device Type	STOE IPDS2T
Empirical formula	$C_{94}H_{118}B_4Mo_4N_{24}O_8Si_2$
Moiety formula	$2(C_{38}H_{50}B_2Mo_2N_{12}O_4Si) \cdot 3(C_6H_6)$
Formula weight	2195.30
Temperature	123(2) K
Crystal system	monoclinic
Space group	$P2_1/c$
Unit cell dimensions	a = 14.8974(6) Å α = 90°
	b = 17.4530(6) Å β = 90.071(3)°
	c = 38.2970(15) Å γ = 90°
Volume	9957.4(7) Å^3
Z, ρ_{calc}	4, 1.464 g/cm^3
μ	0.584 mm^{-1}
F(000)	4520.0

Crystal size	0.25 × 0.18 × 0.1 mm^3
Absorption correction	Integration
Tmin; Tmax	0.7877; 0.9474
Radiation	MoKα (λ = 0.71073)
2Θ range for data collection	5.06 to 51.998°
Completeness to theta	0.986
Index ranges	-18 ≤ h ≤ 17, -21 ≤ k ≤ 14, -47 ≤ l ≤ 41
Reflections collected	45255
Independent reflections	19308 [R_{int} = 0.1153]
Data/restraints/parameters	19308/1/1253
Goodness-of-fit on F^2	0.975
Final R indexes [I>=2σ (I)]	R_1 = 0.0843, wR_2 = 0.1879
Final R indexes [all data]	R_1 = 0.1595, wR_2 = 0.2028
Largest diff. peak/hole	1.75/-0.63 e $Å^{-3}$

5.2.39 [Tp'$(CO)_2$MoSiC(H)C(TMS)Mo$(CO)_2$Tp'] (32-Mo)

Device Type	STOE IPDS2T
Empirical formula	$C_{45}H_{60}B_2Mo_2N_{12}O_4Si_2$
Moiety formula	$C_{39}H_{54}B_2Mo_2N_{12}O_4Si_2 \cdot C_6H_6$
Formula weight	1102.74
Temperature	123.15(2) K
Crystal system	triclinic
Space group	P-1
Unit cell dimensions	a = 10.5935(5) Å α = 81.479(4)°
	b = 11.6755(6) Å β = 79.889(4)°
	c = 21.0837(11) Å γ = 78.060(4)°
Volume	2494.7(2) $Å^3$
Z, ρ_{calc}	2, 1.4679 g/cm^3
μ	0.605 mm^{-1}
F(000)	1129.8
Crystal size	0.24 × 0.15 × 0.06 mm^3
Absorption correction	Integration
Tmin; Tmax	0.7839; 0.9522
Radiation	MoKα (λ = 0.71073)
2Θ range for data collection	5.56 to 50.5°
Completeness to theta	0.969
Index ranges	-14 ≤ h ≤ 14, -15 ≤ k ≤ 15, -28 ≤ l ≤ 28
Reflections collected	23748
Independent reflections	8749 [R_{int} = 0.0577]
Data/restraints/parameters	8749/0/627
Goodness-of-fit on F^2	0.700
Final R indexes [I>=2σ (I)]	R_1 = 0.0379, wR_2 = 0.989
Final R indexes [all data]	R_1 = 0.0556, wR_2 = 0.1065
Largest diff. peak/hole	0.65/-1.09 e $Å^{-3}$

5.2.40 [Tp'(CO)$_2$WSiC(H)C(TMS)W(CO)$_2$Tp'] (32-W)

Device Type	Bruker X8-KappaApexII
Empirical formula	$C_{60}H_{75}B_2N_{12}O_4Si_2W_2$
Moiety formula	$C_{39}H_{54}B_2N_{12}O_4Si_2W_2 \cdot 3.5(C_6H_6)$
Formula weight	1473.82
Temperature	100 K
Crystal system	tmonoclinic
Space group	$P2_1/c$
Unit cell dimensions	a = 22.1107(7) Å α = 90°
	b = 15.1225(5) Å β = 99.4527(9)°
	c = 19.1852(4) Å γ = 90°
Volume	6327.8(3) Å^3
Z, ρ_{calc}	4, 1.547 g/cm^3
μ	3.725 mm^{-1}
F(000)	2948.0
Crystal size	0.12 × 0.08 × 0.06 mm^3
Absorption correction	Empirical
Tmin; Tmax	0.6190; 0.7460
Radiation	MoKα (λ = 0.71073)
2Θ range for data collection	5.338 to 55.998°
Completeness to theta	0.981
Index ranges	$-28 \le h \le 29$, $-19 \le k \le 19$, $-14 \le l \le 25$
Reflections collected	37861
Independent reflections	15036 [R_{int} = 0.0346]
Data/restraints/parameters	15036/19/742
Goodness-of-fit on F^2	1.020
Final R indexes [I>=2σ (I)]	R_1 = 0.0318, wR_2 = 0.0561
Final R indexes [all data]	R_1 = 0.0525, wR_2 = 0.0624
Largest diff. peak/hole	1.09/-0.88 e Å^{-3}

5.2.41 [Tp'(CO)$_2$MoSiC(H)C(Ph)Mo(CO)$_2$Tp'] (33-Mo)

Device Type	STOE IPDS2T
Empirical formula	$C_{56}H_{66}B_2Mo_2N_{12}O_4Si$
Moiety formula	$C_{42}H_{50}B_2Mo_2N_{12}O_4Si_2 \cdot 2(C_7H_8)$
Formula weight	1212.79
Temperature	123(2) K
Crystal system	monoclinic
Space group	$P2_1/c$
Unit cell dimensions	a = 17.4737(5) Å α = 90°
	b = 19.4440(4) Å β = 100.292(3)°
	c = 35.9503(14) Å γ = 90°
Volume	12017.9(6) Å^3
Z, ρ_{calc}	8, 1.341 g/cm^3
μ	0.491 mm^{-1}
F(000)	5008.0

Crystal size	0.24 × 0.21 × 0.12 mm^3
Absorption correction	Integration
Tmin; Tmax	0.7839; 0.9522
Radiation	MoKα (λ = 0.71073)
2Θ range for data collection	5.046 to 50.5°
Completeness to theta	0.902
Index ranges	-17 ≤ h ≤ 25, -20 ≤ k ≤ 28, -56 ≤ l ≤ 45
Reflections collected	61518
Independent reflections	19645 [R_{int} = 0.0531]
Data/restraints/parameters	19645/172/1447
Goodness-of-fit on F^2	0.834
Final R indexes [I>=2σ (I)]	R_1 = 0.0430, wR_2 = 0.0899
Final R indexes [all data]	R_1 = 0.0757, wR_2 = 0.0958
Largest diff. peak/hole	0.68/-0.45 e $Å^{-3}$

5.2.42 [(η^5-C_5H_4Me)$(CO)_2$Mn=Pb(Cl)(C_6H_3-2,6-Mes_2)] (35)

Device Type	Nonius KappaCCD
Empirical formula	$C_{32}H_{32}ClMnO_2P$
Moiety formula	$C_{32}H_{32}ClMnO_2P$
Formula weight	746.16
Temperature	123(2) K
Crystal system	monoclinic
Space group	P2/c
Unit cell dimensions	a = 25.6073(10) Å α = 90°
	b = 16.5712(7) Å β = 125.895(2)°
	c = 17.2243(5) Å γ = 90°
Volume	5921.0(4) $Å^3$
Z, ρ_{calc}	8, 1.674 g/cm^3
μ	6.222 mm^{-1}
F(000)	2912.0
Crystal size	0.30 × 0.18 × 0.14 mm^3
Absorption correction	Semi-empirical from equivalents
Tmin; Tmax	0.2569; 0.4762
Radiation	MoKα (λ = 0.71073)
Θ range for data collection	1.71 to 28°
Completeness to theta	0.994
Index ranges	-33 ≤ h ≤ 33, -21 ≤ k ≤ 21, -22 ≤ l ≤ 22
Reflections collected	36184
Independent reflections	7117 [R_{int} = 0.0681]
Data/restraints/parameters	7117/43/341
Goodness-of-fit on F^2	1.014
Final R indexes [I>=2σ (I)]	R_1 = 0.0372, wR_2 = 0.0919
Final R indexes [all data]	R_1 = 0.0628, wR_2 = 0.0996
Largest diff. peak/hole	1.815/-2.112 e $Å^{-3}$

5.2.43 [{(η^5-C_5H_4Me)$(CO)_2$MnPbC_6H_3-2,6-Mes_2)}$_2$(μ-Br)][B{C_6H_3-2,6-$(CF_3)_2$}$_4$] (38)

Device Type	STOE IPDS2T
Empirical formula	$C_{102}H_{81}BBrF_{25}Mn_2O_4Pb_2$
Moiety formula	$C_{64}H_{64}BrMn_2O_4Pb_2$, $C_{32}H_{12}BF_{24}\cdot(C_6H_5F)$
Formula weight	2460.65
Temperature	123(2) K
Crystal system	monoclinic
Space group	$P2_1/c$
Unit cell dimensions	a = 12.7495(3) Å α = 90°
	b = 20.0446(5) Å β = 92.340(2)°
	c = 38.0335(8) Å γ = 90°
Volume	9711.7(4) Å^3
Z, ρ_{calc}	4, 1.683 g/cm^3
μ	4.221 mm^{-1}
F(000)	4816.0
Crystal size	0.25 × 0.12 × 0.09 mm^3
Absorption correction	Integration
Tmin; Tmax	0.4184; 0.7025
Radiation	MoKα (λ = 0.71073)
Θ range for data collection	2.91 to 28°
Completeness to theta	0.983
Index ranges	$-16 \le h \le 16$, $-26 \le k \le 19$, $-33 \le l \le 50$
Reflections collected	60793
Independent reflections	23044 [R_{int} = 0.0745]
Data/restraints/parameters	23044/424/1309
Goodness-of-fit on F^2	0.851
Final R indexes [I>=2σ (I)]	R_1 = 0.0442, wR_2 = 0.0834
Final R indexes [all data]	R_1 = 0.0993, wR_2 = 0.0938
Largest diff. peak/hole	1.218/-1.070 e Å^{-3}

5.2.44 [(η^5-C_5H_4Me)$(CO)_2$Mn≡Pb(C_6H_3-2,6-Mes_2)][B{C_6H_3-3,5-$(CF_3)_2$}$_4$] (39)

Device Type	Bruker X8-KappaApexII
Empirical formula	$C_{64}H_{44}BF_{24}MnO_2Pb$
Moiety formula	$C_{32}H_{32}MnO_2Pb$, $C_{32}H_{12}BF_{24}$
Formula weight	1573.93
Temperature	100(2) K
Crystal system	triclinic
Space group	P-1
Unit cell dimensions	a = 13.3867(8) Å α = 85.690(3)°
	b = 13.4191(8) Å β = 81.207(3)°
	c = 16.8130(10) Å γ = 86.676(3)°
Volume	2973.0(3) Å^3
Z, ρ_{calc}	2, 1.758 g/cm^3
μ	3.161 mm^{-1}
F(000)	1544.0

Crystal size	0.11 × 0.09 × 0.04 mm^3
Absorption correction	Empirical
Tmin; Tmax	0.7224; 0.8840
Radiation	MoKα (λ = 0.71073)
Θ range for data collection	3.09 to 28°
Completeness to theta	0.992
Index ranges	$-17 \leq h \leq 17$, $-17 \leq k \leq 17$, $-22 \leq l \leq 22$
Reflections collected	133935
Independent reflections	14271 [R_{int} = 0.0638]
Data/restraints/parameters	14271/0/845
Goodness-of-fit on F^2	1.082
Final R indexes [I>=2σ (I)]	R_1 = 0.0339, wR_2 = 0.0550
Final R indexes [all data]	R_1 = 0.0391, wR_2 = 0.0565
Largest diff. peak/hole	0.961/-1.016 e $Å^{-3}$

5.2.45 *trans*-[H(dmpe)$_2$Mn=SnCl(C$_6$H$_3$-2,6-Mes$_2$)] (40)

Device Type	Bruker X8-KappaApexII
Empirical formula	$C_{36}H_{58}ClMnP_4Sn$
Moiety formula	$C_{36}H_{58}ClMnP_4Sn$
Formula weight	823.78
Temperature	100(2) K
Crystal system	monoclinic
Space group	$P2_1/n$
Unit cell dimensions	a = 10.3998(6) Å α = 90°
	b = 17.9090(9) Å β = 90.258(2)°
	c = 20.9073(12) Å γ = 90°
Volume	3893.9(4) $Å^3$
Z, ρ_{calc}	4, 1.405 g/cm^3
μ	1.222 mm^{-1}
F(000)	1704.0
Crystal size	0.41 × 0.21 × 0.02 mm^3
Absorption correction	empirical
Tmin; Tmax	0.6342; 0.9760
Radiation	MoKα (λ = 0.71073)
Θ range for data collection	2.99 to 28°
Completeness to theta	0.998
Index ranges	$-13 \leq h \leq 13$, $-23 \leq k \leq 19$, $-27 \leq l \leq 26$
Reflections collected	40054
Independent reflections	9387[R_{int} = 0.0301]
Data/restraints/parameters	9387/0/406
Goodness-of-fit on F^2	1.012
Final R indexes [I>=2σ (I)]	R_1 = 0.0235, wR_2 = 0.0520
Final R indexes [all data]	R_1 = 0.0335, wR_2 = 0.0551
Largest diff. peak/hole	0.575/-0.436 e $Å^{-3}$

5.2.46 *trans*-[H(dmpe)$_2$Mn≡Sn(C$_6$H$_3$-2,6-Mes$_2$)][B{C$_6$H$_3$-3,5-(CF$_3$)$_2$}$_4$] (41)

Device Type	Nonius KappaCCD
Empirical formula	$C_{74}H_{75}BF_{25}MnP_4Sn$
Moiety formula	$C_{36}H_{58}MnP_4Sn$, $C_{32}H_{12}BF_{24}\cdot(C_6H_5F)$
Formula weight	1747.66
Temperature	123(2) K
Crystal system	monoclinic
Space group	P2/c
Unit cell dimensions	a = 19.4964(3) Å α = 90°
	b = 15.7107(4) Å β = 97.7733(12)°
	c = 25.8856(6) Å γ = 90°
Volume	7856.0(3) Å^3
Z, ρ_{calc}	4, 1.478 g/cm^3
μ	0.660 mm^{-1}
F(000)	3536.0
Crystal size	0.42 × 0.35 × 0.20 mm^3
Absorption correction	Semi-empirical from equivalents
Tmin; Tmax	0.7690; 0.8793
Radiation	MoKα (λ = 0.71073)
Θ range for data collection	1.05 to 28°
Completeness to theta	0.984
Index ranges	$-25 \le h \le 25$, $-19 \le k \le 20$, $-22 \le l \le 34$
Reflections collected	50740
Independent reflections	18639 [R_{int} = 0.0503]
Data/restraints/parameters	18639/166/993
Goodness-of-fit on F^2	0.998
Final R indexes [I>=2σ (I)]	R_1 = 0.0445, wR_2 = 0.1166
Final R indexes [all data]	R_1 = 0.0768, wR_2 = 0.1281
Largest diff. peak/hole	1.379/-0.891 e Å^{-3}

5.2.47 *trans*-[H(dmpe)$_2$MnSn(C$_6$H$_3$-2,6-Mes$_2$)] (43)

Device Type	Bruker D8-Venture
Empirical formula	$C_{36}H_{58}MnP_4Sn$
Moiety formula	$C_{36}H_{58}MnP_4Sn$
Formula weight	788.33
Temperature	100(2) K
Crystal system	monoclinic
Space group	$P2_1/c$
Unit cell dimensions	a = 16.5079(5) Å α = 90°
	b = 17.1719(5) Å β = 95.130(10)°
	c = 13.5638(4) Å γ = 90°
Volume	3830.3(2) Å^3
Z, ρ_{calc}	4, 1.367 g/cm^3
μ	9.607 mm^{-1}
F(000)	1636.0

Crystal size	0.12 × 0.06 × 0.005 mm^3
Absorption correction	Multi-scan
Tmin; Tmax	0.3919; 0.9535
Radiation	CuKα (λ = 1.54178)
2Θ range for data collection	5.374 to 143.862°
Completeness to theta	0.994
Index ranges	-18 ≤ h ≤ 20, -20 ≤ k ≤ 18, -16 ≤ l ≤ 14
Reflections collected	28548
Independent reflections	7442[R_{int} = 0.0465]
Data/restraints/parameters	7442/0/397
Goodness-of-fit on F^2	1.082
Final R indexes [I>=2σ (I)]	R_1 = 0.0420, wR_2 = 0.1069
Final R indexes [all data]	R_1 = 0.0458, wR_2 = 0.1110
Largest diff. peak/hole	3.46/-0.98 e $Å^{-3}$

5.2.48 *trans*-[H(dmpe)$_2$Mn=Sn(H)(C$_6$H$_3$-2,6-Mes$_2$)] (44)

Device Type	Bruker X8-KappaApexII
Empirical formula	$C_{36}H_{59}MnP_4Sn$
Moiety formula	$C_{36}H_{59}MnP_4Sn$
Formula weight	789.33
Temperature	100(2) K
Crystal system	monoclinic
Space group	$P2_1/c$
Unit cell dimensions	a = 16.5090(15) Å α = 90°
	b = 17.1338(16) Å β = 94.8347(19)°
	c = 13.5102(13) Å γ = 90°
Volume	3807.9(6) $Å^3$
Z, ρ_{calc}	4, 1.377 g/cm^3
μ	9.664 mm^{-1}
F(000)	1640.0
Crystal size	0.6 × 0.32 × 0.32 mm^3
Absorption correction	empirical
Tmin; Tmax	0.2368; 0.7536
Radiation	CuKα (λ = 1.54178)
2Θ range for data collection	5.372 to 135.484°
Completeness to theta	0.999
Index ranges	-19 ≤ h ≤ 19, -20 ≤ k ≤ 20, -16 ≤ l ≤ 16
Reflections collected	91495
Independent reflections	6898[R_{int} = 0.0623]
Data/restraints/parameters	6898/72/399
Goodness-of-fit on F^2	1.029
Final R indexes [I>=2σ (I)]	R_1 = 0.0391, wR_2 = 0.1045
Final R indexes [all data]	R_1 = 0.0392, wR_2 = 0.1046
Largest diff. peak/hole	2.65/-1.91 e $Å^{-3}$

5.2.49 SiBr(SiBr$_2$Tbb)(SIdipp) (45)

Device Type	STOE IPDS-2T
Empirical formula	$C_{56}H_{99}Br_3N_2Si_6$
Moiety formula	$C_{51}H_{87}Br_3N_2Si_6$, C_5H_{12}
Formula weight	1208.64
Temperature	123 K
Crystal system	monoclinic
Space group	$P2_1/c$
Unit cell dimensions	a = 13.9362(5) Å α = 90°
	b = 24.0059(9) Å β = 99.552(3)°
	c = 20.1186(7) Å γ = 90°
Volume	6637.4(4) Å^3
Z, ρ_{calc}	4, 1.210 g/cm^3
μ	1.965 mm^{-1}
F(000)	2552.0
Crystal size	0.24 × 0.18 × 0.06 mm^3
Absorption correction	integration
Tmin; Tmax	0.6676; 0.8117
Radiation	MoKα (λ = 0.71073)
2Θ range for data collection	5.328 to 53.998°
Completeness to theta	0.961
Index ranges	$-11 \le h \le 17$, $-30 \le k \le 26$, $-25 \le l \le 25$
Reflections collected	29293
Independent reflections	13969 [R_{int} = 0.0634, R_{sigma} = 0.1009]
Data/restraints/parameters	13969/0/629
Goodness-of-fit on F^2	0.858
Final R indexes [I>=2σ (I)]	R_1 = 0.0431, wR_2 = 0.0795
Final R indexes [all data]	R_1 = 0.0845, wR_2 = 0.0876
Largest diff. peak/hole	0.71/-0.87 e Å^{-3}

5.2.50 (*Z*)-(SIdipp)Si═Si(Br)Tbb (46)

Device Type	STOE IPDS-2T
Empirical formula	$C_{56}H_{99}BrN_2Si_6$
Moiety formula	$C_{51}H_{87}BrN_2Si_6$, C_5H_{12}
Formula weight	1048.82
Temperature	123 K
Crystal system	monoclinic
Space group	$P2_1/n$
Unit cell dimensions	a = 13.1765(7) Å α = 90°
	b = 13.9782(5) Å β = 90.972(4)°
	c = 34.8750(19) Å γ = 90°
Volume	6422.5(5) Å^3
Z, ρ_{calc}	4, 1.085 g/cm^3
μ	0.785 mm^{-1}
F(000)	2272.0
Crystal size	0.18 × 0.09 × 0.03 mm^3
Absorption correction	integration
Tmin; Tmax	0.7696; 0.9219
Radiation	MoKα (λ = 0.71073)

2Θ range for data collection	4.874 to 56°
Completeness to theta	0.982
Index ranges	$-17 \le h \le 17$, $-17 \le k \le 12$, $-33 \le l \le 45$
Reflections collected	30370
Independent reflections	14849 [R_{int} = 0.0866, R_{sigma} = 0.3241]
Data/restraints/parameters	14849/2/586
Goodness-of-fit on F^2	0.631
Final R indexes [I>=2σ (I)]	R_1 = 0.0476, wR_2 = 0.0591
Final R indexes [all data]	R_1 = 0.1981, wR_2 = 0.0835
Largest diff. peak/hole	0.46/-0.43 e Å^{-3}

5.2.51 [MnH(dmpe)$_2$(μ-dmpe)] (2-Mn)

Device Type	STOE IPDS2T
Empirical formula	$C_{30}H_{82}Mn_2P_{10}$
Moiety formula	$C_{30}H_{82}Mn_2P_{10}$
Formula weight	862.54
Temperature	123(2) K
Crystal system	monoclinic
Space group	$P2_1/c$
Unit cell dimensions	a = 13.8201(5) Å α = 90°
	b = 14.9557(4) Å β = 102.749(3)°
	c = 11.0811(4) Å γ = 90°
Volume	2233.88(13) Å^3
Z, ρ_{calc}	2, 1.282 g/cm^3
μ	0.943 mm^{-1}
F(000)	924.0
Crystal size	0.25 × 0.25 × 0.25 mm^3
Absorption correction	numerical
Tmin; Tmax	0.7984; 0.77984
Radiation	MoKα (λ = 0.71073)
Θ range for data collection	2.99 to 28°
Completeness to theta	0.999
Index ranges	$-18 \le h \le 18$, $-19 \le k \le 19$, $-14 \le l \le 14$
Reflections collected	22101
Independent reflections	5400[R_{int} = 0.0327]
Data/restraints/parameters	5400/2/204
Goodness-of-fit on F^2	0.948
Final R indexes [I>=2σ (I)]	R_1 = 0.0245, wR_2 = 0.0533
Final R indexes [all data]	R_1 = 0.0352, wR_2 = 0.0553
Largest diff. peak/hole	0.345/-0.277 e Å^{-3}

5.3. List of Abbreviations

2D	two dimensional
ATR	attenuated total reflection
br	broad
*t*Bu	tert-butyl substituent
ca.	circa
calcd.	calculated
Cp	cyclopentadienyl ligand (C_5H_5)
Cp*	pentamethyl cylcopentadienyl ligand (C_5Me_5)
CV	Cyclic voltametry
$\Delta\nu_{1/2}$	half height width
d	doublet
dec.	decomposition
DEPT	distortionless enhancement by polarisation transfer
DFT	density functional theory
DME	1,2-dimethoxyethane
dmpe	1,2-bis(dimethylphosphino)ethane
E	heavier Group 14 element (Si – Pb)
EA	elemental analysis
Eind	1,1,3,3,5,5,7,7-octaethyl-*s*-hydrindacen-4-yl
equiv.	equivalents
EPR	electron paramagnetic resonance
Et_2O	diethylether
et al.	and others
FT	Fourier transform
Fig.	Figure
HMBC	Heteronuclear multiple bond correlation
HMQC	Heteronuclear multiple quantum coherence
in situ	in the reaction mixture
in vacuo	under vacuum
IMe_4	1,3,4,5-tetramethylimidazol-2-ylidene
Idipp	1,3-bis(2,6-diisopropylphenyl)imidazol-2-ylidene

IR	Infra red
Mes	2,4,6-trimethylphenyl
Mes*	2,4,6-tri-*t*-butylphenyl
m.p.	melting point
NMR	nuclear magnetic resonance
NOE	nuclear overhauser effect
Ph	phenyl substituent
ppm	parts per million
PPN	Bis(triphenylphosphane)iminium chloride
PMe_3	trimethylphospane
q	quartet
quint	quintet
RT	room temperature
s	singlet
sept	septet
SIdipp	1,3-bis(2,6-diisopropylphenyl)imidazolidin-2-ylidene
t	triplet
Tbb	C_6H_2-2,6-$[CH(SiMe_3)_2]_2$-4-*t*Bu
THF	tetrahydofuran
Tp	trispyrazolylborate
Tp’	tris(3,5-dimethyl-1-pyrazolyl)borate
Trip	2,4,6-triisopropylphenyl
UV	ultra violet
Vis	visible
vs	very strong
vt	virtual triplet
vw	very weak
X	halogen

5.4. Scientific contribution from this work

5.4.1 Scientific publications from this work

1. *Manganese-Tin Triple Bonds: A New Synthetic Route to the Manganese Stannylidyne Complex Cation trans-[H(dmpe)$_2$Mn≡Sn(C$_6$H$_3$-2,6-Mes$_2$)]$^+$ (dmpe = Me$_2$PCH$_2$CH$_2$PMe$_2$, Mes = 2,4,6-trimethylphenyl).*

A. C. Filippou, P. Ghana, U. Chakraborty, G. Schnakenburg, *J. Am. Chem. Soc.* **2013**, *135*, 11525.

2. *Si=Si Double Bonds: Synthesis of an NHC-Stabilized Disilavinylidene.*

P. Ghana, M. I. Arz, U. Das, G. Schnakenburg, A. C. Filippou, *Angew. Chem. Int. Ed.* **2015**, *54*, 9980.

5.4.2 Conference contributions

1. *Open-Shell Ferracyclobutadienes*.

A. C. Filippou, U. Das, M. Straßmann, P. Ghana, O. Schiemann, E. Schubert, Y. N. Jahromy. Chemistry@Spin Centers II (SFB 813), International Symposium, Bad Honnef, Germany, 24 – 26 September **2014**, Book of Abstracts, p. 15.

2. *Metal-Silicon Multiple Bonds: Metallasilylidynes and Metallasilacumulenes*.

P. Ghana, G. Schnakenburg, A. C. Filippou. The 14th International Symposium on Inorganic Ring Systems *(*IRIS 14*)*, Regensburg, Germany, 26 – 31 July **2015**, Book of Abstracts, P027.

3. *Metal-Germanium Multiple Bonds: Open-Shell Germylidyne Complexes With a Ge-Centered Unpaired Electron.*

P. Ghana, G. Schnakenburg, A. C. Filippou. 15th International Conference on the Coordination and Organometallic Chemistry of Germanium, Tin and Lead (ICCOC-GTL 2016), Pardubice, Czech Republic, 28 August – 2 September, **2016**, Book of abstracts, PP31.

4. *Synthesis and Reactivity of an NHC-Stabilized Disilavinylidene.*

P. Ghana, S. Krämer, G. Schnakenburg, A. C. Filippou. 2016 Reaxys PhD Prize Symposium, London, United Kingdom, 22 – 23 September **2016**.

5. An NHC-Stabilized Disilavinylidene: Synthesis, Structure and Reactivity

P. Ghana, S. Krämer, G. Schnakenburg, A. C. Filippou, The 12th International Conference of Heteroatom Chemistry, Vancouver, British Columbia, June 11 – 16, **2017**, Book of abstracts, P50

5.4.3 Scientific Lectures

1. *"Stabilization of Highly Reactive Tetrelylidyne Complexes by Scorpionate Ligands"* – presented at the Inorganic Chemistry Colloquium, University of Bonn, 29th January **2015**.

2. "*Triple Bonds of Si - Pb with Transition Metals stabilized by Scorpionate Ligands*: *Potential Precursors for Open Shell Species*" – presented at the Doktoranden-Workshop: Graduate Talks on Chemistry@Spin Centers, Trier, 30th September – 2nd October. **2015**.

Accolades & awards

- Selected as one of the top 45 finalists of **2016** Reaxys PhD Prize.
- Won *Dalton Transactions* best poster prize at the ICCOC-GTL 2016 conference, Pardubice, Czech Republic, **2016**.
- Won *Thieme* best poster prize at the ICHAC-12, 2017 conference, Vancouver, British Columbia, **2017**.

6 References

[1] P. Jutzi, *Angew. Chem. Int. Ed.* **1975**, *14*, 232.

[2] R. West, *Science* **2004**, *305*, 1724.

[3] A. G. Brook, F. Abdesaken, B. Gutekunst, G. Gutekunst, R. K. Kallury, *J. Chem. Soc. Chem. Comm.* **1981**, 191.

[4] R. West, M. J. Fink, J. Michl, *Science* **1981**, *214*, 1343.

[5] J. P. Desclaux, *At. Data Nucl. Data Tables* **1973**, *12*, 311.

[6] L. Pauling, *The Nature of the Chemical Bond*, 3rd ed., Cornell Univ., USA, **1960**.

[7] L. H. Pu, B. Twamley, P. P. Power, *J. Am. Chem. Soc.* **2000**, *122*, 3524.

[8] M. Stender, A. D. Phillips, R. J. Wright, P. P. Power, *Angew. Chem. Int. Ed.* **2002**, *41*, 1785.

[9] A. D. Phillips, R. J. Wright, M. M. Olmstead, P. P. Power, *J. Am. Chem. Soc.* **2002**, *124*, 5930.

[10] A. Sekiguchi, R. Kinjo, M. Ichinohe, *Science* **2004**, *305*, 1755.

[11] P. P. Power, *Organometallics* **2007**, *26*, 4362.

[12] T. Sasamori, K. Hironaka, Y. Sugiyama, N. Takagi, S. Nagase, Y. Hosoo, Y. Furukawa, N. Tokitoh, *J. Am. Chem. Soc.* **2008**, *130*, 13856.

[13] Y. Murata, M. Ichinohe, A. Sekiguchi, *J. Am. Chem. Soc.* **2010**, *132*, 16768.

[14] S. Ishida, R. Sugawara, Y. Misawa, T. Iwamoto, *Angew. Chem. Int. Ed.* **2013**, *52*, 12869.

[15] Y. Sugiyama, T. Sasamori, Y. Hosoi, Y. Furukawa, N. Takagi, S. Nagase, N. Tokitoh, *J. Am. Chem. Soc.* **2006**, *128*, 1023.

[16] Y. Peng, R. C. Fischer, W. A. Merrill, J. Fischer, L. H. Pu, B. D. Ellis, J. C. Fettinger, R. H. Herber, P. P. Power, *Chem. Sci.* **2010**, *1*, 461.

[17] J. Y. Li, C. Schenk, C. Goedecke, G. Frenking, C. Jones, *J. Am. Chem. Soc.* **2011**, *133*, 18622.

[18] T. J. Hadlington, M. Hermann, J. Y. Li, G. Frenking, C. Jones, *Angew. Chem. Int. Ed.* **2013**, *52*, 10199.

[19] T. J. Hadlington, C. Jones, *Chem. Commun.* **2014**, *50*, 2321.

[20] R. C. Fischer, L. H. Pu, J. C. Fettinger, M. A. Brynda, P. P. Power, *J. Am. Chem. Soc.* **2006**, *128*, 11366.

[21] P. P. Power, *Chem. Commun.* **2003**, 2091.

[22] E. O. Fischer, G. Kreis, C. G. Kreiter, J. Muller, G. Huttner, H. Lorenz, *Angew. Chem. Int. Ed.* **1973**, *12*, 564.

[23] S. J. Mclain, C. D. Wood, L. W. Messerle, R. R. Schrock, F. J. Hollander, W. J. Youngs, M. R. Churchill, *J. Am. Chem. Soc.* **1978**, *100*, 5962.

[24] M. J. S. Dewar, *Bull. Soc. Chim. Fr.* **1951**, C71.

[25] J. Chatt, L. A. Duncanson, *J. Chem. Soc.* **1953**, 2939.

[26] S. E. Vyboishchikov, G. Frenking, *Chem. Eur. J.* **1998**, *4*, 1439.

[27] R. S. Simons, P. P. Power, *J. Am. Chem. Soc.* **1996**, *118*, 11966.

[28] L. H. Pu, B. Twamley, S. T. Haubrich, M. M. Olmstead, B. V. Mork, R. S. Simons, P. P. Power, *J. Am. Chem. Soc.* **2000**, *122*, 650.

[29] B. V. Mork, T. D. Tilley, *Angew. Chem. Int. Ed.* **2003**, *42*, 357.

[30] A. C. Filippou, O. Chernov, K. W. Stumpf, G. Schnakenburg, *Angew. Chem. Int. Ed.* **2010**, *49*, 3296.

[31] B. E. Eichler, A. D. Phillips, S. T. Haubrich, B. V. Mork, P. P. Power, *Organometallics* **2002**, *21*, 5622.

[32] L. H. Pu, P. P. Power, I. Boltes, R. Herbst-Irmer, *Organometallics* **2000**, *19*, 352.

[33] O. Chernov, *Novel Molecular Si(II) Precursors for Synthesis of the First Compounds with Metal-Silicon Triple Bonds*, Ph. D. Thesis, Bonn Universitäts- und Landesbibliothek, Bonn, **2012**.

[34] A. C. Filippou, K. W. Stumpf, O. Chernov, G. Schnakenburg, *Organometallics* **2012**, *31*, 748.

[35] A. C. Filippou, B. Baars, O. Chernov, Y. N. Lebedev, G. Schnakenburg, *Angew. Chem. Int. Ed.* **2014**, *53*, 565.

[36] K. W. Stumpf, *Germyliden- und Germalidin-Komplexe des Molybdäns*, Ph. D. Thesis, The Rheinische Friedrich-Wilhelms-Universität Bonn, Verlag Dr. Hut, München, **2014**.

[37] J. Hicks, T. J. Hadlington, C. Schenk, J. Y. Li, C. Jones, *Organometallics* **2013**, *32*, 323.

[38] Y. N. Lebedev, *Multiple Bonding of Low-valent Si and Ge to Group 6 and 9 Metals*, Ph. D. Thesis, The Rheinische Friedrich-Wilhelms-Universität Bonn, Verlag Dr. Hut, München, **2014**.

[39] A. C. Filippou, A. I. Philippopoulos, P. Portius, D. U. Neumann, *Angew. Chem. Int. Ed.* **2000**, *39*, 2778.

[40] A. C. Filippou, P. Portius, A. I. Philippopoulos, *Organometallics* **2002**, *21*, 653.

[41] A. C. Filippou, A. I. Philippopoulos, P. Portius, G. Schnakenburg, *Organometallics* **2004**, *23*, 4503.

[42] A. C. Filippou, P. Portius, A. I. Philippopoulos, H. Rohde, *Angew. Chem. Int. Ed.* **2003**, *42*, 445.

[43] A. C. Filippou, H. Rohde, G. Schnakenburg, *Angew. Chem. Int. Ed.* **2004**, *43*, 2243.

[44] A. C. Filippou, A. I. Philippopoulos, G. Schnakenburg, *Organometallics* **2003**, *22*, 3339.

[45] A. C. Filippou, N. Weidemann, G. Schnakenburg, H. Rohde, A. I. Philippopoulos, *Angew. Chem. Int. Ed.* **2004**, *43*, 6512.

[46] A. C. Filippou, N. Weidemann, A. I. Philippopoulos, G. Schnakenburg, *Angew. Chem. Int. Ed.* **2006**, *45*, 5987.

[47] A. C. Filippou, N. Weidemann, G. Schnakenburg, *Angew. Chem. Int. Ed.* **2008**, *47*, 5799.

[48] H. Hashimoto, T. Fukuda, H. Tobita, M. Ray, S. Sakaki, *Angew. Chem. Int. Ed.* **2012**, *51*, 2930.

[49] T. Fukuda, T. Yoshimoto, H. Hashimoto, H. Tobita, *Organometallics* **2016**, *35*, 921.

[50] A. Lülsdorf, *Current Ph.D thesis*, The Rheinische Friedrich-Wilhelms-Universität Bonn, **2013 - 2017**.

[51] N. Wienkenhöver, *Current Ph. D. Thesis*, The Rheinische Friedrich-Wilhelms-Universität Bonn, **2013 - 2017**.

[52] L. Arizpe, *Current Ph.D Thesis*, The Rheinische Friedrich-Wilhelms-Universität Bonn, **2012 - 2017**.

[53] D. Hoffmann, *Neuartige Ylidinkomplexe des Niobs: Synthese und Reaktionen*, Master Thesis, Universität Bonn, Springer Fachmedien Wiesbaden GmbH, Bonn, **2016**.

[54] U. Chakraborty, *Multiple Bonds between Group 7 Transition metals and Heavier Tetrel Elements (Ge-Pb)*, Ph. D. Thesis, The Rheinische Friedrich-Wilhelms-Universität Bonn, Verlag dr. Hut, München, **2013**.

[55] A. C. Filippou, U. Chakraborty, G. Schnakenburg, *Chem. Eur. J.* **2013**, *19*, 5676.

[56] B. Blom, *Reactivity of ylenes at Late Transition Metal Centers*, Ph. D. Thesis, The Rheinische Friedrich-Wilhelms-Universität Bonn, Cuvillier Verlag; Göttingen, **2011**.

[57] I. Papazoglou, *Current Ph.D thesis*, The Rheinische Friedrich-Wilhelms-Universität Bonn, **2012 - 2017**.

[58] P. G. Hayes, Z. G. Xu, C. Beddie, J. M. Keith, M. B. Hall, T. D. Tilley, *J. Am. Chem. Soc.* **2013**, *135*, 11780.

[59] A. C. Filippou, A. Barandov, G. Schnakenburg, B. Lewall, M. van Gastel, A. Marchanka, *Angew. Chem. Int. Ed.* **2012**, *51*, 789.

[60] C. Lindlahr, *Neuartige Tetrelaylidinkomplexe der Gruppe 6 mit Trialkylphosphanliganden*, Ph. D Thesis, The Rheinische Friedrich-Wilhelms-Universität Bonn, Verlag Dr. Hut, München, **2015**.

[61] F. Fischer, H. Tropsch, *Brennst. Chem.* **1926**, *7*, 97.

[62] A. Y. Khodakov, W. Chu, P. Fongarland, *Chem. Rev.* **2007**, *107*, 1692.

[63] S. Takemoto, H. Matsuzaka, *Coord. Chem. Rev.* **2012**, *256*, 574.

[64] J. C. Peters, A. L. Odom, C. C. Cummins, *Chem. Commun.* **1997**, 1995.

[65] J. B. Greco, J. C. Peters, T. A. Baker, W. M. Davis, C. C. Cummins, G. Wu, *J. Am. Chem. Soc.* **2001**, *123*, 5003.

[66] A. Hejl, T. M. Trnka, M. W. Day, R. H. Grubbs, *Chem. Commun.* **2002**, 2524.

[67] M. H. Stewart, M. J. A. Johnson, J. W. Kampf, *Organometallics* **2007**, *26*, 5102.

[68] M. Tachikawa, E. L. Muetterties, *Prog. Inorg. Chem.* **1981**, *28*, 203.

[69] J. S. Bradley, *Adv. Organomet. Chem.* **1983**, *22*, 1.

[70] M. I. Bruce, P. J. Low, *Adv. Organomet. Chem.* **2004**, *50*, 179.

[71] W. A. Herrmann, *Angew. Chem. Int. Ed.* **1986**, *25*, 56.

[72] D. Mansuy, *Pure. Appl. Chem.* **1980**, *52*, 681.

[73] D. Mansuy, J. Lecomte, J. Chottard, J. Bartoli, *Inorg. Chem.* **1981**, *20*, 3119.

[74] K. Tatsumi, R. Hoffmann, M. H. Whangbo, *J. Chem. Soc. Chem. Comm.* **1980**, 509.

[75] V. L. Goedken, M. R. Deakin, L. A. Bottomley, *J. Chem. Soc. Chem. Comm.* **1982**, 607.

[76] S. L. Latesky, J. P. Selegue, *J. Am. Chem. Soc.* **1987**, *109*, 4731.

[77] M. Etienne, P. S. White, J. L. Templeton, *J. Am. Chem. Soc.* **1991**, *113*, 2324.

[78] W. Knauer, W. Beck, *Z. Anorg. Allg. Chem.* **2008**, *634*, 2241.

[79] S. H. Hong, M. W. Day, R. H. Grubbs, *J. Am. Chem. Soc.* **2004**, *126*, 7414.

[80] I. A. Cade, A. F. Hill, C. M. A. McQueen, *Organometallics* **2009**, *28*, 6639.

[81] A. L. Colebatch, R. L. Cordiner, A. F. Hill, K. T. H. D. Nguyen, R. Shang, A. C. Willis, *Organometallics* **2009**, *28*, 4394.

[82] A. F. Hill, M. Sharma, A. C. Willis, *Organometallics* **2012**, *31*, 2538.

[83] R. D. Young, A. F. Hill, G. E. Cavigliasso, R. Stranger, *Angew. Chem. Int. Ed.* **2013**, *52*, 3699.

[84] E. Solari, S. Antonijevic, S. Gauthier, R. Scopelliti, K. Severin, *Eur. J. Inorg. Chem.* **2007**, 367.

[85] R. L. Miller, P. T. Wolczanski, A. L. Rheingold, *J. Am. Chem. Soc.* **1993**, *115*, 10422.

[86] W. Gade, E. Weiss, *J. Organomet. Chem.* **1981**, *213*, 451.

[87] W. A. Herrmann, J. Weichmann, R. Serrano, K. Blechschmitt, H. Pfisterer, M. L. Ziegler, *Angew. Chem. Int. Ed.* **1983**, *22*, 314.

[88] N. M. Kostic, R. F. Fenske, *J. Organomet. Chem.* **1982**, *233*, 337.

[89] W. A. Herrmann, H. J. Kneuper, E. Herdtweck, *Angew. Chem. Int. Ed.* **1985**, *24*, 1062.

[90] H.-J. Kneuper, Ph. D. Thesis, Technische Universität München, München, **1986**.

[91] H. J. Kneuper, E. Herdtweck, W. A. Herrmann, *J. Am. Chem. Soc.* **1987**, *109*, 2508.

[92] F. Ettel, G. Huttner, W. Imhof, *J. Organomet. Chem.* **1990**, *397*, 299.

[93] W. A. Herrmann, E. Voss, E. Guggolz, M. L. Ziegler, *J. Organomet. Chem.* **1985**, *284*, 47.

[94] C. Zybill, D. L. Wilkinson, G. Muller, *Angew. Chem. Int. Ed.* **1988**, *27*, 583.

[95] G. Schnakenburg, *Quantenchemische Untersuchungen an Tetrela-Ylidin-Komplexesn der 6., 8. and 9. Nebengruppe*, Ph. D. thesis, The Rheinische Friedrich-Wilhelms-Universität Bonn, **2008**.

[96] H. Lei, J. D. Guo, J. C. Fettinger, S. Nagase, P. P. Power, *Organometallics* **2011**, *30*, 6316.

[97] D. Hoffmann, Bonn, p. Personal communication.

[98] S. Trofimenko, *J. Am. Chem. Soc.* **1966**, *88*, 1842.

[99] S. Trofimenko, *Scorpionates: The Coordination Chemistry of Polypyrazolylborate Ligands*, Imperial College: London, **1999**.

[100] M. D. Curtis, K. B. Shiu, W. M. Butler, J. C. Huffman, *J. Am. Chem. Soc.* **1986**, *108*, 3335.

[101] S. Trofimenko, *Chem. Rev.* **1993**, *93*, 943.

[102] R. Castro-Rodrigo, M. A. Esteruelas, A. M. Lopez, M. Olivan, E. Onate, *Organometallics* **2007**, *26*, 4498.

[103] K. G. Bader, *Metallorganische Substituenten und Hauptgruppenelemente. Beeinflussung von Struktur und Reaktivität an Komplexen mit einer Übergangsmetall-Indium Bindung*, Ph. D. Thesis, Humboldt Universität zu Berlin, Berlin, **1998**.

[104] A. A. Saleh, B. Pleune, J. C. Fettinger, R. Poli, *Polyhedron* **1997**, *16*, 1391.

[105] K. H. Pannell, D. Jackson, *J. Am. Chem. Soc.* **1976**, *98*, 4443.

[106] B. T. Carter, M. P. Castellani, A. L. Rheingold, S. Hwang, S. E. Longacre, M. G. Richmond, *Organometallics* **2002**, *21*, 373.

[107] A. C. Filippou, O. Chernov, B. Blom, K. W. Stumpf, G. Schnakenburg, *Chem. Eur. J.* **2010**, *16*, 2866.

[108] K. Suzuki, T. Matsuo, D. Hashizume, K. Tamao, *J. Am. Chem. Soc.* **2011**, *133*, 19710.

[109] T. Sasamori, N. Tokitoh, *Bull. Chem. Soc. Jpn.* **2013**, *86*, 1005.

[110] T. Agou, N. Hayakawa, T. Sasamori, T. Matsuo, D. Hashizume, N. Tokitoh, *Chem. Eur. J.* **2014**, *20*, 9246.

[111] B. V. Mork, T. D. Tilley, A. J. Schultz, J. A. Cowan, *J. Am. Chem. Soc.* **2004**, *126*, 10428.

[112] M. Hirotsu, T. Nunokawa, K. Ueno, *Organometallics* **2006**, *25*, 1554.

[113] A. C. Filippou, O. Chernov, G. Schnakenburg, *Angew. Chem. Int. Ed.* **2011**, *50*, 1122.

[114] B. V. Mork, T. D. Tilley, *J. Am. Chem. Soc.* **2001**, *123*, 9702.

[115] K. Ueno, S. Asami, N. Watanabe, H. Ogino, *Organometallics* **2002**, *21*, 1326.

[116] T. Watanabe, H. Hashimoto, H. Tobita, *Angew. Chem. Int. Ed.* **2004**, *43*, 218.

[117] K. Takanashi, V. Y. Lee, T. Yokoyama, A. Sekiguchi, *J. Am. Chem. Soc.* **2009**, *131*, 916.

[118] T. Watanabe, H. Hashimoto, H. Tobita, *Chem-Asian J* **2012**, *7*, 1408.

[119] T. Watanabe, H. Hashimoto, H. Tobita, *J. Am. Chem. Soc.* **2006**, *128*, 2176.

[120] F. Cadet, S. Garrigues, M. d. l. Guardia, *Encyclopedia of analytical chemistry*, John Wiley & Sons, Chichester, **2012**.

[121] P. Ghana, M. I. Arz, U. Das, G. Schnakenburg, A. C. Filippou, *Angew. Chem. Int. Ed.* **2015**, *54*, 9980.

[122] K. Ueno, M. Sakai, H. Ogino, *Organometallics* **1998**, *17*, 2138.

[123] M. Okazaki, E. Suzuki, N. Miyajima, H. Tobita, H. Ogino, *Organometallics* **2003**, *22*, 4633.

[124] E. Suzuki, M. Okazaki, H. Tobita, *Chem. Lett.* **2005**, *34*, 1026.

[125] R. Begum, T. Komuro, H. Tobita, *Chem. Lett.* **2007**, *36*, 650.

[126] E. Suzuki, T. Komuro, M. Okazaki, H. Tobita, *Organometallics* **2009**, *28*, 1791.

[127] K. Dannappel, R. Nienhaus, M. Schurmann, B. Costisella, K. Jurkschat, *Z. Anorg. Allg. Chem.* **2009**, *635*, 2126.

[128] B. Baars, *Dissertation*, The Rheinische Friedrich-Wilhelms-University of Bonn (Bonn), **2017**.

[129] P. Jutzi, A. Mix, B. Rummel, W. W. Schoeller, B. Neumann, H. G. Stammler, *Science* **2004**, *305*, 849.

[130] P. Jutzi, G. Reumann, *J. Chem. Soc .Dalton. Trans.* **2000**, 2237.

[131] P. Jutzi, K. Leszczynska, B. Neumann, W. W. Schoeller, H. G. Stammler, *Angew. Chem. Int. Ed.* **2009**, *48*, 2596.

[132] P. Jutzi, K. Leszczynska, A. Mix, B. Neumann, B. Rummel, W. Schoeller, H. G. Stammler, *Organometallics* **2010**, *29*, 4759.

[133] P. Jutzi, N. Burford, *Chem. Rev.* **1999**, *99*, 969.

[134] P. Jutzi, D. Kanne, C. Kruger, *Angew. Chem. Int. Ed.* **1986**, *25*, 164.

[135] T. Kuhler, P. Jutzi, *Adv. Organomet. Chem.* **2003**, *49*, 1.

[136] A. C. Filippou, P. Ghana, U. Chakraborty, G. Schnakenburg, *J. Am. Chem. Soc.* **2013**, *135*, 11525.

[137] R. B. King, *Inorg. Nucl. Chem. Lett.* **1969**, *5*, 905.

[138] H. Wadepohl, U. Arnold, H. Pritzkow, M. J. Calhorda, L. F. Veiros, *J. Organomet. Chem.* **1999**, *587*, 233.

[139] B. Cordero, V. Gomez, A. E. Platero-Prats, M. Reves, J. Echeverria, E. Cremades, F. Barragan, S. Alvarez, *Dalton. Trans.* **2008**, 2832.

[140] H. Rohde, *Synthese und Untersuchungen der Reaktivität von Stannylidinkomplexen*, Ph. D. Thesis, The Rheinische Friedrich-Wilhelms-Universität Bonn, Bonn, **2007**.

[141] C. S. Creaser, M. A. Fey, G. R. Stephenson, *Spectrochim Acta A* **1994**, *50*, 1295.

[142] J. C. Jeffery, F. G. A. Stone, G. K. Williams, *Polyhedron* **1991**, *10*, 215.

[143] J. Vicha, R. Marek, M. Straka, *Inorg. Chem.* **2016**, *55*, 1770.

[144] R. S. Simons, L. H. Pu, M. M. Olmstead, P. P. Power, *Organometallics* **1997**, *16*, 1920.

[145] M. Weidenbruch, A. Stilter, J. Schlaefke, K. Peters, H. G. Vonschnering, *J. Organomet. Chem.* **1995**, *501*, 67.

[146] S. Patai, *The chemistry of organic germanium, tin and lead compounds, Vol. 1*, John Wiley & Sons, Ltd., Chichester, West Sussex, **1995**.

[147] W. D. Woodul, E. Carter, R. Muller, A. F. Richards, A. Stasch, M. Kaupp, D. M. Murphy, M. Driess, C. Jones, *J. Am. Chem. Soc.* **2011**, *133*, 10074.

[148] M. P. Egorov, O. M. Nefedov, T. S. Lin, P. P. Gaspar, *Organometallics* **1995**, *14*, 1539.

[149] A. Sekiguchi, T. Fukawa, M. Nakamoto, V. Y. Lee, M. Ichinohe, *J. Am. Chem. Soc.* **2002**, *124*, 9865.

[150] J. D. Cotton, C. S. Cundy, D. H. Harris, A. Hudson, M. F. Lappert, P. W. Lednor, *J. Chem. Soc. Chem. Comm.* **1974**, 651.

[151] R. K. Siwatch, S. Kundu, D. Kumar, S. Nagendran, *Organometallics* **2011**, *30*, 1998.

[152] P. Pyykko, M. Atsumi, *Chem. Eur. J.* **2009**, *15*, 12770.

[153] Y. Q. Ding, H. W. Roesky, M. Noltemeyer, H. G. Schmidt, P. P. Power, *Organometallics* **2001**, *20*, 1190.

[154] S. Nagendran, S. S. Sen, H. W. Roesky, D. Koley, H. Grubmuller, A. Pal, R. Herbst-Irmer, *Organometallics* **2008**, *27*, 5459.

[155] S. P. Green, C. Jones, P. C. Junk, K. A. Lippert, A. Stasch, *Chem. Commun.* **2006**, 3978.

[156] D. Geiß, *Neue Synthesestrategien für Übergangsmetallkomplexe mit ungesättigter germanium- und siliziumbasierter Ligandensphäre*, Ph. D. Thesis, The Rheinische Friedrich-Wilhelms-Universität Bonn; Verlag Dr. Hut, München, **2015**.

[157] G. G. Hlatky, R. H. Crabtree, *Coord. Chem. Rev.* **1985**, *65*, 1.

[158] M. A. Esteruelas, L. A. Oro, *Chem. Rev.* **1998**, *98*, 577.

[159] L. Schlapbach, A. Zuttel, *Nature* **2001**, *414*, 353.

[160] W. Grochala, P. P. Edwards, *Chem. Rev.* **2004**, *104*, 1283.

[161] A. W. C. van den Berg, C. O. Arean, *Chem. Commun.* **2008**, 668.

[162] C. Perthuisot, M. X. Fan, W. D. Jones, *Organometallics* **1992**, *11*, 3622.

[163] G. S. Girolami, C. G. Howard, G. Wilkinson, H. M. Dawes, M. Thorntonpett, M. Motevalli, M. B. Hursthouse, *J. Chem. Soc .Dalton. Trans.* **1985**, 921.

[164] W. A. Herrmann, H. J. Kneuper, E. Herdtweck, *Chem. Ber.* **1989**, *122*, 437.

[165] F. Ettel, G. Huttner, L. Zsolnai, C. Emmerich, *J. Organomet. Chem.* **1991**, *414*, 71.

[166] F. Ettel, M. Schollenberger, B. Schiemenz, W. Imhof, G. Huttner, L. Zsolnai, *J. Organomet. Chem.* **1994**, *476*, 207.

[167] F. Ettel, M. Schollenberger, B. Schiemenz, G. Huttner, L. Zsolnai, *J. Organomet. Chem.* **1994**, *476*, 153.

[168] M. Weidenbruch, A. Stilter, W. Saak, K. Peters, H. G. von Schnering, *J. Organomet. Chem.* **1998**, *560*, 125.

[169] B. E. Eichler, L. H. Pu, M. Stender, P. P. Power, *Polyhedron* **2001**, *20*, 551.

[170] T. B. Grindley, R. D. Curtis, R. Thangarasa, R. E. Wasylishen, *Can. J. Chem.* **1990**, *68*, 2102.

[171] T. Matsumoto, Y. Matsui, M. Ito, K. Tatsumi, *Chem-Asian J* **2008**, *3*, 607.

[172] M. A. Stewart, C. E. Moore, T. B. Ditri, L. A. Labios, A. L. Rheingold, J. S. Figueroa, *Chem. Commun.* **2011**, *47*, 406.

[173] P. Pyykko, S. Riedel, M. Patzschke, *Chem. Eur. J.* **2005**, *11*, 3511.

[174] P. G. Hayes, C. W. Gribble, R. Waterman, T. D. Tilley, *J. Am. Chem. Soc.* **2009**, *131*, 4606.

[175] A. Sekiguchi, T. Fukawa, V. Y. Lee, M. Nakamoto, *J. Am. Chem. Soc.* **2003**, *125*, 9250.

[176] A. C. Filippou, O. Chernov, G. Schnakenburg, *Chem. Eur. J.* **2011**, *17*, 13574.

[177] D. Matioszek, N. Katir, N. Saffon, A. Castel, *Organometallics* **2010**, *29*, 3039.

[178] W. P. Leung, W. K. Chiu, T. C. W. Mak, *Organometallics* **2012**, *31*, 6966.

[179] M. A. Fernandes, M. Layh, B. Omondi, *Acta. Crystallogr. C* **2002**, *58*, o384.

[180] M. Majumdar, I. Omlor, C. B. Yildiz, A. Azizoglu, V. Huch, D. Scheschkewitz, *Angew. Chem. Int. Ed.* **2015**, *54*, 8746.

[181] M. Ray, Y. Nakao, H. Sato, S. Sakaki, T. Watanabe, H. Hashimoto, H. Tobita, *Organometallics* **2010**, *29*, 6267.

[182] D. Melzer, E. Weiss, *J. Organomet. Chem.* **1984**, *263*, 67.

[183] A. Schnepf, C. Schenk, *Angew. Chem. Int. Ed.* **2006**, *45*, 5373.

[184] H. Braunschweig, P. Brenner, R. D. Dewhurst, M. Kaupp, R. Muller, S. Ostreicher, *Angew. Chem. Int. Ed.* **2009**, *48*, 9735.

[185] S. Seebald, B. Mayer, U. Schubert, *J. Organomet. Chem.* **1993**, *462*, 225.

[186] H. G. Alt, J. S. Han, R. D. Rogers, *J. Organomet. Chem.* **1993**, *445*, 115.

[187] A. M. Martins, R. Branquinho, J. L. Cui, A. R. Dias, M. T. Duarte, J. Fernandes, S. S. Rodrigues, *J. Organomet. Chem.* **2004**, *689*, 2368.

[188] M. Abrantes, F. A. A. Paz, A. A. Valente, C. C. L. Pereira, S. Gago, A. E. Rodrigues, J. Klinowski, M. Pillinger, I. S. Goncalves, *J. Organomet. Chem.* **2009**, *694*, 1826.

[189] Y. P. Wang, W. D. Tang, H. Y. Cheng, T. S. Lin, *J. Organomet. Chem.* **2013**, *729*, 68.

[190] S. S. Batsanov, *Inorg. Mater.* **2001**, *37*, 871.

[191] F. A. Carey, R. J. Sundberg, *Advanced Organic Chemistry*, 5th ed., Springer, New York, **2007**.

[192] M. Kira, T. Iwamoto, S. Ishida, H. Masuda, T. Abe, C. Kabuto, *J. Am. Chem. Soc.* **2009**, *131*, 17135.

[193] H. Braunschweig, K. Kraft, T. Kupfer, K. Radacki, F. Seeler, *Angew. Chem. Int. Ed.* **2008**, *47*, 4931.

[194] J. H. van'tHoff, *Arch. Neerl. Sci. Exactes Nat.* **1874**, *9*, 445.

[195] J. A. L. Bel, *Bull. Soc. Chim.* **1874**, *22(2)*, 337.

[196] O. A. D. y. M. Aldoshin, L. O. Atovmyan, A. N. Chekhov, M. I. Al'yanov, *Koord. Khim.* **1980**, *6*, 936.

[197] A. I. Boldyrev, P. V. Schleyer, R. Keese, *Mendeleev Commun.* **1992**, 93.

[198] A. I. Boldyrev, X. Li, L. S. Wang, *Angew. Chem. Int. Ed.* **2000**, *39*, 3307.

[199] S. L. Yao, C. van Wullen, X. Y. Sun, M. Driess, *Angew. Chem. Int. Ed.* **2008**, *47*, 3250.

[200] S. Ishida, T. Iwamoto, M. Kira, *Heteroatom Chem* **2011**, *22*, 432.

[201] F. Lips, A. Mansikkamaki, J. C. Fettinger, H. M. Tuononen, P. P. Power, *Organometallics* **2014**, *33*, 6253.

[202] A. V. Protchenko, M. P. Blake, A. D. Schwarz, C. Jones, P. Mountford, S. Aldridge, *Organometallics* **2015**, *34*, 2126.

[203] M. E. Fasulo, P. B. Glaser, T. D. Tilley, *Organometallics* **2011**, *30*, 5524.

[204] F. B. Lips, P. P. Power, *Abstr. Pap. Am. Chem. S.* **2014**, *247*.

[205] A. C. Diz, R. H. Contreras, M. A. Natiello, H. O. Gavarini, *J. Comput. Chem.* **1985**, *6*, 647.

[206] J. C. Hierso, *Chem. Rev.* **2014**, *114*, 4838.

[207] R. H. Holm, *Chem. Rev.* **1987**, *87*, 1401.

[208] L. K. Woo, *Chem. Rev.* **1993**, *93*, 1125.

[209] C. E. Laplaza, A. R. Johnson, C. C. Cummins, *J. Am. Chem. Soc.* **1996**, *118*, 709.

[210] A. R. Fox, C. R. Clough, N. A. Piro, C. C. Cummins, *Angew. Chem. Int. Ed.* **2007**, *46*, 973.

[211] E. O. Fischer, A. Daweritz, *Angew. Chem. Int. Ed.* **1975**, *14*, 346.

[212] M. H. Chisholm, E. E. Delbridge, A. R. Kidwell, K. B. Quinlan, *Chem. Commun.* **2003**, 126.

[213] B. A. Burroughs, B. E. Bursten, S. Chen, M. H. Chisholm, A. R. Kidwell, *Inorg. Chem.* **2008**, *47*, 5377.

[214] K. K. Pandey, P. Patidar, P. P. Power, *Inorg. Chem.* **2011**, *50*, 7080.

[215] S. Hino, M. Brynda, A. D. Phillips, P. P. Power, *Angew. Chem. Int. Ed.* **2004**, *43*, 2655.

[216] L. H. Pu, B. Twamley, P. P. Power, *Organometallics* **2000**, *19*, 2874.

[217] Y. K. Park, Y. G. Lee, G. S. Kim, *B. Kor. Chem. Soc.* **1996**, *17*, 138.

[218] S. T. Haubrich, P. P. Power, *J. Am. Chem. Soc.* **1998**, *120*, 2202.

[219] H. Braunschweig, M. Burzler, T. Kupfer, K. Radacki, F. Seeler, *Angew. Chem. Int. Ed.* **2007**, *46*, 7785.

[220] E. O. Fischer, J. Chen, K. Scherzer, *J. Organomet. Chem.* **1983**, *253*, 231.

[221] Y. Ortin, N. Lugan, R. Mathieu, *Dalton. Trans.* **2005**, 1620.

[222] N. R. Bunn, S. Aldridge, D. L. Kays, N. D. Coombs, A. Rossin, D. J. Willock, J. K. Day, C. Jones, L. L. Ooi, *Organometallics* **2005**, *24*, 5891.

[223] S. Hino, M. Olmstead, A. D. Phillips, R. J. Wright, P. P. Power, *Inorg. Chem.* **2004**, *43*, 7346.

[224] P. S. Skell, K. J. Klabunde, F. A. Fagone, *J. Am. Chem. Soc.* **1972**, *94*, 7862.

[225] M. Lein, A. Krapp, G. Frenking, *J. Am. Chem. Soc.* **2005**, *127*, 6290.

[226] R. C. Fischer, P. P. Power, *Chem. Rev.* **2010**, *110*, 3877.

[227] M. Cordonnier, M. Bogey, C. Demuynck, J. L. Destombes, *J. Chem. Phys.* **1992**, *97*, 7984.

[228] M. Bogey, H. Bolvin, C. Demuynck, J. L. Destombes, *Phys. Rev. Lett.* **1991**, *66*, 413.

[229] N. Wiberg, S. K. Vasisht, G. Fischer, P. Mayer, *Z. Anorg. Allg. Chem.* **2004**, *630*, 1823.

[230] M. Asay, A. Sekiguchi, *Bull. Chem. Soc. Jpn.* **2012**, *85*, 1245.

[231] H. W. Roesky, *J. Organomet. Chem.* **2013**, *730*, 57.

[232] R. S. Ghadwal, R. Azhakar, H. W. Roesky, *Acc. Chem. Res.* **2013**, *46*, 444.

[233] Y. Z. Wang, G. H. Robinson, *Inorg. Chem.* **2014**, *53*, 11815.

[234] E. Rivard, *Struct Bond* **2014**, *156*, 203.

[235] Y. Z. Wang, Y. M. Xie, P. R. Wei, R. B. King, H. F. Schaefer, P. V. Schleyer, G. H. Robinson, *Science* **2008**, *321*, 1069.

[236] Y. Xiong, S. L. Yao, S. Inoue, J. D. Epping, M. Driess, *Angew. Chem. Int. Ed.* **2013**, *52*, 7147.

[237] R. S. Ghadwal, H. W. Roesky, S. Merkel, J. Henn, D. Stalke, *Angew. Chem. Int. Ed.* **2009**, *48*, 5683.

[238] A. C. Filippou, O. Chernov, G. Schnakenburg, *Angew. Chem. Int. Ed.* **2009**, *48*, 5687.

[239] A. C. Filippou, Y. N. Lebedev, O. Chernov, M. Strassmann, G. Schnakenburg, *Angew. Chem. Int. Ed.* **2013**, *52*, 6974.

[240] H. Y. Cui, C. M. Cui, *Dalton. Trans.* **2011**, *40*, 11937.

[241] S. M. I. Al-Rafia, R. McDonald, M. J. Ferguson, E. Rivard, *Chem. Eur. J.* **2012**, *18*, 13810.

[242] M. J. Cowley, V. Huch, H. S. Rzepa, D. Scheschkewitz, *Nat. Chem.* **2013**, *5*, 876.

[243] Y. H. Gao, J. Y. Zhang, H. F. Hu, C. M. Cui, *Organometallics* **2010**, *29*, 3063.

[244] Y. N. Lebedev, U. Das, O. Chernov, G. Schnakenburg, A. C. Filippou, *Chem. Eur. J.* **2014**, *20*, 9280.

[245] S. U. Ahmad, T. Szilvasi, S. Inoue, *Chem. Commun.* **2014**, *50*, 12619.

[246] A. Jana, V. Huch, D. Scheschkewitz, *Angew. Chem. Int. Ed.* **2013**, *52*, 12179.

[247] D. Geiss, M. I. Arz, M. Strassmann, G. Schnakenburg, A. C. Filippou, *Angew. Chem. Int. Ed.* **2015**, *54*, 2739.

[248] A. Jana, I. Omlor, V. Huch, H. S. Rzepa, D. Scheschkewitz, *Angew. Chem. Int. Ed.* **2014**, *53*, 9953.

[249] J. Xu, Y. H. Ding, D. M. Andrada, G. Frenking, *Chem. Eur. J.* **2014**, *20*, 9216.

[250] R. S. Ghadwal, H. W. Roesky, S. Merkel, D. Stalke, *Chem. Eur. J.* **2010**, *16*, 85.

[251] S. M. I. Al-Rafia, A. C. Malcolm, R. McDonald, M. J. Ferguson, E. Rivard, *Angew. Chem. Int. Ed.* **2011**, *50*, 8354.

[252] S. Khan, G. Gopakumar, W. Thiel, M. Alcarazo, *Angew. Chem. Int. Ed.* **2013**, *52*, 5644.

[253] S. M. I. Al-Rafia, M. R. Momeni, R. McDonald, M. J. Ferguson, A. Brown, E. Rivard, *Angew. Chem. Int. Ed.* **2013**, *52*, 6390.

[254] E. Rivard, *Dalton. Trans.* **2014**, *43*, 8577.

[255] A. K. Swarnakar, S. M. McDonald, K. C. Deutsch, P. Choi, M. J. Ferguson, R. McDonald, E. Rivard, *Inorg. Chem.* **2014**, *53*, 8662.

[256] N. Wiberg, W. Niedermayer, G. Fischer, H. Noth, M. Suter, *Eur. J. Inorg. Chem.* **2002**, 1066.

[257] M. Ichinohe, R. Kinjo, A. Sekiguchi, *Organometallics* **2003**, *22*, 4621.

[258] G. Dolgonos, *Chem. Phys. Lett.* **2008**, *466*, 11.

[259] A. V. Protchenko, A. D. Schwarz, M. P. Blake, C. Jones, N. Kaltsoyannis, P. Mountford, S. Aldridge, *Angew. Chem. Int. Ed.* **2013**, *52*, 568.

[260] S. H. Zhang, H. X. Yeong, H. W. Xi, K. H. Lim, C. W. So, *Chem. Eur. J.* **2010**, *16*, 10250.

[261] S. H. Zhang, H. X. Yeong, C. W. So, *Chem. Eur. J.* **2011**, *17*, 3490.

[262] H. Tanaka, M. Ichinohe, A. Sekiguchi, *J. Am. Chem. Soc.* **2012**, *134*, 5540.

[263] S. Inoue, C. Eisenhut, *J. Am. Chem. Soc.* **2013**, *135*, 18315.

[264] A. F. Holleman, E. Wiberg, *Lehrbuch der Anorganischen Chemie,*, Aufl.101 ed., deGruyter, Berlin, **1995**.

[265] D. F. Shriver, M. A. Drezdzon, *The Manipulation of Air-Sensitive Compounds*, Wiley, New York, **1986**.

[266] O. Burghaus, M. Rohrer, T. Gotzinger, M. Plato, K. Mobius, *Meas. Sci. Technol.* **1992**, *3*, 765.

[267] S. Stoll, A. Schweiger, *J. Magn. Reson.* **2006**, *178*, 42.

[268] S. Trofimenko, *J. Am. Chem. Soc.* **1967**, *89*, 6288.

[269] S. Trofimenko, *J. Am. Chem. Soc.* **1967**, *89*, 3170.

[270] R. C. Smith, J. D. Protasiewicz, *Eur. J. Inorg. Chem.* **2004**, 998.

[271] A. Saednya, H. Hart, *Synthesis-Stuttgart* **1996**, 1455.

[272] K. Ruhlandtsenge, J. J. Ellison, R. J. Wehmschulte, F. Pauer, P. P. Power, *J. Am. Chem. Soc.* **1993**, *115*, 11353.

[273] R. S. Simons, S. T. Haubrich, B. V. Mork, M. Niemeyer, P. P. Power, *Main Group Chem.* **1998**, *2*, 275.

[274] M. L. Luetkens, A. P. Sattelberger, H. H. Murray, J. D. Basil, J. P. Fackler, R. A. Jones, D. E. Heaton, *Inorg. Syn.* **1989**, *26*, 7.

[275] R. J. Burt, J. Chatt, W. Hussain, G. J. Leigh, *J. Organomet. Chem.* **1979**, *182*, 203.

[276] G. Brauer, *Handbuch der Präparativen Anorganischen Chemie* **1975**, *2*, 721.

[277] J. Kouvetakis, A. Haaland, D. J. Shorokhov, H. V. Volden, G. V. Girichev, V. I. Sokolov, P. Matsunaga, *J. Am. Chem. Soc.* **1998**, *120*, 6738.

[278] L. H. Pu, M. M. Olmstead, P. P. Power, B. Schiemenz, *Organometallics* **1998**, *17*, 5602.

[279] N. Weidemann, *Dreifachbindungen zu den schwereren homologen Elementen des Kohlenstoffs*, Ph. D. Thesis, Humboldt-Universität zu Berlin, Cuvillier verlag, Göttingen **2008**.

[280] P. Jutzi, C. Leue, *Organometallics* **1994**, *13*, 2898.

[281] T. E. Muller, J. C. Green, D. M. P. Mingos, C. M. McPartlin, C. Whittingham, D. J. Williams, T. M. Woodroffe, *J. Organomet. Chem.* **1998**, *551*, 313.

[282] J. L. W. Pohlmann, F. E. Brinckmann, *Z. Naturforschung B* **1965**, *20*, 5.

[283] N. A. Yakelis, R. G. Bergman, *Organometallics* **2005**, *24*, 3579.

[284] I. Krossing, *Chem. Eur. J.* **2001**, *7*, 490.

[285] M. Brookhart, B. Grant, A. F. Volpe, *Organometallics* **1992**, *11*, 3920.

[286] W. Rudorff, E. Schulze, *Z. Anorg. Allg. Chem.* **1954**, *277*, 156.

[287] G. Becker, G. Gresser, W. Uhl, *Z Naturforsch B* **1981**, *36*, 16.

[288] J. K. Ruff, W. J. Schlientz, R. E. Dessy, J. M. Malm, G. R. Dobson, M. N. Memering, *Inorg. Syn.* **1974**, *15*, 84.

7 Oath of compliance with the principles of scientific integrity

I hereby affirm that this dissertation was prepared independently at the Institute of Inorganic Chemistry, University of Bonn under the supervision of Prof. Dr. A. C. Filippou, and that all references and additional sources have been appropriately cited.

Priyabrata Ghana

Bonn, 2017